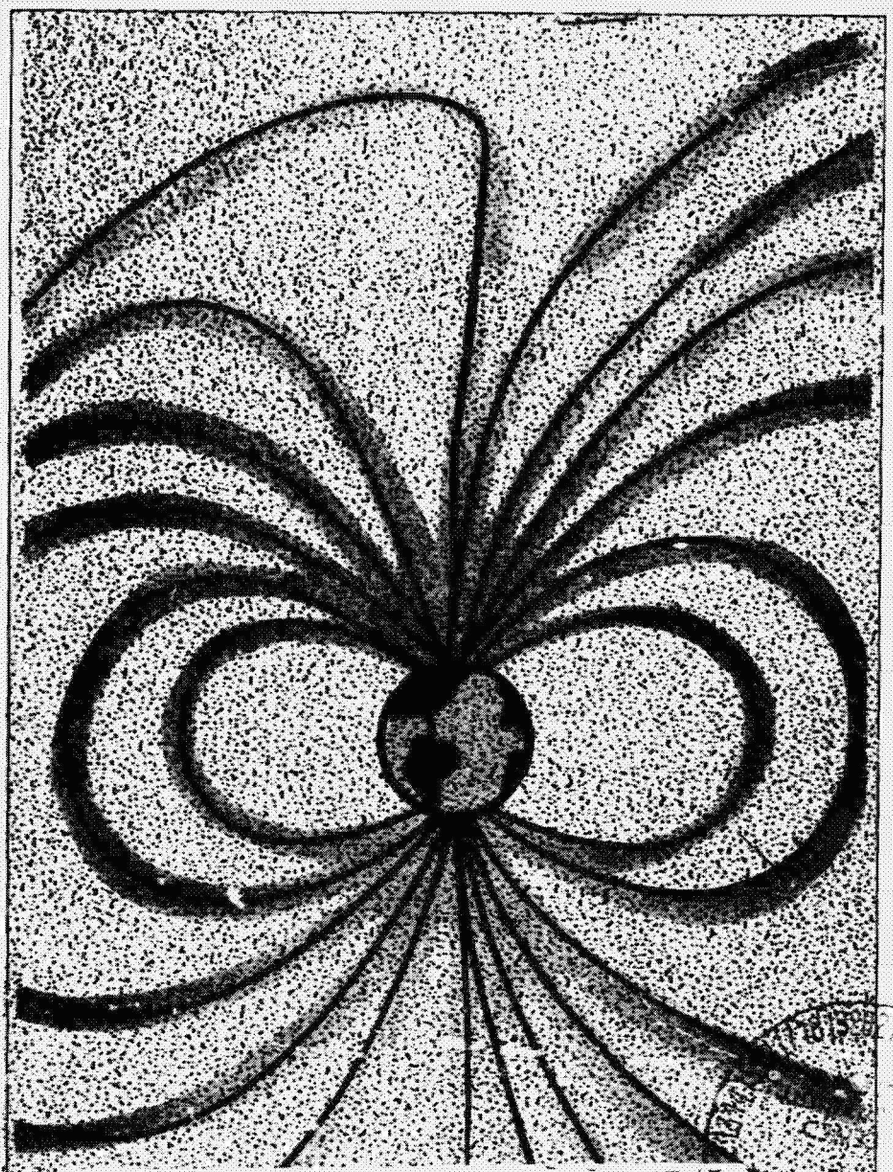
PROCEEDINGS

CR 73350

AVAILABLE TO THE PUBLIC



N69-33951 (ACCESSION NUMBER)
(PAGES)
NASA-CR-73357 (NASA CR OR TMX OR AD NUMBER)
N69-33978 (THRU)
1 (CODE)
23 (CATEGORY)
FACILITY FORM 602

Symposium on Space
Magnetic Exploration
and Technology
Reno, Nevada
August 28-30, 1967

Co-sponsored by
University of Nevada
and Nasa Ames

CR 73350
AVAILABLE TO THE PUBLIC

P R O C E E D I N G S

SYMPOSIUM ON SPACE MAGNETIC EXPLORATION AND TECHNOLOGY

Reno, Nevada
August 28, 29, 30, 1967

Co-sponsored by

University of Nevada
and
NASA/Ames Research Center

Edited By
Ernest J. Iufer
NASA/Ames Research Center

UNIVERSITY OF NEVADA
General University Extension
Continuing Education
Reno, Nevada

TABLE OF CONTENTS

	PAGE
FORWARD	1
CONTRIBUTIONS OF MAGNETIC FIELD RESEARCH TO SPACE SCIENCE, Alois W. Schardt	3
A REPORT ON THE SECOND INTERNATIONAL CONFERENCE ON MAGNET TECHNOLOGY, A. A. Halacsy	19
SOME FEATURES OF SECULAR VARIATION OF THE GEOMAGNETIC FIELD, Robert L. DuBois	26
THE ARGONNE 16-FT. BORE SUPERCONDUCTING MAGNET, J. R. Purcell	32
REVIEW OF SUPERCONDUCTING MAGNETOMETERS, Victor W. Hesterman, William S. Goree and Frank M. Chilton	41
AN ULTRA SENSITIVE MAGNETOMETER AND GRADIOMETER USING WEAKLY COUPLED SUPERCONDUCTORS, A. L. Morse and D. L. Judge	65
MAGNETIC FIELD COMPUTATIONS AND MEASUREMENTS ON THE EXCITERS FOR THE ARGONNE PION FOCUSING HORN, H. Vogel and S. Vegors	79
SYSTEMS OF COILS TO PRODUCE MAGNETIC FIELDS OF PRESCRIBED UNIFORMITY IN REGIONS OF DESIRED SHAPE, George A. Rinard	89
DESIGN AND PERFORMANCE OF A MICROWAVE MOTOR, Jan K. Sedivy	103
A VECTOR MAGNETOMETER SYSTEM FOR DETECTION OF IONOSPHERIC CURRENTS BY SOUNDING ROCKETS, Paul A. Cloutier	118
COMPUTER AIDED ANALYSIS AND DESIGN OF SPACE INSTRUMENT SYSTEMS, Robert M. Munoz	133
DIGITAL OFFSET FIELD GENERATOR FOR SPACECRAFT MAGNETOMETERS, R. C. Snare and G. N. Spellman	155
AVERAGE INTERPLANETARY MAGNETIC FIELD FOR ANGULAR MOMENTUM CALCULATIONS, Jerry L. Modisette	167
DEMAGNETIZATION METHODS FOR SPACECRAFT SYSTEMS AND COMPONENTS, Charles A. Harris	174
MAGNETIC PROPERTIES OF SELECTED SPACECRAFT MATERIALS, P. W. Droll and E. J. Iufer	189

TABLE OF CONTENTS (Continued)

	PAGE
STABILITY MEASUREMENTS OF FLUXGATE MAGNETOMETERS, W. I. Linlor, R. M. Munoz and M. J. Prucha	198
A HIGHLY STABLE FLUXGATE MAGNETOMETER FOR SPACE EXPLORATION, D. I. Gordon, R. H. Lundsten, R. Chiarodo and H. H. Helms, Jr.	235
A MAGNETOMETER TEST ENVIRONMENT USING AN EXPANDABLE SUPERCONDUCTING ENCLOSURE, R. E. Brown	247
NEAR-EARTH MAGNETOMETER FLIGHTS WITH THE OV1 SERIES SPACECRAFT, Kenneth O. Downing and Gordon D. Hall	258
MAGNETIC CLEANLINESS PROGRAM FOR THE LUNAR SURFACE AND PIONEER MAGNETOMETERS, L. Howard Roberts	271
A MAGNETICALLY SHIELDED CHAMBER USED IN SIMULATING SPACE ENVIRONMENT, J. Dale Barry, Paul J. Coleman, Jr., Uri Fehr and Larry L. Simmons	290
MAGNETIC TESTS ON THE ATS-1 SPACECRAFT, L. L. Simmons . . .	308
NEW NONLINEAR MAGNETIC ANALYSIS OF SATURATED ELECTRO-MECHANICAL ENERGY CONVERTERS, E. A. Erdelyi	314
A LOW-FIELD FACILITY FOR LOW-FREQUENCY MEASUREMENTS AT 1×10^{-9} GAUSS, David Cohen (Not available for publication)	
EFFECTS OF MAGNETIC FIELDS UPON BIOLOGICAL SYSTEMS, C. C. Conley, P. W. Droll, W. J. Mills and Patricia A. Corsaut .	339
MARINER VENUS 67 MAGNETIC CONTROL, J. G. Bastow	350
MAGNETIC TESTS OF THE OGO AND ERS SATELLITES, G. T. Inouye	363
APPLICATION OF RESONANCE TECHNIQUE FOR MEASURING SATELLITE MAGNETIC DIPOLE MOMENT, Barry E. Tossman	379

F O R W A R D

Exploration of the magnetic fields found in space has proven to be a remarkably rewarding avenue of scientific investigation. Anticipated progress will continue to present major challenges to scientists and engineers concerned with the development of field measurement systems and spacecraft producing sufficiently low magnetic fields. The effectiveness by which these challenges are met will depend to a large measure on the quality and timeliness of the communication between those engaged in research and development and those in design and test.

The Symposium for Space Magnetic Exploration and Technology, sponsored jointly by the University of Nevada and NASA - Ames Research Center was convened to provide an opportunity for scientists and engineers to exchange information on recent developments bearing on generation, compensation, measurement and calculation of very-low frequency magnetic fields. The papers presented at this symposium are contained in these proceedings. Results of recent spacecraft development programs are described, together with reviews of recent research in allied areas frequently used as resource and reference.

Ernest J. Iufer
August 28, 1967

Contributions of Magnetic Field Research to Space Science

Alois W. Schardt
National Aeronautics and Space Administration

N69-33952

This meeting is concerned primarily with magnetic field measurements and instrumentation; I decided, therefore, to introduce the subject with a short survey of the scientific results which can be deduced from measurements conducted in space. The scientific phenomena which can be investigated with the help of magnetic field measurements are summarized in Table I. Magnetic fields in the range from one to several hundred gauss are predicted to be found near the major planets. In particular, the radio emission of Jupiter can be explained if this planet has a large magnetic field. There are theoretical reasons to expect that other planets like Saturn, Uranus, and Neptune are also endowed with a strong field. At the surface of the Earth, a magnetic field has a magnitude of 0.2 to 0.6 gauss. Geomagnetic investigations have been conducted for centuries and still constitute a most fruitful endeavor.

The circulation of the Earth's core was deduced by Vestine et al.[1] on the basis of secular changes of the main field and is shown in Figure 1. Closer to the surface of the Earth, large scale irregularities of the crust also affect the surface field and initial attempts have been made to recognize these features on the basis of airplane surveys which may be followed later with low altitude satellite surveys of the whole Earth. The ionospheric current systems, such as Sq and the auroral electro-jet, produce measurable changes of the surface fields and have been investigated in detail with low satellites and sounding rockets. Of particular interest are currents flowing around the geomagnetic poles as discussed by Akasofu[2].

A region of lower magnetic fields exists further above the surface of the Earth, with a field strength in the range of 50 to 50,000 gamma. (1 gamma - 10^{-5} gauss). In this region, the magnetic field traps energetic charged particles and produces the well known radiation belts. In the radiation belts, the magnetic field determines the path of the particles and, conversely, the particles react back on the magnetic field. The main phase of a geomagnetic storm illustrates this process. The storm field observed during the period from July 7-14, 1966, is shown in Figure 2. At the time shown by the arrows in Figure 2, the OGO-III satellite passed very rapidly through the radiation belts; it was thus possible to obtain a nearly instantaneous measurement of the particle distribution near the equator as a function of distance from the surface of the Earth. Dr. Frank's[3] data shown in Figure 3, give the flux of 31 to 49 keV protons as a function of L. The L parameter represents essentially the distance at which the trapped particles cross the geomagnetic equator expressed in units of Earth radii; therefore, L=4 is roughly 16,000 miles from the center of the Earth. A relatively low flux existed prior to the storm; the total flux increased

TABLE I

MAGNETIC MEASUREMENTS

MAGNETIC FIELD	MAGNETOMETER	PHENOMENA OF INTEREST
1 - 700 g		Jupiter, Saturn, Uranus, Neptune
0.1 - 0.7 g	Proton precession Rb or Cs vapor (Fluxgate)	Main geomagnetic field Motion of Earth's core Crustal anomalies Ionospheric current systems
10 - 50,000 γ	Rb or Cs vapor Fluxgate Helium	Radiation Belts Magnetic Sturms Bow Shock, Magnetopause Venus, Mars
0.1 - 20 γ	Fluxgate Helium	Interplanetary field near Earth Solar Modulation
0.01 - 10 γ	(Fluxgate) (Superconducting)	Interplanetary medium at $\geq$5 A.U. Galactic magnetic field

$1\gamma = 10^{-5}$g

TABLE II

RESIDUAL SPACECRAFT FIELD IN 10^{-5}g

MARINER II	130
MARINER IV	35
MARINER V	12
ATS I	140
OGO	2
IMP I	0.5
PIONEER VI	0.25

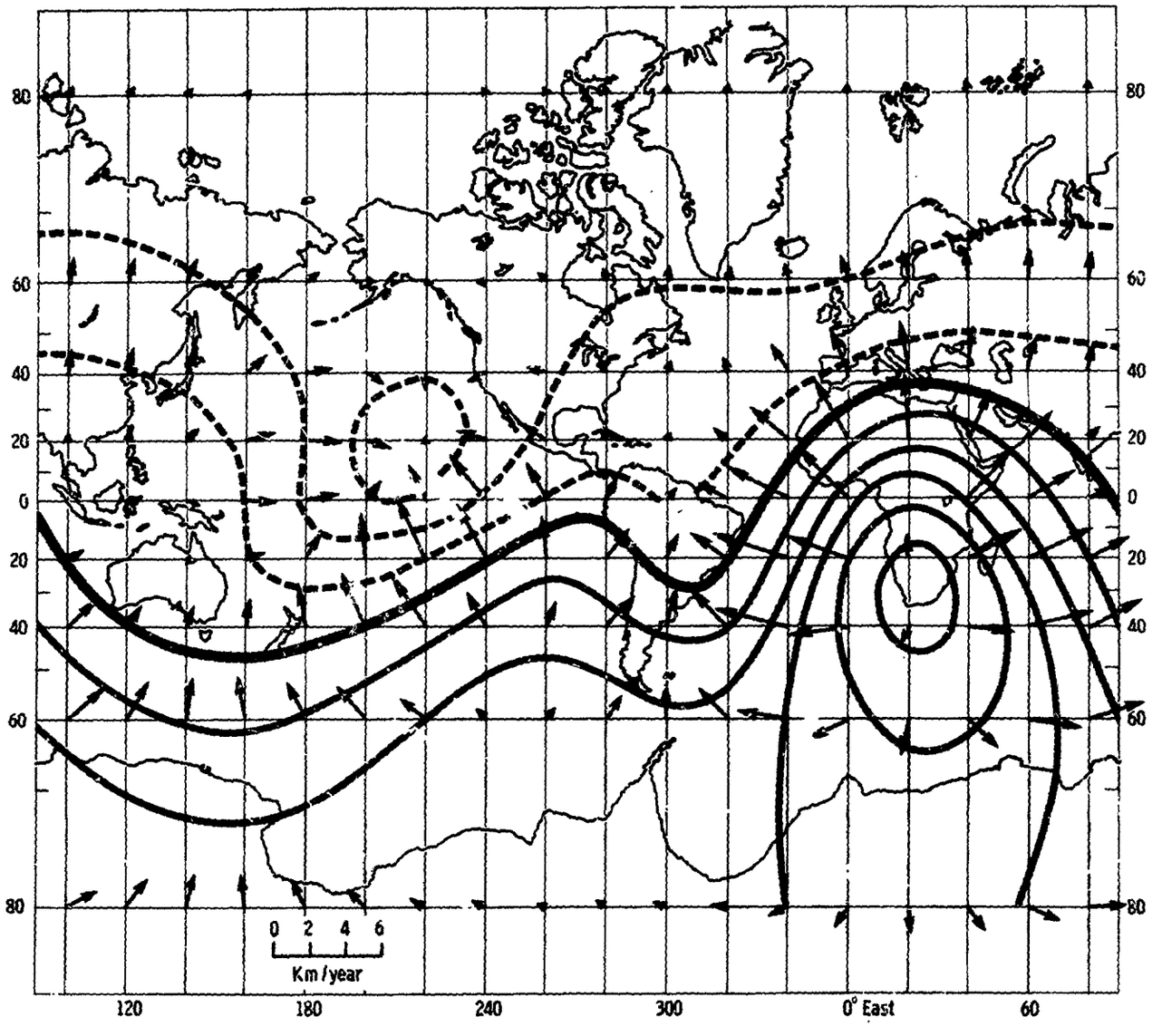
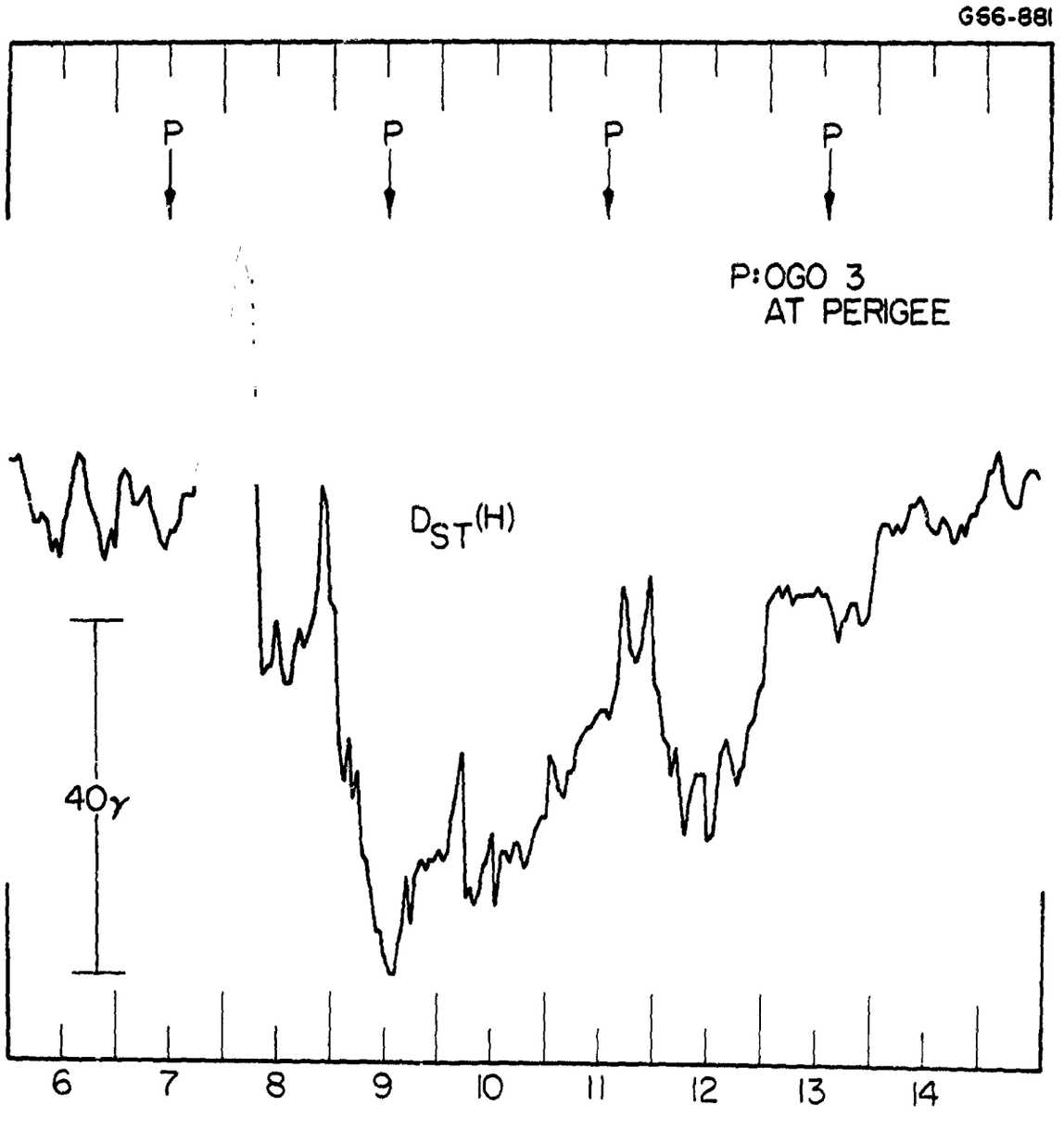


Figure 1

Irrotational part of core surface velocity for epoch 1960.


G66-881
P
P
P
P
P: OGO 3
AT PERIGEE
D_{ST}(H)
40γ
6
7
8
9
10
11
12
13
14
JULY 1966
Figure 2

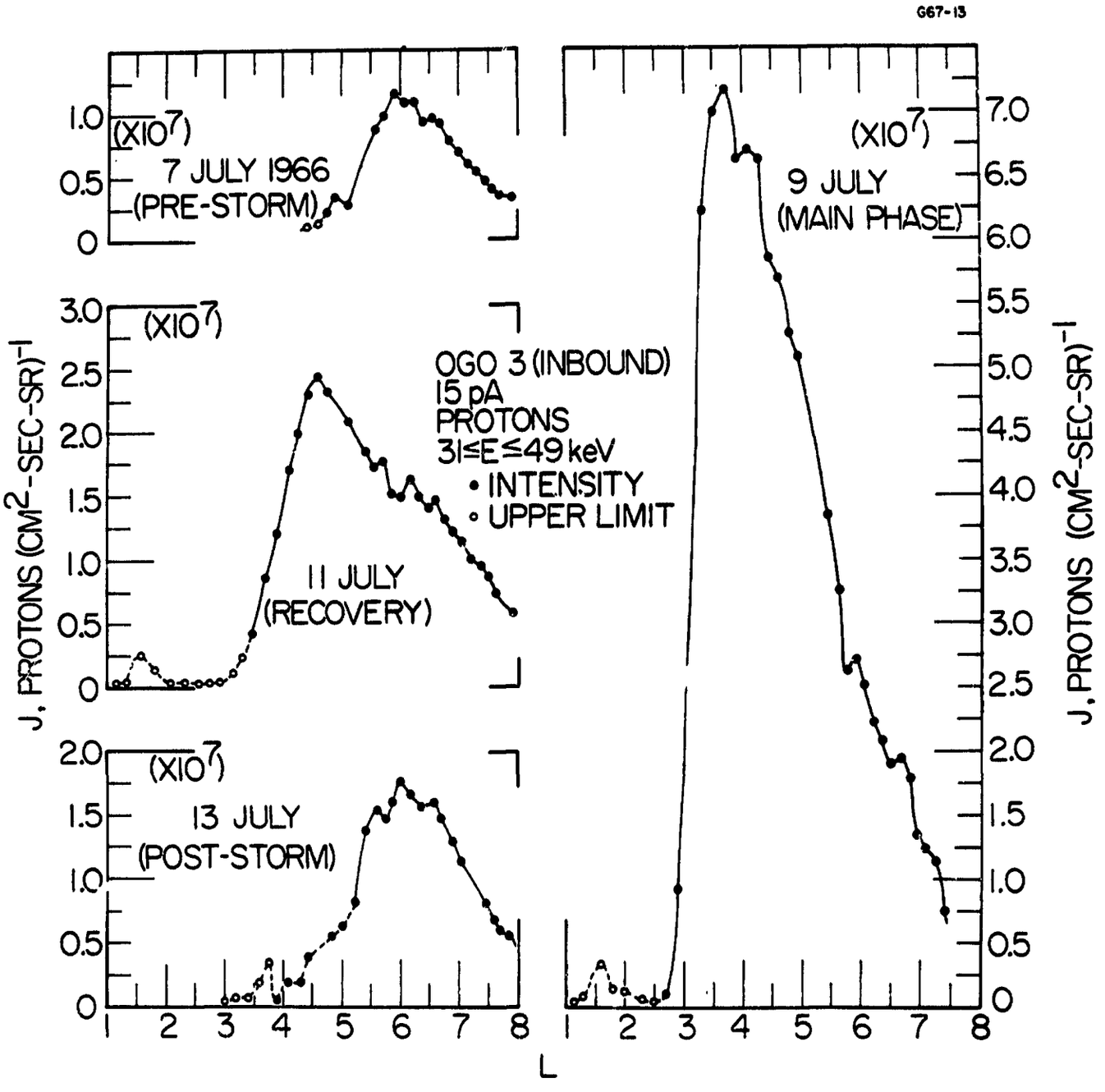

G67-13
7 JULY 1966
(PRE-STORM)
11 JULY
(RECOVERY)
13 JULY
(POST-STORM)
9 JULY
(MAIN PHASE)
(X10^7)
OGO 3 (INBOUND)
15 pA
PROTONS
31≤E≤49 keV
• INTENSITY
◦ UPPER LIMIT
J, PROTONS (CM^2-SEC-SR)^-1
L

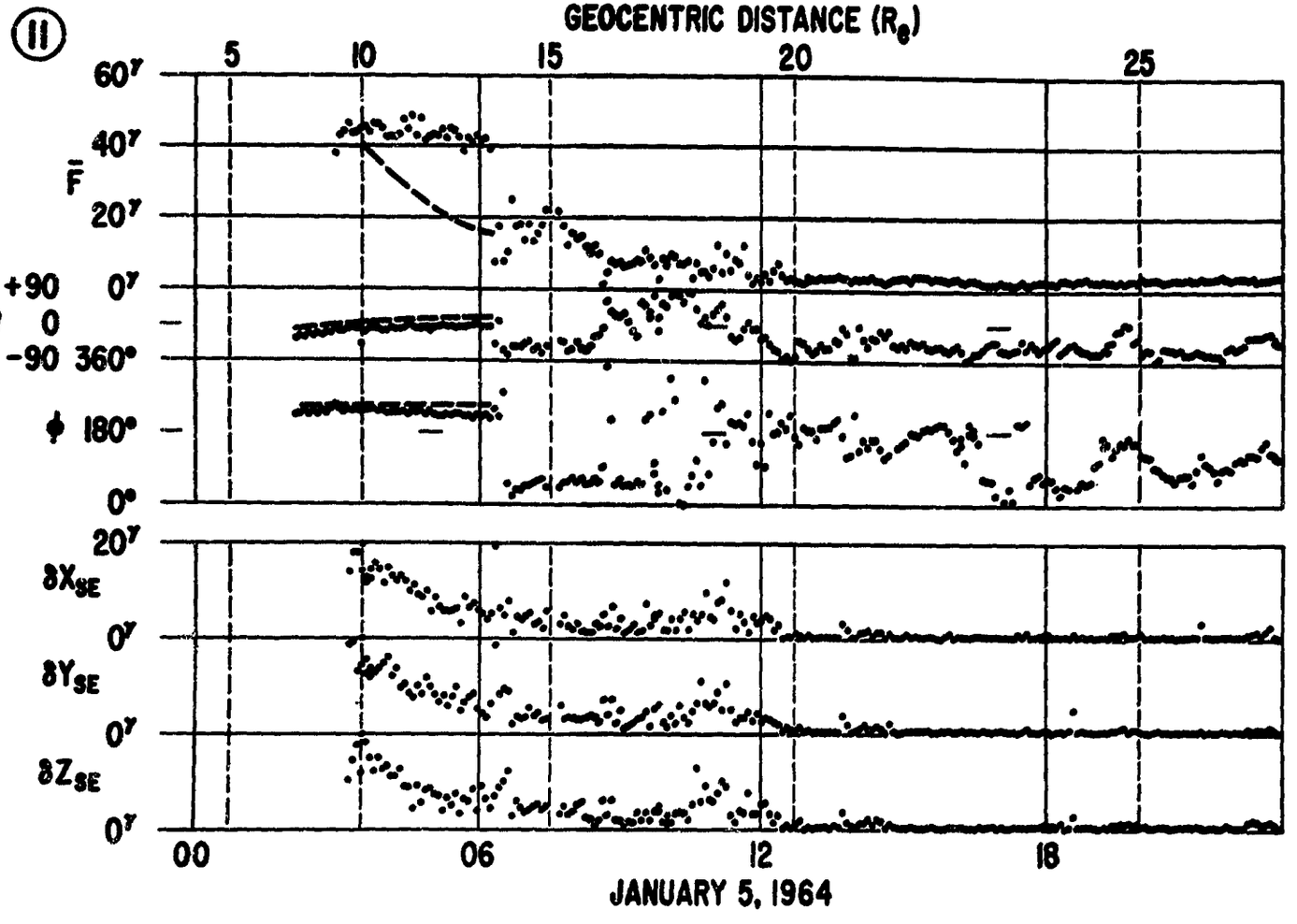
FIGURE 3

by an order of magnitude during the main phase of the storm, and then decayed as the magnetic field recovered. The diamagnetic effect of the trapped particles found by Dr. Frank[3] is adequate to account for the observed decrease in the main field. These measurements, I believe, constitute the first time the ring current particles have been observed and permitted a quantitative explanation of changes in the surface field during a magnetic storm.

An example of magnetic field measurements beyond the radiation belts is shown in Figure 4 (after Ness[4]). The satellite moved away from the Earth towards the Sun. The dashed line gives the expected magnetic field, based on an extrapolation of the geomagnetic dipole. In the region between about 10 and 13 Earth radii, the field does not decrease as expected, but has a value of about 40 to 50 gamma, then decreases abruptly to a value between 10 and 20 gamma. From 13 to nearly 20 Earth radii, the field varies wildly in both magnitude and direction with no resemblance to an expected dipole extrapolation. Magnetic measurements, taken on an orbit in which the satellite moves away from the Earth in the antisolar direction, are characterized by a magnetic field which remains well above the extrapolated dipole value out to 200,000 miles. On the basis of these measurements, a model of the magnetosphere has been formulated (Figure 5). The abrupt decrease in field, shown in Figure 4, is called the magnetospheric boundary; inside this boundary the influence of the Earth's magnetic field predominates, outside the boundary is a transition region which is bounded on the solar side by a shock front. These features are produced by the interaction of the solar wind and the magnetosphere. This phenomenon is analogous to the flow of supersonic gas past an obstacle. In this case, however, the solar wind plasma is collisionless and particle field interactions play a role similar to that of molecular collisions in the aerodynamic case.

At this point, I would like to mention a new technique which has been pioneered by Dr. Luest of the Max Planck Institute in Germany. A magnetic measurement gives the field vector at one point in space; as the satellite moves, one can obtain a succession of such point measurements. However, in studying such regions as the magnetosphere, we are interested in plotting out magnetic field lines, and, if possible, follow their motion with the plasma. If one releases an ion cloud in a magnetic field, the motion of individual ions is restricted to spiraling around field lines. Dr. Luest has released barium vapor in space which is subsequently ionized by sunlight. The resulting Ba ions can then be observed from the ground by optical techniques because the ions scatter sunlight very efficiently. A number of such releases have been conducted successfully both in the auroral zone and under magnetically quiet conditions. In the future, this technique may also prove to be useful for investigating the outer radiation belts and the tail of the magnetosphere.

Since the Earth is a planet in the solar system, the behavior of the Sun and its influence on its environment is of major interest to us. Again magnetic fields play an important role in solar phenomena. In situ measurements at the surface of the Sun are impossible, but optical techniques have permitted remote sensing of the solar magnetic field. At a



Magnetic field data from orbit No. 11 January 5, 1964 illustrating outbound traversal of magnetopause boundary at 13.6 R_e and shock wave boundary at 19.7 R_e.

Figure 4

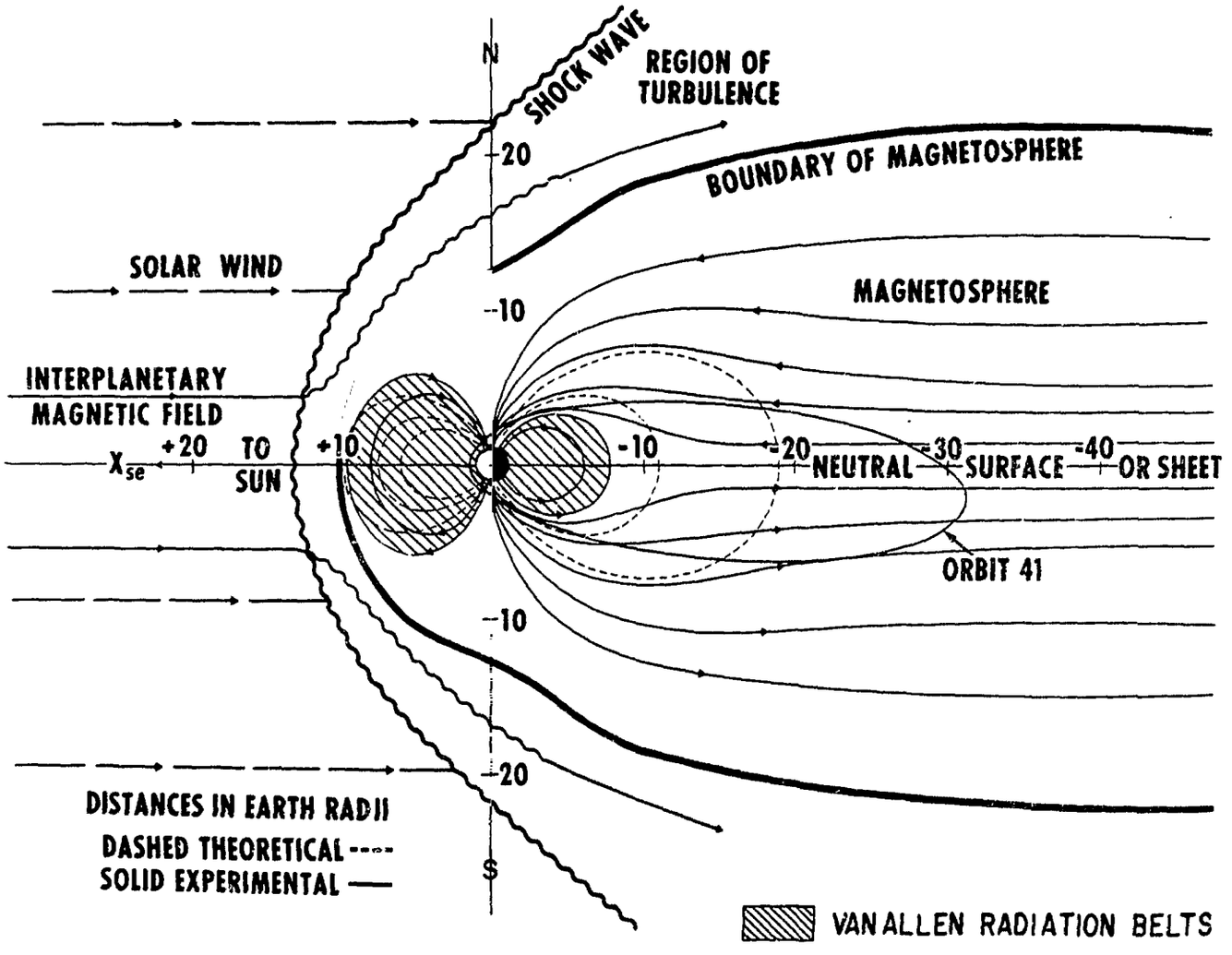


Illustration of the interpretation of the IMP-1 magnetic field data field topology within the magnetosphere in the noon-midnite meridian plane. The relative position of the neutral surface or sheet in the earth's magnetic tail and the co-rotating magnetic field lines supporting trapped particle motion are indicated. These include the classical Van Allen radiation belts. The collisionless shock and magnetosphere boundaries are extrapolated to the polar regions indicating a depression but the relative position of a polar neutral point and the size of the boundary are not experimentally determined. Cylindrical symmetry about the earth sun line has been assumed for the boundary of the earth's magnetic tail in this presentation.

FIGURE 5

sunspot, the field is substantially higher than in the surrounding areas. The high field inhibits the circulation of the surface material; therefore, decreases the amount of heat which can be convected out from the interior of the Sun. At sunspots, continued convection of the plasma can produce unstable field configurations. A triggering mechanism must exist which permits the sudden release of this energy in a solar flare. In this process, high energy particles are formed. These solar cosmic rays constitute a substantial radiation hazard to manned operations in space.

The outer solar corona is sufficiently hot that the ionized hydrogen existing in that region is no longer gravitationally bound to the Sun and can escape at a slow rate. The escaping plasma, called the solar wind, carries with it the solar field that existed in the outer corona. Figure 6 shows an artist's concept of this process. The solar wind has a density of a few protons per cubic centimeter and moves radially away from the Sun with the speed of roughly a million miles per hour (300 to 400 km per second). The magnetic field lines determine the trajectory of the solar cosmic rays.

A systematic study has been performed by Wilcox and Ness[5] of the average structure of the extended solar magnetic field as observed near the Earth. They found that the field near the Earth has, in general, the same polarity as the average polarity found at the surface of the Sun, and that the field exhibits a distinct sector structure. Four sectors of alternate fields directed towards and away from the Sun, as shown in Figure 6, were observed in early 1964. Sectors persist for many solar rotations and evolve slowly as the surface field of the Sun changes. The corotation of this field structure with the Sun is illustrated in Figure 8. In this instance, an apparent reversal in field direction was observed, both with Pioneer VI and Explorer XXVIII satellites[6]. It took 57½ minutes for the field to rotate from one spacecraft to the other; as shown in the insert of Figure 8, the two measurements exhibit the same features.

Beyond the Earth, the exploration of the solar system out toward galactic space offers many challenges. As the solar wind expands further, both its density and magnetic field strength continue to decrease. Therefore, at some distance from the Sun, estimated to occur between 10 and 100 A.U., the influence of the galactic medium will be observable. Even with present rocket technology, a distance of 10 A.U. can be reached with a flight time of a few years. It is therefore feasible to start exploring these features within the next decade.

The fruitful methods of geomagnetic investigations can also be applied to exploring other bodies in the solar system. Already, preliminary measurements of the Moon's magnetic field and of the interaction of the Moon with the solar wind were performed with Explorer XXXV. Ness et al.[7] have shown that the Moon has a negligible magnetic moment and that no shock is formed in the solar wind due to interactions with the Moon. Interpretation of these measurements is complex, but it will be possible

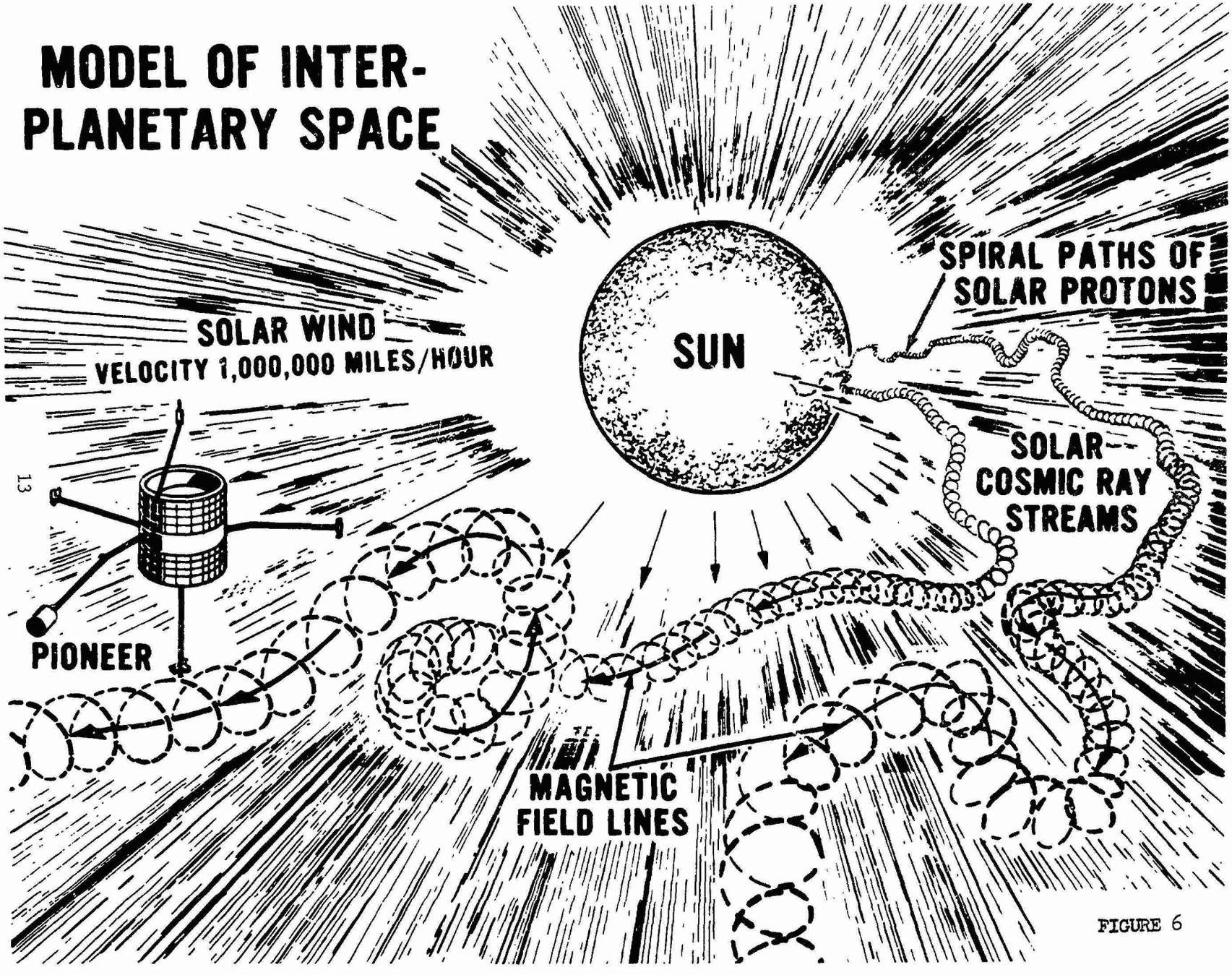

MODEL OF INTER-
PLANETARY SPACE
SOLAR WIND
VELOCITY 1,000,000 MILES/HOUR
SUN
SPIRAL PATHS OF
SOLAR PROTONS
SOLAR
COSMIC RAY
STREAMS
PIONEER
MAGNETIC
FIELD LINES

FIGURE 6

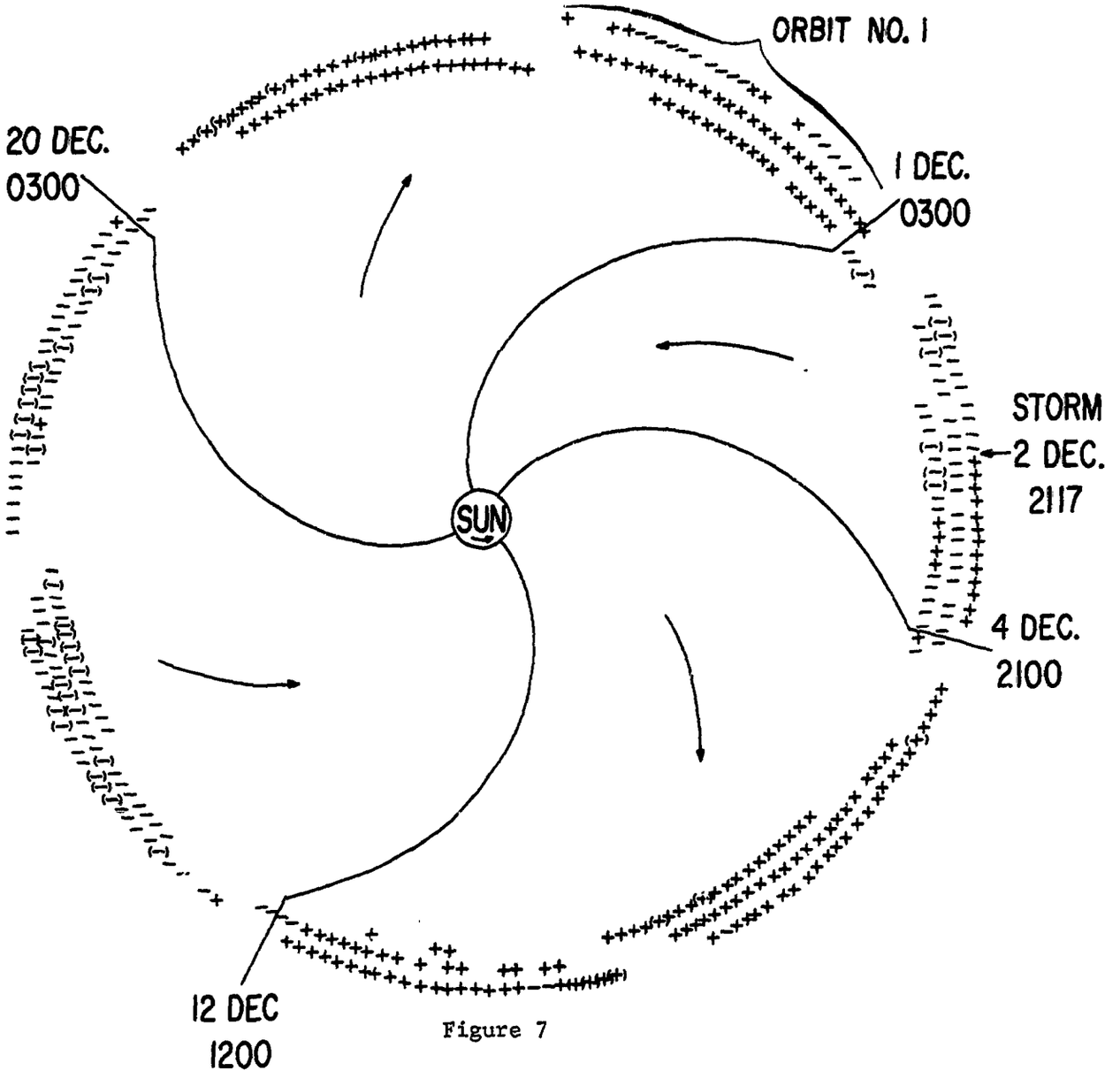

ORBIT NO. 1
20 DEC.
0300
1 DEC.
0300
STORM
2 DEC.
2117
4 DEC.
2100
SUN
12 DEC
1200

Figure 7

PIONEER AND EXPLORER SHOW SOLAR MAGNETIC FIELD ROTATION

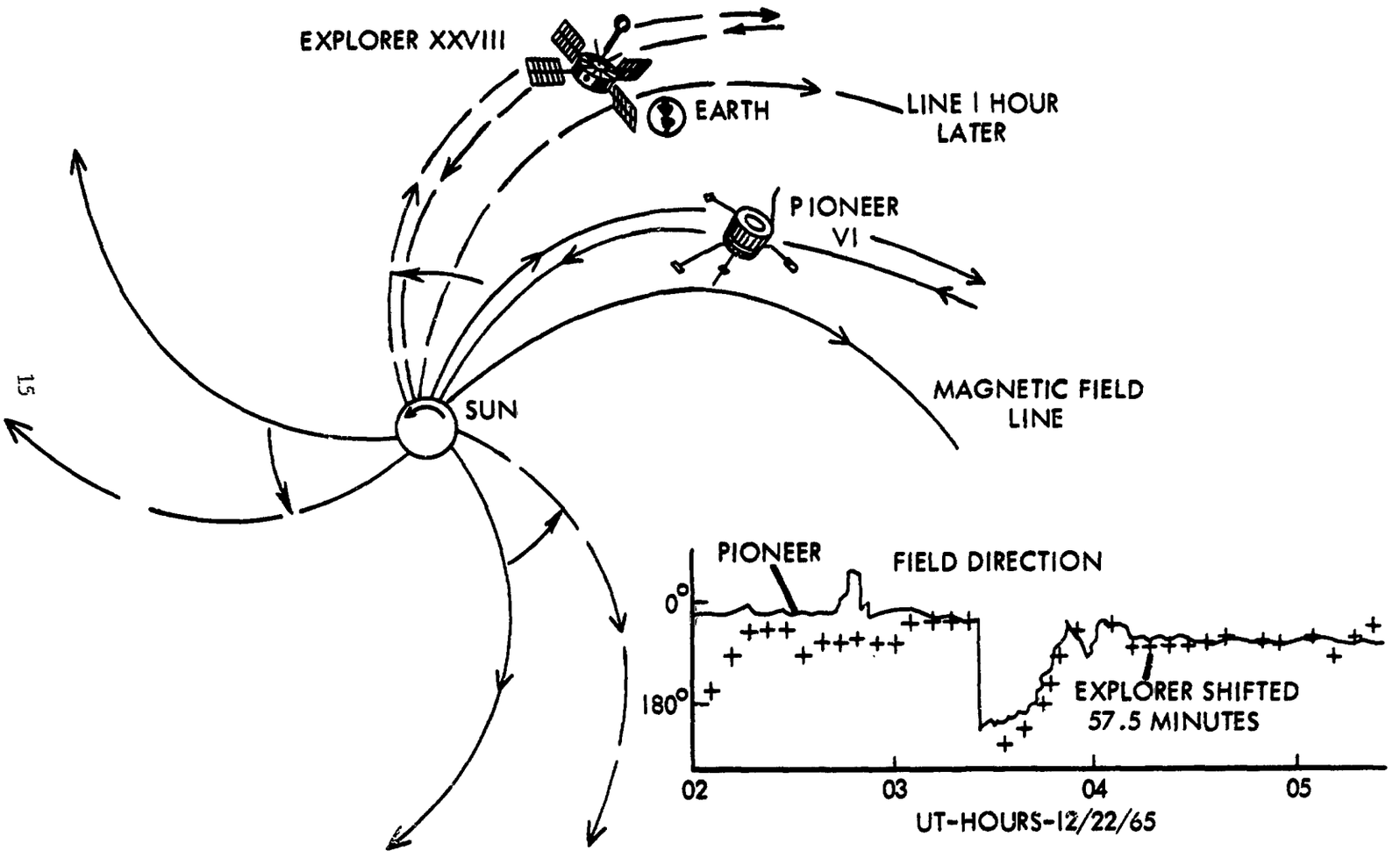


Figure 8

to determine the conductivity of the Moon and use this value as a basis for placing an upper limit on the internal temperature of the Moon. Mars resembles the Moon in some aspects, it would thus be most interesting to repeat these investigations at Mars. An investigation of the strong fields of Jupiter and other planets will provide important information, not only on the internal structure of these planets which is responsible for the strong fields, but also on their radiation belts.

In summary, the outstanding problems in space continue to pose major challenges to everybody interested in measuring magnetic fields, primarily on the low field end, .01 gamma accuracy. The design of a spacecraft to conduct such measurements will take even more effort than has been expended on this problem in the past. Reliability requirements will continue to pose problems because both the spacecraft and instruments will have to operate for many years. With present propulsion techniques, we have to allow almost two years to reach Jupiter and several times that much to go beyond 10 A.U.

REFERENCES

(1) Vestine, E. H.; R. H. Ball; and A. B. Kahle: Nature of Surface Flow in the Earth's Central Core. Rand Corporation, Memorandum RM-5192-NASA, to be published in Journal of Geophysical Research, 1967

(2) Akasofu, Syun-Ichi: Electrodynamics of the Magnetosphere and Geomagnetic Sturms. Space Science Review, Vol. 6, 1966, pp. 21-143

(3) Frank, L.A.: On the Extraterrestrial Ring Current During Geomagnetic Sturms. Journal of Geophysical Research, Vol. 72, 1967, pp. 3753-3767

(4) Ness, N.F.; C. S. Scearce, and J. B. Seek: Initial Results of the IMP I Magnetic Field Experiment, Journal of Geophysical Research, Vol. 69, 1964, pp. 351-3569

(5) Wilcox, J. M. and N. F. Ness: Quasi-Stationary Co-rotating Structure in the Interplanetary Medium. Journal of Geophysical Research, Vol. 70, 1965, pp. 5793-5805

(6) Ness, N.F.: Simultaneous Measurements of the Interplanetary Magnetic Field. Journal of Geophysical Research, Vol. 71, 1966, pp. 3319-3324

(7) Ness, N. F.; K. W. Behannon; C. S. Scearce and S. C. Canterano: Early Results from the Magnetic Field Experiment on Lunar Explorer 35. To be published in Journal of Geophysical Research.

Figure 1 - Irrotational part of core surface velocity for epoch 1960 (reference 1)

Figure 2 - DST field of magnetic storm in July 7-14, 1966 (reference 3)

Figure 3 - Flux of low energy protons constituting the ring current of July 1966 magnetic storm (reference 3)

Figure 4 - Magnetic field data from orbit No. 11, January 5, 1964, of Explorer XVIII. This is an outbound traverse of the Magnetopause and bow shock (reference 4)

Figure 5 - Model of the terrestrial magnetosphere (reference 4)

Figure 6 - Model of Interplanetary Space

Figure 7 - Sector structure of solar magnetic field during December 1963 to February 1964 (reference 5)

Figure 8 - Pioneer VI and Explorer XXVIII record of solar magnetic field rotation (reference 6)

A REPORT ON THE SECOND INTERNATIONAL CONFERENCE ON MAGNET TECHNOLOGY

Dr. A. A. Halacsy
Professor, University of Nevada

N69-33953

The Second International Conference on Magnet Technology was held at Oxford, England on June 10 - 14, 1967. It was a continuation of the First International Conference on Magnet Technology held at Stanford, California, two years ago.

The First Conference was sponsored by the Stanford Linear Accelerator Center, Stanford University, and by the Lawrence Radiation Laboratory, University of California. Both, of course, are supported by the U.S. Atomic Energy Commission. The Co-chairmen of the first conference, Dr. Brechna and Dr. Gordon, expressed a hope that this conference will continue and this materialized this year when the conference was held in England and sponsored by the Science Research Council of England, The Institution of Electrical Engineers of England, the Institute of Physics, and the Physics Society of England, and the International Union of New and Applied Physics. The host of the conference was the University of Oxford and the conference was held in the Oxford College of Technology, about two miles east of the center of Oxford. The Chairman of the Conference, Mr. Pickavance, and most of the members of the committees came from the Rutherford Laboratory, the big nuclear research center of England.

The Conference was really international--even more international than the first conference. Nine countries were represented in the first conference--nineteen in the second one. Of course, most of the total number of participants, which was over 300 this year, came from England--around 130. The second group was represented by the United States, Switzerland and France. Each of these had between 30 and 40 people at the Conference. About 15 Germans were present, and four or five people from Italy and the Netherlands each. The rest of the countries were represented by one or two people, but it was interesting to note that about eight or ten people were from behind the Iron Curtain.

More than 100 papers were presented. This means that every third participant presented a paper. We have about the same ratio at our conference here. It indicates a very active participation and looks very good. Still, 100 papers seemed a bit too much for such a conference; particularly when one considers that all these were jammed in two and a half days, the same time we have for 24 papers here. Too many papers jammed in a conference is a familiar and ever-spreading disease of conferences today. Of course, the Oxford Conference couldn't solve any of it except by scheduling two or even three parallel sessions. We all know that this is not too good, because some people would like to participate at two or three sessions simultaneously. We aim to avoid such a situation at this present conference, and we will have time for discussion. The lack of time for discussions was felt very badly at

the Oxford Conference, where only one and perhaps two discussions were permitted after each paper. The rest was advised to contact the author personally. This is, of course, not a unique experience at todays conferences, but certainly is not a good one and certainly is destroying the very idea of a conference. It is my personal opinion that papers cannot be uniform to the same length, and discussions limited to the same number of minutes. Sometimes five or ten minute presentations are more valuable than a three hour talk. Some subjects need an hour presentation whereas some subjects can be presented in ten minutes. As a consequence of the lack of sufficient discussions and as far as I know, at least two groups decided to get together rather informally next year, just to exchange notes and opinions, and discuss their common interest freely. One group is interested in super-conductive magnets, and another group is interested in magnetic field calculations. This latter group is close to our subject in our present conference, and I was asked to get this group together some time next year. So if anybody is working on magnetic field analysis or calculations, please keep in contact with me, sign up and you will be welcome to a completely informal discussion next summer.

We, here at this conference, are discussing magnetics related to rather very weak magnetic fields whereas the Oxford Conference discussed magnetics in connection with rather high magnetic fields, and high power. Still, about one-fifth of the papers presented dealt with subjects interesting or related to weak magnetic fields too.

It was also most interesting to note the great change in thinking about super-conductive magnets. I well recall the feelings at a cryogenics conference about four or five years ago where the general opinion was that in spite of advances in super-conductive technology, super-conductive magnet coils are and will not be economic ever. This opinion is completely reversed today, and the biggest single group of papers, more than a quarter of all papers presented at the Oxford Conference were on super-conductive coils. Superconductivity is interesting to us here, because and for instance: Space-technology is interested in super-conductive magnetic shielding, then strong magnetic fields are required inside the satelites for their operation and super-conductive magnetic coils are very reasonable in order to produce such fields or to replace permanent magnets. A French paper presented definite results by using super conductive cores instead of iron, in magnets. The rare metals like holmium and dysprosium, are useful for this purpose. It is known for approximately 10 years that these metals, which are not ferro-magneti' at room temperature become ferro-magnetic at super-conductive temperatures and saturate higher than iron. The price is beginning to come down, and therefore they can be considered as core material in super-

conductive magnets, where iron is useless. A super-conductive mass-spectrometer is already using these materials as core in France.

More than a quarter of the papers dealt of course with high power magnets for high energy physics. These are accelerator magnets, mass-spectrometer magnets, bubble-chamber magnets, various other magnets for plasma research, etc. Magnetooptics was also discussed.

About a tenth of the papers dealt with power supplies for magnets. This group is also disinteresting for us here, so I won't mention much about it except that several power supplies for high stability and high accuracy were reported. Such highly accurate power sources of course are interesting in any magnet laboratory, so in a magnet laboratory for investigating weak fields too.

Two groups of papers were really interesting to us in connection with weak magnetic fields. First, papers on the measurement of fields. Such papers were about 10% of all the papers. Second, papers on calculation of magnetic fields, and also some papers discussing production of homogenious fields.

All these papers, which are mostly interesting to us, came from only three countries. Most of them came from the United States. The rest from Switzerland, and from England.

Half of the papers on measurement of fields were presented by people of the Lawrence Radiation Laboratory. Six Lawrence Radiation Laboratory papers numbered from seventeen to twenty-two could be considered as sections of a long paper. They described the Lawrence Radiation Laboratory "Rapid-Mapper" Magnet Measuring System, developed during the course of processing about four million magnetic field measurements in the past four years. The Rapid-Mapper performs a variety of automatic and semi-manual D.C. measurements. In the automatic mode, the machine positions a probe sequences the measurements and records the data for computer analysis. The third generation of "Rapid-Mapper" is now in the planning stage and will be controlled by a digital computer. In addition to its predecessors it will be able to make digital pulsed field measurements and will also do error checking at the time of measurement. It is to be used first for magnetic studies on a 200 GEV accelerator model.

A rotating coil gauss meter is the sensor in the system. AC signals are detected with 0.01% resolution and with 0.1% accuracy. Techniques of using search coils and integrators have been improved during the past few years to an accuracy better than 0.01% of this combination.

The probe is positioned along a line with an accuracy of 0.0005, inch.

The flux standard is a square root flux standard stable to 0.01% and adaptable from one million to one hundred million maxwell turns. Power is generated by reversing the magnetization of a temperature controlled and temperature compensated toroidal transformer. The core of this transformer is made of a nickel-iron alloy with a square hysteresis loop. One of the latest measurements with this Lawrence Radiation Laboratory system was reported as made in March 1967, on an alternating gradient cyclotron magnet at Texas A & M University. Similar measurements are planned for the alternating gradient cyclotron at the University of Maryland next fall.

Of course, the Lawrence Radiation Laboratory "Rapid-Mapper" was designed for measuring rather high fields in specialized magnets. The Swiss report from CERN, the European Center for Nuclear Research, was more interesting. They reported on a technique used for the rapid field mapping of a big ring magnet. Two "field-locked" proton-resonance magnetometers are used, and the frequency difference between a reference unit and mapping unit is recorded automatically. Each unit has a systematic error less than 2 ppm, and a statistical error of the same order on individual measurements. Proton-resonance is also used for field-stabilization and it may be interesting in low-field laboratories as such.

Another CERN report dealt with a permeameter for testing toroidal steel samples. The classical Rowland method is used with semi-conductor switching and electronic integration. The curve of first magnetization, coercivity and remanent field is measured.

A report from the Rutherford High Energy Laboratory listed the three main disadvantages of nuclear magnetic resonance equipment. First, the method does not give a direct and automatic measurement of the field; second, difficulties can arise in magnets with field gradients, and third, there are problems with regard to signal to noise ratio. To overcome these disadvantages, a high stability Hall effect probe system was developed. Recognizing that the Hall-coefficients are sensitive to temperature, temperature effects have been reduced by closely controlling the temperature of the Hall plate by mounting the plate inside a "change-of-state' type oven. The remaining cyclic variation in temperature is 0.002 ^{o}C. The changes in Hall voltage due to temperature variations are then in the order of 1 ppm, which is about the same as reported for magnetic resonance methods. The control current of the Hall plate is supplied from a source with a long term stability of better than five parts in one hundred thousandths.

The Hall voltage is measured with a digital voltmeter. The long term stability of the system was found to be better than 1/200 of a percent over a period of two weeks.

A report from Argonne National Laboratory described a high speed digital field measuring system used for a bubble-chamber magnet. The system measured 1728 field points during a 17 second circular sweep with a polar coordinated manipulator. The resolution was about 10 gauss in a 46,000 gauss field.

There was a unique paper--Number 36, by Dr. Colonias of Lawrence Radiation Laboratory, describing the technique by which a magnet-geometry--that is, a two-dimensional section of an iron-core is drawn on cathode ray oscilloscope screen using a light pen. When a computer program is used for magnetostatic programs, the output of which is connected with the same cathode-ray tube, the field appears in the form of a mesh of equipotential and flux lines. The dimensions of the core can be altered by using a light pen and the resulting new field appears again automatically on the screen.

Five other papers dealt with magnetic field calculations. The only one not from this country was from the Swiss Oerlikon Company which recently merged with the Brown-Boveri Company. They are world-wide known producers of beam handling magnets for high energy physics experiments and they presented a two-dimensional method particularly suited for super-conducting magnets with constant current density windings. The method uses infinite harmonic series.

Dr. Beth of Brookhaven National Laboratory explained the very ingenious new method of calculating field energy and forces on conductors in a two dimensional magnetic field. He maps the physical area by a transformation into a plane, the two axes of which are the vector-potential and the scalar-potential; an area of this new vector-and scalar-potential plane is proportional to the field energy. This seems to be a very powerful technique--particularly if one is interested in forces on conductors. Of course, the vector and scalar-potentials must be known by some other method. Though Dr. Beth's method is for two dimensional cases, it would be interesting to investigate if it would not be adaptable for three dimensions as well.

Dr. Foss of Carnegie University described his computer program, which is a modified relaxation program for calculating magnetic fields, basically in two but possibly in three dimensions, and also in the presence of a magnetizable material. It is a kind of program of an alternating relaxation calculation of the flux density and the permeability. It is written in Algol and requires about 4,000 instructions and calculates an average mesh

point in about 300 memory cycles. The program was designed mostly for the needs of magnets used in higher energy physics. It looks rather complex, and in order to be useful for a rather detailed study of a magnetic field, needs a computer with an extremely great memory which hardly exists today.

I, myself in cooperation with Professor Clark and Mr. Dunks of the University of Nevada, presented a paper on three dimensional calculation of a magnetic field. It dealt with the three dimensional fields without iron. It is, in essence a computerization of Biot-Savart law. The computer program is extremely simple, and may form a part of a more sophisticated calculation of the magnetic field of satellites. It is recognized that any magnetic field is composed of a field of magnetomotive force gradients generated by currents or magnetic moments of magnetizable materials, which magnetic moments in turn are generated by the electric currents, or may be magnetic moments of permanent magnets. The field of electric currents can be calculated, as presented at Oxford and we are working now on the other parts of the more generalized case. It is hoped that more would be ready for reporting by next summer.

A calculation of magnetic fields can go in two directions. The usual way is to list currents and magnetic materials with magnetic moments and then calculate the field. Such calculations are needed mostly in High Energy Physics, which instigated interest in such calculations originally. However, it must be recognized that the aim is to build magnets for a desired magnetic field and not to calculate the field of an existing magnet. This, of course, requires work in a direction exactly opposite to the one done today. This reverse process encounters considerably greater difficulties than taking a magnet and calculating its field and this is the reason why very little was done in that line so far. The process was almost always to choose a magnet, calculate its field, then modify the magnet. Calculate the field again, and so forth until the desired field was arrived at. This background explains the great importance of Dr. Halbach's paper from Lawrence Radiation Laboratory which described the PISA system. PISA means a Program for Inversion of System Analysis which determines the geometry of a magnet for producing the desired field. It is most likely that a tremendous amount of work will develop for this same purpose in the future.

Visits were arranged to principal sites of British nuclear research, as for instance to the Rutherford High Energy Laboratory which, as most of you know, is adjacent to Harwell, and to the Culham Laboratory. Of course, several other visits were made possible. Several factories offered tours of their facilities producing power supplies, and materials and equipment for super-conductive magnets and for instance, I visited the Daresbury Nuclear Laboratory close and in cooperation with Liverpool

University which was opened just last May by the Prime Minister of Britain. These excursions contributed a lot to the value of the Conference.

Conferences, of course, have their social side too, and so the Second International Conference of Magnet Technology also included several other activities--a civic reception by the Mayor of Oxford in the City Hall, a conference banquet, visit to Stratford-on-Avon to the Shakespeare Memorial Theatre for a performance of Coriolanus which was instead of Macbeth because the principal actor of Macbeth was seriously ill. The Macbeth performance originally planned gave rise to the wonderful idea to include quotations from Macbeth in the Conference program. Those were very appropriate and with real English humor. One affixed as a motto to the list of session Chairmen was: "Oh, who can be roused, amazed, temperate and furious, loyal and neutral in a moment."

SOME FEATURES OF SECULAR VARIATION OF THE GEOMAGNETIC FIELD

Robert L. DuBois*

N69-33954

REFERENCE

DuBois, Robert L., "Some Features of Secular Variation of the Geomagnetic Field," Space Magnetic Exploration and Technology Symposium (August 1967), University of Nevada, Reno.

ABSTRACT

To describe completely secular variation, data are needed from preobservatory time, and archaeomagnetic studies provide such information. Archaeomagnetism uses the standard instrumentation of paleomagnetism and determines the paleodirection of the geomagnetic field from the direction of remanent magnetism of specimens of baked clays. Specimens for these studies are collected from fire hearths or kilns at various archaeological sites and range in age from 300 B.C. to modern. The dating is based on a tree-ring chronology.

Results suggest that values for inclination of the earth's magnetic field, as adjusted to Tucson, Arizona, range from 40° to 60° and can be represented on an irregular curve. Changes in declination are from 13°E to 13°W.

Secular variation as indicated by a polar data representation curve (PDRC) has a 1350-year period of counter-clockwise motion that encircles the present geographic pole. The PDRC has three small clockwise loops, approximately 120° apart, and of about 200-400 years duration. The angular standard deviation of all site mean directions is 5.9°.

* School of Geology and Geophysics, University of Oklahoma, Norman, Oklahoma.

INTRODUCTION

The remanent magnetism in baked clay associated with fire hearths, burnt walls or floors of prehistoric Indian dwellings, records accurately the direction of the earth's magnetic field. It can be used to extend our knowledge of geomagnetism beyond that available through direct measurements represented in observatory data. The resulting data can document the amplitude and time variation of secular variation and can be used indirectly to establish a magnetic chronology for dating archaeological sites. Archaeomagnetic measurements of the type discussed in this paper were first made by Thellier and Thellier (1,2) and their methods have been followed by many other investigators throughout the world. The results presented have been determined for specimens of baked clay collected from archaeological sites in Arizona, New Mexico, and Texas over a geographic area approximately 1,000 km in diameter.

DISCUSSION OF SAMPLES AND DATING

The materials used in these experiments were collected mainly from the peripheries of fire hearths of dated Indian sites. Dating of the sites is based on a tree-ring chronology and the sites range in age from 300 B.C. to modern. Work is now progressing to extend the ages studied back to some 5,000 years B.C. The fire hearths, more or less circular in shape, generally occupy either a central position in the room or to one side directly in front of the entrance. In either position, they are not a random feature in the ancient dwelling, but a structure specially constructed for its purpose and lined with special clay brought in from the outside. The thickness of the clay lining ranges from about 0.5 inch to several inches, and some hearths have a raised rim of clay extending several inches above the general level of the floor. The finished hearth is between 8 inches and 3 feet in diameter, and between 6 and 12 inches in depth. Before collecting specimens from a given fire hearth, the geomagnetic characteristics are determined in the vicinity to assess the presence of anomalously magnetic effects. The procedures used assure that the magnetic field at the sample site corresponds to regional patterns of geomagnetic variation.

Ideally the specimens collected are small columns about 1.25 inches high and 1.25 inches in diameter. They are made by carefully excavating the material from around the core using small probe-like tools. The column remains attached at the base until a cubical brass mold is placed over it and filled with plaster. Orientation of the mold is accomplished by use of a special device which contains a compass needle and two precision levels perpendicular to each other. The resulting sample is an oriented column of baked clay embedded in cube which presents a uniform geometrical shape for subsequent measurements.

EXPERIMENTAL METHODS

Eight to ten individually oriented specimens are collected from a fire pit. Measurements of the direction of the remanent magnetism is made on an astatic or spinner magnetometer (3). In using the astatic magnetometer, the specimen is centered below the magnet suspension and

measurements of deflection are made in the 0°, 90°, 180°, 270°, and 360° positions for each face of the cube. This procedure allows the determination of each of the orthogonal coordinates of the magnetic vector eight times. From the resulting measurements, the direction and amplitude of the remanence can be calculated and various precision parameters indicative of the internal consistency of the measurements estimated. Reproducibility of the direction, as determined by repeated measurements on the same specimen, is within 0.2°. To assess the magnetic stability of the specimens measured, thermal demagnetization experiments and storage tests are performed.

RESULTS

Results are presented for the time span 600 to 1600 A.D. (Figure 1) with magnetic measurements made on some 70 fire hearths that have mean directions which can be calculated at the 95 percent confidence level to lie within a cone with a 3° or less radius inscribed about the mean. When corrected to Tucson, changes in inclination are found to range from 40° to 60°. A minimum inclination occurred at 800 A.D., with a value of 40°, and a second minimum of 45° occurred at approximately 1550 A.D. Maximum inclinations occurred around 500 A. D. and 1150 A. D., with values approaching 60°. Modern-day measurements also give inclinations of approximately 60°. Changes in declination range from some 13°E to 13°W of true north. Easterly declinations were recorded around 600 A.D., again at 900 A.D. and 1550 A.D. and also in modern times. The most westerly declination occurred during 1200 A.D. The curves representing changes in declination and inclination are irregular, but may be capable of resolving some frequencies of secular variation. The curve showing changes in inclination for the years 600 to 1200 A.D. suggests major variations with a period of about 800 years. During the years 600 to 1000 A.D., declination seems to have had a variation with a frequency of approximately 400 years, and this value, which is about one-half that of inclination, seems to agree quite well with the model that attributes secular variation to westward drift. The curve representing declination for the years 1200 to 1500 A.D. seems to suggest variations with a period of 70 to 100 years; again this is about one-half the period represented by the curve for inclination. The data on magnetic directions can be used to develop a polar data representation curve (Figure 2) which would show the position of the calculated magnetic pole for a dipole field as representative of the measured values of declination and inclination. The resulting polar data representation curve encircles the present geographic pole in a counter-clockwise manner with a 1350-year period. The curve has three small clockwise loops approximately 120° apart. These loops seem to develop over 200 to 400 years. The average pole position calculated for all of the sites studied so far would be essentially coincident with the present geographic pole, 88.5°N and 105.0°W. The angular standard deviation of the various site mean directions about this over-all direction is 5.9°. This value is a statistical representation of secular variation for the range of the time studied and should be useful in interpreting other paleomagnetic results.

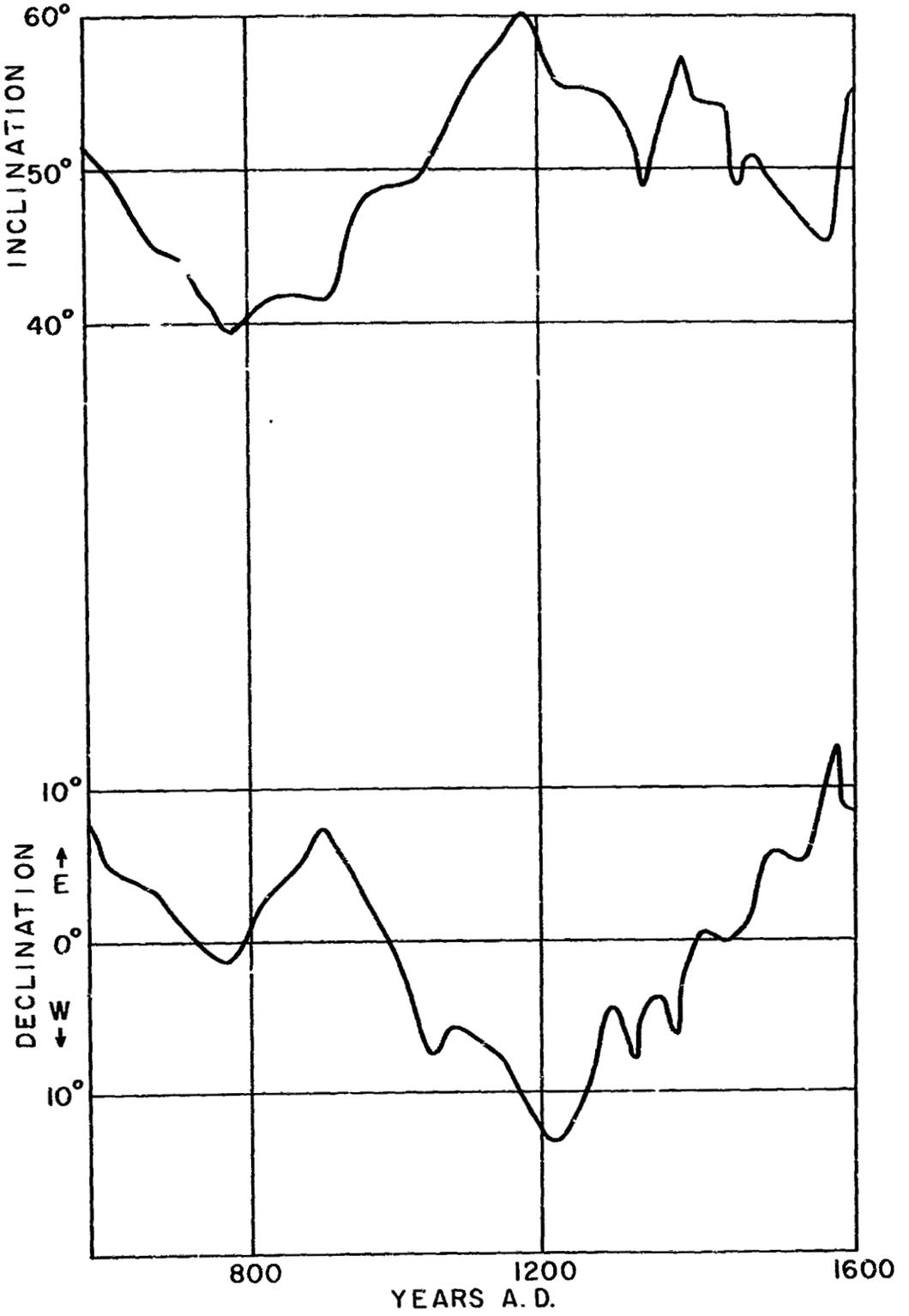


Figure 1. Change of the geomagnetic field in southwestern United States.

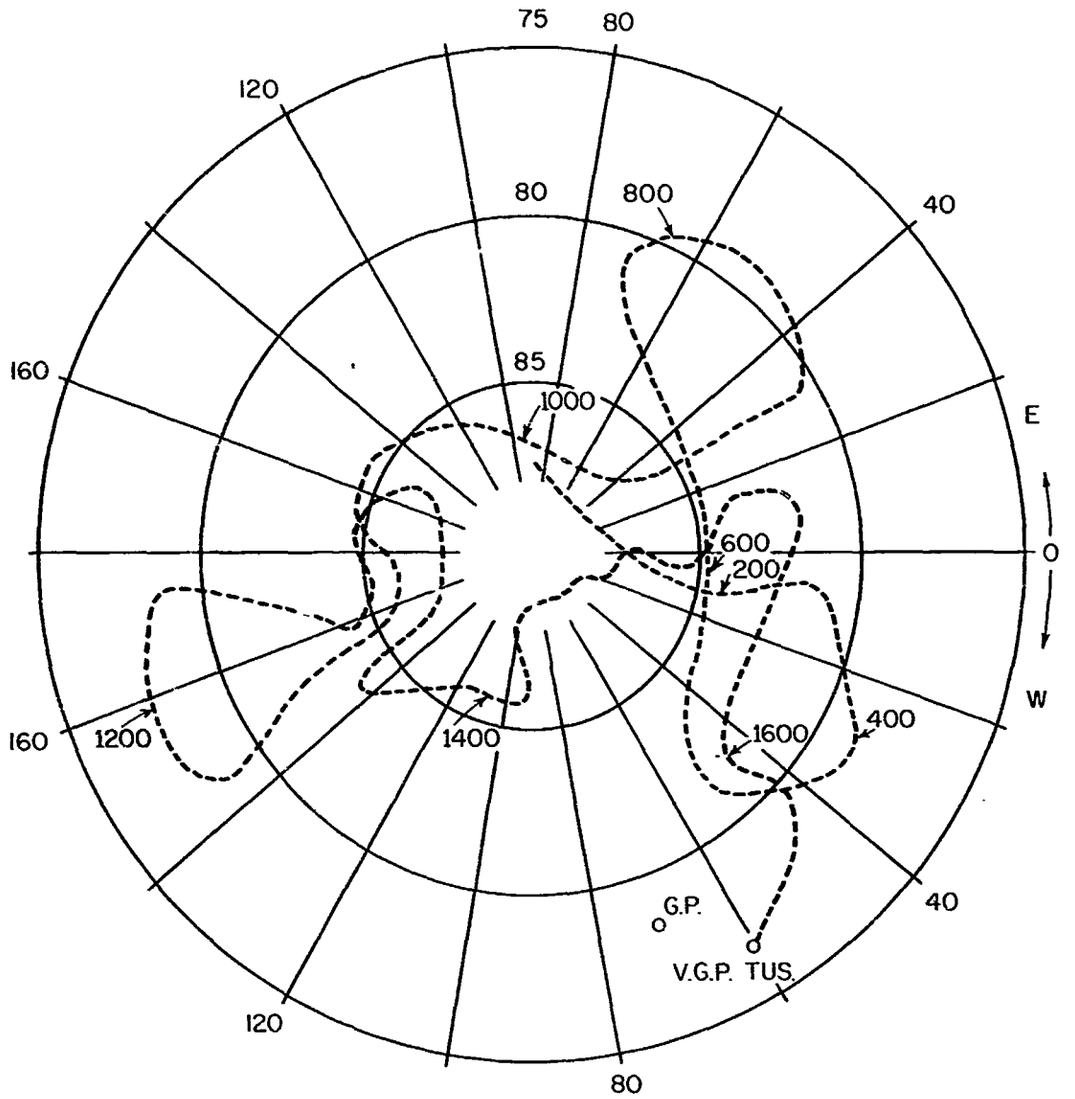


Figure 2. Archaeomagnetic polar data representation curve for southwestern United States.

REFERENCES

1. Thellier, E., and Thellier, D., C. R. Acad. Sci. Paris, 233, 1476 (1951).

2. Thellier, E., and Thellier, D., C. R. Acad. Sci. Paris, 234, 1464 (1952).

3. Collinson, D. W., Creer, K. M., and Rudcorn, S. K., Methods in Paleomagnetism, Elsevier Pub. Co., Amsterdam (1967).

N 69-33955

THE ARGONNE 16-FT BORE SUPERCONDUCT

J. R. Purcell
Argonne National Laboratory, Argonne, Illinois

INTRODUCTION - This paper describes the design approach for building a 16-ft bore superconducting magnet for the large 12-ft liquid hydrogen bubble chamber under construction at Argonne National Laboratory. Both conventional (hollow copper conductor) and superconducting coils were designed in considerable detail and compared on a parameter-to-parameter basis. The superconducting coil was chosen because it compared favorably with the conventional coil. Its design appears to be safe, feasible, and reliable, and - in addition - large savings in power costs can be realized.

The magnet system is designed to provide an 18 kG field. To produce the same magnetic field in a conventional coil, 10 MW of power is required plus an additional 750 kW for the cooling-water circulation pumps. The power requirements of the superconducting coil are not expected to exceed 200 kW, which is almost entirely for refrigeration. This expectation is based on steady-state operation and will depend to some extent upon the efficiency of the thermal insulation.

Detailed capital cost estimates were made for both the conventional and superconducting systems. Although the superconducting coil and refrigeration system are considerably more expensive than the conventional copper coil, this disadvantage is counterbalanced by the fact that the 10 MW power supply and cooling systems are not needed. Within the accuracy of the estimates, the capital costs of the two systems are the same. Operational costs are much lower for the superconducting system.

The superconducting magnet utilizes a 1600-ton, carbon-steel return path and the coils are enclosed in a toroidal container. A cross section of the bubble chamber is shown in Fig. 1. Completion of the magnet system is expected in early 1969.

---

*Work performed under the auspices of the U. S. Atomic Energy Commission.

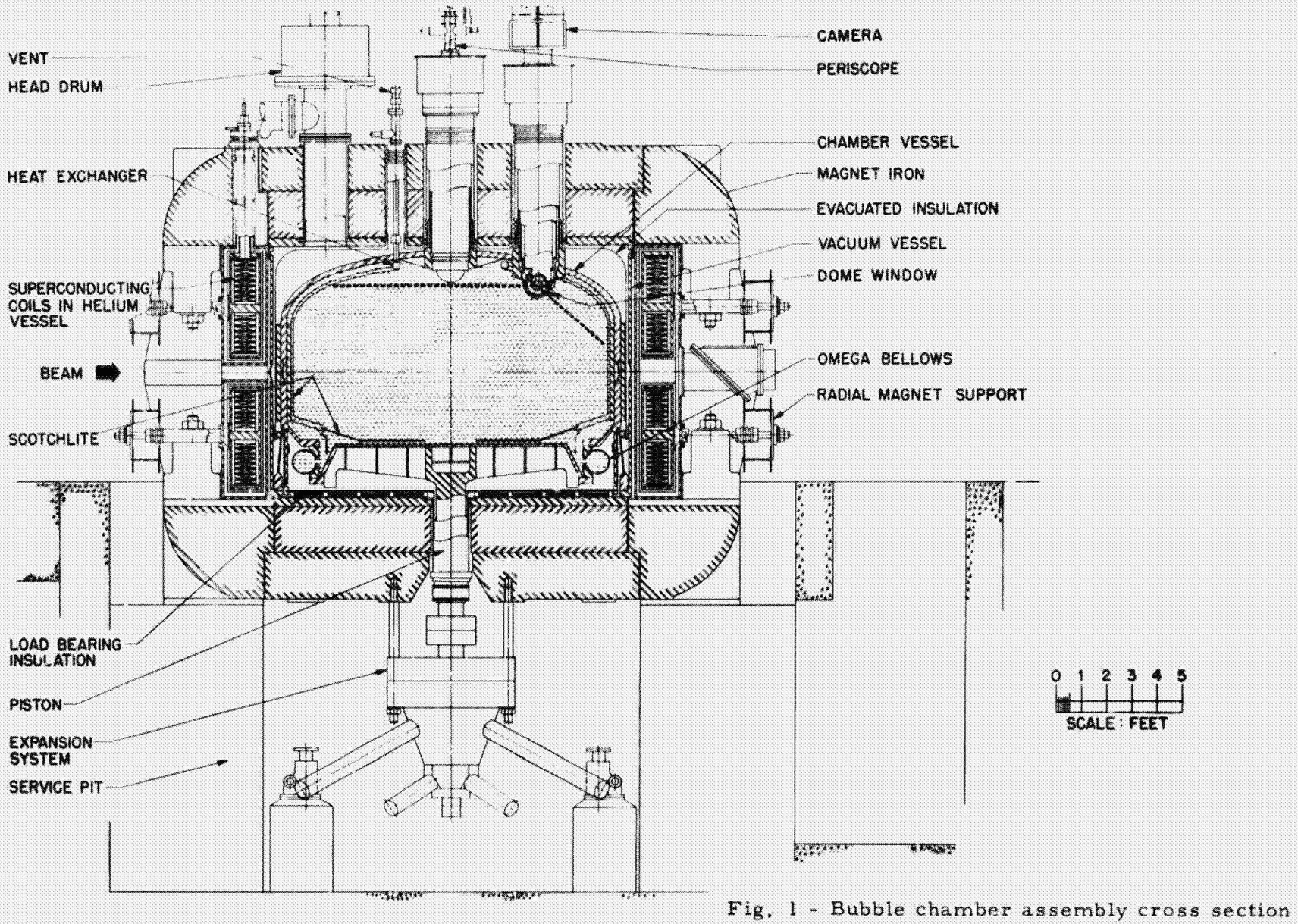


Fig. 1 - Bubble chamber assembly cross section

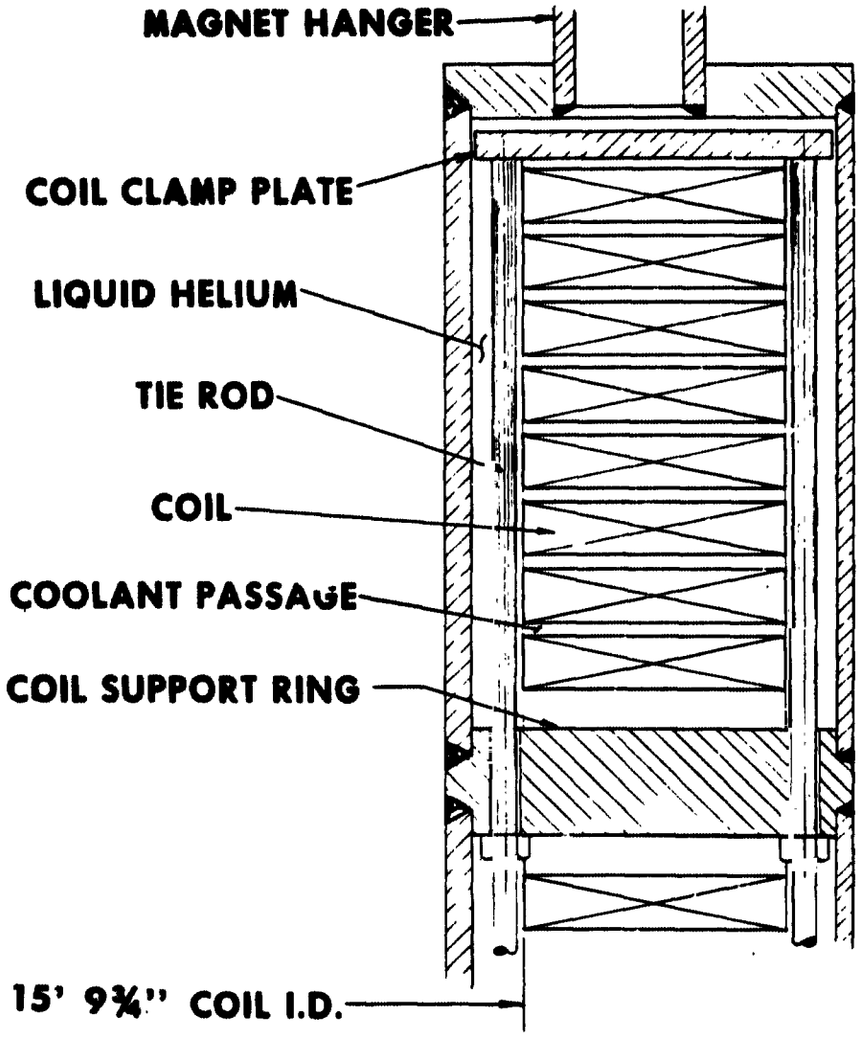
SUPERCONDUCTORS AND STABILITY - The 12-ft hydrogen bubble chamber's energizing coil is designed for fully stabilized operation based in part on other work.[1, 2, 3] Thus, disturbances that tend temporarily to upset the superconductor or even short sections of defective superconductor, will not have a detrimental effect on the operation of the coil.

Copper was chosen as the stabilizing material for the coil because it has high electrical and high thermal conductivity, because it has adequate mechanical strength, and because its low temperature properties (electrical, thermal, and mechanical) are well known. Furthermore, it is readily available in the required quantities, and its fabrication techniques are simple and well established.

SUPERCONDUCTING COIL - The coils are wound from a composite strip conductor of copper and superconductor, measuring 2-in wide by 1/10-in thick. Calculated stable current for this conductor is about 4200 amps with the normally observed heat transfer rate of 0.5 W/cm^2. Turn-to-turn insulation is 10-mil teflon containing about 15% glass fibers. The teflon remains somewhat flexible, even at 4K, which will reduce stress concentrations.

The coil has an inside diameter of 16 ft. It consists of two stacks of pancakes; the top and bottom stacks are separated by about 24 in. Details of the coil construction can be seen in Fig. 2. The coils are held in position by an aluminum tie rod assembly, which clamps the coils to the 4-in thick girder ring. Aluminum is used for the clamping bolts to maintain clamping force on the coils as the system is cooled down. The coefficients of thermal expansion are such that the clamping forces increase somewhat at 4K. Aluminum spacers between the coils (not shown) are located every 6 degrees and are faced with thin electrical insulating material. Coefficient of thermal expansion matches the coefficient of the copper-teflon composite of the coil, resulting in very low shear forces on the coil spacer interface.

The interaction of the coil current and the magnetic field gives rise to radial and axial forces (J X B) on the coil. The integrated effect of the radial component of the force is to induce tensile (hoop) stress in the conductor in the circumferential direction. The maximum hoop stress in the windings is 6000 psi at the 18 kG operating field. This stress level is safely supported by the stabilizing copper portion of the composite conductor with negligible resistance increase due to stress.[4] No additional reinforcing is required. The elimination of the need for reinforced conductor greatly simplifies the conductor configuration and circumvents the problems of induced internal thermal stresses due to the difference in the thermal expansion between the basic conductor and suitable reinforcing materials.



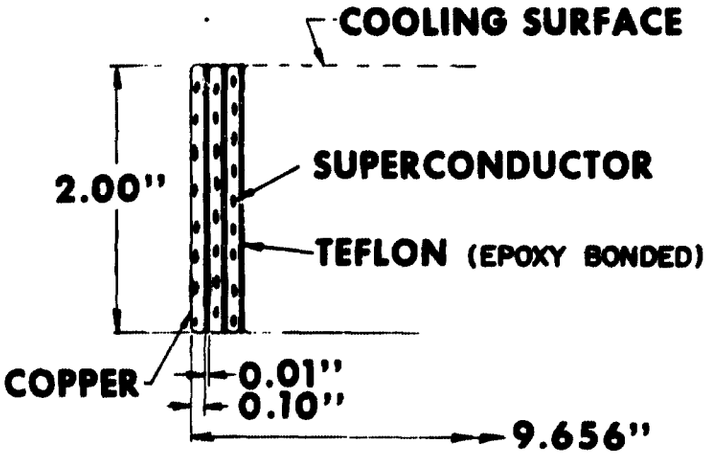


Fig. 2 - Cross section of the helium container, depicting roughly one-fourth of the winding. On the right is shown a detailed coil wafer

Temperature stratification in the helium container is prevented by introducing a mixture of gaseous and liquid helium at the bottom of the tank under the lowest coil. The rising gaseous helium provides sufficient stirring action to maintain a uniform temperature distribution.

The weight of the coil conductor is approximately 100,000 lbs, almost all of which is copper. A cooldown time of about sixty hours is required to cool the conductor and helium vessel.

Table 1 - MAGNET PARAMETERS	
Design Field	18 kG
Design Current	2000 amps
Stable Current (Calculated)	4200 amps
Resistance Ratio of Copper	170-200
Conductor Dimensions	2-in x 0.1-in
Total Conductor Weight	100,000 lbs
Weight of Superconductor (NbTi)	4000 lbs
Hoop Stress on Conductor	6000 psi

The magnet windings are protected against a sudden release of the stored magnetic energy in the event that a portion of the coil reverts to the normal (i.e., resistive) state. A large resistive region may be caused by the drop of the liquid helium level below the top of the coil and the subsequent loss of cooling. Two means of protection are provided. The first method consists of a "dump resistor" (see Fig. 3) which is always in the electrical circuit, connected in parallel with the coil. Should a resistive region develop in the coil, the power supply will be disconnected from the circuit and the coil current will flow through the dump resistor. The energy stored in the magnetic field is then dissipated in the dump resistor at an initial rate of approximately 0.8 MW (2000 A at 400 V for designed operating conditions).

The second protective measure is simply a large vent line that will automatically relieve pressure well below the pressure rating of the helium vessel. These vent lines are sized to carry away the helium fluid at a rate greater than that which can be generated by the magnet being 100% normal. In this condition the magnet would be generating about 200 kW of power. With the liquid helium removed, the entire coil will become normal and the power will be uniformly

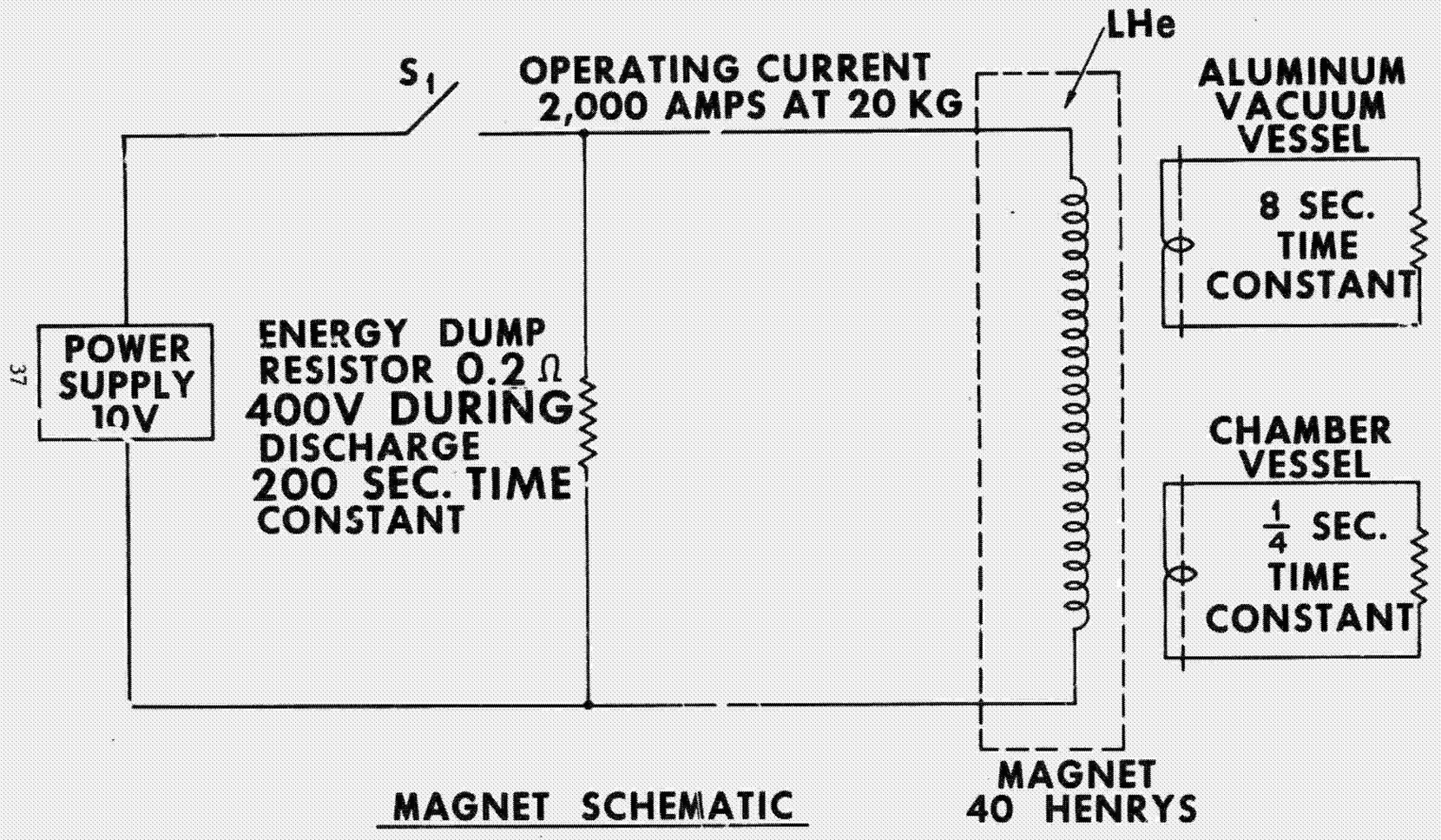


Fig. 3 - Electrical circuit of the superconducting coil

dissipated throughout the windings. If the full-stored magnetic energy of 80 MJ at 18 kG is absorbed by the total thermal mass of the windings, the coil will rise to a temperature of about 90K. Once the liquid helium has been removed from the tank, the temperature rise of the coil will not result in any serious pressure rise of the system.

MAGNET CONTAINER - The magnet coils will be installed in an annular stainless steel vessel which contains liquid helium. This will be surrounded by a refrigerated shield maintained at a temperature of 50K to 70K to intercept heat leakage into the vessel. As may be seen in Fig. 1, openings in the vessel between the upper and lower coils provide passageways for the particle beams to enter the bubble chamber without passing through either the coils or the container material.

The coils and containment vessels will form a single assembly 14.6-ft ID x 18.4-ft OD x 10-ft high, which will be supported from the magnet yoke by eight vertical tubes. These tubes will also provide the passages through which electrical power, refrigeration, and instrumentation are brought to the coils.

Because of the holes in the top of the iron, the net force on the coil assembly centered between the pole faces is expected to be approximately 50,000 lbs downward. The weight of the cryostat will impose an additional load of 200,000 lbs. Vertical adjustment of 1/2-in. in either direction from center is provided to account for mechanical error in coil position, variation in iron permeabilities, and other affects which tend to perturb the downward force. The force on the coil assembly in the vertical direction changes approximately 400,000 lbs per inch of displacement. The eight vertical supports are designed to support one million pounds in tension. The radial instability forces calculated to be approximately 60,000 lbs per inch of radial displacement from magnetic center. This force will be transmitted to the iron by the radial support members (see Fig. 4) located at 90 degree intervals. The system is designed to support a transverse load of 500,000 lbs.

REFRIGERATOR - The steady-state refrigeration requirement of the magnet is estimated to be less than 50 W, but a reasonable cool-down time can be accomplished only with a larger refrigerator. For this reason, and to provide a margin of safety in operation, the refrigeration capacity has been set at 400 W at 4.2K. An additional 500 W of refrigeration at 50K to 70K is provided for thermal shield cooling.

POWER SUPPLY - The power supply capacity is 2000 A at 10V with a current regulation of 0.1%. With the magnet's 40-H inductance, the power supply will charge the magnet at a rate of 0.25 A per second. A full charge will thus be accomplished in about 2.25 hours.

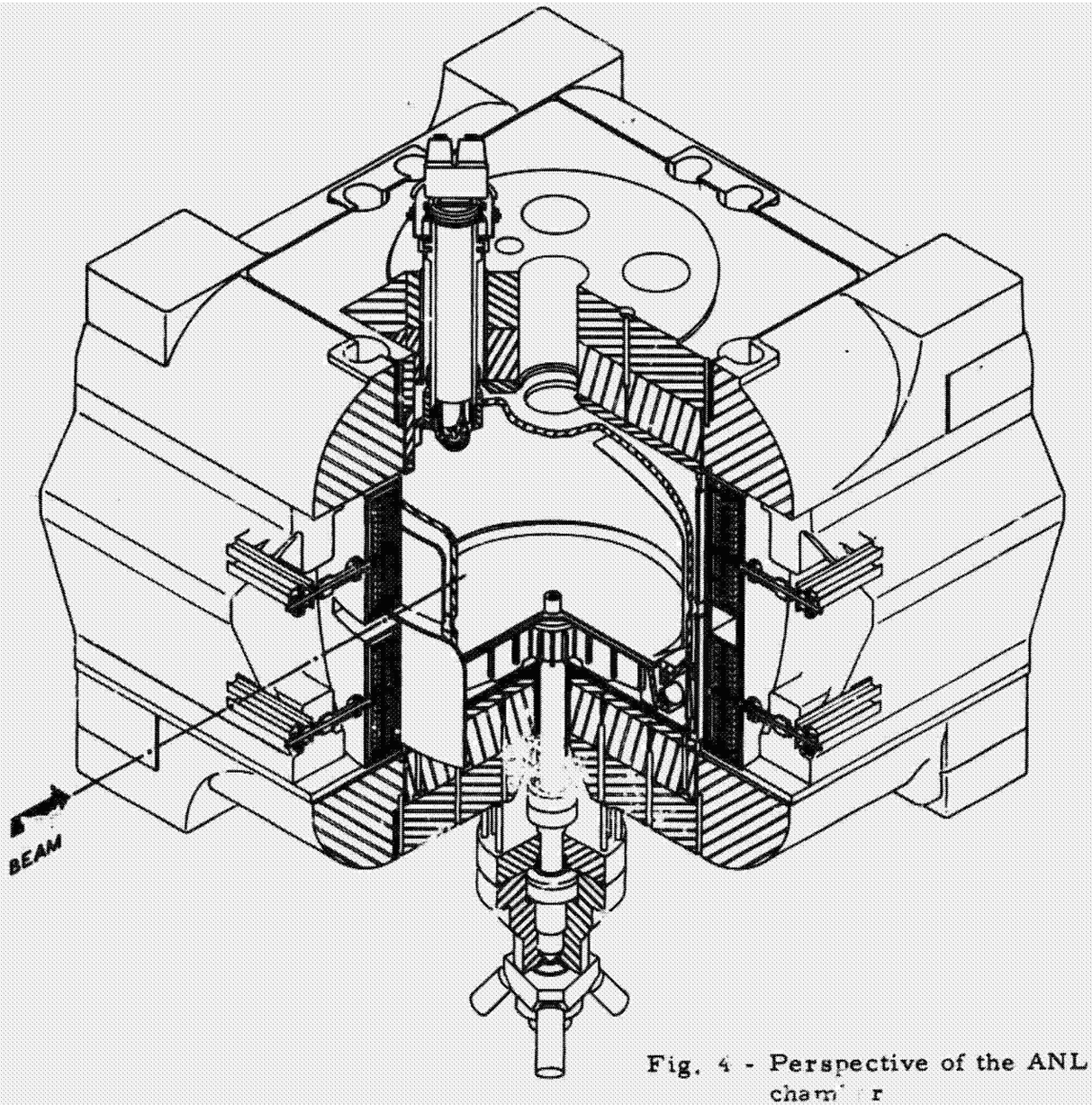


Fig. 4 - Perspective of the ANL 12-ft hydrogen bubble chamber

MAGNET INSTRUMENTATION - The magnet temperature will be monitored throughout the coils during cooldown, using thermocouples down to 40K. At lower temperatures, gallium arsinide diodes will be used.

Potential taps will be placed across every joint within the coils. These will detect bad joints or normal regions between the joints. A separate coil will be wound within the magnet to measure dB/dt. When this is amplified and connected in opposition to the L(di/dt) signal, the resultant signal will represent normal regions within the magnet - even during transient conditions.

REFERENCES

(1) C. Laverick, "Experiments with Superconducting Coils," Proc. of the International Symposium on Magnet Technology, Stanford University, September 1965.

(2) Z. J. J. Stekly, "Terminal Characteristics of Short Samples of Superconductors and Their Effect on Coil Behavior," Proc. of the International Symposium on Magnet Technology, Stanford University, September 1965.

(3) J. R. Purcell and J. M. Brooks, "A Method of Evaluating the Stability of Composite Superconductors," J. of Applied Physics, July 1967.

(4) J. M. Brooks and J. R. Purcell, "Stress Versus Resistivity at Liquid Helium Temperature," Proc. of the IRR, Commission 1, Boulder, Colorado, 1966.

LIST OF FIGURES

1. Cross section of the bubble chamber system.

2. Cross section of the helium container, depicting roughly one-fourth of the winding. On the right is shown a detailed coil wafer.

3. Electrical circuit of the superconducting coil.

4. Perspective of the ANL 12-ft hydrogen bubble chamber.

REVIEW OF SUPERCONDUCTING MAGNETOMETERS*

Victor W. Hesterman, William S. Goree, and Frank M. Chilton
Low Temperature Physics Department
Stanford Research Institute
Menlo Park, California

N69-33956

ABSTRACT

Applications of several of the unique properties of the superconducting state to measure small magnetic fields will be reviewed. The techniques to be described depend primarily on the following properties: zero electrical resistance, allowing the flow of persistent currents; the Meissner effect, which is the expulsion of the magnetic field from the interior of a solid superconductor when it is cooled below its transition temperature; fluxoid quantization; and superconducting tunneling.

We will describe several different magnetometer circuits and discuss their relative merits, methods of signal readout, potential improvements, and intrinsic noise sources. One type of circuit consists of a superconducting pickup coil wound on a core that is thermally switched between the superconducting and normal states. It can make use of the Meissner effect, the quantized-flux effect, or both. Another type of circuit uses the magnetic field dependence of the critical dc Josephson tunneling current. Field sensitivities in the range 10^{-6} to 10^{-9} Gauss have already been obtained.

*Work supported by NASA-Ames Research Center.

I. INTRODUCTION

Much interest has been generated in the last several years in the use of the unique properties of superconductivity to detect and measure extremely small magnetic fields (10^{-6} Gauss and smaller). These basic properties--zero resistance, Meissner effect, quantized flux, and Josephson tunneling--are discussed, and the various types of magnetometer based on these properties are reviewed to clarify their common features and their basic differences. The sensitivity to magnetic fields for actual devices is given and the various sources of noise are considered. The many other applications of superconductivity are too numerous to be covered in this paper, but it is worth mentioning a few to give an idea of how superconductivity is developing as a practical tool.

II. PRINCIPLES UNDERLYING APPLICATIONS OF SUPERCONDUCTIVITY

Zero Resistance

The most evident property of the superconducting state is that of zero resistance. This was the property noticed by Kamerlingh Onnes in 1911 when he discovered superconductivity. The resistance to electrical current flow drops to zero in a fairly narrow region around the transition temperature, T_c. The narrowness of the region of temperature is typical of phase changes, and in a pure Type I superconductor, the transition is narrower than a millidegree.

In superconductors carrying currents, zero resistance results in behavior at all frequencies that is analogous to the high frequency behavior of normal good conductors. The currents are confined to the surface of the conductor. Further, zero resistance with Maxwell's equations implies the exclusion of changes of magnetic flux,

$$\partial \vec{B}/\partial t = 0 \qquad (1)$$

within the body of a superconductor. In Eq. (1) $\vec{B}$ is the magnetic field and t is time.

Meissner Effect

An even more general magnetic field exclusion is observed in superconductors. The Meissner effect pertains to

$$\vec{B} = 0 \qquad (2)$$

inside the superconductor. Equations (1) and (2) apply deep within the body of a superconductor. Near a surface an exponential decay

$$|B(z)| = |B(0)|e^{-z/\lambda} , \tag{3}$$

is observed. In Eq. (3), z measures the distance from the surface into the superconducting sample and λ is the London penetration depth, which is typically of the order of 1000 Å. The flux exclusion represented by Eqs. (1-3) is the principle behind superconducting magnetic shields. By switching a superconducting sample back and forth from superconducting to normal, the flux exclusion of Eqs. (1-3) can be used to measure magnetic field strengths.

Fluxoid Quantization

The superconducting state is a macroscopic quantum state. Thus, classical qua.tities like the velocity of the current carriers, the electrons, are defined in the sense of an expectation value using the wave function for the superconducting state. Just as in the quantum behavior of atomic systems, the existence of the wave function implies various interference effects. One of these interference effects is quantized flux. Quite analogous to the Bohr-Sommerfeld quantization condition, a superconductor obeys

$$\oint (2m\vec{v}_s = 2\frac{e}{c}\vec{A}) \cdot d\vec{x} = nh \tag{4}$$

In Eq. (4), $\vec{v}_s$ is the superconducting electron velocity, $\vec{A}$ is the electromagnetic vector potential, and k is Planck's constant. The electron charge and mass are -e and m, respectively. They appear as 2e and 2m due to the electron pairing that causes superconductivity.

In a wide variety of circumstances, one can consider a contour for this line integral that is deep within the body of a superconducting sample where $v_s = 0$. The second term of the integral is proportional to the magnetic flux,

$$\oint\vec{A}\cdot d\vec{x} = \int\nabla x\vec{A}\cdot d\vec{s} = \int\vec{B}\cdot d\vec{s} ,$$

linking the circuit. In these circumstances, then, the flux is quantized (flux quantum unit = $\Phi_o = hc/2e \simeq 2 \times 10^{-7}$ Gauss-cm^2).

Josephson Tunneling

Another interference effect associated with the superconducting state can be seen in the tunneling that takes place from one superconductor to another through a nonsuperconducting layer. Such a system is usually called a "Josephson junction." The phase of the superconducting wave function on crossing the nonsuperconducting barrier satisfies two equations.

$$\partial\Phi/\partial t = 2eV \tag{5}$$

$$\Phi = \frac{2m}{\hbar}\int_1^2 \vec{v}_s\cdot d\vec{x} - \frac{2e}{\hbar c}\int_1^2 \vec{A}\cdot d\vec{x}, \tag{6}$$

where Φ is the phase difference and V is any voltage across the junction. The essential property of these junctions that makes them so useful is that the magnetic field can penetrate the junction thus providing us with a tool for changing the phase of the superconducting wave function. One aspect of this is called "the dc Josephson effect." In this effect, the voltage across the junction is zero, but a supercurrent can flow if there is a magnetic field penetrating the junction, or if a phase difference is imposed, say by an external source of current. This possibility of a supercurrent in the absence of voltage is implicit in Eqs. (5) and (6). For a junction that is small enough, the maximum zero voltage current flowing, I_{max}, across the junction has a dependence on the external magnetic field similar to that in Frauenhofer diffraction.

$$I_{max} \propto \left| \sin \pi\Phi_J/\pi\Phi_J \right|, \tag{7}$$

where Φ is the flux in the junction measured in units of the flux quantum hc/2e.

Two thin junctions connected in parallel exhibit a diffraction-interference pattern

$$I_{max} \propto 1/\pi\Phi_J \left|\sin \pi\Phi_J \cos[\pi(\Phi_c-\Phi_J)] + \sin^2 \delta\frac{\pi}{2} \sin[\pi(\Phi_c-2\Phi_J)]\right| \tag{8}$$

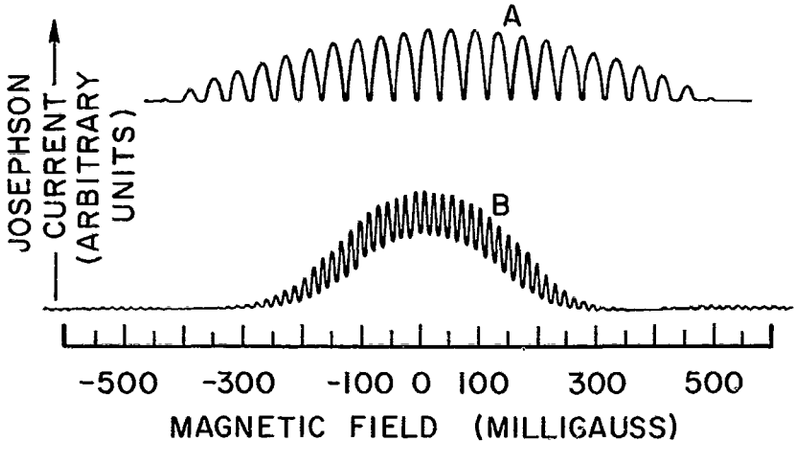
In Eq. (8), Φ_J is now the average of the flux in each of the two junctions, while δ is the flux difference and Φ_c is the total flux through the closed loop or circuit containing the two junctions.

If the junctions are equal, Eq. (8) reduces to the usual optical diffraction-interference formula

$$I_{max} \propto \left| \sin \pi\Phi_J/\pi\Phi_J \cos[\pi(\Phi_c-\Phi_J)] \right|. \tag{8'}$$

If $\delta \neq 0$, then Eq. (8) is not the same as the corresponding optical formula, the distinction being between the real part and the modulus of the complex integral for I_{max}. Note that $\delta \neq 0$ implies that the interference is not complete. At an interference minimum $I_{max} \propto \sin^2 \delta\frac{\pi}{2}(\cos \pi\Phi_J)/\pi\Phi_J$ instead of zero. Because of the difficulties inherent in fabricating junctions, an incomplete interference is the usual situation (see Fig. 1). In principle, the incomplete interference could also be used as a direct measure of field gradient.

If a voltage is present, which from Eq. (5) implies that the phase is time-dependent, rapid current oscillations across the junction are observed.



THE FIELD PERIODICITY IS 39.5 AND 16mG FOR A AND B, RESPECTIVELY. APPROXIMATE MAXIMUM CURRENTS ARE 1mA(A) AND 0.5mA(B). THE JUNCTION SEPARATION IS W = 3mm AND JUNCTION WIDTH ω = 0.5mm FOR BOTH CASES. THE ZERO OFFSET OF A IS DUE TO A BACKGROUND MAGNETIC FIELD.
(AFTER JAKLEVIC, LAMBE, SILVER, MERCEREAU) REF. 27

TA-375522-7

Fig. 1 Experimental Trace of I_{max} versus Magnetic Field Showing Interference and Diffraction Effects.

This is called the "ac Josephson effect." The frequency of these current oscillations obeys the relation

$$\hbar\omega = 2eV, \tag{9}$$

which follows directly from Eq. (5).

The Josephson interference effects reduce measurement of magnetic fields to counting fringes and reduce measurement of voltages to frequency determinations, both of which can be done with extreme accuracy.

III. FLUX-MOTION MAGNETOMETERS

Basically the flux-motion magnetometer generates an emf by changing the coupling between the magnetic field being measured and a sense coil. One method makes use of a superconducting core inside (or near) the sense coil. This core is periodically heated and cooled between the superconducting and normal states. This thermal switching (which can be at kHz frequencies) causes a flux change in the sense coil, which induces an emf in the coil because of the Meissner effect, the quantized-flux effect, or both.[1,2] For the Meissner effect, the amplitude of this emf will be linearly related to B, the magnetic field at the modulator; whereas, for the quantized-flux effect, it will consist of a series of individual quantum steps as shown in Fig. 2. Application of the quantized-flux effect requires that the core be multiply connected (e.g., a hollow cylinder) and small enough so that the individual quantum-flux steps will not be washed out by noise. (The quantized-flux modulator that has been used at Stanford Research Institute was about 0.025 mm in diameter, whereas the Meissner core was about 1 mm in diameter.) If the quantized-flux core has a significant wall thickness compared to the London penetration depth [λ in Eq. (3)], then both the Meissner effect and the quantized-flux effect will be obtained as shown in Fig. 2(c). A magnetometer that uses only the quantized-flux effect generally will not be absolute, since only relative changes about a single quantum step can be detected. This can be overcome if the core is cooled in a zero field environment and the number of quantum steps are counted as the field is applied, or if the output is nulled so that operation is always on one quantum step, or if B is less than Φ_o/A.

Another method of changing the flux linking the coil is to mechanically move a superconducting body in the vicinity of a sense coil. This technique is being used at Stanford University by Professor Fairbank's group.[3] Their approach is to use a superconducting layer on an oscillating quartz crystal placed close to a coil. Both planar and cylindrical geometries are being investigated.

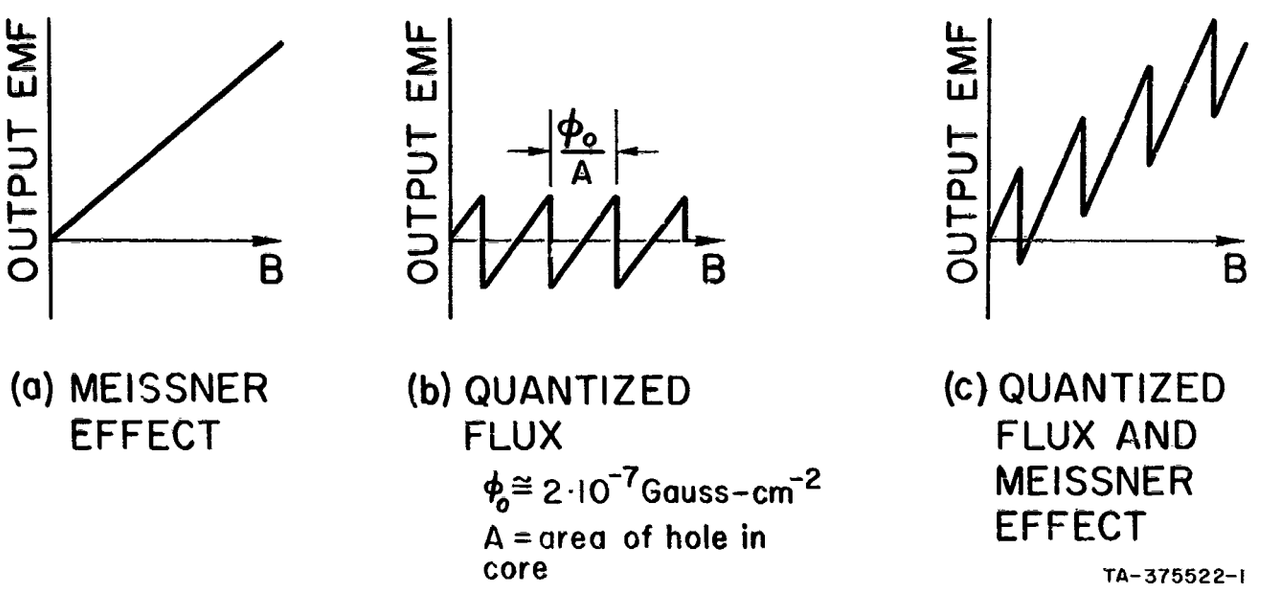


Fig. 2 Output EMF versus Magnetic Field for Flux-Motion Modulators

These various methods of generating an emf in a superconducting coil can be treated alike as far as signal readout is concerned. The general idea is to get the maximum voltage output prior to room temperature amplification so that the maximum signal-to-noise ratio will be obtained. The ultimate sensitivity of a superconducting magnetometer is limited by intrinsic or by intermediate-state noise in the superconductor. The readout circuits that have been used are not basically unique, but they do make use of superconducting components, which give them some unusual qualities. In ordinary electronic circuits, a signal source has some internal resistance associated with it. In the cases being considered here, this internal resistance can be made to approach zero. (This assumes that eddy-currents in the modulator core can be reduced arbitrarily close to zero.) Thus, the load and source resistance cannot be matched. The inductive reactance of the source can be canceled by proper turning with capacitive reactance. The maximum output, therefore, depends on the circuit Q (Q can be as high as 10^4). The maximum Q may be limited by that which can be tolerated from a circuit stability viewpoint or by how long a time constant can be tolerated. (A high Q requires that the measured field is not changing very fast, i.e., the time constant $\tau = 2Q/\omega$, where $\omega = 2\pi$ times the frequency of the measured field.) The sense coil and connecting wires can have zero resistance so that losses and Johnson noise will approach zero. This zero resistance also allows us to obtain very high Q tuned circuits for high voltage amplification; if necessary, a superconducting capacitor also can be used to increase Q. Transformers can be wound with superconducting wire so that impedances can be matched conveniently without lowering the Q. Superconducting shields can be used to prevent extraneous pickup in the transformer or other parts of the circuit. The readout circuit used at SRI is shown in Fig. 3. In this circuit the tuning is accomplished in the secondary of the transformer because this requires a smaller capacitance.

The maximum power output of the Meissner or quantized-flux magnetometer prior to amplification (assuming zero source resistance and an optimized circuit) is given approximately by[3,4]

$$P_o = KB^2 V_c \alpha^2 f Q, \tag{10}$$

where K contains numerical constants and the coupling coefficient of the transformer, B is the magnetic field being measured, f is the frequency of modulation, V_c is the volume of the sense coil, and α is the percent modulation of its inductance. This equation states that P_o is proportional to the change in magnetic field energy each cycle (i.e., $B^2 V_c \alpha^2$) times the Q of the circuit, times the number of times per second that this energy is changed. It is, therefore, advantageous to make f and α as large as possible by proper core design.

Eddy-currents that flow in the core when it is in the normal or the mixed state retard the motion of the magnetic flux within the core. This limits the maximum frequency of modulation for a given α. Thermal time

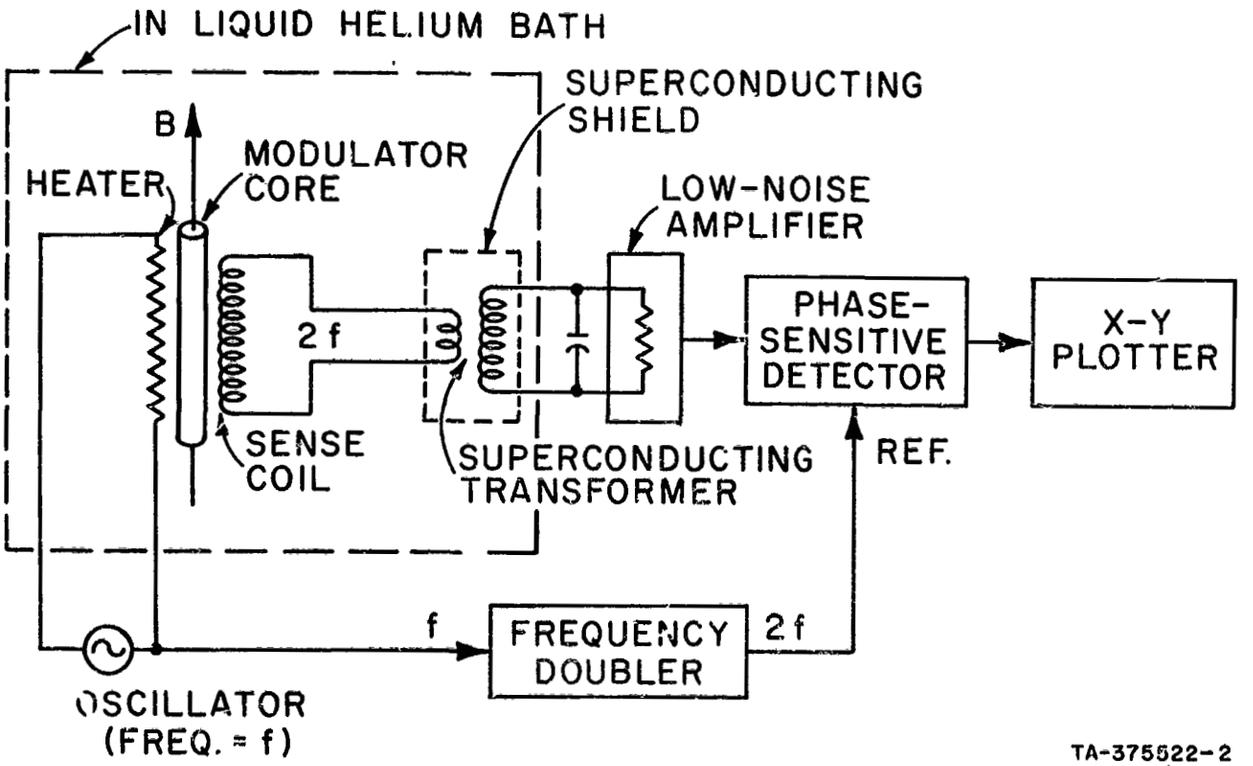


Fig. 3 Magnetometer Readout Circuit used at Stanford Research Institute

constants also can limit the modulation frequency. The Meissner cores tested at SRI have been thick-walled cylinders cast on a coaxial resistive heater. This geometry was used because it was easy to construct, and the initial emphasis was on circuit operation and feasibility. Figure 4 shows the construction of these cores. The thermal time constants for this type of core are of the order of 5 μsec; however, this geometry is quite unfavorable as far as eddy-currents are concerned, and the normal state L/R eddy-current time constants are of the order of 0.5 msec (in the partially superconducting state, L/R would be longer). Experimentally, the modulation dropped significantly at about 500 Hz.[4] It should be possible to build a laminated core of superconducting and insulating layers that would reduce eddy-currents and thereby greatly improve the $\alpha^2 f$ product.

The sensitivity of all of the flux motion magnetometers can be increased by use of a magnetic field amplifier. This consists of a large superconducting single-turn coil for sensing the B field, which is coupled to the magnetometer's previous sense coil. Either direct connection[3] or mutual inductive coupling[2] can be used as shown in Fig. 5. The loop made up of coils 1 and 2 is entirely superconducting so that a persistent current, i, will flow, which is equal to

$$i = \frac{N_1 [A_1 (B-B_0) + \Phi_o]}{L_1 + L_2}, \tag{11}$$

where N_1 is the turns, A_1 the area, and L_1 the inductance of coil 1 and N_2, A_2, and L_2 the same for coil 2; B_0 is the field present when the loop first became superconducting (B_0 can be made zero by momentarily heating a small region of this persistent loop while coils 1 and 2 are in zero magnetic field) and Φ_o is the flux quantum. Normally, $A_1(B-B_0) \gg \Phi_o$. The field B_2 that this current i produces at the modulator is given by

$$B_2 = L_2 i / N_2 A_2 . \tag{12}$$

Therefore, the field amplification factor, A_f, is equal to

$$A_f = B_2/B-B_0 = N_1 A_1 L_2 / N_2 A_2 (L_1+L_2) . \tag{13}$$

However, L_1 is related to A_1 and L_2 to A_2. Maximization of A_f must include these relationships, which depend on the particular coil geometry assumed. Large amplification can be obtained by making coil 1 large in area and of one or few turns and using wide strap conductors to keep its inductance, L_1, small. Field amplification factors of 50 have been obtained with quantized-flux circuits used at SRI, and significantly higher factors should be obtainable. The leakage inductance of the wires connecting coils 1 and 2 must be kept small compared to L_1 and L_2 so that none of the flux, BA_1, will be lost due to leakage flux. Field amplification is important because it increases the signal before the noise of the modulator is introduced. There are three possible disadvantages in the use of field amplifiers: spatial resolution is decreased; the probe is somewhat bulkier; and in the Meissner-effect, the mechanical motion, and the single Josephson magnetometers, the absolute feature

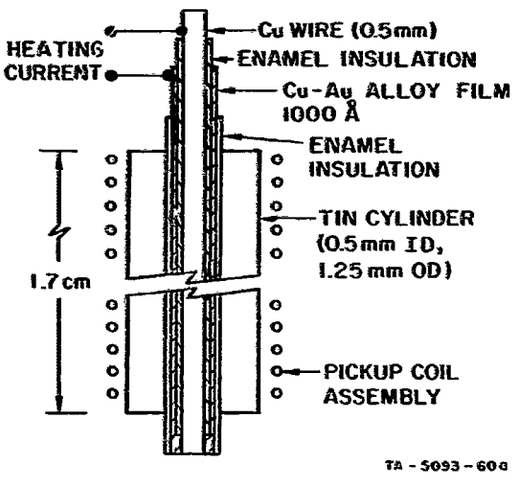


Fig. 4 Meissner Modulator Construction

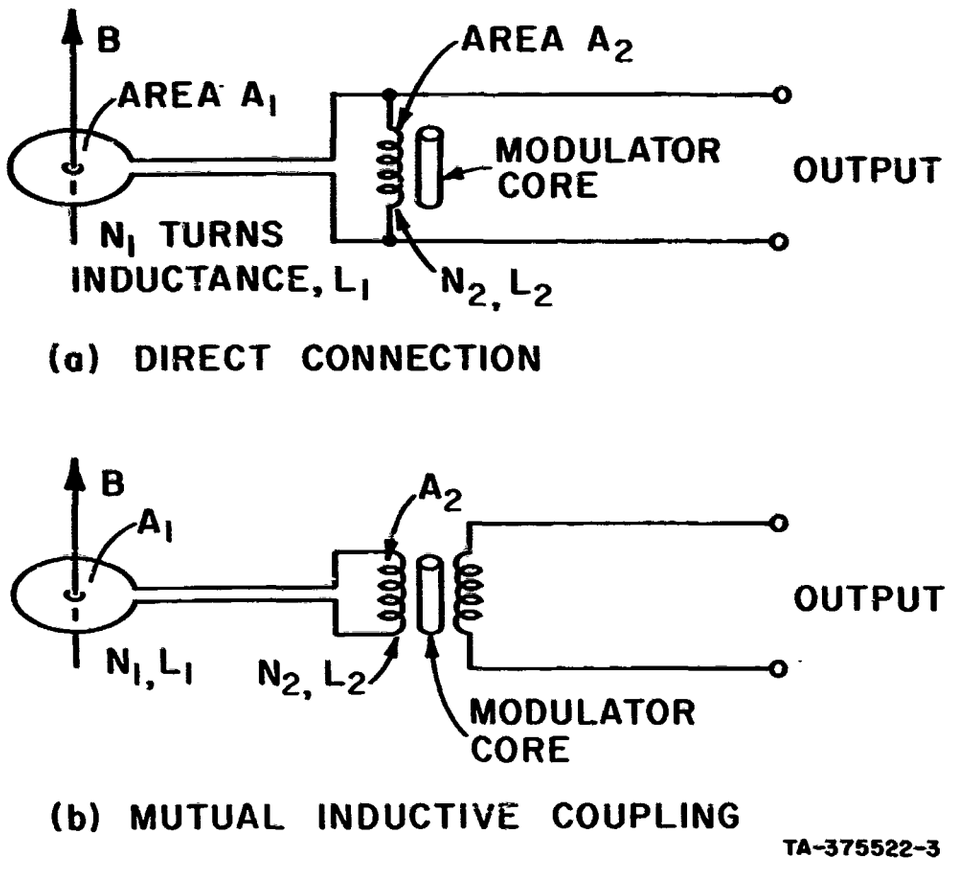


Fig. 5 Field Amplifier for Flux-Motion Magnetometer

is sacrificed--i.e., only a change in magnetic field can be measured unless the magnetometer is cooled in zero field or if the sense coil is rotated 180 degrees. These are not serious limitations for most applications.

If we rewrite Eq. (10) to include the field amplification factor, A_f, we obtain

$$P_o = KB^2 V_c \alpha^2 f Q A_f^2 \quad . \tag{14}$$

Increasing V_c will reduce the maximum obtainable A_f as well as the $\alpha^2 f$ product. Thus, determination of the optimum modulator size becomes very complicated. In magnetometers that have been built, the quantized-flux modulators have been much smaller than the Meissner-effect modulators (0.025 mm vs 1 mm in diameter),[4] but they have had a much higher $\alpha^2 f$ product[3,4] (about 0.1×10^5 Hz vs. very roughly, 0.5×300 Hz).

The quantized-flux modulator makes use of the volume of the hole of the modulator core and, therefore, will have some advantage as far as noise and eddy-currents are concerned. It is currently somewhat more difficult to build reliable quantized-flux modulators, but this might be improved by future developments. The first quantized-flux modulators were intentionally made very small so that the individual quantum steps could best be resolved for the basic investigation of flux quantization.[5] We note that

$$B = \Phi_o / A \quad , \tag{15}$$

where Φ_o is the flux quantum unit (2×10^{-7} Gauss-cm^2) and B, the field in the modulator core, is the quantity sensed. A small area, A, results in a larger and more easily measurable B for an individual quantum of flux. Now that flux quantization is to be used for an instrument, the very small size does not necessarily give optimum magnetic field sensitivity.

If the signal-to-noise ratio is limited by the noise of the room temperature amplifier, then improvement may be obtained by using superconducting properties to construct a low frequency (i.e., below 10 MHz) parametric amplifier with which power gain can be achieved at liquid helium temperatures. Its primary advantage is the possibility of achieving high gain with very low noise. The time varying reactance can be a modulator very similar to the sense coil and core used in the magnetometers discussed above. Although parametric amplification is not new, its application to low frequency (i.e., $<$ 10 MHz) amplification at liquid helium temperatures is very new and has exciting possibilities,[6,7] not only for magnetometers but for other devices where very low noise amplification is important (i.e., infrared bolometers). Perhaps, the main reason that parametric amplification has not been used at low frequencies is the lack of a good high Q, time-varying reactance and high Q circuits at these low frequencies. Superconductivity can easily provide both of these requirements. Very little experimental work has been done to date in this area.[7]

IV. JOSEPHSON JUNCTION MAGNETOMETER

The property that makes the Josephson junction so suitable for use as a magnetometer is its high sensitivity to magnetic fields. A very small magnetic field, B, applied to the junction alters the phase difference of the superconducting wave function, thereby changing the junction's critical current I_c [I_c is the tunneling current above which a voltage appears across the junction as given by Eq. (7)]. Thus, if a dc bias current is applied that is slightly above I_c, a change in voltage results from an applied field change. This is illustrated in Fig. 6 where the V-I characteristic is shown for two different values of B. Not all actual junction characteristics appear as shown in Fig. 6 because of nonuniformities,[8] impurities in the junction,[9] and perhaps other unidentified reasons.

Josephson junctions can be constructed by several techniques. One method is to vapor deposit a superconducting layer, which is then oxidized to form a layer of oxide about 20 Å thick. Another superconducting metal film is then deposited on top of the oxide layer, thereby forming a planar junction. Junctions also can be made by point contact[8,10] and by narrow constrictions[11] in a superconducting thin film. A very simple method of constructing a tunneling junction was suggested by Clarke.[12] A ball of solder (using conventional tin-lead radio solder) is cast around a 2-mil niobium wire that has been stripped of insulation and allowed to oxidize. The solder will not wet the wire but can be made to encompass it, thus forming a cylindrical junction. These have been called SLUGs.[12] In a SLUG, the cylindrical field in the junction, B_j, is established by passing a current through the center wire. The cylindrical junction has the virtue of being shielded from stray magnetic fields by the superconducting solder.

Since the insulation is so thin, irregularities and imperfections can be a serious problem for any type of Josephson junction. Control of the insulation thickness is desirable since the critical current is an exponential function of the thickness. Thicker insulation results in a lower critical current. Typical critical currents are from 1 to 500 μa.

Electrical readout from a Josephson junction can best be accomplished by replacing the dc bias current (see Fig. 6) with a sinusoidal current that is centered about I = 0 and whose amplitude is adjusted so that its peaks occur on the steep part of the V-I characteristic. The amplitude of the resulting ac output voltage will be related to the magnetic field. This ac voltage can be amplified with a high Q tuned circuit and then fed to a phase-sensitive detector in a manner similar to that shown in Fig. 3 for a flux-motion magnetometer.

Two Josephson junctions can be used to build a more sensitive magnetometer, as shown in Fig. 7. In this case, the current I that can flow before

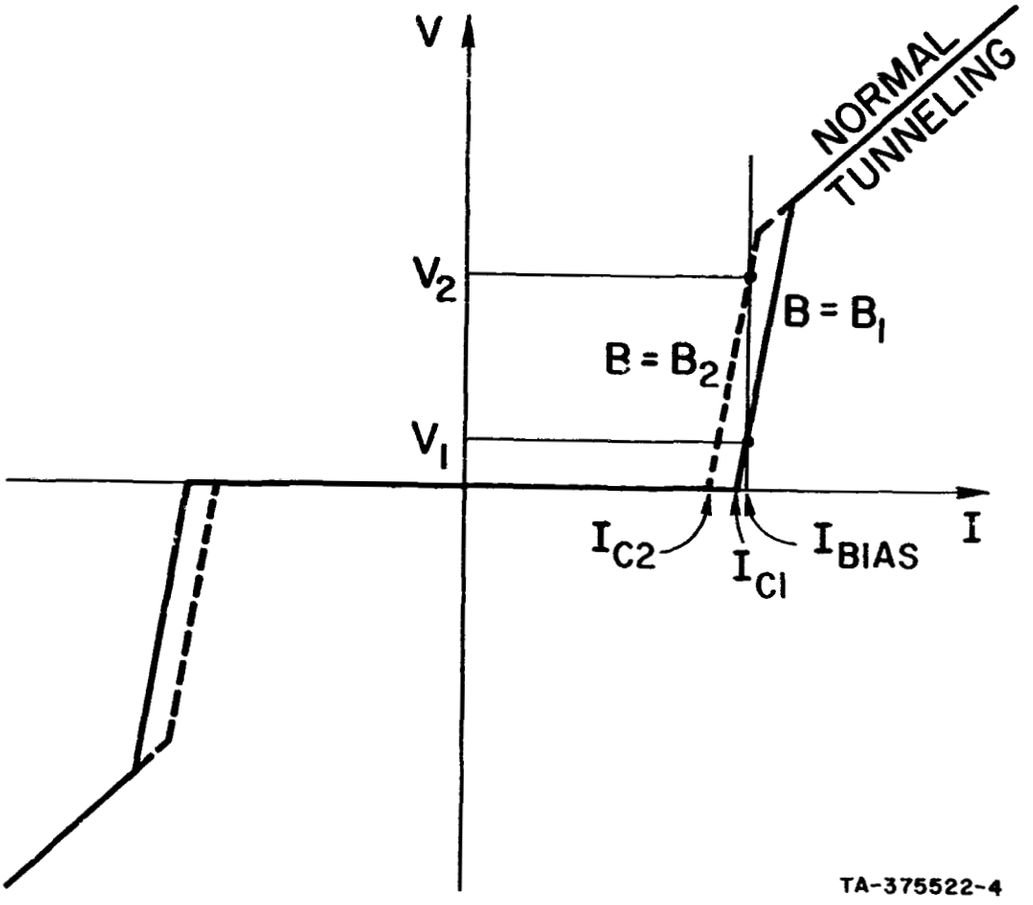


Fig. 6 V-I Characteristic of a Josephson Junction

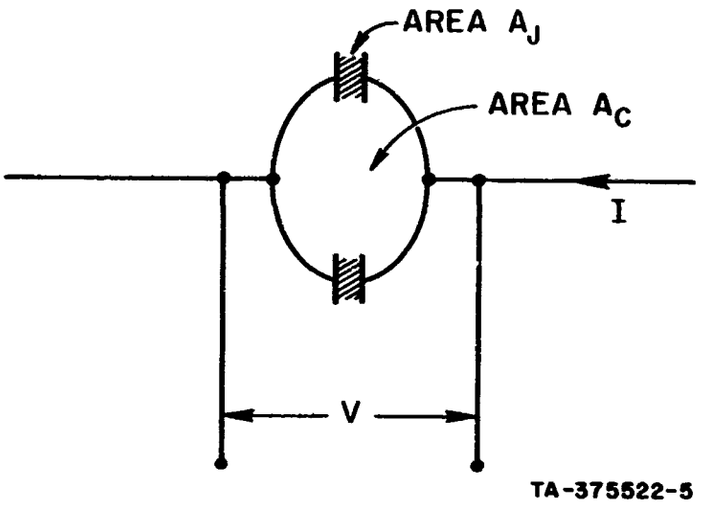


Fig. 7 Magnetometer Using Two Josephson Junctions

a voltage, V, is developed is given by Eq. (8). The increased sensitivity compared to the single junction is a result of the interference effect since A_c is greater than A_j. The active area, A_j, is limited by an effect similar to the Meissner effect,[13] i.e., only the edges of a large junction are effective. The maximum area, A_c, is limited by the current change, $\Delta I = \Phi_o/L$, which can be detected with the existing noise level.[8]

Greater sensitivity can be achieved if the magnetic field is sensed with a one-turn superconducting coil and the single or double Josephson junction is used to sense the magnetic field due to this current.[13] This is illustrated in Fig. 8 for a cylindrical junction (SLUG). Since the flux is conserved in the superconducting coil, the applied field, B, times the coil area, A (shaded area above the axis), must be equal and opposite to the flux produced by I_p (the cross-hatched area below the axis). Note that the field in the junction due to I_p (i.e., B_j) is much larger than the applied field. Essentially, this is a field amplifier coil similar to those described for the flux-motion magnetometer described above (see Fig. 5). It senses a large amount of the uniform magnetic field and concentrates it in a small region near the wire. The field amplification factor, A_f, for a cylindrical junction on a round wire is given by

$$A_f = B_j/B = A/2\pi rL' \quad , \tag{16}$$

where L is the total inductance of the loop, A its area, and r the radius of the wire. This assumes that the loop was made superconducting in zero field. The junction can be separated from the loop by use of a low-inductance strip transmission line (a pair of closely-spaced strips) and placed in a superconducting shield.[4] A field amplifier built at SRI[4] had a measured amplification factor of about 20. Larger values should be possible.

V. SENSITIVITY AND NOISE

The Meissner-effect magnetometers studied at SRI probably exhibit the maximum noise of any of the devices we are considering. With these magnetometers we have measured fields as low as 10^{-6} Gauss without the use of a field amplifier. The same detectors also have been used in a system for measuring static magnetic susceptibility where sensitivities as good or better than the best magnetic balance have been obtained.[2] The quantized-flux magnetometer is approximately one order of magnitude more sensitive in its present state than the Meissner-effect devices we have studied, giving a sensitivity of 10^{-7} to 5×10^{-8} Gauss.[2] Even better sensitivities have been obtained with Josephson junction detectors. Weak-link tunneling junctions have been used in various configurations to obtain magnetic field sensitivity as good as approximately 10^{-10} Gauss.[10] The measurements by Vant-Hull[14] (discussed earlier) of thermal magnetic noise in superconductors were made using a double junction Josephson interferometer where the instrument noise level

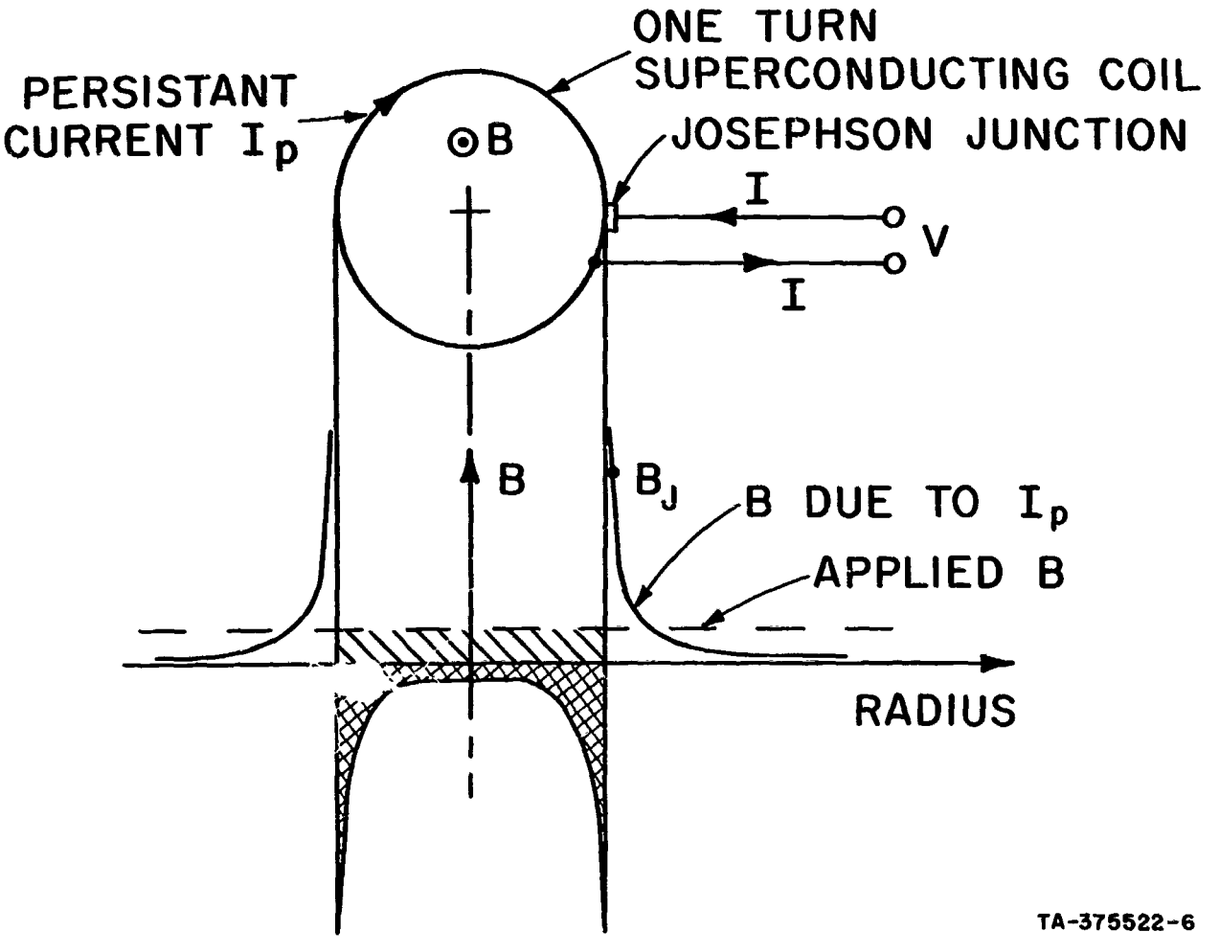


Fig. 8 Use of a Field Amplifier Coil for a Josephson Junction Magnetometer

was approximately 1/1000 of a flux unit. This noise level corresponded to voltage fluctuations of 10^{-18} to 10^{-19} volt in the sample. Clarke[12] has designed a very simple technique for building Josephson junction devices and has constructed magnetometers with sensitivities of 10^{-8} Gauss and dc voltmeters with sensitivities as good as 10^{-14} to 10^{-15} volt. We have used Clarke's technique to build a magnetic field gradiometer with which field gradients of approximately 10^{-7} Gauss-cm have been measured.[1]

Although superconducting instrumentation is a new area of research and development, devices several orders of magnitude more sensitive than those possible with other techniques have been built and demonstrated, both in the laboratory and, in some cases, in the field.

A thorough understanding of the noise associated with superconducting devices is needed before the ultimate sensitivity can be predicted. This noise can be considered in three separate categories:

1. External noise produced by external or environmental sources, such as rf pickup and temperature fluctuations.

2. Transition or intermediate state noise caused by operating the superconducting device in, or switching it through, the state between normal and superconducting.

3. Intrinsic noise characteristic of the superconducting state.

The noise from external sources has set the most severe limitations on sensitivity in most superconducting devices. In the following discussion, external noise includes noise from device components that are normal metals and from superconductors heated above the critical temperature during operation of the device.

The response of Josephson junctions is very sensitive to electromagnetic radiation, especially in the microwave frequency range, and special care must be used to avoid external noise from radio stations, etc. High-frequency filters in all electrical leads to the junction have been used by Mercereau[15] to reduce rf pickup.

Recent measurements by Vant-Hull et al.[14] of the fluctuations in magnetic field near a Type I superconductor both above and below its critical temperature indicate that the Johnson noise is reduced below the noise level of the measuring instrument at the superconducting transition, $\simeq 10^{-18}$ volt. These measurements can be used to set a lower limit on the noise spectrum of quantized-flux and Meissner devices, since in these devices, a superconducting element is intentionally heated above its critical temperature once each cycle. While the temperature is $> T_c$, this thermal noise certainly will be present. Additional noise will be caused by eddy-currents. We feel that the noise due to

eddy-current shielding of the flux motion in Meissner-effect magnetometers is a most serious limitation. This is because the sensitivity of a Meissner magnetometer depends on the rapid movement of magnetic flux contained within the core by thermally cycling a superconducting core. Core materials with a large Meissner effect, i.e., Type I superconductors such as tin and indium, also have a very low residual resistivity, leading to large eddy-currents and efficient shielding.

Another noise source associated with thermally-switched superconducting devices is the boiling of liquid helium in contact with the device and the associated temperature fluctuations. Noise of this type has been identified by Johnson and Chirlian[16] in cryotrons, by SRI in the Meissner-effect magnetometers,[4] and by Bussieres and Leonard[17] in heated wires immersed in liquid helium. Pierce[3] has found that this type of noise can be reduced in quantized-flux magnetometer circuits by mounting the modulator horizontally in the helium bath and winding the pickup coil with space between turns so that gas bubbles can readily escape from the space between the modulator and the pickup coil. Also, the diameter of the pickup coil is made about twice that of the modulator. This allows helium to circulate freely around the modulator, and the corresponding reduction in noise and increased operating frequency appears to more than compensate for the reduced coupling between the modulator and the pickup coil.

An example of transition noise is fluctuations in the Meissner effect from cycle to cycle, possibly caused by flux trapping. This may produce noise analogous to shot noise in semiconducting devices, because the flux is quantized and deviations in the amount of flux excluded each cycle would be in the integral flux units. A possible intermediate state noise source in quantized-flux magnetometers is associated with the transitions at $\pm$ half integral flux quantum. At these points the current must change from plus to minus its maximum value. We have observed a definite width to this transition[2] but have been unable to analyze it precisely.

The rate of the flux exclusion process used with the Meissner-effect magnetometers is drastically limited by eddy-currents, especially during the transition to the superconducting state when the resistance approaches zero. Any variation in these eddy-currents would appear as fluctuations in the emf generated by switching the modulator. Josephson junction devices depend, in general, on the operating characteristics of the junction or junctions when the tunneling current exceeds the critical or zero voltage value. As we have discussed earlier, when a tunneling junction is operating in the region above the critical current, the tunnel current oscillates at the Josephson frequency,

$$\nu = 2eV/h \ , \qquad (17)$$

and the phase of the paired electrons continually changes in time. Burgess[18] and Scalapino[19] have discussed the possible thermal and shot noise power spectrum for tunnel junctions. Also the fluctuation of the superconducting order

parameter has been discussed by these authors and by Ferrell.[20] Kamper[21] has noted that the line width of the high-frequency radiation from a Josephson junction is an extremely sensitive measure of the Johnson noise in the voltage bias. He has described the use of this line width as an absolute thermometer for temperatures as low as a millidegree. Of course, this is not an intrinsic noise source; but since the junction must be biased at a finite voltage, it is a practical limit to sensitivity.

Noise intrinsic to the superconducting state has received very little experimental or theoretical study. Several experiments to measure noise in persistent currents have served only to set limits on the noise power.[22,23] A recently published paper by van Ooijen and van Gurp[24] reports observed noise which they have characterized as shot noise. This is presumably due to random motion of the quantized fluxoids. Vant-Hull et al.[14] studied the thermal-magnetic noise of niobium above and below its critical temperature, T_c, and found little decrease in the noise at T_c. This is in contrast to their studies of Type I superconductors where the noise decreased by almost two orders of magnitude at T_c. These noise studies and the reproducibility and stability of junction construction have not advanced far enough to calculate accurately the noise spectrum of a given device, but progress is being made in this direction.

VI. GENERAL APPLICATIONS AND FUTURE PROSPECTS

We have described the physical principles involved in superconducting devices and specific applications of these principles to devices for measuring magnetic fields and, in several cases, for measuring very small voltages. Of course, these unique properties of superconductors have been applied to other areas of instrumentation and device development far too numerous to cover in this paper. A few examples of these other applications will suffice to give a general idea of the possible widespread use.

The zero resistance property has been used in the construction of high field solenoids, electromagnetic cavities, and computer elements. Quantized flux has been used for computer elements and for the production of true zero magnetic field environments. Josephson tunneling has been used as a radiation detector in the microwave and infrared spectrum, where power as small as 10^{-13} watt for a 1-cycle bandwidth has been detected. In a recent experiment tunneling has been used to measure the fundamental constant e/h about one order of magnitude more accurately than previously known.[25] A rather complete survey of the literature on superconducting devices, which includes numerous references on those and other applications, was published in March 1967 and lists approximately 1300 references of specific devices, patents, and research related to devices.[26] This indicates the considerable amount of basic research and experimental data available to those interested in applying the unique properties of superconductors to devices.

Much work remains to be done before the ultimate performance of superconducting devices can be realized. Probably the most significant area for investigation is that of noise and noise limitations. We have described several of these factors such as thermal noise, shot noise, thermal fluctuation in tunneling junctions, eddy-current noise in thermally-switched superconductors, and pickup from external sources. In general, this description is not complete in that exact equations or design formulas for calculating the noise power spectrum are not yet available. In many cases, the construction techniques of the devices introduce considerable error into the performance and make it even more difficult to compute an accurate noise spectrum.

We feel that the prospects for future application of superconductivity to devices are very bright. Magnetic field sensitivities as good as 10^{-12} to 10^{-13} Gauss, bolometer sensitivities to the order of 10^{-15} watt/cycle bandwidth, and voltage sensitivities as good as 10^{-19} volt may be possible once a better understanding is obtained of the noise properties of superconductors.

REFERENCES

1. Goree, William S. and Troy W. Barbee, Jr., "Sensitive Instruments Using Superconducting Properties," Proc. Int'l. Cryogenic Engr. Conf., Kyoto, Japan, April 1967, to be published.

2. Deaver, Jr., Bascom S. and William S. Goree, "Some Techniques for Sensitive Magnetic Measurements Using Superconducting Circuits and Magnetic Shields,"Rev. Sci. Instr. 38, 311 (1967).

3. Pierce, J.M., "A Persistent-Current Magnetometer with Novel Applications," Proc. Symposium on the Physics of Superconducting Devices, Charlottesville, Virginia, April 1967, to be published.

4. Goree, W.S., B.S. Deaver, Jr., V.W. Hesterman, and T.W. Barbee, Jr., "Cryogenic Magnetometer Development," Final Report for NASA-Ames Research Center, Contract NAS 2-2088, SRI Project 5093, Stanford Research Institute, Menlo Park, Calif., June 1967.

5. Deaver, Jr., Bascom S. and William M. Fairbank, "Experimental Evidence for Quantized Flux in Superconducting Cylinders," Phys. Rev. Letters 7, 43 (1961).

6. Ries, Roger P. and C.B. Satterthwaite, "A Superconducting Parametric Amplifier for the Measurement of Small dc Voltages," Proc. Symposium on the Physics of Superconducting Devices, Charlottesville, Virginia, April 1967, to be published.

7. Kamper, R.A., private communication.

8. Zimmerman, J.E. and A.H. Silver, "Macroscopic Quantum Interference Effects through Superconducting Point Contacts," Phys. Rev. 141, 367 (1966).

9. Jaklevic, R.C. and J. Lambe, "Molecular Vibration Spectra by Electron Tunneling," Phys. Rev. Letters 17, 1139 (1966).

10. Forgacs, R.L. and A. Warnick, "Digital-Analog Magnetometer Utilizing Superconducting Sensor," Rev. Sci. Instr. 38, 214 (1967).

11. Parks, R.D., J.M. Mochel, and L.V. Surgent, Jr., "Critical-Field Behavior of a Microscopic Superconducting Bridge," Phys. Rev. Letters 14, 331a (1964).

12. Clarke, J., "A Superconducting Galvanometer Employing Josephson Tunneling," Phil. Mag. 13, 115 (1966).

13. Ferrell, Richard A. and Richard E. Prange, "Self-Field Limiting of Josephson Tunneling of Superconducting Electron Pairs," Phys. Rev. Letters 10, 479 (1963).

14. Vant-Hull, Lorin, Randall A. Simpkins, and John T. Harding, "Disappearance of Thermal Magnetic Fluctuations in a Superconductor," Phys. Letters 24A, 737 (June 1967).

15. Mercereau, J.E., private communication.

16. Johnson, A.K. and P.M. Chirlian, "The Cryotron as an Ultra-Low Noise Amplifier, Elimination of Excessive Cryotron Noise," IEEE Trans. on Magnetics MAG-2, 390 (1966).

17. Bussieres, P. and A.C. Leonard, "Noise Associated with Heat Transfer to Liquid Helium II," Cryogenic Engr. News 2, 32 (May 1967).

18. Burgess, R.E.,"Quantization and Fluctuations in Superconductors," Proc. Symposium on the Physics of Superconducting Devices, Charlottesville, Virginia, April 1967, to be published.

19. Scalapino, D.J., "Current Fluctuations in Superconducting Tunnel Junctions," ibid.

20. Ferrell, R.A. and H. Schmidt,"Critical Fluctuations in Superconductors," to be published.

21. Kamper, R.A., "Millidegree Noise Thermometry," Proc. Symposium on the Physics of Superconducting Devices, Charlottesville, Virginia, April 1967, to be published.

22. Knol, K.S. and J. Volger, "Is a Superconductor Free from Noise," Physica 19, 46 (1953).

23. Fink, H.J. and A. Zacharias, "Current Fluctuations in a Superconducting Circuit Carrying a Circulating Current," Phys. Rev. 135, A1 (1946).

24. van Ooijen, D.J. and G.J. van Gurp, "Motion and Pinning of Flux in Superconducting Vanadium Foils Studied by Means of Noise," Philips Res. Repts. 21, 343 (1966).

25. Parker, W.H., B.N. Taylor, and D.N. Langenberg, "Measurement of 2e/h Using the ac Josephson Effect and its Implications for Quantum Electrodynamics," Phys. Rev. Letters 18, 287 (1967).

26. Goree, William S. and Edgar A. Edelsack, "Superconducting Devices, A Literature Survey," a cooperative effort of Stanford Research Institute and the Office of Naval Research, March 1967, copies available from Defense Documentation Center, Bldg. 5, Cameron Station, Alexandria, Va. 22314. AD No. 651376.

27. Jaklevic, R.C., J. Lambe, A.H. Silver, J.E. Mercereau, "Macroscopic Quantum Interference in Superconductors," Phys. Rev., 140, A1628 (1965).

SYMPOSIUM

ON

SPACE MAGNETIC EXPLORATION AND TECHNOLOGY

An Ultra Sensitive Magnetometer and Gradiometer Using Weakly Coupled Superconductors

A. L. Morse and D. L. Judge
TRW Systems, Space Sciences Laboratory

N69-33957

In a superconductor the relatively weak interaction between electrons via distortion of the crystal lattice is no longer masked by thermal disorder. The electrons then tend to arrange themselves in a regular lattice in somewhat ıe same way as a liquid upon solidification. This produces a correlation in electron position and momentum which makes it impossible for one of these electrons to gain or lose less energy than that required to remove it from the electron lattice. Since the energy lost per collision, which gives rise to ordinary ohmic resistance, is much smaller than this energy gap, resistance vanishes.

With the discovery of flux quantization[1] and superconducting tunneling[2] with its associated very low saturation current, it became possible to design and construct magnetometers of much greater sensitivity than previously thought possible. Flux densities as low as 10^{-9} gauss have been detected with a TRW cryogenic magnetometer and it is expected that this threshold value may be lowered three or four orders of magnitude in the near future. Such sensitivity permits a determination of magnetic gradients and even higher multipole moments in the earth's field, from which it is possible to determine the nature and source of various anomalies such as those associated with the magnetopause.

Many of the dynamic characteristics of a superconducting circuit are determined by the inductance and capacitance of its components. At low frequencies the inductance is predominant, leading to a relation between the voltage history and the current given by $I = L^{-1}\int V(t)dt$, where L is the inductance and V(t) is the voltage imposed across the circuit. If the external flux Φ through such a loop is changed by an amount $\Delta\Phi$, there will be an induced EMF given by $V(t) = -d\Phi(t)/dt$ so that $\Delta I = -L^{-1}\int d\Phi$ or $\Delta I = -L^{-1}(\Delta\Phi)$, and since the flux associated with a current I through an inductance L is given by $\Delta\Phi = L(\Delta I)$, the total flux will remain constant. It is possible to concentrate essentially all of the induced flux in one part of the circuit. This flux concentration can be made quite large, for example, by forcing all of the circulating current through an extremely short and narrow neck. Since a superconductor becomes normal when the local field exceeds a certain temperature dependent critical value, it is possible to determine when the induced flux causes saturation by observing the inductive voltage kick when the narrow neck becomes normal.

Using only these characteristics of a superconductor, viz., the perfect conductance below a critical current or flux density, it is feasible to construct a magnetometer that would determine the change in flux between successive measurements. The induced current flowing in the superconducting circuit could be determined at any time in one of the following ways. The required critical current could be reduced until saturation is reached by 1) varying the flux concentration near the neck, for example, by closely approaching the narrow neck with a superconducting plane, 2) increasing the temperature of the neck, or 3) imposing a suitable magnetic field parallel to the plane of the superconducting loop. Alternatively, the current could be increased to the critical valve by 4) changing the flux in the loop a known amount, 5) adding an external current through leads attached to each side of the loop or neck, a known fraction of which would add to the current flowing through the narrow neck.

The sensitivity of the above method is determined by the following considerations. First, the circulating current associated with a flux change of 1 gamma-cm^2 or 10^{-5} maxwells is about 10^{-5} amps in a low inductance (10^{-8} henrys) 1 cm^2 loop. If this current were interrupted in 100 μsec, there would be a resultant voltage pulse with an amplitude of 10^{-9} volts, which would be difficult to detect. Therefore a less direct approach is required. If two approximately equal narrow necks, or more generally, weak links are used, and an external current is applied so that it flows in parallel through each link, then when one of the links saturates, all of the external current will be forced to flow through the other link and will immediately cause it to saturate. Thereafter a voltage will appear across the parallel combination determined by the "normal" resistance of the links. This method requires that the external current be greater than half the saturation current of the strongest link, and the signal is a change in the net critical current of the order of 10^{-5} amps/gamma of flux change during the time both links are superconducting. It also requires that when the first link reaches saturation, its resistance jumps to and remains at a finite level, that is, its resistance cannot be a function of current only as was first assumed.

With the discovery of flux quantization a number of the above problems were eliminated. If a superconducting ring is formed which contains a nonintegral number of flux quanta, sufficient current will spontaneously flow around the ring to bring the number of flux quanta to the nearest integer. The necessary energy is provided by a decrease in the latent heat of the superconducting phase transition, i.e., the total energy is substantially lower with the electron correlation broken at one or more points with an insulating gap or barrier. This provides a potential which motivates correlated pairs of electrons to cross the barrier if possible, and reform or rejoin the electron lattice on the other side. This process is similar in many respects to that involved in forcing an ice cube through a screen or mesh. Since only correlated electrons which can lose no energy are involved, there can be no dc voltage drop as long as the correlation is maintained and a dc current flows. Similarly,

if a dc voltage is maintained there can be no dc current flow. Electron pairs crossing a barrier with a voltage drop, V, must lose all the energy they gain on the way across in one step as they "condense" or recorrelate on the other side. This leads to the production of a photon of energy E = hf where E = 2 eV, and a frequency of f = 2 eV/h. These effects, associated with weakly coupled superconductors were first predicted theoretically by Josephson,[3] and weak links having these characteristics have become known as Josephson Junctions.

Superconducting circuits involving Josephson Junctions can be adequately described by three very simple equations [Equations (1), (2), and (3)]. The first of these states that the super current through a point junction is proportional to the discontinuity of the super wave function at the junction, and hence to the sine of the phase shift across the junction. The second equation states that the phase shift around any closed path lying within a superconductor must be $2\pi n$ where n is an integer or more simply that the super wave function is single valued, and that the phase shift around a closed loop is proportional to the amount of flux enclosed by the loop. This condition leads immediately to flux quantization when the closed path lies entirely within a superconductor. The third equation states that the phase difference between two superconductors which are not connected is arbitrary but the time rate of change of the phase shift is proportional to the voltage difference between them.

These three equations along with the conventional equations of E&M completely describe superconducting circuits. In the following pages two superconducting circuits will be analyzed to illustrate the application of these equations.

$$I_j = I_m \sin \phi \tag{1}$$

$$\frac{1}{2\pi} \oint \vec{\nabla}\phi \cdot \vec{dl} = \frac{1}{\Phi_o} \int \vec{B} \cdot \vec{dS} = \Phi/\Phi_o \tag{2}$$

$$\frac{\partial \phi}{\partial t} = \frac{2\ eV}{h} = 2\pi\left(\frac{V}{\Phi_o}\right) \tag{3}$$

where

I_j is the Josephson current

I_m is the maximum current that can flow without loss of correlation

ϕ is the phase discontinuity of the superwave function

Φ_o is the flux quantum given by $\Phi_o = h/2e$

The Response of a Single Point Contact Josephson Junction

In such a geometry, (see Figure 1), only Equations (1) and (3) are needed. Here C is the capacitance between the two superconductors, and R the impedance of the voltage source v. The current flowing through the junction at time t is given by

$$I_j = I_m \sin\left(\frac{2e}{h} \int_{-\infty}^{t} V\, dt\right) \tag{4}$$

where $\phi = (2e/h)\int V\, dt$ is a voltage impulse and is analogous to the relation $p = F\, dt$ for momentum. A voltage impulse of one nanovolt-microsecond (i.e., 10^{-15} volt-sec), produces a phase change of 3.04 radians. This response of 3.3×10^{-16} volt-sec/radian or 5.74×10^{-18} volt-sec/degree is the same for all superconductors.

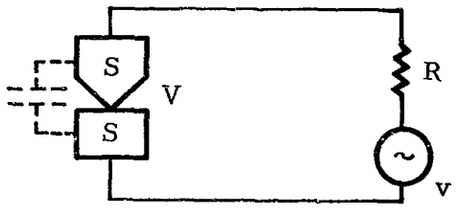


Figure 1

The voltage, V across the junction, will be given by

$$\frac{d(CV)}{dt} = I - I_j$$

or

$$C\dot{V} = \frac{v - V}{R} - I_m \sin\left(\frac{2e}{h} \int_{o}^{t} V\, dt\right) \tag{4}$$

In terms of the phase across the junction Equation (4) becomes

$$\frac{d^2\phi}{dt^2} + \frac{1}{RC}\frac{d\phi}{dt} + \frac{2eI_m}{hC} \sin\phi = \left(\frac{2e}{h}\right)\frac{v(t)}{RC} \tag{5}$$

The nature of the variation of ϕ, the phase shift across the junction, can be seen by considering the result of a step change in v at t = 0. For t < 0, we have

$$\phi = \phi_o,\ V = 0,\ I = \frac{v_o}{R}$$

and

$$\sin \phi_o = \frac{I}{I_m}$$

for $t > 0$ we have

$$\phi = \phi_o + \delta\phi(t)$$

$$\frac{d^2(\delta\phi)}{dt^2} + \frac{1}{RC}\frac{d(\delta\phi)}{dt} + \frac{2e}{h}\frac{I_m}{C}\sin\left[\phi_o + \delta\phi(t)\right] = \left(\frac{2e}{h}\right)\frac{v_o + \delta v}{RC}$$

Since $\delta\phi$ is small,

$$\sin(\phi_o + \delta\phi) = \sin\phi_o + \delta\phi\cos\phi_o$$

leaving

$$\frac{d^2(\delta\phi)}{dt^2} + \frac{1}{RC}\frac{d}{dt}(\delta\phi) + \left(\frac{2eI_m}{hC}\cos\phi_o\right)\delta\phi = \left(\frac{2e}{h}\right)\frac{\delta v}{RC} \qquad (6)$$

From Equation (6) it is evident that there will be a resonance of the system at

$$f = \frac{1}{2\pi}\sqrt{\frac{2eI_m}{h}\frac{\cos\phi_o}{C}}$$

This is not the "quantum" frequency, however, which is produced when $v/R > I_m$, but simply describes the tendency of the phase to overshoot when adjusting to the value required for the junction to carry the "demand" current. If the applied voltage contains a high frequency ac component, there will be a nonlinear reactance causing the average dc voltage drop across the junction to be an integral multiple of the Josephson voltage associated with the frequency of the ac component as given by Equation (3) with

$$\frac{\delta\phi}{\delta t} = f \text{ and } V = \frac{fh}{2e}$$

Figure 2 shows several oscilloscope traces obtained with such a system using a frequency of 900 MHz. The vertical deflection is produced by the voltage across the junction while the horizontal deflection indicates the current through the junction.

The Response of Two Parallel Point Contact Josephson Junctions

In the case of two parallel point contacts as shown in Figure 3 the analysis is as follows.

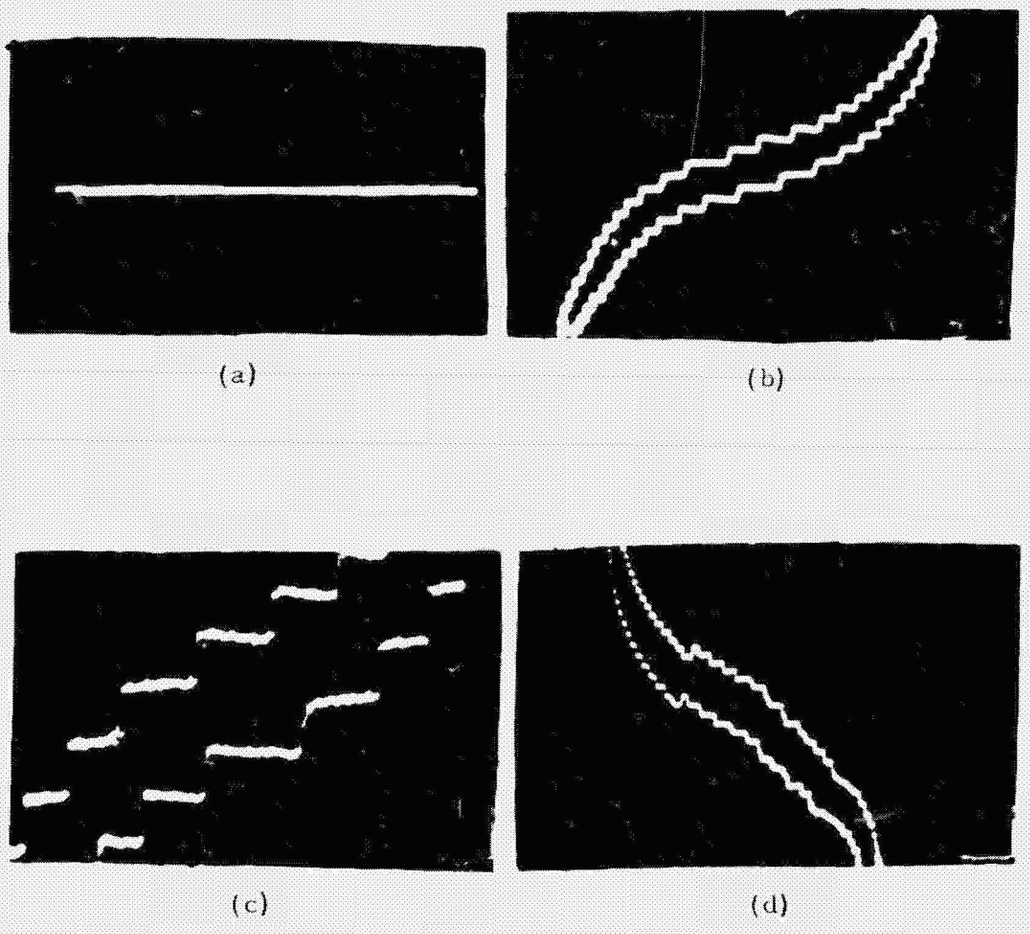


Figure 2. V-I Characteristics of Pb Josephson Junctions
T = 4.2°K

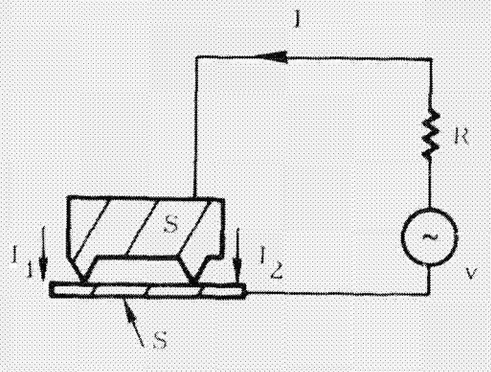


Figure 3. Two Parallel Point Junctions

Let ϕ_1 and ϕ_2 be the phase shifts across junctions 1 and 2, respectively, I_{1m} and I_{2m} their maximum currents, I_1 and I_2 the instantaneous currents, $\vec{B}$ the external magnetic field and $\vec{A}$ the area enclosed by the superconducting loop. Further, let the magnetic flux within the loop due to I_1 and I_2 be given by L_1I_1 and L_2I_2, respectively.

From Equation (2) we have

$$\oint \vec{\nabla}\phi \cdot \vec{dl} = 2\pi \left(\frac{\vec{B} \cdot \vec{A} + L_1 I_1 + L_2 I_2}{\Phi_o} \right) = 2\pi n + \phi_1 + \phi_2$$

and from Equation (1)

$$2\pi \left(\frac{\vec{B} \cdot \vec{A} + L_1 I_{1m} \sin \phi_1 + L_2 I_{2m} \sin \phi_2}{\Phi_o} \right) = 2\pi n + \phi_1 + \phi_2 \quad (9)$$

If L_1I_{1m}/Φ_o and L_2I_{2m}/Φ_o are $\ll 1$

$$\phi_1 + \phi_2 = \frac{B \cdot A}{\Phi_o} - 2\pi n$$

and

$$I = I_1 + I_2 = I_{1m} \sin \phi_1 + I_{2m} \sin \phi_2$$

and the maximum current is

$$I_m = \left(I_{1m}^2 + I_{2m}^2 - 2 I_{1m} I_{2m} \cos \frac{BA}{\Phi_o} \right)^{1/2}$$

This "interference" of the wave function phase at the two junctions results in the parallel combination having a maximum resistanceless current which varies with the magnetic flux and has a period of Φ_o. When (L_1I_{1m}/Φ_o) and (L_2I_{2m}/Φ_o) are $\gg 1$, Equation (9) becomes:

$$L_1 I_{1m} \sin \phi_1 + L_2 I_{2m} \sin \phi_2 = \left(2\pi n - \frac{BA}{\Phi_o} \right) \Phi_o$$

The maximum current that can be carried with both junctions superconducting, assuming that junction two is the first to reach saturation, is given by:

$$I_m = \frac{2\pi n\Phi_o}{L_1} - \frac{BA}{L_1} - \left(\frac{L_2}{L_1} - 1\right) I_{2m} \qquad (10)$$

If I is varied at a rapid rate compared to the rate of change of BA/Φ_o, this maximum will vary by an amount

$$\Delta I_m = (\pi/L_1)\ \Phi_o \qquad (11)$$

with a flux period of $BA = \Phi_o$.

Note that in Equation (10) the inductances L_1 and L_2 will be of opposite sign since currents in opposite sides of the loop will produce fluxes of opposite signs. The mean value of I_m will be given by

$$\bar{I}_m = \left[1 + (-L_2/L_1)\right] I_{2m}$$

and the fractional variation is given by:

$$\Delta I_m/\bar{I}_m = \pi\Phi_o/(L_1 - L_2)\ I_{2m}$$

In order to make the variation in I_m easily observable it is essential that the inductances be made small. This requires the use of conductors of large cross section and counter flowing currents wherever possible. In order to be sensitive to a given component of a field, field gradient, etc., it is possible to construct a circuit of such topology that the total flux threading the closed superconducting loop is proportional to the quantity desired. Figure 4 shows the geometry for measuring two of the six components of a field gradient. Similar more complicated arrays could be used to measure any of the higher multipole moments of a magnetic field. It is estimated that using two loops of 10 cm diameter and a base length of 100 cm one could detect field gradients of the order of 10^{-13} gauss/cm. This estimate assumes a 1 percent measurement of the critical current.

Figures 5 and 6 show schematic diagrams of the device as might be used when working with standard laboratory dewar systems. For space applications, the device would be constructed as in Figure 7 with liquid helium being continuously pumped through the system.

The operation of the system as shown in Figures 5, 6, and 7 is as follows:

1) A sinusoidal voltage is applied through leads (a) causing current to flow through the superconducting header (c), through the two weak links (i), and via the superconducting circuit (g) around the holes (h).

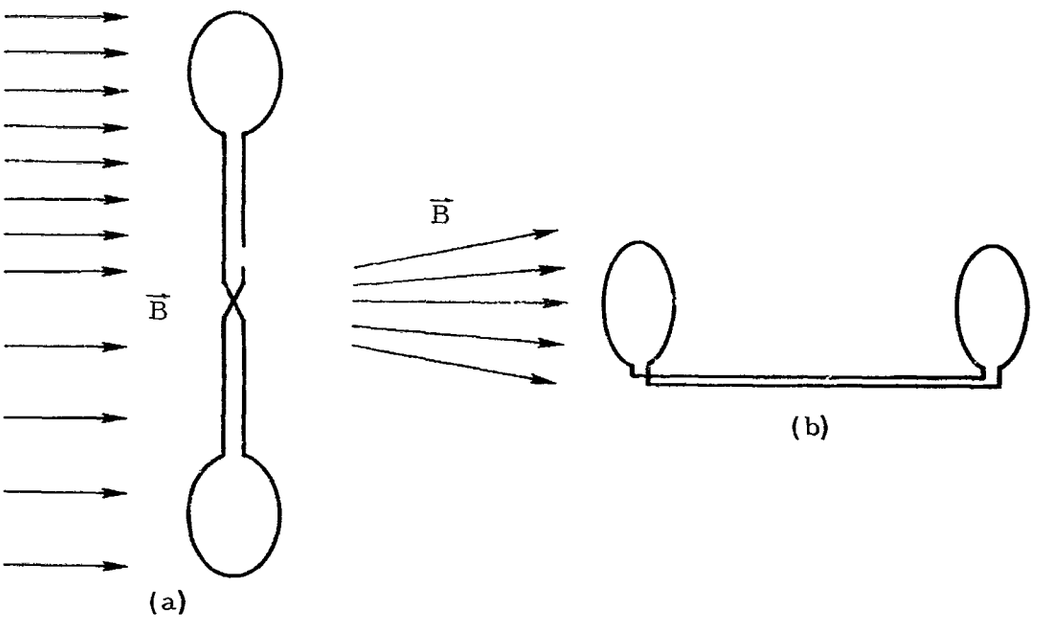


Figure 4. Schematic Geometry for a Gradiometer

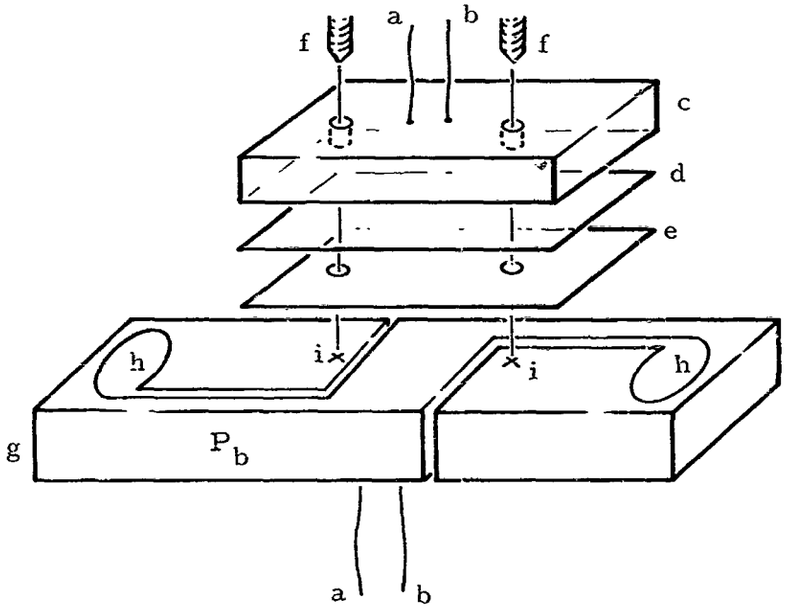


Figure 5. A Gradiometer Sensor

a) Drive leads
b) Voltage measuring leads
c) Superconducting header
d) Flexible superconducting sheet
e) Thin insulating sheet
f) Contact adjusting screw
g) Superconducting circuit
h) Hole for flux
i) Weak links

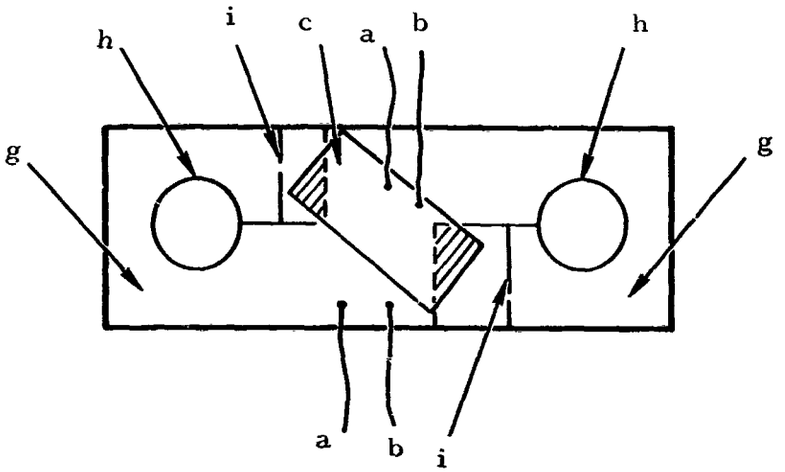


Figure 6. A schematic representation of a gradiometer using a thin superconducting film (g) having weak links at (i). Other symbols are as indicated in Figure 5.

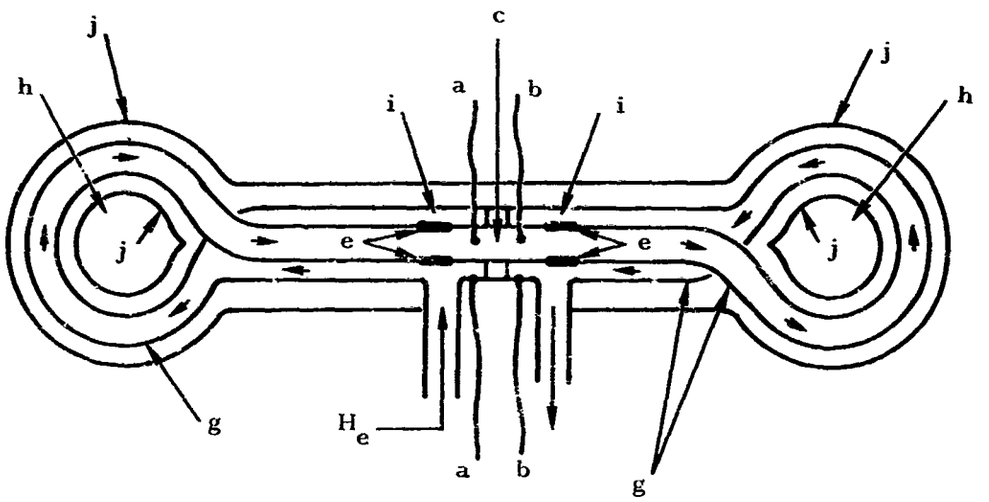
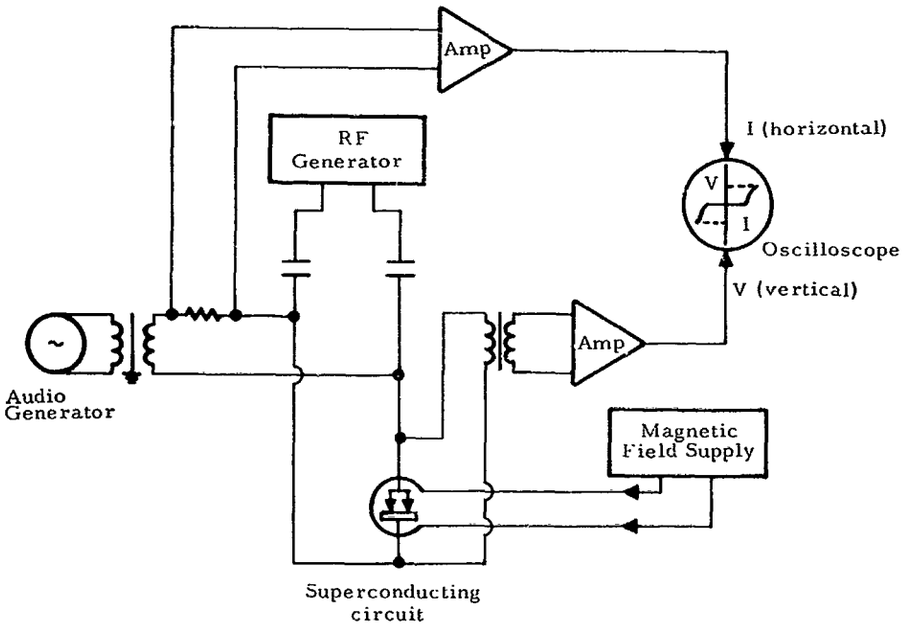


Figure 7. A schematic configuration for a gradiometer of high sensitivity. Such a system, shown here in longitudinal cross section, is designed for a continuous flow of He through its vacuum insulated tubing. Lengths of several meters or more are quite feasible. The weak link can be of either the form indicated in Figure 2 or Figure 3. The superconducting circuit otherwise consists of a lead coating on the inner tubing.

2) When the supercurrent through either of the weak links (i) exceeds the saturation value, a voltage is developed between (c) and (g) which is sensed with the voltage leads (b). If the flux through the two holes (h) is zero, the current at which (i) saturates will be maximum and equal to twice the saturation current of either weak link. If the two fluxes are slightly different an initial circulating current will be present which will add to the drive current at one weak link and subtract at the other, causing a voltage to appear at (b) for a smaller drive current. The useful signal then arises from the voltage which appears when the drive current exceeds the maximum Josephson current for either junction. To determine the critical drive current it is necessary to know only the drive current function and the time, relative to a fixed reference, at which a voltage appears across the junction. For example, for a sinusoidal drive current, the current increases from $t = 0$ to $t = \tau/4$ and there is a unique relation between the current required to produce saturation (maximum Josephson current), the time at which it occurs and the appearance of a voltage across the junctions. The system can thus be calibrated in terms of ΔB, the difference between the fields seen by the two holes (h) versus the time in the current cycle at which a voltage appears across the voltage leads (b).

Figure 8 shows the external circuitry associated with the laboratory measurements of the response of the various devices discussed previously.



Superconducting Shielding

The perfect conductance of a superconductor combined with the Meissner effect makes it possible to construct regions which are nearly field free. The limitations in using this technique are due both to the presence of holes and impurities in the shielding material, and to the self-limiting action associated with the increase in field strength and hence, decrease in T_c at the perimeter of a region where the flux has been excluded. At the same time there is a decrease in field strength in the direction of the field which aids the growth of the superconducting region in these directions. As a result it is possible to obtain complete field exclusion upon cooling only if the superconductor is relatively long and thin, with its long dimension lined up with the magnetic field. In other cases superconducting domains are formed which grow as the temperature is lowered, trapping much of the flux in region that are kept normal by the increased field strength. The flux trapped in this way, or by holes and impurities, is sufficiently mobil that the field inside such a shielded region is modified by fluctuations in the external field.

The magnetic shielding provided by even an extremely crude superconducting envelope however is sufficient to reduce the magnetic fluctuations within that region by a factor of 10^5. In the present Josephson junction investigations we have employed a lead tube having a diameter of 3 inches and a length of 7 inches. The wall thickness of the tube is about 1/16 inch. The ends of the tube are about 90 percent closed, small openings being required for the passage of liquid He throughout the volume enclosed by the lead, as well as for the passage of mechanical apparatus and electrical leads. This shielding system just described is by no means cited as an example of the best one can do. Professor Fairbank of Stanford University has proposed a shielded system in which one would use a "sack" covered with a thin niobium film. This arrangement is to be folded into an extremely small volume cooled below its critical temperature in as low a magnetic field as possible and then opened up to its full volume. Any flux which is trapped in the sack remain constant (a property of superconductors) and thus in opening the sack the flux density must decrease. The efficiency of this process, of course, depends upon the ratio of the volumes before and after extending the sack. One can, of course, imagine a number of variations on this technique.

A pump-like arrangement, that is, a cylinder and piston is another way to achieve the same result. In any case, whatever method may be selected is virtually guaranteed to be far superior to the presently popular technique of using mu-metal or by trade name, netic and co-netic foil. Typically, a well designed mu-metal shield provides a shielding factor of no more than 50 to 100 at the very best. This is to be compared with the lead tube discussed earlier having a shielding factor of 10^5. Of course the price one must pay is that of working with a shield at liquid He temperatures.

Research now underway, by some groups, on practical ways to build high temperature superconductors provides encouragement that in the not far distant future the use of superconductors will not be restricted to cryogenic temperatures. Even without such advances, regenerative dewar systems and new thermal insulators make it presently feasible to orbit cryogenic experiments.

REFERENCES

1. B. S. Deaver and W. M. Fairbanks, Phys. Rev. Letters 7 43 (1961)

2. P. W. Anderson and J. M. Rowell, Phys. Rev. Letters 10 230 (1963)

3. B. D. Josephson, Phys. Letters 1 251 (1962)

H. VOGEL and S. VEGORS*

MAGNETIC FIELD COMPUTATIONS AND MEASUREMENTS ON THE EXCITERS FOR THE ARGONNE PION FOCUSING HORN/

Reference: H. Vogel and S. Vegors
"Magnetic Field Computations and Measurements on the Exciters for the Argonne Pion Focusing Horn"
Spacemagnetic Exploration and Technology Symposium
August 1967
University of Nevada, Reno

N69-33958

1. Introduction

The pion focusing horn of the Argonne National Laboratory includes eight rings - with a total weight of ten tons - wound of transformer-type strip steel (1). Each ring is provided with 76 symmetrically placed toroidal exciting turns; and, the assembly of eight is enclosed by a single-turn toroidal shell. The toroidal shell is to conduct the secondary current, i.e., 300 kA peak. These exciters are the largest toroidal windings wound on laminated iron ever achieved.

Crucial for the successful design of a horn is to make sure that the azimuthal B field is sufficiently free of asymmetries, which would result in eccentric forces on the mechanically weak inner conductor, from interaction with the secondary current. The analysis of the stray field of a steel core with toroidal winding is carried out in this paper. Reported also are measurements, which were to demonstrate sufficient symmetry of the toroidal exciter windings.

Actually, the magnetic field was demonstrated to be 0.2 to 1.0 gauss in the cross-direction to the inner conductor when the exciter turns were fed with d-c current of 400 amperes.

---

* Vogel, Los Alamos Scientific Laboratory, formerly Argonne National Laboratory
Vegors, Idaho State University

/ Work performed under the auspices of the U. S. Atomic Energy Commission, at the Argonne National Laboratory.

2. Field Measurements

The two types of exciters shown in Fig. 1 exist. The fields were measured with a hall probe in a house made of 1/8-in. plate steel. The fields plotted over exciter d-c current in Fig. 2 are typical for exciters of the type shown in Fig. 1a, whereas the fields of the type shown in Fig. 1b were somewhat less than those of Fig. 1a.

Figure 2 shows two curves, one for a winding with rather poor symmetry; and, one for a winding as typically produced for the horn. The poorly-symmetric winding produces a radial field component of substantial magnitude, as one would expect -- because the asymmetry can be replaced by superposing a single current-carrying conductor and a symmetrically-wound toroid.

The well-adjusted winding shows a nonlinear rise with exciter current seen in Fig. 2. The nonlinear field is caused by the inside end of the 14 mil-thick strip steel of which the core is wound. At that edge, the reluctance of the stray field through air; and, the reluctance of the thin space between the innermost and the next lamination, are in parallel. This gives rise to a stray field of the order of 0.5 to 1 gauss when the core is excited to saturation, as seen in Fig. 2.

We shall now show that the field we measured cannot be due to the finite - although symmetric - spacing between conductors.

3. Calculation of the Stray Field in the Inner Space of a Toroidal Winding when the Winding has Azimuthal Symmetry and is Wound on Steel

In Fig. 3, equal and like current filaments of strength I are placed equidistant from the center of a round iron ring of radius a, having a permeability μ. Laplace's equation $\nabla^2\varphi = 0$, written in polar coordinates r, Ψ

$$\frac{\partial^2\varphi}{\partial r^2} + \frac{1}{r}\frac{\partial\varphi}{\partial r} + \frac{1}{r^2}\frac{\partial^2\varphi}{\partial\Psi^2} \qquad (1)$$

Separation of variables is achieved with the integral $\varphi = R\,\Psi$ and the separation constant n^2. The standard solution in parameter form is then

$$\begin{aligned} \Psi &= \sum_{n=1}^{\infty}\left(A_n \cos n\Psi + B_n \sin n\Psi\right) + A_o + B_o\Psi \\ R &= \sum_{n=1}^{\infty}\left(C_n r^n + D_n r^{-n}\right) + C_o + \log r \end{aligned} \qquad (2)$$

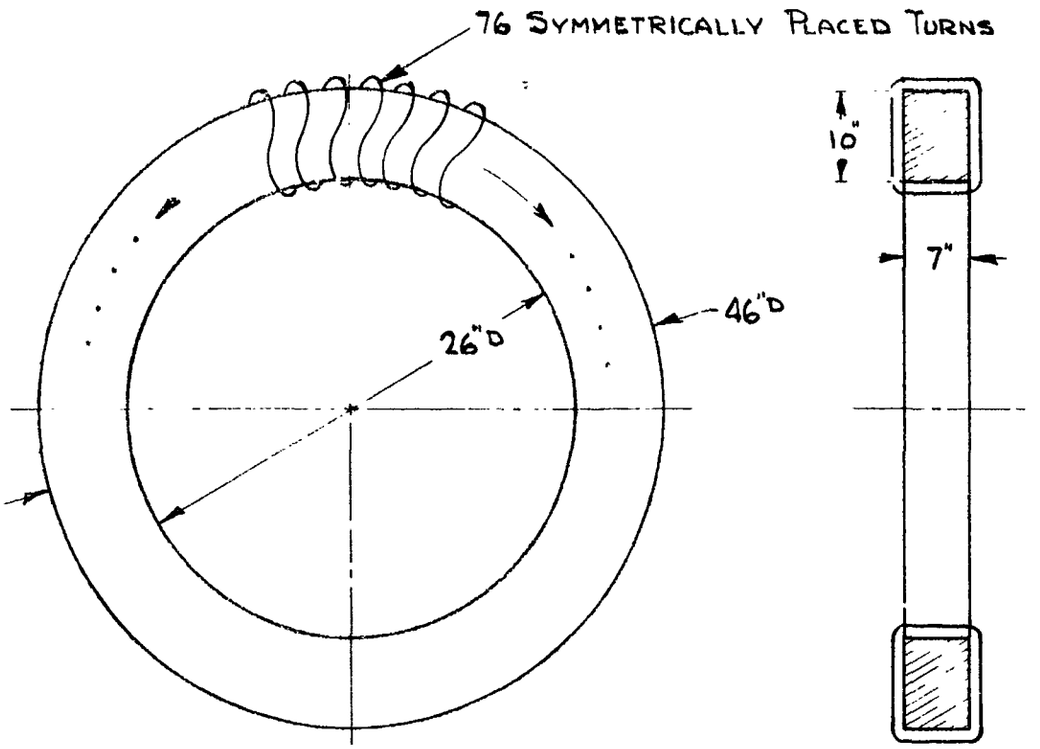


FIG. 1A ALPHA-TYPE ASSEMBLY

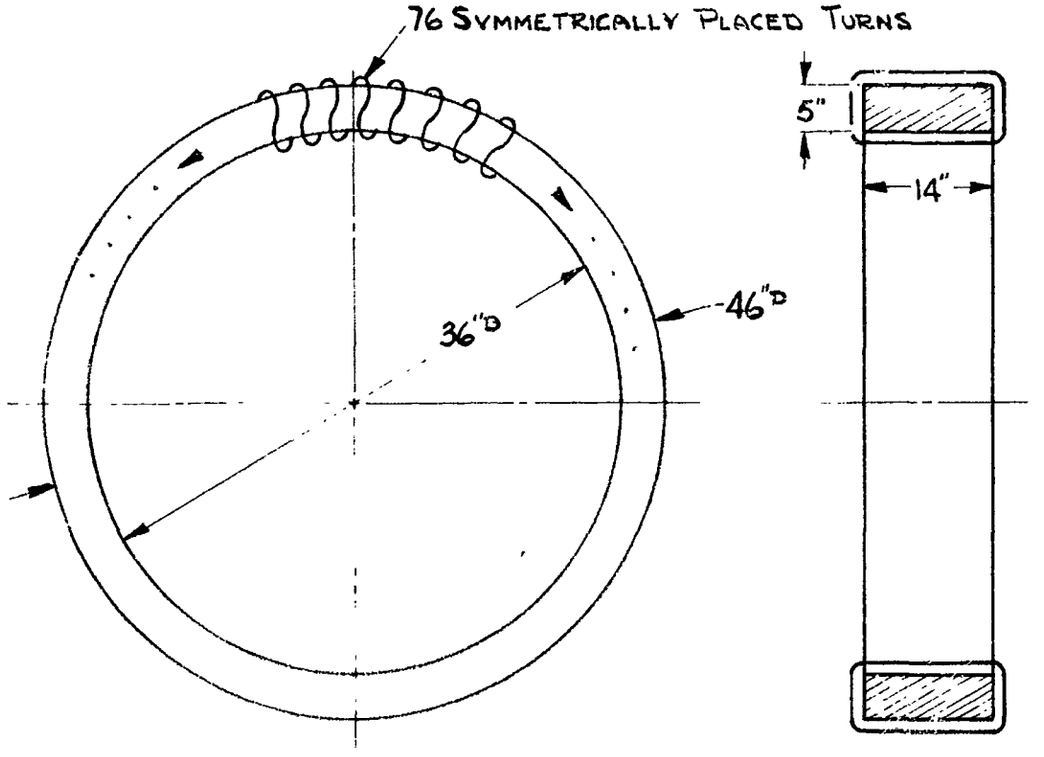


FIG. 1B BETA-TYPE ASSEMBLY

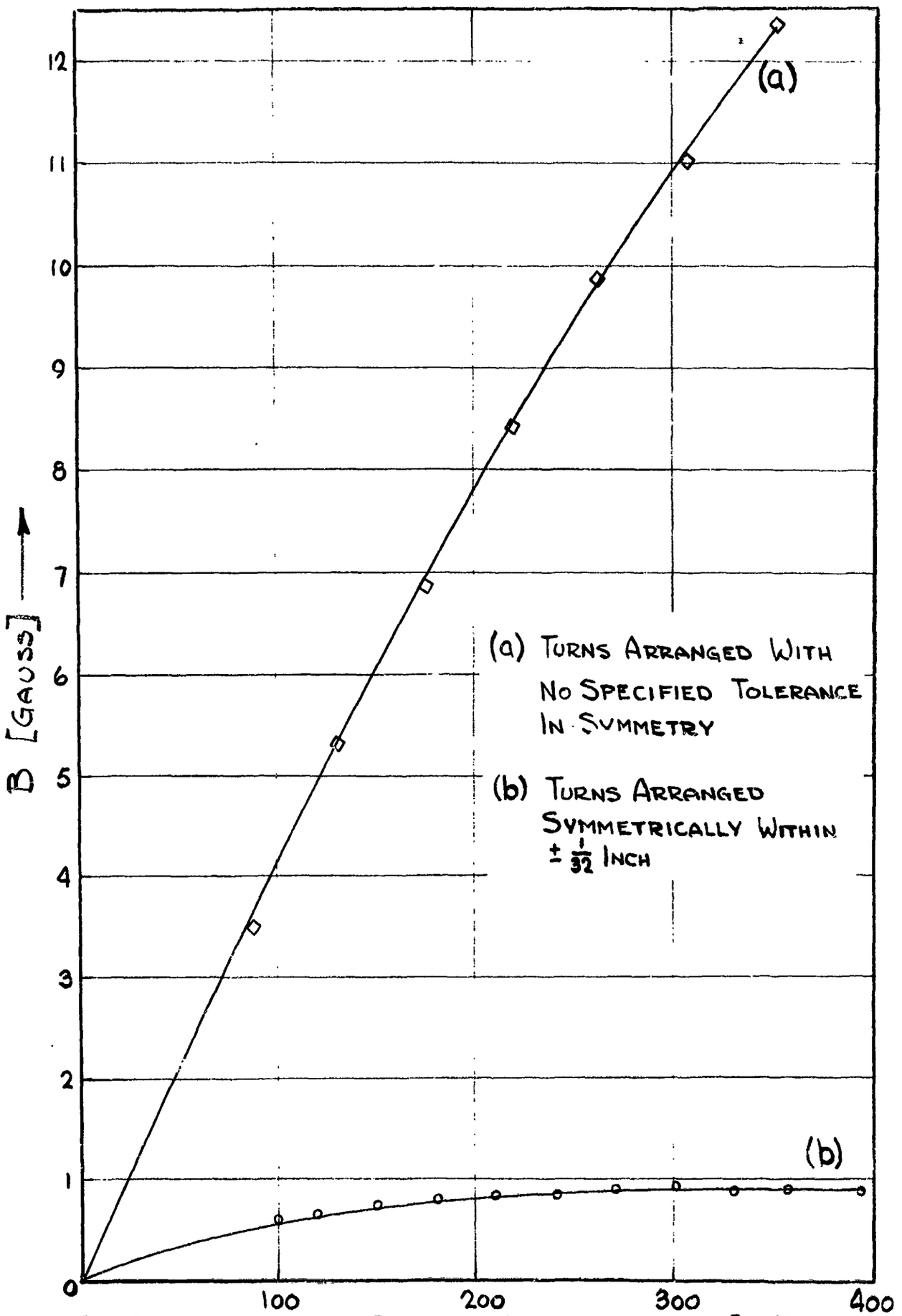


FIG. 2 D.C. EXCITATION CURRENT IN EACH TURN [A]

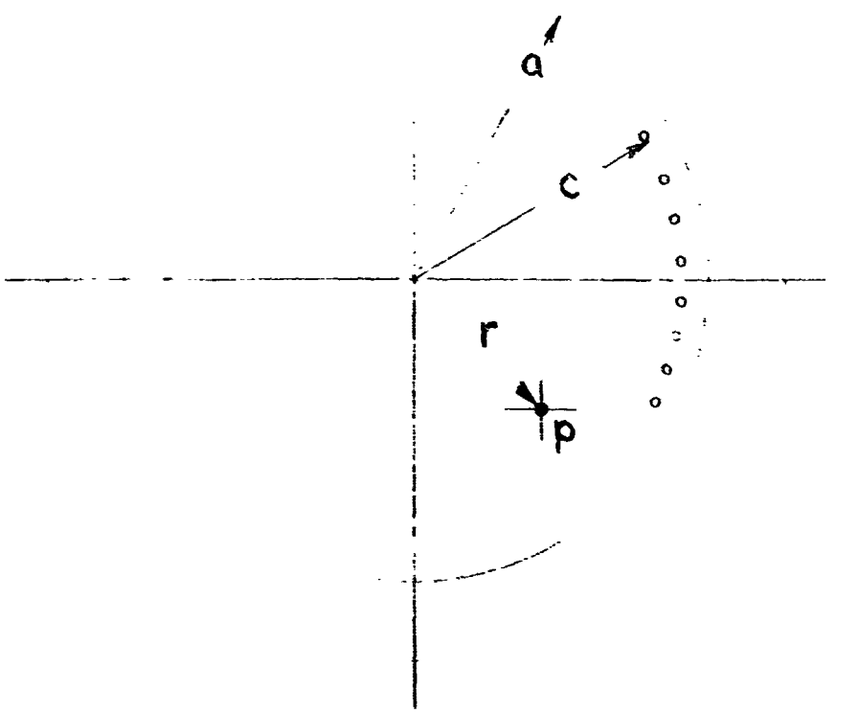


FIG. 3 GEOMETRY TO FIELD COMPUTATIONS AT POINT p OF CURRENT FILAMENT (RADIUS C) IN IRON RING (RADIUS a)

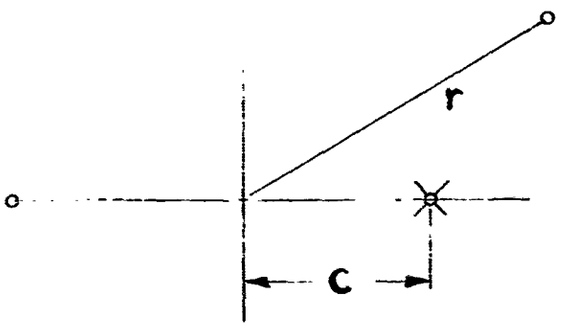


FIG. 4 GEOMETRY TO FIELD OF A CURRENT FILAMENT

By symmetry, and since no current exists at $r = 0$, we must have $A_o = B_o = C_o = D_o = 0$. With the origin of Ψ at the center of a filament, symmetry requires, that $B_n = 0$. Since we have no current in the center, dR/dr cannot have a singularity in the space $0 \leq r < c$; and hence, $D_n = 0$. Thus,

$$\phi_I = \sum_{n=1}^{\infty} C_n r^n B_n \sin n\Psi \qquad (3)$$

where sub I indicates $0 \leq r < c$.

As a result of the assumed symmetry, the field must be invariant under rotation of $2\pi/N$. Hence, the magnetic potential in the region I can be written as

$$\phi_I = \sum_{k=1}^{\infty} A_k r^{kN} \sin kN\Psi \qquad (4)$$

A markedly simple method to find the boundary conditions in region II, i.e., for $c \leq r < a$, is by considering the magnetic moment m induced by the conductors; and, superposing the field from the filament and that from the magnetic moment induced in the iron.

In polar coordinates, the magnetic potential of a single current filament referred to an origin not at it, is given by[1]

$$-\phi = \frac{\Psi}{2\pi} + \frac{I}{2\pi} \sum_{n=1}^{\infty} \frac{1}{r} \left(\frac{c}{r}\right)^n \sin n\Psi , \qquad (5)$$

for $r > c$

where c is the distance filament to origin. We require the radial field of I at the iron boundary $r = a$, which is, for N equally spaced conductors

$$H_r = -\left(\frac{\partial\phi}{\partial r}\right)_{r=a} = \frac{IN}{2\pi a} \sum_{k=1}^{\infty} \left(\frac{c}{a}\right)^{kN} \sin (kN\Psi) \qquad (6)$$

$$-H_\Psi = -\left(\frac{1}{r}\frac{\partial\phi}{\partial\Psi}\right)_{r=a} = \frac{IN}{2\pi a} \sum_{k=1}^{\infty} \left(\frac{c}{a}\right)^{kN} \cos (kN\Psi) \qquad (7)$$

This field will induce a magnetic moment m at the surface point (a,Ψ). Since the iron boundary is round, the normal component of field intensity at this point is $\pm 2\pi m$; where the signs apply to

---

[1] cf. Appendix I

the outside (+) and the inside (-) of the boundary, respectively. Hence, the continuity condition for the flux density can be written

$$\left(H_r + 2\pi m\right) = \mu_r \left(H_r - 2\pi m\right) \tag{8}$$

and thus,

$$2\pi m = \frac{\mu_r - 1}{\mu_r + 1} H_r \equiv y\, H_r \tag{9}$$

or, with Eq. (6),

$$2\pi m = y \frac{IN}{2\pi a} \sum_{k=1}^{\infty} \left(\frac{c}{a}\right)^{kN} \sin kN\psi \tag{10}$$

Eq. (10) gives the distribution of surface polarity expressed as a Fourier series. Each component produces a magnetic force (2)

$$\begin{matrix} H_r \\ H_\psi \end{matrix} = - \frac{IN}{2\pi r} y \left(\frac{cr}{a^2}\right)^{kN-1} \begin{matrix} \sin kN\psi \\ \cos kN\psi \end{matrix} \tag{11}$$

for $c < r < a$

Superposing the field from the filament and that of the induced magnetism yields

$$H_\psi = - \frac{IN}{2\pi r} \left[1 + \sum_{k=1}^{\infty} \left(\frac{c}{r}\right)^{kN} \cos\left(kN\psi\right)\right] - y \frac{IN}{2\pi r} \sum \left(\frac{cr}{a^2}\right)^{kN} \cos kn\psi, \tag{12}$$

and

$$H_r = - \frac{IN}{2\pi r} \sum_{k=1}^{\infty} \left[\left(\frac{c}{r}\right)^{kN} - \left(\frac{a^2}{cr}\right)^{kN}\right] \sin kn\psi \tag{13}$$

As regards the space $r < c$, we have to subtract the current $NI/2\pi$ from H_ψ and take into account that $c/r > 1$, which means, that according to Appendix I we must write r/c instead. Thus Eq. (12) becomes

$$\left(H_\psi\right)_{r<c} = - \frac{IN}{2\pi r}\left[\sum_{k=1}^{\infty} \left(\frac{n}{c}\right)^{kN} \left(1 + y \left(\frac{c}{a}\right)^{2kN}\right)\cos kN\psi\right] \tag{14}$$

Similarly, Eq. (13) becomes

$$\left(H_r\right)_{r<c} = \frac{IN}{2\pi r} \sum_{k=1}^{\infty} \left(\frac{r}{c}\right)^{kN} \left(1 - y \left(\frac{c}{a}\right)^{2kN}\right)\sin kN\psi \tag{15}$$

Comparison of Eq. (14) and (15) with (4) shows, that the integration constant in Eq. (4) is given by

$$A_k = \left[1 - y\left(\frac{c}{a}\right)^{2kN}\right] \Big/ c^{kN}$$

which is easily verified by differentiating Eq. (4).

With the geometry of the toroidal windings (cf. Fig. 1), Eqs. (14) and (15) yield negligible field inside the toroid.

An important conclusion with respect to the space $r<c$ is, that the current filaments can virtually mask the effect of the iron if N is sufficiently large so that

$$y\left(\frac{c}{a}\right)^{2N} << 1.$$

This is the case in the horn with $\frac{c}{a} \sim 0.95$, N = 76.

This means that the roundness of a fictitious cylinder tangent to the winding (i.e., r = c) and the azimuthal symmetry are responsible for the attenuation of the field at $r<c$, whereas the roundness of the iron does not matter. It is for mechanical reasons only that the iron must be round within close tolerance, because a symmetrical toroidal winding is difficult to achieve on an unround core.

Conclusions

The calculations shown demonstrate that the field due to the conductor spacings is negligible as long as the spacing is uniform.

The field measurements demonstrate that the field in the cross-direction to the inner conductor, i.e., near the center of the toroid, is sufficiently independent of the excitation current, i.e., 0.5 to 1 gauss at 400 A excitation. It was shown, that this field saturates as a result of its origin from the end of the steel strip of which the core is wound. Hence, when the horn is pulsed to 300 kA (i.e., 5 kA in the excitation turns) the radial field component at the conductor is expected to be $B_r \approx 1$ gauss.

Acknowledgments

The round wound cores were manufactured at the West Allis, Wisconsin Works of the Allis Chalmers Manufacturing Company; and

some, concurrently, at the Greenville, Pennsylvania Works of the Westinghouse Electric Company.

The symmetrical toroidal windings were manufactured at the Central Shops of Argonne National Laboratory; under the supervision of H. W. Ostrander.

The magnetic and electric measurements on production units were carried out by F. J. Mallen from the Argonne Fabrication and Procurement Services. Many of the measurements on prototype windings were done by E. L. Williams and R. N. Woll.

References

1. H. F. Vogel, W. Brunk, E. Roberts, F. Markley, I. Pollack, H. Hinterberger, V. L. Telegdi, R. Winston, Proc. Int. Sympos. on Magnet Technology, Stanford 1965, p. 653.
2. E. B. Moullin, Principles of Electromagnetism, Oxford, The Clarendon Press, 1955, p. 403f.

Appendix I

Magnetic Potential of a Current Filament Referred to an Origin not at It

Inspecting Fig. 4, one can write for a pair of equal and unlike current elements

$$\frac{2\pi H_\gamma}{I} = \frac{1}{r-c} - \frac{1}{r+c} \qquad \text{for } \gamma = 0 \qquad (1)$$

Expanding Eq. (1) around the origin, we get

$$\frac{2\pi H_\gamma}{I} = \frac{2}{r} \sum_{n=1}^{\infty} \left(\frac{c}{r}\right)^n \cos n\gamma \qquad \begin{matrix} n = 1,3,5.... \\ c/r < 0 \end{matrix} \qquad (2)$$

Similarly, for a pair of equal and like current elements, we get

$$\frac{2\pi H_\gamma}{I} = \frac{1}{r-c} + \frac{1}{r+c}$$

and

$$\frac{2\pi H_\gamma}{I} = \frac{2}{r} \sum_{n=0}^{\infty} \left(\frac{c}{r}\right)^n \cos n\gamma \qquad \begin{matrix} n = 0,2,4.... \\ c/r < 0 \end{matrix} \qquad (3)$$

By superposition, we get the field of one current element of strength I

$$H_\psi = \frac{I}{2\pi r} \sum_{n=0}^{\infty} \left(\frac{c}{r}\right) \cos n\psi \qquad \begin{matrix} n = 0,1,2,3.... \\ c/r < 0 \end{matrix} \qquad (4)$$

Similarly $$H_r = \frac{I}{2\pi r} \sum_{n=0}^{\infty} \left(\frac{c}{r}\right) \sin n\psi$$

If $\frac{c}{r} > 0$, then the expression in parenthesis is to be replaced by $\frac{r}{c}$.

SYSTEMS OF COILS TO PRODUCE MAGNETIC FIELDS OF PRESCRIBED UNIFORMITY IN REGIONS OF DESIRED SHAPE[1]

George A. Rinard[2]

N69-33959

REFERENCE

G. A. Rinard, "Systems of Coils to Produce Magnetic Fields of Prescribed Uniformity in Regions of Desired Shape", Spacemagnetic Exploration and Technology Symposium, (August 1967) University of Nevada, Reno.

ABSTRACT

Most coil systems produce uniform fields over a region that is roughly spherical. The system is more efficient if the shape of the region of uniformity matches the experiment.

This paper describes a technique for determining the arrangement of the coils to produce prolately or oblately spherodial volumes of uniformity. The method is based on expanding the field along a ray in a basic set of polynomials, as, for example, Tschebyscheff polynomials. Systems with very high uniformity may be designed to produce highly eccentric volumes of uniformity.

The results are presented in a form so that given the eccentricity of the region and the degree of uniformity, one may uniquely determine the coil configuration and currents. Although only circular coils are considered, the method is directly applicable to square and other geometrically shaped coils.

KEY WORDS--coils, coil systems, eccentric volume of uniformity, field free, fields, homogeneous magnetic fields, magnetically clean, magnetic field free, Tschebyscheff, Tschebyscheff approximation, uniform fields, uniform magnetic fields.

---

[1]Part of the work described here was done on a Ph. D. dissertation at the University of Missouri, Columbia for Dr. D. L. Waidelich.

[2]University of Denver, Denver, Colorado.

INTRODUCTION

In many experiments, the presence of the earth's magnetic field is undesirable. When such experiments are performed on the surface of the earth, something must be done to reduce the effect of the earth's magnetic field. One way to do this is to generate a field of the same intensity but in a direction opposite to that of the earth's field. The problem then becomes one of producing a field that is essentially uniform over a region which for the desired uniformity will be referred to as the volume of uniformity.

For many experiments the well-known Helmholtz arrangement of two circular coils is adequate. The size of the volume of uniformity was increased greatly by Braunbek by the use of four circular coils all having the same value of ampere turns.(1) In Braunbek's system the field varies less than one part in 10^5 over a sphere whose diameter is roughly the same as the spacing between the two innermost coils. Also, equal ampere turns allows all coils to be connected in series to simplify current control. The same convenience is provided if the ampere turns are an integral ratio. A much larger volume with the same uniformity can be obtained by using more than four coils; however, spacing between coils may limit the size of an object that may be introduced into the coils to one smaller than the volume of uniformity.(2)

Recent interest is in very large coils systems for testing of space craft in a magnetic field-free region. When the coils become very large, the circular shape becomes impractical to construct. For this reason polygonally-shaped coils have been considered.(3) It has been indicated that polygonal coils produce essentially the same uniformity as circular coils if in a system of N coils the polygons have at least 2N sides.(4) However, it should be noted that some square coil systems are equivalent to comparable systems of circular coils.(5)

Practically all of the coil systems designed have used the same criterion for uniformity. This consists of arranging the coils to cancel as many as possible of the coefficients of the Maclaurin series of the axially directed field component, expanded about the center of the coils, usually along the coil's axis. For circular coils this method produces a region which is very nearly spherical as was shown by Garrett.(6) Space vehicles are often of a shape which is more nearly oblately or prolately spherodial; in which case, a spherical volume of uniformity is not necessarily optimum.

This paper describes a technique for determining the arrangement of four circular coils to produce prolately or oblately spherodial volumes of uniformity. Even though only circular coils are considered, this technique is applicable to polygonal coils as well; the field equations for circular coils need only be replaced by those for the polygon system. The method being described will be referred to as the polynomial method. In a system of an odd numer of coils the mid-plane coil obstructs access; for this reason only an even number of coils is considered. Odd numbered coil systems may be examined by allowing the two inner coils to coincide in the x-y plane.

MACLAURIN SERIES METHOD

It is desirable to review briefly the Maclaurin series method since

it forms the basis for the polynomial method.

One of the two vanishingly thin circular coaxial coils of the pth symmetric coil-pair is located at $z = z_p$ (Fig. 1). The radius of the coil is r_p. The coil's spherical coordinants are (r_p, ϕ_p). Due to the axial symmetry of the coil, the field is independent of the azimuthal angle θ.

The magnetic scaler potential for the region inside the coil is given by

$$V_p = \frac{n_p i_p}{2}\left[1 - u_p - (1-u_p^2)\sum_{n=1}^{\infty}\frac{1}{n}\left(\frac{r}{r_p}\right)^n P_n'(u_p)\, P_n(u)\right] \qquad (1)$$

where $u_p = \cos \phi_p$
$u = \cos \phi$.

The axially directed component of the magnetic field intensity of the pth coil is

$$H_{z,p} = -\frac{\partial V_p}{\partial z} . \qquad (2)$$

Using the following relation

$$\frac{\partial}{\partial z}\left[r^n P_n(u)\right] = n r^{(n-1)} P_{n-1}(u) \qquad (3)$$

the axially directed field intensity becomes

$$H_{z,p} = \frac{n_p i_p}{2}(1-u_p^2)\sum_{n=0}^{\infty}\left[\frac{1}{r_p^{(n+1)}}\, P_{n+1}'(u_p)\, P_n(u)\right] r^n . \qquad (4)$$

The total axially directed field is obtained by summing equation 4 over p. Since the coils occur in pairs symmetrical about the origin, all terms involving odd powers of r are zero. The result can be written

$$H_z = \sum_{n=0}^{\infty} a_{2n}\, r^{2n}\, P_{2n}(u) . \qquad (5)$$

Equation 5 may be thought of as the power series expansion for the field about the origin along any ray. For the z axis, u = 1, the power series coefficients are

$$a_{2n} = \sum_{p=1}^{L} n_p i_p \frac{(1-u_p^2)}{r_p^{(2n+1)}}\, P_{2n+1}'(u_p) \qquad (6)$$

where L is the total number of coil pairs.

The Maclaurin series method of solution requires that a_{2n} be zero for n = 1, 2-----(2L - 1). For a system of four coils this requires

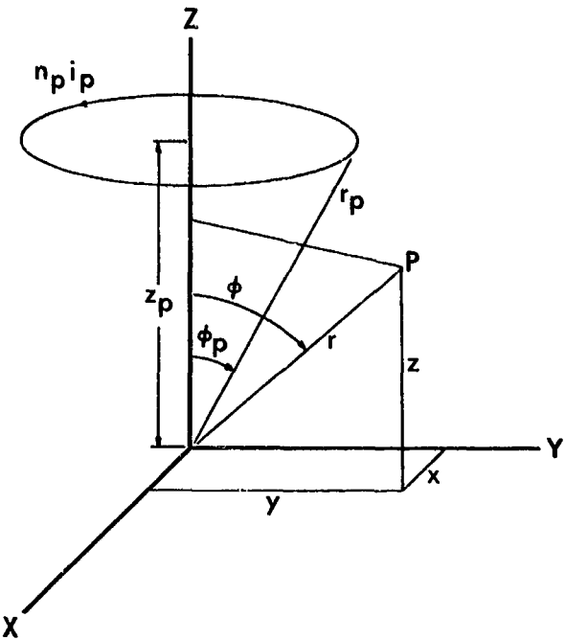


Figure 1. Configuration of one coil of the p^{th} coil-pair.

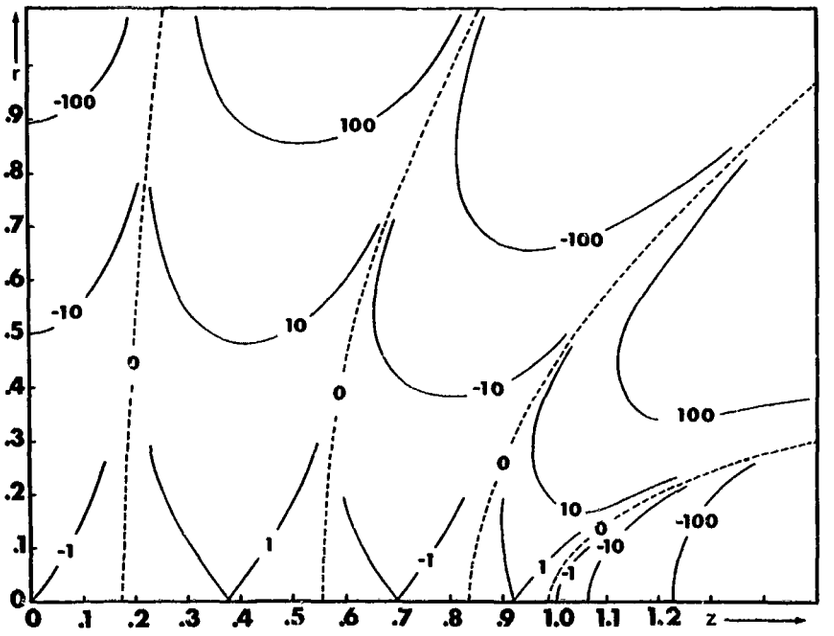


Figure 2. Error contours for the prolate spheroidal case.

$$(1-u_1^2)\,P_3'(u_1)/r_1^3 + T\,(1-u_2^2)\,P_3'(u_2)/r_2^3 = 0 \qquad \text{a)}$$

$$(1-u_1^2)\,P_5'(u_1)/r_1^5 + T\,(1-u_2^2)\,P_5'(u_2)/r_2^5 = 0 \qquad \text{b)} \quad (7)$$

$$(1-u_1^2)\,P_7'(u_1)/r_1^7 + T\,(1-u_2^2)\,P_7'(u_2)/r_2^7 = 0 \qquad \text{c)}$$

where $T = n_2 i_2 / n_1 i_1$.
Solving equation 7a for T

$$T = -\frac{(1-u_1^2)\,P_3'(u_1)}{(1-u_2^2)\,P_3'(u_2)}\,\frac{r_2^3}{r_1^3}\,. \qquad (8)$$

Eliminating T in equation 7b gives

$$\frac{r_2^2}{r_1^2} = \frac{P_3'(u_1)\,P_5'(u_2)}{P_5'(u_1)\,P_3'(u_2)}\,. \qquad (9)$$

Substituting equation 8 and 9 into 7c yields

$$P_3'(u_2)\,P_7'(u_2) - K\left[P_5'(u_2)\right]^2 = 0 \qquad (10)$$

where $K = P_3'(u_1)P_7'(u_1)/P_5'(u_1)^2$ which is constant when coil pair number one is fixed. When the coefficients of the derivative of the Legendre functions are introduced, there results

$$A_8 u_2^8 + A_6 u_2^6 + A_4 u_2^4 + A_2 u_2^2 + A_0 = 0 \qquad (11)$$

where $A_8 = 1407.65625 - 1550.390625K$
$A_6 = -1905.75 + 2067.1875K$
$A_4 = 767.8125 - 836.71875K$
$A_2 = -.05 + 98.4375K$
$A_0 = 3.28125 - 3.515625K$

Thus the solution involves finding the positive real roots of equation 11 which is quartic in u_2^2; if equation 8 and 9 give realizable values, then this root corresponds to the value given by Pitmann and Waidelich.(7) When this value of u_2 is substituted into equation 9 and equation 8, the value of T obtained may be irrational. The solution that gives a value of T that is a rational fraction can be determined by an interation process.

The field produced by the coil system when based on the Maclaurin series method is maximally flat at the center of the system. The deviation of the axially directed component of the field (the field error) is due principally to the first non-zero term in the power series. In the case of four coils, it is proportional to the eighth power of the distance from the origin.

POLYNOMIAL SERIES METHOD

A technique is now given for specifying the axial field component along a ray at any angle to the coil's axis in terms of a series of polynomials. Arranging the coils to cancel lower order terms, other than the constant, yields a field whose major error term has the characteristics of the first non-zero polynomial term. By change of scale, the volume of uniformity may be extended a considerable distance along the ray with a decrease in the size of the other dimensions. For a prolate shape the field is expanded along the coils' axis; for the oblate case it is expanded along the ray from the center of the system normal to the axis. By using the polynomial method the field may be made to oscillate about the desired value over a specified distance along the ray; as a result, the approximation for the polynomial method is no longer best at the origin but the error is spread out along the ray.

The method used to evaluate the coefficients is based on the fact that any polynomial can be uniquely expressed as a linear combination of a basic set of polynomials, where basic implies that there is one polynomial of each degree and the highest order coefficient of each polynomial is not zero.

The power series expression for the axially directed component of field (equation 5) along a ray $\phi = \phi_1'$, may be terminated after N + 1 terms. The value of N is chosen as large as one likes in order to describe the field to the desired accuracy. The truncation yields

$$H_z \doteq \sum_{n=0}^{N} a_{2n}^{(0)} r^{2n} \tag{12}$$

where $a_{2n}^{(0)} = a_{2n} P_{2n}(\cos \phi_1')$.

Since the field is an even function, the basic set of polynomials is chosen to be of even order

$$Q_{2M}(r) = \sum_{n=0}^{M} q_{M,n} r^{2n} \qquad M = 0, 1, 2, \ldots N \ . \tag{13}$$

Solving equation 13 for r^{2N} when M = N and substituting into equation 12 reduces the field expression by two degrees and adds one term involving $Q_{2N}(r)$

$$H_z = \sum_{n=0}^{N-1} a_{2n}^{(1)} r^{2n} + \frac{a_{2n}^{(0)}}{q_{N,N}} Q_{2N}(r) \tag{14}$$

where $a_{2n}^{(1)} = a_{2n}^{(0)} - \frac{q_{N,n}}{q_{N,N}} a_{2n}^{(0)}$. The process may be thought of as adding a term involving $Q_{2N}(r)$ to the 2nth order power series and subtracting the proper amount from each coefficient of the power series to account for its presence; the coefficient of $Q_{2N}(r)$ being chosen to completely absorb the term involving r^{2N}. The process is continued by applying it to the series part of equation 14 and repeating for each new series that arises. If the process is continued N + 1 times, the

truncated power series equation 14 is completely converted to a truncated series of polynomials

$$H_z \doteq \sum_{n=0}^{N} c_{2n}\, Q_{2n}(r) \tag{15}$$

where $c_{2i} = \sum_{j=i}^{N} b_{ij}\, a_{2j}^{(0)}$; $b_{ij} = \dfrac{d_{ij}^{(N-i)}}{q_{ii}}$

and $d_{ij}^{(k+1)} = d_{ij}^{(k)} - \dfrac{q_{N-k,i}}{q_{N-k,N-k}}\, d_{N-k,j}^{(k)}$; $d_{ij}^{(0)} = \begin{cases} 1 & i=j \\ 0 & i\neq j \end{cases}$.

With a system of L-coil pairs, (2L - 1) of the lower order coefficients of equation 15, other than the constant term, may be reduced to zero by proper size and orientation of the coils in the system. This is given by

$$\sum_{j=i}^{N} b_{ij}\, a_{2j}^{(0)} = 0 \qquad i = 1, 2, \ldots (2L-1) \ . \tag{16}$$

Substituting from equations 15 and 6, equation 16 becomes

$$\sum_{n=m}^{N} b_{mn} \sum_{p=1}^{L} n_p i_p \frac{(1-u_p^2)}{r_p^{(2n+1)}} P'_{2n+1}(u_p)\, P_{2n}(\cos\phi_1') = 0 \qquad m = 1, 2 \ldots (2L-1) \ . \tag{17}$$

FOUR-COIL SYSTEM USING TSCHEBYSCHEFF POLYNOMIALS

The set of equation 17 are solved using a basic set of Tschebyscheff polynomials for a system of four coils. The power series coefficients for the four-coil system are from equation 6

$$a_{2n} = n_1 i_1 \left[\frac{(1-u_1^2)}{r_1^{(2n+1)}} P'_{2n+1}(u_1) + T \frac{(1-u_2^2)}{r_2^{(2n+1)}} P'_{2n+1}(u_2) \right] P_{2n}(\cos\phi_1') \tag{18}$$

where $T = n_2 i_2 / n_1 i_1$. The conditions for canceling the three polynomial coefficients c_2, c_4 and c_6 may be written

$$f_{11} + T f_{12} = 0 \qquad \text{a)}$$
$$f_{21} + T f_{22} = 0 \qquad \text{b)} \tag{19}$$
$$f_{31} + T f_{32} = 0 \qquad \text{c)}$$

where $f_{ij} = \sum_{n=1}^{N} b_{in} \dfrac{(1-u_j^2)}{r_j^{(2n+1)}} P'_{2n+1}(u_j)\, P_{2n}(\cos\phi_1')$.

Solving equation 19a for T

$$T = -\frac{f_{11}}{f_{12}} \tag{20}$$

eliminating T from 19b and 19c yields

$$f = \frac{f_{12}}{f_{11}} - \frac{f_{22}}{f_{21}}$$
$$g = \frac{f_{22}}{f_{21}} - \frac{f_{32}}{f_{31}} \quad . \tag{21}$$

From equation 17 it can be seen that for large r_p the solution for a system using the polynomial method approaches as a limit the solution to the system when the power series method is employed. The power series solution can be found directly and for large r_1 it gives a local point for starting the numerical solution of equations 21.

As with the power series method, the value of T may be irrational and a second interation is necessary to obtain values of T that are rational fractions.

The Tschebyscheff polynomials are a natural choice for the basic set of polynomials because of their equal ripple characteristics. The Tschebyscheff expression for the field, along a ray at an angle ϕ_1' to the Z axis, after the maximum number of coefficients have been made to vanish, is

$$H_{z,\phi_1'} = C_0 + C_8 T_8(r) + C_{10} T_{10}(r) + \cdots \quad . \tag{22}$$

Most deviation of the field from c_0 is caused by $c_8 T_8(r)$. Let

$$T_8(r) = \sum_{n=0}^{4} t_{8,2n}\, r^{2n} \tag{23}$$

The field is approximately $H_{z,\phi_1'} \doteq C_0 + C_8 \sum_{n=0}^{4} t_{8,2n}\, r^{2n}$.

The power series expansion for the field along a ray at an angle ϕ_1' to the z axis is truncated at n = 4

$$H_{z,\phi_1'} = \sum_{n=0}^{4} \left[a_{2n} P_{2n}(\cos\phi_1')\right] r^{2n} . \tag{24}$$

Equating coefficients of like powers of r in equation 23 and 24 yields

$$a_0 \doteq C_0 + C_8$$
$$a_{2n} \doteq C_8\, t_{8,2n} \,/\, P_{2n}(\cos\phi_1') \quad n = 1 \text{ to } 4 \, . \tag{25}$$

Substituting equation 25 into equation 12 and dividing by c_0 yields

$$H_z/C_0 \doteq 1 + C_8/C_0 \sum_{n=0}^{4} \frac{t_{8,2n}}{P_{2n}(\cos\phi_1')} r^{2n} P_{2n}(u). \qquad (26)$$

Approximate equal error contours result from the plot of

$$e_N = \frac{|C_0|}{|C_8|} \frac{C_8}{C_0} \sum_{n=0}^{4} \frac{t_{8,2n}}{P_{2n}(\cos\phi_1')} r^{2n} P_{2n}(u) \qquad (27)$$

for e_N equal to a constant. When multiplied by $|c_8/c_0|$ equation 27 gives the deviation of the field from c_0 normalized to c_0.

Figures 2 and 3 are the universal equal error contour maps that result when ϕ_1' takes the values of 0^o and 90^o respectively. These maps are applicable to any four circular coil system whose coil orientation is specified by the Tschebyscheff polynomial method. The values obtained are approximate but give a very good indication of the size and shape of the volume of uniformity.

PRODUCING A DESIRED ECCENTRICITY IN THE VOLUME OF UNIFORMITY

The practical problem of coil design is, given the size and shape of the volume of uniformity, the degree of uniformity and the desired ampere turns ratio, to find the size and spacing of the coils. Figures 4 through 8 were produced in order to facilitate the solution of this problem. Figure 4 gives a plot of the normalized field error, e_N, vrs. the eccentricity of the volume of uniformity. Eccentricity is defined as the ratio of the length (z direction) to width (normal to z axis) of the volume of uniformity.

In designing the coil system e_N is determined from Figure 4 for the desired eccentricity. The normalized maximum field deviation divided by e_N yields $|c_8/c_0|$; this is the ordinate for Figures 5 through 8. Approximate values for all coil dimensions may be determined from these curves. Turns ratios other than those given may be approximated by interpolation. The values thus obtained may be used as a starting point for the numerical solution of equation 20.

Consider a numerical example. A system is to be designed to produce a field uniform in the axial direction to within 0.001% over an ellipsoid with an eccentricity of 2 and a unity ampere turns ratio. Figure 4 gives $e_N = 11.35$ (from which $|c_8/c_0| = 8.82\text{x}10^{-7}$). Approximate values are read from Figures 5 through 8 and used to start the iterative solution.

The iterative solution of equation 20 yields

$u_1 = 0.282000$ $\qquad$ $r_1 = 3.227527$

$u_2 = 0.757110$ $\qquad$ $r_2 = 3.640996$

$c_0 = 0.402412$ $\qquad$ $c_8/c_0 = -8\ 52\text{x}10^{-7}$

$T = 1.000000$

The final step in the design of a coil system should be an actual field plot to determine the field variation for the particular systems. The axial field was evaluated for the example, using the eliptic integral

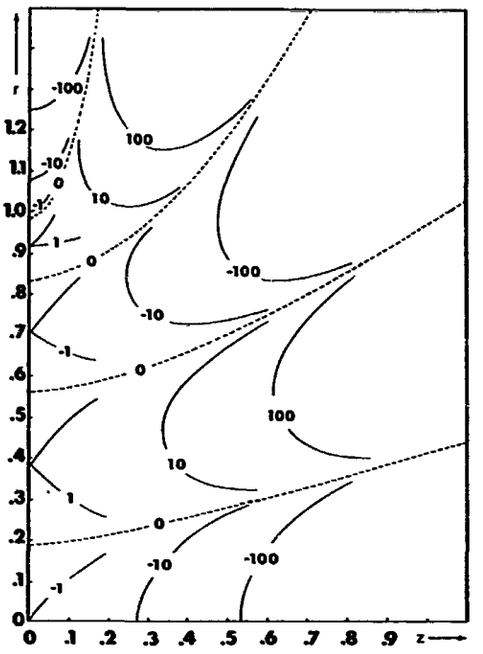


Figure 3. Error contours for the oblate spheroidal case.

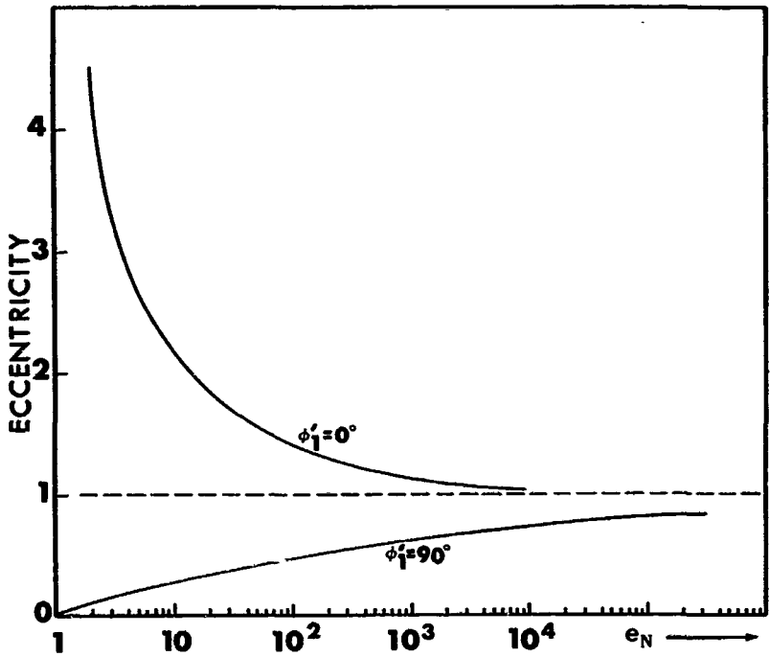


Figure 4. Eccentricity vs. normalized field error.

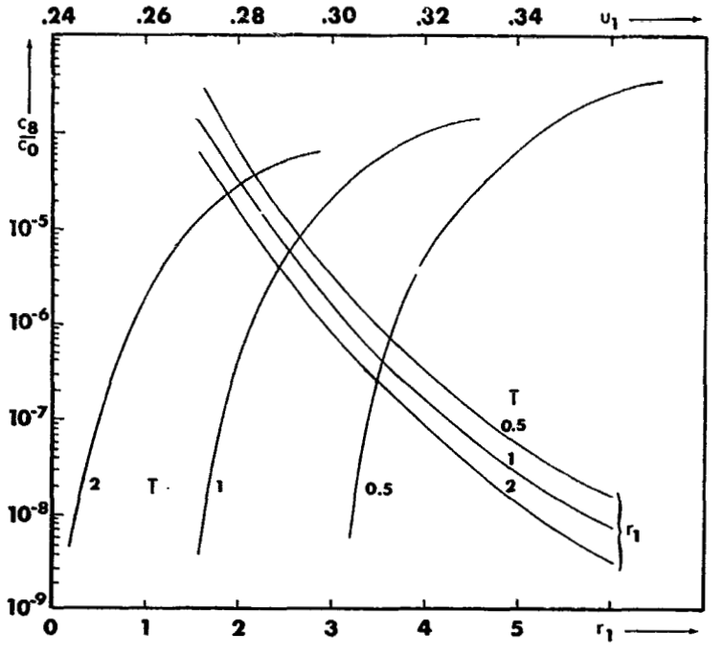


Figure 5. Coordinates for first coil-pair, $\phi_1' = 0°$.

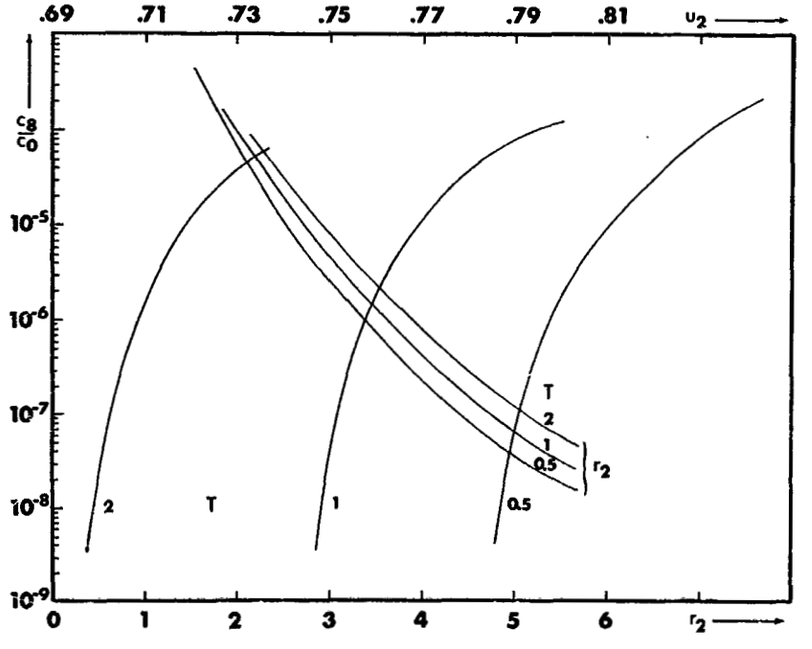


Figure 6. Coordinates of second coil-pair, $\phi_1' = 0°$.

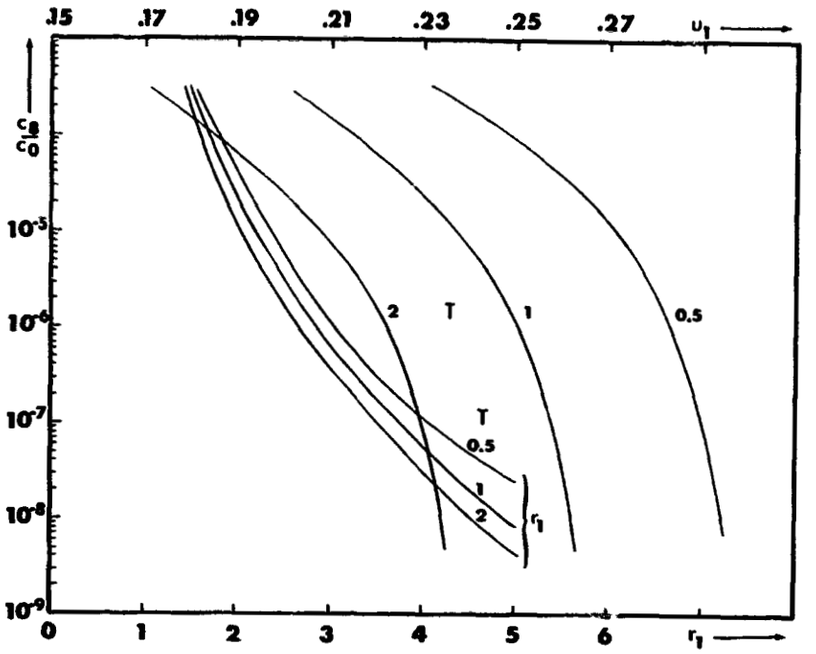


Figure 7. Coordinates of first coil-pair, $\phi_1' = 90°$.

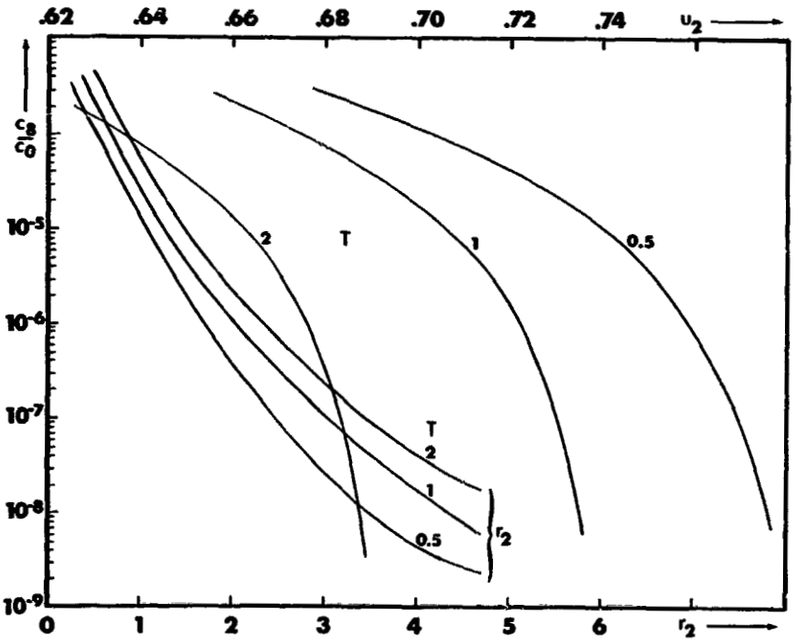


Figure 8. Coordinates of second coil-pair, $\phi_1' = 90°$.

method.(6) Equation 12 could also have been used to evaluate the field error. The variation along the axis and radially is plotted in Figure 9. The eccentricity as determined from Figure 9 is 2.18 which compares well with the value desired. The maximum dimension of the volume of uniformity is 1.09 as determined from Figure 9. The actual desired maximum dimension is divided by 1.09 to determine the scale factor for all dimensions.

SUMMARY

A method has been given for designing a coil system that will produce other than a spherical volume of uniformity. The results indicate that such a system may have much smaller coils when the eccentricity of the working region is high than would a system with a spherical volume of uniformity. The results are presented so that one may determine the unique system that has the desired eccentricity, degree of uniformity and ampere turns ratio.

BIBLIOGRAPHY

(1) Braunbek, Werner. "Die Erzeugung weitgehend homogener durch kreisstrome," Zeitschrift Fur Physik, LXXXVIII (April, 1934), pp. 399-402.

(2) Speiser, M. and D. L. Waidelich. "The Six-Circular-Coil System," Final Report of the Goddard Summer Workshop Program in Measurement and Simulation of the Space Environment, pp. C-113-C-121. Publication X-320-63-264. Greenbelt, Maryland: Goddard Space Flight Center, 1963.

(3) Saperstone, S. H. "Four-Octagonal-Coil Systems,: Report X-320-64-341, pp. C-7-C-16. Greenbelt, Maryland: Goddard Space Flight Center, 1964.

(4) Bloom, A. L., D. J. Innes, R. C. Rempel and K. A. Ruddock. "Octagonal Coil Systems for Canceling the Earth's Magnetic Field," Journal of Applied Physics, Vol. 36, no. 8 (August, 1963), pp. 2560-2565.

(5) Waidelich, D. L., G. Yildirim, M. Speiser, and R. E. Gebhardt. "Four-Square-Coil Systems for the Magnetic Testing of Spacecraft," IEEE Transactions on Aerospace, AS II (October, 1964), pp. 1181-86.

(6) Garrett, Milan Wayne. "Axially Symme' c Systems for Generating and Measuring Magnetic Fields. Part Journal of Applied Physics, XXII (September, 1951), pp. 1091-1107.

(7) Pittman, M. E. and D. L. Waidelich. "Three and Four Coil Systems for Homogeneous Magnetic Fields," IEEE Transactions on Aerospace, AS II (February, 1964), pp. 36-45, also in National Aeronautics and Space Administration Technical Note TN D-2095, (January, 1964).

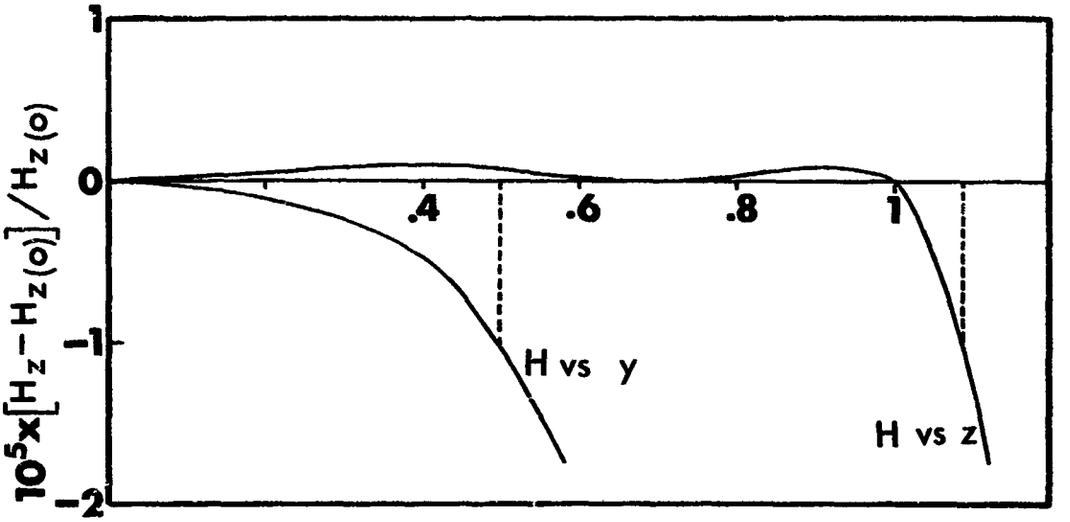


Figure 9. Calculated field error for the example.

JAN K. SEDIVY

"DESIGN AND PERFORMANCE OF A MICROWAVE MOTOR"

Space Magnetic Exploration and Technology Symposium, August 1967
University of Nevada, Reno, Nevada

N69-33960

SUMMARY

This paper describes a microwave motor, its characteristics and properties obtained experimentally in addition to the analytical derivation of induced voltage, current and produced torque. Motors with a power input of approximately 2 Watts operating at a frequency in the neighborhood of 3300 Mc have been built and tested experimentally. The lower limit of operating speed was 20 RPM, the upper limit approximately 1200 RPM. The motor has the advantage of simple construction, contains no commutator; when used in a wave guide reversal of direction of rotation is easily accomplished. Since the microwave energy can be transmitted over large distances the microwave motor may find use and application in control and actuation of space vehicles or components for space program.

INTRODUCTION

With the space age development the possibility of utilization of microwave energy for conversion to mechanical energy may gain a new interest and application. At the present it is possible to produce high microwave power and transmit it to some receiver in space. At the receiving end, however, it may be necessary to use large antennas in order to concentrate the microwave energy. In addition it may be necessary to employ waveguide and operate the microwave motor such that part of the rotor circuit will be inside of the waveguide. The purpose of the waveguide is to guide the microwave power to the rotor circuit; however, it is not essential for the operation of the motor.

Basically the motor resembles a standard D.C. motor except it does not have a mechanical commutator in the rotor circuit. Typical construction is shown in Figure 1. The pickup antenna on the rotor can be mounted inside of a wave guide as it is indicated in the Fig. 1 by dash lines. Dipole or loop antenna can be used in order to pick up the microwave energy. The principle of operation is as follows: The rotor antenna picks up the microwave energy, the diode rectifies the current which in turn flows in the rotor coil; the current interacts with the permanent magnet field and produces a torque. The geometry must be asymmetrical with respect to the rotational axis, otherwise the average component of torque would be zero. Many antenna configurations are, of course, possible and some of them were made and tested experimentally. (Ref. (1) (2) (3) (4)). Dr. Ishii and associates first suggested and investigated experimentally different

Electrical Engineering Department, Marquette University, Milwaukee, Wis.

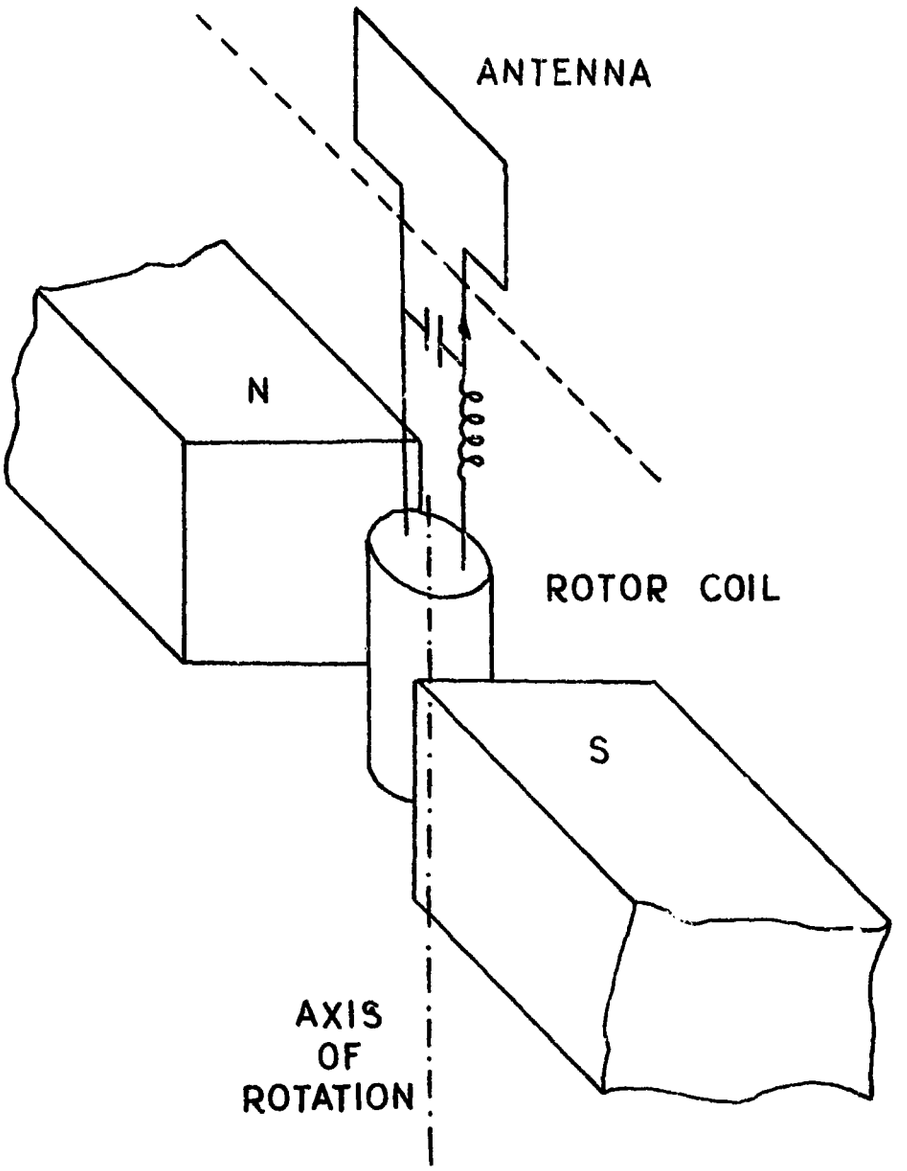


FIG 1.

antenna arrangements outside and inside of a wave guide. These investigators also found experimentally the relations between the speed and the frequency of operation, conditions for speed reversal and speed vs. input power relation. There is no general analysis available for the microwave motor. This paper provides the first step and its aim is to derive the equations for voltage, current and torque for loop antennas in the rotor circuit.

ANALYSIS

This analysis is carried out for a rectangular antenna loop. Since the plane of the antenna loop must be arranged asymmetrically with respect to the rotational axis and with respect to the wave propagation direction and since it is advantageous to use simpler form of harmonic functions, three different coordinate systems are used: x, y, z; x', y', z', x'', y'', z''. The x, y, z system is selected such that the wave propagation is in the positive direction; the flux density wave then has components B_x, B_y and B_z. The x, y, z system is stationary with respect to the stator (Fig.2A.) The x', y', z' system is associated with the rotational axis and is chosen in such a fasion that the z' axis is the axis of rotation of the rotor. The x', y', z' coordinate system is also stationary (Fig. 2B). The x'', y'', z'' coordinate system is tied to the antenna loop and is picked such that the width of the antenna loop is in the x'' direction and the height in the y'' direction. This system rotates with the antenna, which is rigidly connected to the rotor (Fig. 2C). In order to relate the rotating system (x'', y'', z'') with the stationary systems an angle θ is used; θ is equal to zero when the projection into xy (or x'y') plane of z'' axis and negative y axis coincide as seen in Fig. 3. This figure shows the top view of the antenna arrangement for $\theta = 0$. The reason for this choice of coordinates is the simpler form of the transformation relations. From this it follows that

$$\theta = \omega_R t + \delta \tag{1}$$

where ω_R represents the mechanical angular velocity of the rotor and δ is some initial angle. Clockwise rotation has been assumed. With the rotating and stationary coordinate systems established, the next step is to find the magnitude of the flux element through the surface element of the antenna.

$$d\phi = \bar{B} \cdot d\bar{s} = \bar{B} \cdot \bar{r} dA \tag{2}$$

$\bar{B}$ is the flux density vector, $\bar{r}$ is the unit vector perpendicular to surface of the antenna, and dA is the area element of the antenna. The equation of the flux density is

$$\bar{B} = i\, B_x(y,t) + j\, B_y(y,t) + k\, B_z(y,t) \tag{3}$$

where i, j, k are the unit vectors of the x, y, z coordinate system and

$$\begin{aligned} B_x(y,t) &= B_x \sin(\omega_e t - Ky) \\ B_y(y,t) &= B_y \sin(\omega_e t - Ky) \\ B_z(y,t) &= B_z \sin(\omega_e t - Ky) \end{aligned} \tag{4}$$

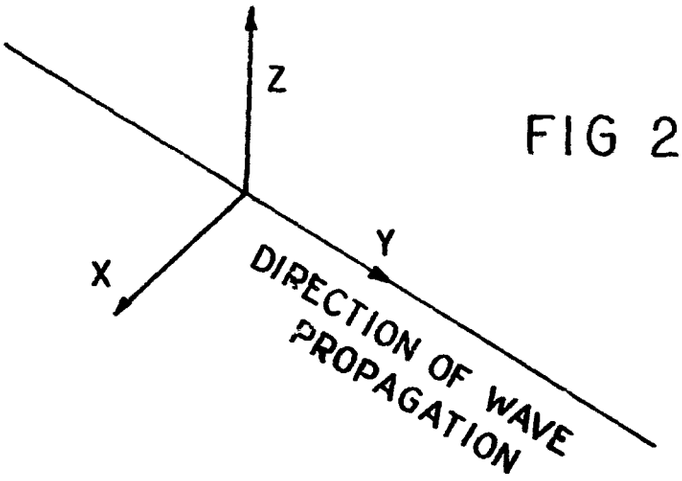


FIG 2A.

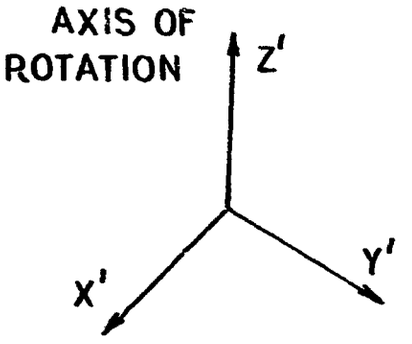


FIG 2B.

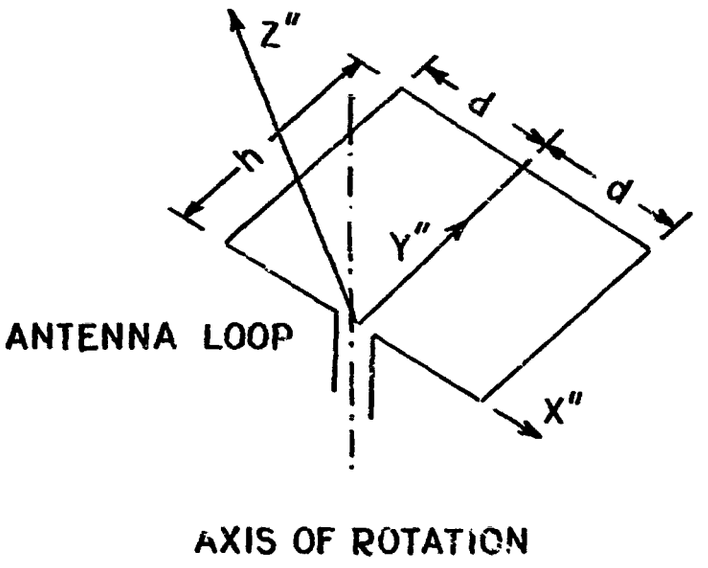


FIG 2C.

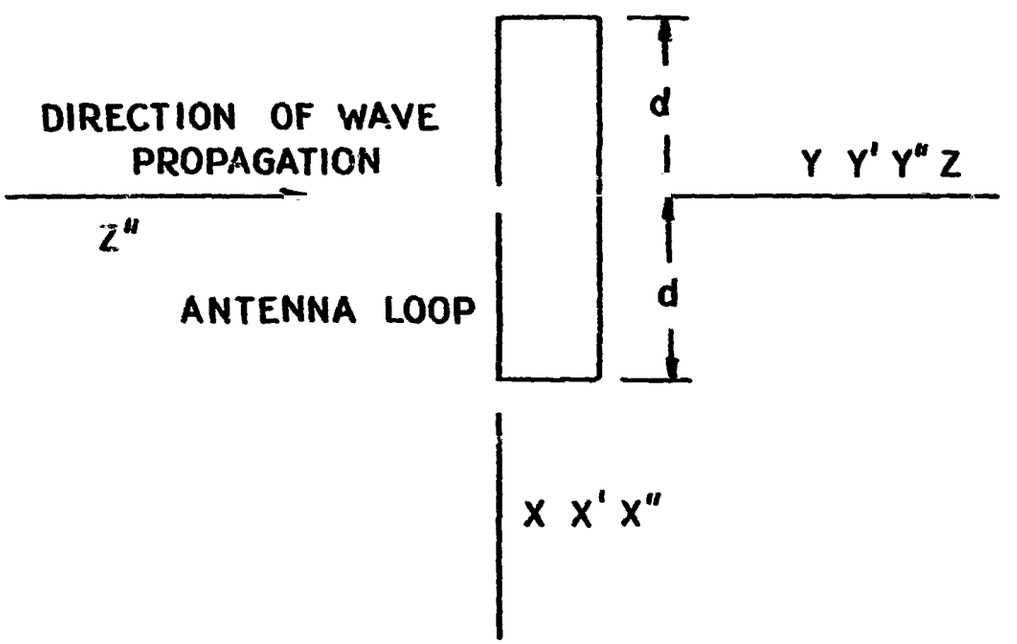


FIG 3.

are the components of the flux density vector propagating in the positive direction of the y-axis. ω_e is the electrical angular velocity of the waves - it is assumed to be equal for all three components - and K represents $2\pi f/v$ expression (f is the frequency of the wave and v is velocity of light). The element $d\bar{s} = \bar{r}\, dA$ is obtained in the following fashion: A unit vector $\bar{r}$ perpendicular to the antenna plane can be represented as

$$\bar{r} = \bar{g} + \bar{p} \tag{5}$$

(Fig.4) When the antenna rotates the end point of the vector $\bar{p}$ describes a circle which has an equation

$$x'^2 + y'^2 = \cos^2\beta \tag{6}$$

where β is the angle between z' and y'' coordinates and it is constant. Because of the relation between x', y', z' and x, y, z coordinate system which is expressed as .

$$\begin{bmatrix} x' \\ y' \\ z' \end{bmatrix} = \begin{bmatrix} 1 & 0 & 0 \\ 0 & \cos\alpha & \sin\alpha \\ 0 & -\sin\alpha & \cos\alpha \end{bmatrix} \begin{bmatrix} x \\ y \\ z \end{bmatrix} \tag{7}$$

it follows that

$$x^2 + y^2 + 2y \frac{\sin\alpha}{\cos\alpha}\, y \cos\alpha \sin\alpha + \frac{\sin^2\alpha}{\cos^2\alpha}\, y^2 \sin^2\alpha = \cos^2\beta \tag{8}$$

where α is the angle between the axis of rotation (z') and z coordinate. It is also a constant. With

$$x = \cos\beta \sin\theta \tag{9}$$

$$y^2 = \frac{\cos^2\beta \cos^2\theta}{\cos^2\alpha + 2\sin^2\alpha + \frac{\sin^2\alpha}{\cos^2\alpha}} = \cos^2\alpha \cos^2\beta \cos^2\theta \tag{10}$$

and

$$z^2 = \sin^2\alpha \cos^2\beta \cos^2\theta \tag{11}$$

Then the equation of the $\bar{p}$ vector becomes:

$$\bar{p} = -i \cos\beta \sin\theta - j \cos\alpha \cos\beta \cos\theta - k \sin\alpha \cos\beta \cos\theta \tag{12}$$

Since the vector $\bar{g}$ can be expressed as

$$\bar{g} = - j \sin\beta \sin\alpha + k \sin\beta \cos\alpha \tag{13}$$

then from Eqs. (5), (12) and (13)

$$\bar{r} = - i \cos\beta \sin\theta - j (\cos\alpha \cos\beta \cos\theta + \sin\beta \sin\alpha) + k (\sin\beta \cos\alpha - \sin\alpha \cos\beta \cos\theta) \tag{14}$$

Also the equation of the antenna plane is:

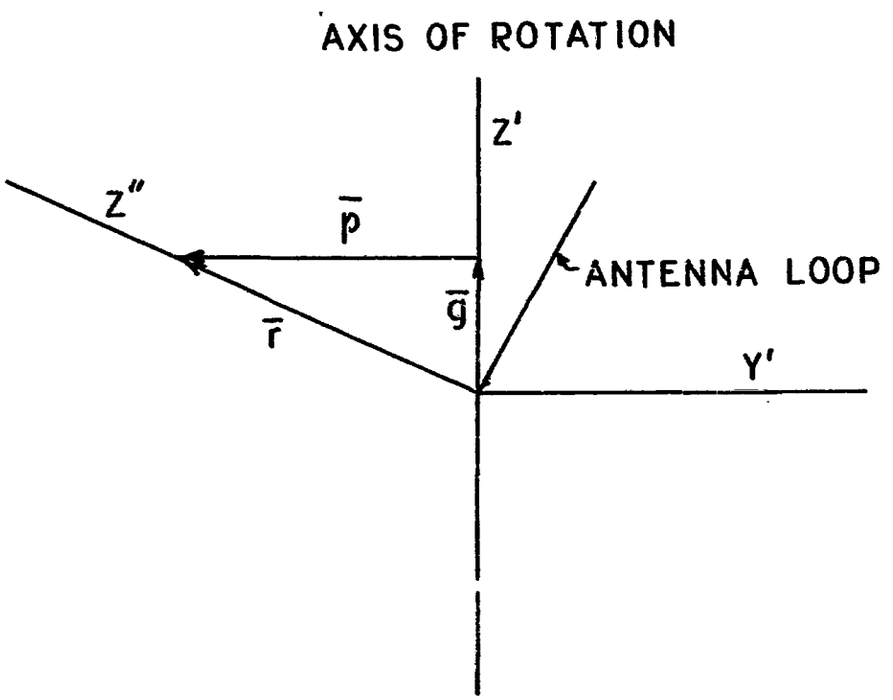


FIG 4.

$$- x \cos\beta \sin\theta - y (\cos\alpha \cos\beta \cos\theta + \sin\beta \sin\alpha) + z (\sin\beta \cos\alpha - \sin\alpha \cos\beta \cos\theta) = 0 \quad (15)$$

From Eqs. (2), (4) and (14) we obtain:

$$d\vec{\Phi} = [i B_x \sin(\omega_e t - Ky) + jB_y \sin(\omega_e t - Ky) + kB_z \sin(\omega_e t - Ky)] \cdot [-i \cos\beta \sin\theta - j(\cos\alpha \cos\beta \cos\theta + \sin\beta \sin\alpha) + k(\sin\beta \cos\alpha - \sin\alpha \cos\beta \cos\theta)] dA \quad (16)$$

The area element dA has, of course, constant magnitude, independent of θ and could be written as:

$$dA = dx'' dy'' \quad (17)$$

From Eq. (7) and because of

$$\begin{bmatrix} x' \\ y' \\ z' \end{bmatrix} = \begin{bmatrix} \cos\theta & \sin\beta \sin\theta & -\cos\beta \sin\theta \\ -\sin\theta & \sin\beta \cos\theta & -\cos\beta \cos\theta \\ 0 & \cos\beta & \sin\beta \end{bmatrix} \begin{bmatrix} x'' \\ y'' \\ z'' \end{bmatrix} \quad (18)$$

it follows that

$$\begin{bmatrix} x \\ y \\ z \end{bmatrix} = \begin{bmatrix} \cos\theta & \sin\beta \sin\theta & -\cos\beta \sin\theta \\ -\cos\alpha \sin\theta & \cos\alpha \sin\beta \cos\theta - \sin\alpha \cos\beta & -\cos\alpha \cos\beta \cos\theta - \sin\alpha \sin\beta \\ -\sin\alpha \sin\theta & \sin\alpha \sin\beta \cos\theta + \cos\alpha \cos\beta & -\sin\alpha \cos\beta \cos\theta + \cos\alpha \sin\beta \end{bmatrix} \begin{bmatrix} x'' \\ y'' \\ z'' \end{bmatrix} \quad (19)$$

Since the antenna lies in the x'' y'' plane (z'' = 0) we obtain from Eqs. (16) and (19)

$$d\vec{\Phi} = [-B_x \cos\beta \sin\theta \sin[\omega_e t - K(-\cos\alpha \sin\theta x'' + (\cos\alpha \sin\beta \cos\theta - \sin\alpha \cos\beta) y'')] - B_y (\cos\alpha \cos\beta \cos\theta + \sin\beta \sin\alpha) \sin[\omega_e t - K(-\cos\alpha \sin\theta x'' + (\cos\alpha \sin\beta \cos\theta - \sin\alpha \cos\beta) y'')] + B_z (\sin\beta \cos\alpha - \sin\alpha \cos\beta \cos\theta) \sin[\omega_e t - K(-\cos\alpha \sin\theta x'' + (\cos\alpha \sin\beta \cos\theta - \sin\alpha \cos\beta) y'')]] dx'' dy'' \quad (20)$$

if we set:

$$a = \cos\alpha \sin\theta$$
$$b = \cos\alpha \sin\beta \cos\theta - \sin\alpha \cos\beta$$
$$c = \cos\beta \sin\theta$$
$$m = \cos\alpha \cos\beta \cos\theta + \sin\alpha \sin\beta$$
$$n = \sin\beta \cos\alpha - \sin\alpha \cos\beta \cos\theta \quad (21)$$

and integrate over the whole area of the antenna we obtain

$$\vec{\Phi} = \int_{-d}^{d} \int_{0}^{h} (-B_x c \sin[\omega_e t - K(-ax'' + by'')] - B_y m \sin[\omega_e t - K(-ax'' + by'')] + B_z n \sin[\omega_e t - K(-ax'' + by'')]) dx'' dy'' \quad (22)$$

Before we carry out the integration it seems necessary to add a few remarks. First of all, with some simplifications, as for example when $\alpha = 0$, $\beta = 0$, then $a = \sin\theta$, $b = 0$, $c = \sin\theta$, $m = \cos\theta$, $n = 0$ one obtains an integral where b is equal to zero. (The choice of $\alpha = 0$ and $\beta = 0$) corresponds to the case where the propagation direction and the unit vector $\bar{r}$ are perpendicular to the axis of rotation). It is thus necessary to substitute the values of a, b, etc., into this integral first and not after the integration has been carried out, because one would obtain expression of the form 1/0. Also, the integration is carried out in the x''y'' coordinates. It is, however, possible to integrate in x, y, coordinate system, but the limits of integration are more involved.

Integrating Eq. (22) one obtains the total flux:

$$\begin{aligned} 0 = {} & \frac{2c\,B_x}{K^2 ab} \sin(Kad) \left[\cos(\omega_e t - Kbh) - \cos(\omega_e t) \right] + \\ & + \frac{2m\,B_y}{K^2 ab} \sin(Kad) \left[\cos(\omega_e t - Kbh) - \cos(\omega_e t) \right] - \\ & - \frac{2n\,B_z}{K^2 ab} \sin(Kad) \left[\cos(\omega_e t - Khb) - \cos(\omega_e t) \right] = \\ & = \frac{2}{K^2 ab} \sin(Kad) \left[(cB_x + mB_y - nB_z) \right] \left[\cos(\omega_e t - Kbh) - \right. \\ & \left. - \cos(\omega_e t) \right] \end{aligned} \tag{23}$$

The induced voltage can now be calculated from Eq. (23) by taking the total derivative with respect to time. It is to be remembered that a, b, c, m, and n contain θ (Eqs. 5, 21) which in turn is a time function (Eq.1). Since $\omega_e \ggg \omega_R$ the rotational component can be completely neglected. Then the equation of induced voltage becomes:

$$e = \frac{2\omega_e}{K^2 ab} \sin(Kad)\,(cB_x + mB_y - nB_z) \left[\sin(\omega_e t) - \sin(\omega_e t - Kbh) \right] \tag{24}$$

For a, b, c, m, and n the values from Eq. (21) can be substituted.

The electromagnetic torque can be derived from the coenergy. For a doubly-excited system the coenergy is

$$W'_{field} = .5\,L_{ss}\,i_s^2 + .5\,L_{rr}\,i_r^2 + L_{rs}\,i_r\,i_s \tag{25}$$

where L_{ss}, L_{rr} and L_{rs} are the self-and mutual inductances of the stator and rotor coils, i_s and i_r represent the stator and rotor current respectively. The torque can then be derived as

$$T = + \frac{\partial W'_{field}}{\partial \gamma} \tag{26}$$

Fig. 5 represents the completely general conditions of position between antenna, rotor coil, horn and stationary stator. The rotor circuit does not contain any ferromagnetic material, thus L_{ss} will be constant and independent of γ. The self-inductance of rotor will depend upon γ and could be represented as:

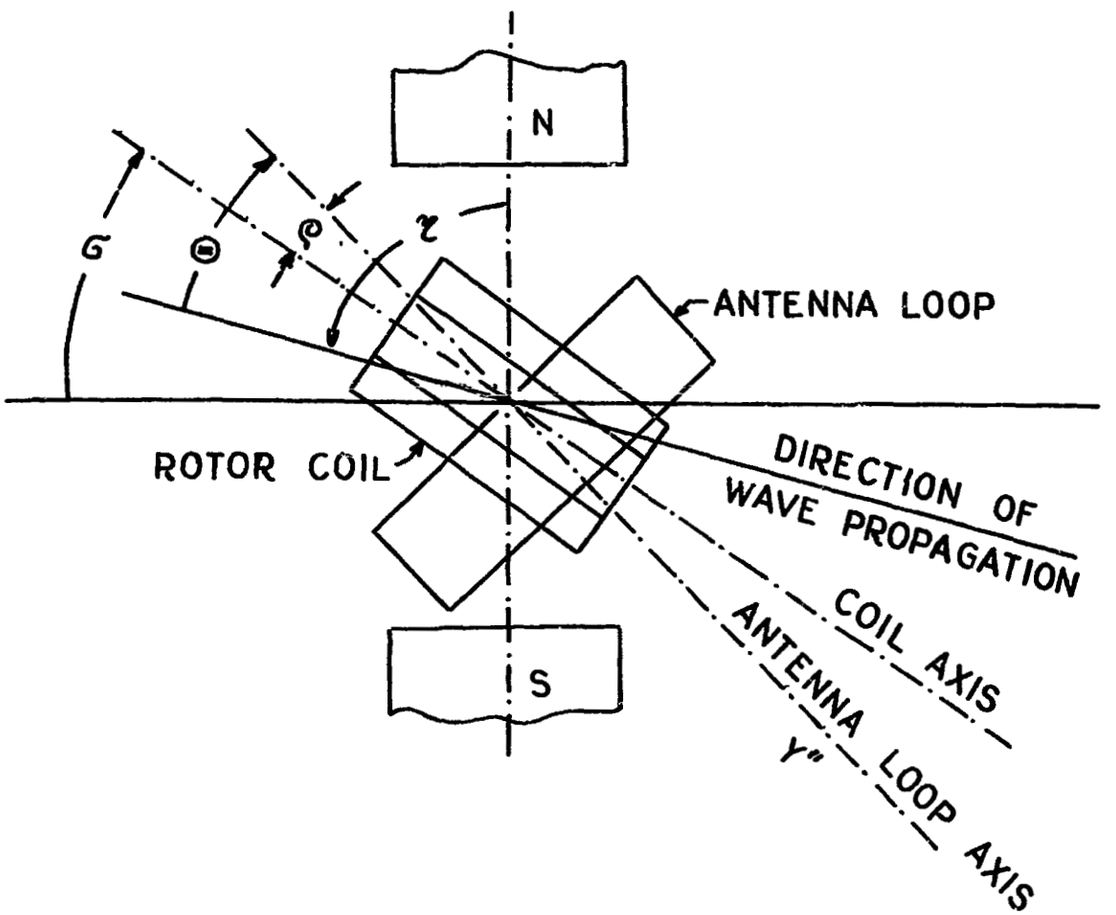

N
S
ANTENNA LOOP
ROTOR COIL
DIRECTION OF
WAVE PROPAGATION
COIL AXIS
ANTENNA LOOP AXIS
γ"

FIG 5.

$$L_{rr} = L_{rro} + L_{rr\eta} \cos 2\eta + \text{higher order terms in } \eta \tag{27}$$

For the mutual inductance between the stator and rotor winding we can write

$$L_{sr} = L_{sro} \cos \eta \tag{28}$$

In order to determine the conditions for an average torque the rotor current must be found. Because of the rectifier in the antenna circuit, the current in the antenna loop is a half-wave rectified sine wave which has an amplitude equal to:

$$I_{Ant} = \frac{2\omega_e \sin(K \cos\alpha \sin\theta\, d)}{K^2 \cos\alpha \sin\theta (\cos\alpha \sin\beta \cos\theta - \sin\alpha \cos\beta)} \cdot$$
$$\cdot \left[B_x \cos\beta \sin\theta + B_y (\cos\alpha \cos\beta \cos\theta + \sin\alpha \sin\beta) - \right.$$
$$\left. - B_z (\sin\beta \cos\alpha - \sin\alpha \cos\beta \cos\theta) \right] \frac{1}{Z} \tag{29}$$

where Z is the impedance of the antenna loop. The average value of the current, as it follows from Eq. (29), will then flow in the rotor coil. Since the Eq. (29) contains sine and cosine terms of the angle θ, the sign of the whole expression will also change. Thus Eq. (29) should be evaluated for given parameters and variable θ, and then the absolute value taken as the resulting amplitude. From Figure 5 it follows that

$$\delta = \frac{\pi}{2} - \gamma + \theta - \varphi$$
$$\delta = \eta + \frac{\pi}{2}$$
$$\eta = \theta - \varphi - \gamma \tag{30}$$

Substituting this expression into the torque relation and from Eqs. (27), (28), and (29) one finds

$$T = i_r^2 \left[(-L_{rr}(\eta) \sin 2(\theta - \varphi - \gamma) + \text{derivatives of higher order of inductance components of the rotor}) \right. \left. -L_{sro} \sin(\theta - \varphi - \gamma) i_s i_r \right] \tag{31}$$

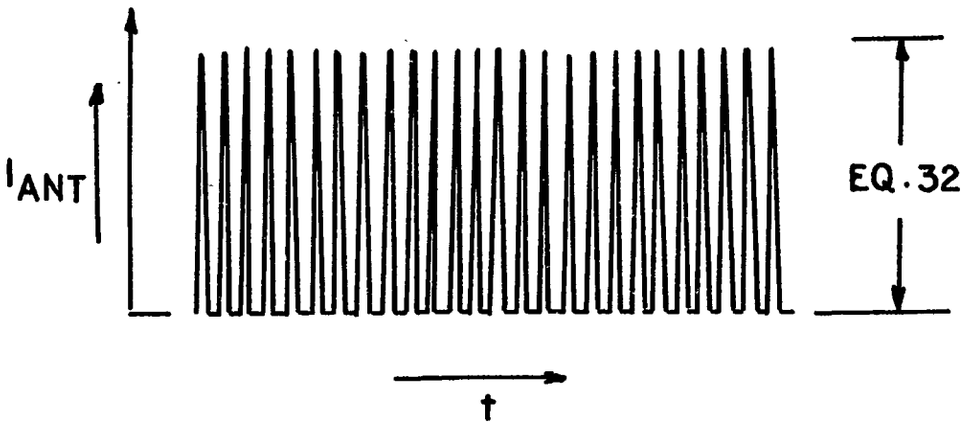
The conditions for existance of an average torque can now be set up. The rotor current in Eq. (31) will be of the form:

$$i_r = \frac{1}{R} I_{Ant} = \frac{1}{\pi} \left[i_{av} + \text{higher order terms in } \theta \right] \quad \text{(Fig.6)} \tag{32}$$

Putting Eq. (32) into Eq. (31) establishes the conditions for which the torque component will be independent of θ. If i_r contains a term proportional to sin 2 θ, the first part of Eq. (31) will produce a torque component which is independent of θ. Thus in this mode an average torque will be produced.

DISCUSSION AND EXPERIMENTAL DATA

The analysis was carried out considering the B-field only; then the voltage can be derived from Faraday's law. The resulting voltage and current equation is rather involved, but not difficult.



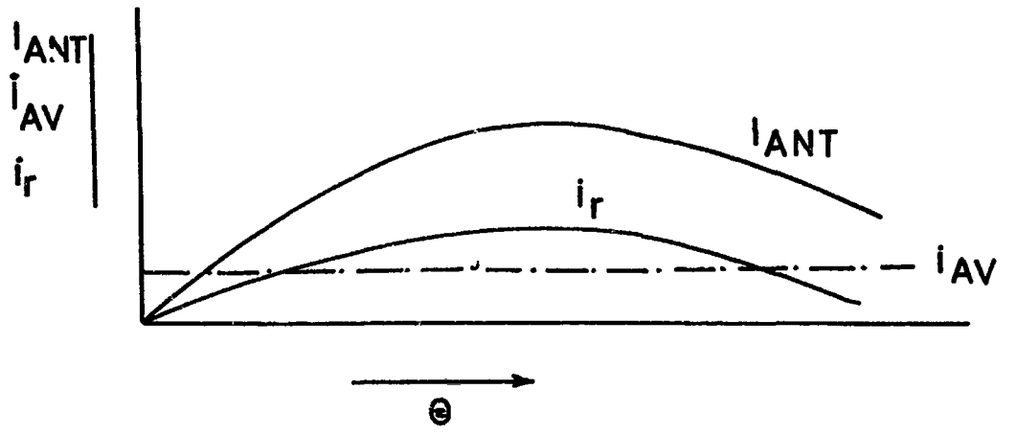


FIG 6.

Much of the experimental data are available as given in the references. The salient features and characteristics are given here. In the experiments the microwave frequency was approximately 3.4 GHz and the flux density of the permanent magnet had a magnitude of .10 to .20 W/m^2. The microwave input power was on the average 2 Watts. With these basic quantities the following characteristic and properties were obtained by test.

a) The lower limit of speed obtained is approximately 20 RPM, the upper limit 1200 RPM. The speed depends upon the incident power, shape and geometry of the antenna and somewhat upon the microwave frequency. Lower speeds were obtained when using the loop antennas, higher speeds when using dipole and reflector-type antennas in a wave guide. Speed control and direction of rotation can be accomplished by using the microwave motor in a parametric mode.(Ref.6).

b) The speed vs. input power characteristic is a linear relation up to approximately 2 Watts; above 2 Watts the characteristic displays saturation and an increase in input power does not produce proportional increase in speed.

c) For an operation of a rotor antenna in a wave guide the speed changes rather rapidly from zero to a maximum value when the frequency is changed by approximately 2%. For a dipole, two-folded dipole antenna and loop antenna the speed is much less sensitive to frequency changes.

d) The rotor coil current is in the neighborhood of 30 mA. With this value the torque produced would be $.06 \cdot 10^{-6}$ NM per cm of rotor conductor length and per cm of rotor radius. If, for example, the coil has 1000 turns and the coil is 2 cm long the total torque should be approximately $.24 \cdot 10^{-3}$ NM which compares with the experimental data. The efficiency is then approximately 1%.

CONCLUSION

This paper presents theoretical analysis and also salient results of the experimental investigations. The mode of operation of a microwave motor was demonstrated and experimental evidence supports the feasibility of conversion of microwave energy into mechanical energy.

ACKNOWLEDGMENT

The author wishes to express his sincere gratitude to Dr. T. K. Ishii of Marquette University for his interest in the subject and his valued suggestions which are very much appreciated.

REFERENCES

(1) R. C. Garnier, T. K. Ishii: Microwave Power New Motor System, The Electronic Engineer, August 1966, 25, pp 54-56.

(2) R. C. Garnier, T. K. Ishii: Microwave Motor, Proc. IEEE, Vol.52, No. 11, Nov. 64, pp 1380-1381.

(3) R. W. Steinhoff, T. K. Ishii: Pickup Antennas for Waveguide Motors, IEEE Trans. on Microwave Theory and Techniques, Vol. MTT-14, #9, Sept. 1966, pp 438.

(4) T. K. Ishii, R. C. Garnier, R. W. Steinhoff: Electric Motor Energized by Microwaves in a Waveguide. Proc. of NEC, Vol. 22, 1966, pp 259-264.

(5) R. C. Garnier, T. K. Ishii: Microwave Motor Utilizing a Double Antenna and a Double Coil. Proc. IEEE, Vol. 53, No. 2, February 65, pp 178.

(6) T. K. Ishii, R. C. Garnier: Parametric Operation of a Waveguide Motor, Electronics Letters, Vol. 2, No. 10, October 1966.

(7) Stockman, H. E. : Parametric Oscillatory and Rotary Motion, Proc. IRE, 1960, 48, pp 1157-1158.

(8) Woodson-White: Electromechanical Energy Conversion (Book).

LIST OF SYMBOLS

a	Eq. (21)
b	Eq. (21)
c	Eq. (21)
2d	width of the antenna loop
f	frequency of the flux density wave
$\bar{g}$	vector in the axis of rotation. (Fig. 4)
h	height of the antenna
i,j,k	unit vectors in x, y, z coordinate system
i_r	rotor current
i_s	stator current
i_{av}	average value of the rotor current
m	Eq. (21)
n	Eq. (21)
$\bar{p}$	vector perpendicular to the axis of rotation (Fig. 4)
r	unit vector normal to the antenna plane
v	velocity of light
A	area of the antenna
$B_xB_yB_z$	x,y,z components of the flux density waves
I_{Ant}	average value of antenna current
K	$2\pi f/v$
L_{rr}	self-inductance of rotor coil
L_{rro}	average value of the self-inductance of the rotor coil
$L_{rr}(\eta)$	η - dependent component of the rotor coil self-inductance
L_{ss}	self-inductance of stator coil
L_{sr}	mutual inductance between stator and rotor coil
L_{sro}	amplitude of the mutual inductance between stator and rotor
T	torque
W'_{field}	electromagnetic coenergy
Z	impedance of the antenna loop

α	angle between the axis of rotation and z coordinate (z' and z)
β	angle between the axis of rotation and y'' coordinate (z' and y'')
γ	Fig. 5
ζ	angle between stator axis and rotor coil axis (Fig. 5)
θ	Eq. (1)
δ	Eq. (1)
φ	Fig. 5
σ	Fig. 5
ϕ	flux linking the antenna loop
ω_e	angular velocity of the flux density wave
ω_R	angular velocity of rotor

Paul A. Cloutier*

"A Vector Magnetometer System for Detection of Ionospheric Currents by Sounding Rockets"

Space Magnetic Exploration and Technology Symposium
August 1967
University of Nevada, Reno

N69-33961

Abstract

A vector magnetometer employing a scalar alkali-vapor sensor and single switchable bias coil is described. Mathematical analysis of the magnetometer signal for a spinning vehicle is performed, and the vector field components in the vehicle coordinate system are extracted. Use of a vehicle aspect device is discussed, and the translation of the field vector from the vehicle coordinate system to a ground-based geographic coordinate system by vehicle aspect information is performed. Electronics techniques and data reduction methods are described, and the problems of vehicle precession (coning) and time-dependent reference vectors are treated. The theoretical resolution of the magnetometer system is shown to be less than ± 1 gamma scalar magnitude, and less than ± 0.01°.

Key Words

Ionospheric Currents

Vector Magnetometer System

*Department of Space Science
Rice University
Houston, Texas

In order to obtain meaningful vector information on magnetic fields associated with ionospheric current systems at high dip-latitudes, one measures the vector components in a vehicle coordinate system, and then translates the results to a ground-based reference system by knowledge of the vehicle attitude. This places severe requirements on both the magnetic sensor and the vehicle aspect sensor, since the expected change in magnetic field intensity as the vehicle penetrates the current sheet is of order 10^{-4} of the ambient field intensity and the change in the direction of the field vector is a fraction of a degree. In addition, the high spin rate of spin-stabilized sounding rockets (~10 rps) results in rapid changes in the vector components; the magnetometer must be able to track component changes which may be as large as 100,000 gammas per revolution. The aspect sensor must also respond to the rapid aspect changes caused by spin.

Alkali vapor magnetometer sensors are capable of meeting the sensitivity and dynamic range requirements mentioned above, but such sensors measure only total field magnitude. They may be converted, however, to vector instruments by the addition of a magnetic bias system.

Consider the case of a scalar magnetometer with a single-axis bias fixed with respect to some vehicle coordinate system such that the bias axis lies in the yz-plane and is inclined an angle ϵ from the y-axis, as shown in Figure 1. Assume in this case that the magnetometer sensor has no null regions, and that the ambient field of magnitude B_g is inclined at an angle θ from the z-axis with angular velocity ω. At time $t_o = 0$, let the vector B_g lie in the yz-plane. Then if B_o is the bias magnitude, the components of the vector sum of B_g and B_o as a function of time are:

$$B_x = B_g \sin\theta \sin\omega t \tag{1}$$

$$B_y = B_g \sin\theta \cos\omega t + B_o \cos\epsilon \tag{2}$$

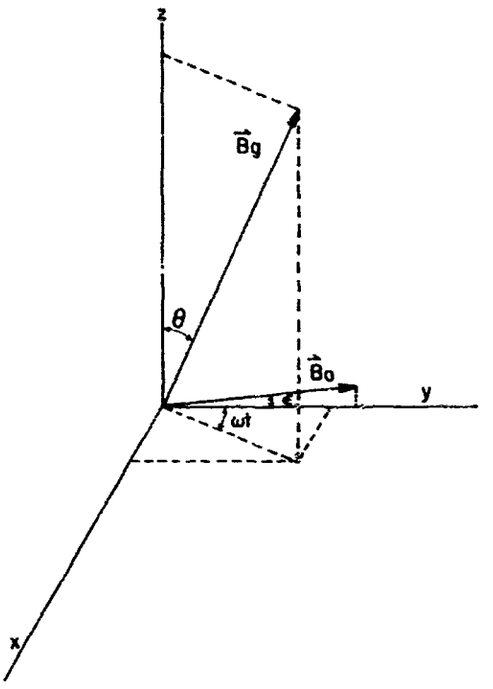


FIG. 1

Vehicle Coordinate System

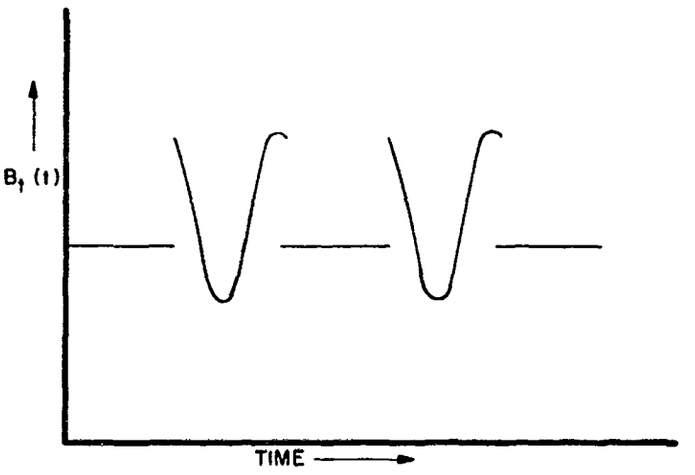


FIG. 2

Total Field Trace

$$B_z = B_g \cos\theta + B_o \sin\varepsilon \tag{3}$$

The sensor output as a function of time is then:

$$B_T = \sqrt{B_x^2 + B_y^2 + B_z^2} = \sqrt{B_g^2 + B_o^2 + 2B_o B_g (\sin\varepsilon\cos\theta + \cos\varepsilon\sin\theta\cos\omega t)} \tag{4}$$

Making the transformation $\cos\omega t = 1 - 2\sin^2 \frac{\omega t}{2}$ we obtain

$$B_T = \sqrt{B_g^2 + B_o^2 + 2B_o B_g (\cos(\theta+\varepsilon) - 2\cos\varepsilon \sin\theta \sin^2 \frac{\omega}{2} t)} \tag{5}$$

where B_T is the magnitude of the total field (sum of ambient plus bias fields) seen by the sensor. This may be written in the form,

$$B_T = \sqrt{X}\sqrt{1 - k^2 \sin^2 \frac{\omega}{2} t} \tag{6}$$

where,

$$X = B_g^2 + B_o^2 + 2B_o B_g \cos(\theta + \varepsilon) \text{ and}$$

$$k^2 = \frac{4B_o B_g \sin\theta \cos\varepsilon}{X}$$

In this form B_T may be recognized as an elliptic function of the second kind. In the special case of $\theta = 0$, B_T is a constant. For a bias vector aligned along the y-axis ($\varepsilon = 0$), the function reduces to the form:

$$B_T = \sqrt{B_g^2 + B_o^2 + 2B_o B_g \sin\theta \cos\omega t} \tag{7}$$

For a bias that is switched alternately on and off at some multiple of the apparent rotation period of B_g, the functional value alternates as shown in Figure 2. For known values of B_o, γ and λ, recovery of the parameters B_g and θ from the functional values may be effected by one of the methods outlined below:

(a) Direct integration of $B_T(t)$

Since an alkali vapor magnetometer produces as a signal a frequency proportional to the field scalar magnitude, integration of $B_T(t)$ may be accomplished electronically through direct counting of the frequency $f(t) = 3.49854\ B_T(t)$ over some time interval. Because of the periodicity of the elliptic function, integration over integral multiples of the rotation period of the vector B_g will yield a result which is more sensitive to changes in the magnitude of B_g than to changes in θ. (This may be easily seen by analogy to a circular function (sine or cosine) for which integration over a complete cycle yields a result completely independent of the amplitude of the rotating component of the vector.) The integral is most sensitive to the value of θ when the interval is one-half cycle or less, centered about a maximum of $f(t)$ ($\lambda t = 2\pi n$, where $n = 0, 1, 2, \ldots$). By the symmetry of the function about the maximum, integration over the range $\lambda t_1 = (2\pi n - \Phi_o)$ to $\lambda t_2 = (2\pi n + \Phi_o)$ yields twice the value of the integral:

$$E(k,\Phi_o) = \sqrt{X} \int_{\frac{2\pi n}{\lambda}}^{\frac{2\pi n + \Phi_o}{\lambda}} \sqrt{1 - k^2 \sin^2 \frac{\lambda t}{2}}\, dt \qquad (8)$$

which is an incomplete elliptic integral of the second kind. The corresponding equation for frequency count C over the interval t_1 to t_2 is:

$$C_{t_2 - t_1} = 3.49854 \quad (2) \quad E(k,\Phi_o) \qquad (9)$$

For a frequency count over some time $(t_4 - t_3)$ with the bias off, we obtain $C_{t_4 - t_3} = 3.49854\ (t_4 - t_3)\ B_g$. If we solve this equation for B_g, then equation (9) for $C_{t_2 - t_1}$ becomes an equation in θ alone, since all other parameters are known. This equation may be solved numerically for θ on a digital computer, either by series approximation of the elliptic function or by interpolation of tabulated values of $E\ (k, \Phi_o)$.

(b) Measurement of $B_\tau(t)$ maximum

This is a simplified case of the previous technique in which integration is replaced by exact measurement of the functional value at its maximum value. In this case, B_g is found by the same method as before, but the value of θ is obtained directly from the equation:

$$\sin\ (\theta + \varepsilon) = \frac{B^2_{\tau(max)} - (B^2_g + B^2_o)}{2B_o B_g} \tag{10}$$

which was obtained by setting $\alpha t = 0$ in the general expression for B_τ. Electronically, an oscillator may be phase-locked to the frequency $f(t)$ until a maximum is detected, at which point the oscillator is de-coupled and held to the peak frequency by phase-locking the oscillator to itself. Count of the frequency of the oscillator over some period of time then yields $B_{\tau(max)}$.

For the special case $\varepsilon \to 0$, an alternate method employing only the function $f(t)$ with the bias on is useful. In this method, the minimum and maximum values of $f(t)$ are measured, giving the two relations:

$$B^2_{\tau(max)} \simeq B^2_g + B^2_o + 2B_o B_g \sin\theta \tag{11}$$

$$B^2_{T(min)} \simeq B^2_g + B^2_o - 2B_o B_g \sin\theta \qquad (12)$$

Addition of the two relations gives a result independent of θ, which may be solved for B_g to yield:

$$B_g = \sqrt{\frac{B^2_{T(max)} + B^2_{T(min)}}{2} - B^2_o} \qquad (13)$$

Substitution of B_g into either the maximum or minimum relations yields the value of θ directly.

(c) Determination of phase with bias on.

In this method, the values of $B_T(t)$ at two times t_1, and $t_2 = t_1 + \frac{\pi}{\omega}$ are compared. At the time when $B_T(t_1) = B_T(t_2)$, $\omega t_1 = \frac{\pi}{2}$ and $\omega t_2 = \frac{3\pi}{2}$, so that:

$$B_T(t_1) = \sqrt{B^2_g + B^2_o} = B_T(t_2) \qquad (14)$$

This relation may be solved for B_g, and measurement of either the maximum or minimum value of $B^g_T(t)$ may be used to evaluate θ.

The previously derived relations represent physically the case of a coordinate system fixed with respect to a spinning vehicle containing a scalar magnetometer sensor with fixed bias system. The quantities ωt, θ, and B_g fix the vector components of B_g in the vehicle coordinate system, and the translation of coordinates from the vehicle system to a ground-based system may be accomplished by determination of vehicle attitude relative to some vector whose coordinates are known in the ground-based system.

For the purpose of analysis, it will be assumed that vehicle attitude relative to this vector will be expressed

by an angle σ between the vector and the vehicle spin axis when the vector lies in some plane fixed relative to the vehicle and containing the vehicle spin axis. For the present purpose, let this plane be the vehicle yz-plane, which also contains the bias axis. Assume also that the direction of the geomagnetic field vector $\vec{B}_g$ is known in the ground-based coordinate system, and that any observed change in the vector $\vec{B}_g$ may be referenced to the unperturbed vector direction and magnitude. Let α_B and β_B denote the zenith angle and north azimuth angle of $\vec{B}_g$ in geographic coordinates, and α_V, β_V and α_z, β_z represent the corresponding angles for the reference vector V and the vehicle spin axis z, respectively. Let Φ denote the angle of vehicle spin between the time vector V crosses the yz-plane and the time a maximum occurs in $B_T(t)$. The relative orientations of the vehicle axis, the reference vector, and the field vector are shown in Figure 3.

The evaluation of the vehicle attitude in the geographic coordinate system, assuming α_B and β_B are known, is straightforward. Denoting the great circle arc between $\vec{B}_g$ and $\vec{V}$ as ψ, by the spherical law of cosines we obtain:

$$\psi = \text{Arccos}\left[\cos\alpha_B\cos\alpha_V + \sin\alpha_B\sin\alpha_V\cos(\beta_B - \beta_V)\right] \qquad (15)$$

Let the angle at $\vec{V}$ between $\vec{B}_g$ and the zenith be χ. Then by the spherical law of sines:

$$\chi = \text{Arcsin}\left[\sin\alpha_B\cos(\beta_B - \beta_V)\ /\sin\psi\right] \qquad (16)$$

Substitution of ψ and χ into the law of cosines allows solution for Ω, the angle at V between the vehicle spin axis and the zenith:

$$\Omega = \text{Arccos}\left[(\cos\vartheta - \cos\psi\cos\sigma)/\sin\psi\ \sin\sigma\right] - \chi \qquad (17)$$

The vehicle axis zenith angle may now be obtained:

$$\alpha_z = \text{Arccos}\left[\cos\alpha_V\cos\sigma + \sin\alpha_V\sin\sigma\ \cos\Omega\right]. \qquad (18)$$

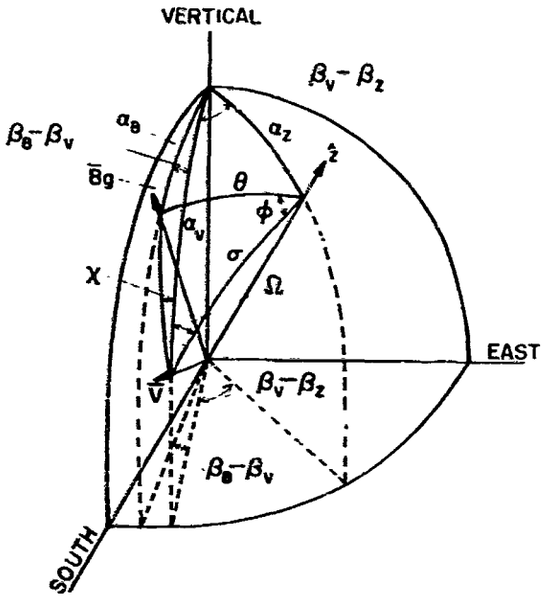


FIG. 3

Designation of Vectors in Geographic Coordinates

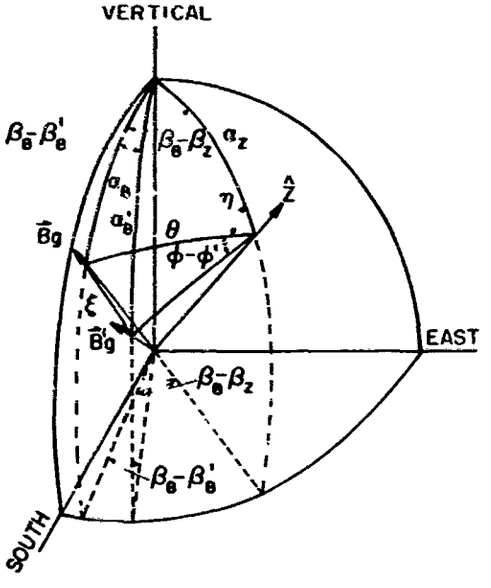


FIG. 4

Field Vector Change in Geographic Coordinates

Likewise, the vehicle axis azimuth angle is:

$$\beta_z = \beta_v - \text{Arccos}\left[(\cos\sigma - \cos\alpha_z\cos\alpha_v)/\sin\alpha_z\sin\alpha_v \right]. \qquad (19)$$

The angle Φ corresponding to the above azimuth and elevation of the vehicle axis is given by:

$$\Phi = \text{Arccos}\left[(\cos\psi - \cos\theta\cos\sigma)/\sin\theta\sin\sigma \right]. \qquad (20)$$

For the case of a vehicle outside the atmosphere, the vehicle attitude should be a smoothly varying function of the time (precession and nutation). Any discontinuous change in the apparent vehicle attitude may be interpreted as a change in the direction of $\vec{B}_g$, since the other reference vector $\vec{V}$ is precisely determined. The apparent change must be along a contour of constant σ, so that the change in direction of $\vec{B}_g$ may be separated into a change in θ and a change in Φ.

If the change occurs at some time t_0, let σ, θ, and Φ denote the measured values at t_0 when the change occurred. The direction of the new field vector $\vec{B}_g$ may be found, and the component changes easily extracted.

Consider the spherical triangles pictured in Figure 4. Let ξ be the great circle arc between the old field vector $\vec{B}_g$ and the new field vector $\vec{B}_g'$, and let η be the angle at the vehicle axis between the zenith and the old field vector. We then obtain:

$$\alpha_B' = \text{Arccos}\left[\cos\alpha_z\ \cos\theta' + \sin\alpha_z\ \sin\theta'\cos(\eta + \Phi - \Phi') \right], \qquad (21)$$

and

$$\beta_B' = \beta_B - \text{Arccos}\left[(\cos\xi - \cos\alpha_B\cos\alpha_B')/\sin\alpha_B\sin\alpha_B' \right], \qquad (22)$$

where,

$$\xi = \text{Arccos}\left[\cos\theta\cos\theta' + \sin\theta\sin\theta'\cos(\Phi - \Phi')\right], \tag{23}$$

$$\eta = \text{Arccos}\left[\cos\alpha_B - \cos\alpha_z\cos\theta)/\sin\alpha_z\sin\theta\right]. \tag{24}$$

The changes in the components in a geographic coordinate system are therefore:

$$\Delta B\ (\text{EAST}) = B_g\sin\alpha_B\sin\beta_B - B_g'\sin\alpha'_B\sin\beta'_B \tag{25}$$

$$\Delta B\ (\text{SOUTH}) = B_g\sin\alpha_B\cos\beta_B - B_g'\sin\alpha'_B\cos\beta'_B \tag{26}$$

$$\Delta B\ (\text{VERTICAL}) = B_g\cos\alpha_B - B_g'\cos\alpha'_B \tag{27}$$

For a vehicle which has no angular motion except spin, the elements θ and Φ should be constant in time due to the vehicle motion, so that any change in the field direction will be readily recognized. The more general, realistic motion of the vehicle above the atmosphere is that of combined spin, precession, and nutation. A complete analysis of the dynamics of the vehicle requires introduction of techniques not pertinent to this discussion, but in general the various motions may be described by superposition of cyclic functions. The precession motion may be viewed as periodic motion of the vehicle spin axis in a cone centered about a fixed direction in space, and nutation as a modulation of the coning motion by still another periodic function. For a well-balanced vehicle, nutation effects are minor, and will not be considered in the following discussion. When precession is significant, extrapolation of the vehicle position depends on the form of the precessional curve expressed in geographic coordinates. This shape is in general rather complicated, as will be seen from the following analysis. Let α_c and β_c respectively represent the zenith angle and north azimuth angles of the center of precession. Let σ represent the half-angle of the cone, and $\omega_c(t - t_0)$ the phase of the coning motion measured along the cone from the highest

point of the cone, as shown in Figure 5.

The zenith angle and north azimuth angle of the vehicle spin axis are given by:

$$\alpha_z = \text{Arccos}\left[\cos\alpha_c\cos\rho + \sin\alpha_c\sin\rho\cos\dot{x}_c(t - t_0)\right] \qquad (28)$$

$$\beta_z = \beta_c - \text{Arccos}\left[(\cos\rho - \cos\alpha_c\cos\alpha_z)/\sin\alpha_c\sin\alpha_z\right] \qquad (29)$$

Extrapolation of a precessing vehicle's attitude thus requires fitting a center of precession and precession half-angle to a known portion of the curve of the vehicle's attitude.

A further complication is introduced by the possibility of the reference vector direction being a function of time, or vehicle geographic position, or both. The following analysis uses the solar aspect angle as an example.

Because of the change in the vehicle's latitude and longitude and the westward movement of the sun with time during a flight, the sun's geographic attitude vector changes direction (with time) in the ground-based coordinate system. Knowledge of the sun's declination (δ), the equation of time (E), Local Standard Time (LST), and the vehicle latitude and longitude as a function of time allow the sun vector direction to be expressed in the ground-base coordinate system. Let the vehicle's latitude and longitude be represented by λ and L, respectively. Denoting the standard meridian for the time zone by L_s, the hour angle H of the sun in degrees at the vehicle longitude is given by:

$$H = 15(12^h - LST - E) - (L - L_s) \qquad (30)$$

From the diagram given by Figure 6, it may be seen that the solar zenith angle at the vehicle position is:

$$\alpha_v = \text{Arccos}\left[\sin\lambda\sin\delta + \cos\lambda\cos\delta\cos H\right] \qquad (31)$$

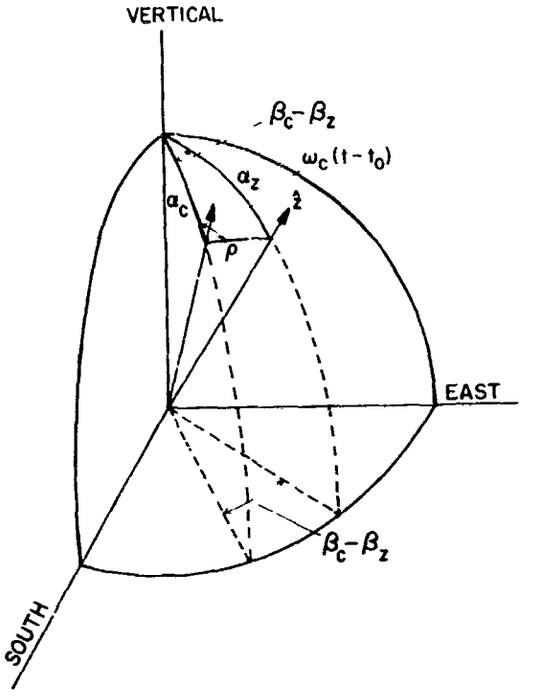


FIG. 5

Vehicle Precession in Geographic Coordinates

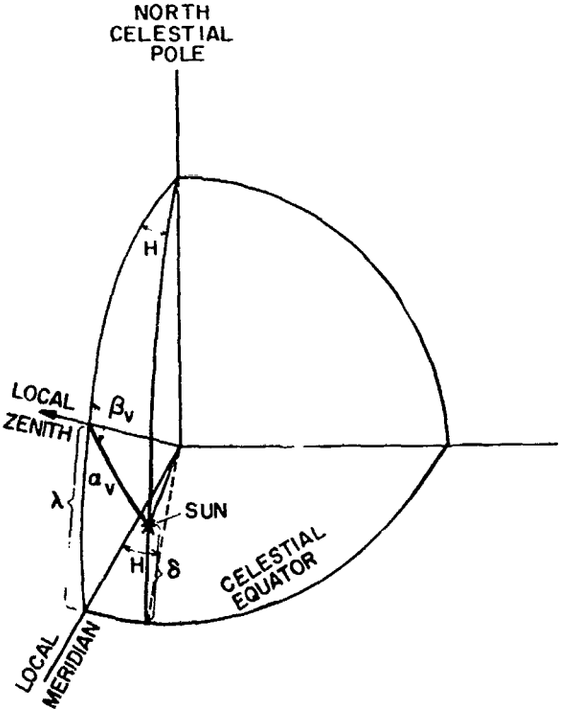


FIG. 6

Solar Attitude in Geographic Coordinates

The solar azimuth is given by:

$$\beta_v = \text{Arcsin}\left[\cos\delta \sin H / \sin\alpha_v\right] \tag{32}$$

The vehicle position obtained from radar tracking data allows the determination of the solar vector direction at any time in the flight.

The analysis thus far has assumed no restriction on the field of view of either the aspect sensor or the magnetometer sensor. When the actual angular field of view of both are considered, care must be taken to optimize a vehicle trajectory and attitude with respect to the direction of the sun and the field. In some instances, the configuration of the bias coil, magnetometer sensor, and solar aspect sensor within the vehicle must be altered. In addition, severe coning may not be tolerated, so that vehicle dynamics must also be considered.

Errors and Approximations

By equation 7, the change in θ with respect to a change in the total (measured) field is:

$$\frac{d\theta}{dB_T} = \frac{2B_T}{\sqrt{(2B_o B_g \cos\omega t)^2 - (B_T^2 - B_g^2 - B_o^2)^2}}$$

$$= \frac{B_T}{B_o B_g \cos\omega t \cos\theta} \tag{33}$$

If the value of B_T used is a maximum of the elliptic function, then $\omega t = 0$. Taking values of B_T, B_g, and θ computed from an actual flight (NASA 14.243 UE, $t^T = 0^g + 77$ seconds), which were 55746 gammas, 53204 gammas, and 9.11 degrees, respectively, we obtain:

$$\frac{d\theta}{dB_T} \sim 6 \times 10^{-3} \text{ degrees/gamma} \qquad (34)$$

For a cesium vapor magnetometer sensor with a resolution of less than 1 gamma (scalar), the angular accuracy is thus less than .01 degree.

The angular resolution in the angle Φ is governed by the uncertainty in the measurement of the time between the maximum in the total field B_T and the yz-plane crossing of the reference vector. A maximum resolution of 0.1 degrees is practically attainable by solar or lunar aspect devices now in use.

Acknowledgments: This work was supported by NASA contract No. NSR-44-006-023.

REFERENCES

Dessler, A. J. Geomagnetism, Satellite Environment Handbook (second edition), F. S. Johnson, ed., Stanford University Press, Stanford, 1965.

Milne-Thomson, L. M., Jacobian Elliptic Functions and Theta Functions, Handbook of Mathematical Functions, M. Abramowitz and I. A. Stegun, ed., National Bureau of Standards Publications, 1964.

Struve, O., Elementary Astronomy (5th edition), Oxford University Press, Oxford, 1959.

COMPUTER AIDED ANALYSIS AND DESIGN OF SPACE INSTRUMENT SYSTEMS

Robert M. Muñoz

N69-33962

INTRODUCTION

Each of us has either directly or indirectly come in contact with the general purpose digital computer and it should be no surprise that the digital computer has invaded the field of space instrument system development. The scientific community has come to regard the computer as a valuable tool for performing many useful functions and my objective will be to show how a general purpose digital computer can be used with some material benefit in the development of a space instrument system. The topics to be discussed are more or less generally related to the development of any instrument system but the emphasis will be placed on a noncomprehensive set of problems related to the development of a fluxgate magnetometer system at the Ames Research Center. Since a large scale general purpose digital computer such as the 7040/7094 DCS system in use presently at Ames has such great computing power it will certainly not be possible to discuss all the potential uses in space instrument design. However, some of the more important aspects of circuit and system design along with certain computer experiments made to test the mathematical model of a simulated instrument system will be discussed. Several examples will be presented as case histories of some of these methods and it should be relatively easy from these to conceive many other areas within the design and development task where the computer can be effectively used.

SPACE INSTRUMENT SYSTEMS

Space instrument systems are certainly not entirely separable from other ground based and flight instrument systems but there are certain characteristics which do prevail more frequently in the space instruments and which are troublesome enough to be worthwhile considering. Most space instruments are relatively unique. Production runs for space instruments, if they can be called that, are usually keyed to very few of a kind and often each instrument within a run differs, at least in small ways, from others within the same run. The uniqueness of the space instrument is important in that it allows new state-of-the-art ideas to be implemented but at the same time, it denies sufficient use experience to provide satisfactory estimation of performance and reliability by prior experience. The first launch of many space instruments usually gives the experimenter his first real look at instrument performance in the operating environment.

Short development cycles are commonplace for space instruments. The crisis atmosphere generated by the launch schedule is felt very strongly after an instrument has been accepted for space flight and, to a lesser extent, the same pressure applies even before such instruments are proved to be more or less feasible for space flight. Commercial instrument systems, although bound by a number of other restraints, are seldom bound by schedules as confining as the launch schedule.

No user feedback is possible with the space instrument. To some degree flight qualification programs make up for the lack of user feedback which is

provided commercial instrument manufacturers by those who buy and use commercial laboratory test equipment. These users form a block of interested critics and can provide a manufacturer the benefit of suggested changes or at least a demand for improvements. All this of course takes time, time which is usually not available in the short development cycle for space instruments.

Space instruments are as a rule very high precision devices. The cost of the space mission, and scientific curiosity in general would seem to be justification enough for the demand for high precision but additional impetus for high accuracy instrumentation is given by those who select flight payloads because the competition between various experimenters proposing for the same space mission is keen, and the better instruments are flown. In conjunction with this requirement for high accuracy, the space instrument system is usually very light weight, low in power consumption and small enough to fit in the flight payload.

There are a number of other differences between space instrument systems and other instrument systems but these I believe are a representative set and each constitutes a major difficulty in the development process, a difficulty which can to some extent be alleviated by means of intelligent use of a digital computer.

CYCLE OF DEVELOPMENT

There are probably as many ways to produce a satisfactory design for a space instrument as there are space instruments but engineering techniques do become somewhat stylized and the more successful techniques are well known and are disseminated in the literature. Instruments don't always go through the stages of system design, circuit design, breadboard fabrication and breadboard testing but they often do and some of these steps can be computerized.

If we consider a space instrument such as the Ames Magnetometer [Ref. 1], the cycle of development probably starts with the choice of a general approach to make the physical measurement, in this case the fluxgate technique for measuring the interplanetary magnetic field. The choice of general approach, however, does not lend itself to computer aided methods. We have to rely on human beings with their unique judgement factors and enlightened preferences for this phase of development.

Once the general approach has been selected, the development cycle continues with a feasibility study which is usually conducted to see if the desired physical parameters can be measured and the desired engineering and scientific objectives can be accomplished altogether. Here again the computer cannot help very much although it can assist in some of the routine tasks of bookkeeping and mathematical analysis that may go along with a feasibility study. The designer usually depends upon his experience, ability, and judgement to say whether an instrument is indeed feasible. If it is, he can proceed directly to the third step in the cycle, the instrument system design.

System design is a well-developed engineering art and can be assisted greatly by computer methods. In the example to be presented later, the Ames version of a topological network analysis program of Calahan is used with inputs in the form of the poles and zeros of system transfer functions to provide

a Bode analysis of system stability for a version of the Ames Magnetometer. The IBM control system analysis program MA01X is very useful in providing root locus analysis of continuous and sampled data systems but no example of the use of this program will be given at this time. Having selected a satisfactory instrument system, we can now proceed to the 4th step, the development of subsystem components and circuits necessary to perform the system functions.

Many seminars and symposia have been held in the last two years on computer aided circuit design and analysis. As a matter of interest, Dr. Calahan from the University of Michigan conducted such a course at Ames recently. [Ref. 6] It is clear from current theory and practice that the computer can perform the analysis functions of circuit design better and faster than any designer can do by hand. ECAP, NET I, SCEPTRE, POTTLE, CIRCUS, and many other programs are available to do general circuit analysis. An example of circuit analysis using the topological analysis program of Calahan will be presented later. A comparitive description of the various methods of circuit analysis is given in reference [3]. Although there are many analysis programs in existence, very few network synthesis programs are available in generally useful form. In the near future more attention will probably be given to the activity of computer aided synthesis but at the present time the designer fulfills this function and the computer checks his results. In some cases analysis programs have been used in feedback schemes to arrive at an optimized circuit or system design after having started from only a general concept of system topology. This approach is costly in computing time and subject to certain difficulties which arise from the definitions used for the optimum solution. When better synthesis programs are made available, the computer will be even more effective in space instrument design.

Now, with system design and circuit design complete, it is possible to proceed to a breadboard stage and check the results of the effort made heretofore. Fabrication and tests of an instrument system in breadboard form gives the designer a verification or rebuttal of his efforts and no completely adequate computer simulation of the breadboard phase is possible because hardware usually speaks for itself. Approximations that are made for the sake of analysis are sometimes not adequate and adjustments of values for circuit elements, tuning of filters, selecting of transistors and related activities will always be a part of the development of the space instrument system so long as real-world components are used but the computer can replace, or at least augment, many of the tests that are usually done in breadboard hardware. Transfer functions through the breadboard instruments can be simulated on the computer if enough is known about the system design. If a mathematical model has been used in the development of the system, this mathematical model along with whatever modifications necessary due to circuit and sub-system design should suffice as the basic computer model for performance simulation. Problems not readily amenable to analysis by hand methods can be solved more easily within the computer. If tests indicate that changes in system characteristics are necessary, it is probably more easy to effect these changes in the computer than it would be in breadboard hardware. An example of a new method of system simulation using the theory of digital filters will be presented later to illustrate how the computer can aid in the space instrument system design process.

In summarizing the roll of the digital computer in the development of space instruments, it can be seen that the computer is readily adapted to system design and analysis as well as subsystem and circuit analysis. The computer can be used to simulate a completed system design and provide some information that heretofore has been provided only in breadboard tests. If used in this way, the computer expedites the development process and makes it easier to obtain a more reliable design. The cost of developing a capability in computer aided design and analysis techniques cannot be entirely neglected. For those who have access to a large scale computer the difficulty lies mainly in acquiring a repertoire of useful programs and subroutines for doing their kind of work and for those who are not so fortunate, computing services can be obtained from any one of a large number of organizations specializing in renting computer time through the use of teletype terminal units located in the users facilities and connected to a time-shared computer by means of telephone lines.

COMPUTER AIDED SYSTEM DESIGN

One version of the Ames Magnetometer designed for measurement of the magnetic field on the surface of the moon is presently being developed jointly by Ames and Philco Ford Space and Reentry Systems Division. Figure 2 shows the functional block diagram of the sensor electronics subsystem for this Lunar Surface Magnetometer. The main point of difference between the sensor electronics subsystem of this mission and others such as the one presently flying on the interplanetary monitoring probe spacecraft lies in the addition of an integrator in the forward path. The integrator changes the operation of the subsystem from a type 0 servo to a type 1 servo. For those not familiar with this terminology, it simply means that the design with an integrator is theoretically capable of operating without static errors due to changes in the performance of components within the forward path. This approach was selected because temperature variations on the surface of the moon are expected to be much larger than those encountered in most spacecraft and such a subsystem design should, with some reservations, allow satisfactory operation at these temperatures. The design temperature range is -30 to +65° Centigrade.

An interesting problem which turned up during the course of development of this subsystem and which will be discussed briefly here was the saturation of the input to the integrator at frequencies above 10 cycles. This problem was not discovered until late in the development cycle and the computer was used effectively to demonstrate the nature of the problem and show means of correcting it. Figure 3 shows a mathematical model of the sensor electronics subsystem of the Ames Lunar Surface Magnetometer. The characteristics of those elements of the forward path excluding the integrator were analyzed in laboratory tests and approximated by the filter function shown in the left hand block. Figure 4 shows a comparison between the performance characteristics of the actual system with those of the mathematical model as derived by means of computer analysis. Using the mathematical model of Figure 3, a frequency analysis was made of the total closed loop system and found to be satisfactory as shown in Figure 5 but when an investigation was made of the fluctuations of signal at the input to the integrator, a problem was discovered. Signal levels were found to be as much as 20db beyond the full scale capability of the

STEPS IN THE CYCLE OF DEVELOPMENT OF THE SPACE INSTRUMENT SYSTEM

- CHOICE OF GENERAL INSTRUMENTATION APPROACH
- FEASIBILITY STUDY
- SYSTEM DESIGN
- CIRCUIT DESIGN
- BREADBOARD FABRICATION
- BREADBOARD TEST AND EVALUATION

FIGURE 1

NATIONAL AERONAUTICS AND SPACE ADMINISTRATION
AMES RESEARCH CENTER, MOFFETT FIELD CALIFORNIA

FUNCTIONAL BLOCK DIAGRAM OF SENSOR ELECTRONICS SUB-SYSTEM

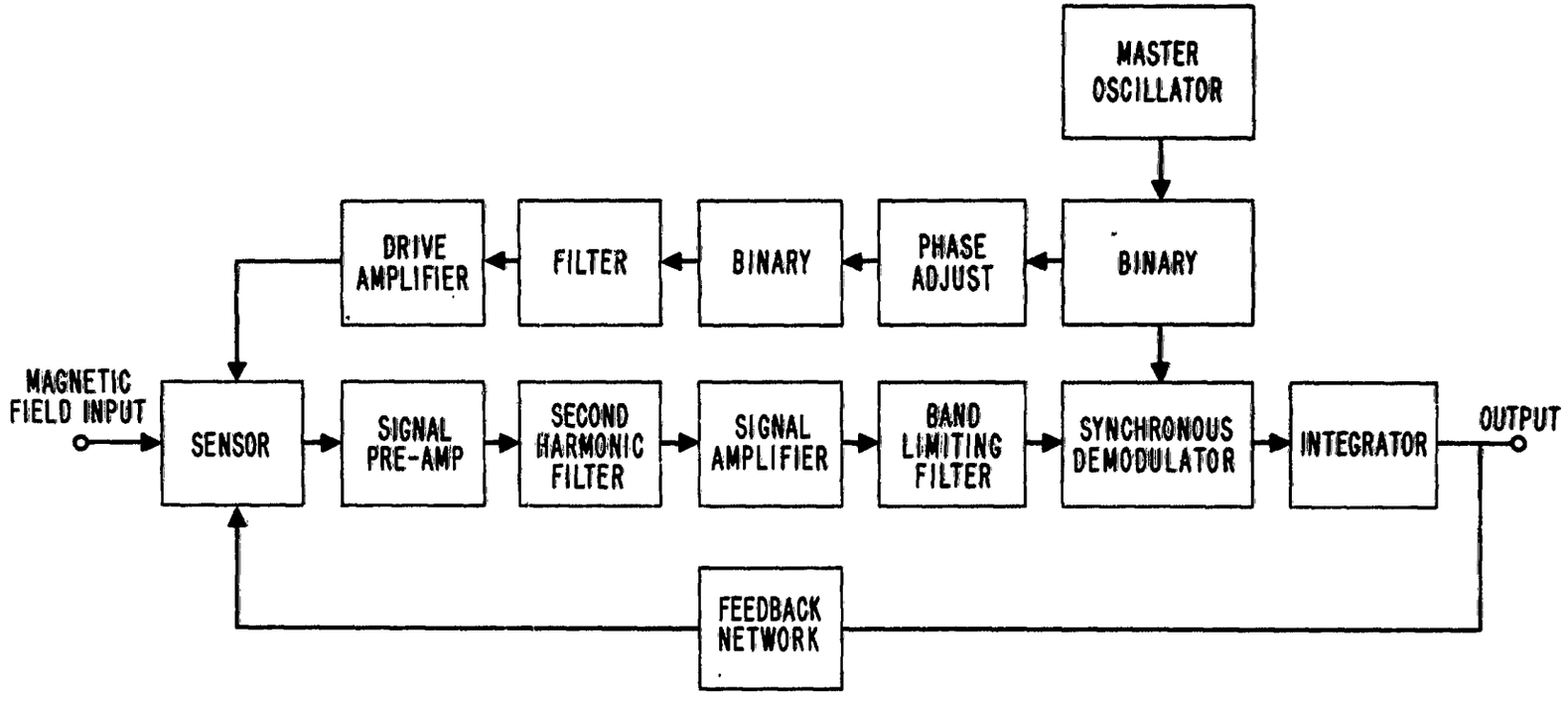


FIGURE 2

NATIONAL AERONAUTICS AND SPACE ADMINISTRATION
AMES RESEARCH CENTER, MOFFETT FIELD, CALIFORNIA

MATHEMATICAL MODEL OF THE SENSOR ELECTRONICS SUB-SYSTEM OF THE AMES APOLLO MAGNETOMETER

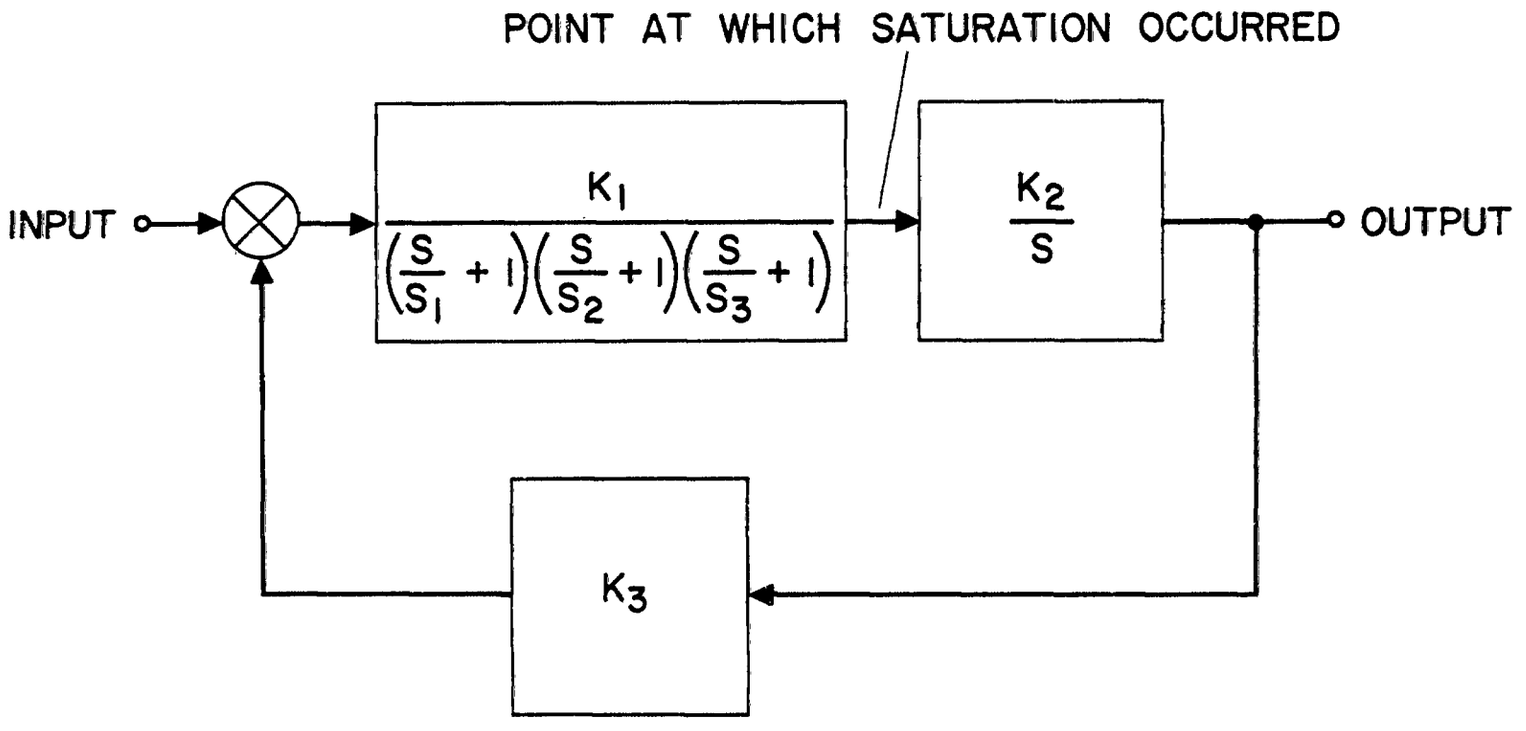


FIG.3

NATIONAL AERONAUTICS AND SPACE ADMINISTRATION
AMES RESEARCH CENTER MOFFETT FIELD CALIFORNIA

COMPARISON OF THEORETICAL AND ACTUAL OPEN LOOP CHARACTERISTICS

(NOT INCLUDING INTEGRATOR)

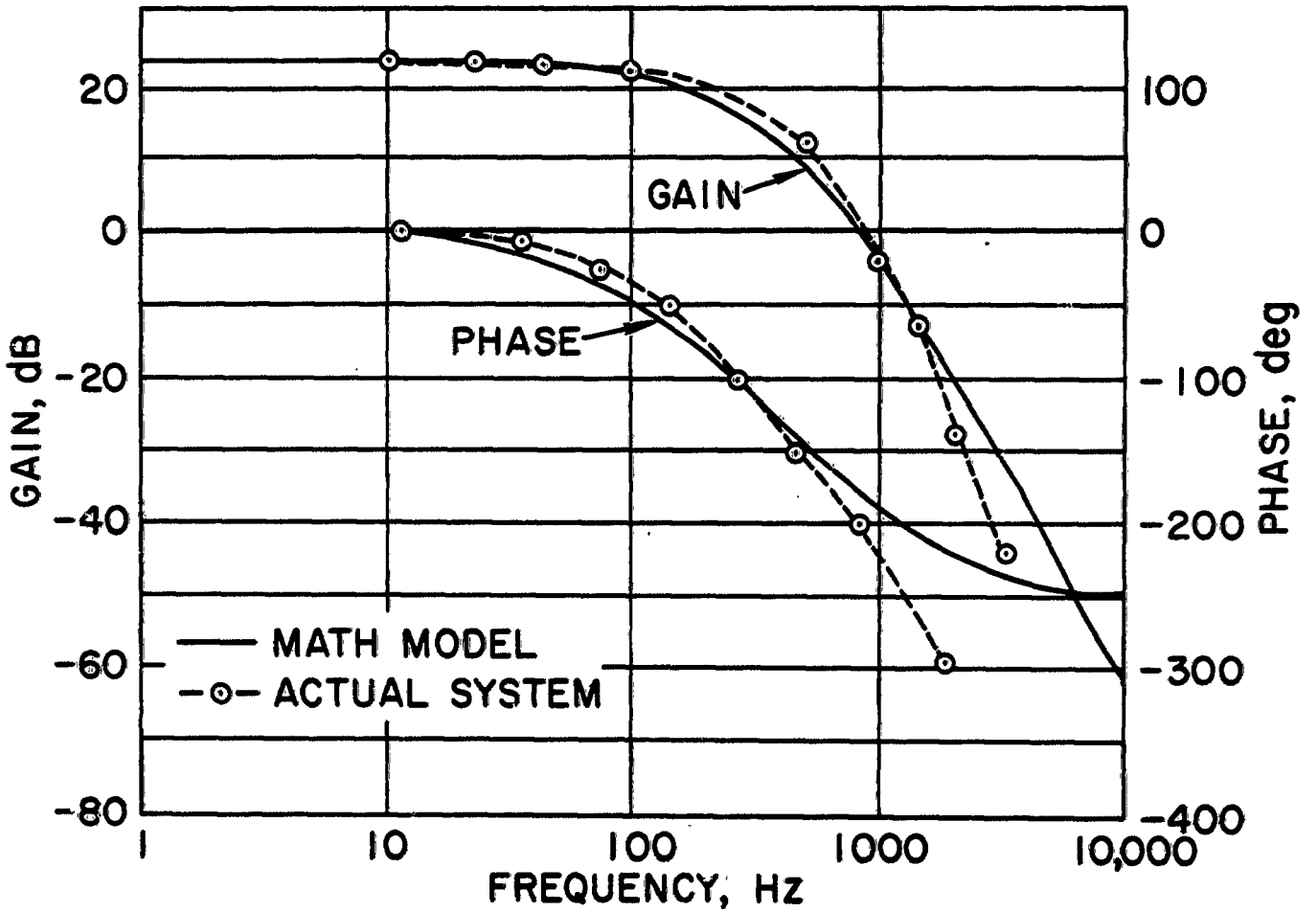


FIGURE 4

NATIONAL AERONAUTICS AND SPACE ADMINISTRATION
AMES RESEARCH CENTER, MOFFETT FIELD, CALIFORNIA

FREQUENCY CHARACTERISTICS OF THE CLOSED LOOP SENSOR ELECTRONICS SUB-SYSTEM

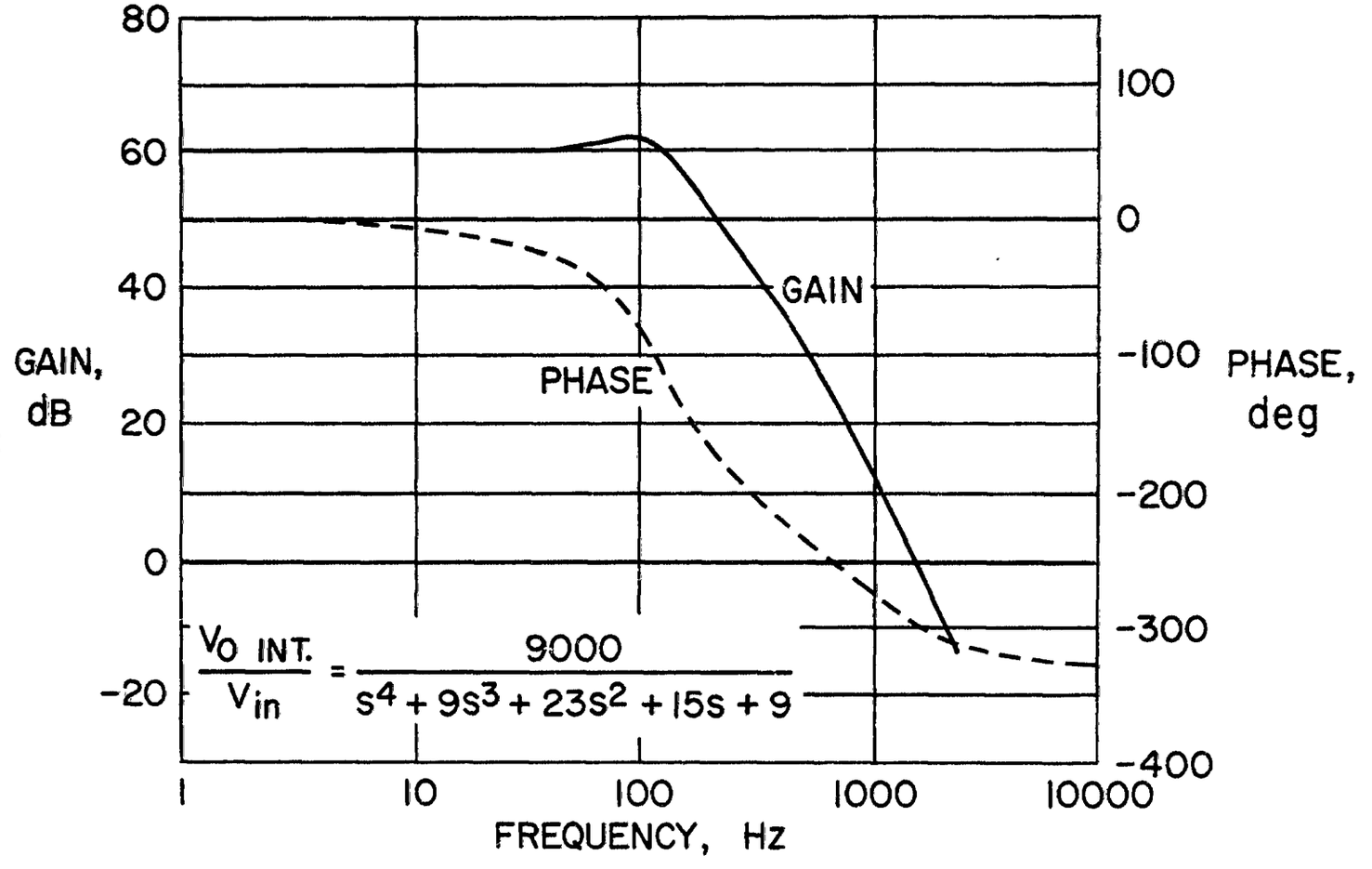


FIG. 5

NATIONAL AERONAUTICS AND SPACE ADMINISTRATION
AMES RESEARCH CENTER, MOFFETT FIELD, CALIFORNIA

hardware. The problem did not manifest itself until signals approaching full scale were encountered at frequencies between 10 and 500 HZ. (See Figure 6)

In order to remove this problem, it was necessary to increase the gain of the integrator to a point which caused a system instability. The gain was high enough to cause the poles of the system closed loop transfer characteristic to lie in the right half plane and it became necessary to apply some form of compensation to regain the stability that we formally had. Without going into any great detail at this point because time will not allow it, I will merely indicate that, with the aid of the computer, many types of compensation were investigated and it was found that complex zeros placed judiciously in the S plane were a satisfactory form of compensation and an RLC network placed at the input to the integrator can easily provide such compensation. Figure 7 shows the saturation characteristics once again. From this figure it is clear that the system will not saturate until the frequency of approximately 500 cycles is reached and then if additional dynamic range of 5 db were allowed, no saturation would occur at all. Better forms of compensation using more complex networks are certainly possible but for this design study, the effort was stopped at this point and the feasibility of implementing complex zero compensation within the constraints of weight and power was investigated.

COMPUTER AIDED CIRCUIT DESIGN

In order to maintain some continuity in the discussion an example of a computer aided circuit design was selected from the sensor electronics system shown in Figure 2. That block in Figure 2 titled Second Harmonic Filter represents a fairly complex 6th order band pass filter with two rejection points, one at approximately 6 KHz and the other at approximately 12KHz. The synthesis of the filter was performed by hand using approximate methods which are too lengthy to be discussed here; however, Figure 8 shows the synthesized circuit configuration. The fundamental design problem rests in ascertaining whether the approximations made in the synthesis procedure are valid. Calculations of the 6th order filter with real values of circuit Q are simply not practical to do by hand. Several days of computation were necessary to check the results based on analysis of the lossless prototype of this filter.

Again the topological circuit analysis program was used to analyze the frequency and time responses of the second harmonic filter but in this case, resistance, capacitance and inductance values were used as inputs to the program rather than the mathematical description of the circuit or transfer function. The result of the computer analysis obtained after approximately half a minute are shown in Figures 9 and 10. From the computer studies of the filter we obtain a verification of the fact that the assumptions made in synthesis were practical assumptions. The attentuation at notch frequencies with practical filter Q's is seen to be approximately 60db and phase characteristics within the passband are not drastic enough to cause any significant problem of system instability. All this was done in a very short time without the need for producing breadboard hardware but, hardware tests did confirm these results. The dissimetry noticable in the pass-band of Figure 9 is due simply to a lack of perfect tuning of the coils and is not an essential part of the design.

SATURATION CHARACTERISTICS OF THE INTEGRATOR INPUT
(BEFORE COMPENSATION)

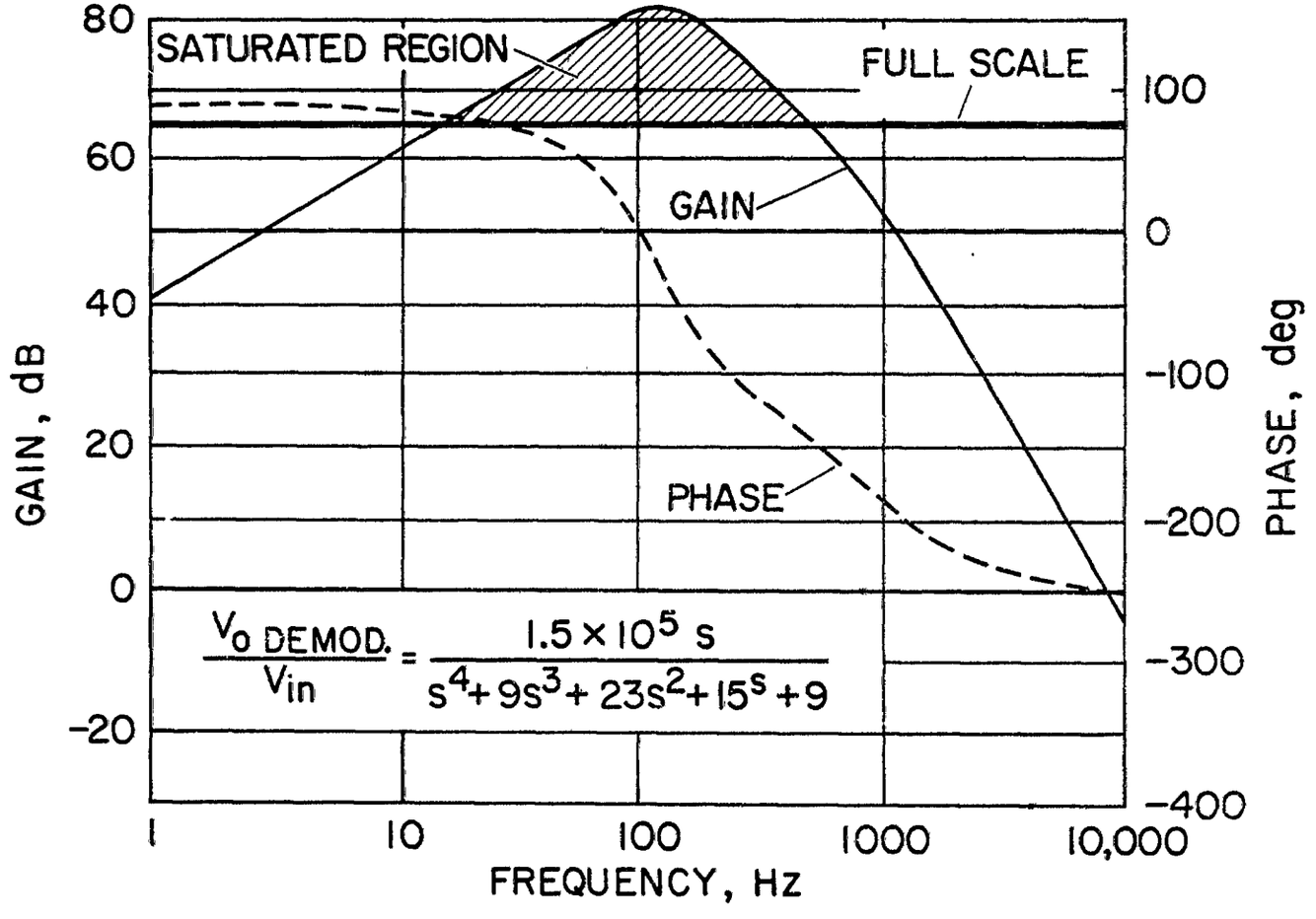


Figure 6

NATIONAL AERONAUTICS AND SPACE ADMINISTRATION
AMES RESEARCH CENTER MOFFETT FIELD CALIFORNIA

SATURATION CHARACTERISTICS OF THE INTEGRATOR INPUT
(AFTER COMPENSATION)

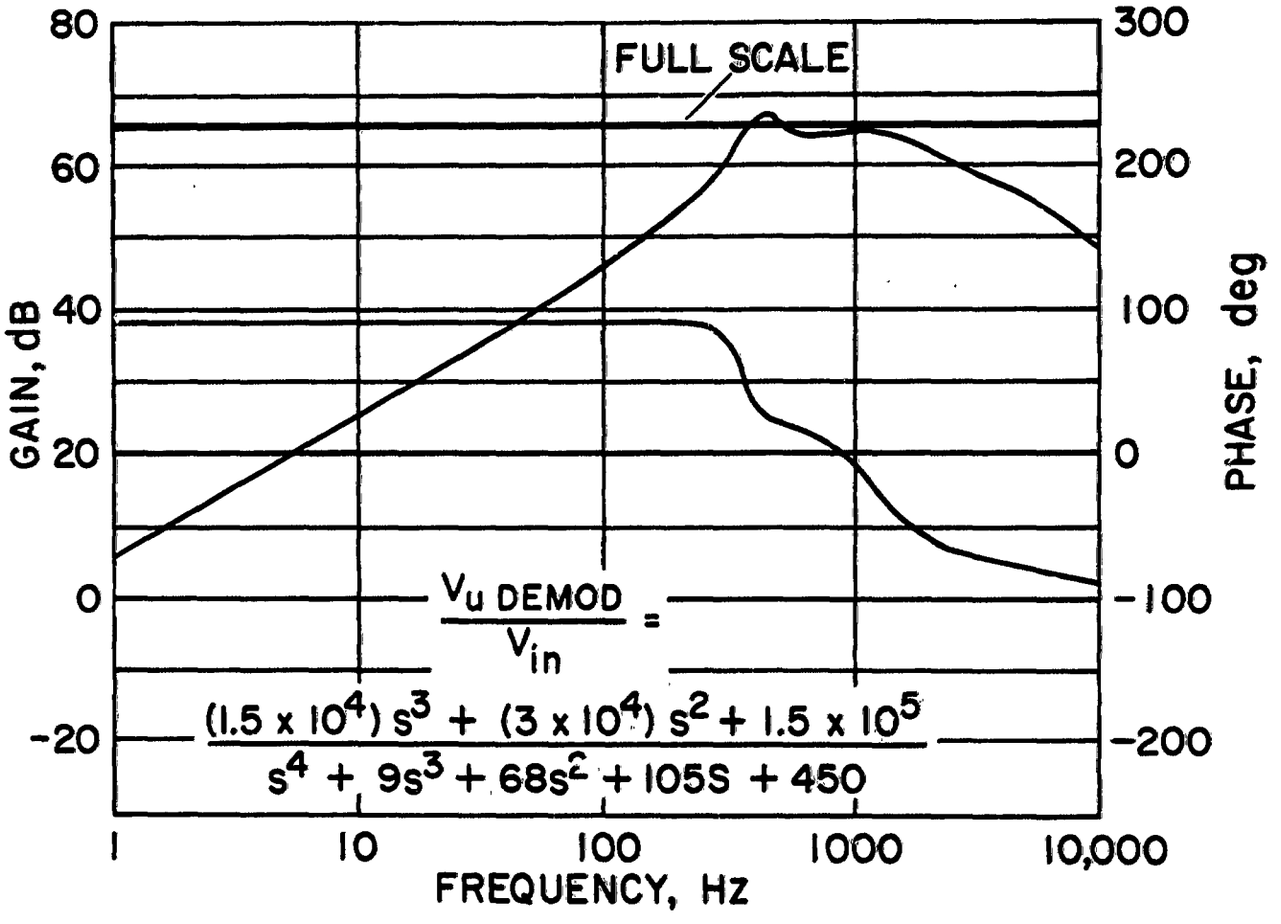


Figure 7

NATIONAL AERONAUTICS AND SPACE ADMINISTRATION
AMES RESEARCH CENTER, MOFFETT FIELD CALIFORNIA

2nd HARMONIC FILTER OF THE AMES MAGNETOMETER

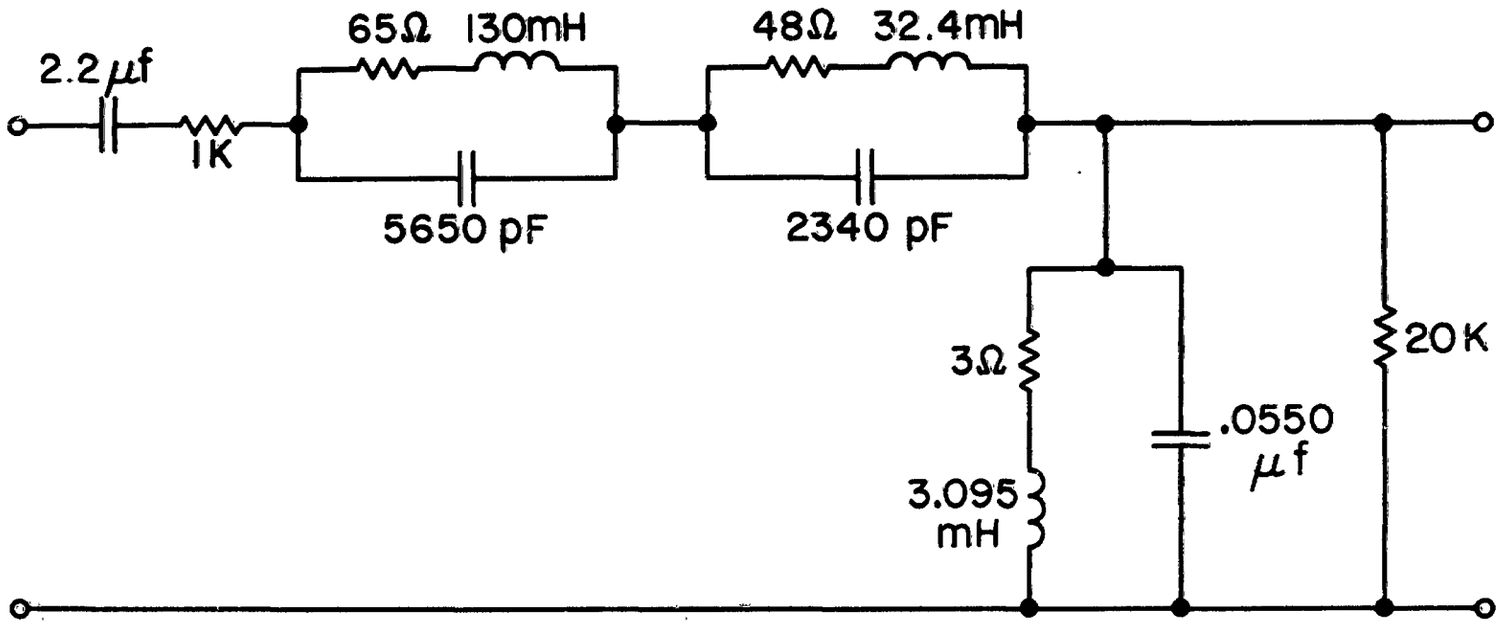


FIGURE 3

NATIONAL AERONAUTICS AND SPACE ADMINISTRATION
AMES RESEARCH CENTER, MOFFETT FIELD, CALIFORNIA

FREQUENCY RESPONSE OF THE SECOND HARMONIC FILTER OF THE AMES MAGNETOMETER

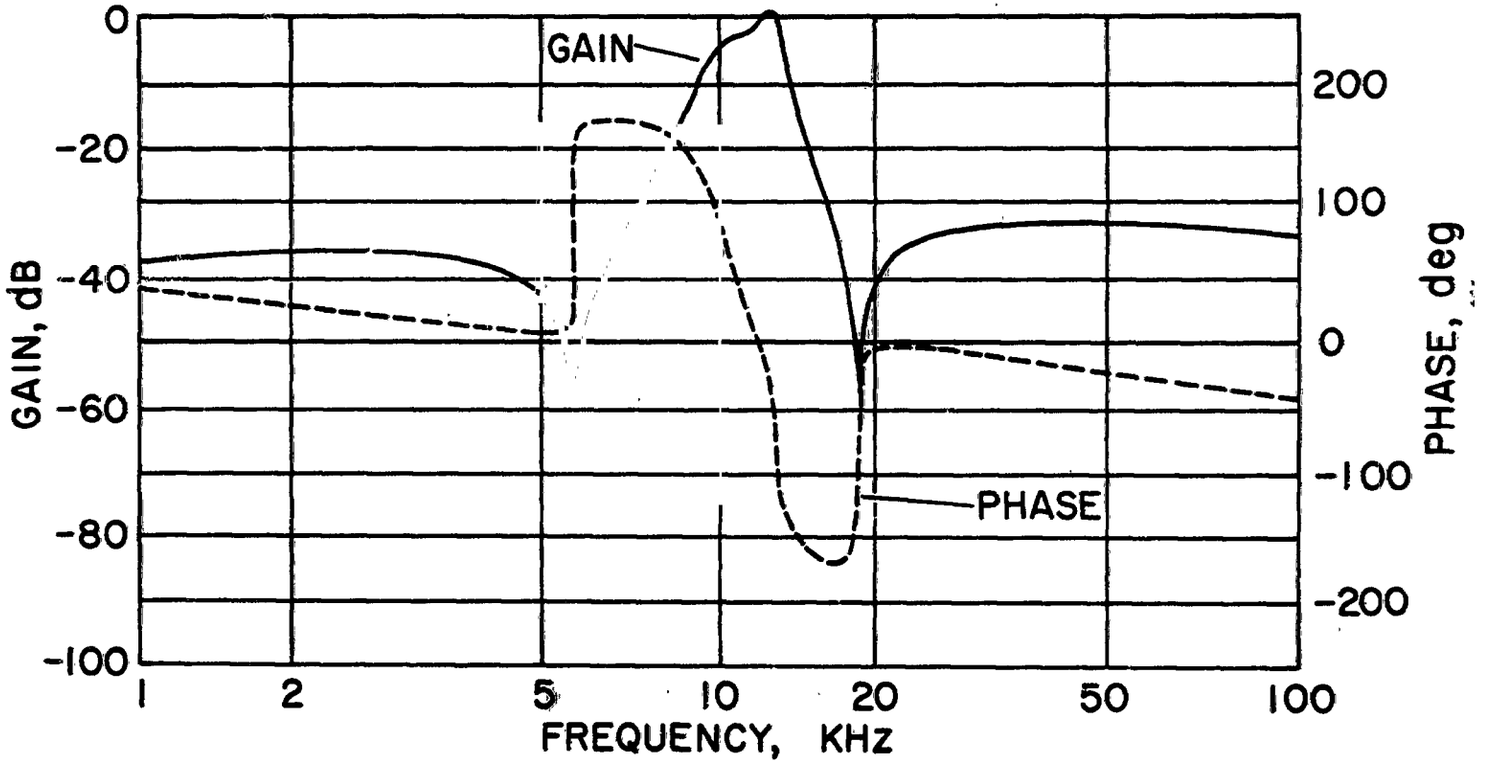


Fig. 9

NATIONAL AERONAUTICS AND SPACE ADMINISTRATION
AMES RESEARCH CENTER, MOFFETT FIELD, CALIFORNIA

MAGNETOMETER SYSTEM SIMULATION

Perhaps the most effective use made of the digital computer in the design of the Ames Magnetometer system has been in hybrid system simulation. Figure 11 shows a functional block diagram of the magnetometer system including not only sensor electronics subsystems but also the spin demodulator subsystem, the sampling filter, and the sampler, each a part of the flight hardware. Along with these elements of flight hardware, it is necessary to include the simulated magnetic field input and a data reconstruction filter in order to perform meaningful tests on the systems ability to measure magnetic field. The general approach adopted in this computer breadboard system simulation was as follows:

1. A mathematical analysis was performed on each subsystem component and a mathematical model in the form of a subsystem transfer function in the frequency domain was developed for analog sub-systems. The digital sub-systems and logical operations are already in a form convenient for computer processing.

2. A digital filter approximating the transfer characteristics of the analog subsystems was synthesized by means of the bilinear transform method. Digital functions were accepted without transformation.

3. A program relating the digital filter equivalents of each of the subsystem components was written to simulate the entire system in numerical form in the computer.

The process seems a bit complicated at first glance but when looked at carefully, the largest difficulty is seen to be that of generating the digital filter equivalents to analog subsystem transfer functions. Again the computer has been a great help in this area. We are at present developing a generally useful digital filter synthesis program to perform this function and when completed this program will reduce the difficulty of the task to that of merely obtaining analog transfer functions in the S domain, an operation which is usually performed by the designer whether using the computer or not. For those interested in digital filters, Rader and Gold [Ref. 5] and Chapter 7 of Kuo and Kaiser's book [Ref. 2] provides a good starting point.

System simulation is by no means a new discipline, many compiler programs with various levels of capability exist. Thomas Naylor et. al. [Ref. 7] and Kuo and Kaiser et. al. [Ref. 2] discuss many software packages that help ease the burden of simulating some classes of systems. SIMSCRIPT, SIMPAC, and BLODI, are a few of the many simulation languages of general utility. Because each of these compiler languages has certain limitations and because, to use them effectively requires special training in the semantics of the language, the approach adopted here was to retain the flexibility provided by the higher level language, Fortran IV, at the expense of a somewhat longer programming time. Where many different simulations of a particular type are encountered, the special simulation languages offer a real advantage.

The results of one preliminary test performed in the computer on a simulated version of the Ames Magnetometer are shown in Figure 12. The objective of this test was to demonstrate the kind of output that would result in the

time domain if the system were subjected to a random variation of magnetic field input and if no sample filtering were employed. This should show graphically what the effects of sample aliasing are when presented as a time history. As you can see, there is not much significance to the relationship between the random variable inputs and the reconstructed outputs. These data contain large errors due to signal aliasing.

The errors discussed here are produced in any sampled data system where the data band is allowed to extend beyond half the sampling frequency or the niquist frequency. This is so because the spectral distribution of the sampled data of one frequency band is overlayed or summed with that of another data band. The fundamental sampling theorem [Ref. 8] has been violated and our effort was directed toward measuring the effect quantitatively.

After performing a number of similar experiments using sample filters of various orders in conjunction with a random number generator simulating the interplanetary field, it was found that the second or third order filter with a cutoff frequency of approximately 0.3 HZ provides an adequate attenuation of the aliasing frequency spectrum. Figure 13 is a plot of error versus the order of the sample filter.

Though it is certainly possible to compute errors in the time domain for simple data input functions such as sine waves, it is extremely difficult to do this for the more complex waveforms such as the random input used in this model of the magnetic field. A considerable amount of beneficial systems information can be derived on breadboard hardware tests but in hardware it is very difficult to change parameters such as filter order. This however represents no difficulty to the computer. It simply means the change in the difference equation representing the sample filter subsystem.

The approach of system simulation is certainly not new but the methods suggested by this procedure are relatively new. In the recent past the analog computer and the digital differential analyzer, a specialized form of digital computer, have been used to do this but there capability was quite limited because of the requirement for nonstandard hardware and the difficulty of programming such devices. The techniques employed in this simulation are completely adaptable to the general purpose digital computer which is widely used today. No fundamental computer language limitation exists however most of the circuit analysis programs as well as the system simulation program discussed here were written in Fortran IV.

CONCLUSIONS

The original objective of this paper was to discuss the relationship between the computer and space instrument system design especially the design of the Ames Magnetometer. A number of advantages and disadvantages of system and subsystem design have been discussed and an example of the system design of the sensor electronics subsystem of the Ames Magnetometer was given as an illustration. A large number of digital computer programs for circuit analysis were mentioned and an example of circuit analysis of a 6th order filter used in the magnetometer sensor electronics was presented. The big advantage of both system and circuit analysis by computer lies in the fact that the computer can perform these functions faster and more accurately than the designer can do by hand. The third and perhaps the most important means of using the

STEP RESPONSE OF THE SECOND HARMONIC FILTER OF THE AMES MAGNETOMETER

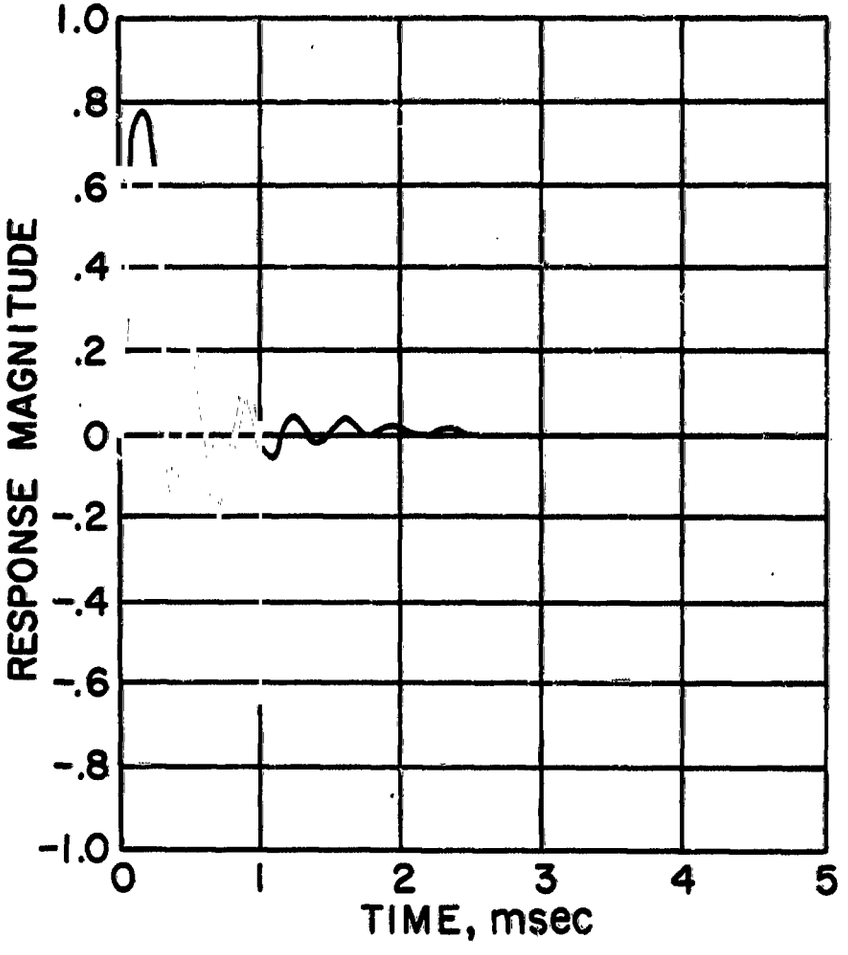
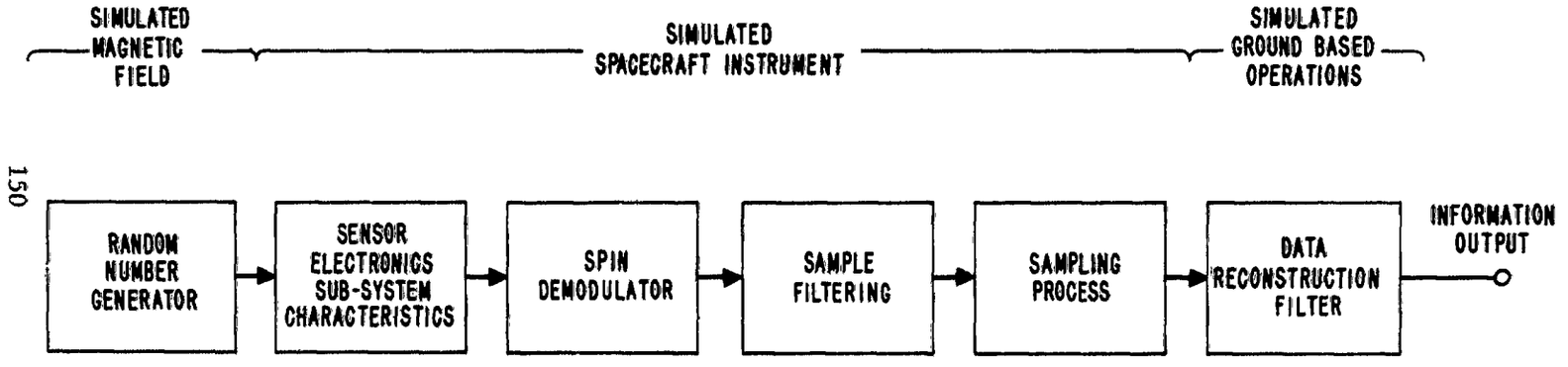


FIGURE 10

NATIONAL AERONAUTICS AND SPACE ADMINISTRATION
AMES RESEARCH CENTER, MOFFETT FIELD, CALIFORNIA

FUNCTIONAL BLOCK DIAGRAM OF THE AMES MAGNETOMETER COMPUTER EXPERIMENT



150

FIGURE 11

NATIONAL AERONAUTICS AND SPACE ADMINISTRATION
AMES RESEARCH CENTER, MOFFETT FIELD, CALIFORNIA

COMPARISON OF SIMULATED SYSTEM OUTPUT WITH RANDOM FUNCTION INPUT

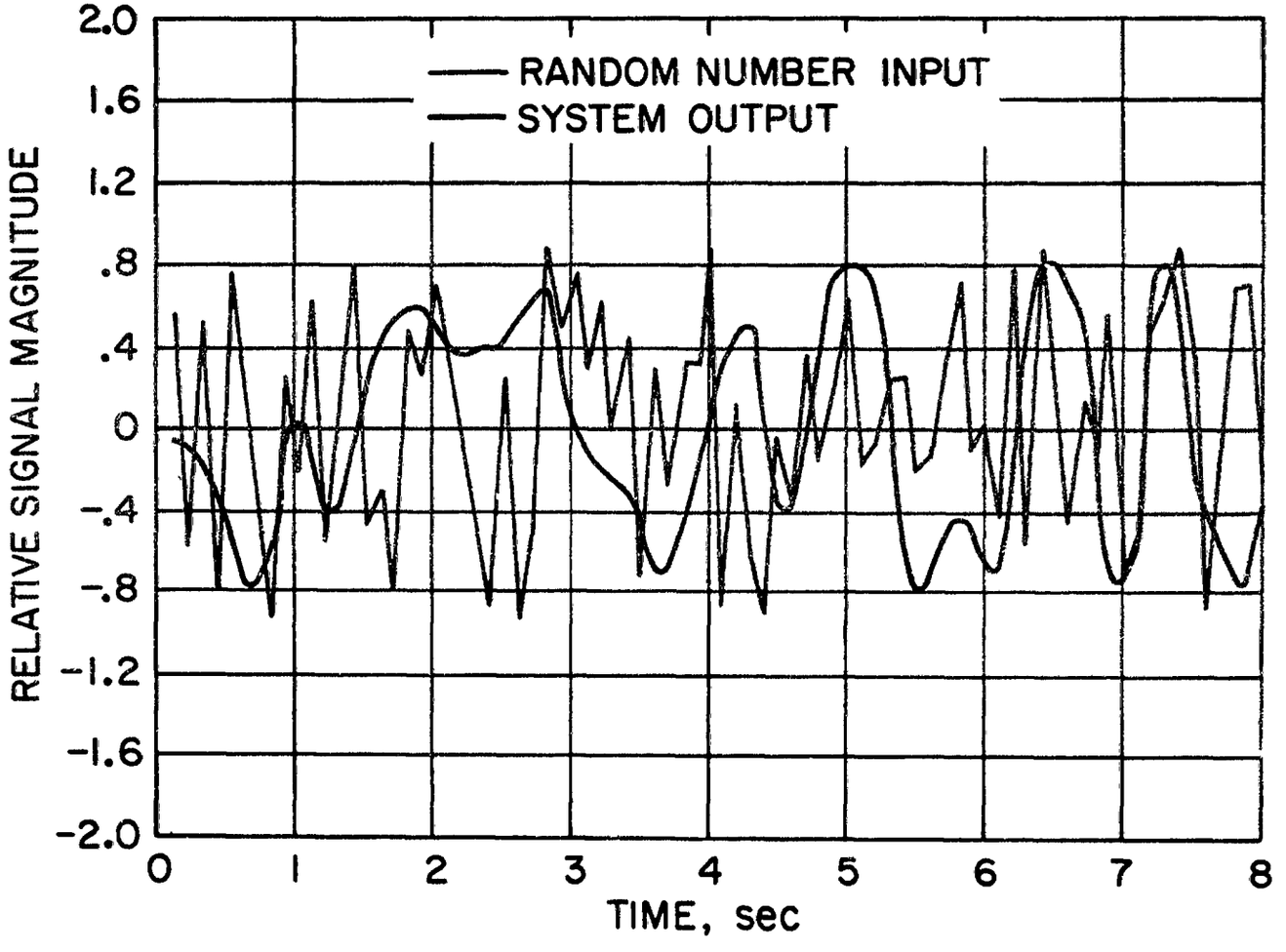


FIGURE 12

NATIONAL AERONAUTICS AND SPACE ADMINISTRATION
AMES RESEARCH CENTER, MOFFETT F D, CALIFORNIA

A COMPARISON OF ERROR VS THE ORDER OF THE SAMPLE FILTER

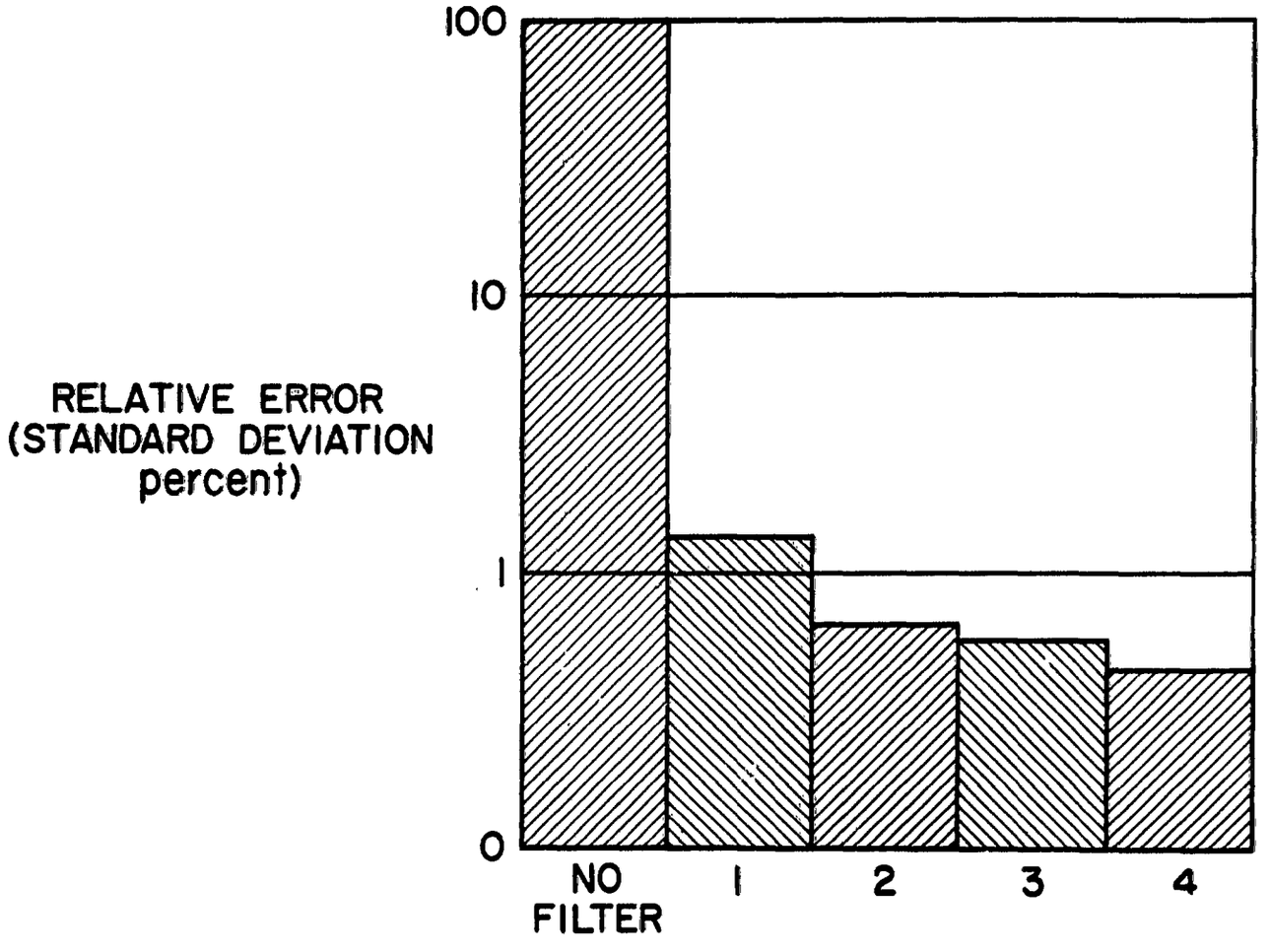


FIGURE 13

NATIONAL AERONAUTICS AND SPACE ADMINISTRATION
AMES RESEARCH CENTER, MOFFETT FIELD, CALIFORNIA

computer in the design development cycle by simulating the performance of the total integrated system was also discussed. A new method of approximating the transfer functions of subsystem components by generating a difference equation of the digital filter equivalent of the subsystem and integrating a number of difference equations thus found into a computer model of the total system functioning in the time domain provides answers for system performance that are too difficult to derive by conventional methods. An example investigation of sample aliasing in the Ames Magnetometer System was presented.

The benefits of using the digital computer in space instrument system design are many and the penalities, once a digital computing capability has been established, are relatively few. The largest single penality for those who already have a computer is that of obtaining and putting into use the already available analysis programs. As additional program materials in both the analysis and the synthesis disciplines become available, the advantages of computer aided design will become greater and the disadvantages will become less making it possible to do even more careful and sophisticated design.

ACKNOWLEDGEMENTS

The assistance of Msrs. R. Seeback and R. Moyer is gratefully acknowledged. Their efforts in programming and debugging program materials as well as running test problems on the Ames computer was a vital part of the task.

References

[1] R. M. Munoz, "The Ames Magnetometer," Proceedings of the 1966 National Telemetering Conference, Boston, Massachusetts, May 1966.

[2] F. F. Kuo, J. F. Kaiser, et. al, "System Analysis by Digital Computer," J. Wiley and Sons, 1966.

[3] R. M. Munoz, "Methods of Computer Aided Circuit Analysis," as yet unpublished report, NASA Ames Research Center, May 1967.

[4] W. J. Kerwin, R. M. Munoz, M. J. Prucha, "An Improved Magnetometer for Deep Space Use," presented at IEEE National Aerospace Electronics Conference, May 1964.

[5] C. M. Rader and B. Gold, "Digital Filter Design Techniques in the Frequency Domain," IEEE Proceedings, Vol. 55, No. 2, Feb. 1967, pp. 149-171.

[6] D. A. Calahan, "Computer Analysis and Optimization of Circuits" to be published in the near future by McGraw Hill.

[7] T. H. Naylor, J. L. Balintfy, D. S. Burdick, K. Chu, "Computer Simulation Techniques" J. Wiley and Sons, 1966.

[8] B. M. Oliver, J. R. Pierce, C. E. Shanon, "The Philosophy of Pulse Code Modulation" Proc. IRE Vol. 36, No. 11, pp. 1324-1331, Nov. 1948.

R.C. Snare[1] and G.N. Spellman[2]

DIGITAL OFFSET FIELD GENERATOR FOR SPACECRAFT MAGNETOMETERS

Snare, R.C., Spellman, G.N., "Digital Offset Field Generator For Spacecraft Magnetometers", Spacemagnetic Exploration and Technology Symposium, (August 1967) University of Nevada, Reno.

N69-33963

ABSTRACT

A digital offset field generator has been developed which accurately extends the dynamic range of a sensitive magnetometer. This system enables the use of a sensitive magnetometer to resolve small magnetic field fluctuations in the presence of fields of large value. The circuitry is described in some detail and its application in instruments for the first Applications Technology Satellite and the fifth Orbiting Geophysical Observatory is discussed.

Key Words: Offset Field Generator, Magnetometer

INTRODUCTION

The design of a magnetometer for space flight often involves a trade-off between dynamic range and resolution. The magnetometer for near earth, highly eccentric orbits presents a problem as it requires a large dynamic range to remain linear at both perigee and apogee. An example of this large dynamic range is the field seen by the first Orbiting Geophysical Observatory (OGO-1) with perigee and apogee values which vary between roughly 40,000γ and 10γ.

There has been significant interest recently in resolving small field changes of less than 1γ at flux levels as large as 60,000γ. A magnetometer system has been developed which employs an accurate offset field generator that provides a wide dynamic range for a high resolution magnetometer. This system has been successively used on instruments for the first Applications Technology Satellite (ATS-1) and OGO-E.

[1]Institute of Geophysics and Planetary Physics, University of California at Los Angeles.

[2]Marshall Laboratories, Torrance, California.

EARLY MAGNETOMETER DEVELOPMENTS

Many early spacecraft magnetometers were designed to provide a single output from each axis. The maximum output would be scaled to represent the maximum value of the field expected for the planned orbit or, as in some cases, the maximum value of the field expected in certain regions of interest. This selection criteria often resulted in an instrument of large dynamic range. The resolution of such an instrument was limited by the resolution of the data system and instruments with a resolution of ten gamma or a hundred gamma were not unusual.

A technique used on a variety of spacecraft instruments was to provide several different values of dynamic range. The dynamic range was selected by a ground command transmitted to the spacecraft or possibly the range was automatically selected during flight by a detector circuit of the instrument. Examples of this type of instrument are fluxgate magnetometers for Explorer 6 with ranges of ±25γ, ±50γ and ±10,000γ (Coleman, 1960) and for OGO-1 with ranges of ±30γ and ±500γ (Heppner et al., 1967).

A magnetometer was prepared for the ABLE-5 spacecraft which provided automatic scale switching with dynamic ranges of ±32γ, ±320γ and ±3200γ. Upon ground command these scales could be increased to ±500γ, ±5000γ and ±50,000γ respectively. This provision was to be activated during launch of the spacecraft such that the magnetometer would remain on scale during the boost phase. Also included was a system which upon ground command could apply offset fields to the sensor in steps of 40γ with a total range of -160γ to 200γ. The purpose was to provide a means of offsetting spacecraft fields such that the magnetometer could operate in its most sensitive mode in the presence of a spacecraft perm field which might ordinarily keep the magnetometer on one of its less sensitive scales (G.M. Takahashi, 1960). While this technique enhances the resolution of the instrument when operating in low fields, the resolution of the least sensitive scale is often less than desirable.

An early automatic offset field generator was used on the magnetometer for Sputnik 3 as reported by Dolginor et al., 1961. The system provided sixteen offset steps, each of 3000γ to offset a magnetometer with a dynamic range of ±2,400γ. Thus the system had a total dynamic range of 43,000γ. The system used several rotary stepping switches and was operated from batteries (Fig. 1). Although the usefulness of the offset field generator was demonstrated on Sputnik 3, the accuracy of the system left something to be desired by todays standards.

DIGITAL OFFSET FIELD GENERATOR

The purpose of the offset field generator is to apply a localized field at the sensor which opposes the ambient field and places the basic magnetometer within its linear dynamic range. This is accomplished by supplying stable currents in discrete steps to an auxiliary coil wound around the magnetometer sensor. This extends the dynamic range of the overall instrument without altering the resolution of the basic magnetometer.

The block diagram of a magnetometer and offset field generator is shown in Fig. 2. The basic magnetometer is of the saturable core, closed

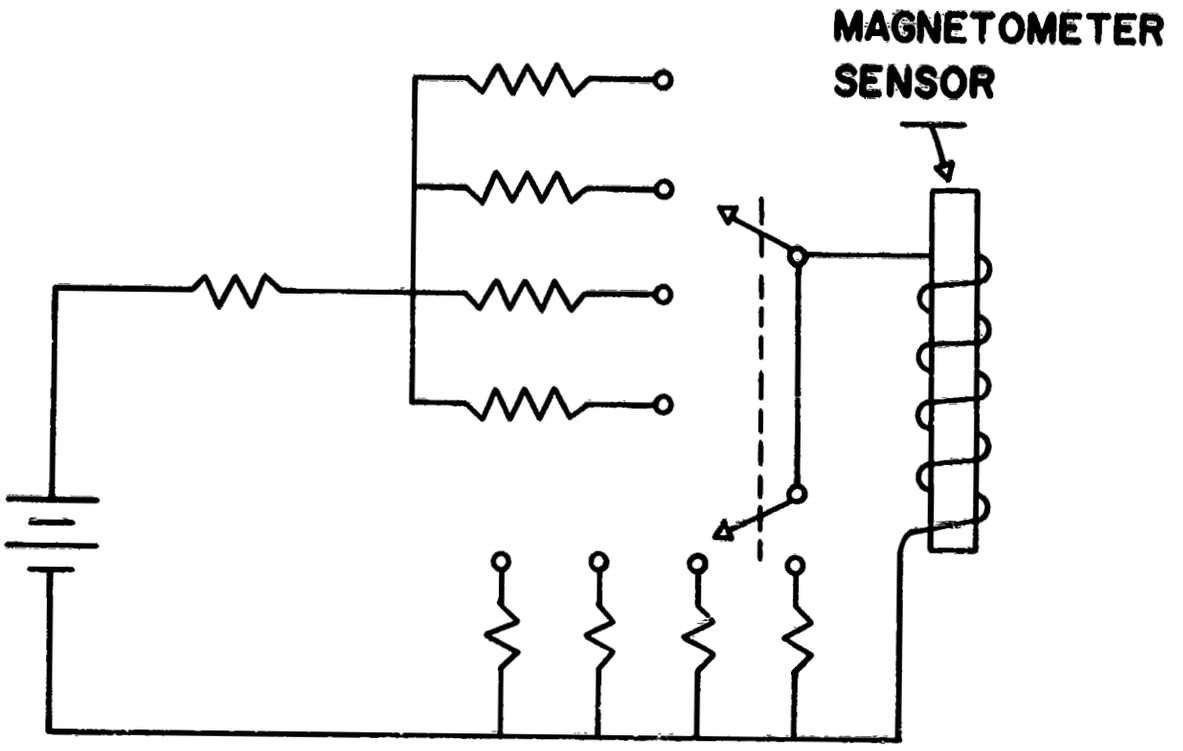


Fig. 1 Cffset field generator for Sputnik 3 magnetometer.

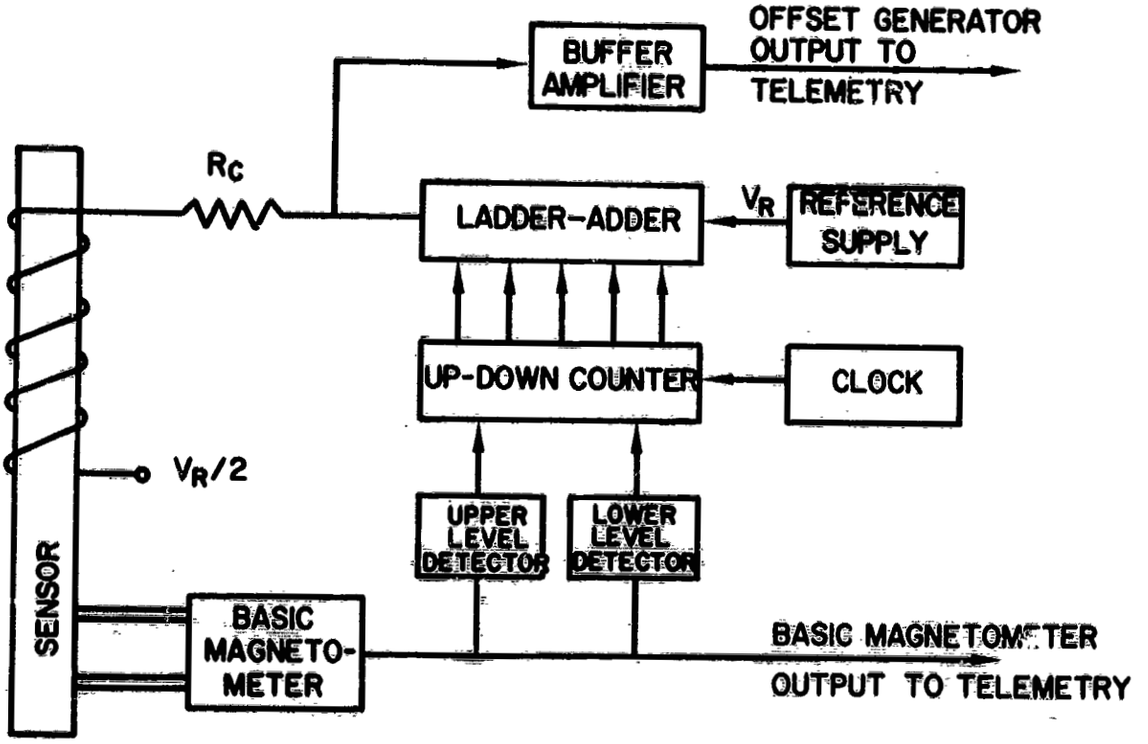


Fig. 2 Digital offset field generator block diagram.

loop type with ample feedback to insure stable gain, linearity and flat frequency response. The analog output of the basic magnetometer may be scaled to produce the desired resolution.

The purpose of the level detectors is to indicate an off scale condition of the basic magnetometer. When this occurs a count is either added to or subtracted from the up-down counter. Each binary in the up-down counter drives a switch of a ladder-adder type digital to analog converter (Fig. 3). The output of the ladder-adder is a linear function of the state of the up-down counter. The calibrate resistor (R_C of Fig. 2) scales the current applied to the sensor coil and is selected during system calibration. When the output of the basic magnetometer activates either level detector, the offset field generator applies an incremental offset field to the sensor such that the basic magnetometer output is returned to center scale.

It will be noted that the offset coil on the sensor is returned to $V_R/2$. When the count in the up-down counter is 10000..., i.e., the most significant bit is a "1" and all others are "0", the output voltage of the ladder-adder will be $V_R/2$. In this condition no current will flow in the coil and the zero offset condition is established. The ladder output voltage may vary up or down from $V_R/2$ and provide both positive and negative values of offset fields.

CIRCUITRY

The OGO-E and ATS-1 magnetometer while different in many respects, share the same basic circuit blocks. The following is a description of some of those blocks with special attention given those factors which effect the accuracy of the system.

The up-down counter is of a standard type using Texas Instruments integrated circuits. The binaries are the SN510A type and the routing gates use the "pulse-exclusive-or" type SN5121. The output of the SN510A binary is capable of driving both the relay and the solid state switch modules which will be described later.

The up-down counter is controlled by two threshold circuits which sense the zero volt level and the five volt level at the basic magnetometer output. The threshold circuit uses a 2N2060 matched differential pair of transistors as shown in Fig. 4. The threshold circuits are switched within 5 millivolts of the desired threshold over the temperature range of $-15^{\circ}C$ to $+55^{\circ}C$.

A digital to analog conversion ladder was constructed as shown in Fig. 3. The equivalent circuit for the ladder converter can be arrived at as shown in Fig. 5. It can be seen that regardless of the state of the ladder switches ($S1-S_n$), the output impedance of the ladder remains fixed at R.

The accuracy and stability of the digital to analog conversion performed by the ladder is dependent on the accuracy and stability of the ladder resistors, the reference voltage V_R and the offset voltage of each

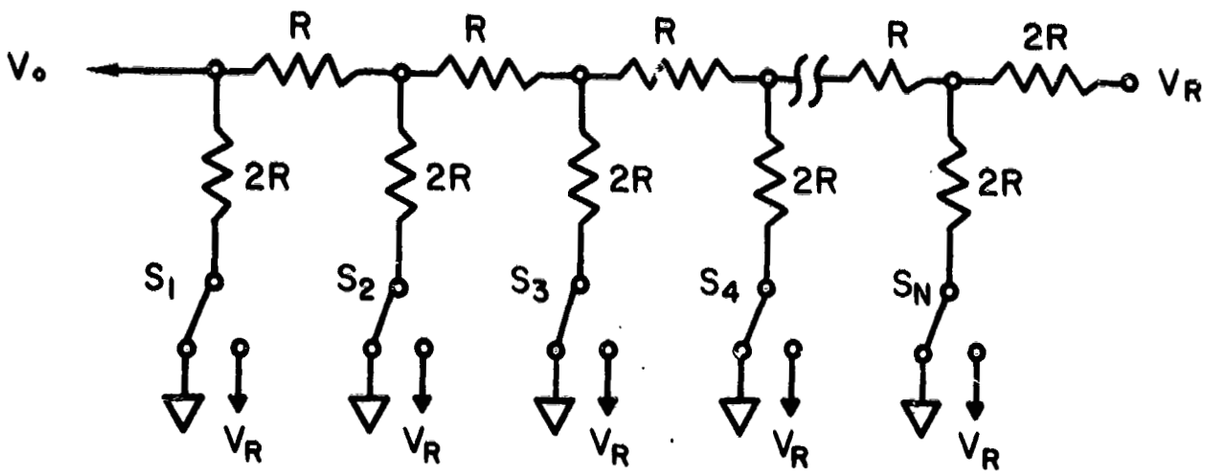


Fig. 3 Ladder-adder circuit of N bits.

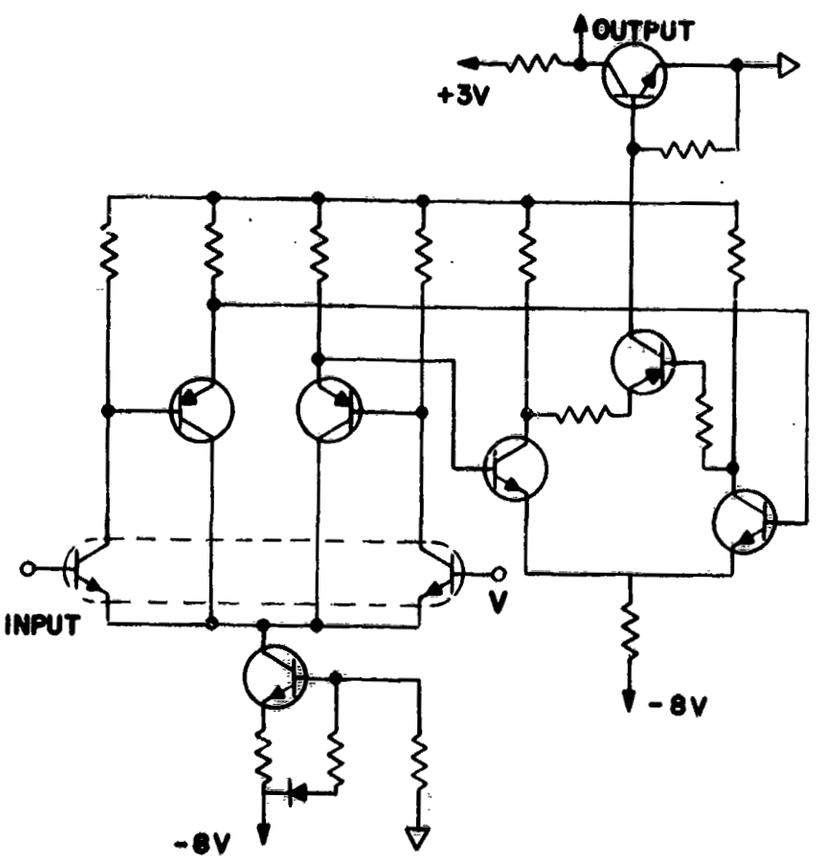


Fig. 4 Threshold detector schematic diagram (V is connected to either 0V or 5V for upper or lower level detection).

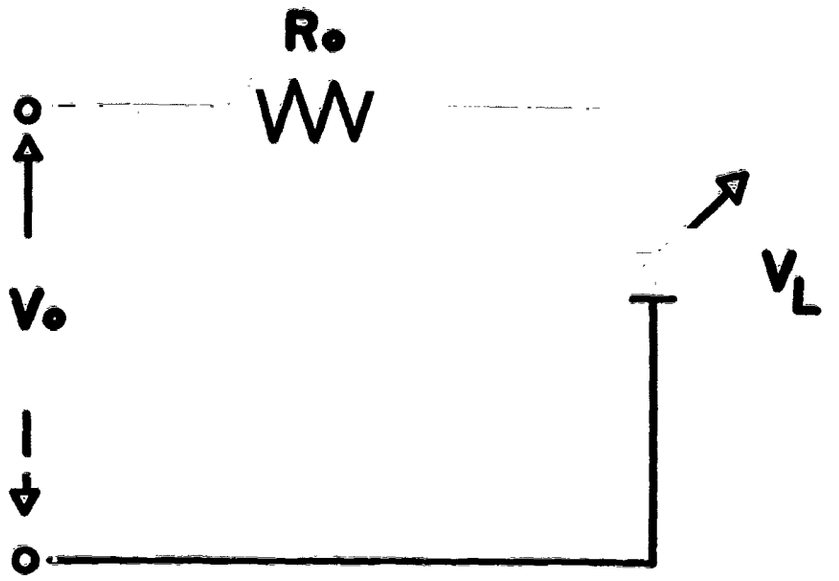
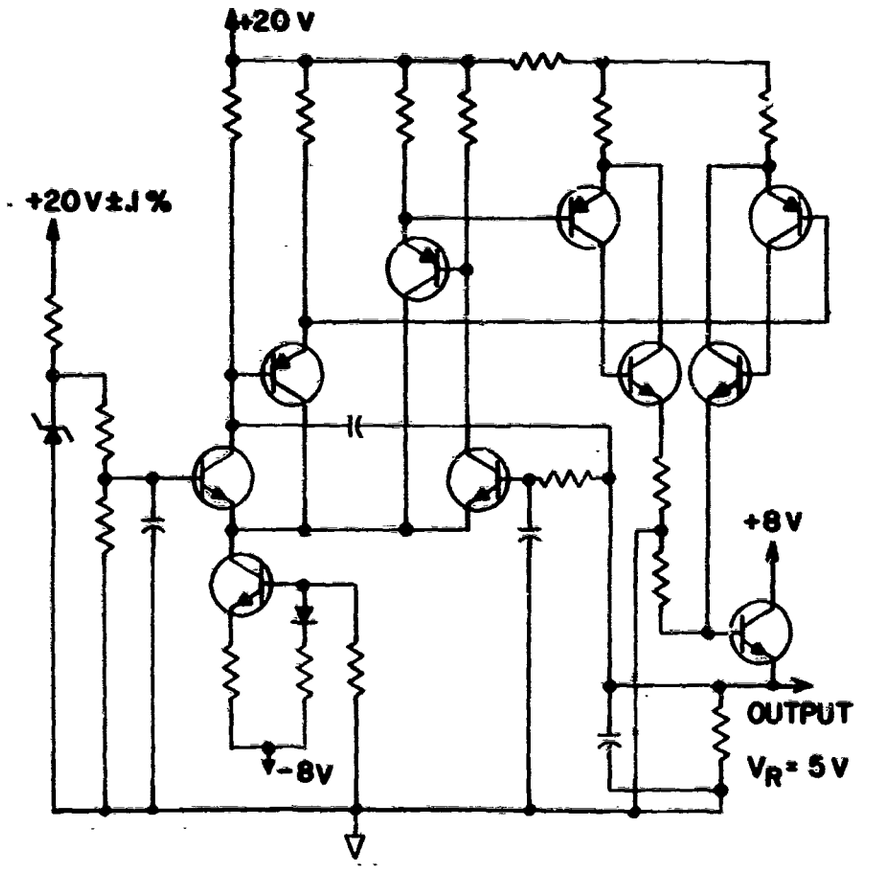


Fig. 5 Equivalent circuit of ladder-adder (the output resistance is constant at R_O, the Thevenin voltage V_L is a function of the position of the switches of the ladder-adder).



F.g. 6 Reference voltage supply schematic.

switch. It is seen that an extremely stable reference voltage must be generated. The reference voltage supply uses a highly stable Fairchild reference diode (Fig. 6). This diode has a temperature coefficient of 5 μv/C°. The Zener reference source is buffered by a d.c. differential amplifier. This amplifier has a very high open loop gain and is fed back to a closed loop gain of unity. The large open loop to closed loop gain ratio can give rise to oscillation problems in this type amplifier. However, in this application the frequency response is carefully rolled off to a very low value. The nigh open loop to closed loop gain ratio gives the advantage of a high input impedance and a low output impedance. Both of these characteristics are requirements. This Zender diode, although extremely stable, has a high dynamic impedance. The current through this diode must be invariant. The voltage supplied to the Zener is pre-regulated (+20V ± .1%) and the buffer amplifier must have sufficient input impedance so as not to load the Zener's circuit. The input stage of the reference amplifier uses a matched pair of transistors. The tracking of the V_{BE} offset between the two sides of this pair is better than 5 μV/C°. The total drift of these amplifiers has been measured to be less than 350 μV over a 40°C change in temperature.

The switch S1 and adjacent resistor (Fig. 3) correspond to the most significant bit of the ladder. An error in the value of the resistor or an increase in the offset associated with S1 is more critical than an equal error in one of the less significant bits of the ladder. Considerations of speed and system reliability make the use of semiconductor switches preferable to relay switches, however, the offset voltage associated with transistor saturation can be excessive in the more significant bit positions. System accuracy considerations may dictate the use of relays for the most significant bits. Careful selection of relays is required as an offset voltage may be generated by the potential between dissimilar metals used in a relay. The error voltage caused by an offset in the ladder switches is given by equation 1 as reported by Arthur, 1964.

$$\Delta V \approx \frac{\partial V}{\partial E_1} \Delta E_1 + \frac{\partial V}{\partial E_2} \Delta E_2 + \ldots + \frac{\partial V}{\partial E_n} \Delta E_n \qquad (1)$$

Where E_n is the voltage supplied by the switch S_n and V is the ladder output voltage. It can be seen that the output error is most sensitive to variations in offset voltage of the most significant bit position (ΔE_1).

The accuracy requirements for each switch in the ladder decrease from the most significant bit position to the least significant position. It is therefore possible that a good compromise between ladder speed and accuracy is to use relay switches in the most significant positions and transistor switches in the least significant positions. It is seen that as the ladder is counting either up or down the cycling rate of the switches decreases as you progress from the least significant bits to the most significant bits.

The semiconductor switch used on the offset field generator is shown in Fig. 7. This circuit offers a maximum offset of less than 750 μv at 0°C. The worst case variation of this offset has been shown to be less than 400 μv over a 40°C range. This corresponds to an error of 16 x 10^{-3} percent of the reference voltage or 160 PPM.

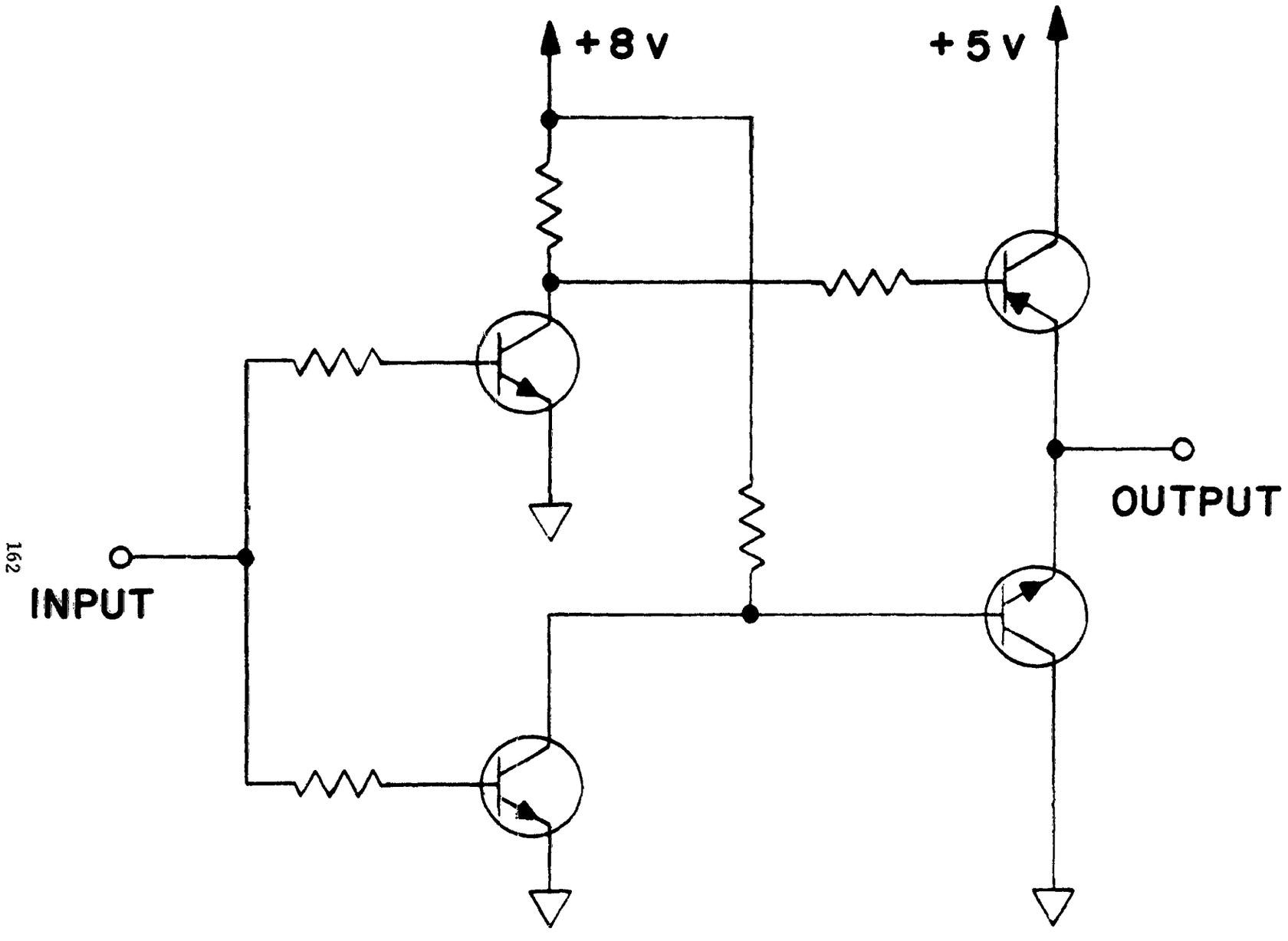


Fig. 7 Solid state switch schematic.

The ladder-adder resistors were precision wire wound resistors made of Karma[3] which was chosen because of its non-magnetic properties and low temperature coefficient. All resistors were custom wound from the same spool of wire to insure the temperature coefficient of all resistors would be identical and track one another over the temperature range. The resistors were selected to be within .02% of the specified value at 25°C with a temperature coefficient of ± 5PPM per °C. The change in output voltage due to a temperature variation of 50°C can be expected to be .025%.

The error in output voltage caused by a variation in the resistance of an individual ladder resistor $\left(\frac{\partial V}{\partial R}_n\right)$ has been analyzed by Arthur, 1964 The error depends upon the state of each switch in the ladder and can be calculated for any state of the counter. The total variation in output voltage when the ladder is in its center scale position is approximately equal to the thermal variations of an individual resistor of the circuit.

The wire wound around the sensor to generate the offset field must be carefully selected. It must have a very low temperature coefficient of resistance such the current through the coil does not change with the temperature. The wire must also be non-magnetic. There are a number of excellent wire types which meet this requirement, however, an added requirement is that of low resistivity. The resistance of this wire must be low enough such that the combination of the output impedance of the ladder and coil resistance is not too large to allow the required current to flow. The wire selected was Advance[4], this wire has a resistance of approximately 2.54 ohms per foot if number 30 wire is used.

MAGNETOMETER FOR OGO-E

The orbit for OGO-E is highly eccentric with magnetic field values ranging from roughly 40,000γ to <10γ. It was required that the instrument cover this entire range of fields with the best resolution obtainable. The spacecraft has a pulse code modulation data system with eight bit digitization of the 0V to 5.12V input voltage. This corresponds to a resolution of 20 millivolts. The basic magnetometer sensitivity was selected such that 20 millivolts represents 1/3γ. This gives a dynamic range of ±16γ centered about +2.5V for the basic magnetometer output. The least significant offset step of the offset field generator was scaled for 16γ. To conserve power the instrument has two offset field generators, a coarse offset field generator with seven bits and a medium offset field generator with six bits. The least and most significant bits of the medium offset field generator are scaled for 16γ and 512γ respectively. The least and most significant bits of the coarse offset field generator are scaled for

[3]Karma, a trade name of Driver Harris Company

[4]Advance, a trade name of Driver Harris Company

1,024γ and 65,536γ respectively. As previously mentioned, when the most significant switch of each ladder is on and all other switches are off, both offset field generators are in the zero offset condition. The dynamic range of the two ladders are +496γ to -512γ and 64,512γ to -65,536γ. The total dynamic range of the instrument which is the sum of the coarse and medium offset field generators and the basic magnetometer is +64,924γ to -66,064γ. The magnetometer can resolve 1/8γ even in the presence of a field of maximum value. It should be made clear that this is the resolving power of the instrument and not its absolute accuracy.

The seven bit coarse offset field generator uses relay switches. The resistors for the coarse ladder are 375 Ω and 750 Ω. The coarse offset winding on the sensor has a coil constant of 22γ/ma and has a d.c. resistance of 135 Ω. The calibrate resistor is approximately 300 Ω and is the same type of resistor as those of the ladder-adders. The seven bit medium offset field generator uses semiconductor switches. The resistors for the medium ladder are 25K Ω and 50K Ω. The medium offset winding on the sensor has a coil constant of 7.5 γ/ma and has a d.c. resistance of 139 Ω. The calibrate resistor is approximately 37K Ω.

The room temperature accuracy of the instrument at ±10,000γ was found to be within 50γ or .5%. Some of this error can be attributed to the test facility and to errors in the alignment of the sensor assembly within the test chamber. Some of the inaccuracy may be due to errors in the original set-up and calibration of the magnetometer. It is difficult to determine the exact amount of error to assign to each factor.

Temperature tests have been made over the range of 0°C to +50°C on both the sensor assembly and the electronics package. Variations were found to be within 30γ of the room temperature value at ±10,000γ or .3%. Some error can be attributed to thermal variation in the sensor assembly holding fixture which changes the sensor alignment as a function of temperature.

It can be seen that this type of instrument is limited by the test and calibration facility available. In our case the magnetometer may be more accurate at high field values than the test facility. Alignment of the sensor assembly within the calibration coil is another serious problem. The orthogonality of the calibration facility coils and the orthogonality of the sensor assembly elements also limit the accuracy of the measurements.

The OGO-E magnetometer has three orthogonal axes each with coarse and medium offset field generators. For additional information on the OGO-E magnetometer see Snare and Benjamin (1966).

ATS-1 MAGNETOMETER

The ATS-1 spacecraft was placed in schyncronous equitorial orbit at 5.6 earth radii on December 6, 1966. The spacecraft was spin stabilized at 100 rpm. The magnetometer has two sensors which lie in a plane that also contains the spin axis, with each sensor at 45° to the spin axis (Barry and Snare, 1966). The outputs of the two basic magnetometers are passed through sum and difference amplifiers to resolve the fields normal and parallel to the spacecraft spin axis. The dynamic range of each basic

magnetometer was ±50γ, ±100γ and ±200γ. The instrument remained in the most sensitive condition (±50γ) except when the normal field was greater than the dynamic range of the basic magnetometer. When the normal field exceeded the dynamic range, the instrument automatically switches to a sensitivity of greater dynamic range.

The nominal field at the position of the spacecraft was expected to be 125γ with a diurnal variation and solar wind modulated variations of unknown amplitude. Another significant factor was that the instrument was mounted on a magnetically dirty spacecraft. The magnetometer sensor was mounted on a boom whose total length was a spectacular seven inches. The perm field of the spacecraft and stray fields due to current loops at the location of the sensor was unknown when the instrument was being designed. Because of these variations in the geomagnetic field and the uncertainty of the spacecraft fields, an offset field generator was used in conjunction with each magnetometer axis.

Each offset field generator had six bits. The least significant step was scaled for 25γ. The zero step of the ladder was offset 125γ and the ladder had a dynamic range of -675γ to +925γ. This zero step offset was selected because of the nominal orbital field value of 125γ. With the zero offset, the offset field generator had an even range in each direction of ±800γ.

Because of the limited dynamic range of the offset field generator, solid state switches had low enough offset voltage such that relay switches were not required. The resistors of the ladder were 25K Ω and 50K Ω. The coil constant of the sensor winding was 15.3 γ/ua and a d.c. resistance of 150 Ω. The calibrate resistor was approximately 25K Ω.

To date the ATS-1 magnetometer has been successively operating in orbit for nine months with a total operating time of 4500 hours.

ACKNOWLEDGMENTS

The principal investigator for these projects is Professor Paul J. Coleman, Jr. of the Department of Planetary and Space Science, University of California at Los Angeles. Early development of the magnetometer was funded under NASA Grant NsG 249-62. Project funding was from NASA contracts NAS 5-9570 (ATS-1) and NAS 5-9098 (OGO-E). The detailed design, packaging and fabrication of the instrument was performed by Marshall Laboratories, Torrance, California under contract to the University of California. Special acknowledgment is given to C.R. Benjamin of Marshall Laboratories for significant contributions in system and circuity design.

BIBLIOGRAPHY

Arthur, Allan A., "Digital-To-Analog Conversion Ladders", Electro-Technology, Nov. 1964, pp. 60-64.

Barry, J.D., Snare, R.C., "A Fluxgate Magnetometer for the Applications Technology Satellite", IEEE Transactions on Nuclear Science, Vol. NS-13, No. 6, Dec. 1966.

Coleman, Jr., P.J., "Signal Processing for Space Vehicle Experiments", IRE Transactions, Fifth National Symposium on Space Electronics and Telemetry, Sept. 1960.

Dolginov, S. Sh., Eroshenko, E.G., Zhuzgov, L.N., Pushkov, N.V., and Tyurmina, L.O., "Magnetic Measurements with the Second Cosmic Rocket", Artificial Earth Satellites, Vol. 5, Plenum Press, New York 1961.

Heppner, J.P., Sugiura, M., Skillman, T.L., Ledley, B.G., Campbell, M., OGO-A Magnetic Field Observations, Goddard Space Flight Center, Publication X-612-67-150, March 1967.

Snare, R.C., Benjamin, C.R., "A Magnetic Field Instrument for the OGO-E Spacecraft", IEEE Transactions on Nuclear Science, Vol. NS-13, No. 6, Dec. 1966.

Takahashi, G.M., Engineering Electronic Design Final Completion Report, ABLE-5 Fluxgate Magnetometer, Space Technology Laboratories report No. STL/TN-60-0000-02102, June 1960.

Average Interplanetary Magnetic Field for Angular Momentum Calculations

Jerry L. Modisette

N69-33964

Modisette (1967) and Weber and Davis (1967) have analyzed the angular momentum lost from the sun to the solar wind, and have shown that the torque on the sun can be calculated by assuming the solar wind plasma to rotate as a rigid body out to the Alfvén radius and to be discoupled at greater distances. Dicke (1964) had predicted a similar result from unpublished work. Modisette (1967) also showed that the torque on the sun is, to a close approximation, proportional to the square of the radial component of the solar magnetic field.

The proper value of the average solar magnetic field is of considerable astrophysical interest, since as shown by Figure 1, the e-folding time for decay of the solar rotation becomes equal to the age of the sun at a surface field of about 3 gauss. Stronger fields produce shorter decay times, while weaker fields such as the generally quoted 1 gauss produce insignificant decays in solar rotation.

Because the torque is proportional to the square of the field strength, small areas with strong fields can be important contributors to the effective solar field, which is the rms average. For example, if 10% of the surface is covered with a 10 gauss field, this area alone would produce an rms average field of about 3 gauss, even if there is no field on the other 90% of the surface.

There are two sources of data available for determining the average solar magnetic field. There are direct measurements based on observations of Zeeman splitting of lines in the solar spectra, and there are inferred values obtained by extrapolating the field measured in interplanetary space. In a sense both sources amount

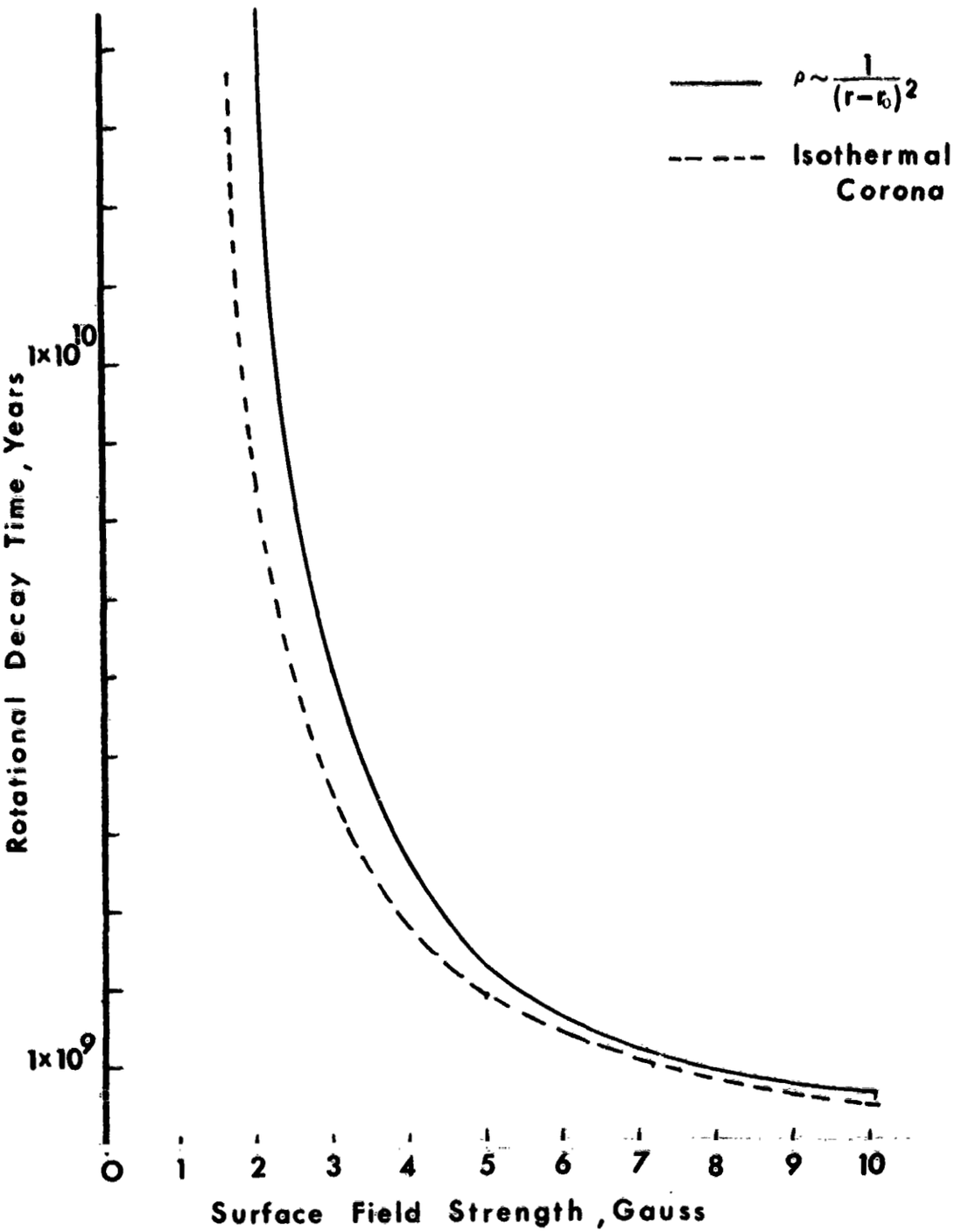


FIGURE 1. Time Constant for Decay of Solar Rotation for a Solar Wind Velocity of 500 km/sec, a Density of 5 ions/cc.

to extrapolations as far as the torque is concerned since it is the radial component of the field at the Alfvén radius which actually determines the torque on the sun.

Bumba and Howard (1965) have published maps of the solar magnetic field for August 1959 and February 1964. The periods shown represent a time of peak solar activity and a minimum period. From their field maps it is possible to integrate areas within contours and calculate average fields. However, one immediately has the problem of deciding what field strengths to consider as contributing to the interplanetary field, since for very strong fields one would not expect the field lines to be drawn out into space. Table I shows the results of averaging the fields with fields stronger than 10 gauss omitted from the calculation.

Table I

August 1959

Contour	Fraction of Area Enclosed	B_{avg}	Δ Area	$(\Delta A) B^2$
2 gauss	0.53	4 gauss	0.28	4.5
6 gauss	0.25	8 gauss	0.14	8.0
10 gauss	0.11	10 gauss	0.11	11.0
15 gauss	negligible			

$$B_{rms} = \sqrt{(4.5) + (8.0) + (11.0)} = 4.8 \text{ gauss}$$

February 1964

Contour	Fraction of Area Enclosed	B_{avg}	Δ Area	$(\Delta A) B^2$
2 gauss	0.145	4	0.130	2.1
6 gauss	0.015	8	0.014	0.9
10 gauss	0.001	10	0.001	0.1
15 gauss	negligible			

$$B_{rms} = \sqrt{2.1 + 0.9 + 0.1} = 1.8 \text{ gauss}$$

Note: The field is taken to be zero outside the 2 gauss contour. Assuming the average field outside the 2 gauss contour to be one gauss increases the rms average by 0.05 gauss for August 1959 and by 0.2 gauss for February 1964.

The 10 gauss cutoff was selected rather arbitrarily as corresponding to the stronger fields observed at 1 AU ($\approx$ 20 gamma based on a $1/r^2$ extrapolation), and because the dimensions of stronger field regions are so small that the fields are believed to be closed at the sun.

It is apparent from Table I that the stronger field regions are the major contributors to the rms average, so that the question of what fields are drawn out into space is quite important.

The magnetic field in interplanetary space is of more immediate interest in determining the torque on the sun, since it obviously has been drawn out and will contribute. Most of the measurements, unfortunately, have been made at times of relatively little solar activity, so that an average over a solar cycle cannot be made based on interplanetary measurements alone.

Measurements of the interplanetary magnetic field have been reported for Mariner II (Neugebauer and Snyder, 1967), Pioneer V (Greenstadt, 1966), and Imp I (Wilcox, et al., 1967). In addition, C. P. Sonett and David S. Colburn have made Imp III data available to the author. Table II shows the rms averages obtained. Table II also shows the corresponding solar field, obtained by extrapolating the interplanetary measurement back to the sun by an inverse-square law.

Table II

Vehicle	Date	Interplanetary Field	Solar Field
Pioneer V	March 12-May 6, 1960	6.9 γ	3.19 gauss
Mariner II	Aug. 29-Nov. 15, 1962	4.6 γ	2.1 gauss
Imp I	Dec. 10, 1963-Feb. 12, 1964	3.08 γ	1.56 gauss
Imp III	Oct. 22-Dec. 29, 1966	4.47 γ	2.06 gauss

It appears from Table I and Table II that the rms magnetic field of the sun varies from one or two gauss at sunspot minimum to about five gauss at sunspot maximum with the rms average over a sunspot cycle being 3-4 gauss. However, this result depends rather heavily on the cutoff selected in analyzing the solar measurements. Interplanetary field measurements through solar maximum will establish the average with greater confidence.

An average magnetic field of 3 or 4 gauss gives a torque on the sun producing an e-folding decay of the solar rotation in 3 to 6 billion years which is comparable to the age of the sun. It is possible that at other periods the sun was more active and had a stronger magnetic field. It appears that magnetic torques are capable of explaining the small amount of the solar system angular momentum in the sun.

It should be emphasized that the rather high value of the field results largely from strong fields existing a small part of the time. It is therefore important that accurate measurements of these fields be extended over the entire solar cycle, and that rms averages be carefully determined.

References

Bumba, V. and Robert Howard, 1965, "Large Scale Distribution of Solar Magnetic Fields", Astrophys. J. 141, 1502-1512.

Dicke, R. H., 1964, "The Sun's Rotation and Relativity", Nature 202, 432-435.

Greenstadt, E. W., 1966, "Final Estimate of the Interplanetary Magnetic Field at 1 AU from Measurements made by Pioneer V in March and April 1960", Astrophys. J. 145, 270-295.

Modisette, Jerry L., 1967, "Solar Wind Induced Torque on the Sun", J. Geophys. Res. 72, 1521-1525.

Neugebauer, Marcia and Conway W. Snyder, 1967, "Mariner II Observations of the Solar Wind", J. Geophys. Res. 72, 1823-1828.

Weber, Edmund J. and Leverett Davis, Jr., 1967, "The Angular Momentum of the Solar Wind", Astrophys. J. 148, 217-227.

Wilcox, J. M.; K. H. Schatten; and N. F. Ness, 1967, "Influence of Interplanetary Magnetic Field and Plasma on Geomagnetic Activity During Quiet Sun Conditions", J. Geophys. Res. 72, 19-26.

DEMAGNETIZATION METHODS FOR SPACECRAFT SYSTEMS AND COMPONENTS

Charles A. Harris

N69-33965

Goddard Space Flight Center
Greenbelt, Maryland

INTRODUCTION

Since the commencement of the magnetic test programs for the IMP and OGO spacecraft systems and components, demagnetization has been employed as a means of restoring the object to a nearly zero virgin magnetic state. Between 1962 and 1963 D.C. demagnetization was employed at the Component Magnetic Test Facility (CMTF). More recently demagnetization has been performed by substituting a 60 Hz A.C. field for the D.C. schedule. Under normal conditions a ferromagnetic material can be demagnetized by the application of a demagnetizing force with an initial field strength amplitude equivalent to the coercive force of the material. A field of this magnitude would then ensure removal of the remanence resulting from prior saturation of the material.

However, in the testing of the spacecraft subsystems there are practical reasons why the demagnetization field magnitude has been maintained at a level of 50 Oersted or less. For example, facilities to generate more intense fields throughout larger volumes are either very costly or are incompatible with requirements for generating gradient free low intensity fields (zero to a few gammas) needed for other magnetic tests. In addition, some spacecraft carry on-board permanent magnet devices (mass spectrometers, klystrons, compensating magnets) whose intended function would be impaired by even partial demagnetization. There

is the possibility of inducing damaging mechanical and electrical forces with the spacecraft by exposure to very intense fields. Also, apart from the deliberate magnetization of permanent magnets and the magnetic inspection of components and welds, it is extremely unlikely that components or subassemblies will be exposed to magnetizing fields in excess of 10 or 15 Oersteds except under controlled test conditions. Therefore the 50 Oersted level of field should result in completely demagnetizing "soft" ferrous materials which have low coercivity and, in addition, reducing the field strength of "hard" ferrous materials which have not been magnetized with fields above this level. This will not reduce the moment of an ALNICO magnet however, and therefore will not alter the operating characteristics of components which include magnets. Figure 1, therefore, presents examples of the hysteresis curves for both hard and soft ferrous materials and indicates the wide difference between the two saturation levels.

The sequential exposure of a component or assembly to a known magnetization field followed by demagnetization provides a well defined magnetic history for the test item and is a means of establishing a relatively stable and predictable magnetic characteristic. Even if the exposure sequence is omitted, demagnetization alone can still be used to establish a relatively stable magnetically clean condition. Therefore there is a continuing need for improved methods to accomplish this task. As a result, a series of tests have been performed in order to compare the relative merits of A.C. and D.C. demagnetization techniques and to enable the selection of the method most suitable for demagnetization of spacecraft systems and components. In order to demagnetize materials properly, the following procedures should be included in the process.

1. Gradual and continuous reduction of the area under hysteresis curve to zero by cycling through a series of gradually diminishing hysteresis loops.
2. Maximum amplitude or initial field strength equal to or in excess of the maximum coercivity of the material to ensure removal of the saturated remanence.
3. Return of object to a demagnetized isotropic condition similar to a virgin state by producing a scattering effect which in turn results in a completely random orientation of the domains in the material.

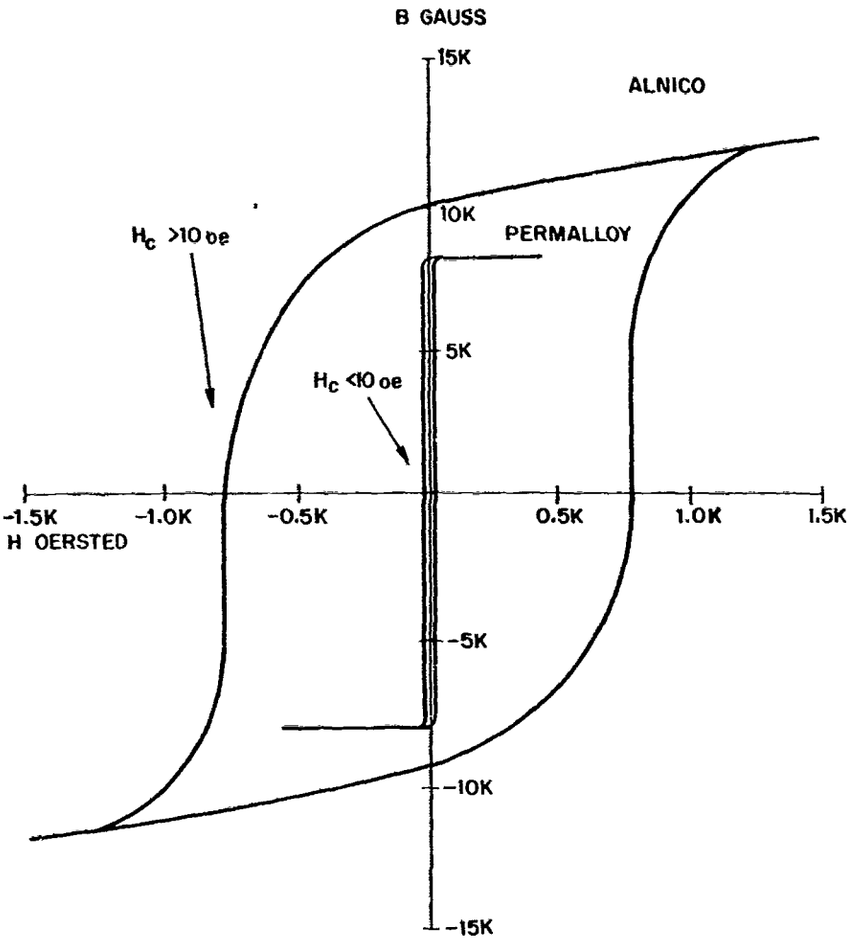


Figure 1–Hard and Soft Material Hysteresis Curves.

While the aforementioned requirements can be satisfied by either A.C. or D.C. demagnetization processes, a third method which does not satisfy these conditions can also be used for demagnetization. This technique, normally called the "recoil method," is not customarily employed since it actually results in a pseudo deperm by leaving the test item in an anisotropic condition. By trial and error the magnetization of "softer" elements is reversed to provide compensation for the remanence of the "harder" elements. The stability of such a multipole system comprising both soft and hard elements would then be uncertain. Therefore, only the A.C. or D.C. demagnetization processes have been investigated.

TEST OBJECTIVE

In order to evaluate the demagnetization techniques a series of tests was designed which would provide the following information:

1. Effectiveness of demagnetization process in reducing the residual field intensity.
2. Data to be used in comparing the results between 60 Hz A.C. and D.C. demagnetization.
3. Relationship between intensity of applied field and remanent magnetization of object.
4. Comparison between 3-axis and single axis (moment) demagnetization.
5. Feasibility of demagnetizing in earth's ambient field.
6. Other miscellaneous factors affecting the demagnetization process (L/D ratio, shape, eddy current loss).

Some of the problems and limitations of the two general categories (A.C. and D.C.) of demagnetization techniques involve:

1. Induction of large circulating currents within the spacecraft circuitry associated with 60 Hz A.C.
2. High current switching requirements which are handled by relays for D.C. deperming.
3. Induced voltages which can affect cancellation coils.

While these problems are not insurmountable, it would appear that they should be taken into consideration and included in the actual demagnetization requirements. From the standpoint of the problems associated with (1) and 3) those demagnetization systems which include either A.C. or D.C. pulsing demagnetization are undesirable. A proposed solution would be to develop a D.C. rotation demagnetization capability which could be substituted for both the D.C. (pulsing) and A.C. systems. Whereas, the 60 Hz A.C. deperm can employ a variable autotransformer to vary the field, the D.C.—pulsing system requires a succession of field pulses of reversed polarity which can be diminished to a minimum field strength magnitude of zero. The sequence for such a system is displayed in Figure 2. The proposed D.C.— rotation method employs a diminishing D.C. field (refer to Figure 3) similar to the D.C. pulse deperm of Figure 2 but excludes the field reversal requirements. As seen by the test item, the D.C. field effectively becomes a low frequency A.C. field in view of the fact that the object is rotating in the applied D.C. field. There are several advantages to this system which make it more preferable to either the A.C. or D.C. pulsing systems; for example, power supply problems are simplified; ambient field effects are cancelled; there is greater uniformity and control of the deperming process; and though automatic controls are convenient, they are not mandatory. The last and final test objective then is to compare all three methods of demagnetization in order to determine if the D.C. rotation technique would indeed be practical.

TEST RESULTS

Prior to the actual deperm tests, consideration was given to the selection of test samples which might correspond to expected spacecraft components. Thus, one sample was obtained which represents an actual spacecraft electronics subassembly while the others were selected to represent various thicknesses and lengths of objects. The particular rods which were selected had approximate demagnetization factors which varied from 0.08 to 0.001 and contained low or moderate eddy current loss characteristics.

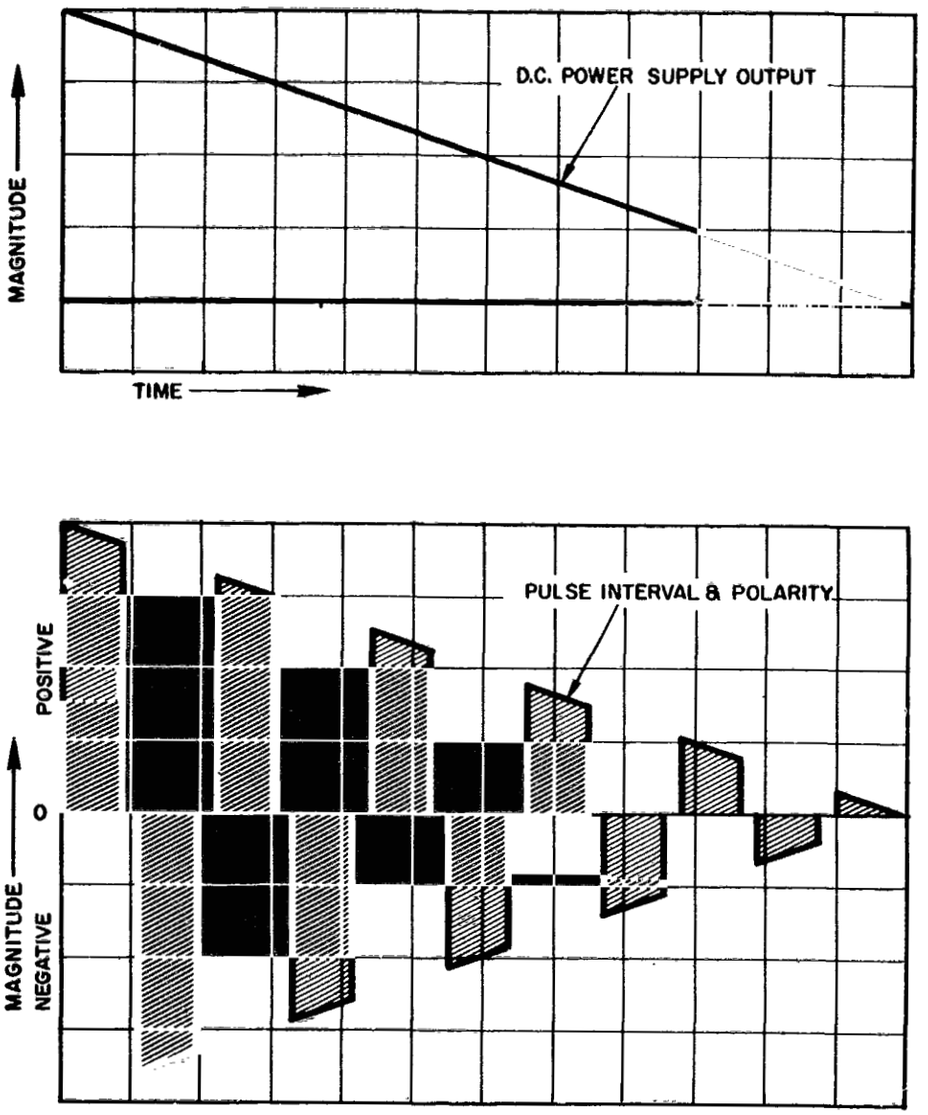


Figure 2–D.C. Pulse Demagnetization Sequence.

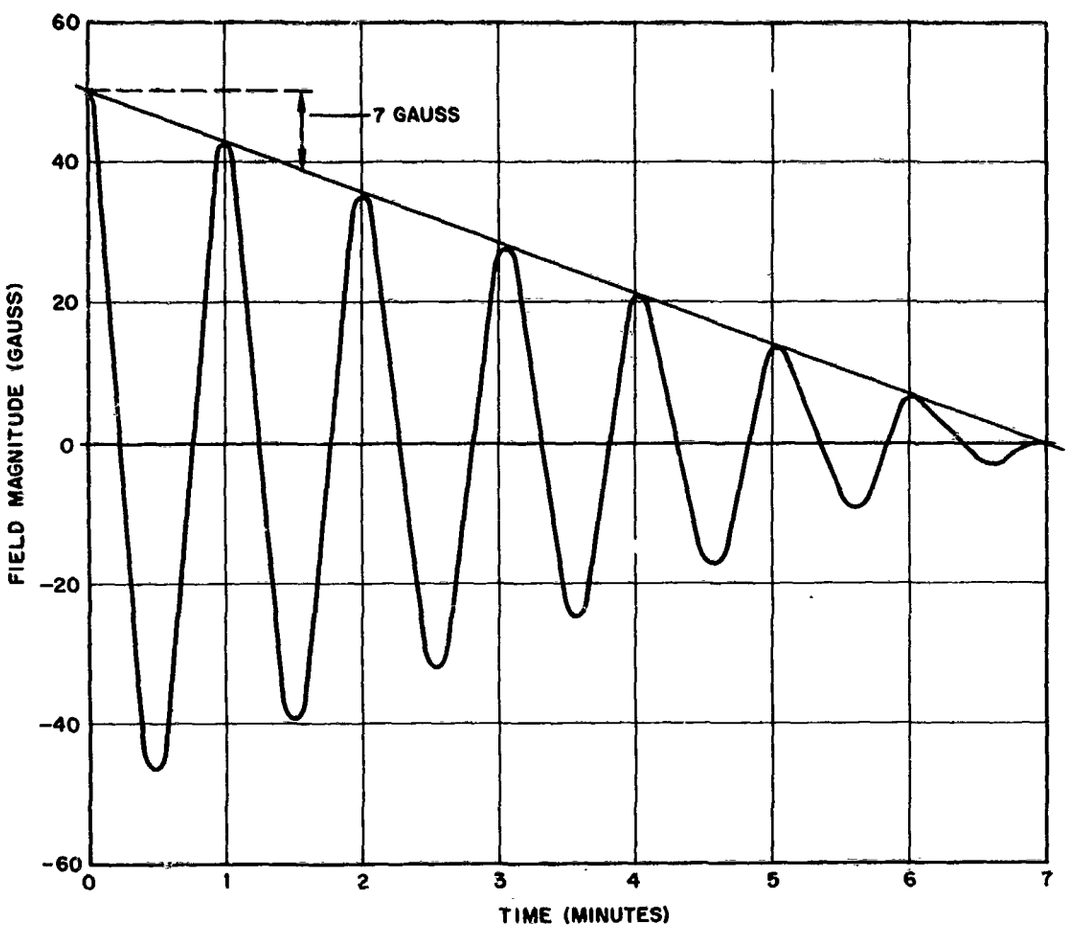


Figure 3–D.C. Rotation Deperm Sequence.

50 Gauss Deperm Results - Figure 4, is a comparison graph which indicates the percentage deperm results, obtained with the various samples for each of the three demagnetization states. In the case of four samples, each method of demagnetization reduced the remanent 25 gauss exposure field magnitude at least 90%. While there remained less than 5% difference between the three methods, the D.C. rotation system produced the most effective results in each case.

3.5 L/D Steel Rod - As depicted by Figure 4 which includes the demagnetization results for the various samples, only slight differences in the effectiveness of the three methods could be found. The one exception was the 3-1/2" length rod which had a much greater thickness (1 inch diameter). Here again the D.C. rotation method tends to prove slightly more effective than the 60 Hz A.C. and substantially more effective than the D.C. pulse demagnetization. In addition to the 50 gauss field results, treatments involving various field levels were also performed. Figure 5 has then been prepared to illustrate graphically the results obtained under these conditions. Although the A.C. method proves effective when the demagnetization field magnitude is less than 25 gauss, the D.C. rotation method becomes more effective as the magnitude is increased. Examining the results obtained with the 1" diameter rod, the following facts can be noted:

1. At levels of 50 gauss the D.C. rotation deperm was 2-3% more effective than the A.C. deperm.
2. Increasing the D.C. rotation magnitudes from 25 to 50 gauss resulted in a 10% improvement in the deperm results (81-85% reduction at 25 gauss and ≥95% at 50 gauss).

It is of particular interest to note the eddy current effects which are attributed to the less effective A.C. deperm. For example, as the diameter of a rod approaches and exceeds 1" the eddy currents generated by a 60 Hz field can become appreciable. In the case of a 1" diameter rod the ratio of field applied (H_a) to surface field (H_s) would be approximately 0.9. So for a 50 gauss 60 cycles A.C. field the rod will generate an opposition field of 5 gauss (H_s=45 gauss). Furthermore, with a 2"

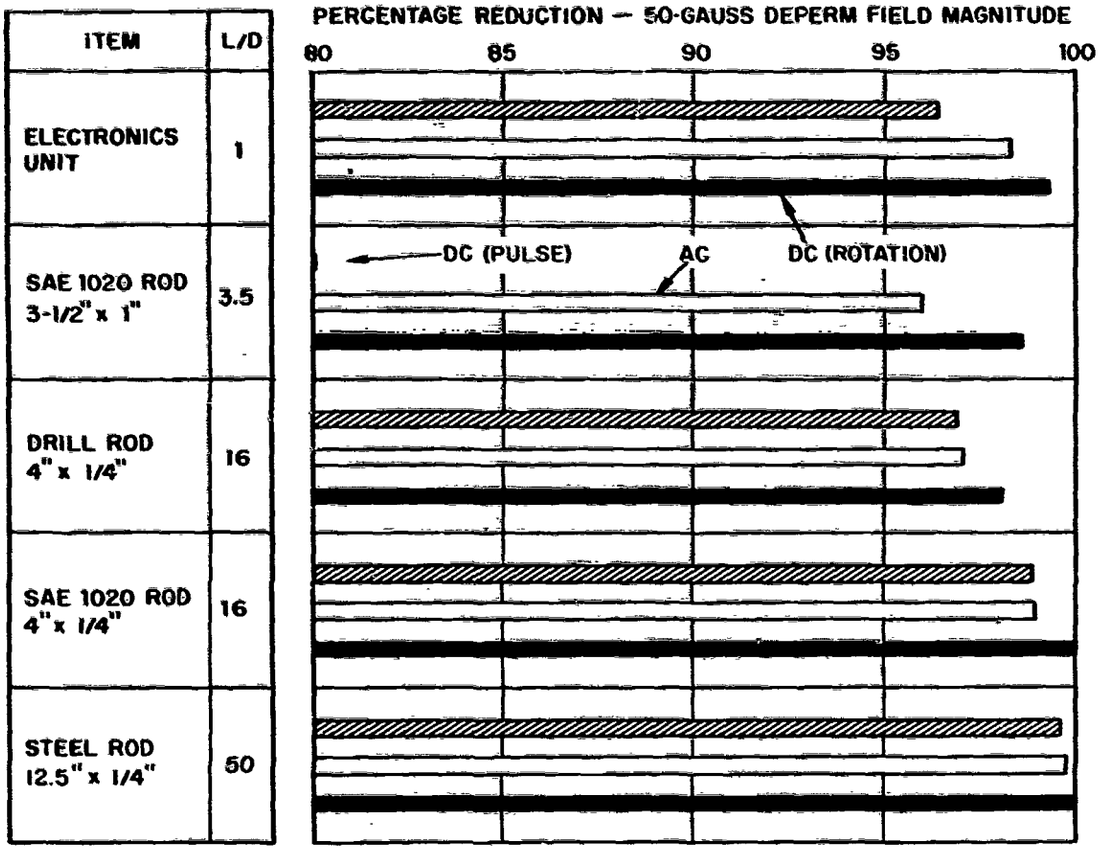


Figure 4–Deperm Test Results.

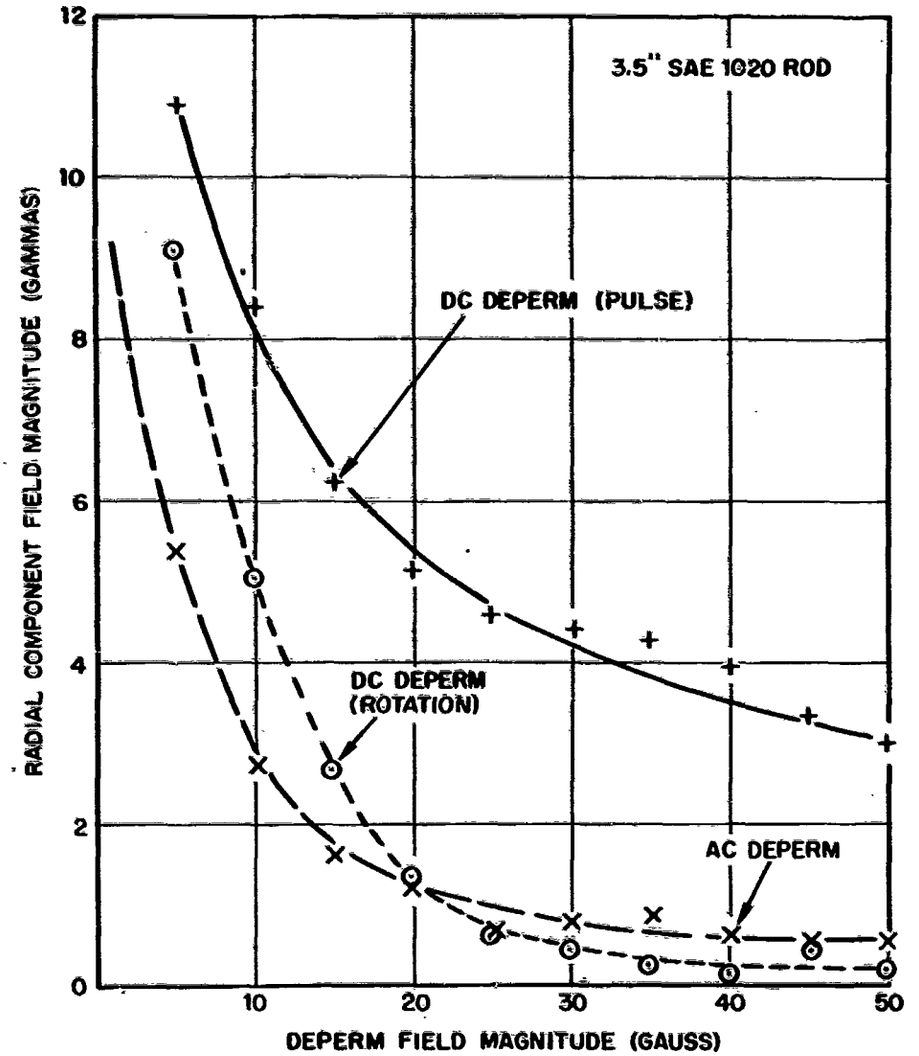


Figure 5–1" Diameter Rod Deperm Results.

diameter rod this ratio would approach 0.33 resulting in a 1/3 field reduction. These eddy current effects could be remedied by reducing the A.C. field frequency in which case the H_a/H_s ratio would diminish. However, this would require sources of controllable, high power, low frequency A.C. which are not readily available.

As a further note, there are instances where A.C. will not always result in an isotropic distribution of the material domains. This condition would prevail for a magnetic substance which had a cubic anisotropy. This material would be expected to have a domain distribution at the demagnetization state which would be confined to within 55° about the axis of the A.C. field. In order to eliminate this problem, a rotating field capability would be required.

Electronics Unit - The advantage of D.C. rotation demagnetization in relation to field magnitudes in excess of 25 gauss is illustrated in Figure 6 which displays the test results for the electronics unit. Although the composition of this spacecraft subassembly is such that the three methods tested produce effective deperms, there is still a decided difference between the results obtained with each method. In addition to the comparison data presented in Figure 6, the following tables summarize the A.C. and D.C. rotation test results. As evidenced by the hysteresis loop and normal magnetization curve for the unit, the 25 to 50 gauss (Figure 6) these curves would then have to be readjusted.

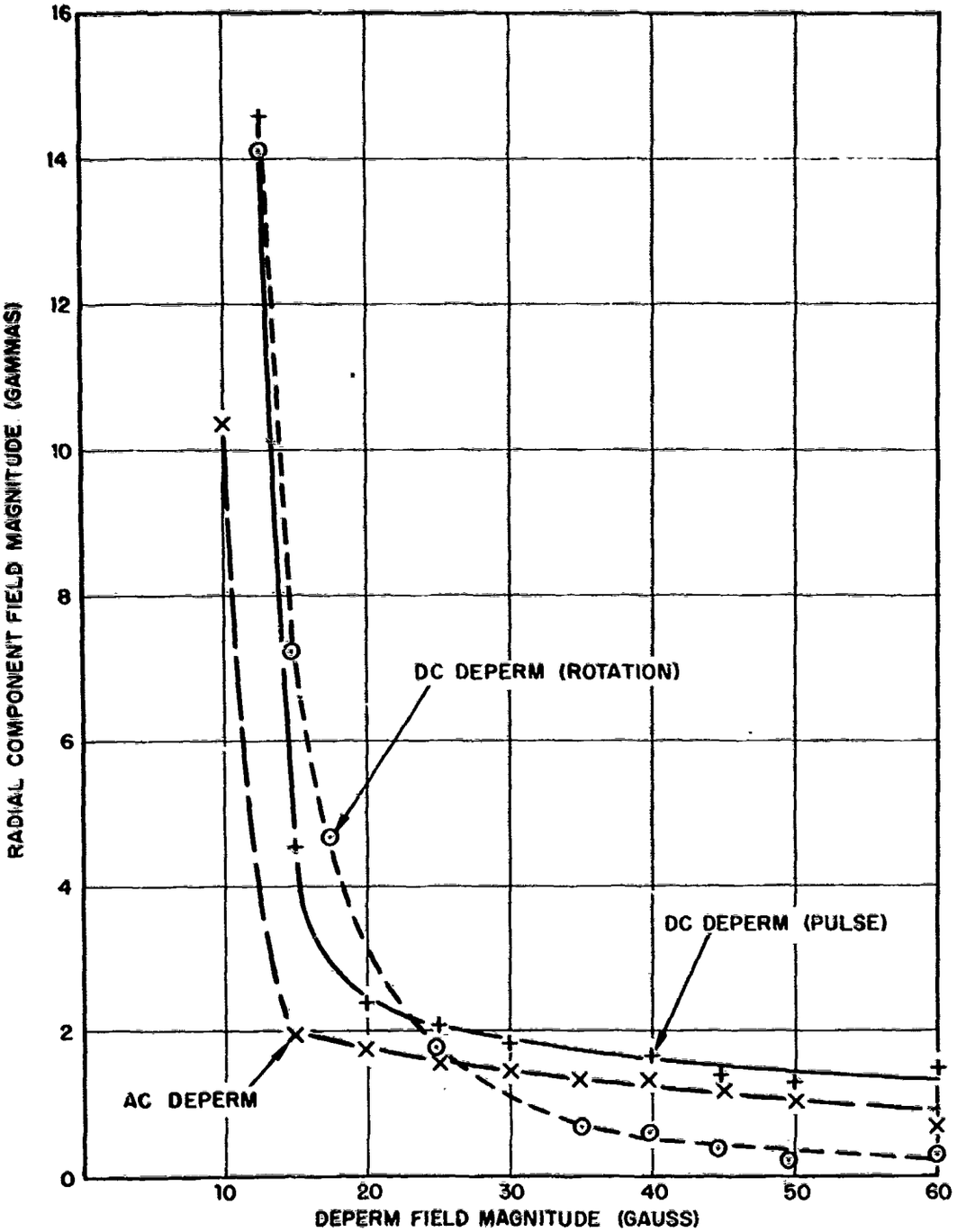


Figure 6–Electronics Unit Deperm Results.

TABLE I

Summary of A.C. Test Results
1. By increasing the deperm magnitude by a factor of two (25 to 50 gauss) the remanent perm magnitude was reduced 60% (1.8 to 1.1 gammas).
2. By incorporating rotation of the assembly while deperming in earth's field, results comparable to a zero (background) field deperm were obtained.
3. With the assembly and coil aligned east-west (D field magnitude zero) a satisfactory deperm could be obtained without rotation; however, the results were less effective than a zero field deperm (remanent field magnitude approximately twice as great).
4. Repetition of the deperm treatment (unit not re-exposed) results in slight reduction of remanent perm magnitude (5 to 10 percent reduction).
5. Application of the deperm field along three individual axes of the assembly resulted in a cleaner deperm than a single axis deperm (along moment). This included either a single axis (moment) or 3 axis exposure.

TABLE II

Summary of D.C. Rotation Test Results
1. By comparison, the D.C. rotation method of demagnetization resulted in the most effective deperm (2-3% better than A.C.).
2. Although it was possible to vary the deperm cycle, effective results were obtained by employing a minimum of 7 to 10 complete field reversals.
3. A decidedly ineffective demagnetization treatment was obtained when the sweep rate was accelerated or diminished during the deperm sequence.

While the D.C. rotation deperm sequence consisting of seven field reversals would prove effective when applied to most materials, other combinations of field decrease and assembly rotation could be selected. In this particular case the speed of rotation of the assembly was 1 rpm which was identical to the power supply sweep drive rate. Variation of the deperm sequence could be accomplished by adjusting the rate of rotation of the assembly from 0 to 11 rpm and/or setting the sweep drive at 1 or 10 rpm. Thus, the deperm sequence could be shortened from a time interval of less than 7 minutes to just one minute if desired (rotation speed 10 rpm-sweep drive 10 rpm) while still obtaining the normal 7 field reversals. Obviously, these alternatives improve the versatility of the system as compared to the 60 Hz A.C. deperm. The selection of sequences which include fewer or more field reversals could be varied from test item to test item as necessary. Actual results which were obtained for various rotation and sweep rates, the corresponding number of full wave field reversals and the related increments of field magnitude between each cycle are presented in Table III. The data verifies the fact that little is to be gained from the efficiency standpoint by prolonging the deperm sequence unless there is a mechanical or other limitation on the rate of rotation.

TABLE III

D.C. Rotation Deperm Sequence (50 Gauss Field Magnitude)

Assembly Rotation Speed (rpm)	Power Supply Sweep Drive Speed (rpm)	No.of Full Wave Field Reversals (shots)	Approximate Field Increment between shots(gauss)	Percent Deperm Achieved
1	1*	7	8	97.5
2	1	14	4	97.6
11	1	75	1	97.7
1	10**	<1	50	0
5	10	3	14	95.4
7	10	5	10	97.5
11	10	7	7	97.5

*Total time required 6-2/3 minutes (identical to D.C. pulse deperm)

**Total time required 40 seconds (normal A.C. deperm <10 seconds)

CONCLUSIONS AND RECOMMENDATIONS

The demagnetization tests which were performed indicated the following:

1. Demagnetization with a pulsing D.C. field is the least effective of all three methods.

2. Rotation of the object is desirable when an earth's field deperm is attempted.

3. Although the results tend to favor the D.C. rotation deperm over the 60 Hz A.C., effective demagnetization of spacecraft subassemblies could be achieved by either method. When eight IMP or OGO spacecraft assemblies were demagnetized by both methods the maximum and minimum percentages of effective deperm were as follows:

   A.C. = 99 and 45

   D.C. rotation = 99 and 46

In view of the favorable deperm results obtained with the D.C. rotation method and especially because of the advantages of such a system, i.e., variable frequency rates, reduction of eddy current and rise time effects, and elimination of circuit breaking, it is recommended that this method be utilized in the demagnetization of spacecraft. Generation of non-alternating D.C. field presents no difficulty and with the presently available Helmholtz coils and turntables, the D.C. rotation method could be employed in the demagnetization of the IMP or ISIS spacecraft in a facility such as the ACTF.

P. W. Droll[1] and E. J. Iufer[1]

MAGNETIC PROPERTIES OF SELECTED SPACECRAFT MATERIALS

N69-33966

REFERENCE: P. W. Droll and E. J. Iufer, "Magnetic Properties of Selected Spacecraft Materials," University of Nevada and Ames Research Center, NASA, Cosponsored Symposium on Space Magnetic Exploration and Technology (August 1967).

ABSTRACT: This paper summarizes the results of an investigation of the magnetic properties of selected spacecraft materials. Experimental measurements describing the effects of magnetic field exposure, shock, vibration, and temperature on the induced and remanent dipole moment of Kovar, Dumet, Invar, Nickel, 304SS, 410SS, and 416SS rod specimens are presented. Analysis of the data indicates that temperatures of 77° K to 390° K, shock to 50 g, and vibration to 25 g produce negligible effects on dipole moment for specimens having length-to-diameter ratios of 5.5. The remanent and induced moments of rod samples having length-to-diameter ratios of 40 or less are linearly related to magnetizing forces less than 25 oersteds. By means of the data provided, predictions of the dipole moment can be made for these materials if the alloy, demagnetization factor, magnetizing field, volume, and length-to-diameter ratio are known.

Nomenclature

B	magnetic induction (B_r, residual induction; B_{rs}, retentivity; B_s, saturation induction)
D	diameter
H	magnetizing force, magnetic field strength (H_a, applied field; H_c, coercive force; H_{cs}, coercivity)
I	intensity of magnetization
L	length
M	magnetic moment
m	length to diameter ratio
N	demagnetizing factor
R	measurement range
V	volume
μ	permeability, normal
μ'	permeability, apparent

[1]Research Scientist, Ames Research Center, NASA, Moffett Field, California 94035.

Introduction

Recent emphasis on the systematic exploration of the boundary of the Earth's magnetosphere and beyond has served to set strict limitations on the magnitude of magnetic fields produced by the spacecraft. To assure that spacecraft fields do not degrade the accuracy of the flight magnetometers, maximum field intensities of 1 nanotesla (1 gamma) are being specified for the complete spacecraft. This specification is related to current flight magnetometer sensitivity of 0.1 nanotesla and the 4 to 10 nanotesla quiescent level of the interplanetary magnetic field. As listed in Table 1, the fields of previously flown spacecraft (1), which were of sufficient interest to be reported, range from approximately 0.2 to 58.8 nanotesla at a range of 2 meters (nominal sensor location). Design of spacecraft complying with 1 nanotesla, or less, require close attention to the magnetic properties of all materials used in fabrication.

Although achievement of a low-moment spacecraft design would be realized by elimination of all ferromagnetic materials, a large percentage of electronic parts still contain magnetic materials. Therefore, it is extremely useful to know the magnetic properties of these essential components to provide a basis for design and prediction of spacecraft fields.

Much information on the types of materials used in the design of conventional magnetic circuits may be found in the literature. The magnetic properties of the materials studied in this report are incidental to their application, and consequently, little or no information can be found on their pertinent magnetic properties. Experimental measurements have been made to provide the missing information under conditions simulating the environmental exposures occurring during the manufacture, transportation, and launch of spacecraft.

By means of the Tables and Curves found in this report, it is possible to make estimates of the magnetic moments of spacecraft components.

Basic Relationships in Ferromagnetism

There are two basic magnetic quantities and an arbitrary constant from which all other magnetic quantities are derived (2). They are magnetic induction, B, magnetizing force, H, and permeability, μ_o. Magnetic induction is the quantity measured by the mechanical force experienced by a current-carrying conductor in a magnetic field. The measure of the ability of an electric current to produce magnetic induction at a given point is called the magnetizing force, H. Permeability is the ratio of the magnetic induction to the

corresponding magnetizing force. The value assigned to the permeability of free space, μ_o, determines the system of units and is equal to $4\pi \times 10^{-7}$ henries per meter in the MKS system and to unity in the c.g.s.-e.m.u. system used in this report.

With the definitions of B, H, and μ, a dynamic set of characteristics may be defined. If a demagnetized closed ring specimen is subjected to increasing values of H, there is a corresponding but nonlinear increase in B. This effect is illustrated in Fig. 1, and is called the normal induction or virgin magnetization curve. The hysteresis of the material is characterized by the partial retention of the induction when H is reduced to zero. If the material were previously magnetized to saturation, the induction retained is called the retentivity, B_{rs}; for lower exposure levels, the term residual induction B_r is used. The negative magnetizing force at which B_r becomes zero is called the coercive force, H_c, and the moment at which B_{rs} becomes zero is called the coercivity, H_{cs}.

Magnetic induction is made up of two components: one induced in the space occupied by the specimen (H) and the other due to the intrinsic magnetization of the specimen ($4\pi I$). That is

$$\bar{B} = \bar{H} + 4\pi\bar{I}$$

or

$$\bar{I} = \frac{\bar{B} - \bar{H}}{4\pi} \qquad (1)$$

and $\bar{I}$ is the intensity of magnetization (3). Equation (1) is sometimes called the magnetic equation of state because it describes the behavior of ferromagnetic media in a magnetic field.

These equations assume homogeneity in the magnetic circuit typified by torroidal core structures. However, spacecraft, magnetic material shapes can often be approximated by slender cylinders. The relatively high reluctance of space as compared to that of the material causes the net magnetizing force inside the rod to be less than the applied field. Classically this dimunition is attributed to the formation of fictitious poles at the ends of the rod. As a result, the hysteresis curve for the rod specimen appears to be sheared in comparison with the hysteresis curve of closed rings as shown in Fig. 1.

For rod specimens (4) the equation of state is

$$\bar{H} = \bar{H}_o - N\bar{I}$$

or the equivalent

$$\bar{H} = \bar{H}_o - N\left(\frac{\bar{B} - \bar{H}}{4\pi}\right) \qquad (2)$$

Where $\bar{H}$ is the magnetizing field acting on the middle of the rod, $\bar{H}_o$ the applied field equal to that which would exist if the specimen were removed and $\bar{B}$ the flux density measured at the middle of the rod. N represents the demagnetizing factor to accommodate for specimen shape with a finite length to diameter ratio (m). It is assumed that $\bar{H}$, $\bar{B}$, and $\bar{I}$ are parallel to $\bar{H}_o$ and uniform throughout the specimen, which permits the vector notation to be discarded.

The normal permeability of a ferromagnetic material is defined as $\mu = B/H$ measured on a closed loop specimen. The magnetic induction is measured for known values of H, and μ is calculated. For a cylindrical specimen made from the same material the effective permeability (μ') is less and may be defined by

$$\mu' = \frac{B}{H_o} \qquad (3)$$

Substituting (3) and the definition of normal permeability into equation (2) yields

$$\frac{1}{\mu - 1} = \frac{\mu}{\mu'(\mu - 1)} - \frac{N}{4\pi} \qquad (4)$$

If $\mu \gg 1$

$$\frac{1}{\mu} = \frac{1}{\mu'} - \frac{N}{4\pi}$$

For known values of H_o, N, and μ the induction B may be calculated from equation (3). Substituting equation (4) into (2) yields

$$H = \frac{H_o[1 + (N/4\pi)] - (NB/4\pi)}{1 - (N/4\pi)} \qquad (5)$$

The intensity of magnetization is obtained by substituting (5) into (1) and

$$I = \frac{1}{4\pi}\left\{B - \frac{H_o[1 + (N/4\pi)] - (NB/4\pi)}{1 - (N/4\pi)}\right\}$$

The magnetic moment, M, of a body is equal to the volume integral of the vector, I, and for rods, assuming M is parallel to L is

$$M = IV$$

After calculating the magnetic moment of the rod, the magnetic fields can be calculated at any range using the dipole approximation. The on axis field of a magnetic dipole is given by

$$H = \frac{2M}{R^3}$$

where R is the distance from the geometric center of the specimen to the point of measurement. Therefore, the external magnetic field produced by cylindrical shaped specimens can be calculated if the permeability, magnetizing force, and the length-to-diameter ratio is known. However, because of the simplifying assumptions, experimental measurements are relied upon to determine the curve relating permeability to the intensity of magnetization and to find the curves for residual induction and coercive force.

Materials Selection

Seven ferromagnetic materials commonly used for spacecraft electronic or structural purposes were selected for this study. These materials and their uses are listed in Table 2. The purity and some properties of these materials, shown in Table 3, were verified by independent measurement. The geometrical shapes of the specimens studied are listed in Table 4.

Experimental Apparatus

The magnetic field measurements of the specimens were made in the Ames Research Center 12-foot coil facility (5). The Earth's magnetic field was canceled to eliminate induced moments in the specimens during residual induction measurements. High field

intensities were generated using a multiturn coil approximately 10 cm long and 10 cm in diameter which produced fields from zero to 400 gauss uniform to ±3% over the volume of the specimens. The low field intensities were generated using a solenoid 61 cm in length and having a bore approximately 15 cm in diameter. The magnetic field intensities of the specimens were measured with a fluxgate magnetometer[2] sensitive to 0.2 gamma.

Experimental Procedure

Induction Measurement

The magnetic induction tests were performed on demagnetized specimens. The stray fields of the coil were compensated using circuitry built into the magnetometer. After placing the specimens in the unenergized coil, the current was adjusted to provide a preselected magnetizing force and the resulting field intensity measured by the magnetometer was recorded. The specimen was then withdrawn and demagnetized in preparation for the next higher exposure level.

Residual Induction Measurements

The procedures used for the residual magnetic induction measurements were similar to the tests for magnetic induction. The demagnetized specimens were placed in the coil and exposed to a known magnetizing force. After the coil was de-energized, the residual magnetic fields of the specimens were measured using the magnetometer under zero ambient field conditions.

Coercive Force Measurements

Coercive force measurements were made after each specimen had been exposed to a known magnetizing force. The residual magnetic induction was brought to zero by applying a momentary magnetizing force in the direction opposite to the initial exposure. Values for the initial exposure and for the reversed exposure which reduced the residual induction to zero were recorded. Conventional coercive force measurements are made during application of a magnetizing force which reduces the induction to zero. However, for these studies, momentary exposures were used to realistically simulate the exposures received by spacecraft.

Vibration and Shock Effects Measurements

Vibration stresses were induced into the specimens using a M.B. Electronics Model 2750MB amplifier with a Model C11-D calibrator/exciter system. The accelerometer used to monitor the g levels was a Columbia Model 504-3 with a Model 602 Dial-A-Gail amplifier. The drive unit was set up at a remote location to avoid magnetic interference. A nylon shaker fixture which held the specimens was connected horizontally to the exciter system via a 182 cm (6 ft) thin-walled aluminum push rod, 1.5 cm in diameter. Dead load deflection of the push rod was reduced by use of a two point suspension near its center. The natural resonant frequency of the rod and fixture was determined to be outside the vibration frequency band of interest. An acceleration level of 25 g was induced in the samples over a frequency range of from zero to 2000 Hertz for a period of time not exceeding 300 seconds to simulate the launch environment. The specimens were first vibrated while in a 25 oersted magnetizing force to determine the induced moment effects and then vibrated after a momentary exposure to a 25 oersted magnetizing force to determine residual moment effects.

The specimens were subjected to shock stresses by dropping the specimens on a hard surface from an elevation of approximately 30 cm to obtain a shock level of approximately 50 g. Shock tests were performed on the specimens after they were subjected to a magnetizing force of 25 oersted to determine if the residual magnetic induction would change.

Temperature Effects Measurements

The influence of temperature on B_r stability was determined by exposing specimens to a 100 gauss magnetizing force and then varying the temperature. Measurements of the magnetic field intensity were performed on specimens at 330° K and 77° K.

Error Analysis

The estimated error in the calculated induction field values is ≤100%. The error is attributed to the following: (a) variations in properties resulting from composition or processing and (b) nonuniform magnetization intensity over the entire cylindrical shape. The estimated uncertainty of the calculated values of magnetic moment obtained from measurements of the external field is considered to be less than 5% including random and systematic errors.

Temperature measurement uncertainties of 15° K at the elevated temperature and 3° K at the low temperature resulted primarily from the inability to attach thermocouples directly to the specimens.

Experimental Results

The materials tested can be divided into two types according to application: The first type, consisting of Kovar, Invar, Dumet, and Nickel, is used in the manufacture of electronic parts and is presented together in the graphs. The second type, consisting of 416, 410, and 304 stainless steel, is used in the manufacture of structures and fasteners and is similarly grouped.

Induction Properties

The induction moments of seven different materials were obtained for various length to diameter ratios as a function of magnetizing force. Also, the induction moment of Kovar was measured as a function of length to diameter ratio at one level of magnetizing force.

The induction moments of Kovar, Invar, and Dumet are shown in Fig. 2. The Kovar and Invar samples, tested in configuration A (m = 5.5) exhibit a very linear response to magnetizing forces less than 100 oersteds. However, the Kovar and Dumet samples in configuration B (m = 40), show a tendency to saturate at the 100 oersted level. The test results on the 416SS, 410SS, 304SS, and Nickel samples in configuration A did not tend to saturate

[2]Forster-Hoover M. F. 5050

as the magnetizing force approached the 100 oersted level. Figure 3 illustrates typical data as a function of magnetizing force. The 410SS and 416SS data are plotted as one curve because their characteristics are very similar, see Table 2.

The effect of m on the induced moment of Kovar samples tested in configurations B through L at a magnetizing force level of 1 oersted is shown in Fig. 4, and listed in Table 13. The low level of magnetizing force was chosen to assure that the specimen would not saturate in configuration L (m = 240). However, the theoretical induced moment curve does show a tendency to saturation at high m values. The results of this test illustrate a very important design consideration. That is, if a long piece of magnetic lead material were reduced in length, by an order of magnitude, the induced moment of the lead would be diminished by approximately two orders of magnitude. Reducing the m value is then an effective method of reducing induced moment.

Residual Induction Properties

The residual induction moments of all the materials are shown in Figs. 5 and 6, and listed in Tables 5 through 12. The results shown in Fig. 5 indicate that the residual induced moment of Kovar and Dumet with high values of m(40) approach saturation at relatively low levels of magnetizing force. In fact, it could be inferred that they will saturate very close to the 30 oersted level. It appears that the knee of the Dumet curve is closer to the 20 oersted level. The Kovar and Invar samples with m's of 5.5 show linear characteristics over the magnetizing force range with only slight tendencies to saturate. Curves similar in shape to the Kovar and Invar, m = 5.5, were obtained for Nickel, 416SS and 410SS as shown in Fig. 6. A general comparison of Figs. 5 and 6 indicate that all of the materials except 304SS are equally magnetic. Since 304SS is an austenitic stainless, it should exhibit lower magnetizations.

Coercive Force Properties

The coercive force properties of all the configuration A materials except Dumet, were obtained as a function of magnetizing force. These results are shown in Fig. 7. The data illustrate that 304SS is the only material exhibiting a linear response to magnetizing force over the range of zero to 100 oersteds. That is, a fixed percentage of the magnetizing force, if applied in the opposite direction in the sample will always reduce the residual induction to a zero value. It should be noted that a similar condition exists for the other materials at magnetizing forces less than approximately 25 oersteds.

Vibration and Shock Effects on Properties

The vibration and shock levels which were determined from known levels of the THOR DELTA launch environment, were induced into the specimens in configuration A. The specimens were subjected to vibration levels while in a magnetizing field of 25 oersteds and again in zero ambient field after momentary exposure at the same level. They were subjected to shock stresses on the order of 50 g after a momentary exposure of 25 oersteds. The results of those tests indicate that mechanical effects on the magnetic properties of specimens with m = 5.5 are negligible (less than 5%) for magnetizing fields of 25 oersteds.

Temperature Effects on Properties

The samples in configuration A were subjected to temperatures of 390° K and 77° K after exposure to a 25 oersted magnetizing force. Data obtained with specimens at these temperatures showed a negligible change.

Discussion

Comparisons of experimental data with values of induction moment calculated for Kovar (6), Invar (7), Nickel (8), 416SS (8), are shown in Figs. 2 and 3.

Reasonably good agreement is shown for all specimens at the high levels of magnetizing force because the permeability is becoming more nearly constant. Better agreement could be obtained if equation (3) were expanded to account for the nonuniform intensity of magnetization in cylindrical specimens. A closer approximation to B might be obtained by integrating B over the length of the rod to find some average value correction factor. Bozarth (3) suggests the need for "some kind of averaging." The figures indicate that the experimental and theoretical values agree within a factor which ranges from about 1.2 to 2.

No theoretical model was found which would permit accurate calculation of the residual induction moment as a function of magnetizing force. An attempt was made to apply a hyperbolic demagnetization curve approximation based on permanent magnet materials to these specimens; however, the development proved invalid. In lieu of a mathematical model, one can use the residual induction moment data contained in this report for estimating the residual moment of parts. Recalling that the induction B is always larger than the B_r, for a given exposure level, one may calculate a worst case remanent moment using the equations for induction.

Conclusions

An analytical model of the induction moment of rod specimens, based on formulas available in the literature, was derived. Experimental verification of the model was accomplished by demonstrating the influence of permeability, demagnetization factor, magnetizing force, and volume on the materials. The model was found to give a reasonably accurate prediction of induction moment for specimens whose length to diameter ratio ranged from 5 to 100. Analysis of the induction moment experimental data indicates the following:

The calculated value of induction moment was always larger than the experimental value.

All of the controlled expansion alloys studied have similar magnetic properties and their induction moments are approximately linear for magnetizing environments less than 30 gauss.

The magnetic moment of a cylindrical specimen can decrease two orders of magnitude for a decrease in length to diameter ratio of one order of magnitude.

Efforts to develop an analytical model for calculating the coercive force and the residual induction

moment were not successful. The experimental measurements covering the length-to-diameter ratios and the magnetic field exposure levels of interest in spacecraft design support certain generalizations: For any one material, the residual induction moments are at least an order of magnitude less than the induction moments for a given magnetizing force. The residual induction moment may be linearly extrapolated to low field values for magnetizing forces less than 25 gauss. For probable spacecraft exposure field levels (1-10 gauss), there is little basis for distinguishing between the controlled expansion alloys on the basis of their residual induction moments.

The coercive force measurement data indicate that all of materials tested with a length to diameter ratio of 5.5 are similar in their response to magnetizing forces of less than 10 gauss. In addition, the ratio of the coercive force to the magnetizing force tends to be a constant value of approximately 0.5 for the 10 gauss field level.

From the standpoint of material selection, there is apparently no basis for selecting Dumet in preference to Kovar from a magnetic moment standpoint.

The use of linear extrapolation techniques to estimate residual induction moment of specimens having length-to-diameter ratios in the order of five is apparently valid for standard exposure fields of 25 gauss or less.

References

1. C. L. Parsons, "Magnetic Testing of Spacecraft," Proceedings of the Magnetics Workshop, compiled by J. G. Bastow, Jet Propulsion Laboratory, TM 33-216, September 15, 1965.

2. R. L. Sanford, and I. L. Cooter, "Basic Magnetic Quantities and the Measurement of the Magnetic Properties of Materials." National Bureau of Standards Monograph 47, May 1962.

3. R. M. Bozarth, "Ferromagnetism," D. Van Nostrand Company, Inc., p. 3, 1951.

4. R. M. Bozarth, and D. M. Chopin, "Demagnetizing Factors for Rods," J. Appl. Phys., vol. 13, pp. 320-326, May 1942.

5. E. J. Iufer, and P. W. Droll, "Space Magnetic Environment Simulation for Spacecraft Testing," to be presented at ASTM/IES/AIAA Second Space Simulation Conference (September 1967), Am. Soc. Testing Mats., 1967.

6. "Kovar Expansion Alloy," Application Data Sheet 52-461, Westinghouse Electric Corporation, Los Angeles, California, May 1965.

7. "Carpenter Alloys for Electronic, Magnetic and Electrical Applications," The Carpenter Steel Company, Reading, Pennsylvania, 1963.

8. "Electrical Materials Handbook," Allegheny Ludlum Steel Corporation, Pittsburgh 22, Pennsylvania, 1961.

TABLE 1--Magnetic fields of some interplanetary spacecraft.

Spacecraft	Date	Post 25 gauss[a] magnetizing force	Demagnetized[a]
OGO-A (8)	4/15/64	146.8	58.8
Explorer (8) IMP-C	7/30/64	15.7	0.6
Explorer XXI (8) IMP-B	8/14/64	12.3	0.5
Pioneer VI	12/16/65	1.6	0.2
Pioneer VII	8/17/66	1.5	0.2

[a]Approximate measurement range, 2 meters.

TABLE 2--Materials selected for study.

Materials	Use	Comment
Nickel	Electronic components	A standard lead material; good weldability
Kovar	Electronic components	Controlled expansion alloy; useful lead material - has coefficient of thermal expansion matching glass
Dumet	Electronic components	Standard lead material, good weldability
Invar	Electronic components	Controlled expansion alloy
410 stainless steel	Structural	General purpose stainless steel. Excellent availability; good resistance to chemicals and atmosphere
416 stainless steel	Structural	Free machining modification of type 410
304 stainless steel	Structural	Low carbon modification of 302SS. Excellent atmosphere resistance and machinability

TABLE 3--Chemical and physical properties of rod specimens.

Material	Source	Major constituents, %									Rockwell hardness		Comment
		C	Cr	Fe	Mn	Ni	P	Si	S	Co	B	C	
Nickel	Pacific Metals	0.03	---	---	---	PC*	---	0.08	---		90.5		Cold drawn heat #N7050A
Kovar	Westinghouse Electric Co.	---	---	53.00	0.46	29.00	---	0.01	---	17.53	82.8		Heat #920050
Dumet	General Electric Company	---	---	57.00	1.00	42.00	---	---	---	---	---		Has copper sheath
Invar	Carpenter steel	0.08	---	PC	0.87	35.74	---	0.31	---	---	94.0		Cold drawn heat #66719
410SS	Carpenter steel	0.12	12.13	PC	0.53	---	0.01	0.33	0.01	---	98.5		Cold drawn heat #810491
416SS	Ames Research Center Stock item	0.01	12.85	PC	0.82	---	0.02	0.36	0.26	---	98.5		Annealed grain size ASTM #9
304SS	Carpenter steel	0.07	18.30	PC	0.94	8.47	0.03	0.64	0.02	---		28.5	Cold drawn heat #67844

*Principal constituent - remainder of percentage.

TABLE 4--Geometrical properties of rod specimens.

Configuration	Length, cm	Diameter, cm	Volume, cubic cm	M
A	5.080	0.952	3.62	5.47
B	5.080	0.127	0.06	40.00
C	7.62	0.127	0.10	60.00
D	10.16	0.127	0.13	80.00
E	12.70	0.127	0.16	100.00
F	15.24	0.127	0.19	120.00
G	17.78	0.127	0.22	140.00
H	20.32	0.127	0.26	160.00
I	22.86	0.127	0.29	180.00
J	25.40	0.127	0.32	200.00
K	27.94	0.127	0.35	220.00
L	3048	0.127	0.38	240.00

TABLE 5--Results of nickel tests.
[$N/4\pi$ = 0.036, m = 5.4, V = 3.621 cm]

Magnetizing force, oersted	Normal permeability	Field intensity, theoretical, gamma	Field intensity, experimental, gamma	Induction moment, theoretical, gauss-cm^3	Induction moment, experimental, gauss-cm^3	Residual induction moment, experimental, gauss-cm^3	Coercive force, experimental, oersted
0.5	*	---	14.7	---	2.08	---	---
1.0	1000	54.9	27.8	7.8	3.9	0.0	---
5.0	720	271.8	124.0	38.5	17.6	0.2	2.3
10.0	410	528.1	280.0	74.8	39.6	0.7	---
15.0	287	770.4	420.0	109.1	59.5	1.8	7.5
20.0	220	999.2	568.0	141.5	80.4	3.3	---
25.0	180	1217.3	717.0	172.4	101.5	5.2	12.9
35.0	---	---	---	---	---	10.8	18.2
100.0	58	3754.2	3313.0	531.5	469.1	75.0	42.1

*Data unavailable.

TABLE 6--Results of Kovar tests.
[$N/4\pi$ = 0.036, m = 5.4, V = 3.6 cm^3, R = 30.48 cm]

Magnetizing force, oersted	Normal permeability	Field intensity, theoretical, gamma	Field intensity, experimental, gamma	Induction moment, theoretical, gauss-cm^3	Induction moment, experimental, gauss-cm^3	Residual induction moment, experimental, gauss-cm^3	Coercive force, experimental, oersted
0.5	1000	27.4	20.6	3.9	2.9	---	---
1.0	2000	55.7	39.0	7.9	5.5	0.0	---
5.0	2375	279.3	193.0	39.5	27.3	0.2	2.3
10.0	1600	555.3	388.0	78.6	54.9	0.8	---
15.0	1300	829.6	580.0	117.4	82.1	1.8	7.1
20.0	1100	1101.8	769.0	155.9	108.9	2.9	---
25.0	900	1369.4	946.0	193.8	133.9	4.2	10.9
35.0	---	---	---	---	---	6.6	14.2
100.0	200	4938.1	4330.0	699.2	613.1	18.1	26.1

TABLE 7--Results of Kovar tests.
[$N/4\pi$ = 0.0018, m = 40, V = 0.064 cm]

0.5	1000	6.4	3.8	0.9	0.5	---	---
1.0	2000	15.7	7.6	2.2	1.1	0.0	---
5.0	2375	81.2	47.5	11.5	6.7	1.3	---
10.0	1600	148.7	88.0	21.0	12.4	2.3	---
15.0	1300	210.5	140.0	29.8	19.8	3.0	---
20.0	1100	266.1	176.0	37.7	24.9	3.6	---
25.0	900	309.5	210.0	43.8	29.7	3.8	---
35.0	---	---	---	---	---	4.1	---
100.0	200	527.9	434	74.7	61.4	4.3	---

TABLE 8--Results of Dumet tests.
[$N/4\pi$ = 0.0018, m = 40, V = 0.064 cm^3, R = 30.48 cm]

0.5	*	---	2.7	---	0.4	---	---
1.0	*	---	5.1	---	0.7	0.0	---
5.0	*	---	30.0	---	4.2	0.8	---
10.0	*	---	68.0	---	9.6	3.0	---
15.0	*	---	98.5	---	13.9	5.1	---
20.0	*	---	134.0	---	18.9	6.6	---
25.0	*	---	163.0	---	23.1	7.6	---
35.0	*	---	---	---	---	8.1	---
100.0	*	---	370.0	---	52.4	9.8	---

TABLE 9--Results of Invar tests.
[$N/4\pi$ = 0.036, m = 5.4, V = 3.6 cm^3, R = 30.48 cm]

0.5	*	---	21.2	---	3.0	---	---
1.0	85	42.1	40.0	6.0	5.7	0.0	---
5.0	500	267.2	203.0	37.8	28.7	0.3	2.6
10.0	610	539.8	411.0	75.4	58.2	1.3	---
15.0	470†	798.5	618.0	113.0	87.5	2.9	8.0
20.0	400†	1054.5	824.0	149.3	116.7	4.8	---
25.0	300†	1289.1	1006.0	182.5	142.4	6.5	10.3
35.0	*	---	---	---	---	9.3	12.3
100.0	*	---	4135.0	---	585.4	19.4	21.0

*Data unavailable.
†Extrapolated.

TABLE 10--Results of 416SS tests.
[$N/4\pi$ = 0.036, m = 5.4, V = 3.6 cm^3, R = 30.48 cm]

Magnetizing force, oersted	Normal permeability	Field intensity, theoretical, gamma	Field intensity, experimental, gamma	Induction moment, theoretical, gauss-cm^3	Induction moment, experimental, gauss-cm^3	Residual induction moment, experimental, gauss-cm^3	Coercive force, experimental, oersted
0.5	*	---	19.8	---	2.8	---	---
1.0	500	50.3	36.8	7.6	5.2	0.0	---
5.0	600	269.7	196.0	38.2	27.7	0.3	2.3
10.0	760	544.6	394.0	77.1	55.8	1.1	---
15.0	647	811.8	592.0	114.9	83.8	2.3	6.8
20.0	550	1074.3	785.0	152.1	111.1	3.7	---
25.0	465	1330.5	964.0	188.4	136.5	5.3	11.7
35.0	---	---	---	---	---	8.6	14.0
100.0	160	4785.8	4090.0	677.6	579.1	27.3	30.0

TABLE 11--Results of 410SS tests.
[$N/4\pi$ = 0.036, m = 5.4, V = 3.6 cm^3, R = 30.48 cm]

0.5	*	---	19.8	---	2.8	---	---
1.0	500	50.3	36.8	7.6	5.2	0.0	---
5.0	600	269.7	196.0	38.2	27.2	0.3	2.3
10.0	760	544.6	394.0	77.1	55.8	1.1	---
15.0	647	811.8	592.0	114.9	83.8	2.3	6.7
20.0	550	1074.3	785.0	152.1	111.1	3.7	---
25.0	---	1330.5	964.0	188.4	136.5	5.3	11.9
35.0	---	---	---	---	---	8.7	14.1
100.0	160	4785.8	4090.0	677.6	579.1	27.2	29.9

TABLE 12--Results of 303SS tests.
[$N/4\pi$ = 0.036, m = 5.4, V = 3.62 cm^3, R = 30.48 cm]

0.5	*	---	0.5	---	0.1	---	---
1.0	*	---	0.8	---	0.1	0.0	0.0
5.0	*	---	3.0	---	0.4	0.0	3.0
10.0	*	---	6.6	---	0.9	0.0	---
15.0	*	---	10.2	---	1.4	0.0	9.0
20.0	*	---	13.5	---	1.9	0.0	---
25.0	*	---	16.2	---	2.3	0.1	15
35.0	*	---	---	---	---	0.2	20
100.0	*	---	80.0	---	11.3	3.1	59.1

*Data unavailable.

TABLE 13--Theoretical and experimental induction moments of Kovar as a function of L/D ratio H_o = 1 oersted, μ = 2000.

(L/D) m	$N/4\pi \times 10^{-5}$	Volume, cm^3	Measurement, range-cm	Field intensity, theoretical, gamma	Field intensity, experimental, gamma	Induction moment, theoretical, gauss-cm^3	Induction moment, experimental, gauss-cm^3
240	6.2	0.385	152.4	3.1	1.7	54.6	30.1
220	7.4	0.353	139.7	3.6	2.0	48.9	27.[illegible]
200	9.0	0.321	127.0	4.2	2.0	43.3	20.[illegible]
180	11.0	0.289	114.3	5.0	2.6	37.7	19.4
160	14.0	0.257	101.6	6.1	3.0	31.9	15.[illegible]
140	18.0	0.225	88.9	7.5	4.7	26.3	16.[illegible]
120	25.0	0.193	76.2	9.2	6.3	20.4	13.[illegible]
100	36.0	0.161	63.5	11.6	9.1	14.8	11.[illegible]
80	54.0	0.129	50.8	15.0	11.2	9.8	7.3
60	90.0	0.096	38.1	19.7	20.0	5.4	5.5
40	180.0	0.064	25.4	27.1	---	2.2	---

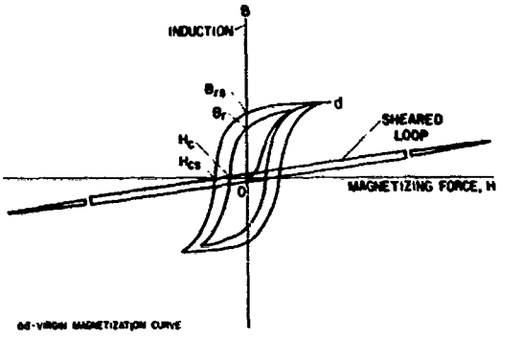


Fig. 1--Normal and sheared hysteresis loops.

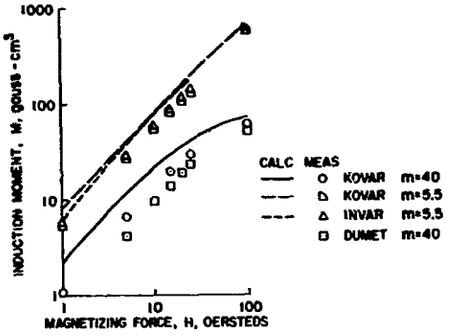


Fig. 2--Effect of magnetizing force on induction moment.

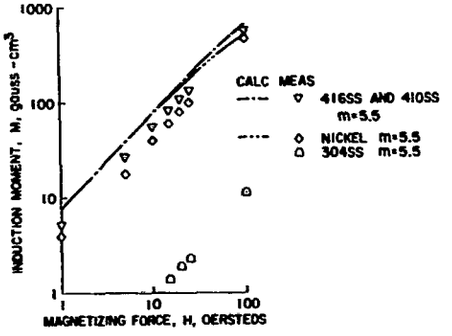


Fig. 3--Effect of magnetizing force on induction moment.

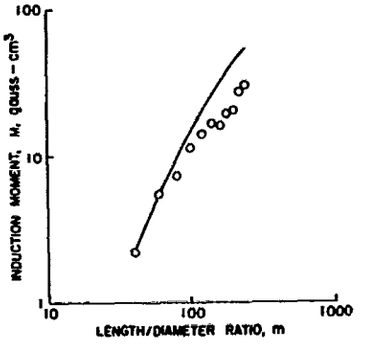


Fig. 4--The effect of length-to-diameter ratio on induction moment for Kovar.

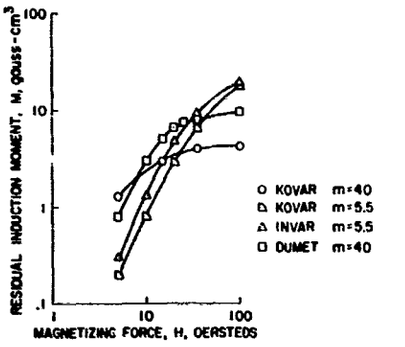


Fig. 5--Effect of magnetizing force on residual induction moment.

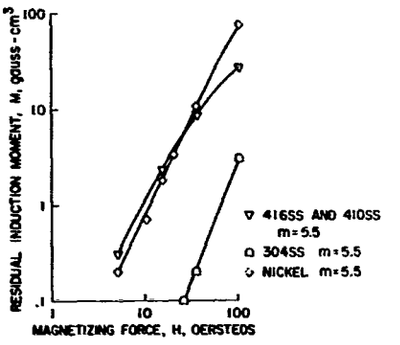


Fig. 6--Effect of magnetizing force on residual induction moment.

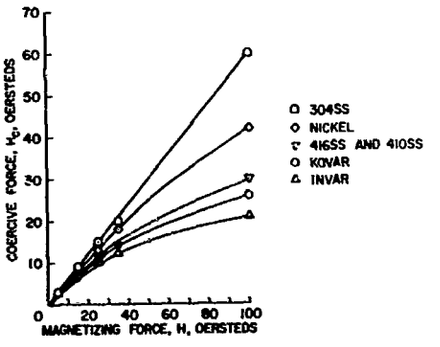


Fig. 7--Effect of magnetizing force on coercive force.

STABILITY MEASUREMENTS OF FLUXGATE MAGNETOMETERS

W. I. Linlor, R. M. Munoz, and M. J. Prucha*

N69-33967

INTRODUCTION

Interplanetary magnetic fields are of great interest to space scientists. Their intensities are relatively low (of the order of ten gamma, equivalent to 10^{-4} gauss) compared to earth magnetic fields, implying that measurements should be reliable to less than a fraction of a gamma uncertainty. Therefore considerable effort has been expended by spacecraft designers to provide a vehicle which is "magnetically clean", as well as by magnetometer system designers to obtain an instrument that is accurate and stable.

This paper has the purpose of describing stability measurements of the Ames fluxgate magnetometer (1) particularly in regard to effects of temperature changes. A brief description will be given of the sensor for convenient reference. The associated electronics is described in Ref. 1. Most of the presentation will be concerned with the "offset", which can be defined as the indicated reading in a "zero" field; alternatively, it is the algebraic mean of readings along a given axis taken in the zero and 180-degree directions.

Prime interest is the stability (or constancy) of the offset under systematic variation of test conditions. Both the sensor and its associated electronics may contribute to the value of the offset; variation of the parameters that affect only the sensor or only the electronics determines the relative contribution of each to the offset.

*NASA-Ames Research Center, Moffett Field, California

DESCRIPTION OF SENSOR

A fluxgate magnetometer utilizes the nonlinear B-H characteristics of magnetic materials when driven into saturation. Many alternative configurations are possible; the present arrangement consists basically of an iron core, exciting winding, sense winding, and feedback winding. As shown in Fig. 1, the iron core has the shape of a flattened ellipse or "race-track". The ampere-turns of the exciting winding on each leg aid the other so that the magnetic flux follows an essentially closed path within the iron core. A photograph of the iron core and exciting winding is shown in Fig. 2. Surrounding the iron core and its winding is the sense winding, shown in Fig. 3. In the absence of an external magnetic field no voltage would be induced in the sense winding of an "ideal" unit, because a flux change in one leg would be counterbalanced by the flux change in the other leg. An ambient magnetic field alters the symmetry properties of the flux changes, thus producing a second harmonic in the sense winding whose amplitude is proportional to the component of the ambient magnetic field along the axis of the sensor. A "feedback" winding which is similar to the sense winding is added for circuit response reasons.

A simplified perspective drawing of the sensor is given in Fig. 4. A functional block diagram of the electronics system is shown in Fig. 5. In Table 1 is given a summary of the performance characteristics.

The material used as the core of the sensor is 4-79 molybdenum permalloy tape having a width of 1/16 inch and thickness of 0.0005 inch. Three wraps of the tape are carefully wound on a ceramic core 1-3/4 inches long. The exciting winding consists of approximately 700 turns total, divided equally between the two halves on the legs of the core. The exciting voltage is sinusoidal, 4.0 volts peak-to-peak, 5 KC frequency; the exciting current has the waveform shown on Fig. 6a, with a peak-to-peak value of 180 milliamperes. The peak value produces a magnetizing force approximately twenty times larger than that necessary to saturate the core. The sense winding consists of about 3,000 turns, yielding a sensitivity of approximately 25 microvolts RMS per gamma at 10 KC. The feedback winding consists of about 700 turns, producing a feedback constant of 20 gamma per microampere.

The induced voltage waveform in the core, obtained by a pickup loop surrounding one leg, is shown in Fig. 6b (superimposed on waveforms of Fig. 6a). The induced voltage in the sense winding, for an essentially zero ambient magnetic field, is shown in Fig. 6c, for which each vertical division represents 0.2 volt, and each horizontal division represents 50 microseconds.

Because the primary concern of this paper is the stability of the sensor, no description of the electronics will be given; the system is essentially that described in Ref. 1.

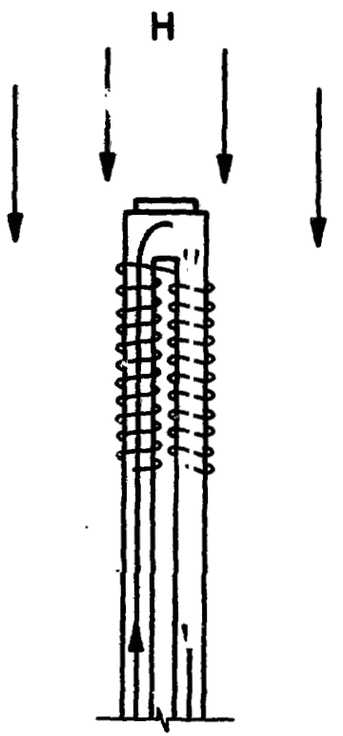


Fig. 1. Core and drive winding schematic

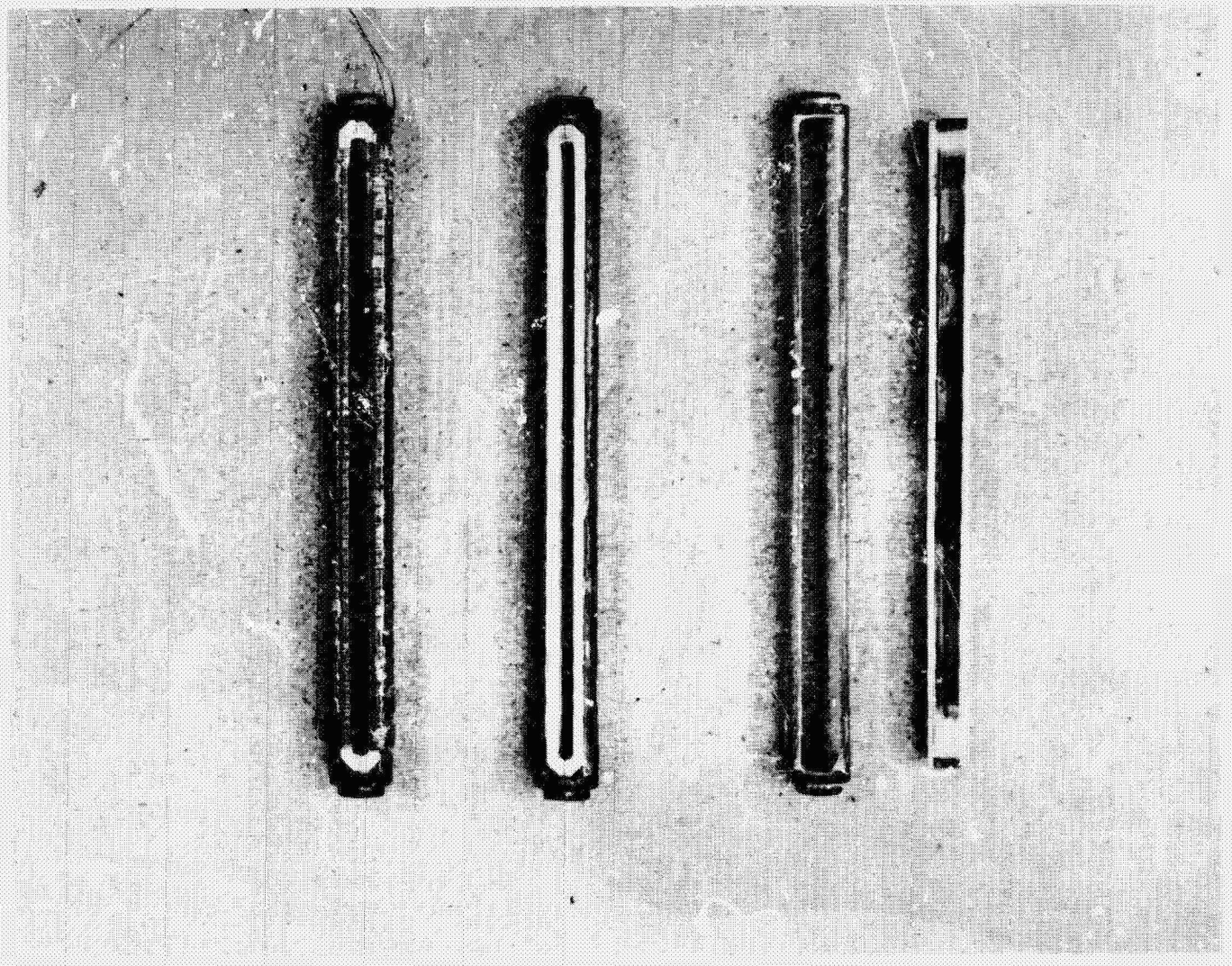


Fig. 2. Core assembly

Fig. 3. Sense winding

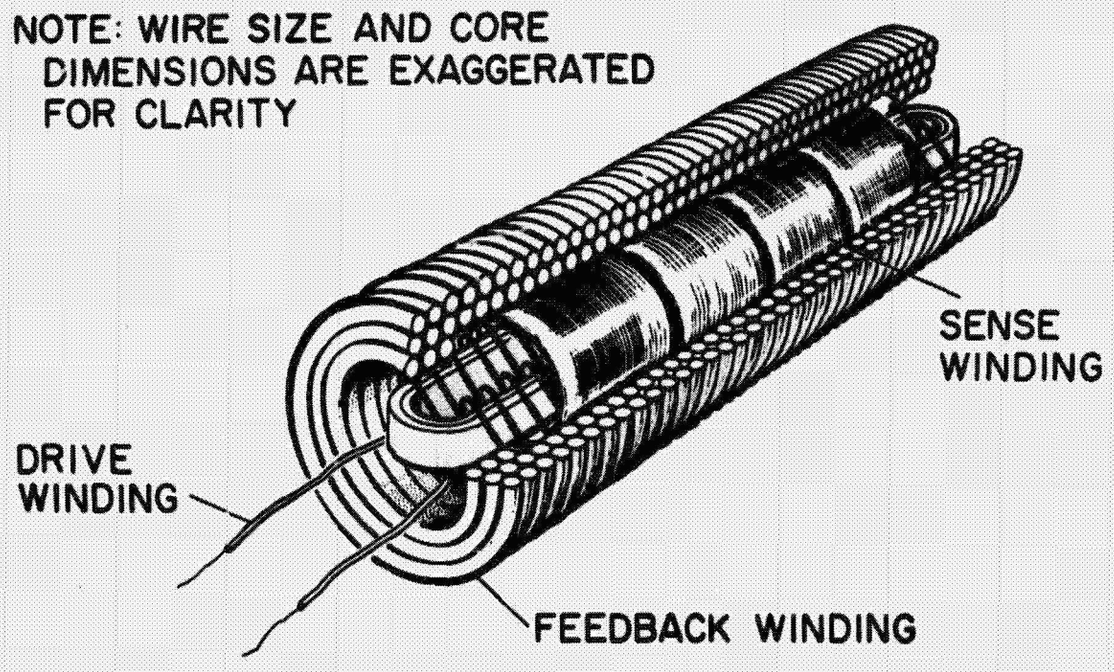


Fig. 4. Simplified view of Ames flux-gate sensor

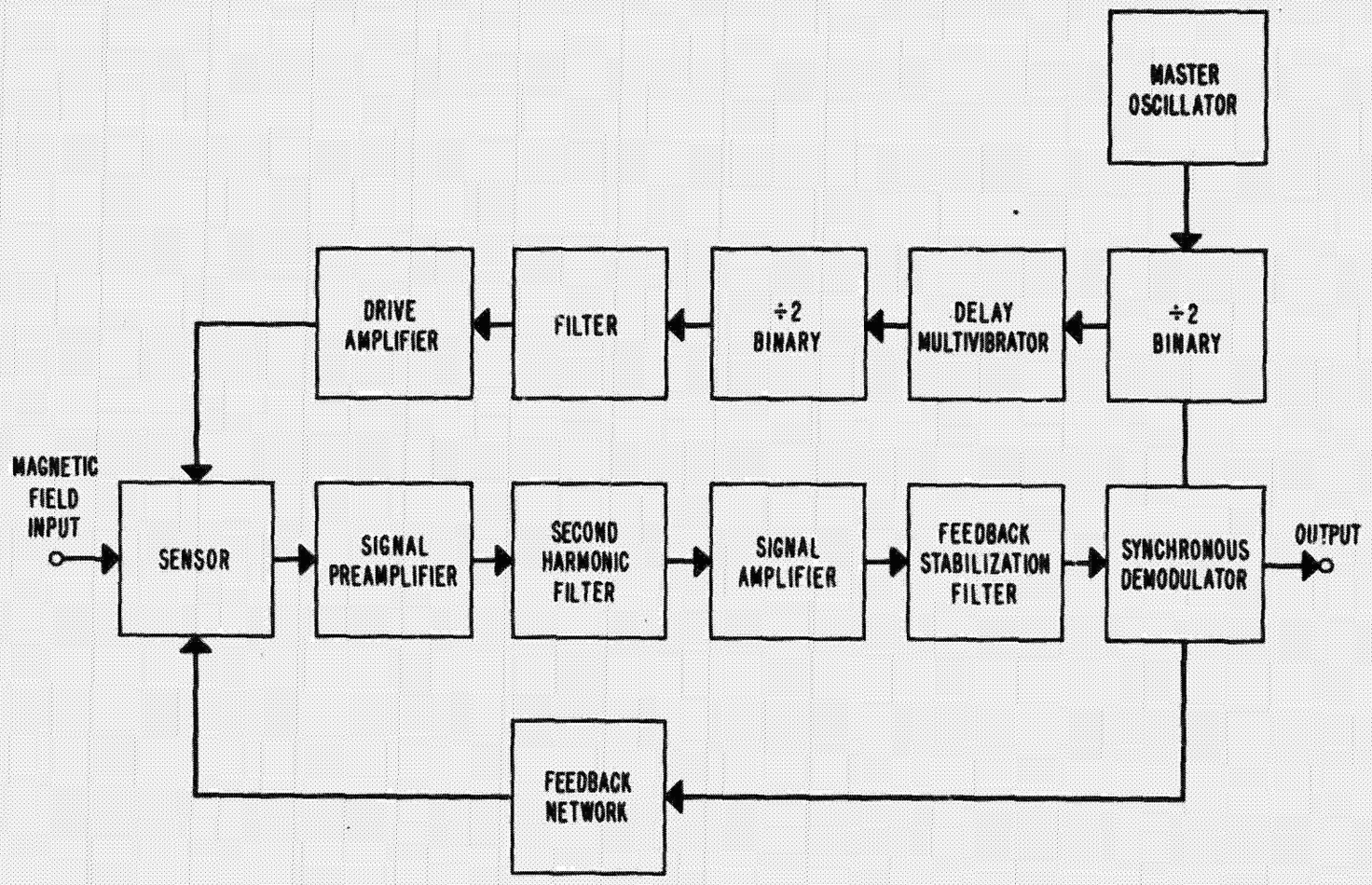


Fig. 5. Functional block diagram of the single axis sensor electronics sub-system

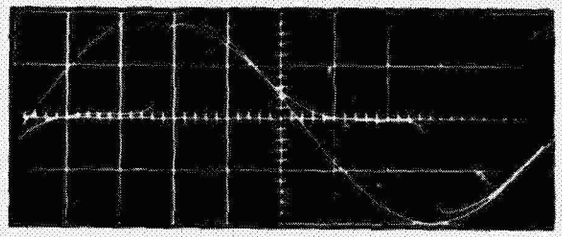


Fig. 6a. Exciting current waveform

1 vertical div. = 1 volt

1 vertical div. = 50 milliamps

1 horiz. div = 20 microsec

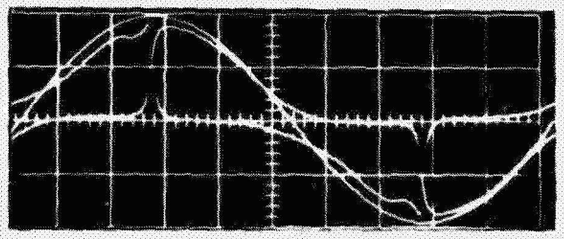


Fig. 6b. Induced voltage waveform in core

1 horiz. div. = 20 microsec

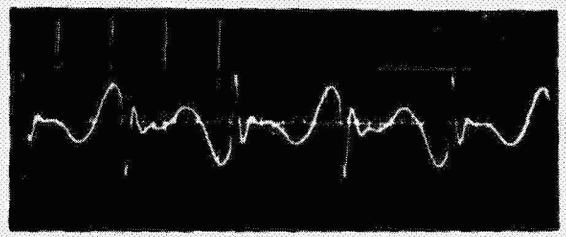


Fig. 6c. Sense winding voltage waveform

1 vertical div = 0.2 volt

1 horiz. div = 50 microsec

TABLE 1

SENSOR PERFORMANCE CHARACTERISTICS

Exciting winding voltage	4.0 volts sinusoidal, peak-to-peak, 5 KC
Exciting winding current	180 milliamperes peak-to-peak
Scale factor	Approximately 25 microvolts RMS per gamma at 10 KC
Scale factor change with drive level	Less than 20% change for 20% change in drive voltage
Feedback winding coil constant	20 gamma per microamp
Self-resonant frequency of sense winding	Greater than 150 KC
Sense winding voltage	Less than 0.3 volts peak-to-peak, with secondary winding cables attached.
Second harmonic feed-through	Less than 1 gamma equivalent when the drive contains 1 millivolt of second harmonic
Noise	Less than 0.3 gamma peak-to-peak in the frequency band from d-c to 10 cps, measured for 1 minute
Size	Approximately 2 inches long and 0.5 inch diameter
Weight	25 grams, less cable
Power	Approximately 40 milliwatts
Linearity	Within ± 1% of reading relative to offset level
Full scale	Plus or minus 100 gamma

DESCRIPTION OF FLUX-TANK

The low-field environment for operation of the sensors is provided by a "flux-tank", constructed by Marshall Laboratories, ML-186-1. A schematic drawing is given in Fig. 7, with labels to indicate the major components. The dimensions and materials of the four closed-end concentric cylindrical cans are given in Table 2; the outer can is made of steel for structural rigidity. The inner cans are made of high-permeability mu-metal for magnetic shielding; they are supported and spaced from each other by foam and epoxy plastic. Access to the interior is obtained by removal of the top cover, which is an assembly of four separate slip-over can lids.

TABLE 2

FLUX-TANK DIMENSIONS AND MATERIAL

Cylinder Number	Material	Thickness Inches	Height Inches	Diameter Inches
1	Mu-metal	0.050	26	8
2	Mu-metal	0.050	27-1/8	9-1/8
3	Mu-metal	0.050	32-7/8	14-7/8
4	Steel	0.090	34	16

A solenoid coil for calibration is mounted concentrically within the inner shield can. It is 24 inches long, 7 inches diameter, having approximately 360 turns; its coil constant is 0.35 microamperes per gamma. Precision-regulated current for the coil is supplied by the Marshall Laboratories control unit ML 109-2, in decade steps calibrated in gammas.

Temperature variation within the flux-tank is obtained by circulation of air through the interior. Heated or chilled air from an external source is pumped into the manifold extending to the bottom portion of the flux-tank; return air is drawn from the top part. The air temperature within the flux-tank is obtained by a mecury-in-glass thermometer, and also by measurement of the resistance of a thermistor suspended about 5 inches above the sensor. Resolution of temperature measurements is approximately 0.1° C.

Sensor cables and thermistor leads are brought out of the flux-tank through a slot at the top edge of the tank. The turntable control shaft (see below) and the air manifold pass through holes in the lid. The solenoid connections are built into the flux-tank through the bottom to an external connector.

The sensor being tested is clamped in a holder mounted on a turntable having its plane of rotation parallel to the axis of the flux-tank. When the sensor is vertical, its axis coincides with the flux-tank axis. The turntable is rotated by means of a 20:1 worm gear driven by a hand crank on a shaft extending through the lid assembly; one full turn of the crank rotates the sensor by 18 degrees. Indexing is provided by a turns-counting dial at the hand crank.

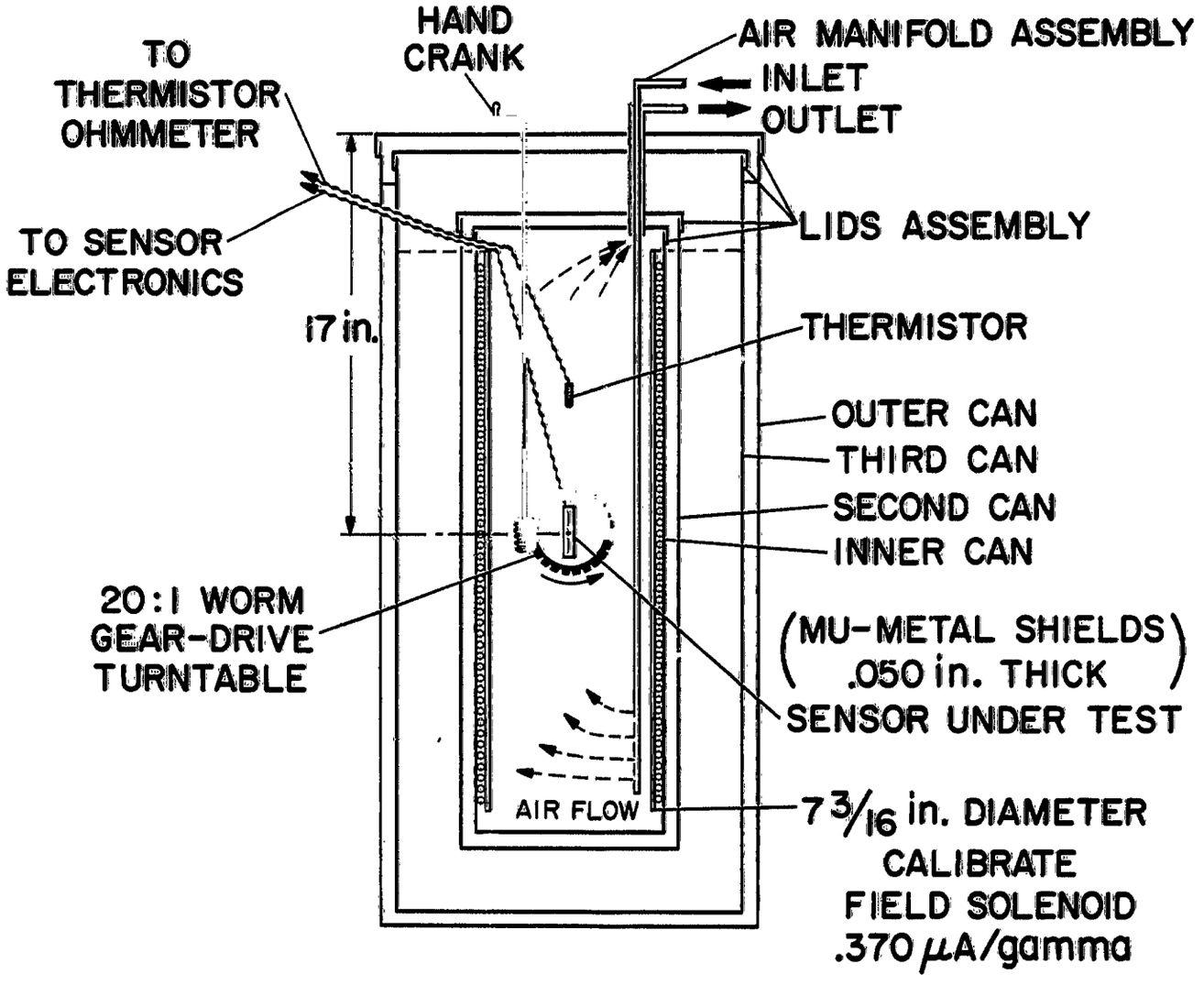


Fig. 7. Schematic drawing of flux-tank

At a time t_1, readings are taken at successive angular positions of the sensor axis spaced 18 degrees apart, for a full 360-degree circle, as indicated in Fig. 8. The total of 20 readings is taken in less than two minutes. Thus individual offsets are obtained for 10 axes, spaced 18 degrees apart, and the average of these 10 values represents the offset for the time t_1.

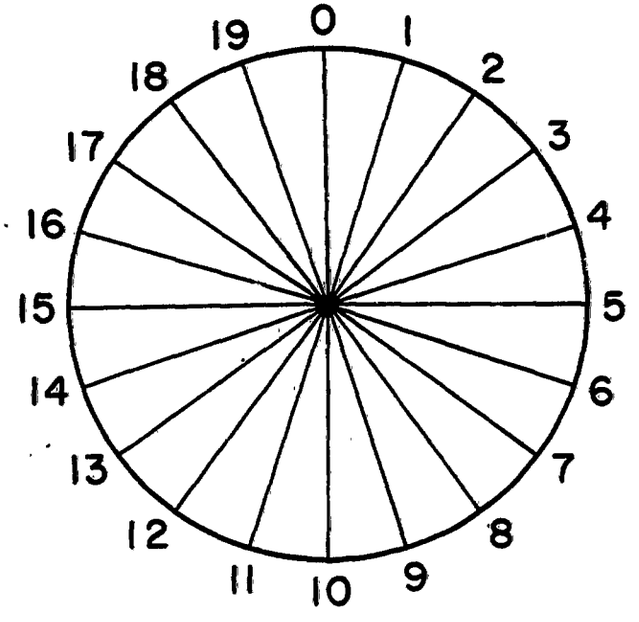
TESTS OF FLUX-TANK

Effects associated with the presence of the flux-tank which might alter the offset values were investigated. Basically these include the space and time variations of the magnetic field within the flux-tank, produced by either internal or external causes. For example, a magnetic field gradient within the tank could produce a pseudo-offset if the axis of rotation of the sensor did not coincide with its "magnetic center." As another example, if the residual magnetic field within the tank changed during the time required for taking data, the offset would be correspondingly changed. Another effect could be eddy currents in the walls, produced by the sensor magnetic fields, which depend on the angular position of the sensor axis, thereby yielding offsets that are dependent on the axis angle.

The residual magnetic field at the center of the flux-tank, with the lid clamped in place and a settling-down interval of about fifteen minutes, is less than 10 gammas, a typical value is 3 gammas. A magnetic field gradient at the same place is about 3 to 5 gammas per inch. These values do not vary by more than a few percent per hour during normal operating conditions. Of course, the sudden alteration in the location of external magnetic objects (such as the arrival or departure of a truck outside the laboratory) is noted by a few gamma change within the tank. Temperature changes of the tank affect the residual field: with the inside temperature at 0° C, the field at the center of the flux-tank is about 6 gammas, at +40° C it is about zero gammas.

Changes in the earth's magnetic field, or disturbances caused by external currents produce less than 0.1 gamma change inside the flux-tank. An exploratory test to evaluate such effects was performed by placing a solenoid coil (17 inches long and 11 inches in diameter) near the flux tank; it was energized so as to produce a one-gauss magnetic field at the surface of the flux-tank, thus simulating an approximate doubling of the earth's magnetic field. With the axis of the external coil perpendicular to the flux-tank axis at its mid-point, the offset of the sensor changed by 0.05 gamma. With the external coil coaxial with the flux-tank, the offset of the sensor changed by less than 0.05 gamma. The residual field within the flux-tank changed by less than 0.5 gamma for the perpendicular case, and by about 2 gamma for the coaxial case.

Eddy currents in the tank walls appear to have negligible effect on the offset. This was determined by measuring the offset of a sensor for test conditions as follow: a copper plate (4 inches by 5 inches by 1/8 inch thick) was held on a movable non-magnetic support at distances of 3



1. READINGS ARE TAKEN ON TEN AXES, EQUALLY SPACED.
2. AVERAGE OFF-SET IS PLOTTED.
3. READINGS ARE TAKEN EVERY 20 MINUTES.

Fig. 8. Axes for data

inches and 9 inches from the center of the sensor. Sensor offsets were taken for these two positions of the copper plate, and turned out to be identical. No change in the residual field was observed.

Rotation of the sensor about its "magnetic center" is determined by values of the offsets for the axes that are spaced 18 degrees apart. If the offset for the vertical axis is appreciably different from that for the horizontal axis, for example, this is an indication that the sensor is improperly centered in its holder. Tests were performed to evaluate effects of positioning errors by deliberately moving the sensor in its holder. Results are given in Table 3, which lists the offset values for the ten axes, for three positions of the sensor in its holder: a) the nominal position, b) sensor displaced + 1/4 inch, c) sensor displaced - 1/4 inch.

TABLE 3

EFFECT OF LOCATION OF SENSOR IN ITS HOLDER

Axis Angle	Offset in Gammas		
	Nominal Position	+1/4 inch	-1/4 inch
0 (vertical)	-0.90	-1.10	-0.15
18	-0.90	-0.85	-0.50
36	-0.90	-0.60	-1.00
54	-0.90	-0.25	-0.95
72	-0.90	-0.10	-1.60
90 (Horizontal)	-0.90	-0.25	-1.55
108	-0.85	-0.45	-1.20
126	-0.75	-0.70	-0.65
144	-0.75	-0.95	-0.20
162	-0.85	-1.05	-0.05
180 (Vertical)	-0.90	-1.10	-0.15
Average Value:	-0.86	-0.63	-0.78

It is clear from these data that the location of the sensor in its holder is important; however, averaging the offsets for the 10 angles tends to compensate for location errors. The sensor can be readily located in its holder to within 1/32 inch.

For the stability tests to be described later, the sensor was not moved in its holder, and so offset readings as a function of time were very little affected by misalignment factors. Of course the sensor was adjusted as closely as possible to the proper position, such that the offset values were independent of the angular position of the axis.

The time required for taking the data (twenty readings) was less than two minutes. During this interval the residual field and field gradient within the flux-tank changed a negligible amount.

It should be noted that the instrumentation provides a digital read-out. Noise in the system limits observation of the value of the magnetic field to about 0.1 gamma, although interpolation is possible to 0.05 gamma. The average of 10 observations is thus obtained with an approximate reliability of 0.01 gamma.

OFFSET DUE TO TAPE STRESS

A brief investigation of the effect of tape stress on the value of the offset was made. A sensor was constructed on a ceramic core which was deliberately parted in the middle, so that the tape could be stretched by a cord attached to one part of the ceramic core, the other part being anchored. The sensor was mounted in a fixed position in the flux tank, with the cover in place. A nylon cord passed through a hole in the cover, over a pulley, to a pan, which could be loaded with suitable weights. The sensor could not be rotated through 180 degrees, of course. The variation in the indicated sensor reading as the pan weight load was modified is interpreted as the variation in the sensor offset. The temperature was approximately constant. The results are given in Fig. 9. This shows a definite relation between the offset and the strain, although there is no simple proportionality. As an order-of-magnitude relation, the offset was approximately 4 gamma for a tension of 10,000 pounds per square inch on the magnetic tape. The result is not surprising, because magneto-strictive effects of magnetic materials are well known.

These results suggest that changes of temperature, producing stresses in the tape because of differential expansion or contraction, can produce variations in the offset of a sensor.

OFFSET DUE TO CIRCUIT VARIABLES

For the laboratory investigation of the offset, various modifications of the electronics circuit from the flight configuration were necessary, such as insertion of meters and oscilloscopes, connection boxes, etc. These modifications in general produced an increase in the offset of a given sensor, typically about 1/2 to 1 gamma. Even switching instrument scale-ranges introduced (in a special case) as much as several gamma offset.

In order to minimize offset effects of the instrumentation, a "standard" set of circuit elements was selected. All of the circuits remained energized continuously during the tests. A storage battery was employed to avoid line supply problems.

STABILITY MEASUREMENTS

With various preliminary investigations completed, the main problem was addressed: for a given sensor in a flux-tank, and a given set of electronics, how constant are the readings with time?

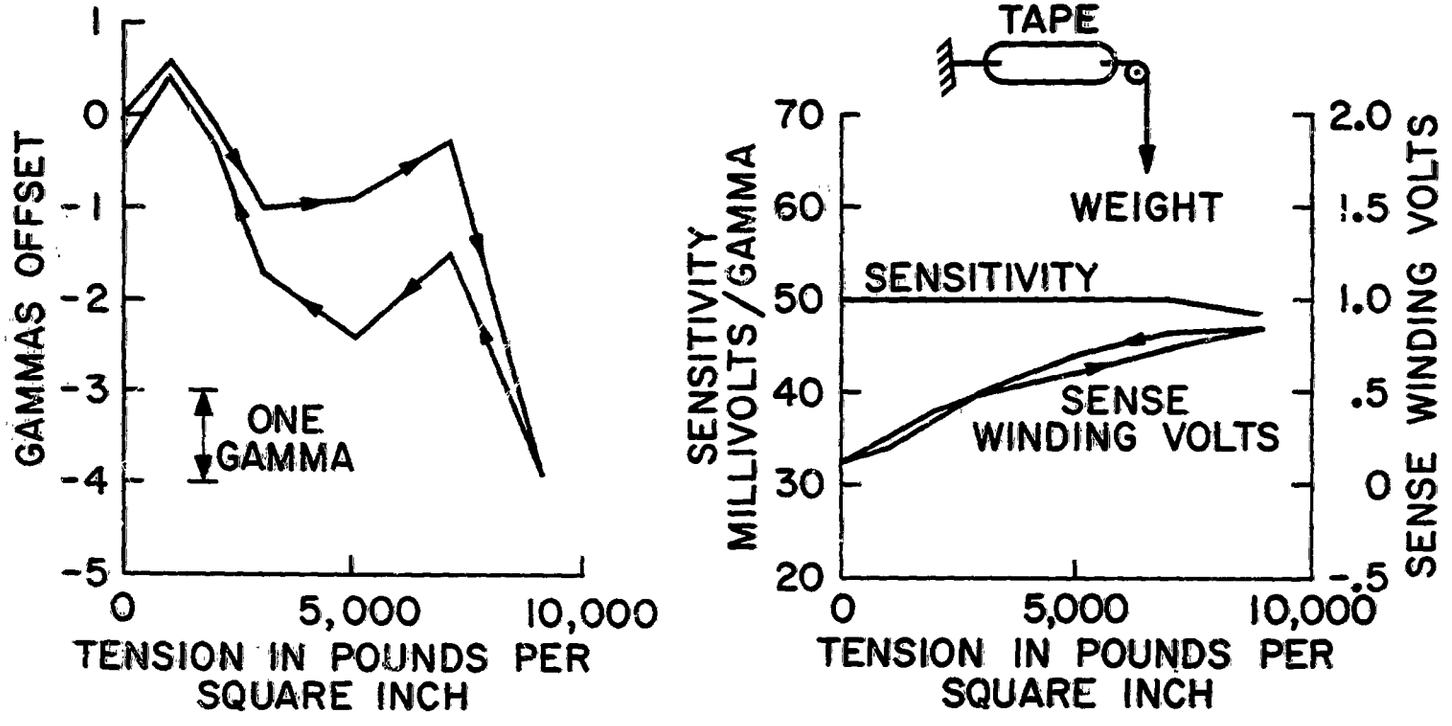


Fig. 9. Strain test of sensor

As described previously, at time t_1 readings were taken every 18 degrees, for a full 360-degree circle; the total of 20 readings was taken in less than two minutes. Individual offsets were thus obtained for 10 axes, spaced 18 degrees apart, and the average of these 10 values represented the offset for time t_1.

At time t_2, similar readings were taken by the same individual, and so on, for times t_3, t_4, etc. The time interval between readings ranged from 12 minutes to 20 minutes, depending on how rapidly the offsets changed.

For each offset, the temperatures were measured in the flux-tank, in the room, and in the vicinity of the electronics package.

The duration of the time vs. offset runs extended to as much as three weeks for some sensors. At no time during the runs was the power turned off, or modifications made to the setup.

One effect became evident quite early: the offset readings were fairly stable in the morning, but showed "spikes" about 0.5 gamma high, extending over several hours, in the afternoon. Several alternative explanations were considered for this effect, such as an increase in vehicular traffic in the afternoon, or currents, or power problems, etc. None of these was adequate or consistent. Temperature variation was considered as a possibility, but because the increase in temperature in the flux-tank was only a few degrees during the afternoon, this did not seem sufficient to cause differential-expansion strains (and magnetostriction effects). There was a reluctance to heat the flux-tank deliberately, because of the possibility of thus introducing a major variable.

An example of the time vs. offset values is given in Fig. 10; the temperature within the flux-tank is also plotted, showing an essentially constant temperature (within 0.2 degree) in the morning, followed by a one-degree increase in the afternoon. The offset is seen to increase from 0.1 gamma in the morning to 0.6 gamma in the afternoon.

For the same sensor (E5) and electronics configuration, and with no changes in the experimental conditions, another time vs. offset graph is shown in Fig. 11. This shows an offset between 0.4 and 0.5 gamma. The temperature within the flux-tank was essentially constant during the entire day, as closely as could be read (0.1 degree); such a constant temperature was fortuitous.

The decision was then made to heat the flux-tank by the air line, with an air flow pattern that would avoid direct heating of the sensor. There were no other changes in the test arrangement.

The effect of a temperature change for the test sensor (E5) is shown in Fig. 12. The temperature was quite constant in the morning, during which time the offset was essentially constant at 0.7 gamma following which the afternoon temperature rise produced an increase in the offset to about 1.1 gamma. The next day the offset was back to 0.7 gamma in the

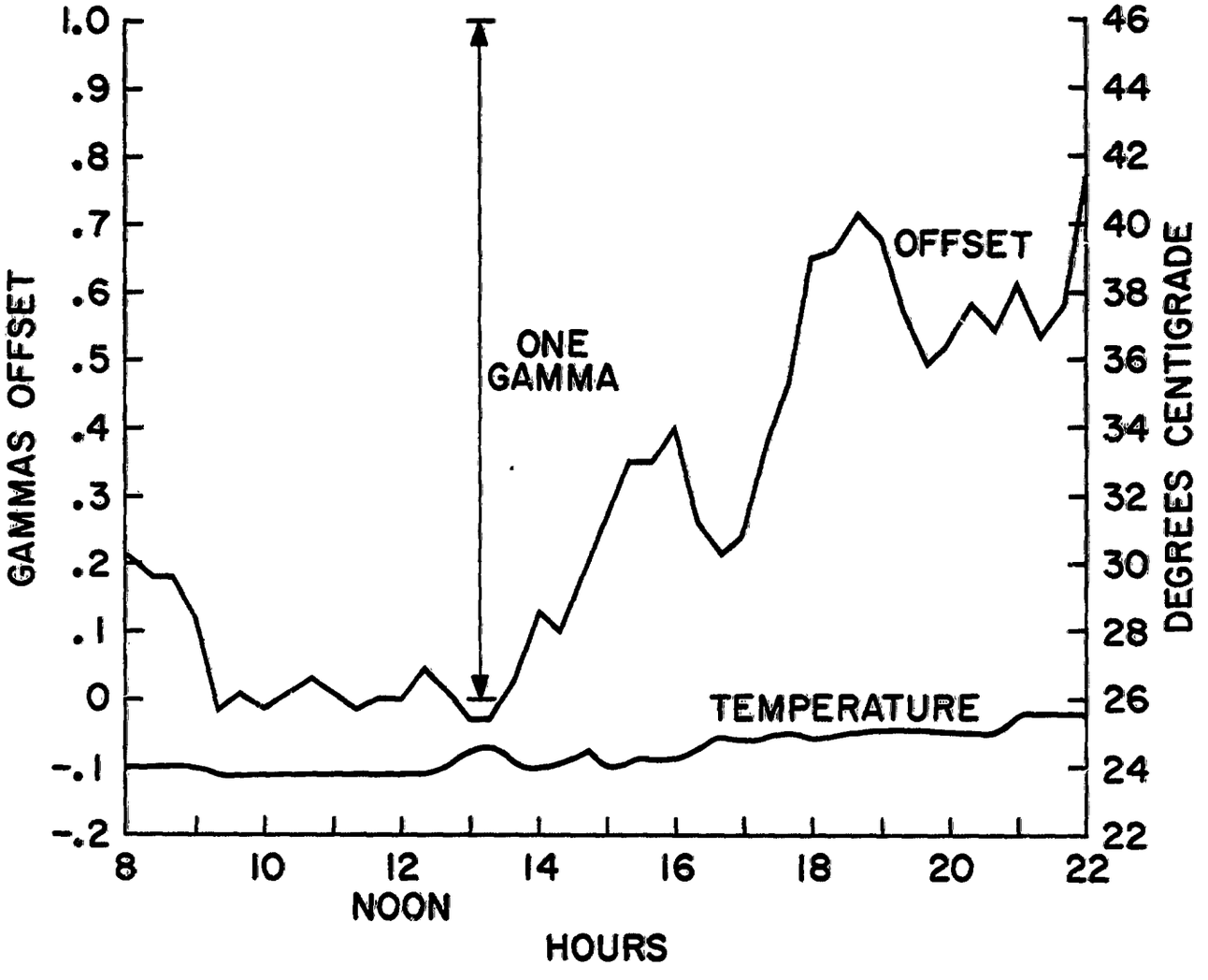


Fig. 10. Stability test, E5

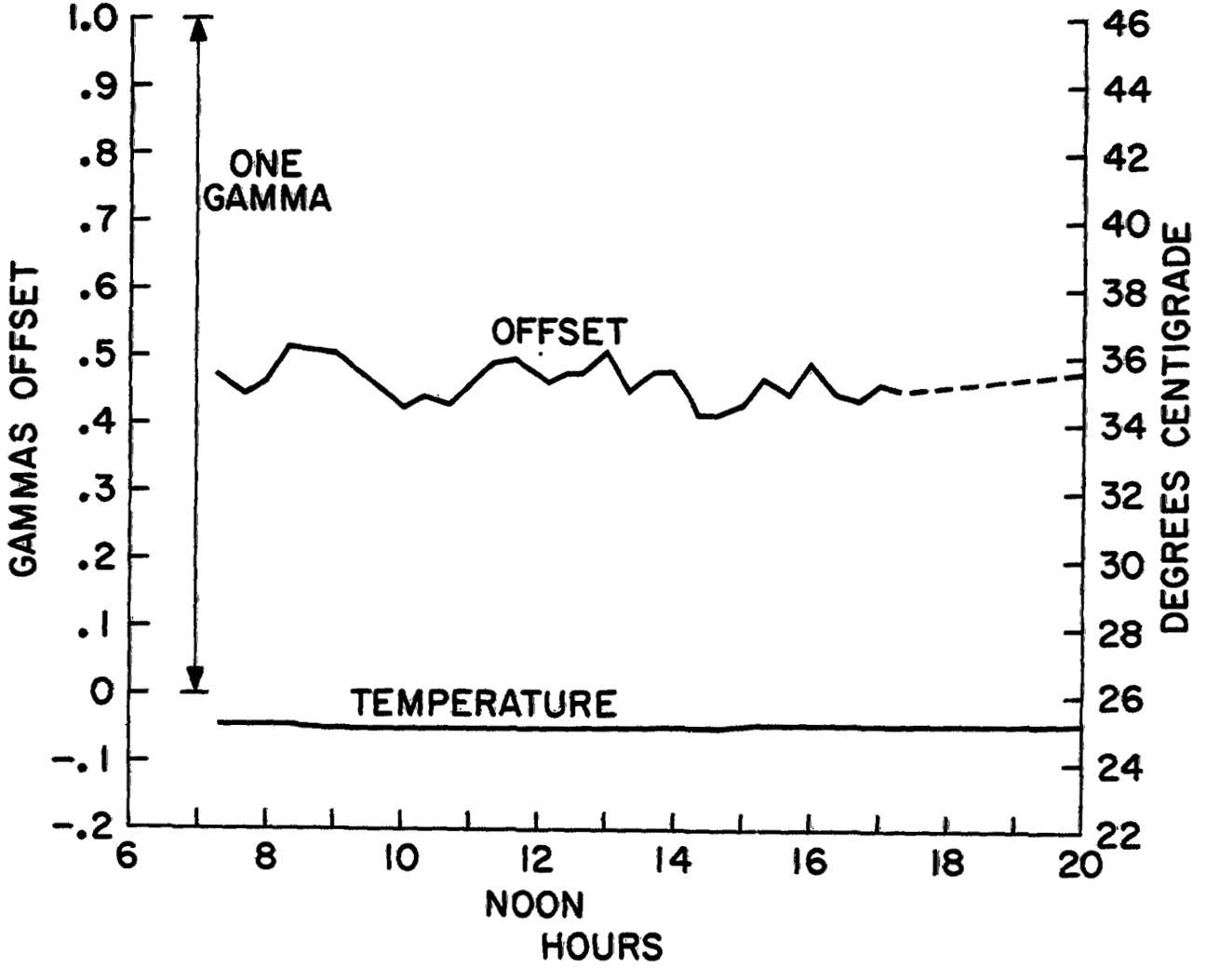


Fig. 11. Stability test, E5

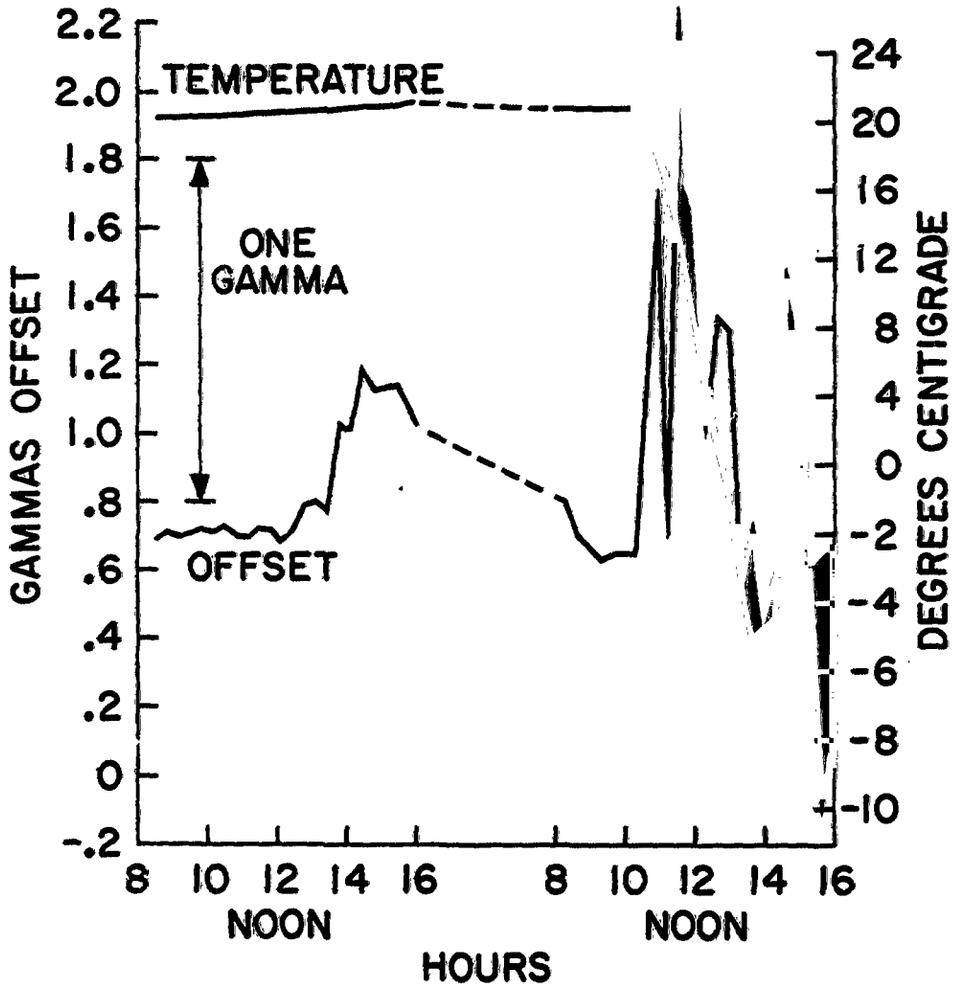


Fig. 12. Stability test, E5

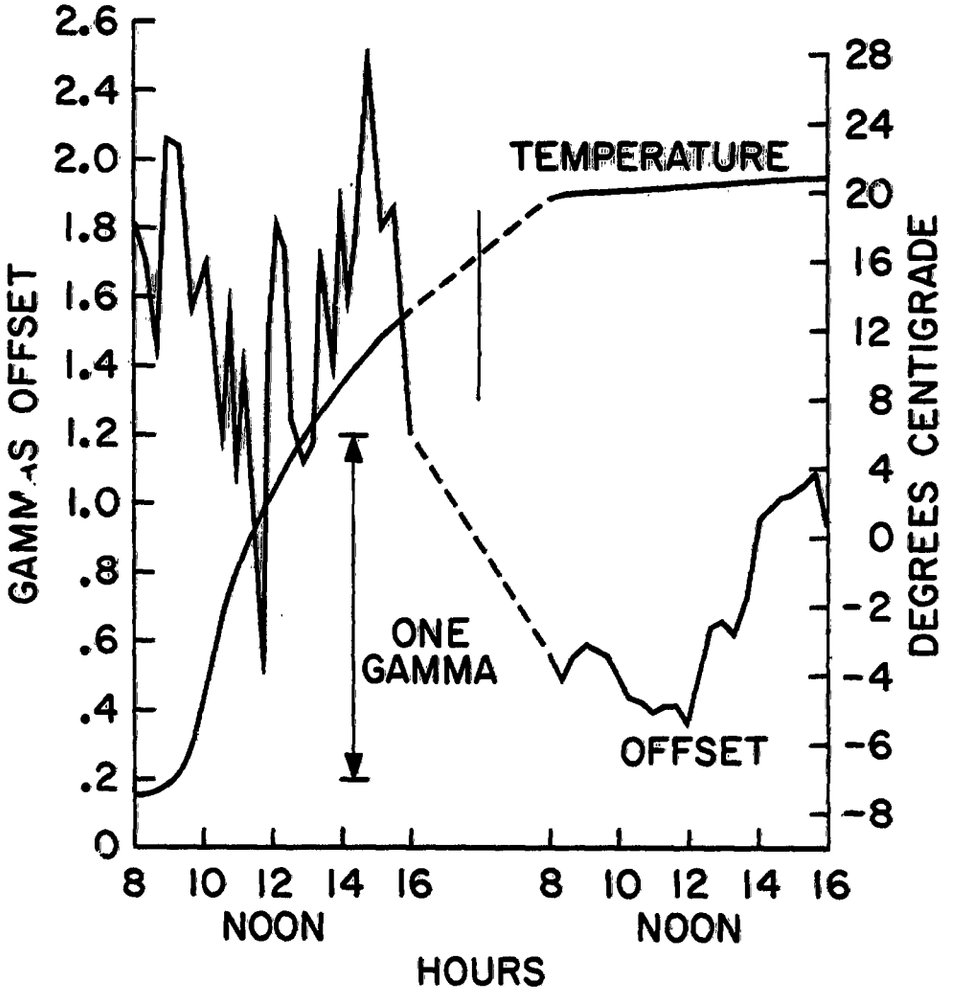


Fig. 13. Stability test, E5

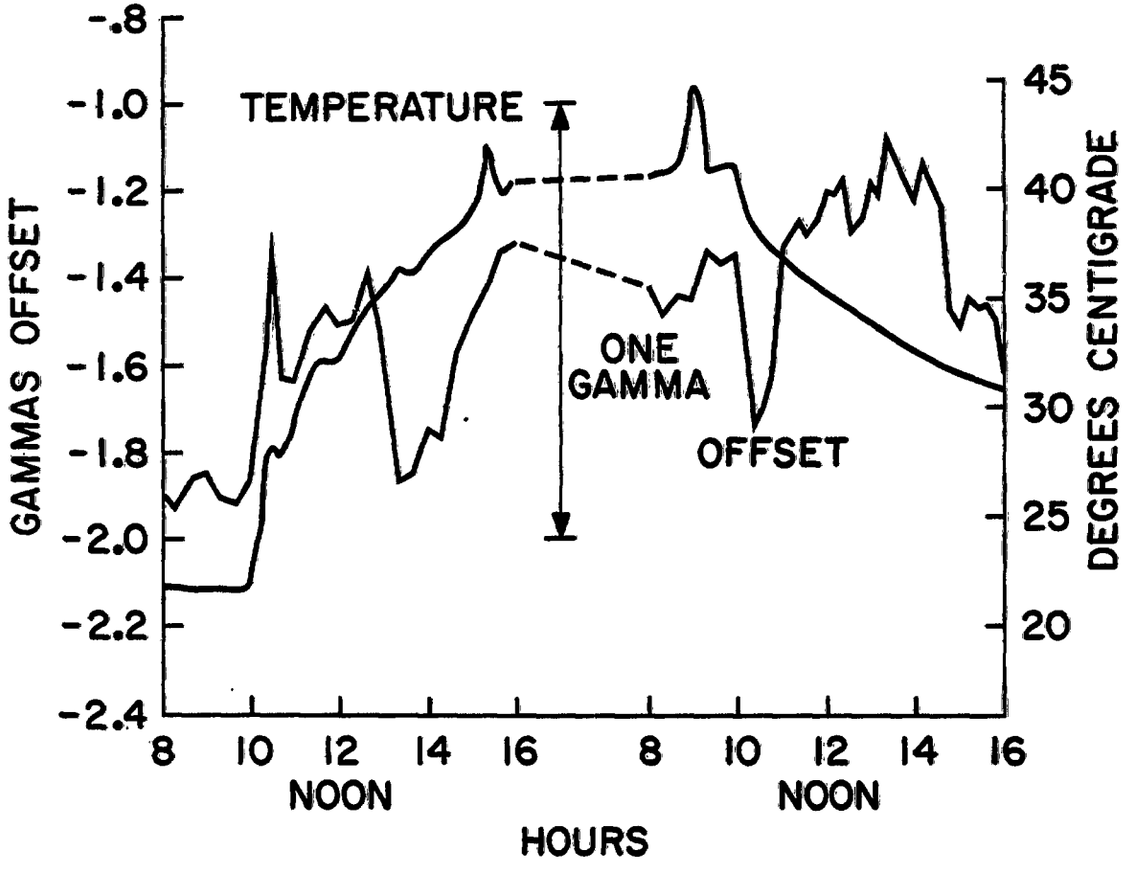


Fig. 14. Stability test, E7

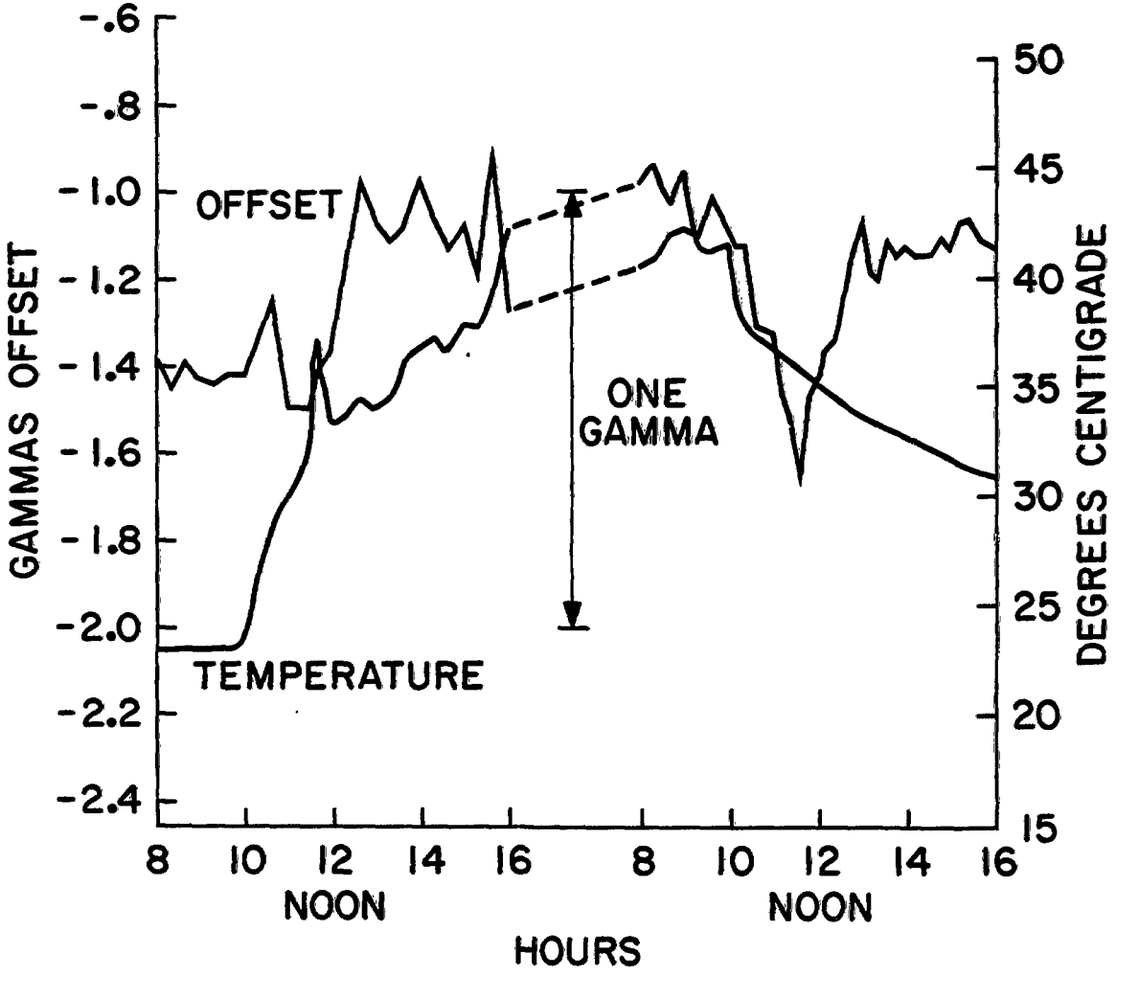


Fig. 15. Stability test, 10B

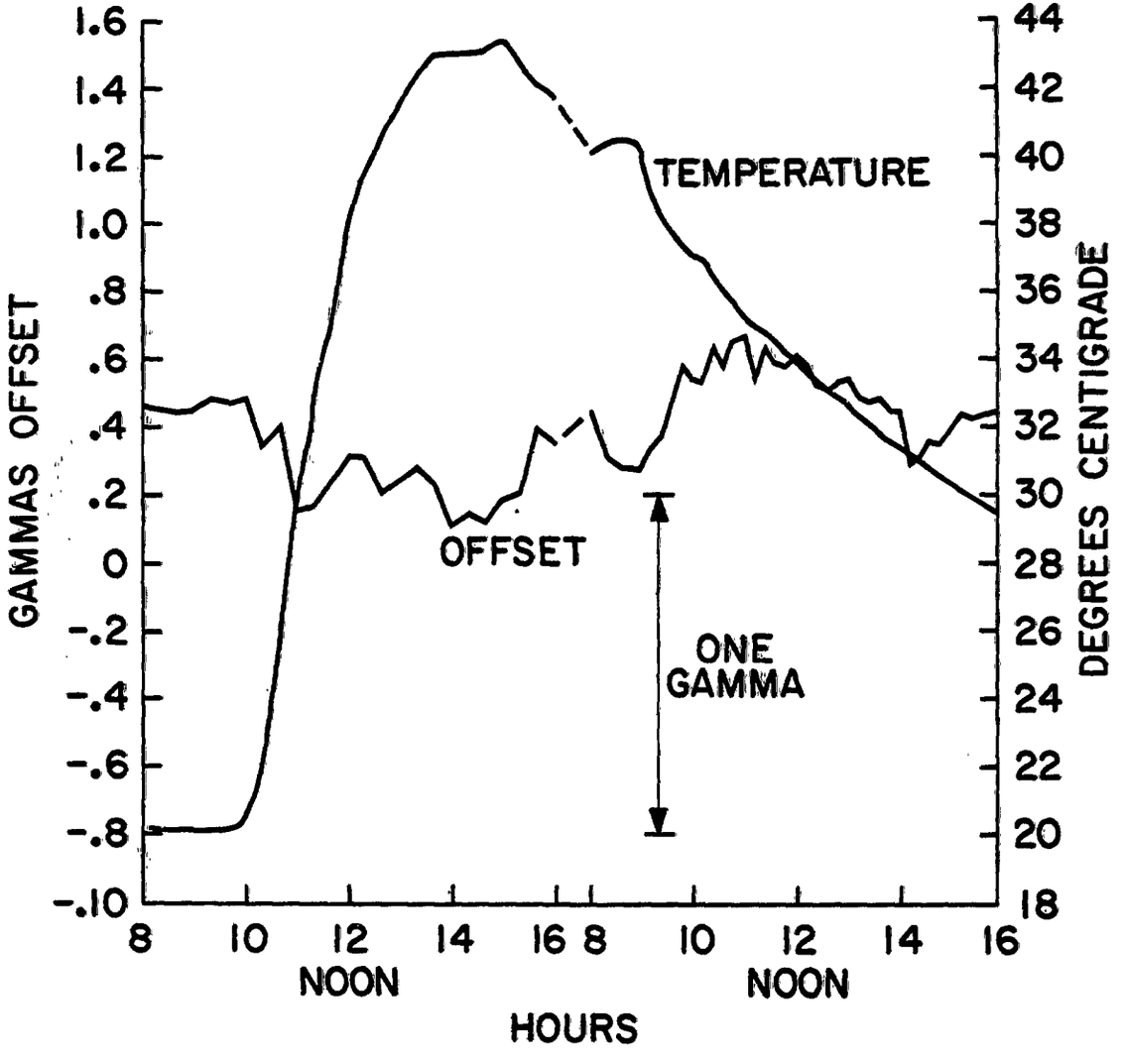


Fig. 16. Stability test, 12

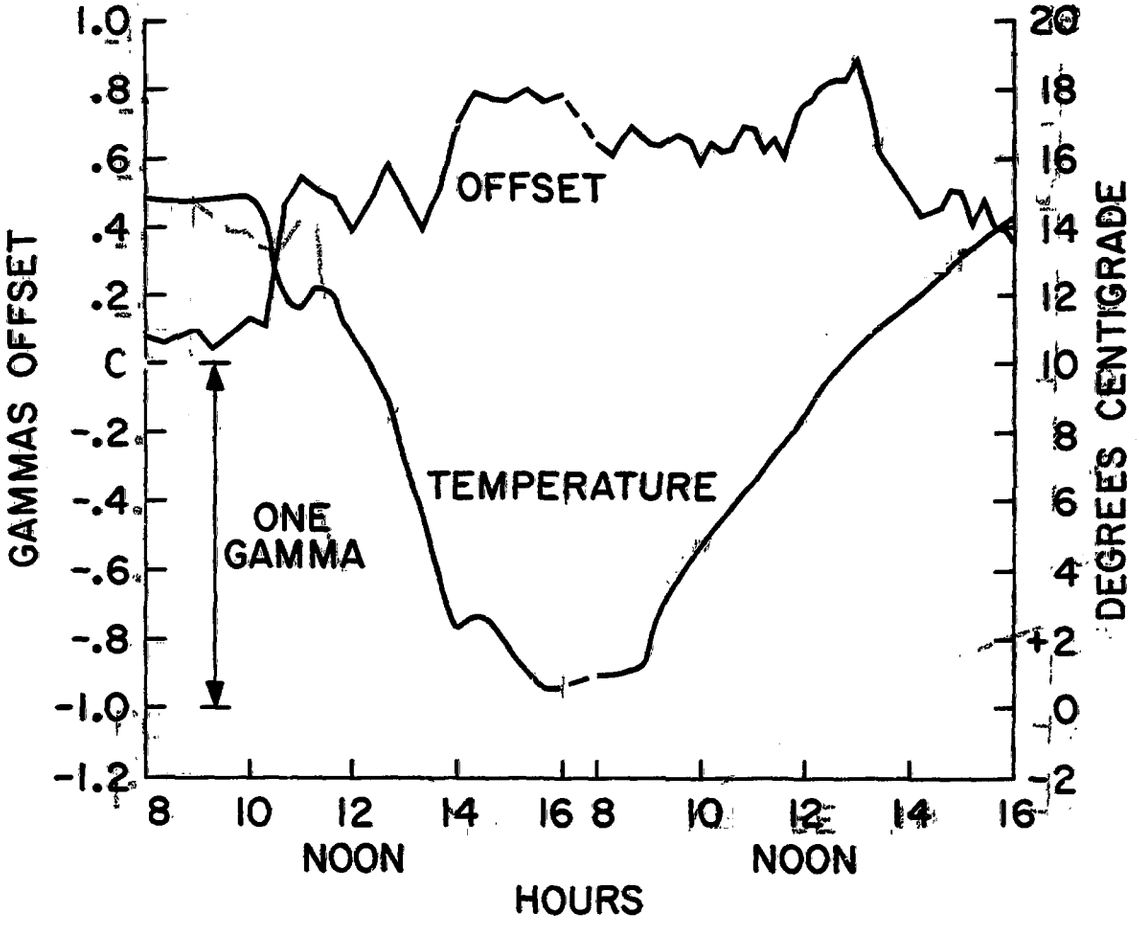


Fig. 17. Stability test, 12

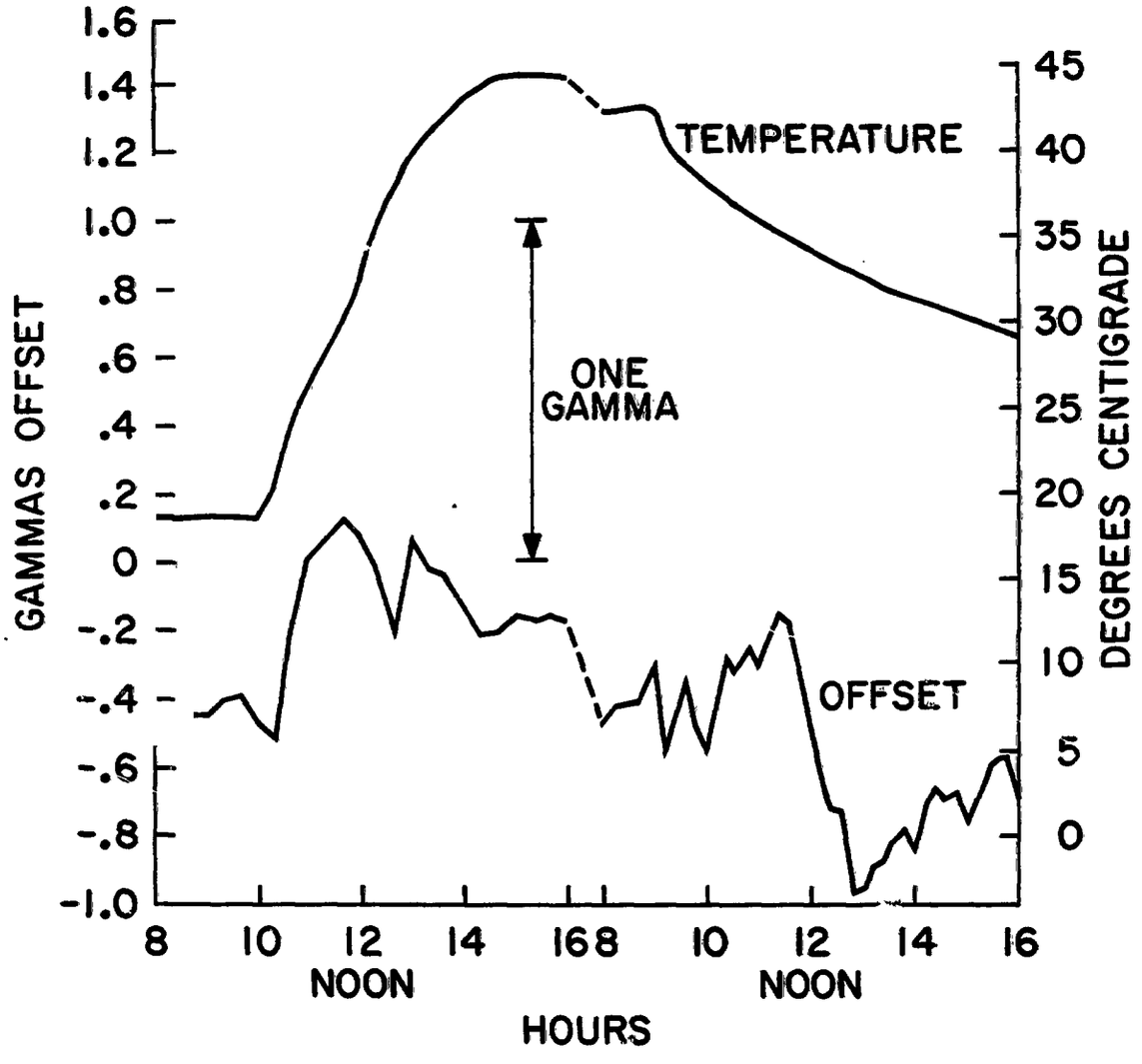


Fig. 18. Stability test, LSM-C6

morning. As soon as the temperature was deliberately changed, in this case by cooling the tank air, the time vs. offset curve showed jagged spikes. The spikes were both positive and negative, while the temperature was changing in only one direction (from 20° C to -4° C). As Fig. 12 shows, the spikes in this case were about 1 gamma in amplitude, during time intervals of about 1 hour.

The effect of a temperature increase is shown in Fig. 13. The same sensor (E5) in the same configuration was employed as for the preceding tests. The temperature increased from -7° C to room temperature (about 21° C) by room heat being conducted through the tank walls, that is, there was no possibility of temperature reversals. Despite the smooth increase in temperature, the sensor displayed offsets that followed no particular pattern. The time vs. offset curve had jagged spikes nearly a gamma in amplitude, ranging from 0.6 gamma to nearly 2.6 gamma.

Fig. 13 shows that when the temperature change became more gradual, the spikes disappeared. However, the offset showed a variation from 0.4 gamma in the morning to about 1.0 gamma in the afternoon, while the temperature increased by about one degree C.

Other sensors displayed much the same characteristics. Fig. 14 shows that for sensor E7, a temperature change from 22° C to 40° C and back to room temperature produced an offset variation from -1.9 gamma to -1.2 gamma, including somewhat jagged spikes in the time vs. offset curve.

Confirmation that the offset is produced by the sensor was obtained by heating of the electronics (using an infrared heat lamp). With the flux-tank maintained at room temperature there was no measurable change in offset. The conclusion seems justified that the "spikes" in offset are caused primarily by sensor temperature changes.

Various experimental sensors were constructed with the goal of minimizing temperature-produced magnetostrictive or related effects. Some sensors were constructed with "cushions" of elastic material at one or both ends. Other sensors had teflon coating between layers of the permalloy tape to prevent possible binding. A sensor was constructed with a beryllium core instead of the ceramic bobbin, so as to match the coefficient of expansion of the tape. These procedures reduced the offset variations caused by temperature to some extent, but did not eliminate them entirely. Representative results are shown in Fig. 15 for experimental sensor 10B (heating above room temperature, followed by cooling). The variations in offset with time are less violent than for the previous sensors; however, variations of about one-half gamma during several hours occurred.

For another experimental sensor, Figs. 16 and 17 show the variation of offset with time for the respective situations of a) heating above room temperature followed by cooling, and b) cooling below room temperature followed by heating.

In Fig. 18, offset vs. time curves are given for a sensor which was constructed with great care, by experienced personnel. An offset drift of nearly one gamma was observed in the heating environment.

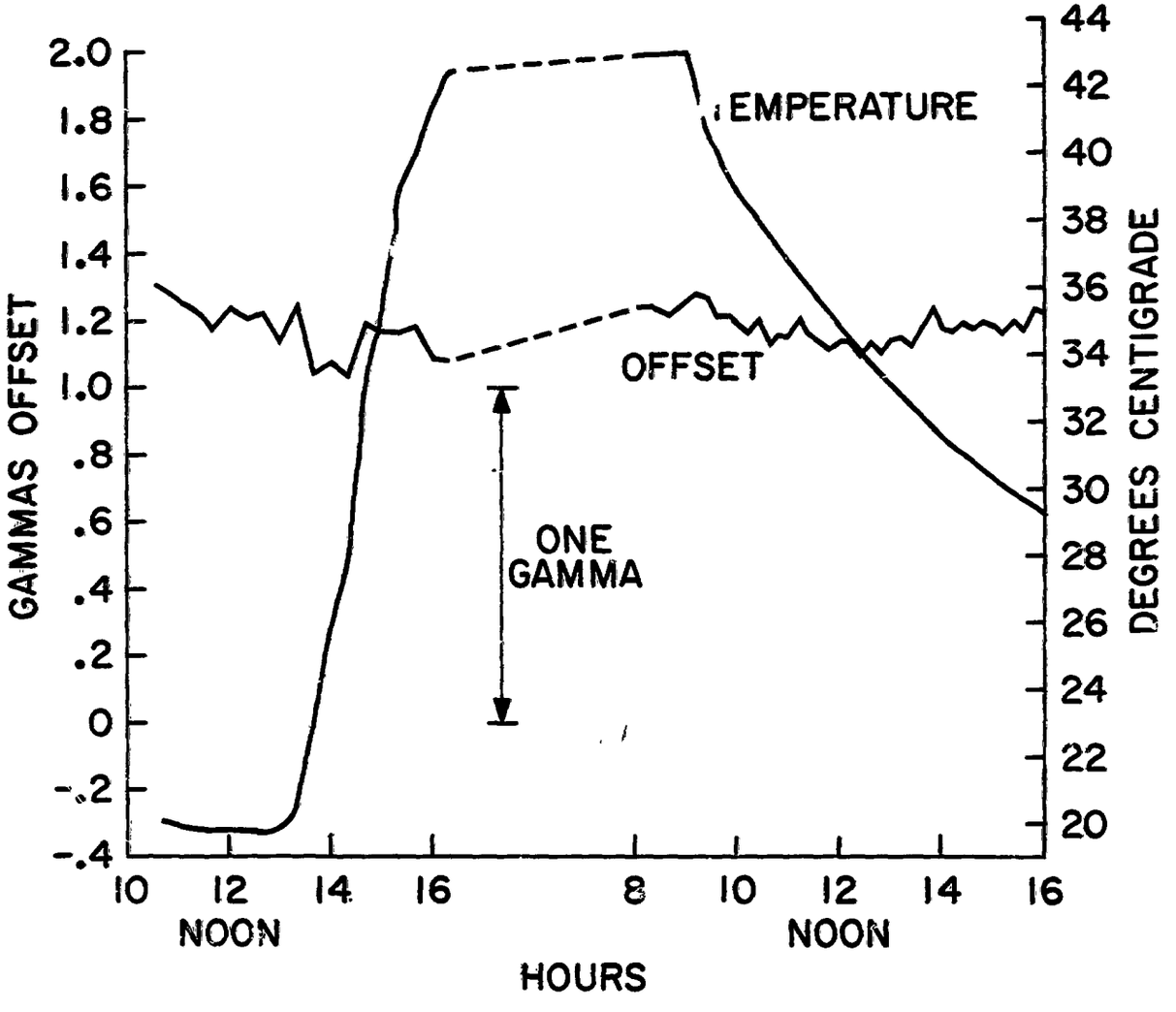


Fig. 19. Stability test, ring core

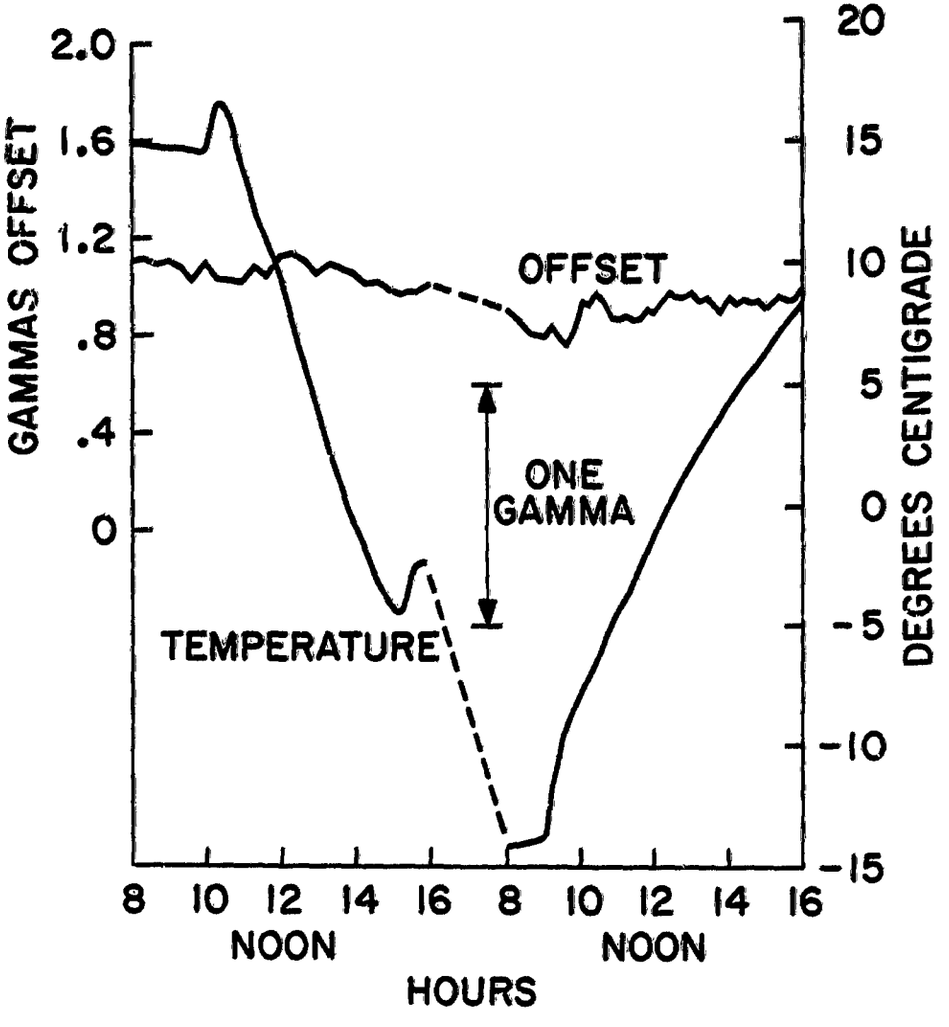


Fig. 20. Stability test, ring core

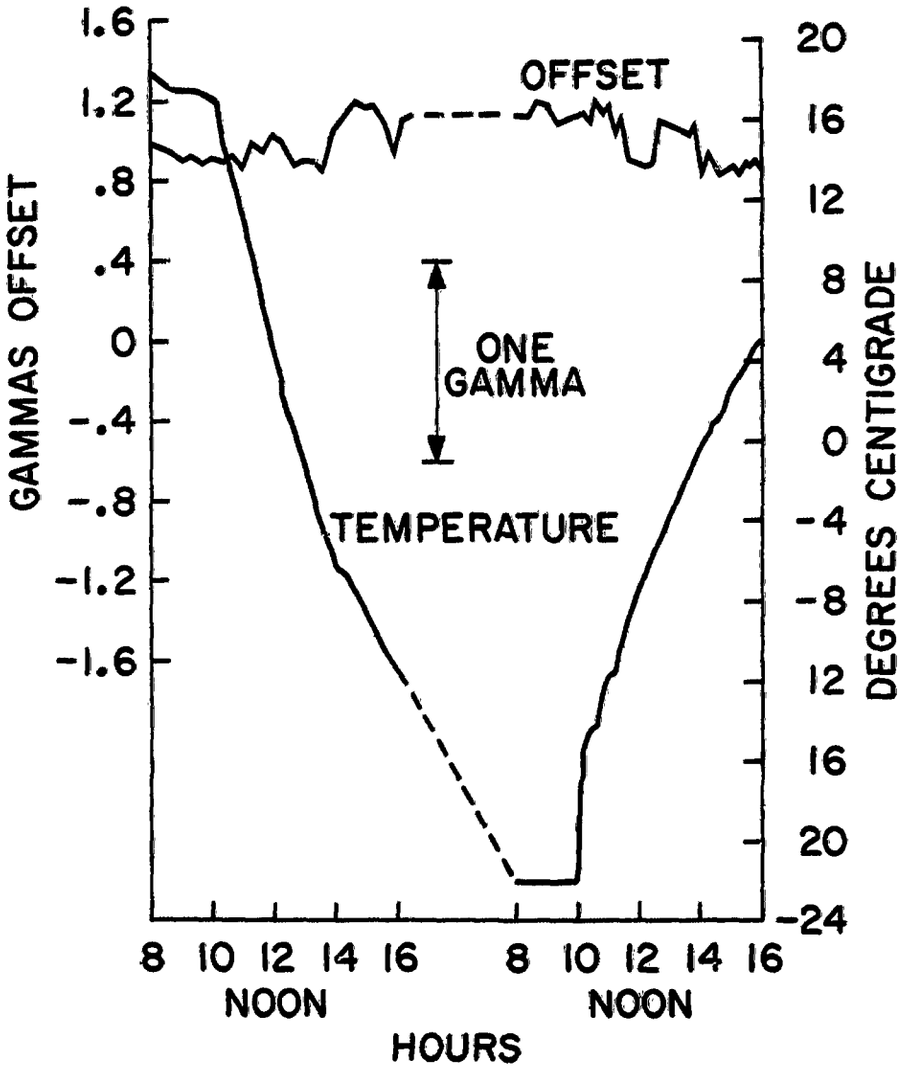


Fig. 21. Stability test, ring core

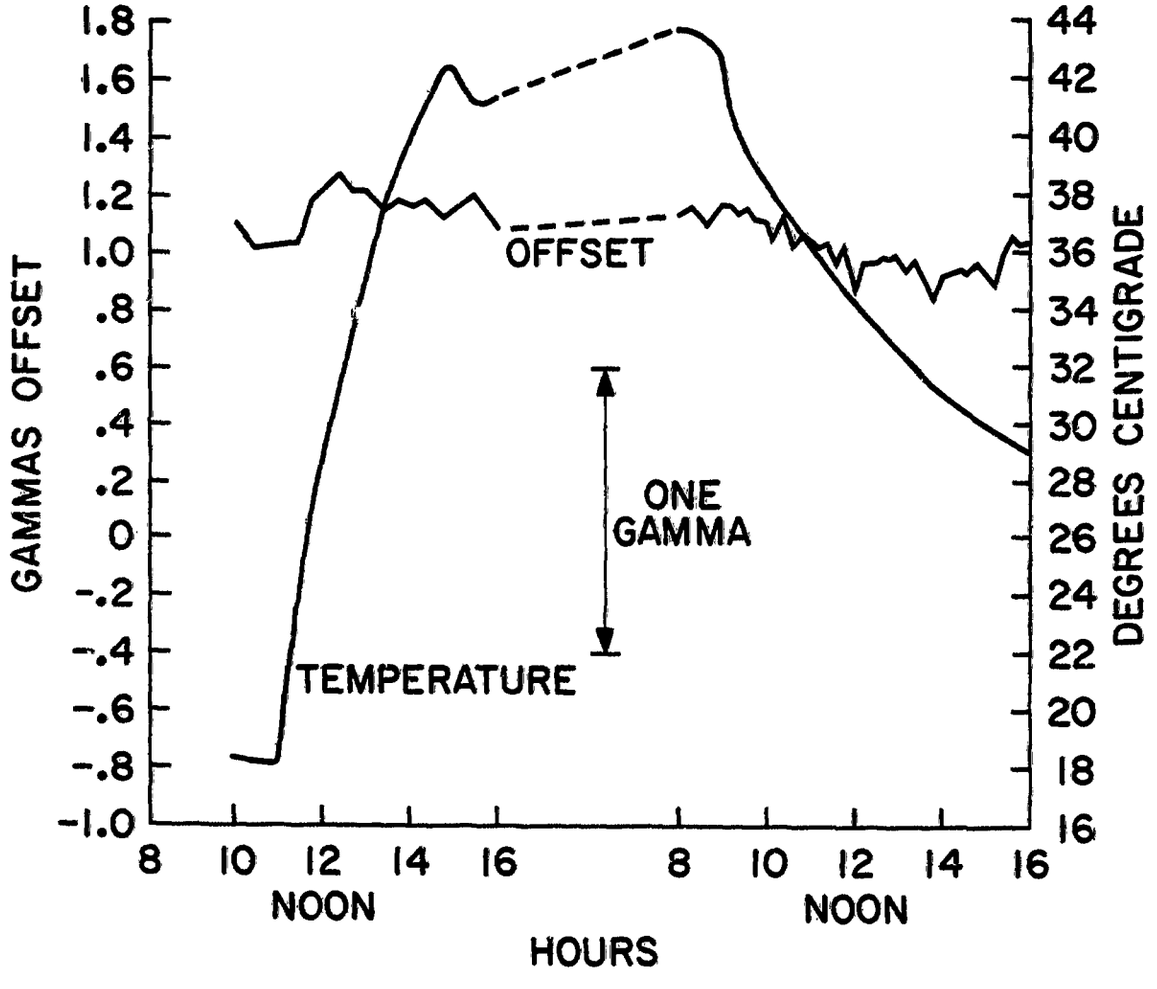


Fig. 22. Stability test, ring core

The data obtained so far suggest that the "race-track" sensor configuration may have basic difficulties associated with its construction. This point of view is supported by tests of a "ring-core" sensor constructed by Mr. Dan Gordon and his associates at the Naval Ordnance Laboratory (2). No description of the ring-core sensor will be given here because it is described in another paper being presented at this Symposium by Mr. Gordon. The offset vs. time curves for a ring-core sensor are given in Figs. 19 and 20 for the respective situations of a) heating above room temperature followed by cooling, and b) cooling below room temperature followed by heating. Results of repetitions of these same tests to check reproducibility are given in Figs. 21 and 22. It will be noted that the excursions in offset with time caused by the temperature changes are considerably smaller than with the "race-track" sensors.

PROSPECT FOR THE FUTURE

In order to obtain a magnetometer system whose precision and reliability is 0.1 gamma or better, the conclusion from the present investigation is that multi-unit sensor assemblies should be designed and operated in combinations as follow:

a. Two or more sensors operating in rapid sequence from the same electronics. Because offset drifts for one sensor are independent of those for the other, whereas external signals are correlated in time, the occurrence of offset drifts can be identified. Thus, the ambient magnetic field can be measured to within the noise of the system, or about 0.1 gamma.

b. Two or more sensors operating simultaneously, in opposition, to yield the magnetic field gradient. Such measurements are a sensitive method of measurement for local magnetic field sources, such as spacecraft current loops. For special situations, this type of information would yield a first approximation to Curl B.

c. For arrays having three, four, or more vertexes, with three-axis sensor units at each vertex, combinations of electronics can yield simultaneous individual values, sums, differences, products, etc., thus providing information regarding sensor drifts, magnetic field gradients, Curl B, energy density, and related quantities.

REFERENCES

(1) "An Improved Magnetometer for Deep Space Use," by William J. Kerwin, Robert M. Munoz, and M. John Prucha, IEEE/AIAA National Aerospace Electronics Conference, Dayton, Ohio, 1964.

(2) "A Highly Stable Fluxgate Magnetometer for Space Exploration," by D. I. Gordon, R. H. Lundsten, R. Chiarodo, and H. H. Helms. Paper to be presented at this Symposium.

APPENDIX - POSSIBLE FACTORS INVOLVED IN OFFSET

For convenient reference, the following is a list of manufacturing or operating parameters which in principle can cause offsets in the range of a fraction of a gamma or more.

A. Variations in manufacture of sensors

1. Different techniques by different workers
2. Different sources of supply of components

B. Manufacturing tolerances

1. Non-symmetry in tape and location on bobbin halves
2. Non-symmetry in number of turns and location on bobbin halves
3. Non-symmetry in location of drive and sense windings
4. Variations in tape winding tension
5. Variations in potting procedures
6. Variations in potting compound

C. Magnetic tape history

1. Composition
2. Manufacturing and annealing
3. Handling, bending, and cutting stresses
4. Exposure to magnetic fields

D. Sensor history

1. Shock and vibration
2. Exposure to magnetic fields
3. Exposure to temperature excursions
4. Annealing steps, if any

E. Impurities

1. Polishing of ceramic on wire brush
2. Iron dust within or on sensor

3. File or screwdriver deposits

4. Impurities in potting compound

F. Temperature (sensor and/or electronics)

G. Temperature rate of change (sensor and/or electronics)

H. Temperature gradients (sensor and/or electronics)

I. Strains within sensor due to temperature coefficient of expansion

J. Strains within sensor due to mounting or handling

K. Humidity (sensor and/or electronics)

L. Effect of ends of sensor (remanent field effects)

M. Electronic factors

1. Second harmonic in sensor drive feeding through to sense winding

2. Second harmonic generated at "front end" of amplification chain, due to non-linearity of response; i.e., large-signal effect of spikes in the sense winding voltage

3. Interaction between feedback winding and sense winding

4. Eddy currents due to unexpected loops, producing timing asymmetry effects

5. Effect of drive level

N. Flux-tank problems and effects

1. Magnetic field gradients; axis of rotation of sensor not coinciding with its magnetic center

2. Effect of removing and replacing cover, altering gradients

3. Variable location of sensor in tank on successive tests

4. Effect of angular position of sensor in tank

5. Effect of walls of tank

a. Eddy currents

b. Sources of remanent magnetism

c. Time variation of remanent magnetism

6. Temperature effects on tank remanent magnetism

7. Earth field fluctuations

8. Power line and earth current magnetic field variations

9. Iron object motions near flux-tank (trucks outside, etc.)

0. Circuit variables

1. Power supply voltage fluctuations

2. Power supply second harmonics

3. Lead lengths and IR drop

4. Insertion or removal of voltmeters and ammeters

5. Instrument scale-range changes

6. Insertion or removal of junction boxes

7. Insertion or removal of oscilloscopes

8. Use of coupling loops for waveform sampling

9. Plug contact effects: variable resistance and/or rectification

10. Faulty contacts within circuit

11. Thermoelectric loops

12. Battery effects in loops (including perspiration on plug contacts)

13. DC leakage into sense or feedback windings

14. Ground currents due to improper grounding or component failure

15. "Cross-talk" between adjacent circuits or experiments

16. Switching transients (random phase energizing)

LIST OF FIGURES

1. Core and drive winding schematic
2. Core assembly
3. Sense winding
4. Simplified view of Ames flux-gate sensor
5. Functional block diagram of the single axis sensor electronics sub-system
6a. Exciting current waveform
6b. Induced voltage waveform in core
6c. Sense winding voltage waveform
7. Schematic drawing of flux-tank
8. Axes for data
9. Strain test of sensor
10. Stability test, E5
11. Stability test, E5
12. Stability test, E5
13. Stability test, E5
14. Stability test, E7
15. Stability test, 10B
16. Stability test, 12
17. Stability test, 12
18. Stability test, LSM-C6
19. Stability test, ring core
20. Stability test, ring core
21. Stability test, ring core
22. Stability test, ring core

PRECEDING PAGE BLANK NOT FILMED.

Space Magnetic Exploration and Technology Symposium
August 1967, University of Nevada, Reno

A HIGHLY STABLE FLUXGATE MAGNETOMETER FOR SPACE EXPLORATION

D. I. Gordon, R. H. Lundsten, R. Chiarodo, H. H. Helms, Jr.*

N69-33968

ABSTRACT

A new fluxgate magnetometer, highly stable with time and temperature, was developed jointly by the NASA Ames Research Center (ARC) and the Naval Ordnance Laboratory (NOL). Incorporating ARC electronic circuitry for drive and detection and an NOL ring-core as the magnetometer sensor, the new magnetometer now has a zero offset level adjustable to less than 0.1 gamma, which fluctuates less than ± 0.1 gamma in 24 hours at constant temperature, and shifts less than 0.4 gamma when temperature is shifted from -30°C to + 60°C. Room temperature noise is less than 0.2 gamma peak-to-peak in the frequency band of 0-10 Hz. Stability and noise measurements were made in the NOL superconducting shield as well as in the ARC flux tank.

The electronics, developed by ARC, supplies fundamental drive power with negligible second harmonic content for exciting the fluxgate sensor. The detection channel receives the output signal from the fluxgate core sense winding, selects and amplifies only the second harmonic component, and demodulates this to provide an analog output voltage proportional to the field. Negative feedback from demodulator to sensor is used for circuit stability and system linearity.

Core material for the highly stable sensor is NOL developed and produced 6-81 Mo Permalloy tape, which is wrapped on a one-inch diameter non-magnetic metallic bobbin, spot welded and then annealed at high temperature in a dry hydrogen atmosphere. The ring-core drive winding is toroidal while its sense and feedback windings are solenoidal.

KEY WORDS

Magnetometer, fluxgate, stable, space magnetic exploration, Naval Ordnance Laboratory, NOL, NASA, Ames Research Center, ARC, stability, Permalloy, ring-core, sensor

---

* U. S. Naval Ordnance Laboratory, Silver Spring, Maryland

INTRODUCTION

In view of the fact that much about the nature and magnitudes of space magnetic fields is unknown, it is necessary that field measuring instruments have good resolution and accuracy over a wide dynamic range, and that they maintain these capabilities over long periods of time and with variations in temperature. In particular, recent experimenters have indicated that space magnetometers should have the following characteristics:

Resolution:	± 0.2 gamma
Long term stability:	Drift less than ± 0.2 gamma in 24-hour period at constant temp.
Operating temperature:	-30°C to +65°C
Temperature sensitivity:	Less than ± 0.2 gamma change in DC offset due to temperature change
Absolute null offset in zero field:	Less than 0.3 gamma

This paper describes a highly stable fluxgate magnetometer whose performance exceeds the above requirements. It consists of an electronics package containing driver and detection channels, developed by the NASA Ames Research Center (ARC), and a ring-core fluxgate sensor developed by the Naval Ordnance Laboratory (NOL). Its stability with time and temperature was measured at NOL with the sensor in a superconducting shield (1), where static magnetic fields are less than 0.1 gamma and static gradients are less than 0.1 gamma per inch and where attenuation to a-c fields is $\sim 10^6$. Measurements have also been made using a flux tank (2) at ARC.

In its present state of development this magnetometer has a zero offset which can be adjusted to less than 0.1 gamma and which fluctuates less than ± 0.1 gamma in 24 hours at constant temperature. It also shifts less than 0.4 gamma in the temperature range from -30°C to +60°C. Room temperature noise is less than 0.2 gamma peak-to-peak in the frequency band of 0-10 Hz.

ELECTRONICS

The electronics system used with the NOL ring-core sensors was developed by ARC and is described in detail elsewhere (3), (4). The system provides a 5 kHz* sine wave drive for the sensor core and detects the second harmonic output which is the predominant signal developed for an applied d-c field.

---

* Nominal drive frequency

The circuit consists of master oscillator, binaries, drive amplifiers, signal amplifiers, demodulator and associated filters.

A crystal controlled master oscillator provides a stable 20 kHz square wave from which the sensor drive and detector reference signals are derived. Two binary circuits are used to divide the 20 kHz oscillator signal into 10 kHz and 5 kHz square waves. The 10 kHz signal from the first binary is fed to a delay multivibrator and then to the second binary. The multivibrator provides a time delay for synchronizing the magnetometer system.

The 5 kHz square wave output from the second binary contains about 0.1% second harmonic which must be reduced before it can be used to drive the sensor core. This reduction is accomplished by using a fourth order band pass filter which produces a sine wave with less than 0.002% second harmonic distortion. This signal serves as the input for a low impedance amplifier which provides the sine wave voltage drive for the sensor core.

The signal output from the sensor due to the external field is preamplified by a low distortion emitter follower. This amplified signal contains, besides the second harmonic (10 kHz) due to the detected field, a large fundamental component (5 kHz) due to feedthrough from the drive to secondary windings. There are also present third and fifth harmonics of similar magnitude as well as other odd harmonics. In order to eliminate these odd harmonics the output from the preamplifier is filtered by a 2.5 kHz band pass filter at 10 kHz with 70 dB attenuation at 5 and 15 kHz.

The filtered signal is further amplified by a signal amplifier with a 5:1 sensor feedback ratio and a voltage gain of 70 dB. The amplified signal is converted into a low frequency analog signal between dc and approximately 100 Hz by a demodulator circuit. A fraction of the demodulator output voltage is fed back to a set of windings on the sensor core in such a phase as to cancel part of the field seen by the sensor. This feedback is used to increase the system's linearity for large ranges of field, and to increase stability against voltage changes in the system.

SENSOR

The sensor is of ring-core construction, with the drive windings wound in toroidal fashion on the ring. See Figure 1a. Sense and feedback windings are wound as solenoids on a fiberglass-filled epoxy bobbin of rectangular cross-section, as shown in Figure 1c. The assembled sensor is shown in Figure 2. The use of a closed ring-core instead of two parallel open cores was first demonstrated by Geyger (5). The primary advantages of closed core sensors are: (1) low driving power, because of the lower magnetizing current required for saturation since there is no self-demagnetization of the core, and (2) high resistance to sensor perm because of more uniform magnetization of the sensor volume due to uniform winding distribution over the whole core, i.e.,

no end regions where the magnetizing field is low. Flattened toroids (i.e., racetrack configuration) also have the above two advantages, but to a lesser extent, because the curved ends of the racetrack are not covered by magnetizing windings. Hence, the approximation to a true closed core in a tape-wound racetrack is less than in a tape-wound circular ring. The ring-core has additional advantages. First, because of its circular symmetry, the ring-core can easily be rotated within its sense winding for offset nulling without changing the alignment axis of the sensor. This provides an additional degree of freedom in making the original zero-field reading adjustment of the sensor-electronics combination. Second, fabrication of the sensor is relatively simple, since "non-magnetic" metallic bobbins and bobbin core fabrication techniques can be used. Uniformity of tape tension during the tape wrapping operation can easily be maintained, and because of the constant radius of curvature there are no concentrated stress points in the tape of the finished core. As a further effort at minimizing mechanical stress in the cores, and in improving uniformity of the end product, the NOL procedure includes high temperature annealing of the tape-wound bobbins after the tape-wrapping operation. Third, toroidal drive windings are easily applied with existing winding machines. When this procedure is followed sensors with low offset, low noise, and high stability can be produced with a high production yield.

SENSOR CORE FABRICATION

In general, the investigation of low noise materials for this work was limited to molybdenum-permalloy alloys because of their low magnetostriction, low magnetic crystal anisotropy, low coercive force, and high permeabilities. The fundamental magnetostriction constants for various crystalline orientations and for unoriented polycrystalline materials are mainly a function of composition and for binary nickel-iron alloys these constants are known to become zero in the 80 to 83% nickel range. Since no particular effort was made to obtain specific crystalline orientations in the present study it was deemed desirable to use a composition having a zero magnetostriction value for the polycrystalline unoriented condition. This alloy contains about 81.3% nickel. Fortunately, a variation of cooling rate during the final anneal affects the atomic ordering of this alloy such that the crystal anisotropy constant can be changed from positive to negative and consequently permits minimizing of the anisotropy energy.

The effect of molybdenum on the magnetostriction and crystal anisotropy of nickel-iron alloys has only been evaluated on a limited scale. This work has been covered in a short review by English and Chin (6). Previous investigation of low noise materials at NOL showed the desirability of adding 4% or 5% molybdenum to the binary nickel-iron alloys. These studies led to investigation of alloys containing higher molybdenum additions. Finally, an alloy consisting of 6% molybdenum - 81.3% nickel - remainder iron was selected as being most appropriate for the present application. Some magnetic data have been reported on this alloy in the cube textured condition by Odani (7).

In the present study the processing techniques, annealing cycles, and thickness gauge were considerably different from those reported by Odani; therefore, it cannot be assumed that the orientation textures were similar in both cases. It is quite possible that a better defined crystal orientation might provide even further improvement in the properties obtained in the present development.

The 6 Mo - 81.5 Ni-Fe alloy used in the subject magnetometer is prepared by induction melting electrolytic iron and nickel in a hydrogen atmosphere, adding molybdenum, and pouring in helium. The resultant slab is hot rolled to 0.100" thickness and then homogenized for four hours at 850°C. The material is subsequently cold reduced to 0.008" thickness, strip annealed in hydrogen at 1050°C, and then cold reduced about 94% on a cluster mill to a final thickness of 0.0005". The material is slit to desired width, cleaned, insulated with magnesium oxide, and finally wound on a non-magnetic bobbin, Inconel X-750, which had previously been machined to shape using a stellite tool. Each core contains exactly 12 turns of 0.0005" material and the outer turn of tape is spot welded to hold the core shape during anneal.

The tape cores are firally annealed in pure dry hydrogen (dew point < -90°F) for 1½ hours at 1000°C and furnace cooled using a cooling rate of approximately 35°C/hour through the critical ordering range (600°C to 400°C).

SENSOR ASSEMBLY

The annealed bobbin core is wrapped with an insulating tape and wound with 200 turns of #36 heavy formvar copper wire. This number of drive windings gives the maximum sensitivity and a minimum noise figure. A preliminary screening evaluation of sensitivity and noise determines the bobbin cores to be used in sensors.

A glass-filled non-magnetic epoxy (Reapoxy #111) is used to cast a rectangular coil form. The sense windings of 2200 turns of #44 H.F. copper wire are uniformly distributed among the four grooves on the coil form. The 1104 turns of the feedback windings, #36 H.F. copper wire, are wound over the sense windings in the same manner. The start and finish ends of the windings are then soldered to a terminal board that is epoxied across one of the open ends of the coil form. See Figure 1c.

To complete the assembly of the sensor, the bobbin core with its drive windings is mounted on a phenolic turntable (Figure 1b) and the unit is then placed into the coil form. A 0.020 inch non-magnetic axle is fitted through holes in the coil form and turntable. This allows the turntable to be rotated within the coil form so that zero offset can be minimized. Drive winding ends and lead cables are then soldered to the terminal board. A protective cover cast from epoxy is fitted around the coil form and the terminal board end is potted to hold the cables and wires in position. Figure 2 shows the assembled sensor.

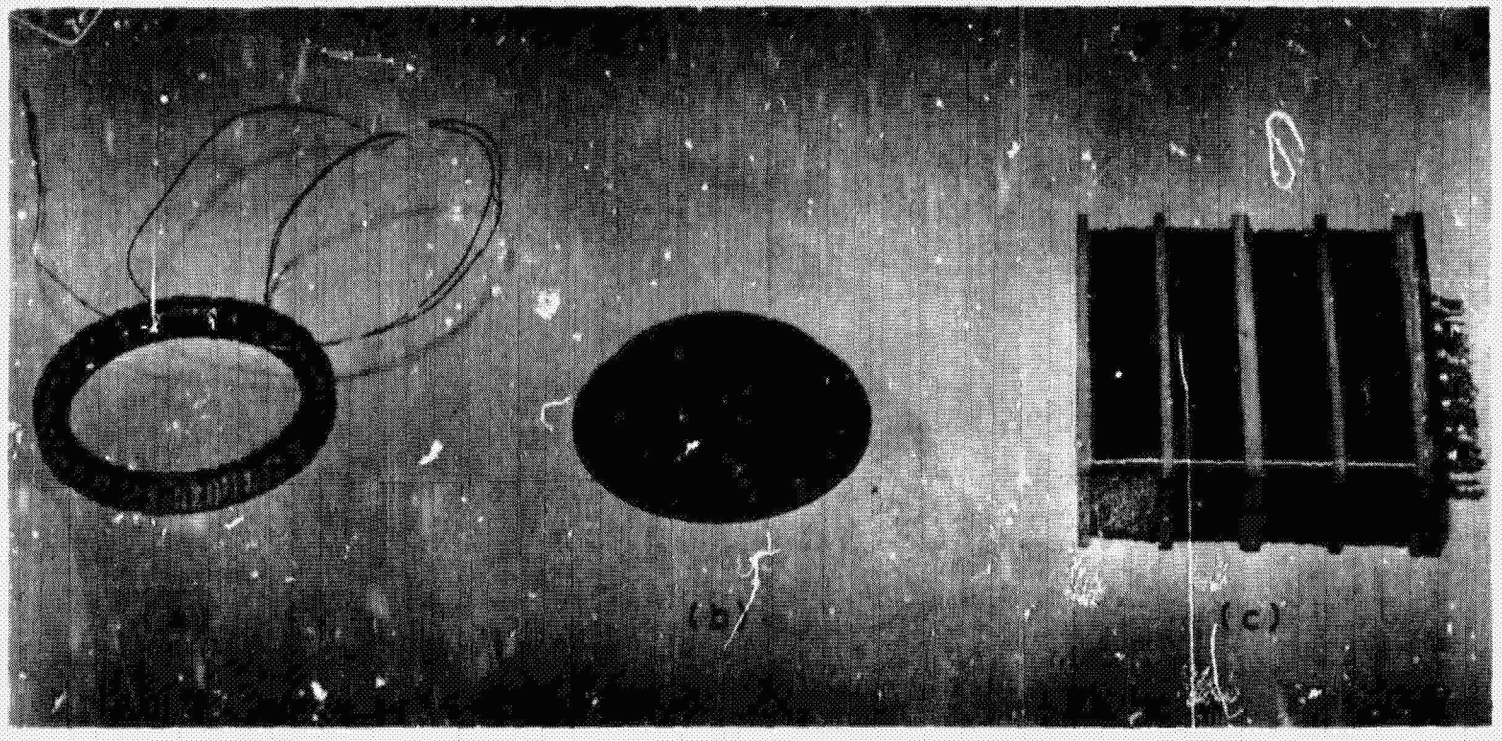


FIG. 1 (a) Ring-Core With Toroidal Drive Windings
(b) Turntable for Ring-Core Zero Offset Adjustment
(c) Sense and Feedback Windings on Rectangular Coil Form for Ring-Core



FIG. 2 NOL Ring-Core Sensor and Cable Assembly

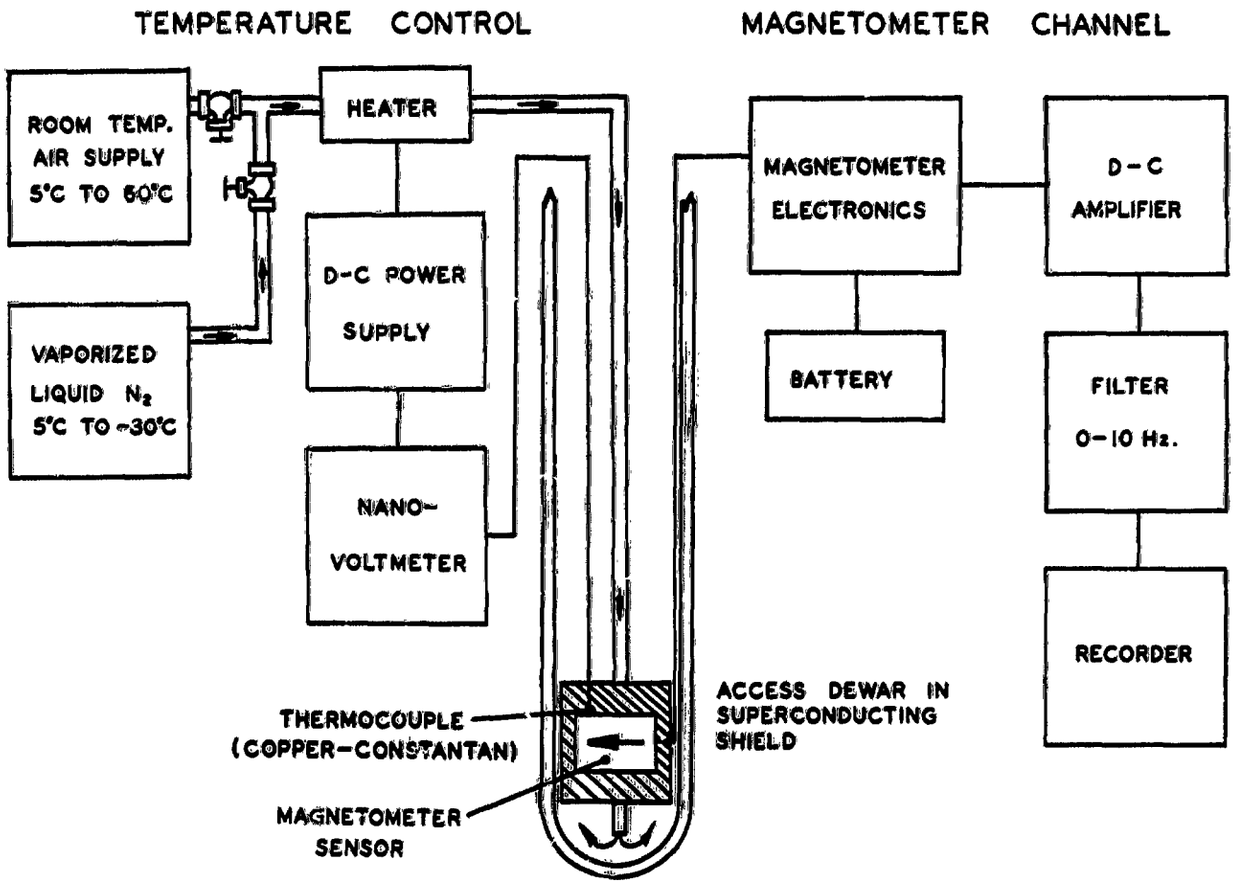


FIG. 3 Schematic of Test Arrangement for Evaluating Magnetometer Stability. Sensor is in temperature controlled region within superconducting shield.

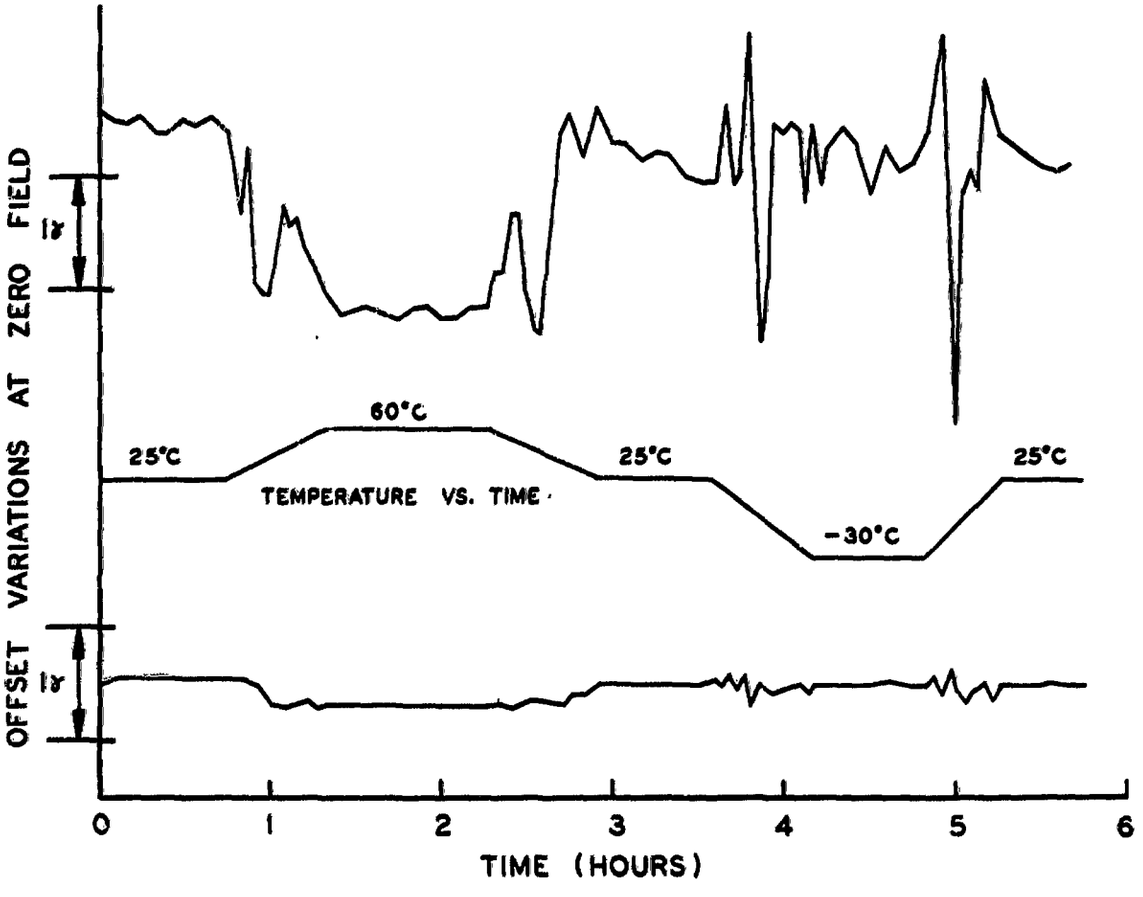


FIG. 4 Zero-Offset vs Time During Temperature Test Cycle (a) Racetrack Sensor (b) Ring-Core Sensor (c) Temperature of Sensor

Prior tc the stability tests of the sensor, minimum offset adjustment is made by rotating the ring-core on its turntable. After adjustment the ring-core turntable is cemented in place. Upon completion of this operation, a phenolic cover is epoxied across the remaining open end of the coil form and the sensor is ready for evaluation in the superconducting shield.

PERFORMANCE EVALUATION IN SUPERCONDUCTING SHIELD

All sensors are evaluated in the highly stable, low field environment provided by the NOL superconducting shield (1). The working volume of the access dewar inside the superconducting enclosure has a 1.75" diameter and a usable length of three inches. Typical values of field, gradient and noise attenuation within this temperature access volume in the superconducting shield are:

Field:	$< 0.1\ \gamma$
Gradient:	$< 0.1\ \gamma$/inch
Noise attenuation:	Transverse -- 5×10^5 at bottom to 10^4 at 3"
	Axial -- 2×10^7 at bottom to 2×10^5 at 3"

The temperature in the access dewar is controlled by a system employing an air supply, a resistance heater, and a thermocouple-controlled power supply. See Figure 4. The thermocouple output is sensed by a Keithley Micro-millivoltmeter. Using negative feedback and a remote sensing power supply the temperature is controlled to ± 0.1°C in the range of 5°C to 60°C. The same feedback system is used with a supply of evaporating liquid nitrogen to control to ± 0.25°C in the range of -30°C to 5°C.

Each sensor is evaluated for stability by measuring its offset and noise values during a temperature cycle. The temperature cycle consists of an hour at room temperature, a period of heating to 60°C at a rate of ~ 1°C/minute, an hour at 60°C, cooling to room temperature at ~ 1°C/minute, a half hour at room temperature, cooling to -30°C at ~ 2°C/minute, an hour at -30°C, heating back to room temperature at ~ 2°C/minute, and lastly one hour at room temperature.

The magnetometer electronics supplied by ARC is powered by a 8.3 volt wet-cell battery which is continually kept at full charge by a trickle charge device. The output of the electronics package is amplified by a Dana d-c amplifier with a bandwidth of 0 to 20 kHz. The amplified signal is fed into a Dytronics Filter set at a bandwidth of 0 to 10 Hz and then into a Sanborn Recorder Type 320 where a plot of signal vs time is obtained. A continuous record of offset and noise values for the magnetometer syste vs time which can be related to temperature is thereby obtained.

RESULTS

Sample curves of offset vs time during the temperature cycling evaluation tests in the superconducting shield are shown in Figure 4. Curve (a) is for a sensor of racetrack configuration supplied to NOL by ARC. Curve (c) is typical of the ring-cores evaluated to date. Average results for the first four ring-core sensors and data for the racetrack sensor evaluated are as follows:

	NOL Ring-Cores	Racetrack
Fluctuations at constant temp.	± 0.10 γ	± 0.35 γ
Fluctuations during temp. changes	± 0.15 γ	± 1.75 γ
Offset difference/high-low temp.	0.35 γ	1.40 γ
Offset difference/start to end	0.10 γ	0.40 γ

These results were confirmed by ARC, who also made longer time stability checks and showed that offset fluctuations were less than ± 0.10 gamma in 24 hours at constant temperature. Room temperature noise for the ring-core sensors fabricated to date ranges from 0.10 to 0.20 gamma peak-to-peak in the 0-10 Hz frequency band.

CONCLUSION

Combining an NOL ring-core sensor with the ARC drive and detection electronics produces a fluxgate magnetometer, which is highly stable with time and with sensor temperature. Measurements in a superconducting shield at NOL and in a fluxtank at ARC show that zero stability is exceptionally good, both for long periods at constant temperature and during relatively rapid temperature transitions. Differences in zero-offset level between high and low temperature sensor conditions and between start and end of a temperature test cycle are quite small. The improved operating stability of this fluxgate magnetometer should be useful in meeting some of the higher performance requirements for space magnetic exploration.

REFERENCES

(1) R. E. Brown, "A Magnetometer Test Environment Using an Expandable Superconducting Enclosure," Space Magnetic Exploration and Technology Symposium (August 1967) Univ. of Nevada, Reno

(2) W. I. Linlor, R. M.Munoz, M.J Prucha, "Stability Measurements of Fluxgate Magnetometers," Space Magnetic Exploration and Technology Symposium (August 1967) University of Nevada, Reno

(3) Wm. T. Kerwin, Robert M. Munoz and M. John Prucha, "An Improved Magnetometer for Deep Space Use," IEEE/AIAA National Aerospace Electronics Conference, Dayton, Ohio, May 1964

(4) R. M. Munoz, "The Ames Magnetometer," Paper presented at National Telemetering Conference, Boston, May 1966

(5) W. A. Geyger, "New Type of Flux-Gate Magnetometer," J. Appl. Phys., 33, 1280 (1962)

(6) A. T. English and G. Y. Chin, "Metallurgy and Magnetic Properties Control," J. Appl. Phys., 38, 1183-1187 (March 1967)

(7) Y. Odani, "Magnetic Properties of Cube-Textured 6-81.3 Mo-Permalloy," J. Appl. Phys., 35, Part 2, 865-866, (March 1964)

ACKNOWLEDGEMENT

This work is sponsored by National Aeronautics and Space Administration.

Space Magnetic Exploration and Technology Symposium
August 1967, University of Nevada, Reno

A MAGNETOMETER TEST ENVIRONMENT USING AN EXPANDABLE SUPERCONDUCTING ENCLOSURE

R. E. Brown *

N69-33969

ABSTRACT

A volume containing a reduced magnetic field may be obtained inside a lead foil sack by opening the folded sack at 4.2°K when the lead is superconducting. A multi-stage magnetic flux vacuum pump based upon this idea was used to reduce earth's field to below 10^{-6} oersted in a volume of several cubic inches. The superconducting sack shields this volume against the magnetic field fluctuations of the laboratory environment. The estimated noise level in the low field space is 10^{-8} oersted. A glass dewar inserted into the sack permits working in the low field space at controlled temperatures near room temperature. This system has had extensive use for the study of the long term stability of flux-gate magnetometer sensors destined for use in space exploration.

KEY WORDS

superconducting shield, magnetic shield, flux pump, magnetometer test

---

INTRODUCTION

When placed in zero magnetic field, flux-gate magnetometers generally have a residual output signal called the zero offset. As long as the zero offset is constant with time, magnetometer readings may be converted to absolute field measurements by subtracting the zero offset signal. When a shift in the zero offset is suspected, it may be redetermined by turning the sensor 180°. To reduce the number of times this sensor reversal must be performed in flight, it is desirable for magnetometers used in space exploration to have a stable zero offset.

* U. S. Naval Ordnance Laboratory, Silver Spring, Maryland

The offset is customarily attributed to imperfections in both the sensor and the associated electronics. The test environment to be described below was developed for use in a study of the origin and stability of the sensor offset alone (1). The requirements set by the sensor study and met or exceeded by this test environment were (a) A magnetic field approaching zero (less than 10^{-6} oersted) so that the zero offset signal may be isolated and kept under continuous observation. (b) A magnetic field that is uniform to within 10^{-6} oersted over the sensor volume. (c) Magnetic field fluctuations less than 10^{-7} oersted during a test period of several hours. (d) Control of sensor temperature in the range -30°C to +60°C.

A test space containing a low magnetic field is commonly obtained in one of two ways. Earth's field either is canceled out by a coil system or is diverted around the test space by an enclosure of high magnetic permeability. With sufficient expenditure of effort the requirements listed above can perhaps be met by these more conventional means. We decided instead to develop a test system using the magnetic shielding capabilities of superconductors for two reasons. (a) The potential for field reduction and noise suppression in a superconducting enclosure is greater than with any other magnetic shielding method (2). (b) There was a need to check magnetometer sensor offset studies performed in a conventional flux-tank by making similar measurements in a different kind of test environment.

THE MAGNETIC FLUX VACUUM PUMP

It was shown in a previous report (2) that magnetic noise attenuation by a factor of at least 10^{-8} could be obtained easily inside a superconducting hollow cylinder. Since the test environment required a low magnetic field as well, the scheme shown in Figure 1 was proposed. At A in the figure an axial magnetic field is depicted inside a lead foil hollow cylinder. At B the foil cylinder has been flattened at room temperature so that a smaller magnetic flux is contained in the cylinder cross-section. At C the lead foil cylinder has been reopened after cooling it below the superconducting transition temperature of the lead. The field configuration does not return to state A because the perfectly conducting walls of the cylinder do not admit the external field. Thus the field inside the cylinder at C has been reduced from its value at A.

A cascaded or multi-stage operation of this flux vacuum pump is possible. After performing one stage of field reduction as described above, the cascading can be achieved by inserting a second flattened cylinder into the first. This second cylinder must be kept above its superconducting transition temperature until it is in place in the reduced field region inside the first cylinder. When superconducting, the second cylinder may be reopened, and the field inside should be lower than it was inside the first cylinder.

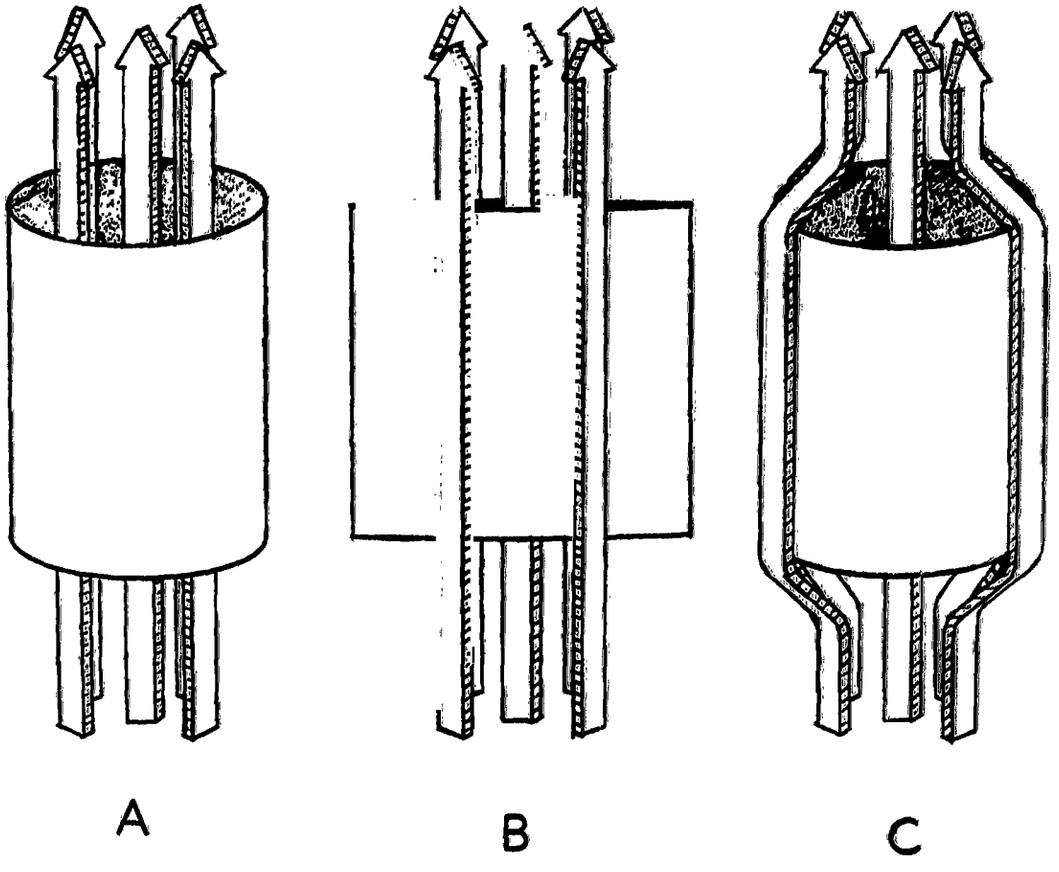


FIG. 1 The magnetic flux vacuum pump operating sequence

In most of our later work a lead foil sack has been used, which resembles a hollow cylinder closed at one end. The folding of the sack is more intricate than simple flattening. The field reduction factor per stage of the pump can be as high as several hundred as shown in Table 1, and it is found to be roughly constant per stage. The final transverse field shown for the second stage in Table 1 represents the noise level of the flux-gate magnetometer used to make this particular measurement, and the field reduction factor of 80 is thus a minimum value.

DETAILS OF CONSTRUCTION AND FLUX-PUMP OPERATION

The sacks are made of lead foil .0015 inch thick. This lead foil was supplied on 18 inch wide rolls by American Metal Climax, Inc., who make it for use in packaging. The lead is certainly of no more than technical purity. Each sack is made from a rectangular piece of foil 28 inches long and 6.8 inches wide. The piece is folded double to halve the long dimension, and the edges are welded together by careful melting with a flame. The result is a sack 14 inches long and about 6.7 inches wide when flattened.

Four fingers made from 1/8 inch thick cloth base phenolic are glued to each sack with Weldwood Contact Cement to form the structure shown in Figure 2. In this figure the open end of the sack is at the top and the welded seams are along the vertical edges. This particular sack has been folded into its compact form and then unfolded so that the creases show the folding scheme. On the right are two clips formed from sheet aluminum that are used to fasten together the compact form of the sack package. The nylon fishline attached to each clip enables removal and retrieval of the clips when the sack is ready to be opened in the liquid helium dewar. The sacks are generally used only once although refolding results only in the appearance of a few pinholes in the foil.

A handle 28 inches long made from 1/4 inch diameter thin wall stainless tubing is attached to the top of each of the phenolic fingers so that they may be manipulated from the top of the helium dewar when opening the sack. The compact form of the sack package is shown on the right in Figure 3 with the handles and aluminum fastening clips in place. On the left in Figure 3 an opened sack is shown below the fixture used for the opening operation and with the silvered glass room temperature access dewar extending into the sack. This access dewar permits working near room temperature in the low field space inside the sacks. Its inside diameter is 1.75 inches and outside diameter 2.5 inches. The opening fixture fits into a 6-inch inside diameter liquid helium dewar. From the top of the helium dewar the operator can pull four traveling loops of nylon string in the opening fixture to apply an outward force to each of the tubing handles at a point near the top of the phenolic fingers. The lead foil easily undergoes permanent deformation at 4.2°K without cracking or tearing. Although the foil is stiffer at 4.2°K than at room temperature, the force required to open a sack is estimated to be increased by less than five times.

TABLE 1

FIELD REDUCTION IN THE MAGNETIC FLUX VACUUM PUMP

Starting Field at Bottom of Sack (oersted)	Final Field at Bottom of Sack (oersted)	Field Reduction Factor
	First Stage	
0.3 axial	6×10^{-4} axial	500
0.2 transverse	4×10^{-4} transverse	500
	Second Stage	
6×10^{-4} axial	$\sim 10^{-6}$ axial	~600
4×10^{-4} transverse	$< 5 \times 10^{-6}$ transverse	> 80

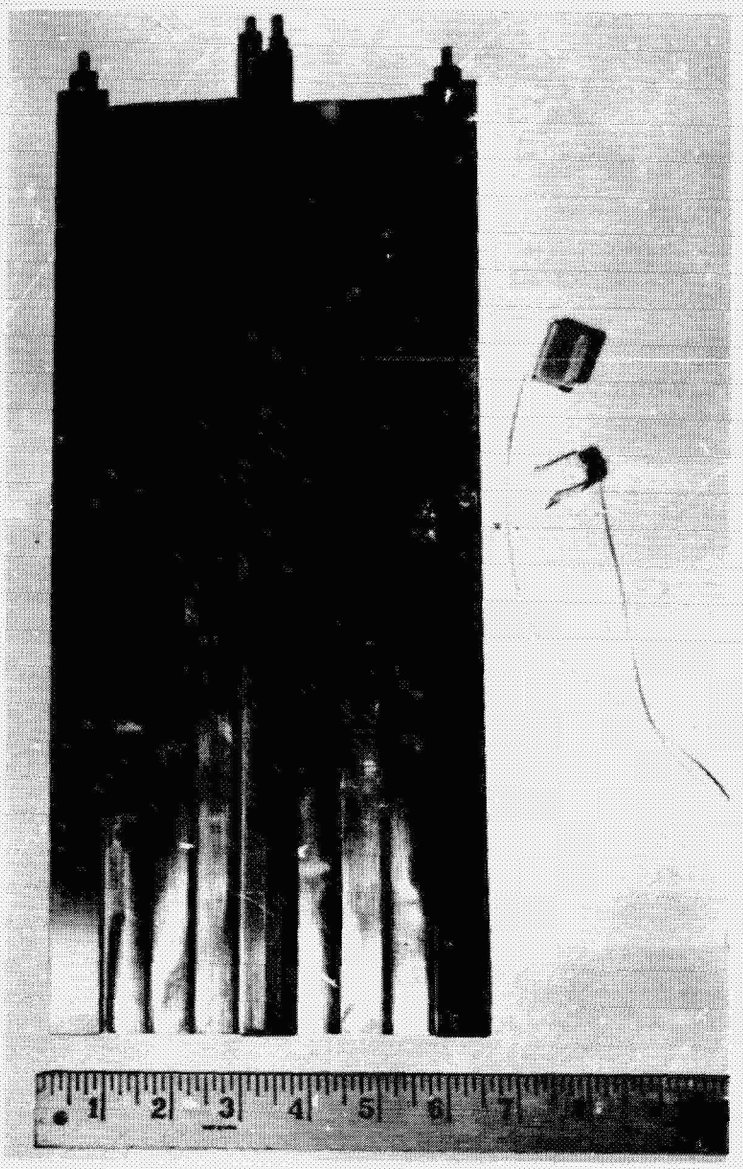


FIG. 2 The lead foil sack for one stage of the flux vacuum pump

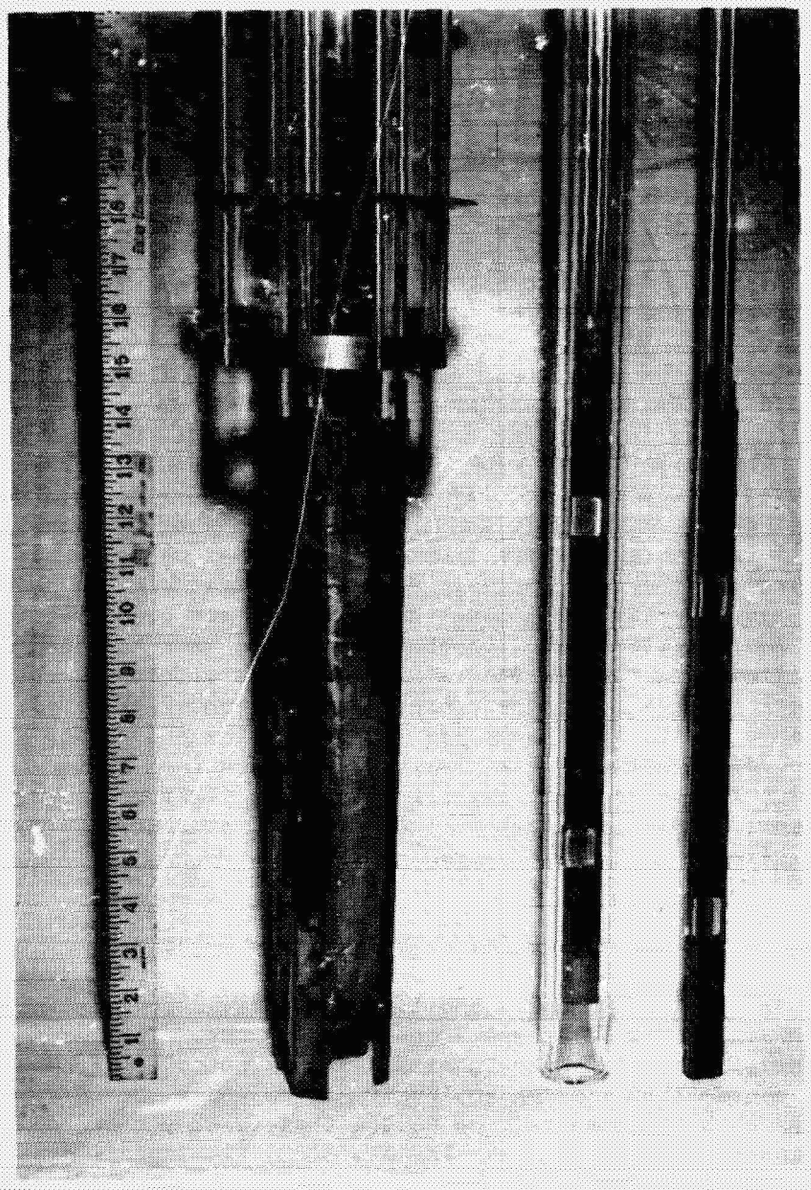


FIG. 3 First and second stage sacks folded and ready for use and an opened sack in the opening fixture

In the center of Figure 3 is shown a second stage folded sack package hanging inside a glass vacuum jacket that has an open bottom. The package hangs from a detachable hook at the top of the jacket. The vacuum jacket keeps the lead foil sack in the normal state when the assembly is immersed in liquid helium. A slight over-pressure of helium gas applied at the top of the jacket prevents liquid helium from entering the bottom opening. When the second stage sack is in position in the lowered field region inside the first stage sack, liquid helium is permitted to enter the bottom opening. The jacket is then detached and lifted out of the helium dewar leaving the second stage package behind. All materials that enter a low field region are checked to assure non-magnetic character.

Figure 4 shows an overall view. The small coil system shown around the plastic helium dewar reduces earth's field to about .01 oersted near the liquid helium level. The operating sequence of the flux-pump is as follows: The first folded sack is precooled in liquid nitrogen and then lowered slowly into the liquid helium dewar filled to a depth of about 16 inches. Presumably the normal-superconducting transition in the lead foil occurs near the liquid helium level where the field has been reduced by the coil system. After this first sack has been opened, a second sack and its enveloping vacuum jacket are precooled in liquid nitrogen and inserted into it. When the second sack has been cooled to liquid helium temperature, the vacuum jacket is withdrawn, the second folded sack package is punched through the bottom of the first sack, and the remnants of the first sack are withdrawn from the dewar. This latter operation prevents the physical situation from becoming too cluttered. The second sack may now be opened. This cascading can be carried easily to higher stages, but we are at present unable to measure the small fields that are expected to result.

PERFORMANCE OF THE MAGNETIC TEST ENVIRONMENT

Figure 5 shows the axial and transverse field profile inside the access dewar for the first and second stage sacks. The zero position is the lowest possible sensor position and is not the bottom of the sack. The coil system that reduces ambient field to about .01 oersted near the top of the sack has been left on during these measurements as it is during sensor stability tests. The distorted field profile in the first sack indicates the presence of trapped flux in the lead foil. The flux-gate magnetometer used to make these measurements had a noise level slightly less than 10^{-6} oersted and indicated no field up to 4 inches above the lowest sensor position in the second sack. Not all components of the field gradient can be measured with high sensitivity sensors, but no gradient as large as 10^{-6} oersted per inch could be found at the lowest position in the second sack. The field profile in the lower portion of the second sack has been found to remain unchanged for as long as 100 hours.

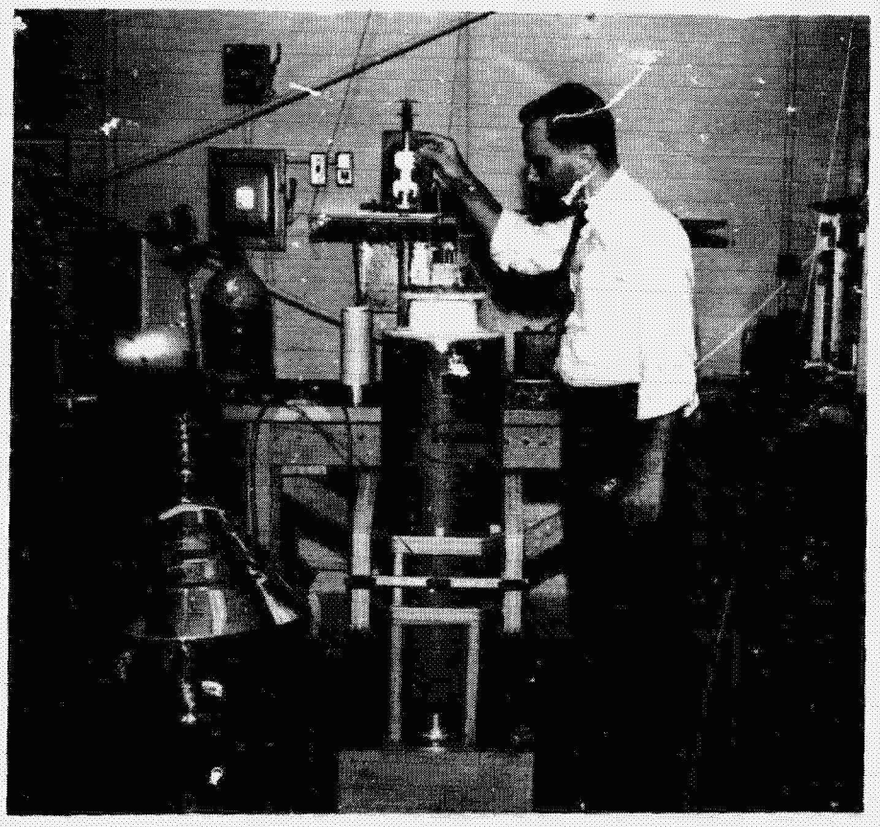


FIG. 4 An overall view of the apparatus

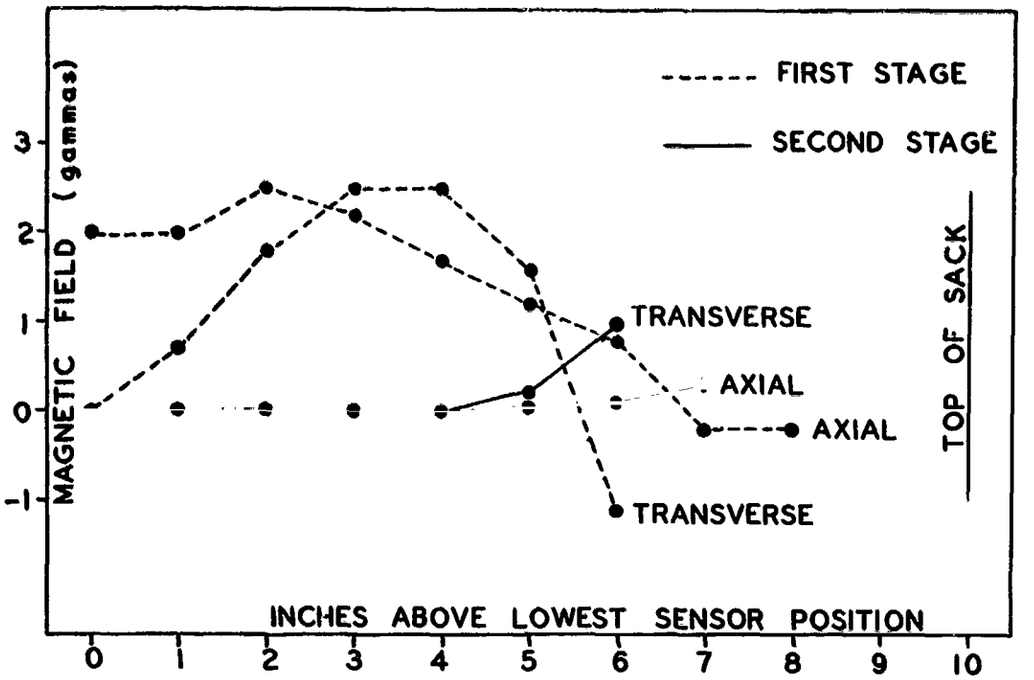


FIGURE 5. FIELD PROFILE IN SACKS.

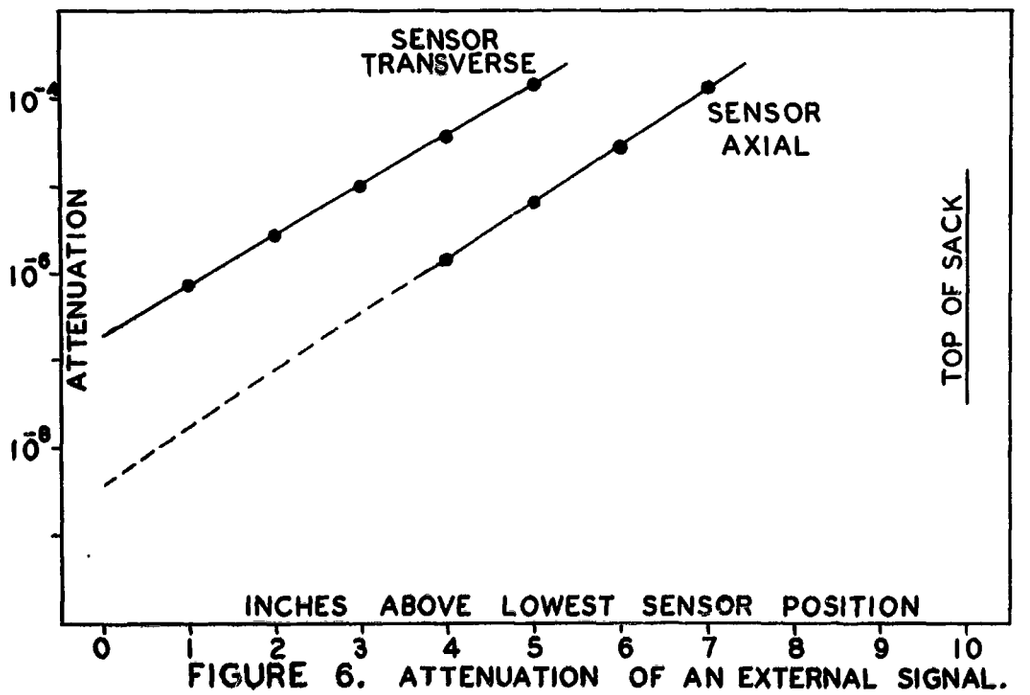


FIGURE 6. ATTENUATION OF AN EXTERNAL SIGNAL.

The attenuation of a magnetic signal applied at the top of the sack is shown in Figure 6. This signal was 0.2 oersted in the worst direction, which is transverse. The attenuation follows closely a linear logarithmic law. The attenuation one would infer for the sensor in the axial orientation and at the lowest position requires a long extrapolation which may be questionable.

Temperatures above room temperature are obtained at the sensor location in the access dewar by conducting a stream of heated air to the bottom of the dewar. A copper-constantan thermocouple is attached to the sensor under test, and the thermocouple output controls the power supplied to a heater in the air stream. For temperatures below room temperature the air supply is replaced by a stream of cold nitrogen gas issuing from a dewar containing liquid nitrogen and a heater of fixed power input to induce a constant boil-off. The thermocouple still controls a heater in this gas stream. Temperature control at the sensor location is ± 0.5°C in the range -30°C to +60°C.

The major heat leak into the liquid helium comes from the room temperature access dewar. With this dewar in place liquid helium consumption is about 2 liters per hour. With the access dewar removed, this rate drops to 3 liters per 24 hours. A better insulated access dewar would diminish materially the operating cost. The system is normally kept in operation for a week at a time.

REFERENCES

(1) D. I. Gordon, R. H. Lundsten, R. A. Chiarodo and H. H. Helms, Jr., "A Highly Stable Fluxgate Magnetometer for Space Exploration," Paper presented at this symposium.

(2) Proceedings of the Magnetics Workshop, JPL Tech. Memo No. 33-216, 1965, p 227, Rev.Sci. Instr. 36, 1378 (1965)

ACKNOWLEDGEMENT

This work is sponsored by National Aeronautics and Space Administration.

NEAR-EARTH MAGNETOMETER FLIGHTS WITH THE OVI SERIES SPACECRAFT

by

Kenneth O. Downing and Gordon D. Hall
General Dynamics Convair
San Diego, California

N69-33970

INTRODUCTION

A relatively large number of the spacecraft currently being launched are in near-earth orbits ranging from 100 to 1000 nautical miles. Of the many varieties of experiments being flown into this region of space studies such as that of incoming, trapped, and backscattered energy particles auroral and airglow distributions, and others using directional detectors require that the spatial orientation of the spacecraft be known in order that the data can be correctly interpreted. In these regions of space the geomagnetic field predominates and the field vectors are known to an accuracy that encourages the use of a magnetometer solar aspect system to determine the spacecraft orientation. Assuming that the field distortions caused by the spacecraft are negligible and that a modern PCM telemetry system is being used, the spacecraft attitude can be determined to an accuracy of several degrees, especially if the solar aspect data is considered to be primary and the magnetometer is used to resolve the roll position of the spacecraft about the sun spacecraft vector. Thus the magnetometer is being flown as a part of the spacecraft engineering system rather than as an experiment for field studies.

NEAR-EARTH ORBIT CONSIDERATIONS

Since the near-earth magnetic field is typically 10^4 gamma and higher, the intrinsic field of the spacecraft can be much higher than is allowable for lunar and deep space probes without introducing appreciable error into the magnetometer data. Consequently the components and systems engineers have a far wider latitude in the selection of materials and physical design than for deep space probes. However, the economic and schedule requirements typical of near-earth spacecraft do not allow for excessive testing, overdesign, nor the luxury of extensive redesign as the result of testing.

The near-earth engineer has an additional concern: Although he is often allowed ten milligauss or more intrinsic field at the magnetometer, the effective dipole of the spacecraft will interact with the ambient geomagnetic field to produce a torque on the spacecraft which may be significant if a low torque attitude control system, such as a gravity gradient device is being employed. Thus a boom installation for the magnetometer is not a solution to the stray field problem if attitude control perturbations are present.

OV1 SPACECRAFT

General Dynamics Convair has successfully designed and flown numerous spacecraft of the OV1 series into these orbits, several of which have contained aspect magnetometers including some which were stabilized by means of the Convair Vertistat gravity gradient attitude control system. Our experience in the design and test of these spacecraft may be of interest to others working on this type of program as well as to engineers designing "off-the-shelf" equipment.

The OV1 spacecraft consists of a right cylindrical section containing the experimental payload and a faceted hemispherical solar cell dome on each end, Figure 1, one housing the telemetry and power electronics and the other housing the spacecraft power battery. The magnetometers are mounted under the aft solar dome (inside the spacecraft), Figure 2. These are three axis flux-gate units commonly of $\pm$ 600 milligauss range, although $\pm$ 200 and $\pm$ 100 milligauss magnetometers are also flown.

CONVAIR MAGNETIC TEST FACILITY

Tests on the Convair spacecraft are conducted at a new magnetic test facility located at Convair's Kearny Mesa plant in San Diego. It is a twelve coil system having four coils along each of three axes, one axis being north-south, one east-west, and the third vertical, Figure 4. The coils extend twenty feet along each axis, and are squares twenty feet on a side, rather than the more common circular design. The apertures to the working volume inside the coils are 4.7 feet by 5.1 feet in the north-south direction and 4.7 feet by 4.9 feet in the east-west direction. The coil system is installed in a wood building assembled with aluminum nails. The building contractor was made aware of our requirements and concern, and all construction materials, concrete aggregate, etc., were tested before being used.

Each of the twelve coils has a primary winding and two compensating windings, Table I. The four primary coils along each axis are electrically connected in series and are used to reduce the field to zero or to any specified value up to 50,000 gamma at the center of the coil system. The compensating windings,

Table 1. Four-square 20 ft. coil system specifications.

	AXES		
	N-S	E-W	VERTICAL
DIMENSIONS (FT.)	19.2	20.0	18.3
APERATURE (FT.)	4.7 X 5.1	4.7 X 4.9	4.9 X 5.1
MAIN POWER WINDING			
TURNS/COIL SET	80	80	80
RESISTANCE/COIL SET (OHMS)	4.0	4.0	4.0
COIL SET CONSTANT (GAMMA/AMP)	8,650	8,290	9,020
COMPENSATING WINDING NO. 1	10 - 20	10 - 20	10 - 20
TURNS PER COIL			
COMPENSATING WINDING NO. 2	1	1	1
TURNS PER COIL			

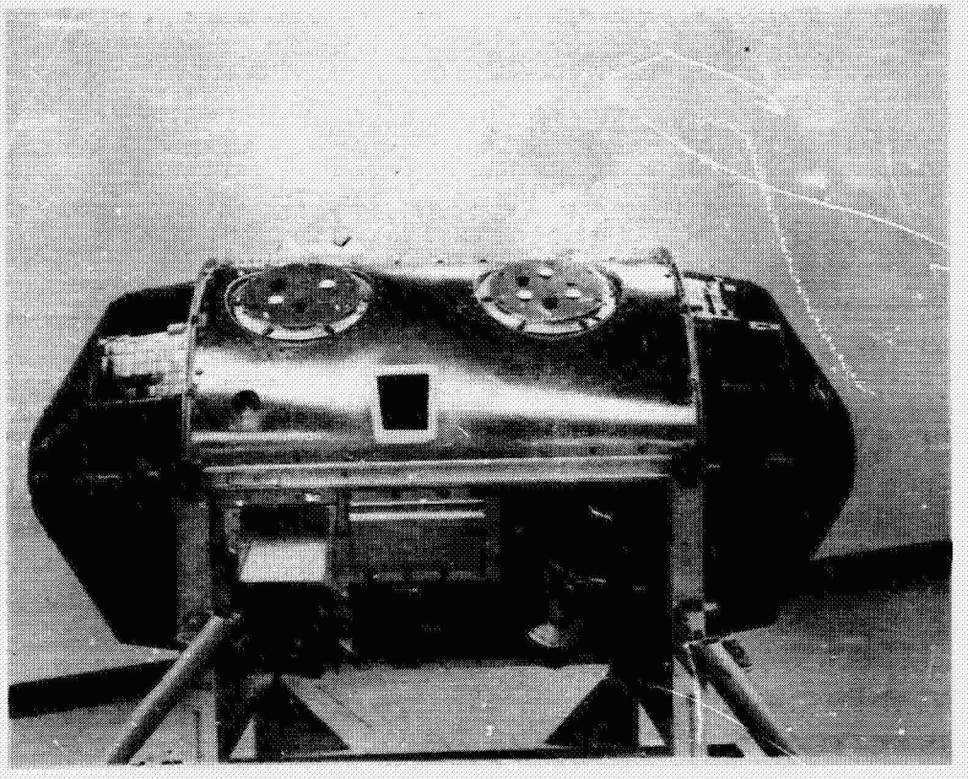


Figure 1. OV1 spacecraft with solar domes installed.

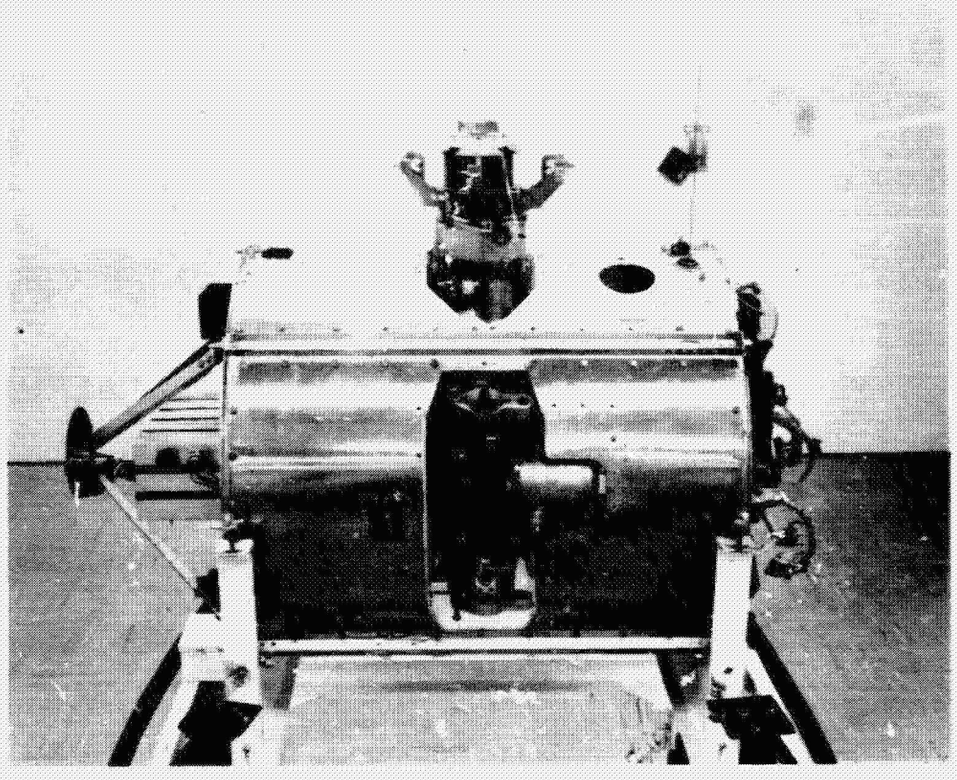


Figure 2. OV1 spacecraft with solar domes removed showing magnetometer.

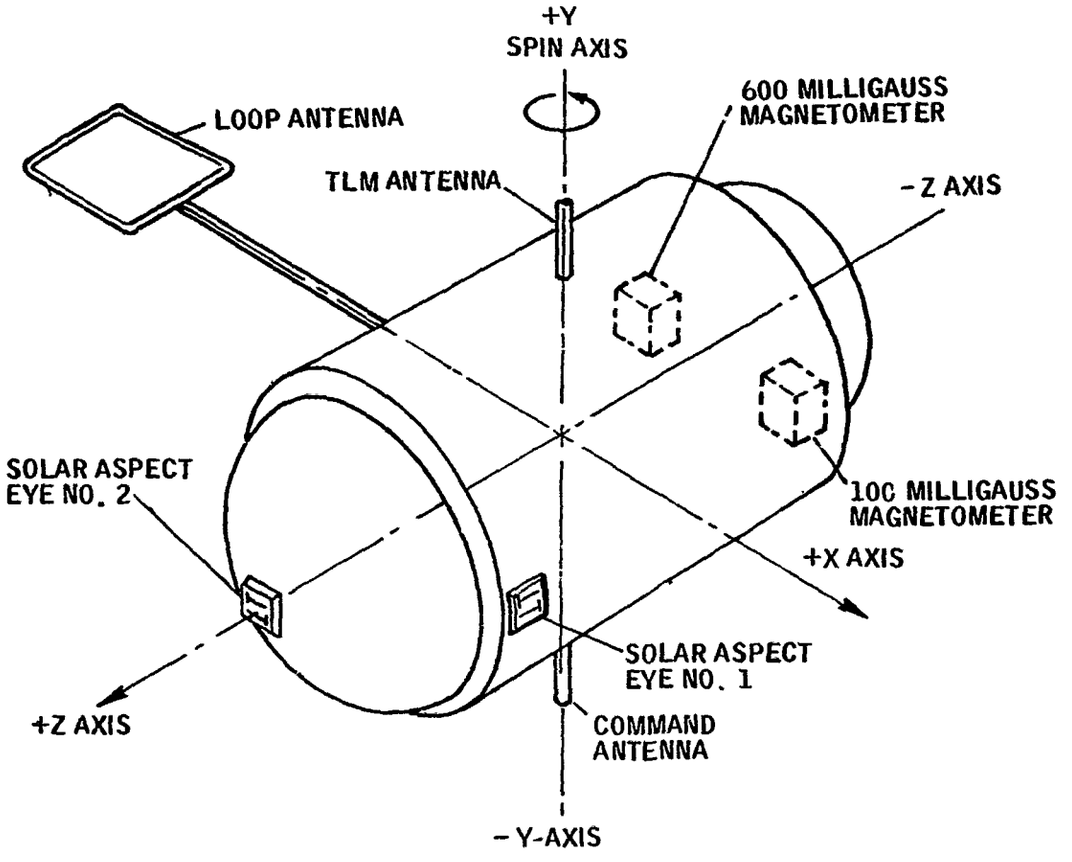


Figure 3. OV1 spacecraft solar aspect sensor and magnetometer locations.

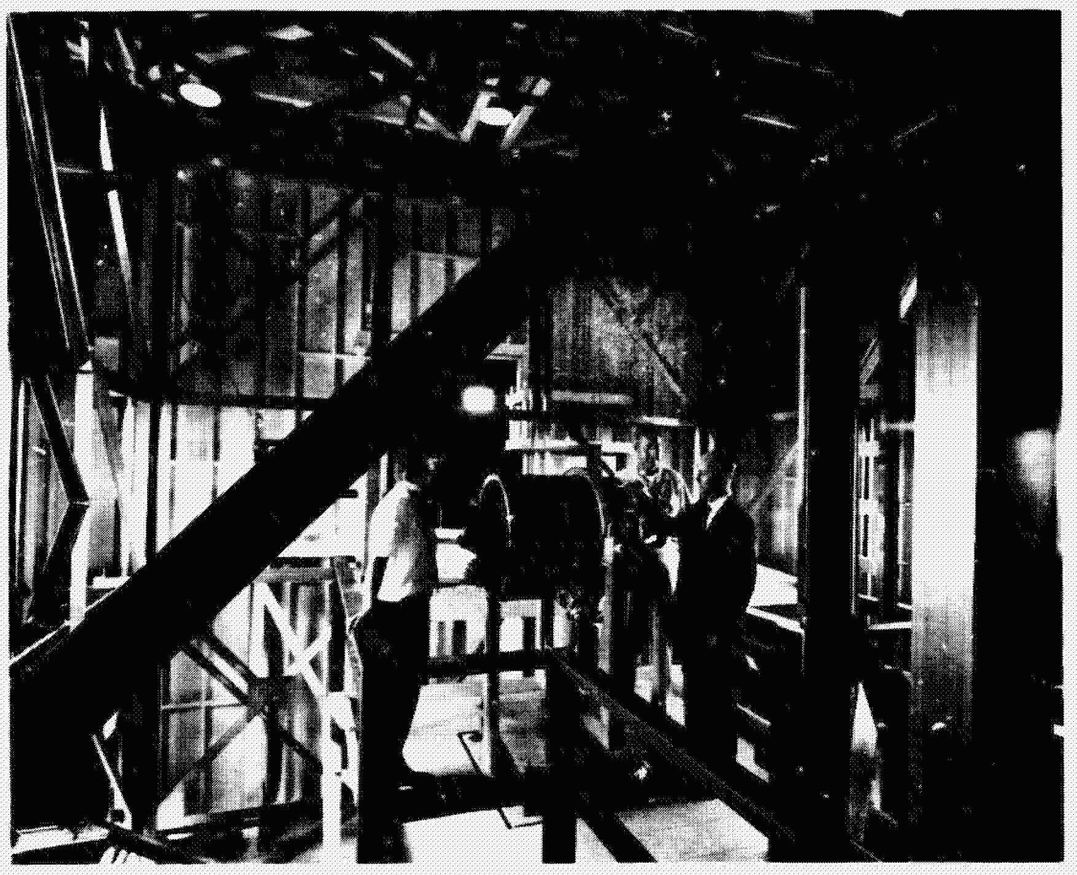


Figure 4. Four-square 20 ft. coil system with OV1 spacecraft installed.

which are electrically isolated from each other, are used to cancel any gradients which exist in the working volume. These windings are capable of cancelling any gradient up to 500 gamma per foot.

The system is designed to provide a working volume of five feet on a side within which the field varies by no more than one gamma, end to end. There is a 10 gamma variation over a volume six feet on a side, a 50 gamma variation over a volume eight feet on a side, and a 100 gamma variation over a volume nine feet on a side. The system is not yet operating within these specifications; these can only be accomplished with a closed-loop control system, extensive experimentation to cancel the residual gradients, and the removal of presently installed electronics and air conditioning equipment. The closed-loop control instrumentation and power amplifiers have not yet been purchased; hopefully funds to bring the facility to its design capability will become available within a year.

The coil system is currently in operation, although with less strict field tolerances, to perform magnetic surveys of the OV1 spacecraft both to determine the spacecraft field at the magnetometer and to determine the effective dipole of the spacecraft in each of its three flight axes, pitch, roll, and yaw for those flying Vertistat attitude control systems.

MAGNETIC FIELD SOURCES

It is axiomatic that a low budget spacecraft never has a negligible magnetic field. The three common sources of this field are:

1. permanent magnets,
2. the induced field surrounding highly permeable material, and
3. electrical current loops.

To measure the effect of the spacecraft fields on the magnetometer data, the flight magnetometers themselves are commonly used to make the measurements although when time permits these are removed and a more accurate laboratory magnetometer is installed in the same location. With the spacecraft installed in the coils and the field reduced to near zero the field measured by the magnetometers is the resultant of permanently magnetized material and that produced by current loops. Current loop effects are removed simply by turning off the spacecraft; the remaining field is due entirely to the permanently magnetized material. Current loop effects are then determined by operating the spacecraft through each of its commanded operational modes. Because of the proximity of the magnetometer to the battery the spacecraft is operated using the battery during these tests. It has been established that the fields due to solar cell panel

operation are small, apparently due to the intricate pattern of the wiring of the series-parallel solar cell network.

The fields due to these two effects are assumed to be fixed in magnitude and direction and so can be removed during flight data reduction. Where there are permanent fields there also exist induced fields and these are not fixed, but are a complex function of the ambient geomagnetic field. Consequently the typical magnitude of the induced fields needs to be determined and then considered as an error band around the flight data plots. The field in the coils is brought to a magnitude approximating that at the nominal flight altitude. Magnetometer readings are taken, the spacecraft is rotated 180 degrees, and the readings repeated. Since the permanent and current loop fields rotate with the spacecraft, the induced field is one half of the difference between the two readings. By repeating this with the ambient field in several orientations relative to the spacecraft an average value for the induced field is obtained.

MAGNETIC DIPOLE MOMENTS

Knowledge of the effective dipole moment perpendicular to each of the three principal flight axes is required for Vertistat stabilized spacecraft because of the low restoring torque of the gravity gradient system. In a typical installation for 500 nautical mile altitude, a 500 pole-centimeter dipole could produce attitude errors of 1^{o} to 10^{o} depending upon the dipole orientation. The same dipole, however, if due for instance to a DC motor in the telemetry tape recorder would cause a one milligauss field at the magnetometer--which is negligible.

To determine the dipole moment perpendicular to a given axis the spacecraft is rotated about that axis in a zero field while monitoring the signal of a stationary magnetometer probe located along the radial direction in the plane. Because of the complex nature of the spacecraft field the probe must be some distance large compared with the source separation to sense a dipole pattern. This places the probe outside the working volume of coil system, but since the probe is being held stationary in a fixed ambient field the ambient field can be compensated in the magnetometer and accurate readings obtained. The strength and position of the maximum and minimum points in the spacecraft field are noted as it is rotated. The dipole moment in the plane is then calculated from the relationship

$$M = (5r^3)\, B_{max}$$

where M is the dipole moment in pole-centimeters, r is the distance from the probe to the axis in meters, and B_{max} is the maximum magnetic field amplitude in gamma. The orientation of the dipole moment in the plane is determined by the angular location of B_{max}. The dipole moment obtained by this method represents the projection of the total dipole moment into the selected plane, the plane of

rotation. The spacecraft frequently have multiple sources in a given axis. However, at large distances a dipole approximation is sufficiently accurate for the magnetic moment determinations.

MAGNETIC DESIGN PROBLEMS

The OV1 spacecraft is basically an inexpensive carrier adaptable to a large variety of experimental payloads. The physical envelope is quite restricted requiring that the magnetometer be unavoidably close to other packages. Consequently it is imperative that steps be taken during design phase to recognize and avoid potential problems.

One of the problems is the permanent magnet parts in equipment--for instance, DC motors in the tape recorder and latching relays in the command and logic system. On OV1 these are placed on the opposite end of the spacecraft from the magnetometer and the net effect on the data is one or two milligauss. More important is the equipment mounted in the experiment payload section because of its proximity to the magnetometer. In those cases where it does not affect the operation of the equipment small bar magnets are epoxyed to the case of the disturbing package and are effective in reducing the dipole moment and the field at the magnetometer. In another instance, the packages were not compensated individually, but several small magnets were attached to the spacecraft to reduce the combined effect of all packages. Figure 5 shows a typical dipole moment curve in the spin axis plane both before and after compensation with permanent magnets applied to the spacecraft structure. The peak average field was reduced from 26 gamma to 4 gamma, or a moment reduction from 800 pole-cm. to 120 pole-cm.

In a recent updating of the Vertistat gravity gradient system it became necessary to reduce the stray fields of two wide gap C-shaped magnets employed in the damping mechanism without reducing their field in the gap. This was accomplished by replacing each C magnet with two bar magnets, the air gap on one end acting in the damping mechanism and the one on the other end acting to counteract the stray fields of the first at large distances.

Shielding permanent magnets reduces the permanent field, but at the expense of increasing the induced field by the addition of the high permeability shielding material. This technique, although we do use it, is used with caution.

The choice of structural materials is important, although aluminum is so universally used that there is seldom a problem here. However, a detector or other package may contain permeable materials for other than structural reasons, for example a transformer or shielding. Materials with effective permeabilities greater than unity are acceptable provided that the induced field

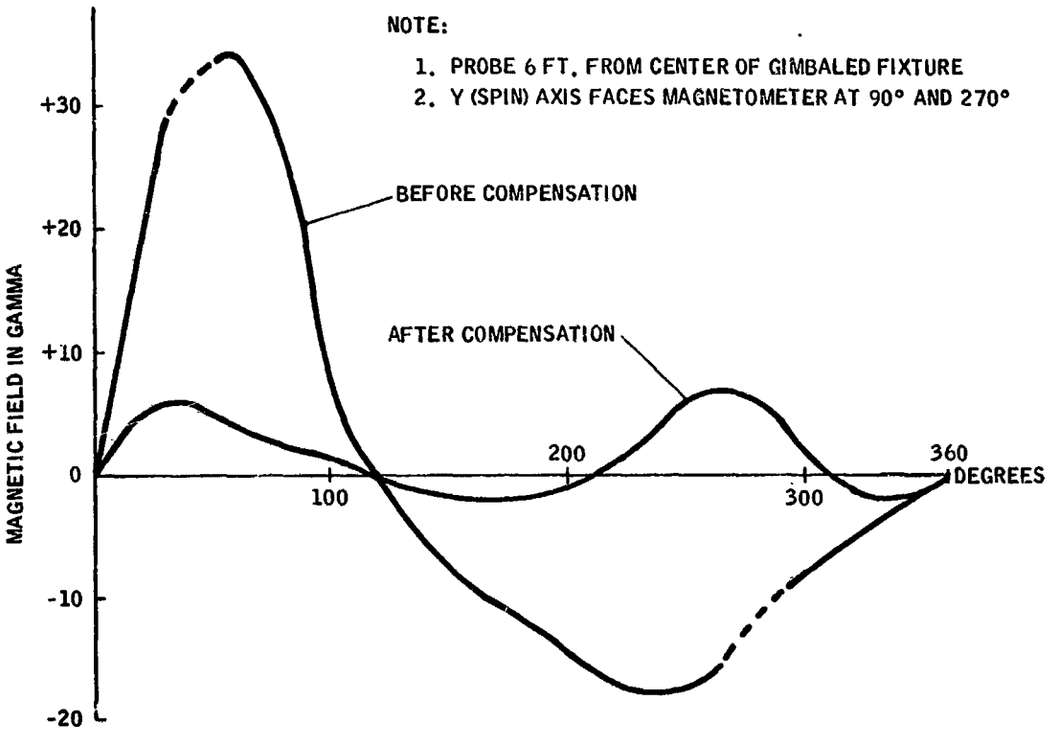


Figure 5. Typical dipole data (moment) in spin axis plane of spacecraft.

at the magnetometer is within tolerable limits. For example, a rod one-half inch diameter and six inches long if placed in a 0.3 oersted field would induce the following fields:

PERMEABILITY	B (18 INCHES)
1.5	1.4 gamma
10	1.9
100	8.9
1000	48.

Even if the induced field is acceptable one must be concerned with the material's remanence since spacecraft are commonly exposed to fields of 25 gauss during flight acceptance vibration tests. If use of the permeable material is unavoidable, it should place the package as far from the magnetometer as possible. To date the remanence values have not been sufficiently high to require deperming of the spacecraft.

The position of the magnetometers adjacent to the main power battery on the OV1 spacecraft has caused considerable comment. The effect of the battery is quite small. The silver-cadmium cells have a negligible induced field. Typical operating current drain is 1.5 amperes creating a field from internal battery current of seldom more than one milligauss at the magnetometer. Occasionally a package will have a high current relay or calibration pulse which will appear as a pulse on the magnetometer output, but these are ignored during data reduction. Inside the battery, cell interconnections and heavy current wiring are arranged to reduce the external field. This was not the case in the early OV1 batteries in which the wire routing was down one side of the battery and up the other. Changing to a compensating wire and cell layout in the battery reduced the external field by a factor of two. Heavy current wire leading from the battery is twisted pair, but elsewhere in the spacecraft no special precautions are taken.

The net field at the magnetometer of an OV1 spacecraft varies considerably from one model to the next, depending on the experiment payload being flown. Typical values are in the following ranges:

Permanent field	1 to 10 milligauss
Induced field	1 to 10 milligauss
Current loop field	0.5 to 1 milligauss

The effective spacecraft dipole moment is typically 400 to 700 pole-centimeters.

In summary, by these techniques the OV1 spacecraft flown to date have been magnetically clean--by the standards which they have had to meet. It is a low budget and very practical approach to the common problem of flying magnetometers in the near-earth environment for purposes other than magnetic field studies.

MAGNETIC CLEANLINESS PROGRAM FOR THE LUNAR SURFACE AND PIONEER MAGNETOMETERS

L. Howard Roberts
Philco-Ford Corporation
Space and Re-Entry Systems Division

N69-33971

This paper outlines the program required to build space flight equipment conforming to strict "magnetic cleanliness" specifications. The selection of parts, materials and construction techniques utilizing both integrated circuits and discrete components are discussed in terms of the design and development of the Pioneer interplanetary magnetometer and the Lunar Surface Magnetometer. Magnetic test data produced by these programs are summarized and analyzed.

1.0 INTRODUCTION

This paper outlines the magnetic properties control program required to satisfy strict "magnetic cleanliness" specifications. This work was carried out on the Pioneer interplanetary magnetometer and the Lunar Surface Magnetometer Programs, NASA Contracts NAS2-3397 and NAS2-3554. The specification for these instruments is as follows:

> "At the radius of three feet from the centroid of the instrument, the steady-state magnetic field induced by the instrument shall be less than plus or minus 2 gamma and the fluctuating magnetic field shall be held to less than plus or minus 0.5 gamma after being subjected to a standardizing magnetic field of 25 gauss. Changes in operational mode shall not change the magnetic field of the instrument other than as noted above."

Forewarning of the severity of this specification was provided by the fact that on a previous Philco-Ford contract, one subsystem of about 1/5 the complexity of either magnetometer was measured to have a magnetic field of 20 gammas at 3 feet after exposure to a 25 gauss field. While satisfying the magnetic cleanliness requirements of that program, the result pointed out that the magnetic cleanliness techniques then in practice would not be adequate for the magnetometers; i.e., based purely on a parts count, either magnetometer might be expected to have a magnetic field on the order of 100 gammas at 3 feet after a 25 gauss exposure.

Three basic guidelines were developed and served as the foundation of the magnetic cleanliness programs:

1. Elimination of all "hard" (permanent) magnetic materials

2. Reduction of fields due to "soft" magnetic material

3. Reduction of current-induced magnetic fields.

The implementation of each of these guidelines is discussed in Section 2. Results and conclusions are presented in Section 3.

2.0 MAGNETIC CLEANLINESS PROGRAM

2.1 GUIDELINE 1: ELIMINATION OF ALL "HARD" (PERMANENT) MAGNETIC MATERIALS

Any permanent magnet is constrained by the 2 gamma at 3 feet specification and adds directly to the instrument magnetic field. Inclusion in the design of permanent magnets would have required the use of other permanent magnets to achieve cancellation. Associated uncertainties in the manner in which the magnets track as a function of time, temperature, and shock were deemed unnecessary additions to an already complicated magnetic cleanliness program. Permanent magnetic materials therefore were excluded from use in the magnetometers. Implementation of this guideline was achieved via materials, parts, and design specifications. As examples, 2-phase ac servo motors instead of dc motors and mechanically actuated switches instead of latching relays were specified.

2.2 GUIDELINE 2: REDUCTION OF FIELDS DUE TO "SOFT" MAGNETIC MATERIAL

The utilization of "soft" magnetic materials was not permitted except for Kovar or Nickel leads and cases, and magnetic circuits. "Soft" magnetic materials as defined herein are those materials which may be depermed to zero, but which acquire and retain a "magnetization" when exposed to a magnetic field. It is this soft material which is most detrimental to instrument performance, since, aside from the specification, the magnetic field read by the instrument due to this source is a pure uncertainty in the data. It is this area that received the primary attention of the magnetics control program.

The magnetics control program was, in fact, primarily concerned with the implementation of this guideline which was achieved via a combination of parts selection, packaging, and screening.

2.2.1 Selection of Parts

The initial phase of the magnetic cleanliness program was to determine which of the large number of part types available to the design engineers were acceptable from a magnetic cleanliness standpoint. Subsequent screening of 100% of all parts has shown that the parts are, in fact, sufficiently repeatable to permit selection decisions based on a small measurement sample.

Integrated Circuits

The real purpose of the selection tests was to find an integrated circuit package that would be acceptable from the magnetic cleanliness point of view. Integrated circuits are of primary importance in this program since on the order of 1000 are used in each magnetometer. Further, magnetic measurement data was unavailable for integrated circuits of any description. Some results of the integrated circuit selection tests are given in Table 1.

TABLE 1 - INTEGRATED CIRCUIT MAGNETIC SIGNATURE DATA

PACKAGE	LEAD LENGTH	MAGNETIC FIELD AT 3" AFTER 25 GAUSS EXPOSURE - MEASUREMENT IN LEAD AXIS
Fairchild Black Ceramic (14 Lead)	5/16"	310 Gammas
	3/16"	124 Gammas
	.030"	10 Gammas
Fairchild B-H Forbes (14 Lead)	3/8"	128 Gammas
	3/16"	38.5 Gammas
	0.1"	9 Gammas
	0.06"	4.5 Gammas
Signetics (Corning Glass) Package (10 Lead)	5/16"	300 Gammas
	.125"	31 Gammas
	.06"	17 Gammas
Fairchild TO-84 Package (6 Lead)	3/16"	15 Gammas
	.03"	4 Gammas
Fairchild TO-84 Package (10 Lead)	.06"	15 Gammas

The integrated circuit packages selected for use are listed below in Table 2.

TABLE 2 - APPROVED INTEGRATED CIRCUIT PACKAGES

PACKAGE/MANUFACTURER	REMARKS
Fairchild BH/Forbes Flat Pack	This package is a 14-lead, ceramic package and is the best package tested to date for logic circuits and should be used wherever possible. Unfortunately this all glass package is not suitable for the high power dissipating linear circuits.

PACKAGE/MANUFACTURER	REMARKS
Signetics	This package is a 14-lead glass and Kovar package suitable for either logic elements or linear integrated circuits. It is not as good as the Fairchild BH/Forbes Flat Pack for logic elements or the TO-84 for linear circuits but is much superior to the standard TO-5 case which was deemed unacceptable.
TO-84	The TO-84 package is all Kovar with 10 Kovar leads. This package is somewhat superior to the Signetics package from the magnetic standpoint, and is a standard package for some linear integrated circuits.

Transistors

As in the case of integrated circuits, the large number of transistors utilized in each magnetometer necessitated an investigation of the available packages to guide selection. Results of this study are presented in Table 3.

TABLE 3 - TYPICAL TRANSISTOR MEASUREMENT DATA

PACKAGE	LEAD LENGTH	TYPICAL MAGNETIC FIELD AT 3" AFTER EXPOSURE TO 25 GAUSS FIELD - MEASURING ALONG LEADS
TO-18 Std. Nickel Can	.06"	25 Gammas
TO-18 (Fairchild) Nickel Silver Can	.06"	13 Gammas
TO-18 (Siliconix) Nickel Silver Can	.06"	5 Gammas
TO-46 (Short Version of TO-18)	3/16" .06"	15 Gammas 3 Gammas
Fairchild FK Package (4-Lead 80X80 Mil Ceramic)	.1" .06"	5 Gammas 2 Gammas
TO-5	1/16"	60 Gammas
RO-52A (Short Version of TO-5)	1/16"	25 Gammas

Here, the TO-46 was chosen as the standard transistor package, based on a reliability and magnetics trade-off between the TO-46 and the Fairchild FK package. Standard TO-5's were permitted only when absolutely necessary, the more desirable choice being the RO-52A. Transistors with the TO-18 standard Nickel can were excluded from the design.

Diodes

The standard glass DO-7 diode case with Dumet or Kovar leads was utilized wherever necessary. Some few reference diodes in standard TO-18 cans were accepted since they derive from standard transistor lines and are available in no other configuration.

Passive Elements

Resistors and capacitors are without exception specified to be nonmagnetic. In some isolated instances, resistors with Kovar end caps were accepted. For the most part, Angstrohm and Allen-Bradley resistors with oxygen-free copper leads were chosen.

Tantalum capacitors presented a problem since the standard package, used by all major manufacturers utilizes Nickel leads. Where the quantity involved permitted, tantalum capacitors with 180 alloy leads were procured.

Magnetic circuits of both powdered iron and tape-wound cores were used. Recognizing that the iron is prone to spreading stray field, care was taken to achieve stray field cancellation.

2.2.2 Packaging

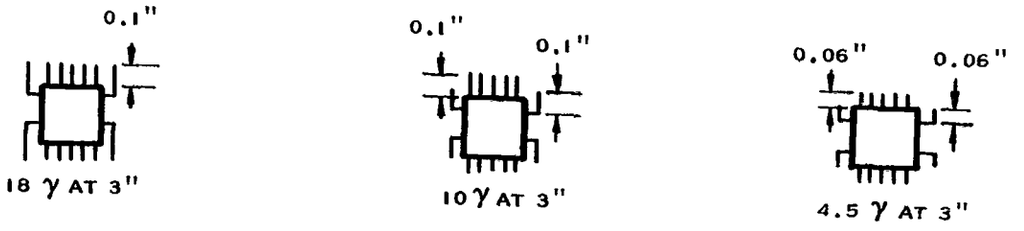
Reduction of instrument magnetic signature is achievable through the use of advanced techniques involving lead clipping, orientation, and close proximity packaging.

Lead Clipping

It is apparent from the data listed in Tables 1 and 3 that if the specification of 2 gammas at 3 feet after 25 gauss exposure is to be met, the minimum feasible lead length must be used. 0.060 inches was determined to be the minimum lead length required for welding. To provide margin for clipping error, possible re-work, and/or operator capability, a lead length of 0.085 inch was specified for all components except for the integrated circuits. For these, a cutting die allowed accurate clipping of the leads to 0.067 inches on 5 integrated circuits simultaneously. The sophisticated packaging technique required to utilize these short lead lengths is discussed in detail below.

Measurements illustrated in Figure 1 indicated the necessity of also clipping the four leads which exit from the sides of the I.C. case to the 0.067 inch length rather than clipping them to be flush with the leads extending from the ends. Figure 1 presents data for a single flat pack.

FIGURE 1 - MAGNETIC FIELD VERSUS LEAD CONFIGURATION



Based on the results shown in Figure 1, it is estimated conservatively that the preferred clipping technique results in a net field reduction of at least 1.7 gamma at 3 feet.

Cordwood Module Packaging

The technique utilized for discrete component packaging permits minimum lead lengths. The cordwood module consists of a number of closely packed discrete components suspended between two parallel 0.007 inch mylar substrates, or Mylars. The leads on each end of a part protrude through a Mylar unless the part with its clipped leads is too short to bridge the gap which is sized to the largest part. In this case, an additional length of 180 alloy ribbon is welded tc each lead on one side of the part. All leads are required to extend beyond the Mylar sufficiently to permit welding of a 0.010 inch by 0.031 inch 180 alloy interconnect ribbon. After welding any excess lead remaining is clipped by hand.

Integrated Circuit Packaging

Perhaps the most novel feature of the packaging design is the method used to package the integrated circuits. In addition to magnetic cleanliness, weight and volume constraints are also severe. A unique packaging approach has been developed which satisfies all three requirements.

The normal method used to mount integrated circuits is to lay the flat pack on a substrate, extend the leads horizontally, bend the leads down to the substrate, and form the weld on the horizontal substrate. This method is depicted in Figure 2.

Installation of an integrated circuit in this manner requires a lead length of about 0.120 inches. The technique developed for the magnetometer programs is to form the substrate rather than the integrated circuit leads. That is, the substrate, having the circuit connections, is made of 0.004 inch Type G-10 glass epoxy with etched 10 ounce copper traces. The board is heated to above its curing point while held in a die. The result is illustrated in Figure 3. The integrated circuit leads

FIGURE 2 - NORMAL INTEGRATED CIRCUIT INSTALLATION

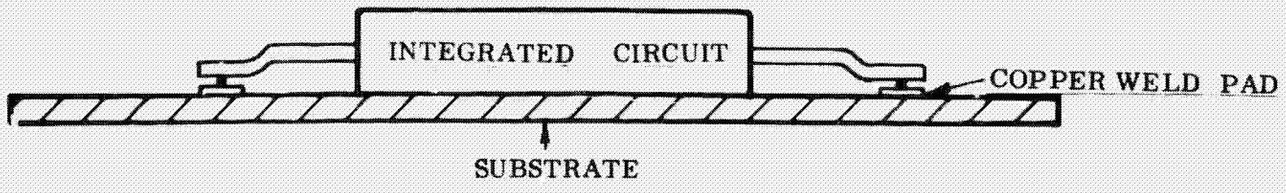
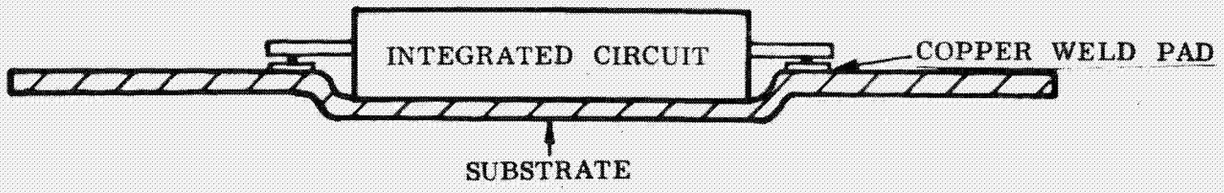


FIGURE 3 - PREFERRED INTEGRATED CIRCUIT INSTALLATION



are then of minimum length, extending horizontally from the flat pack. Note that the side-exiting leads which are also clipped to 0.067 inch from the corner incorporate a 180 Alloy ribbon extension which is welded to the copper pad on the substrate. Figure 4 depicts a substrate with 12 integrated circuits welded in place. Note that there are two different package types mounted on the substrate. The only magnetic material present on the substrate is the lead material on the flat packs.

FIGURE 4 - COMPLETED INTEGRATED CIRCUIT SUBSTRATE



In the early program stages, an attempt was made to determine empirically whether or not there exists a preferred way to stack the integrated circuits into modules; i.e., could the integrated circuits be installed practically in a manner such that some of the circuits shield others. Several configurations were investigated and the resulting data is given in Table 4.

TABLE 4 - RESULTS OF I.C. GEOMETRY TESTS

PARAMETER	CONFIGURATION	TYPICAL RESULTS (PERMED)
Substrate-to-Substrate Alignment	20 TO-84's	
	a. 5 srings of 4 elements, vertically aligned	47 Gammas at 6"
	b. As in a but alternate strings displaced horiz. by 1/2 element	61 Gammas at 6"
Lateral Separation	4 TO-84's	
	a. In-line, cases touching	18 Gammas at 6"
	b. Rectangle, 3/4" X 7/16"	27 Gammas at 6"
Vertical Separation	20 TO-84's (5 Stacks, 4 each)	
	a. .015" Separation	55 Gammas at 6"
	b. .003" Separation	38 Gammas at 6"

The results indicate that the optimum packaging technique is to place the I.C.'s in vertical stacks with minimum separation. This is fortunate, since this represents the simplest scheme from the packaging standpoint.

As indicated in the foregoing discussion, the integrated circuit module packaging design is highly attuned to the magnetic cleanliness requirements. Examples of completed subsystems are shown in Figures 5 and 6.

FIGURE 5 - INTEGRATED CIRCUIT MODULE

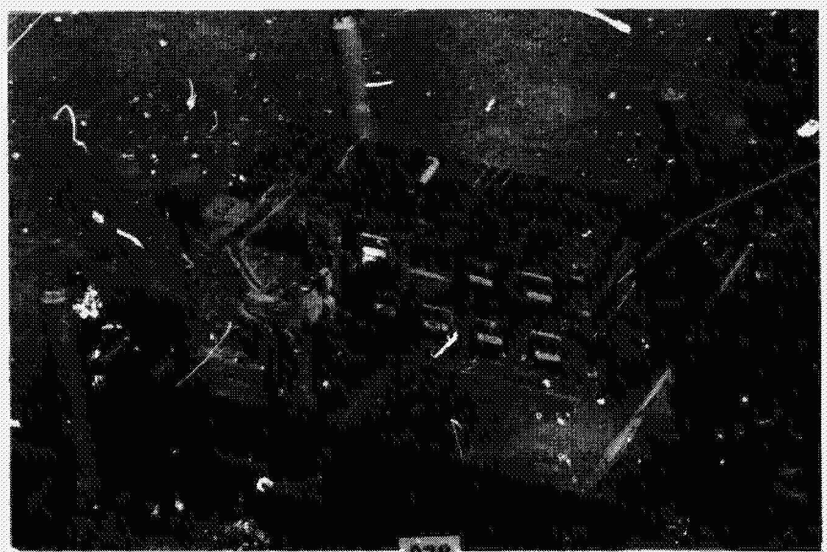
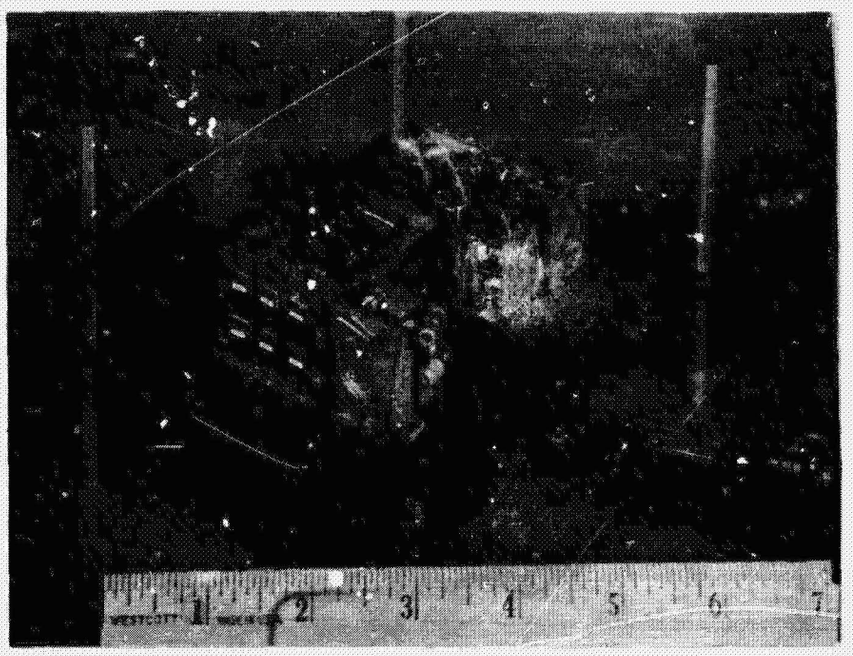


FIGURE 6 - I.C./CORDWOOD MODULE



2.2.3 Screening

In order to meet the magnetic cleanliness requirements, all parts are screened for magnetic properties. Data given in Tables 1 and 3 show the large improvement made in part by clipping the leads. The part value prior to lead clipping is too large to provide meaningful information about the part value when the leads are clipped. For this reason, all parts with leads made of magnetic material have the leads clipped prior to screening.

Parts screening is accomplished in a facility located in incoming inspection station. Parts are screened against pre-determined values, which comprise a specification. Failure to meet this specification results in scrapping of the part.

The screening station consists of a flux tank, perming and deperming facilities, a Hewlett-Packard 428b Magnetometer, and various part holding fixtures. The fixtures are used to hold the parts in quantities of up to 10 at a fixed known distance from the magnetometer probe. This method for holding the parts was implemented to expedite the screening process and to standardize the geometry thereby minimizing measurement uncertainty.

Parts which are located in proximity to the magnetometer sensors are screened to a much more exacting standard than those used in the electronics or mechanical subsystems. In the sensor area, parts must be nonmagnetic to within the sensitivity of the measurement apparatus. The most vexing problem encountered in the screening at this level is that brass, commonly used to solder terminals, spacers, and even structural elements, has traces of iron which render it unusable for this application.

After all parts have been screened individually another screening is performed at the module or subassembly level. Here the intent is to catch any gross mistakes which may have been introduced in subassembly fabrication. One specific instance occurred when an assembly technician replaced two non-magnetic screws in each sensor head by screws from open stock after the proper ones had been misplaced. Undetected, this action would have resulted in an error field of 2-10 gamma at each sensor.

The module screening results will be discussed in Section 3.

2.3 GUIDELINE 3: REDUCTION OF CURRENT-INDUCED MAGNETIC FIELDS

The approach to current-induced magnetic fields is simple, either reduce the current loop area to zero or use a compensating loop. Attention has been directed to the following areas:

a) **Motors** — Bifilar wound motors are used to minimize the effect of windings.

b) **Power Lines** — In all instances, power supply voltages, internal or external are run with their respective returns when making any interconnections in the system. The return is run directly over (or vice versa) the supply voltage, reducing the loop area to the thickness of the motherboard. This appears to be the minimum practical spacing.

c) **Power Subsystem** — The primary sources of stray fields in the power subsystem are the filter chokes. Here there are many turns of wire carrying substantial currents. In all instances, complementary chokes are used. That is, either an inductance is divided between two chokes and the chokes mounted back-to-back, or one choke is installed in the prmary leg and the other in the return leg of a circuit. These chokes are then installed to maximize cancellation of their stray fields.

d) **Sensor Heads** — Both the Pioneer and Lunar Surface (LSM) Magnetometers require electric heaters in the sensor areas. Both use dc current to drive the heaters. The LSM is the more critical of the two, since the heater is located within about 1 inch of the magnetometer sensor and is activated for long periods of time. Testing showed that heater elements can be fabricated to give nearly perfect cancellation. However, all heaters seem to have the problem that attaching the leads to the heaters forms a current

loop of sufficient size to give a field on the order of gammas at the sensor. To solve this problem, two heaters are used, wired in series and oriented such that the fields from the lead area cancel.

e) Modules

No attempt was made to configure the cordwood modules in a manner to minimize the magnetic fields due to current flowing in the components. The currents are generally quite small, and analysis of the geometries involved represents a formidable task.

The integrated circuits are another matter, however. Here, the geometry is rather simple and due to the fact that circuits are packaged in an orderly fashion, some care must be taken to prevent current-generated fields since power on the order of watts may be dissipated within the integrated circuit modules.

The approach used to solve this problem involved using a separate substrate, termed a Voltage-Ground Plane, in conjunction with each integrated circuit substrate. The Voltage-Ground Plane, as the name implies carries power and ground to the integrated circuits. The Voltage-Ground Plane contains holes appropriately positioned to fit over the integrated circuits and is bonded to the substrate. The power and power return conductors are indicated in Figure 7. The patterns are reversed in adjacent substrates, resulting in cancellation as illustrated in Figure 8.

3.0 RESULTS

Perhaps the most interesting result of the magnetic cleanliness program involves the manner in which the contributions of individual parts sum up in the total subsystem or system to give a net contribution. The approach implemented throughout the entire program has been to base control decisions on a linear combination of the individual part contributions. For example, it was on the basis of linear addition of part contributions that the decisions were reached to use a 0.067 inch integrated circuit lead length, and also to clip the side-exiting leads to 0.067 inch, even though the latter necessitates approximately 3000 extra welds per system. Also on the basis of linear addition, it was deemed necessary to use a TO-46 transistor package rather than the more common, and less expensive, TO-18 case.

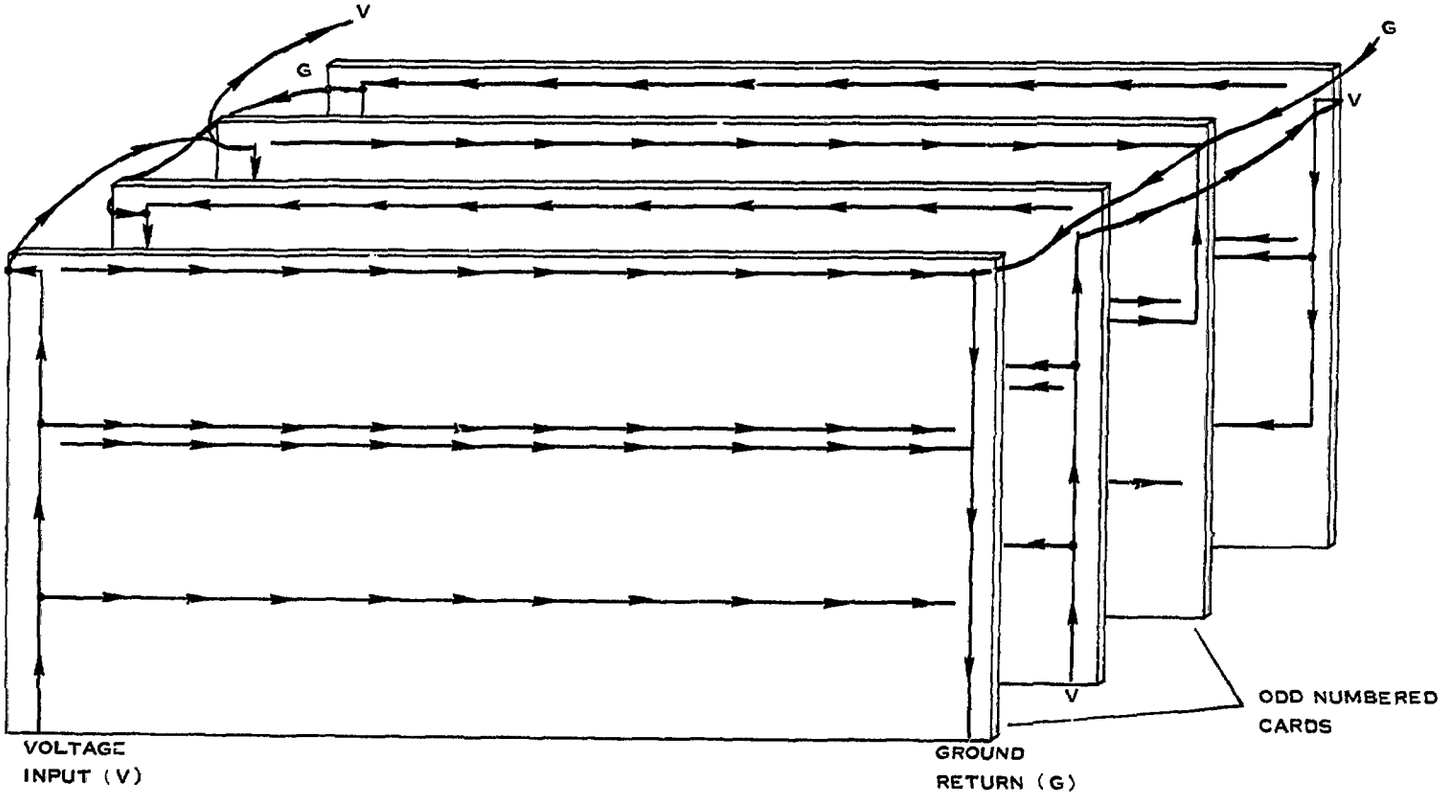
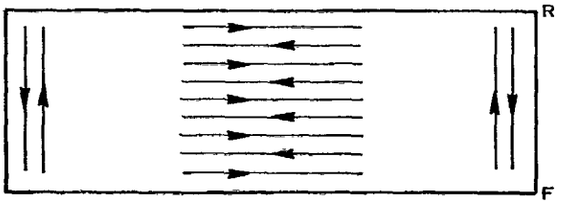


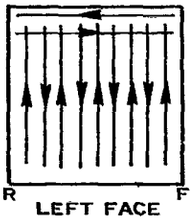
FIGURE 7 - GROUND AND VOLTAGE LINE LAYOUT IN DIGITAL MODULES (ARROWS SHOW CURRENT FLOW)

FIGURE 8 - EFFECTIVE FLAMENTARY CURRENTS IN INTEGRATED CIRCUIT MODULES



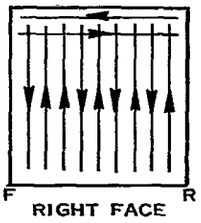
NET ZERO (±1 'UNIT')
VERTICAL DIRECTION
ZERO FOR ODD
NUMBER OF CARDS

TOP VIEW -- POWER, GROUND WIRING IN MODULES



LEFT FACE

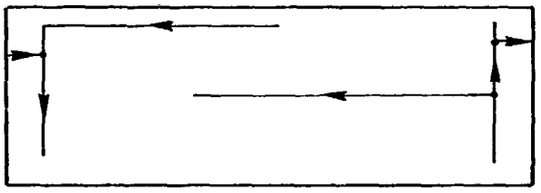
NET (+1) -
HORIZONTAL
CONDUCTORS



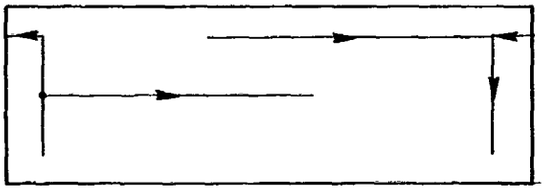
RIGHT FACE

NET ONE 'UNIT'
(±1 UNIT) FROM
VERTICAL CONDUCTORS
NET ONE UNIT FROM
HORIZONTAL CONDUCTORS

NET ZERO FROM HORIZONTAL CONDUCTORS
NET 1 ±1 FROM VERTICAL CONDUCTORS
ZERO FOR EVEN NUMBER OF CARDS



FRONT VIEW - EVEN NUMBER CARDS



FRONT VIEW - ODD NUMBER CARDS

NET ZERO ±1 - MODULE FACE
ZERO FOR EVEN NUMBER OF CARDS

The results indicate general agreement with the assumption of linear addition. It must be noted, however, that measurement values for each part that goes into a system are not recorded. For screening purposes, the part is compared to a limit that has been previously established from measurements on a number of parts of this type. Hence, the only knowledge available is that each part used contributes less than this specified value. By reference to Figure 9 and 10, actual part value may be compared to the specified part value for a relatively large number of parts. From this data, means are established for each part type and these numbers used to estimate the module signature, using linear addition. These numbers may then be compared to the actual measured values. In addition, the estimated module signature derived by addition of part acceptance limit values is used as a gauge for modules acceptance. These signature values are also presented.

The results of the magnetic cleanliness program may be seen from module (subsystem) measurements presented in Tables 5 and 6. In Table 5, the measured values are compared to estimates made using means determined from the data presented in Figures 9 and 10. In Table 6 the measured values are compared to estimates made using the acceptance limits for the electronic parts. An error coefficient is defined which is simply the ratio of measured value to estimated value.

Figure 11a presents both the distribution of the error coefficients derived in Table 5, and the mean value of these coefficients. Figure 11b presents the distribution of error coefficients derived from Table 6. Although the mean value for error coefficients derived from Table 6 is very nearly unity, this result is fortuitous since high accuracy was not required for measurements intended for engineering evaluation only. Furthermore, values for the off-axis components of the part field are little better than engineering estimates, although data was taken on a very limited number of parts.

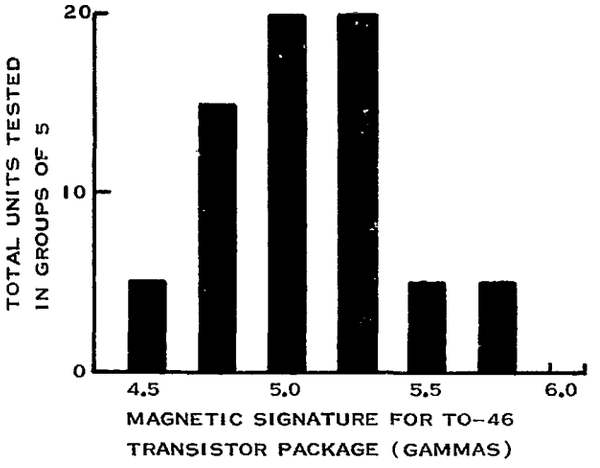
The most meaningful result derives from considering only the Y-axis measurement for each subsystem. The Y-axis is colinear with the part leads and concrete data is available for each part. For the estimate using mean-values for parts (based on Table 5), the mean measured value is 1.11 times the mean estimated value. For the worst-case estimate, (based on Table 6) the mean measured value is 1.07 times the mean estimated value. The consistency of these results indicates that estimates using linear addition are probably accurate to within 10% for this type of circuit packaging.

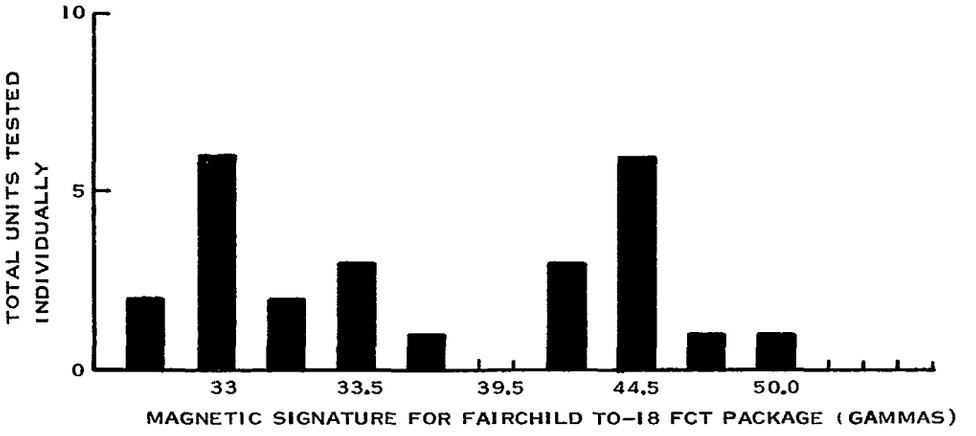
The extent of the program success in eliminating permanent magnetic material is illustrated by the subsystem depermed values shown in Table 7.

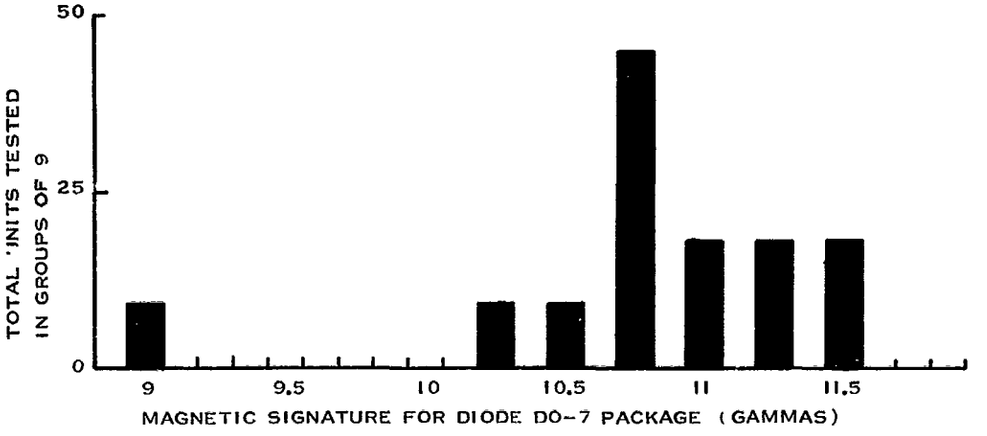
ACKNOWLEDGEMENTS

The author wishes to express his gratitude to Dr. K. L. Rose for his many helpful suggestions in preparing this paper, to Walter Buchler for his help in testing, and to David Whitelaw for his help in data reduction.

FIGURE 9 - TRANSISTOR AND DIODE MAGNETIC DATA DISTRIBUTIONS







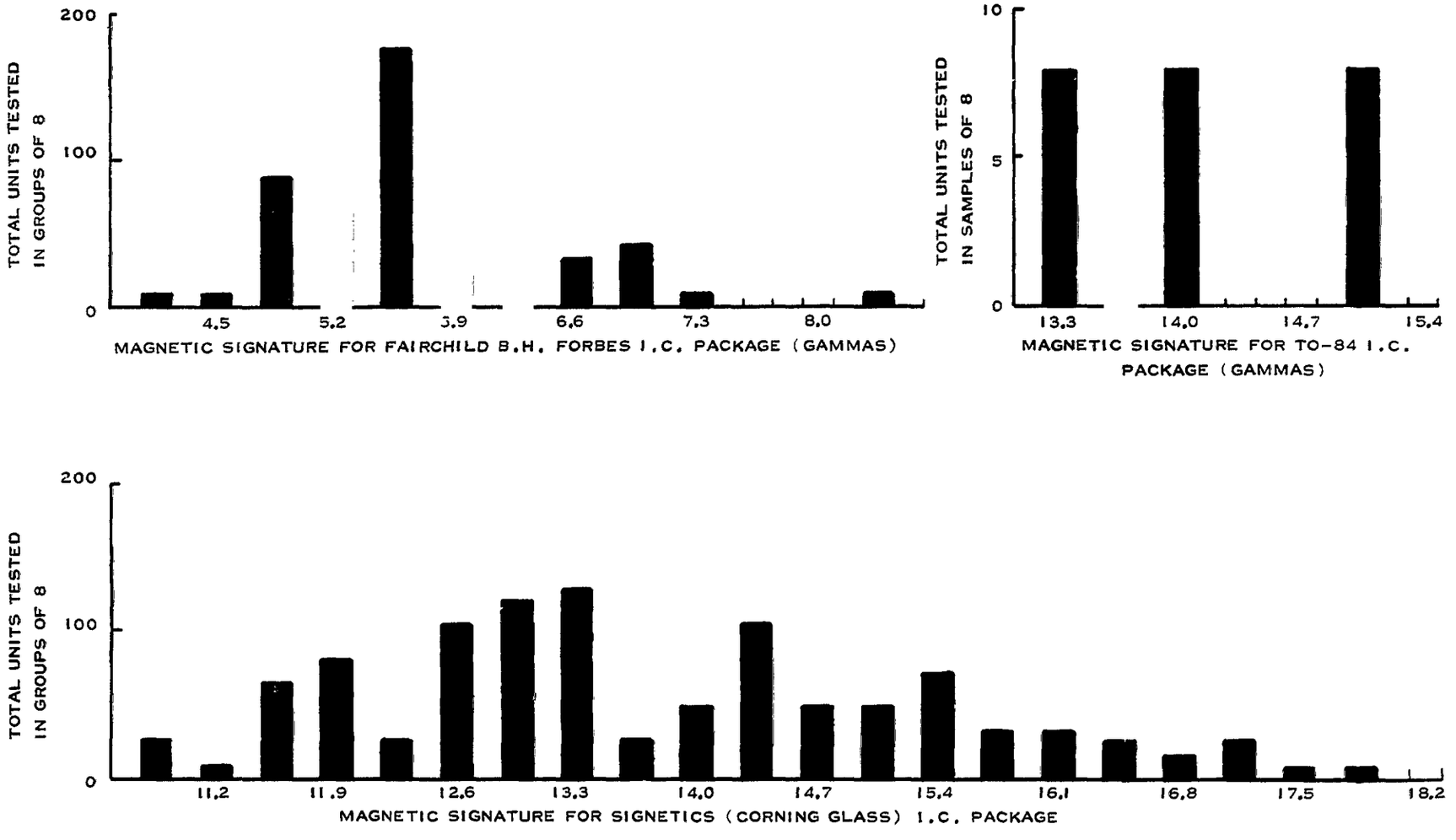


FIGURE 10 - INTEGRATED CIRCUIT MAGNETIC DATA DISTRIBUTIONS

TABLE 5 - MODULE TEST DATA AND ESTIMATES USING PART MEAN VALUES

SUBSYSTEM	ESTIMATE - MEAN VALUES USED (GAMMAS AT 12")			MEASUREMENT (GAMMAS AT 12")			ERROR COEFFICENT		
	X	Y	Z	X	Y	Z	X	Y	Z
LSM Scientific Sequencer	5.26	6.74	.71	5.00	8.80	0.15	.95	1.3	----
LSM Arithmetic/K Register	8.08	9.23	0.95	3.9	14.4	0.35	.48	1.56	----
LSM System Timer	2.89	3.14	2.57	3.0	4.7	4.9	1.04	1.49	1.9
LSM Site Survey	2.42	2.67	.28	1.4	6.5	.1	.58	.41	----
Pioneer Calibrator	12.49	8.81	6.81	9.1	7.6	6.6	.73	.86	.97
Pioneer Sin/Cos Coeff Stor.	1.37	12.45	8.20	0.2	13.0	11.0	----	1.04	1.34
Pioneer Buffer Clock	5.58	5.83	3.48	2.5	6.5	2.0	.45	1.11	.58

TABLE 6 - MODULE TEST DATA AND ESTIMATES USING PART ACCEPTANCE LIMITS

SUBSYSTEM	ESTIMATE - PART VALUES USED (GAMMAS AT 12")			MEASUREMENT (GAMMAS AT 12")			ERROR COEFFICIENT		
	X	Y	Z	X	Y	Z	X	Y	Z
LSM Scientific Sequencer	6.87	9.40	1.02	5.00	8.80	0.15	.73	.94	----
LSM Arithmetic/K Registor	9.85	11.7	1.3	3.9	14.4	0.35	.39	1.23	----
LSM System Timer	4.2	4.6	5.0	3.0	4.7	4.9	.72	1.02	.98
LSM Site Survey	3.3	3.3	.34	1.4	6.5	0.1	.42	1.96	----
Pioneer Calibrator	14.2	10.2	7.6	9.1	7.6	6.6	.63	.74	.87
Pioneer Sin/Cos Coeff Stor.	2.1	18.3	12.6	0.2	13.0	11.0	---	.71	.87
Pioneer Buffer Block	6.6	7.0	4.4	2.5	6.5	2.0	.38	.93	.46

FIGURE 11a - RATIO OF MEASURED VALUE TO ESTIMATED (MEAN VALUE) VALUE

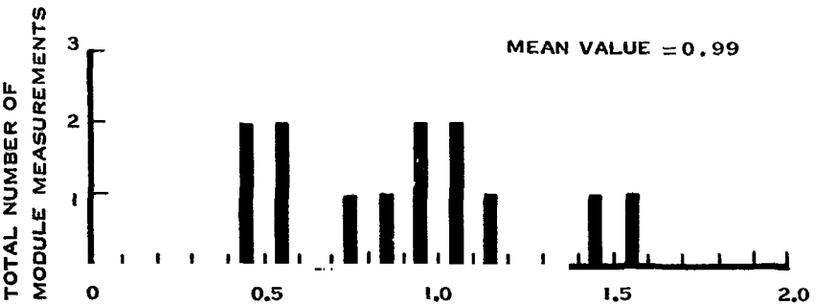


FIGURE 11b - RATIO OF MEASURED VALUE TO ESTIMATED (WORST CASE) VALUE

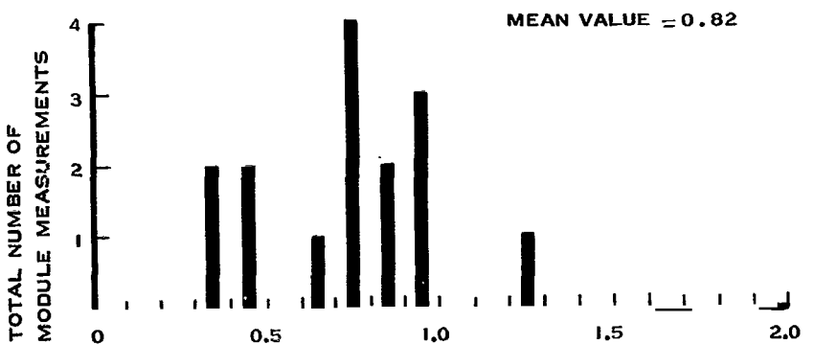


TABLE 7 - LSM MAGNETIC SIGNATURE (GAMMA)

	MEASURED - 12" TEST RADIUS					
	PERMED - 25 GAUSS			DEPERMED		
	X	Y	Z	X	Y	Z
Sensor Electronics	6.3	13.5	4.8	0	.3	.3
Input Driver	1.3	.3	.4	0	0	0
Sensor Driver	.8	2.2	.8	.5	.5	.5
Power Filter	.4	7.0	3.1	0	0	0
Engr Data Elex	14.5	8.9	11.3	.1	.1	0
Transformer Module	.6	1.2	1.4	0	0	0
MPX-A/D Converter	8.2	2.3	5.5	0	0	.1
Cal Offset Bias Gen.	9.4	3.8	3.1	.2	.1	0
Output Data Buffer	.7	.2	3.3	.1	.1	.1
Offset Command Logic	1.0	.1	3.5	.1	.1	0
Engr Data Seq.	.6	.1	2.8	.1	.1	0
Arithmetic Unit	3.9	.4	14.4	0	.3	.1
System Timer	3.0	4.9	4.7	.2	.3	.3
DC/DC Converter	2.1	3.6	2.7	0	.1	.2
Memory	12.0	20.1	15.0	.7	.1	.5
Scientific Sequencer	5.0	.2	8.8	.1	.1	0
Site Survey	1.5	.1	6.5	0	.1	.2
Electro/Mechanical S/S	10.0	5.9	1.1	.2	.5	.4
TOTAL	81.3	73.8	93.2	2.3	2.8	2.7
Equivalent Field at 36" (Total ÷ 27)	3.0	2.7	3.5	.1	.1	.1

J. Dale Barry, Paul J. Coleman, Jr.,
Uri Fehr and Larry L. Simmons[1]

A MAGNETICALLY SHIELDED CHAMBER USED IN SIMULATING SPACE ENVIRONMENT

Barry, J. Dale, Coleman, Jr., Paul J., Fehr, Uri, Simmons, Larry L., "A Magnetically Shielded Chamber Used In Simulating Space Environment", Spacemagnetic Exploration and Technology Symposium, (August 1967) University of Nevada, Reno.

N69-33972

ABSTRACT

A walk-in, magnetically shielded chamber used in the testing and calibration of sensitive space-flight magnetometers is discussed. The chamber is a two-shield cubical design, using a highly permeable, annealed shielding material. The facility includes a large three-dimensional coil array surrounding the chamber and a small, calibrated, double Helmholtz coil array at the geometrical center of the chamber. Within the Helmholtz coils is a non-magnetic temperature chamber in which a magnetometer sensor can be subjected to variations in the ambient temperature of -50°C to +100°C. A non-magnetic fixture used for 360° rotation of a magnetometer sensor is placed within the temperature chamber. In addition, the magnetically shielded chamber is situated upon a non-magnetic table which allows 360° rotation of the complete facility.

Key Words: Shielded, Non-Magnetic, Space, Construction, Helmholtz Coils, Temperature Chamber.

INTRODUCTION

In the development of relatively sensitive magnetometers, it is necessary for the instruments to be tested and calibrated in a magnetically quiet environment. The purpose of this report is to describe a magnetometer testing facility which provides such an environment in the laboratory. More specifically, this facility performs three functions. First, the facility provides a region in the laboratory which is relatively free from magnetic

[1]Institute of Geophysics and Planetary Physics, University of California at Los Angeles.

field gradients and magnetic noise. Second, it provides a means of generating, within this region, the magnetic fields which are desired for testing and calibration of the magnetometer probe. Third, it provides, within this same region, a means of varying the temperature of the magnetometer probe being tested.

The magnetic environment in the laboratory normally includes the following types of fields: the earth's magnetic field which varies slightly with time, permanent magnetic fields produced by ferromagnetic materials, time dependent magnetic fields produced by electrical circuits in nearby machinery, and induction fields produced by magnetically permeable materials in the presence of ambient laboratory magnetic fields.

In such an environment, a calibration or accurate study of the performance of a relatively sensitive magnetometer is impossible. It is possible to remove the instrument and test equipment to a site which is sufficiently remote to be free from the last three types of fields listed. It is then only necessary to compensate for the earth's magnetic field and its variations. An alternative to a remote test site is a magnetically shielded chamber in which the shielding is provided by walls of relatively high permeability. It is a relatively simple matter to construct a small chamber which provides effective shielding against magnetic noise and which is large enough to contain most magnetometer probes. However, if it is desired to produce fairly uniform magnetic fields within the chamber, it is necessary that the chamber be sufficiently large that the walls do not appreciably influence the magnetic fields produced at the center of the chamber. Furthermore, since the properties of magnetically permeable materials vary considerably with temperature, it is necessary that any control of the temperature of the magnetometer probe within the shielded region be performed by a temperature chamber which is contained within the shielded volume and insulated from the shielding walls.

In any such facility, the accessibility of the temperature chamber and of the mounting fixtures for the magnetometer probe which is to be tested must be considered. Such considerations led us to conclude that a magnetically quiet spherical working volume, eight feet in diameter, would be desirable. However, a study of possible construction techniques indicated that a cubical geometry could be obtained at considerably less expense. As a result, the magnetically shielded chamber provides an eight foot cubical working volume.

The cubical chamber that provides the magnetic shielding has two walls separated by six inches. Each wall is covered with a layer of 4-79 molybdenum permalloy steel .070 inches thick. Access to the inside of the chamber is provided by an inner and outer sliding door. Within the chamber controlled magnetic fields are generated by a triaxial Helmholtz coil array with a nominal coil diameter of 30 inches. A non-magnetic

temperature chamber is centered within this coil array. The completed facility is shown in Figure 1.

In this report, the details of the design during construction of this facility will be described. In addition, the results of various performance tests will be given.

CONSTRUCTION OF THE MAGNETICALLY SHIELDED CHAMBER

As the first step in the construction of the shielded chamber, a wooden framework was constructed from two by fours and sheathed by 1/2-inch plywood sheets to form inner and outer walls separated by approximately six inches.

This steel used to provide the magnetic shielding was 4-79 molybdenum permalloy in the form of sheets 0.0070 inches thick. The metal sheets were precut to the patterns required for the shielding chamber and then annealed by the manufacturer (Allegheny Ludlum Company). These sheets were glued to the plywood walls of the wooden structure. The sheets used on the inner walls were 8 feet in length and 19 inches in width, while those used on the outer walls were 9 feet in length and 17 inches in width. The sheets were attached with the long dimension vertically on the outer wall, and horizontally on the inner wall. The resulting shielded chamber is shown in Figure 2. The spacing between the adjacent sheets on a given wall was approximately 1/4 inch. These quarter inch gaps were covered by strips of shielding material 4 inches wide and of the same length as the wider sheets. Thus, considerable overlap of the shielding material was provided in order to minimize magnetic flux leakage at the 1/4-inch gaps. These 4-inch strips had been predrilled before annealing to provide screw holes every 5-5/8 inches along the length of the strip. These strips were held in place by aluminum screws that pass through 4 inches by 4 inches by 3/32 inch aluminum plates, through the holes provided in the strips, through the 1/4-inch gap between adjacent sheets of shielding material, and anchored in the heavy wooden framework.

The 4 inch by 4 inch by 3/32 inch aluminum plates immediately ahead of the heads of the screws were included to distribute the load produced by the screw over a wider area of the shielding material and thereby to minimize the stress in the shielding material. These details are illustrated in Figure 4. A similar method was employed to improve the shielding at the intersection of adjacent walls. With this type of construction, the gaps between the overlapping magnetic shields are held to less than 0.002 inches.

Access to the inside of the shielded chamber is provided by a rectangular doorway 38-1/2 inches wide and 82-1/2 inches high. The design and construction of the doors with which to seal this doorway to the 0.002 inch gap specifications was one

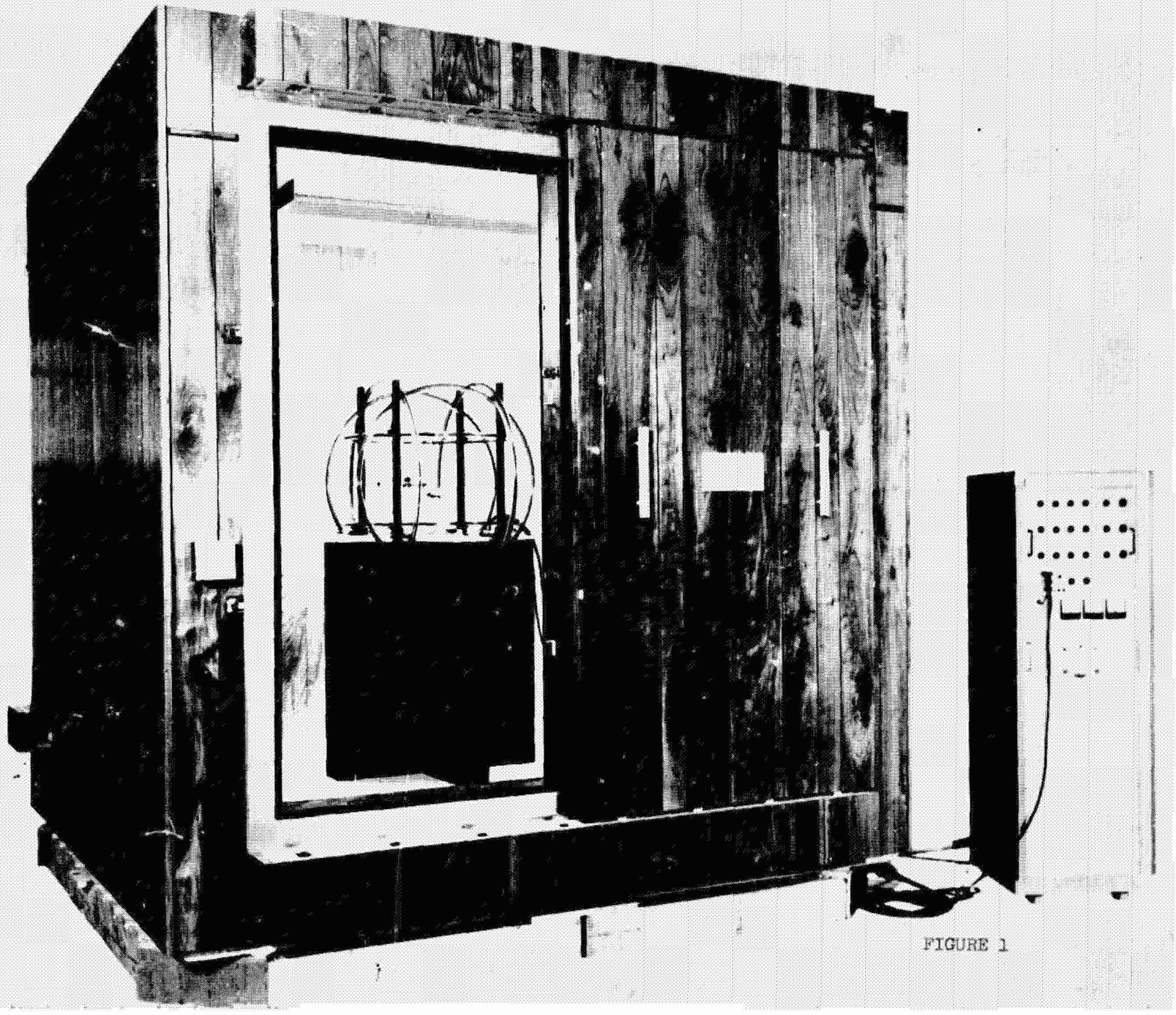
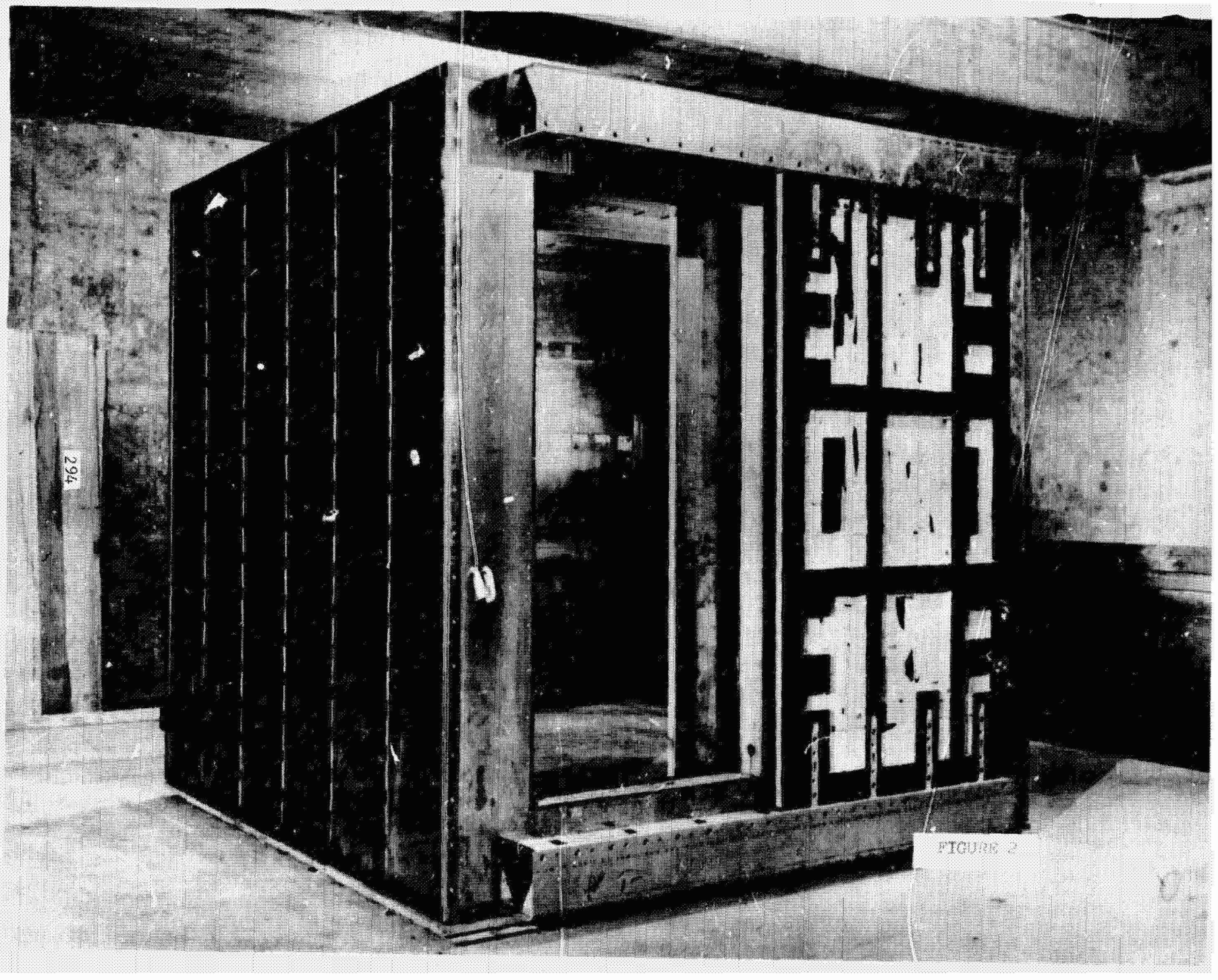


FIGURE 1



294

FIGURE 2

of the more difficult tasks encountered in the development of this facility. Two doors were constructed, each of a heavy wooden framework with the shielding material affixed to only one side of each door in the manner just described. The wooden framework of the doors was from two by fours and 1/4 inch plywood. The doors are 8 inches longer and 8 inches wider than the doorway. They are mounted in such a way that in a closed position, the shielding material on the doors is pressed flat against the shielding material of the chamber walls in an area 4 inches wide running around the edges of the doors.

In order to provide sufficient pressure over this area to insure the desired small gap between the shielding material of the doors and that of the chamber walls, the volume between the inner and outer doors is evacuated slightly in the manner employed by Patton (1962). Both doors are mounted on heavy horizontal aluminum tracks and use plastic rollers. The tracks for the inner door are attached to the floor and ceiling of the chamber and those for the outer door are attached to the outside wall of the chamber at the same heights. The tracks run parallel to the wall of the chamber which contains the doorway. The motion of the door from the closed to the opened position is to first move the outer door directly away from the wall about 2 inches. The door is then rolled parallel to the wall along the tracks until it is clear of the doorway.

Two access ports 6 inches by 6 inches were provided for test connections in opposite walls of the chamber just above the floor level. A third access port 12 inches by 12 inches was provided in the center of the ceiling for air conditioning. In order to minimize the leakage of magnetic fields through the access ports, external shields are attached to the inside and outside of each access port, as may be seen in Figure 2.

The chamber was built upon a wooden pad constructed of two by fours laid parallel to one another and separated by 12 inches. The entire unit was then mounted upon an aluminum turntable to enable the rotation of the chamber about a vertical axis through the chamber's center. This turntable was constructed by first mounting in the concrete laboratory floor a square aluminum plate 59-3/4 inches on a side and 2 inches thick in such a way that the level is maintained to within 0.0001 inch. A circular ball race 54 inches in diameter had been cut in the plate and 72 balls are used to distribute the load. The balls are bronze, 1.250 inches in diameter, and are held in position by a five section spacer. An aluminum plate identical to the one mounted in the floor was then placed upon the resulting ball bearings. Attached to this plate is an aluminum I-beam frame which provides the support for the wooden pad carrying the magnetically shielded chamber. The completed turntable is shown in Figure 3.

FIGURE 3

For the most part, the construction techniques employed in the fabrication of the shielded chamber were relatively standard. However, special handling was required for the permalloy steel. The annealed steel was shipped from the factory in special padded containers. The sheets were handled with vacuum cups. Flexing of the sheets was avoided as much as possible. Drilling, cutting, bending, and heating were kept to a practical minimum. Wiring for lights and vacuum switches was built into the wooden chamber walls. Care was taken to insure that all wiring was run in tightly twisted pairs carrying the input in returned strands to a given point. The completed chamber was covered with a 1/4 inch layer of wood in order to minimize the possibility of damage to the walls due to accidental shocks.

RECTANGULAR COIL ARRAY

In order to measure the performance of the shielded chamber, it is desirable that uniform magnetic fields which can be varied in orientation and magnitude somehow be generated in the region containing the facility. Since a coil array which could provide such a uniform field would be much too large to be contained in the limited space available in the laboratory, such fields cannot in practice be provided. A coil array consisting of three rectangular coils was constructed with their axes mutually orthogonal and with the center of each coil array at the center of the shielded chamber. The geometry of these coils, which had to be completely contained within the laboratory, was far from optimum. However, these coils allow us to obtain valuable data concerning the relative field attenuation provided by the shielded chamber for magnetic fields of various magnitudes and frequencies. The coils also allow us to reduce the earth's ambient field on the chamber wall.

Each of the six coils in this array was wound with two turns of ten conductor ribbon wire giving a total of 20 turns per coil. Each conductor in the ten conductor ribbon wire was AWG 14 wire of the standard C-10 type with a resistance of 2.46 ohms per 1000 feet. The various coil constants for the three rectangular coils are given in Table 1.

TABLE I

RECTANGULAR COIL ARRAY SPECIFICATIONS

Coil	Dimensions (feet)	Separation (feet)
Vertical	26.4 x 29.6	10.0
East-West	12.0 x 29.0	10.0
North-South	12.0 x 24.0	10.0

FIGURE 4

HELMHOLTZ COIL ARRAY

The magnetic fields at the center of the shield chamber are controlled by a triaxial set of Helmholtz coils observable in Figures 1 and 5. The center of this coil array is located at the geometrical center of the shielded chamber. Each coil has two windings. One winding, the null coil, is normally used to cancel any residual DC field within the chamber and the other winding, the calibrate coil, is used to provide the desired calibration or test field. The coils are wound on lucite forms which are mounted on brass angle brackets. Each coil consists of 25 turns of AWG 22 copper wire which has a resistance of 22.76 ohms per 1000 feet. The various coil constants are given in Table 2 for each of the three orthogonal Helmholtz coils.

TABLE 2

HELMHOLTZ COIL ARRAY SPECIFICATIONS

Coil	Radius (null)	Radius (cal.)	K_c (μa/γ)	K_n (μa/γ)
V	35.12 cm	36.07 cm	16.07	15.67
E-W	40.45 cm	41.40 cm	18.27	17.82
N-S	37.77 cm	38.74 cm	17.12	16.73

The fields of the Helmholtz coils are generated by calibrated currents provided by the control unit shown in Figure 4. The unit is basically a constant voltage source coupled to a manually controlled resistive binary ladder. The fields for the calibrate Helmholtz coil are manually switched using dials calibrated in discrete units of 1γ, 10γ, 100γ, and 1000γ with a range of ± 13,332γ. Another dial, not as accurately calibrated, is manually switched in units of 10,000γ with a range of ± 1 gauss.

The fields for the null Helmholtz coil are manually switched using a potentiometer with a range of ± 100 with a resolution of 0.1γ. Another dial provides a field of ± 1200γ in units of 100γ. The polarity is changed by a DPDT toggle switch.

TEMPERATURE CHAMBER

A means of temperature variation of a sensor over a wide range was found to be necessary. Most magnetic devices are sensitive to the ambient temperature to some degree, and space flight magnetometers which are to be evaluated must be calibrated over the temperature ranges anticipated in space.

FIGURE 5

The UCLA facility is now equipped with a second generation temperature system shown in Figure 5. From our initial system we learned that no metallic materials should be included in the system near the sensors and definitely not in any moving parts of the system. For example, an aluminum nut used to position the probes was found to not only contribute a magnetic field but its field was temperature dependent.

Our present system utilizes completely non-magnetic materials, styrafoam walls, phenolic linen supports, and tygon input-output lines. The styrafoam box is contained within the triaxial Helmholtz coil array, and provides a working volume 18 inches high, 14 inches wide, and 14 inches deep. Hot or cold nitrogen is introduced to and expelled from the chamber, through 1/2" I.D. tygon tubing.

The phenolic linen platform used for mounting magnetometer probes may be seen in Figure 5. The platform is attached to phenolic discs at the top and bottom of the chamber through three 1/2" threaded phenolic rods. By adjustment of the support nuts, a probe may be placed in the geometric center of the Helmholtz coil array and aligned in the plane of the coils. The top and bottom rotating phenolic discs are coupled to the stationary chamber through 1/8" teflon bushings to insure smooth operation at both high and low temperatures. A phenolic shaft, which is attached to the top disc, extends out of the chamber with a pointer attached to indicate the position of the probe. The dimensions of the platform and chamber allow evaluation of probes with a maximum overall dimension of 10 inches. The permanent field of a sensor and the relative alignment of two sensors in a probe can be determined in a single operation using two of the orthogonal Helmholtz coils.

The temperature control system is basically a standard liquid nitrogen system. Liquid nitrogen at 25 lb/in.^{2} is supplied to a temperature control console which is located approximately 15 feet from the chamber (see Figure 6). The console then routes the nitrogen through either the heating or cooling section and the hot or cold nitrogen (the nitrogen is always gaseous before leaving the console) is routed to the test chamber through separate insulated 1/2" copper lines.

The heating system consists of a 50 foot evaporation coil made of 1/2" soft drawn copper tubing which is used to preheat the liquid nitrogen. The preheated nitrogen is introduced into a 4500 watt circulation heater which raises the nitrogen temperature to any desired value up to 300°C. The hot gas is next flow-regulated by a 1/2" throttling valve which is in series with an electronically activated solenoid valve. In parallel with the throttle and solenoid valves is a 1/4" bleed valve which provides a continuous, low volume flow of gas to reduce temperature deviations from the desired value. The cooling system is identical with the heating system except no evaporation coil or heater is used.

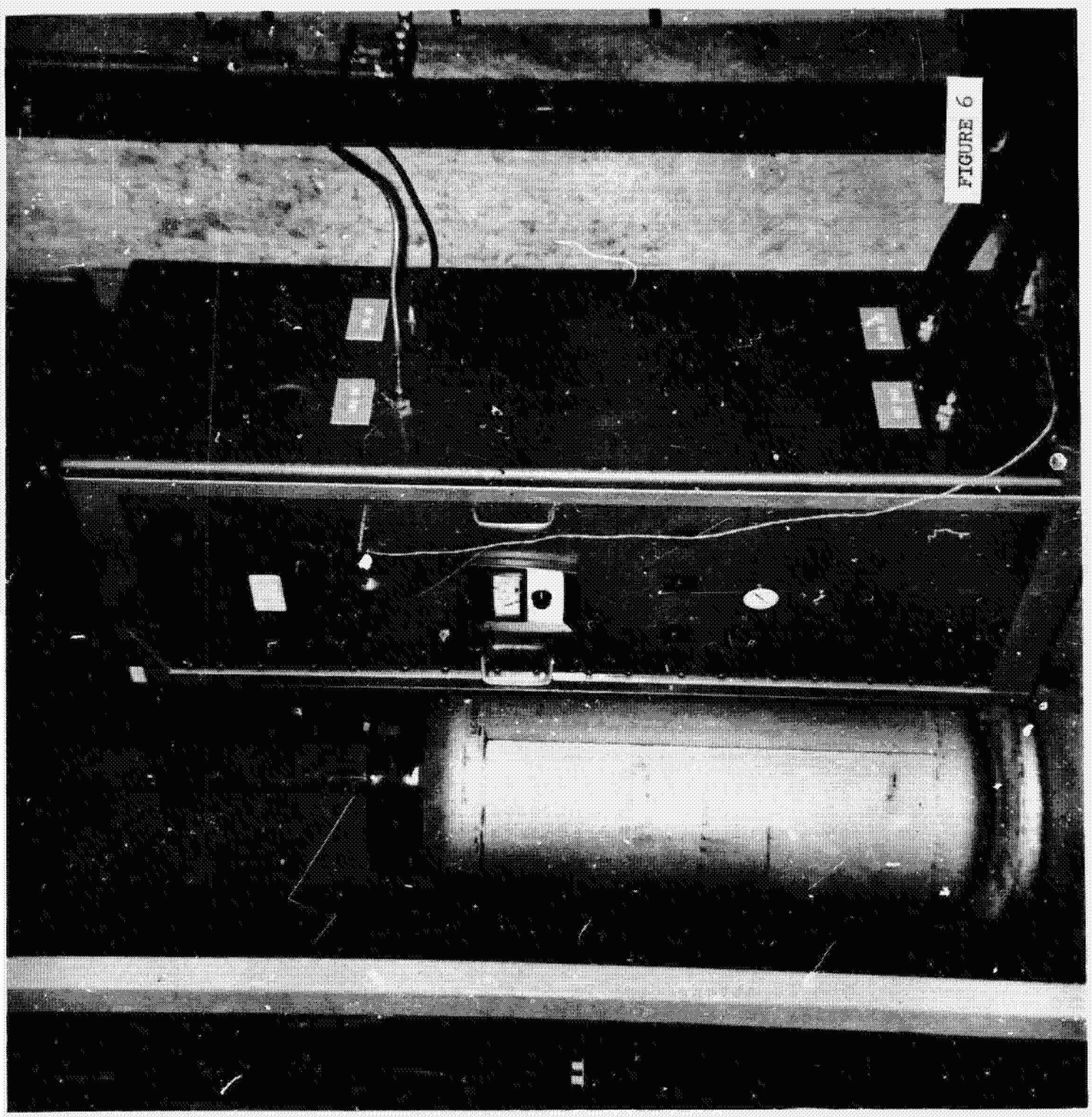


FIGURE 6

The electronic control system consists of a stationary thermistor located within the chamber near the test specimen which detects the ambient temperature. A level detector in the console senses the thermistor output and activates a relay which in turn activates the proper solenoid valve. The chamber and console then constitute a closed-loop system that can maintain any temperature from -50°C to +100°C to within ±0.5°C. By using nitrogen that is hottor or colder than the desired temperature the volume of gas required is substantially reduced.

AIR CONDITIONING

Considerable care is taken to insure that the walls of the magnetically shielded chamber are not subjected to significant temperature variations. The outside walls of the magnetically shielded chamber are protected from temperature variations by the laboratory air conditioning. It is also necessary to protect the inside walls of the shielding chamber from temperature excursions which might be introduced due to heat produced by equipment operating within the shielded chamber or due to losses from the temperature chamber located within the shielded chamber. To do this, special air conditioning for the inside of the shielding chamber is provided. This air conditioning is supplied by a unit rated at 23,000 BTU/Hr and capable of an air flow of 800 Ft^3/min.

The air conditioning unit is located about 20 feet from the shielded chamber. Connections from an aluminum supply duct is connected to the chamber with flexible rings so that the rotation of the chamber is not impaired.

PERFORMANCE

To describe the performance of the magnetically shielded chamber, we consider the attenuation characteristics and the ambient interior field gradients. We distinquish the attenuation characteristics and the ambient interior field gradients. We distinquish the attenuation characteristics as two types, that related to DC magnetic fields and that related to AC magnetic fields. We will use the terms, DC attenuation and incremental attenuation, respectively.

The DC attenuation is of the order 10^2. This value can apparently be changed by simply deperming or perming the walls if one defines the DC attenuation as the ratio of the external field to the internal field. The magnitude of the interior field at the center of the chamber immediately after the shielded chamber was completed and placed upon the rotation table was about 400γ. The walls of the shielded chamber were then depermed

using a small degausser and the center interior field decreased to about 30γ. The field magnitude can be further reduced to about 5γ at the chamber center by careful deperming.

The incremental attenuation was determined by rotating the chamber in the earth's field and by applying various AC magnetic fields with the use of the large rectangular coils. Another method incorporated a portable rotating magnet which was moved perpendicular to a chamber wall from a near distance of 5 feet from the chamber wall to a far distance of 20 ft. The coils and the rotating magnet were calibrated in a location far from any magnetic or permeable materials. These values are comparable to those obtained for other magnetic shielded chambers of similar dimensions.

We have used the rotation capability of the chamber to determine the DC attenuation. This provides the DC attenuation for the wall in the unpermed condition and is also indicative of the incremental attenuation since the interior field can be monitored as the chamber rotates in the uniform earth's field. The field inside the shielded chamber was determined by mapping the field components at one foot intervals.

The interior gradients were found to be a function of the deperming and perming of the chamber walls. For instance, the gradients immediately after chamber assembly and before the wall degaussing were about 20γ per inch. After the first degaussing, gradients of about 1γ per inch were obtained. After several degaussings, we now have gradients of about 0.2γ per inch within a 10 inch diameter sphere at the chamber center. This is well within our main working volume as most of our magnetometer probes have dimensions of less than 6 inches.

We have found that the laboratory noise was much less then expected. During the day, we observe a field variation within the shielded chamber of about 2γ rms. During the late evening and early morning hours we observe a field variation within the shielded chamber of about 0.2γ rms at frequencies less than 10 cps. Consequently, we have found it advantageous to do our most sensitive tests during the late hours. We have also been able to work with the doors open during the day. This has not affected the gradients within the main working volume to an appreciable extent nor has it affected our day time noise levels. The open door also allows us constant visual examination of the sensor orientations, and negates the requirement of enclosing a laboratory assistant within the chamber where his movements may cause unnecessary field variations.

FUTURE IMPROVEMENTS

The facility described has provided an adequate environment for all of its intended uses. However, in the future we anticipate having larger dynamic range, and more sensitive

instruments. We are therefore planning improvements in the following areas.

One area of future improvement will be extending the dynamic range of the Helmholtz coils to $\pm$ 1 gauss. In recent work it has been found desirable to produce fields in the order of the earth's field, but the present coil system is constructed of a wire size that will not support the current required without joule heating which in turn (since we are using a constant voltage system) gives rise to slow field drifts. With a new set of coils we will have the capability of introducing calibrated 1γ or more field steps superimposed on a quiet 1 gauss field.

The styrafoam temperature chamber presently in use is inefficient in that a good hermetic seal is not maintained. A new temperature chamber is being planned that will provide a better seal, with the anticipated result being a further increase in the efficiency of heating and cooling. We anticipate the temperature transition time to be significantly reduced when desired so that thermal shocks may be applied to magnetometer sensors.

Since flight magnetometers in general are vector field measuring devices there are usually three orthogonal sensors. At present we can only rotate about one axis which evaluates only two sensors at a time. In the near future we anticipate installing a new fixture which will provide us with rotation about two orthogonal axes, and will therefore allow complete evaluation of an instrument without reorientation of the probe on the rotating platform.

Due to the interest in and demand for very sensitive magnetometers for space use with resolution of less than 0.01γ, we have plans to alter the magnetically shielded chamber itself. This change will be to introduce a cryogenic magnetic shield into the facility. With such a system, we expect to increase our major attenuation factor and the incremental attenuation factor to greater than 10^6. The cryogenic shield is to be placed in the geometrical center of the magnetically shielded chamber. This is to reduce to a minimum the magnetic fields and gradients which can be trapped in the cryogenic shield when it goes superconducting. The cryogenic shield is to be cylindrical with an interior diameter of 10 inches and a long dimension of 6 feet. It will be possible to rotate the shield about its vertical axis and introduce a device to alter the relative orientation of a probe within the cryogenic shield.

List of Figures

Figure 1. The completed operational magnetically shielded chamber and Helmholtz coil control console. The system is used to provide a field free region in which to test sensitive magnetometers.

Figure 2. The magnetically shielded chamber immediately after construction and prior to installation of the wooden protective covering.

Figure 3. The aluminum turn table upon which the magnetically shielded chamber was placed. The completed facility may be rotated 360° about the vertical axis.

Figure 4. The Helmholtz coil control console used to control the magnetic field produced by the Helmholtz coils in the center of the chamber.

Figure 5. The Helmholtz coil system, non-magnetic temperature chamber, and probe rotation platform. The systems are used in evaluating sensitive magnetometers.

Figure 6. The temperature control console which provides hot and cold nitrogen gas to the non-magnetic temperature chamber. The system is used to maintain any probe temperature between -50°C and +100°C to within ±0.5°C.

ACKNOWLEDGMENT

This project was supported in part by NASA Grant NsG 237-62.

BIBLIOGRAPHY

Patton, B.J., Fitch, J.L., "Design of a Room-Size Magnetic Shield", JGR 67, 1117 (1962).

L. L. Simmons[1]

MAGNETIC TESTS ON THE ATS-1 SPACECRAFT

Simmons, L. L., "Magnetic Tests on the ATS-1 Spacecraft", Spacemagnetic Exploration and Technology Symposium, (August 1967) University of Nevada, Reno.

ABSTRACT

The first Applications Technology Satellite was tested to determine its magnetic properties. The test methods and results are discussed.

Key Words: Magnetic tests, Applications Technology Satellite.

N69-33973

INTRODUCTION

In September and November of 1966 magnetic tests were conducted on the Applications Technology Satellite (ATS-1) spacecraft at the Goddard Space Flight Center. The tests were conducted in the then newly completed 40-foot coil facility located in a remote, relatively quiet area at the Goddard Space Flight Center. Due to the newness of the facility, some desired tests, such as full solar simulation, were not possible, and other tests in which the automatic earth compensation system was employed were of questionable value due to the fact that the system was only partially completed.

The purpose of this paper is to present data on the types of magnetic interference that affect relatively sensitive magnetometers on board spacecraft that have been designed without giving high priority to magnetic contamination or isolation of the magnetometer sensor.

SPACECRAFT MAGNETOMETER

The instrument used in making the measurements described in this paper was the ATS-1 fluxgate magnetometer. Its operation has been described by Barry and Snare (1966). Basically, the instrument consists of two fluxgate magnetometers with the sensors oriented normal to each other, and at 45° with respect to the spacecraft spin axis. The dynamic range of each of these magnetometers is ±50γ. As shown in Figure 1, the axis designated A measures fields along an axis which passes through the main body of the spacecraft, and the B axis does not intersect the spacecraft.

[1]Institute of Geophysics and Planetary Physics, University of California at Los Angeles.

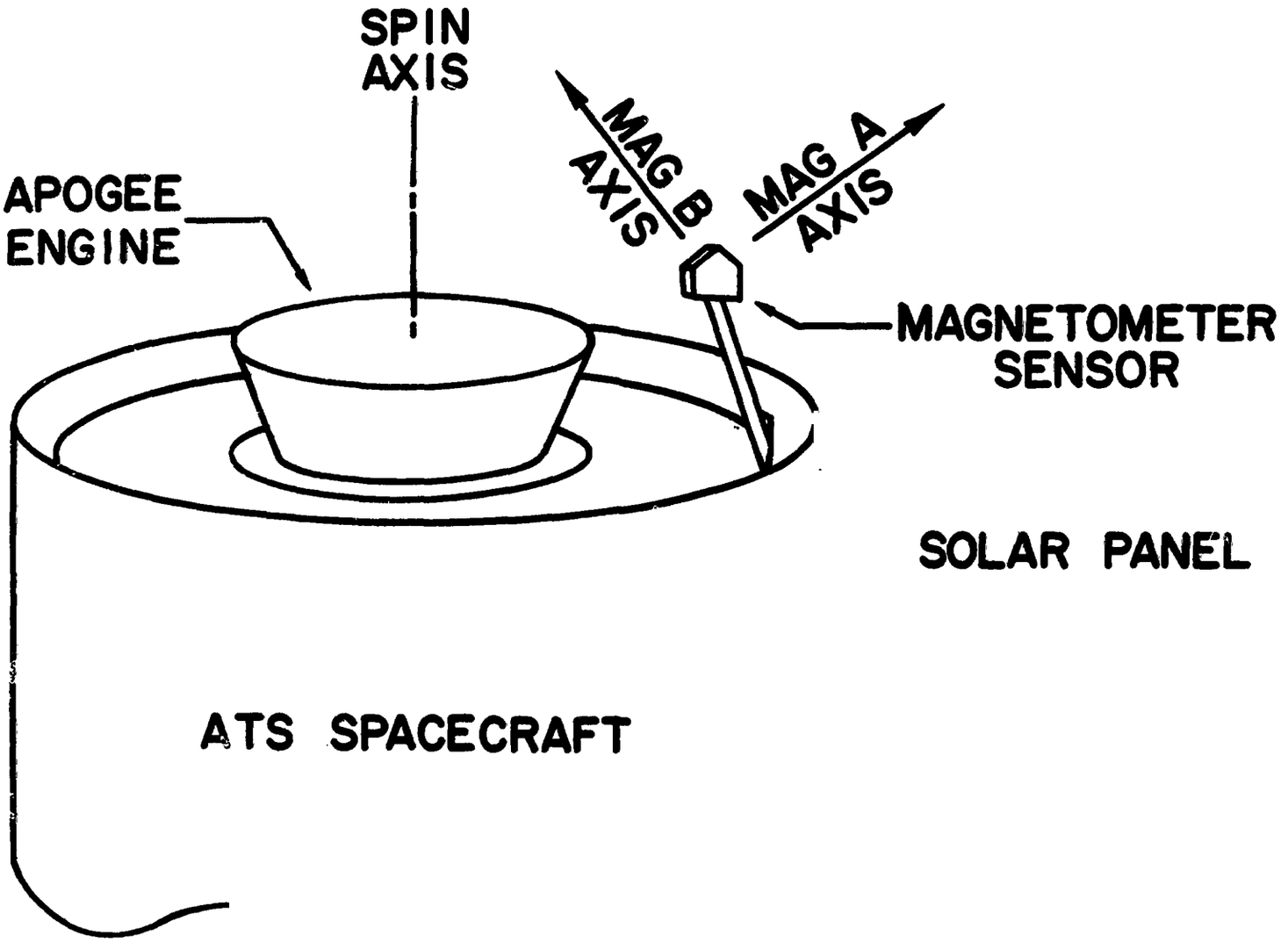


Figure 1

The Applications Technology Satellite

showing the position of the magnetometer sensor

The overall instrument has a dynamic range of +925γ to -675γ which is obtained by extending the range of the basic magnetometer with a digital offset system. The bandwidth of the basic magnetometer is 50 Hz. The large bandwidth is required to allow tracking of large field changes by the digital offset system with sufficient speed to provide overall field data up to frequencies of 2 Hz. The field data from the basic magnetometer are passed through a low-pass filter which cuts off at 2 Hz. The telemetered data has a bandwidth of 2 Hz, which eliminates frequency aliasing of field information.

Another feature of the magnetometer is that in the presence of a large amplitude fluctuating field the sensitivity is automatically changed from ±50γ to either ±100γ or ±200γ depending on the fluctuation magnitude.

SPACECRAFT MAGNETIC DESIGN

Figure 1 indicates the location of the magnetometer probe with respect to the spacecraft. The probe is located only 6 in. from the solar panels, and the total boom length is only 9 in. The boom length and location were determined by considerations of shroud size and relation of sensor to apogee motor rather than the optimum magnetic location.

Due to the proximity of the probe to the spacecraft hardware, the effects of magnetic materials becomes more pronounced. The only magnetic specifications for the spacecraft were those imposed on the scientific instruments. As a result hardware was designed giving main consideration to size and weight, and in some cases to most desirable material. For example, the housing of the Spin Scan Cloud Camera is made of Invar steel as a low thermal expansion characteristic was desired.

D.C. MAGNETIC FIELDS

The D.C. magnetic field of the spacecraft, attributable to magnetic materials on the spacecraft, was measured by rotating the spacecraft through 360° in a zero field environment with spacecraft power off.

Magnetometer data were obtained by removing the spacecraft magnetometer probe from the boom and mounting the flight spare magnetometer probe. An inter-instrument cable was connected from the flight spare probe to the flight spare electronics located approximately 40 ft from the spacecraft. The magnetometer was then powered and monitored by the experiment ground support equipment (G.S.E.). In this configuration no power was needed on the spacecraft to determine the spacecraft permanent field.

The spacecraft was rotated 360°, and the permanent field perpendicular to the spin axis was taken as one-half the difference between the 0° and 180° readings. The fields measured were +50γ and +100γ on the magnetometer's A and B axes, respectively. As stated earlier the facility's automatic earth compensation system was not operational at

this time, but the 0° and 360° field readings were in good agreement. The recordings of the earth's field also showed no significant changes during this test period, so these field values were taken as being due only to the spacecraft.

The parallel component of the spacecraft's permanent magnetic field was measured by holding the G.S.E. operated magnetometer sensor at the location of the magnetometer boom and rolling the spacecraft up to and away from the sensor. The fields measured were 2γ and 25γ on magnetometer axes A and B, respectively. The test was repeated several times, and each test was in good agreement with the original test.

A significant source of D.C. magnetic fields was found to be current loops in the spacecraft power system. As an example, we found a D.C. field shift of about 20γ as a result of current being drawn from the solar panels instead of from the spacecraft batteries.

One day of magnetic testing was devoted to commanding the spacecraft into various operational modes and observing the D.C. magnetic field changes at the magnetometer probe. Table 1 is a list of commands sent and the associated changes in fields. These values are averages from up to seven separate executions of the same command. Note that many commands create fields in excess of 10γ, and also in general they are reversible, e.g., regulator #2 on produced -42γ change on A, and regulator #2 off produced +42γ change on A. In general the fields created by a particular configuration of the spacecraft have no permanent effect; over a period of time in orbit the signatures of these commands can be identified and used to help reduce flight data.

A.C. MAGNETIC FIELDS

A second type of magnetic disturbance present on the ATS-1 prototype spacecraft was what will be called A.C. magnetic fields. In fact some of the fields, such as those observed from the University of Minnesota magnetic electron spectrometer experiment were caused entirely by alternating currents in conjunction with the movement of magnetic materials, such as the Spin Scan Cloud Camera.

Again referring to Table 1, these disturbances were observed to be in the order of 10γ as measured with the ATS-1 fluxgate magnetometer. The basic bandwidth of the instrument is 50 Hz, so the actual peak field amplitude of some of the spikes is unknown. In space flight the telemetered data from the ATS-1 magnetometer have a bandwidth of approximately 2 Hz. Therefore these sources of interference are not observed in the space flight data.

CONCLUSIONS

The pre-flight magnetic tests discussed have provided specific magnetic interference data on each system of the ATS-1 spacecraft. These data have proven useful in evaluating orbital data from the satellite since its launch in December, 1966. However, insufficient time was allocated

Table 1

Current Loop Magnetic Fields

Command No.	Command Description		ΔA	ΔL
	+28v applied to s/c		+ 1	+ 2
	Xmitter and encoder on		+ 6	0
002	PCM encoder #1 on		- 2	+ 1
003	TM Xmitter #4 on (Xmtr #2 off)		- 4	0
335	EME payload regulator on		+10	0
066	EME Power Buss on		+ 5	0
341	UCLA on		4	0
077	PCM Encoder #2 off		- 3	- 1
023	Xmitters 2 and 4 off		+ 5	- 1
212	Xmitters 2 on and 4 off		- 5	0
127	PCM encoder #2 on		- 3	+ 2
211	Repeater #1 mult. access on		+ 5	0
001	Xmitter #1 TWT H.V. on		+ 3	+ 1
253	Repeater #1 off		- 7	- 1
164	Xmitter #2 TWT #3 fil. on		+ 3	+ 3
126	Xmitter #2 TWT H.V. on		+ 7	+11
374	Repeater #2 off		-11	-13
336	Repeater #2 mult. access mode on		+ 5	+ 2
076	Pace #1 on; Pace #2 off		- 6	+12
			or	
			- 2	0
245	Pace #2 on; Pace #2 off		+ 2	- 1
141	Phase shifter drivers on		+ 2	+ 5
232	Xmitter #2 TWT #4 filaments on		- 2	+ 2
313	All pace off		+ 6	-14
207	Phase shifter drivers off		- 3	- 3
357	Wideband Data Mode #1 on		+ 4	0
006	Spin Scan Cloud Camera Reg. on	spike	+ 3	- 3
254	South Frame Limit	noise	+ 3	- 3
060	Wideband Data Mode #2 on		+ 6	0
133	Spin Scan Cloud Camera Reg. off	noise gone	- 1	0
376	Regulator #1 on		+19	-14
150	Wave form generator on/off		2γ p-p spikes	
251	Regulator #2 on		-42	+69
275	Waveform generator #2 on/off	noise	~25γp-p	12γp-p
			no effect	
302	Regulator #1 off		-13	+13
027	Regulator #2 off		+42	-72
124	Regulator on		- 4	+ 7
230	Regulator off		+ 4	- 4
303	Experiment P.S. on		+21	0
113	U. of Minn. on	High freq noise, 6-8γ p-p	+ 3	- 3
172	U. of Minn. off		- 7	2
151	Experiment P.S. off		-17	0
007	UCLA off		- 4	0
125	EME Payload Reg. off		-14	- 1

to this portion of the spacecraft testing. The ATS-1 program provided three days for all magnetic testing of the spacecraft.

On many spacecraft programs, even those with stringent magnetic specifications, a disproportionately small period of time is allocated for magnetic testing. Usually some sort of perm-deperm test is scheduled and, in some cases, the magnetic field of the spacecraft is mapped, but usually detailed testing with solar simulation is not provided. If test time early in a program is made available, many sources of interference can be investigated and, in some cases, significantly reduced.

Permanent D.C. fields, current loop D.C. fields, and A.C. fields all contribute to masking the nature of the physical environment which the instruments are trying to measure. Often these errors may be removed from flight data. In some cases large amounts of time and considerable data reduction expense occur when more stringent magnetic control could be much more simply and economically applied.

ACKNOWLEDGMENTS

This work was supported by the National Aeronautics and Space Administration under contract NAS 5-9570.

REFERENCES

Barry, J.D., Snare, R.C., A Fluxgate Magnetometer for the Applications Technology Satellite, IEEE Trans. Nuc. Sci., NS-13, 333-339, 1966.

NEW NONLINEAR MAGNETIC ANALYSIS OF SATURATED ELECTROMECHANICAL ENERGY CONVERTERS

by E. A. Erdelyi

University of Colorado, Boulder, Colorado

N69-33974

INTRODUCTION

A knowledge of the distribution of magnetic induction in electrical devices is of great importance to the designer interested in finding in advance the performance characteristic of his design. The endeavor to find the magnetic induction is as old as the art of designing electrical apparatus.

Many of the early workers attempted a rigorous mathematical treatment that would yield explicit solutions based on a number of simplifying assumptions, one of which was the assumption of the infinite permeability of iron. A review of previous mathematical and engineering papers dealing with fields in rotating machines is given in Ref. 1, 2, 3, and 4.

With the development of modern rotating machines, the solutions based on infinite or constant permeability became inadequate. The author and his research group have been engaged for some five years in establishing more accurate numerical methods that consider the nonlinear characteristics of the ferromagnetic materials. The method employed is based on the numerical solution of the partial differential equation describing the potential fields in the cross-section of rotating electrical machines. In this procedure, the so-called magnetization characteristic, the relationship between the magnetic intensity $\tilde{H}$ and $\tilde{B}$ is replaced by a curve that can be expressed easily in an explicit formula. The class of problems occurring in rotating electrical machines are based either on the nonlinear equivalent of the Laplacian partial differential equation of the magnetic scalar potential or the quasi-Poissonian partial differential equation of the magnetic vector potential. Homopolar and heteropolar machines are analyzed to demonstrate the method developed in the paper.

NUMERICAL SOLUTION OF THE NONLINEAR MAGNETIC SCALAR POTENTIAL.[1-4]

The Differential Equation

For electrical machines whose current-density fields in a cross-section can be replaced by an infinitesimally thin current sheet, the magnetic-field intensity vector $\tilde{H}$ is best found as the negative gradient of a scalar potential V. The

scalar potential is the solution of a non-linear, quasi-Laplacian that can be expressed as

$$\frac{\partial}{\partial x}\left(\mu \frac{\partial V}{\partial x}\right) + \frac{\partial}{\partial y}\left(\mu \frac{\partial V}{\partial y}\right) = 0 \qquad (1)$$

in rectangular coordinates or in circular polar coordinates as:

$$r\frac{\partial}{\partial r}\left(r\mu \frac{\partial V}{\partial r}\right) + \frac{\partial}{\partial r}\left(\mu \frac{\partial V}{\partial \theta}\right) = 0 \qquad (2)$$

The scalar-potential concept can be used with advantage for homopolar alternators. The cross-section of the rotor of this rotating machine does not contain current fields; the current fields of the stator can be replaced by thin current sheets.

Description of Homopolar Alternators

In a homopolar alternator the electromotive force in the stator winding is induced by a variation of the airgap flux between a maximum value and a minimum value of the same polarity. The flux-linkage charges are caused by the modulation of a uni-directional flux. This modulation is achieved by providing the rotor with saliencies as shown in Fig. 1. The saliencies are called "teeth" in order to distinguish them from conventional salient poles. A period of induced emf. in a conductor corresponds to a complete period of flux modulation. The distance between two consecutive tooth centers, or the distance between two consecutive axes of symmetry of inter-tooth spaces, will correspond to the double pole-pitch of a conventional synchronous machine. If the rotor is provided with N saliencies, then N cycles of emf will be induced in each stator coil by a single revolution of the rotor. At n revolutions per second the frequency of the induced voltages will be

$$F = nN \text{ cps.}$$

The stator of such a homopolar alternator consists of two stacks of laminations separated by a circular excitation coil (or field coil) of rectangular cross-section, coaxial with the shaft of the generator, shown cross-hatched in Fig. 1. The stator laminations are the same as those of an induction motor or of a synchronous machine. The outer cylinder completes the magnetic path as shown in Fig. 1.

The rotor of an HA is a solid forging, forming two identical toothed rings and a shaft. The left and right rings are offset so that a rotor-tooth axis on the left is on the same generatrix as the inter-tooth axis on the right.

Assumptions

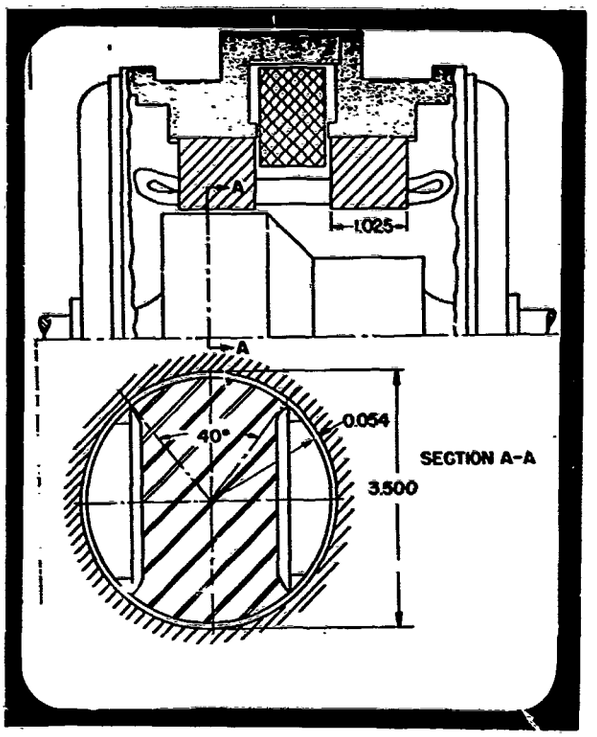


Fig. 1. Cross Section of a Homopolar Alternator

In order to bring the differential equation into the realm of a numerical solution the following simplifying assumptions are made.

1. The field is two-dimensional as shown in Fig. 2. The solution thus will be independent of the z coordinate.

2. The magnetic potential at the boundaries AB and CD and the potential difference between AB and CD in Fig. 2 are constant. The potential difference between AB and CD will be denoted F_f.

3. The material is isotropic.

4. There are no current-density fields at no-load.

5. The magnetization characteristic of the material is represented by a single-valued function. The permeability will be expressed by one or several equations of the form $\mu = (a + b\,|H|)^{-1}$ or any other convenient form.

6. The slotting of the stator region is replaced by a homogeneous material of "synthetic" permeability[5]. This, together with an airgap increased by the usual Carter coefficient, will be used in the analysis instead of full consideration of the slotting.

7. The shaft has a small bore in its center as shown in Fig. 2. This is necessitated by the fact that some terms of the partial differential equation become singular at the origin of polar coordinates.

The Boundary Conditions and Field Vectors

The general solution of Eq. 2 must satisfy the following boundary conditions:

Type 1. Boundary conditions at a contour of applied potential (as contours AB and CD in Fig. 2). Here the potential is given as

$$V(r,\theta) = \text{const} \tag{3}$$

Type 2. Boundary conditions at a line of symmetry (as AD and BC in Fig. 2). The equipotentials at these lines must be normal to the boundary. The condition to be satisfied is therefore

$$\frac{\partial V}{\partial \theta} = 0 \tag{4}$$

Type 3. Boundary conditions at interfaces: Across boundaries at which there is a change of material, this means a change of permeability. The normal component of the magnetic

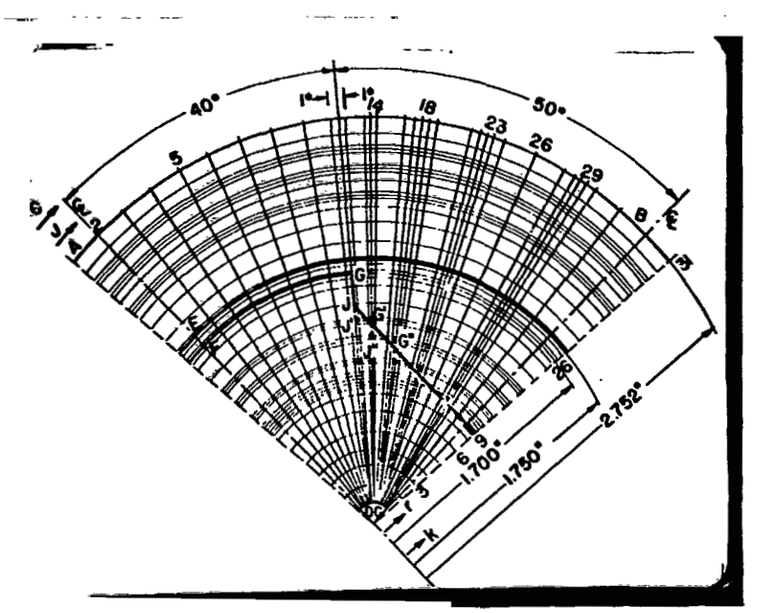


Fig. 2. Mesh System in Polar Coordinates

induction vector B and the tangential component of the magnetic intensity vector H must be continuous. For boundaries Eg, FG, and JI (in the θ direction) this is expressed as:

$$\left(\frac{\partial V}{\partial \theta}\right)_{air} = \left(\frac{\partial V}{\partial \theta}\right)_{iron} \tag{5a}$$

$$\mu_o\left(\frac{\partial V}{\partial r}\right)_{air} = \mu \left(\frac{\partial V}{\partial r}\right)_{iron} \tag{6a}$$

For boundary GJ in the r direction:

$$\left(\frac{\partial V}{\partial r}\right)_{air} = \left(\frac{\partial V}{\partial r}\right)_{iron} \tag{5b}$$

$$\mu_o\left(\frac{\partial V}{\partial \theta}\right)_{air} = \mu\left(\frac{\partial V}{\partial \theta}\right)_{iron} \tag{6b}$$

Type 4. At interface corners (corners G and J in Fig. 2). At such conditions Eqs. 8a, 8b, 9a and 9b have to be simultaneously satisfied.

The magnetic intensity is found everywhere by the formula

$$\tilde{H} = - \text{grad } V \tag{7}$$

and the flux density is found by the constituent relation

$$B = \mu(H) \tag{8}$$

where B is a nonlinear function of H. The permeability can be conveniently expressed by one or several relationships of the form

$$\mu = (a_n + b_n|H|)^{-1} \tag{9a}$$

where a_n and b_n are constants of the ferromagnetic materials.

Or in terms of the magnetic scalar potential

$$\mu = \left\{a_n + b_n\left[\left(\frac{\partial V}{\partial r}\right)^2 + \left(\frac{1}{r}\frac{\partial V}{\partial \theta}\right)^2\right]^{1/2}\right\}^{-1} \tag{9b}$$

Numerical Solution of the Mathematical Model

An explicit solution of the nonlinear partial differential equation 2, satisfying the boundary conditions at the complicated contours, cannot be found. A numerical method in which the partial differential equation is replaced by difference equations that are as numerous as the intersecting meshpoints

of a grid system becomes necessary. The continuous variable is hereby replaced by the value of the potential at the discrete gridpoints. For this purpose the cross-section is subdivided by a convenient system of gridlines; these are either radial lines or concentric circles. Since the side of the saliency is not radial, it becomes necessary to replace the side with finite steps as shown by the line J'G', G'J", J"G", and so on.

In the numerical solution by relaxation a uniform mesh may be chosen. The complicated geometry of the problem and the fact that different domains have different characteristics, suggest, however, that special care be taken in the choice of the mesh. Inside a domain, the mesh chosen can be larger than at the boundaries. Great precaution has to be taken at corners, because at these points the gradient of the potential changes rapidly. Thus, as seen from Fig. 2, in the interior of the air and iron domains, large meshes are generally chosen. In the various air-gap between the rotor and stator iron, the potential gradient is large, and it becomes necessary to introduce a finer mesh. Such a subdivision leads to square and nonsymmetrical meshes.

It is of great computational advantage if each row contains the same number of mesh points, and if each column contains the same number of meshpoints, although the number of mesh points in rows and columns is not generally the same. A systematic method of programming is thus obtained.

Using a method explained in detail in Ref. 1, the following difference expression for the gridpoint J,K denoted as 0 in an irregular mesh shown in Fig. 3 results.

$$V_0 = \frac{\alpha_1\mu_I V_1+\alpha_3\mu_{III}V_3+R_{2k}(\beta_2 V_2+\beta_4 V_4)}{\alpha_1\mu_1+\alpha_3\mu_{III}+R_{2k}(\beta_2+\beta_4)} \tag{10a}$$

where

$$\beta_2 = \alpha_2\mu_{II}R_{2k+1}; \qquad \beta_4 = \alpha_4\mu_{IV}R_{2k-1} \tag{10b,c}$$

$$\alpha_1 = \frac{2}{\delta_1(\delta_1+\delta_3)}; \qquad \alpha_2 = \frac{2}{h_2(h_2+h_4)} \tag{11,12}$$

$$\alpha_3 = \frac{2}{\delta_3(\delta_1+\delta_3;} \qquad \alpha_4 = \frac{2}{h_4(h_2+h_4)} \tag{13,14}$$

Similarly the permeabilities are calculated and one obtains for the permeability of point III on a tangential gridline of Fig. 2

$$\mu_{III} = \left\{a+b\sqrt{\left(\frac{V_7-V_8+V_2-V_4}{2h_2+2h_4}\right) + \left(\frac{V_0-V_3}{R_{2k}\delta_3}\right)}\right\}^{-1} \tag{15}$$

Above equations refer to the so-called no-load operation of

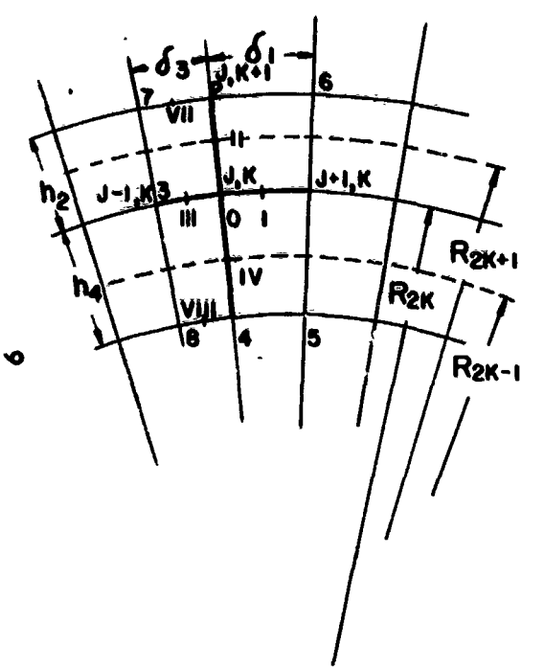


Fig. 3. Detail of Mesh

the alternator. The load currents in the discrete conductors can be replaced by the thin sinusoidally-distributed current sheet at the bore. The scalar potential V then becomes discontinuous at the current density sheet. If the potential at one side of the current sheet is denoted as V_1 and, on the opposite side, as V_2, the discontinuity will be

$$V_1 - V_2 = F \tag{16}$$

The function F is actually the magnetomotive force distribution at the stator bore and can be expressed as

$$F = F_{max}\cos(\pi\tau/x) \tag{17}$$

where

$$F_{max} = A_{max}(\tau/\pi) \tag{18}$$

The potential at a meshpoint on the bore with current sheet will now have two values given as:

$$V_0 = \frac{\alpha_1\mu_1 V_1+\alpha_3\mu_{III}V_3+R_{2k}[\beta_2(V_2\bar{+}F)+\beta_4 V_4]}{\alpha_1\mu_1+\alpha_3\mu_{III}+R_{2k}(\beta_2+\beta_4)} \tag{19}$$

The quantity (V_2-F) is used if the point J_1,K in Fig. 3 is on the current sheet. For the potential at point $J_1,K+1$ shown as 2 in Fig. 3 the quantity (V_2+F) is used. The permeabilities are calculated similarly.

The Iteration Method

Once the difference equations (Eqs. 10 and 19) are established, an overrelaxation method is used for the simultaneous solution of the N equations describing the potentials at the N mesh points.

The nonlinearity of the problem suggests a reality of two sets of quantities. These are the potentials and the permeabilities that are nonlinear functions of the potential gradients. Experience has shown that a one-step solution for both quantities converges slowly, if at all. In this paper alternating iterations are used. In this method an iteration is performed first for the potentials, assuming the permeabilities to be functions of position only. As a second step the permeabilities are calculated by an iteration procedure from the gradients of the new potentials, using Eq. 9b. The iteration processes are then as follows:

First, an initial guess is made for the potential at every point in the mesh. It is not necessary that these guesses be too accurate, although the convergence is faster with accurate initial guesses.

For convenience, the permeabilities at every point in the

mesh are set equal to the permeability of air, and using the assumed values of potential, a new set of permeabilities is calculated, using Eq. 9b. Using the new values of permeability, a new set of potentials is calculated using Eqs. 10 or 19. This iteration procedure is continued until the potentials that satisfy with sufficient approximation all N difference equations are obtained.

In order to determine if the solutions have approximated sufficiently the final values of the scalar potentials, the differences of potential are calculated at certain selected points from one iteration to the next. If the potentials do not change appreciably from one iteration to the next, it is assumed that the computations have converged to values sufficiently close to the real solution.

A Fortran computer program for an IBM 7090 computer has been used to obtain the following objectives:

1) To carry out the overrelaxation procedure;

2) To recalculate the permeabilities;

3) To test the solution for convergence;

4) To calculate the radial magnetic induction at the stator bore, using Eqs. 7 and 3.

The flow chart and the computer program are described in detail in Ref. 2 and 4.

The theory and the computer programs have been applied to a wye-connected 8KVA 3-phase, 0.75 power factor homopolar alternator operating at 18,840 rpm. The nominal frequency is 628 cps; the line-to-line voltage is 85 volts.

For the no-load computation the excitation between $\overline{AB}$ and $\overline{CD}$ in Fig. 2 has been chosen as 1000, 1500 and 2000 ampereturns respectively. The numerical solution has also been established for purely reactive inductive loads for 60-amp. phase current at 1500, 2000 and 2500 ampereturn excitation. The load current establishes a 550-ampereturn armature reaction.

The calculated results have been plotted in Fig. 4a for no-load conditions. The resulting radial component of the airgap magnetic induction is shown in Fig. 4b. A Fourier analysis yielded the fundamental component from which the theoretical no-load-acid-load characteristic has been established. The agreement as seen from Fig. 5 is quite good when the complications of the problem are considered.

MAGNETIC VECTOR POTENTIAL OF HETEROPOLAR MACHINES[8-10].

The cross-section of heteropolar electrical machines contains

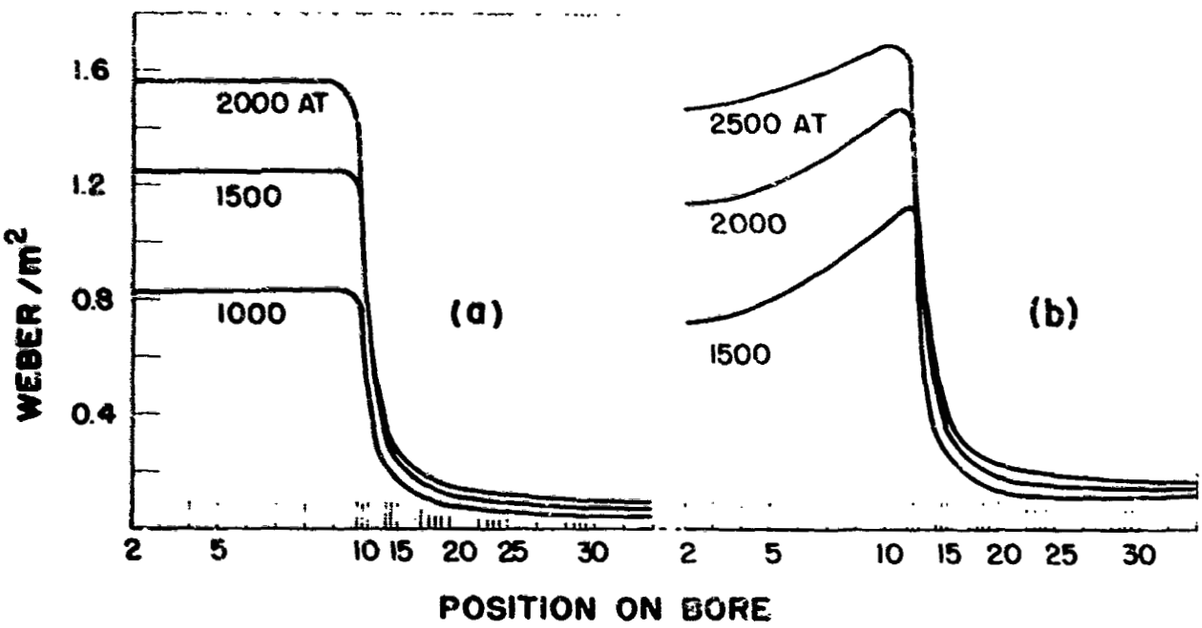


Fig. 4. Flux Distribution in Airgap of Homopolar Alternator
(a) No-Load
(b) Purely inductive load

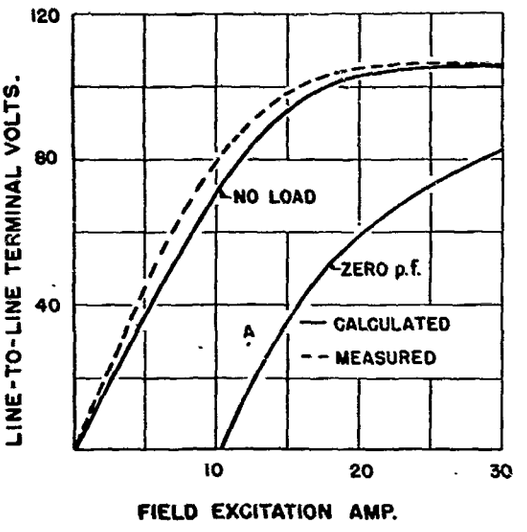


Fig. 5. No-Load and Zero Power Factor Characteristic

current fields even at no-load, as seen. The excitation currents in the field coils represent singularities of the scalar potential field and Poisson's equations have to be applied leading to the vector potential field concept. Experience has shown that the alternating overrelaxation process leads to very slow convergence or to unstable solutions.

The author and his associates have developed a method, largely overcoming the difficulty of slow convergence, that consists of the following:

1) The constitutional relation given by Eq. 9a is reversed and the form suggested by King[6]

$$\tilde{H} = \nu\tilde{B} \tag{20}$$

is used. In this expression ν is the reluctivity of the ferromagnetic material and is obviously the reciprocal of the permeability. This assumption simplifies the partial differential considerably.

The nonlinear dependence of the reluctivity ν on the magnetic induction can be described by one or several expressions of the form

$$\nu = c(1 - d|B|)^{-1} \tag{21a}$$

where c and d are material constants. At high saturation levels the saturation curve can be approached by a straight line. In this region the reluctivity can be defined as

$$\nu = e - f|B|^{-1} \tag{21b}$$

2) A new method of accelerating convergence, first introduced by S. V. Ahamed[7] and then extended by Erdélyi and Ahamed[8] is used. In the procedure, based on Stokes' theorem, the line integrals of the magnetic intensity over closed paths are compared with the enclosed currents. The ratio of these quantities is then used to adjust the potentials in the cross-section by block relaxation.

3) In the alternating process of iterations of potentials and reluctivities, the latter are underrelaxed.

The Differential Equation of the Vector Potential and Boundary Conditions

Assumptions are generally the same as for the scalar potential. It is further assumed that the discrete currents in the field winding and armature-winding conductors are distributed uniformly over the cross-section of the individual coils. In the practical example the cylindrical surfaces on both sides of the airgap are represented by planes. Here again only two-dimensional solutions are considered. The simultaneous solution of Maxwell's equation leads into the assumption of

a divergence-free vector potential, thence to the quasi-Poissonian partial differential equation

$$\frac{\partial}{\partial x}\left(\nu \frac{\partial A}{\partial x}\right)+\frac{\partial}{\partial y}\left(\nu \frac{\partial A}{\partial y}\right) = -J \qquad (22a)$$

in Cartesian coordinates. In circular polar coordinates the vector potential is formed by the solution of the equation:

$$\nu \frac{\partial A}{\partial r} + r \frac{\partial}{\partial r}\left(\nu \frac{\partial A}{\partial r}\right) + \frac{1}{r}\frac{\partial}{\partial \phi}\left(\nu \frac{\partial A}{\partial \phi}\right) = J \qquad (22b)$$

The magnetic induction is then found from the relations

$$\tilde{B} = \text{curl } A \qquad (23)$$

This leads to the field components

$$Bx = \frac{\partial A}{\partial y}; \qquad By = -\frac{\partial A}{\partial y} \qquad (23a)$$

in Cartesian coordinates and in polar coordinates

$$B_r = \frac{1}{r}\frac{\partial A}{\partial \phi}; \qquad B_y = \frac{\partial A}{\partial r} \qquad (23b)$$

Fig. 6 shows a pole-pitch in the cross-section of a typical heteropolar, salient-pole, synchronous machine. The following boundary conditions have to be satisfied:

At air-iron interfaces, at air-current interfaces: The tangential component of the magnetic intensity vector and the normal component of the magnetic induction vector are continuous. This condition has to be satisfied also at infinitesimal distances from the corners formed by two intersecting contours.

At no-load conditions the field is symmetrical to the so-called direct axis $\overline{AB}$ and $\overline{CD}$. The vector potential is, in this case, constant on the axis $\overline{AB}$ and $\overline{CD}$. If one assumes also that the field outside the contour of the machine is zero, then the vector potential is constant over the whole path $\overline{ABCDA}$. The vector potential equipotentials, the so-called flux lines, are orthogonal to the cross axis $\overline{EF}$ and here

$$\left(\frac{\partial A}{\partial x}\right)_{CD} = \left(-B_y\right)_{CD} = 0 \qquad (24)$$

The above symmetries and orthogonalities do not apply if the armature conductors carry currents; the vector potential, however, remains a periodic function, the double pole-pitch as its fundamental period. The vector potential at any point P will be equal in magnitude and opposite in sign to the vector potential P' on the same horizontal gridline a pole-pitch away.

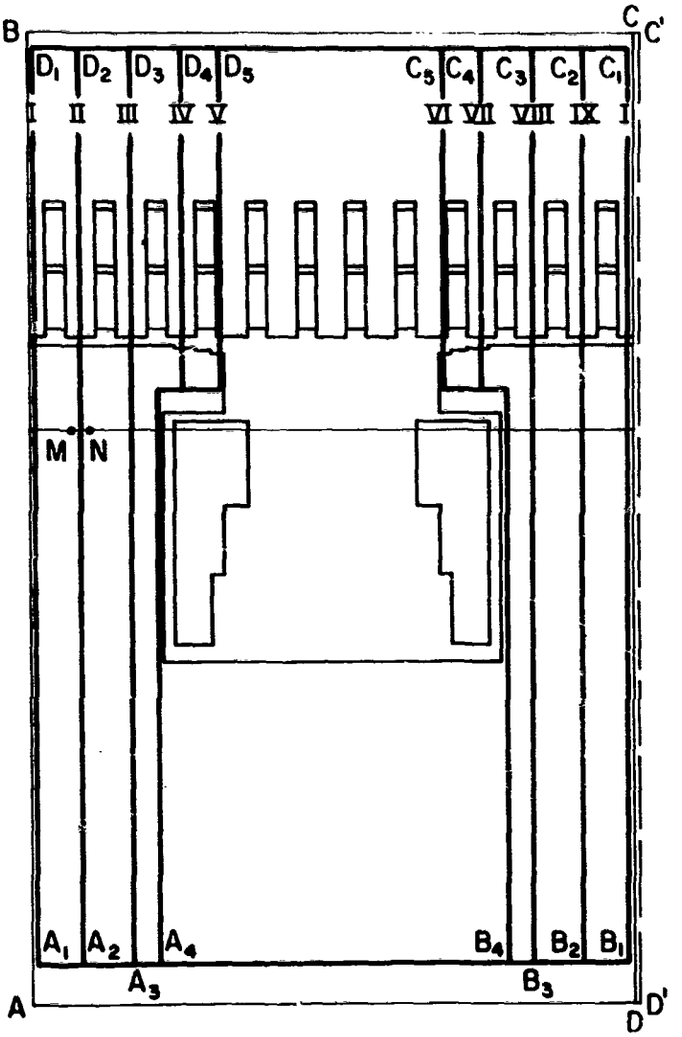


Fig. 6. Cross Section of Salient Pole Synchronous Machine

$$A(P_J) = -A(P'_{J+T}) \tag{25}$$

Discretization of the Partial Differential Equation and the Grid System

As in the case of scalar potential problems the continuous region of the cross-section shown in Fig. 6 is provided with a grid system and the vector potential is then found only for the intersecting gridpoints. Again, great care has to be taken in constructing the grid system. A fine mesh is chosen at boundaries as shown in Fig. 7. It is also advantageous to let the contours coincide with gridlines. Slanted and leveled contours are replaced by staircase-type contours.

Such a grid system leads to square and non-uniform meshes. A typical mesh is shown in Fig. 8. The ν's denote the reluctivities over the area of meshes, and the J's denote the current densities of the meshes. Current-density fields are in air regions, i.e., regions of constant reluctivity.

The first-order approximation of the difference equation at point 0 can be found by using Ampere's law as

$$A_0 = M/N \tag{26}$$

where

$$M = J_0 + A_1\alpha_1(\nu_I\beta_4 + \nu_{II}\beta_2) + A_2\alpha_2(\nu_{II}\beta_1 + \nu_{III}\beta_3) + A_3\alpha_3(\nu_{III}\beta_2 + \nu_{IV}\beta_4) + A_4\alpha_4(\nu_{IV}\beta_3 + \nu_1\beta_1) \tag{27}$$

and

$$N = \alpha_1(\nu_I\beta_4 + \nu_{II}\beta_2) + \alpha_2(\nu_{II}\beta_1 + \nu_{III}\beta_3) + \alpha_3(\nu_{III}\beta_2 + \nu_{IV}\beta_3) + \alpha_4(\nu_{IV}\beta_3 + \nu_I\beta_1) \tag{28}$$

The constants α_1, α_2, α_3, and α_4 in 27 and 28 are defined as

$$\alpha_1 = \frac{2}{h_1\,(h_1 + h_3)} \tag{29a}$$

$$\alpha_3 = \frac{2}{h_3(h_1 + h_3)} \tag{29b}$$

$$\alpha_2 = \frac{2}{h_2\,(h_2 + h_4)} \tag{30a}$$

$$\alpha_4 = \frac{2}{h_4(h_2 + h_4)} \tag{30b}$$

The constants β_1, β_2, β_3, and β_4 in 27 and 28 are defined as

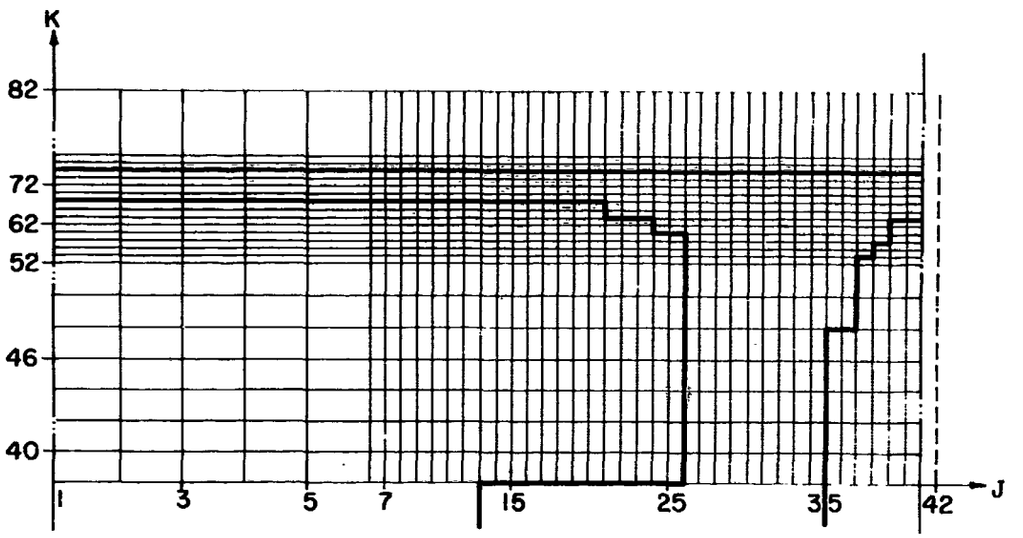


Fig. 7. Detail of Mesh System

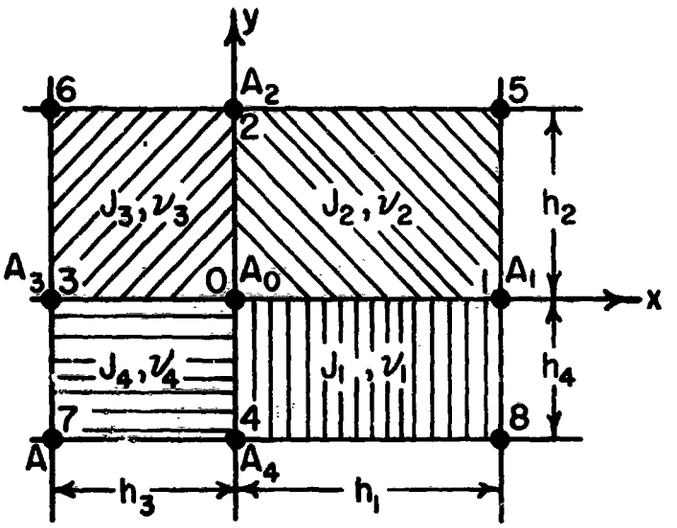


Fig. 8. Mesh in Cartesian Coordinates

$$\beta_1 = \frac{h_1}{h_1 + h_3} \tag{31a}$$

$$\beta_3 = \frac{h_3}{h_1 + h_3} \tag{31b}$$

$$\beta_2 = \frac{h_2}{h_2 + h_4} \tag{32a}$$

$$\beta_4 = \frac{h_4}{h_2 + h_4}. \tag{32b}$$

The reluctivities are calculated from Eq. 21a or 21b using the average values of the magnetic induction in the center of the mesh. This can be shown for mesh $\overline{0184}$ to be

$$B_x = \frac{A_1 - A_8 + A_0 - A_4}{2h_4} \tag{33a}$$

and

$$B_y = \frac{A_1 - A_0 + A_8 - A_4}{2h_1} \tag{33b}$$

The current density J_0 in Eq. 27 is the average value of the current at gridpoint 0 and is defined as

$$J_0 = \frac{J_1 h_1 h_4 + J_2 h_1 h_2 + J_3 h_2 h_3 + J_4 h_3 h_4}{(h_2 + h_3)(h_1 + h_4)} \tag{34}$$

$$|B| = \sqrt{\left[\left(\frac{A_1 - A_8 + A_0 - A_4}{2h_4}\right)^2 + \left(\frac{A_1 - A_0 + A_8 - A_4}{2h_1}\right)^2\right]}. \tag{35}$$

This value of B is used in Eqs. 21a,b for the calculation of reluctivity in the mesh $\overline{0184}$.

The reluctivities in the other three rectangles having gridpoint 0 as a joint corner are determined similarly. In order to avoid a separate location in the computer program for the reluctivity, the reluctivity of each mesh is assigned to the top-right corner of a mesh.

The boundary conditions at interfaces are included automatically in the difference formula Eq. 26. To satisfy the periodicity condition, it is best to start by comparing the lattice points on direct axes $\overline{AB}$ and $\overline{CD}$. An additional gridline C'D' is introduced (as shown in Fig. 6) a pole-pitch away from the gridline next to $\overline{AB}$ for the execution of the periodicity condition.

The Iteration Procedure

Experience with several programs has shown that iteration procedures of magnetic vector-potential problems are best carried out in a sequence of three steps forming one iteration. These are

1. Relaxation of the Potentials
2. Block relaxation for acceleration of convergence
3. Underrelaxation of reluctivities

Relaxation of the Potentials

Initial values are chosen for the potentials and estimates made of the reluctivities. The potentials are then recalculated, replacing the original values with the values obtained by the use of the algorithm of Eq. 26.

Acceleration of Convergence by Block Relaxation

The current fields in the cross-section of the machine constitute singularities in the scalar magnetic-field concept. They do not represent singularities in the vector-potential field concept; the effect of these fields, however, causes a painfully slow convergence of the usual iteration procedure and in many cases leads to divergent behavior. In order to attain convergence, the effect of these fields has to be brought into the calculation procedure in a more definite way. This is accomplished by the use of Stokes' theorem and will be best understood from Fig. 8. First, the line integral of $\tilde{H}$. $d\tilde{\ell}$ is formed on path I, consisting of the points $\overline{ABCDA}$, and then the surface integral of the current densities in the area bounded by path I is found. The ratio of these two quantities is denoted as c_I

$$c_I = (\iint \tilde{J}.\ d\tilde{s}) / (\int \tilde{H}.\ d\tilde{\ell}) \neq 1 \tag{36}$$

The value of c_I should be obviously 1 and will not even be close to unity at the beginning of the iterations. In order to correct this defect all vector potentials are multiplied with c_I.

Next the line integral and surface integral are found for the path II connecting points $\overline{A_2BCD_2A_2}$. The ratio of these integrals is denoted as c_{II}. In order not to disturb the potential relationship found by the first block relaxation, the vector potential A_M in a point M just left of $\overline{D_2A_2}$ is replaced by A'_M defined as

$$A'_M = c_{II}(A'_M - A_N) + A_N \tag{37a}$$

where A_N is the potential on a gridline just right of $\overline{D_2A_2}$ on the same horizontal gridline as point M. The vector potentials on all gridpoints on the horizontal gridline left of M are recalculated as

$$A'_P = A_P - (A'_M - A_M). \tag{37b}$$

The process described for the integration path II is carried out also for all other paths (III-IX shown in Fig. 9). After all these relaxations the periodicity condition will not be satisfied. The potentials on $\overline{AB}$ and $\overline{CD}$ will not be equal in magnitude. As an adjustment, the vector potentials of all grid points of a gridline K_M are reduced by

$$A = (1/2)\,[A(1,K) - A(J_{max},K)] \tag{38}$$

Underrelaxation of Reluctivities

The reluctivities can now be recalculated using Eqs. 21a and 21b. Experience with similar programs indicates that the iterations become more stable if the reluctivity changes are kept in small bounds. For this reason the process includes an underrelaxation of the reluctivities according to the formula

$$\nu_{n+1} = \nu_n - (\nu_n - \nu'_n)\ (1/f) \tag{39}$$

where ν_{n+1} is the reluctivity used in the (n+1)st iteration, ν_n is that used in the nth iteration, and ν'_n is the reluctivity calculated after the nth iteration. The magnitude of f is in the range between 10 and 30.

The Computer Programs

The computer programs, written in Fortran II language, accomplish the following operations:

1. Relax the vector potentials at each gridpoint using Eq. 26.

2. Carry out the block relaxation using Eqs. 36, 37, 38.

3. Underrelax the reluctivities according to Eq. 39.

4. Calculate the radial component of the magnetic induction along the armature periphery using Eq. 23a.

5. Check the convergence of the iterations.

Application of the Vector Potential Method and Solution Obtained.

The theory described in this paper and the computer program

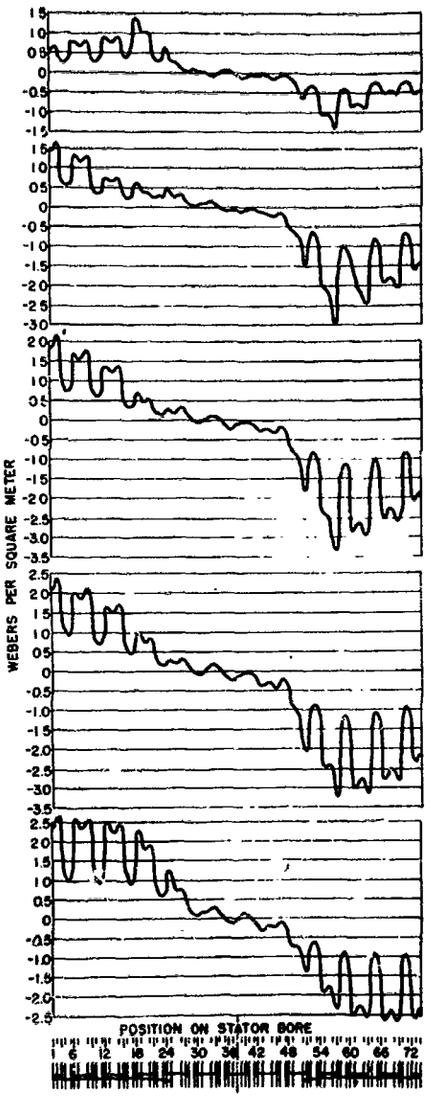


Fig. 9. Airgap Radial Magnetic Inductions in a 3-phase Synchronous Generator at Full Load

of Refs. 8-10 have been applied to large salient-pole synchronous generators and direct-current motors. Here only the results of calculations carried out for a 2750 KVA, 2300 V, 3-phase, wye-connected, 60 cs., 900-rpm, 8-pole alternator at rated current and seven different power-factor angles are reproduced. The design data of the alternator were obtained from the Large Apparatus Division, Westinghouse Electric Corporation, East Pittsburgh, Pennsylvania. The calculations were carried out on the CDC 3600 computer of the National Center for Atmospheric Research in Boulder, Colorado.

Load Conditions and Results

The radial airgap induction at the armature bore has been found for 10,500 At/pole excitation at full load of 696A at seven different power factors. The plot of the results are shown in Fig. 9. The induced voltages have been calculated and found to agree with an accuracy of three per cent as compared with measurements.

CONCLUSION

The methods of solution presented here for scalar-magnetic and vector-magnetic problems are well suited for the predetermination of the behavior of electrical devices incorporating nonlinear ferromagnetic material. The quasi-Laplacian and Poissonian partial differential equations apply to the quasi-stationary regime of the devices and can be used with great advantage for many other devices, like accelerator magnets, for the analysis of magnetohydro-dynamic energy converters. The computational procedures described could also be easily adapted to heat-transfer, fluid-mechanics and other problems of mathematical physics.

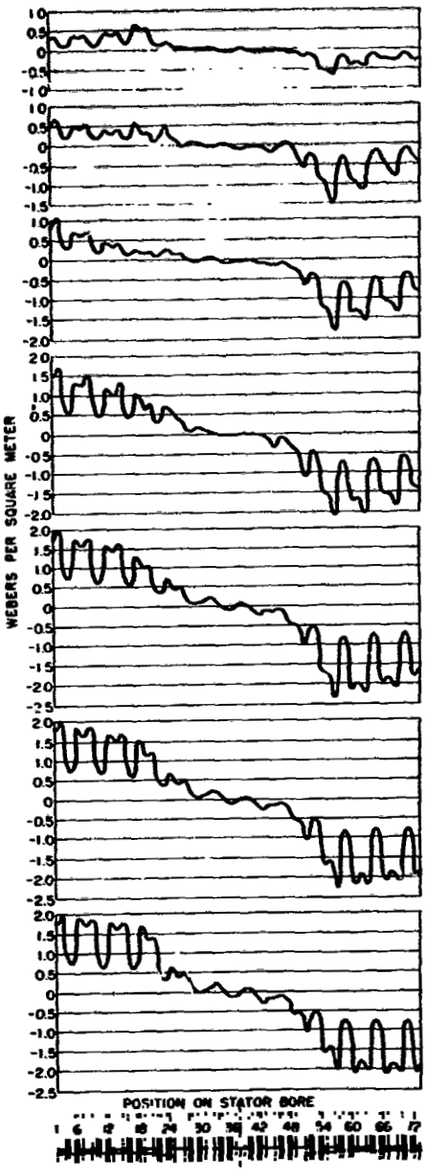


Fig. 10. Airgap Radial Magnetic Inductions in a 3-phase Synchronous Generator at Twice Full Load

REFERENCES

1. F. C. Trutt, E. A. Erdélyi and R. F. Jackson, "The Non-Linear Potential Equation and its Solution for Highly Saturated Electrical Machines," Trans. IEEE on Aerospace, Vol. 1, (1963), No. 2, pp. 430-440.

2. F. C. Trutt, E. A. Erdélyi, "No-Load Flux Distribution in Saturated High-Speed Homopolar Inductor Alternators," Trans. IEEE on Aerospace, Vol. 1, (1963), No. 2, pp. 417-429.

3. E. A. Erdélyi, F. C. Trutt, R. E. Hopkins, "Flux Distributions in Saturated High-Speed Homopolar Inductor Alternators with Purely Reactive Loads," Trans. IEEE on Aerospace, Vol. 1, (1963), No. 2, pp. 407-416.

4. E. A. Erdélyi, F. C. Trutt, R. E. Hopkins, "Saturated High-Speed Homopolar Alternators at Balanced Loads," Trans. IEEE on Aerospace, Vol. 2, (1964), pp. 929, 936.

5. K. K. Surti and E. A. Erdélyi, "The Effects of Slotting on the Flux Distribution in Saturated High-Speed Homopolar Inductor Alternators," Trans. IEEE on Aerospace, Vol. 2, (1964), pp. 937-947.

6. R. W. P. King, Fundamental Electromagnetic Theory, New York: Dover, 1963, p. 139.

7. S. V. Ahamed, "Acceleration of Convergence of Numerical Solutions of Linear and Nonlinear Vector Field Problems," The Computer Journal, (London) Vol. 8, April, 1965, pp. 72-76.

8. E. A. Erdélyi, S. V. Ahamed, R. D. Burtness, "Flux Distribution in Saturated D.C. Machines at No-Load," Trans. IEEE on Power Apparatus and Systems, Vol. 84 (1965), pp. 375-381.

9. S. V. Ahamed, E. A. Erdélyi, "Non-Linear Theory of Salient Pole Machines," Trans. IEEE on Power Apparatus and Systems, Vol. 85, January, 1966, pp. 61-70.

10. E. A. Erdélyi, S. V. Ahamed, R. E. Hopkins, "Non-Linear Theory of Synchronous Machines On-Load," Trans. IEEE on Power Apparatus and Systems, Vol. 85, July, 1966, pp. 792-801.

C. C. Conley[1], P. W. Droll[1], W. J. Mills[1,2], and Patricia A. Corsaut[3]

EFFECTS OF MAGNETIC FIELDS UPON BIOLOGICAL SYSTEMS

REFERENCE: C. C. Conley, P. W. Droll, W. J. Mills and Patricia A. Corsaut, "Effects of Magnetic Fields Upon Biological Systems," Symposium on Space Magnetic Exploration and Technology, University of Nevada, Reno, Nevada, 28-30 August, 1967.

N69-33975

INTRODUCTION

Magnetic field effects upon biological systems have been demonstrated with increasing frequency in recent years, and many reviews of the subject have appeared (1-4). Negative experimental work (5-8) and theoretical discussions refuting the existence of any significant biomagnetic effect also exist (9-10). But qualifying factors that must be considered are the intensity and the temporal aspects of the applied fields and the complexity of the biological systems under study.

Despite the broad range of recent experimentation, from plant magnetotropism (11) to effects on the aging of mammals (12), two major questions seem uppermost in this area; first, whether there is a limit to the magnetic field intensity to which man may be exposed without harm, and second, whether fields of geomagnetic intensity have any biological significance.

Early studies and later surveys of incidental, brief exposures of humans to strong fields have revealed only occasional transient, and apparently harmless, effects (5,6,13,14). Experimental exposures of small primates to kilogauss fields for several hours have shown electrocardiographic changes; but, again, these are limited, transient and apparently reversible without lasting damage (15). One effect, incidental to this discussion, is that of the magnetic phosphene. Discovered and confirmed in the early era of biomagnetic experimentation (16,17), it consists of a subjective visual sensation of light, sometimes faintly blue, when the head is placed within a magnetic field in the kilogauss range. It was soon found (18) that this occurred only in a changing field, and both early and recent theoretical explanations (19,20) invoke the concept of induced electromotive forces, presumably occurring within retinal cell visual pigment macromolecules.

Thus, the experimental application of varying magnetic fields to living organisms introduces the problem of induced electric currents, since, while traditionally diamagnetic, living systems are by no means dielectric. In order to reduce this problem, for this discussion, we have chosen to limit our considerations to the effects of D.C., or static, magnetic fields.

---

[1]Research Scientist, Ames Research Center, NASA, Moffett Field, California 94035

[2]Present Address: V. A. Hospital, Sepulveda, California

[3]Research Technologist.

More chronic exposures to high fields have been limited to lower life forms and, while some striking positive results have been reported (21-28), some suggesting an effect of the magnetic field on biological ion transport mechanisms (29-32), comparable situations involving man are not anticipated on earth. Thus, while the first of our two questions is by no means definitively answered, it can be concluded that exposures of only a few minutes' duration to the high fields around presently available equipment have not been shown to present any significant hazard.

Studies addressed to the second question have not been numerous (33-39). Yet space exploration promises to put man into fields of only milli-, if not micro-gauss strength (40); i.e., effectively eliminating most of the geomagnetic environment to which he and his evolutionary ancestors have become adapted (Table I).

By the use of the Ames space magnetic environment simulation facility (Figure 1), we have observed (38) the effect of nullifying most of the geomagnetic field upon an enzyme response of specialized mammalian cells, *in vivo*, to the inoculation of a foreign biopolymer. Mice were placed within the nulled area of the activated coils during the incubation period, then cells were taken from them for assay of their enzyme content for comparison with cells from animals similarly inoculated but kept in a control area. The cellular response to inoculation was significantly reduced in material from the animals kept in the nulled field (Table 2). The following possibilities, singly, or in combination, are suggested by these findings:

1. The rate of production of enzyme by the macrophages was reduced.

2. A defective enzyme was produced.

3. The enzyme produced underwent accelerated denaturation in the reduced magnetic field.

The presence of paramagnetic transition metals in hydrolytic enzymes of the type assayed in the above study suggests that magnetic field effects on enzymes might derive from direct action on such metals. Cook & Smith (41), Akoyunoglu (42) and Wiley and co-workers (43) have all shown enhancement of enzyme activity following exposure to high magnetic fields. But Maling & Weissbluth (8) found no effect when the enzyme-substrate systems they used were allowed to react in 100 K-gauss fields. Since none of these studies involved acid phosphatase nor the nulled field environment, we made observations of both nulled and high (kilo-gauss) magnetic field effects on the activity of this enzyme as well as two others, *in vitro*. One of the purposes of this paper is to present our findings.

SOME REPRESENTATIVE MAGNETIC FIELD INTENSITIES

ALNICO MAGNET SURFACE	~ 1000 GAUSS	$\simeq 10^8$ GAMMA
SOLAR FLARES, SURFACE	~ 100	$\simeq 10^7$
SUN SURFACE, QUIET	1	$= 10^5$
EARTH	~ 1	$\simeq 7 \times 10^4$ (POLAR)
INTERPLANETARY, STORMY	$\sim 10^{-3}$	$\simeq 100$
MOON, MARS, VENUS	$< 10^{-3}$	< 50 (MOON)
INTERPLANETARY, NORMAL	$\sim 10^{-5}$	$\simeq 5$

AFTER BEISCHER, 1962, REVISED

Table 1.

LABORATORY BUILDING GENERAL

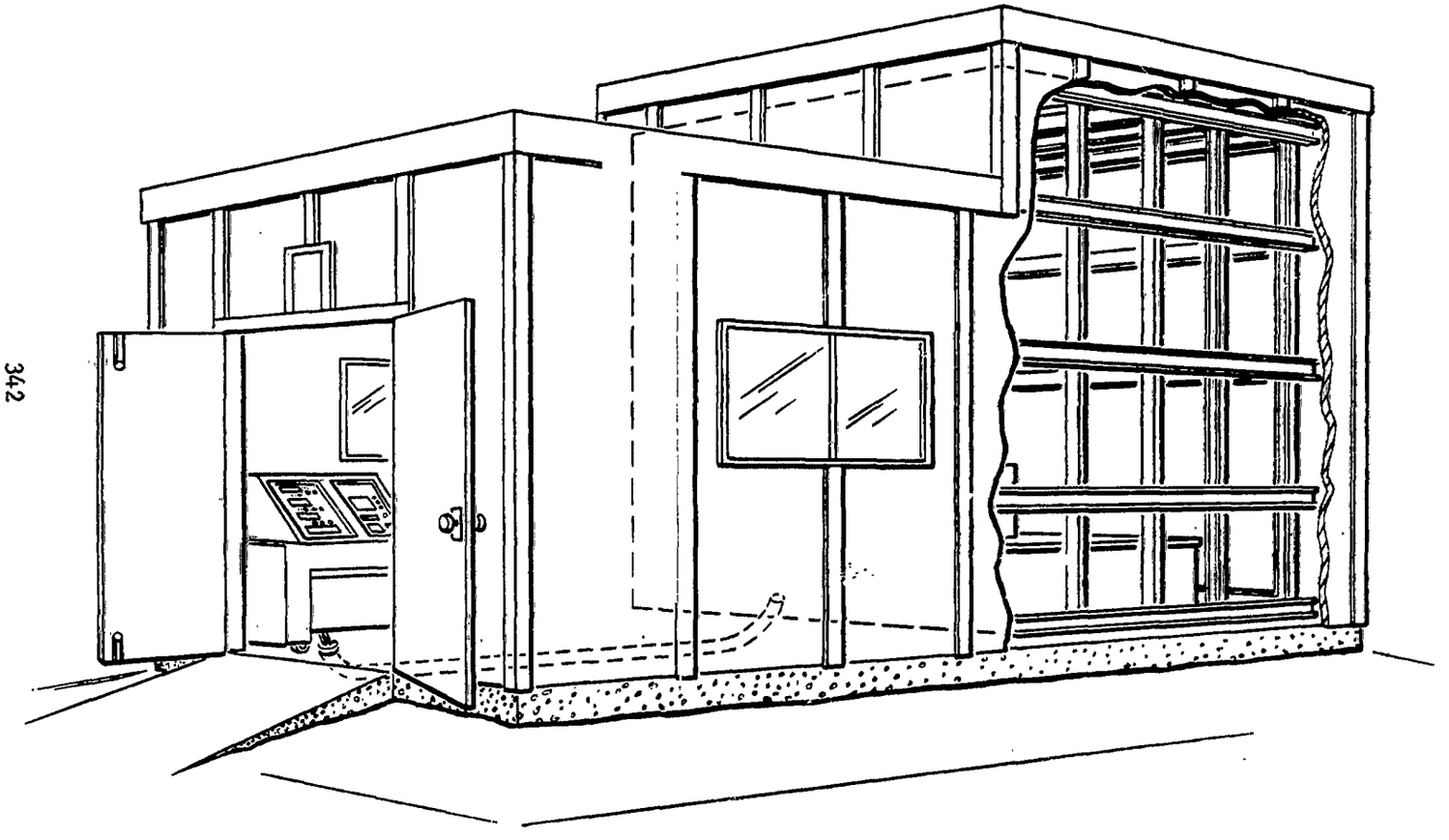


Figure 1. Ames Space Magnetic Environment Simulation Facility.

TABLE OF MEAN RESPONSE OF CONTROL AND LOW FIELD GROUPS VERSUS TIME SEQUENCE OF EXPERIMENTS[a]. (ACID PHOSPHATASE ACTIVITY IN MOUSE PERITONEAL MACROPHAGE SUSPENSIONS EXPRESSED AS μg OF PHENOL RELEASED PER 5 MILLION CELLS $\pm SE_{MEAN}$)

EXPERIMENT NUMBER	1	2	3	4	5	6	TREATMENT MEANS
TREATMENT GROUP:							
LOW FIELD CHAMBER (< 80 gamma)	13.6 ± 2.6	22.6 ± 2.6	16.9[b] ± 1.2	13.5 ± 1.1	5.3 ± 0.5	9.9 ± 0.1	13.6[c]
CONTROL (GEOMAGNETIC FIELD)	21.1 ± 0.8	25.6 ± 3.5	25.3 ± 1.0	18.2 ± 3.5	10.8 ± 3.5	15.1 ± 4.8	19.3[c]
TIME MEANS	17.4	24.1	21.1	15.8	8.0	12.5	16.5

a. EACH MEAN IS BASED ON FOUR OBSERVATIONS
b. ONE OBSERVATION IS MISSING
c. DIFFERENCE BETWEEN TREATMENT MEANS IS SIGNIFICANT AT $p < .001$, BY ANALYSIS OF VARIANCE

Table 2.

METHODS

The nulled field ($< 10^{-4}$ gauss) observations were made in the Ames space magnetic environment simulation facility (Figure 1). Temperature regulation of experimental and control incubation vessels was achieved with a Precision Closed Circuit, circulating constant temperature bath. The high field observations were made using a Varian Model V-4007 6" water cooled electromagnet having V 4037 tapered pole caps with 3" faces providing a uniform field of 5.7 K gauss with 95% homogeneity over a $2\frac{1}{2}$ " diameter.

A closed plastic water bath held the experimental test tubes in groups of 3 within the uniform field area. This was circulated in parallel with the control incubation vessel by means of a Haake Model F constant temperature circulating water pump.

The enzyme-substrate reaction systems used consisted of the quality control standards for alkaline and acid phosphatase, with reactivity assay by the Lowry-Brock method, and SGOT using the Reitman-Frankel assay method. 30 and 60 min. incubation times were used, respectively (44,45).

RESULTS

The results listed in Table 3 show the lack of any significant[4] effect of either high or low field upon the activities of the 3 enzymes. Our results are consonant with those of Maling & Weissbluth, but neither their work nor ours should be construed to contradict the findings of the 3 other groups, since we used fresh, untreated enzyme which was already in contact with the substrate by the time the altered magnetic field was applied, and this application was only for the duration of the reaction period. The earlier workers had all pretreated their enzymes by exposure to high fields for at least an hour, and Wiley's group even showed a correlation between length of exposure and percent enzyme reactivation.

In our *in vivo* experiments (38), the enzyme was released by sonic disruption of the macrophages within 1/2 hour after removal of the mice from the nulled field, so that if a qualitative change in the enzyme had been produced by the field, it could be expected to cause the results we got. The *in vitro* studies presented here, were done with the idea that if altered magnetic fields cause some direct molecular changes in the enzymes, these might produce altered reaction rates when the enzyme-substrate system was exposed during the reaction period. The lack of such an effect on fresh enzymes does not exclude the malformation or denaturation possibilities as operative in the *in vivo* experiments, but it does seem to favor a gradual, cumulative effect of the markedly reduced field as equivalent to the loss of a favorable bias on a complex sequence of cellular events resulting in a quantitative change, i.e., lowered enzyme production.

ENZYME ACTIVITY IN VITRO

LACK OF A SIGNIFICANT EFFECT OF MAGNETIC FIELD VARIATION

ENZYME	ACTIVITY LEVEL * MAGNETIC FIELD			SIGNIFICANCE °	
	Nulled: 10^{-4}G	Geo-: 1/2G	High: 10^{3}G	t	df
Acid Phosphatase	1.21 (±0.01)	1.22 (±0.02)		0.500	28
		1.34 (±0.03)	1.36 (±0.04)	0.444	16
Alkaline Phos phatase	6.02 (±0.18)	5.83 (±0.27)		0.189	78
		5.33 (±0.41)	4.90 (±0.18)	0.962	16
Transaminase (Glutamic-Oxala-cetic)	92.3 (±1.19)	93.2 (±0.99)		0.600	18
		93.5 (±0.74)	94.6 (±0.88)	0.960	16

* P'tase: Lowry-Brock units; SGOT: Reitman-Frankel units; means(± S. E.)

Table 3.

CONCLUSIONS

Thus we are left with an effect apparently requiring more of the physiological milieu than a simple enzyme-substrate system, an effect which may be related more to the rate of production of a specialized enzyme protein than to the activity of that product. A possible inference is that: to be biologically effective, a field may have to act across a rather extensive conduction system, on the molecular scale, and for a fairly long time, in proportion to traditional electrical phenomena; both requirements implying a cumulative action.

---

[4]We thank Mrs. Margaret N. O'Neill for her advice on our statistical treatment.

REFERENCES

1. Valentinuzzi, M. Magnetobiology and Complements of Magnetochemistry. Pub. no. SID 61-283, No. Amer. Aviation, Inc., Downey, Calif., 1961.

2. Davis, L. D., Papajohn, K. and Plavnieks, I. M. Bibliography of the Biological Effects of Magnetic Fields. Fed. Proc. 21: No. 5, Part II. Supplement 12, 1962.

3. Alexander, H.S. Biomagnetics--The Biological Effects of Magnetic Fields. Am. J. Med. Electron. 1:181, 1962.

4. Becker, R.O. The Biological Effects of Magnetic Fields--A Survey. Med Electron. Biol. Engng. 1:293, 1963.

5. Hermann, L. Hat das magnetische Feld directe physiologische Wirkungen? Pflügers Arch. f. d. gesamte Physiol. 43:217, 1888.

6. Peterson, F. and Kennelly, A. E. Some physiological experiments with magnets at the Edison Laboratory. N. Y. Med. J. 56:729, 1892.

7. Halpern, M. H. and Greene, A. E. Effects of Magnetic Fields on Growth of HeLa Cells in Tissue Culture. Nature 202:717, 1964.

8. Maling, J. E., Weissbluth, M. and Jacobs, E. E. Enzyme Substrate Reactions in High Magnetic Fields Biophys. J. 5:767, 1965.

9. Ragle, J. L. On Possible Biological Effects of Magnetic Fields. Aerosp. Med. 35:469, 1964.

10. Piette, L. H. Varian Associates, Palo Alto, Calif., Personal Communication.

11. Audus, L. J. Magnetotropism:A New Plant-growth Response. Nature 185:132, 1960.

12. Barnothy, J. M. Biological Effects of Magnetic Fields. in: Glasser, O. ed., Medical Physics, Vol. 3. Chicago, Yearbook Med. Publ., 1960.

13. Drinker, C. K. and Thomson, R. M. Does the Magnetic Field Constitute an Industrial Hazard ? J. Indust. Hyg. 3:117, 1921.

14. Beischer, D. E. Human Tolerance to Magnetic Fields. Astronautics 7:24, 1962.

15. Beischer, D. E. and Knepton, J. C., Jr. Influence of Strong Magnetic Fields on the Electrocardiogram of Squirrel Monkeys. Aerosp. Med. 35:939, 1964.

16. d'Arsonval, M. A. Production des Courants de Haute Frequence et de Grande Intensite; leurs effets physiologiques. Compt. rend. Soc. Biol. 45:122, 1893.

17. Beer, B. Ueber das Auftreten einer subjectiven Lichtempfindung im magnetischen Felde. Wien. klin. Wchnschr. 15:108, 1902.

18. Magnusson, C. E. and Stevens, H. C. Visual Sensations Caused by changes in the Strength of a Magnetic Field. Am J. Physiol. 29:124, 1911.

19. Dunlap. K. Visual Sensations from an Alternating Magmetic Field Science 33:68, 1911.

20. Valentinuzzi, M. Theory of Magnetic Phosphenes. Am J. Med. Electron. 1:112,1962.

21. Gross, L. and Smith, L. W. Effect of Magnetic Fields on Wound Healing in Mice. Fed. Proc. 20:164, 1961.

22. Cheneveau, C. and Bohn, G. De l'Action du Champ Magnetique sur les Infusoires. Compt. rend. Acad. sc. 136:1579, 1903.

23. Lengyel, J. Die Wirkung des Magnetischen Kraftfeldes auf die Faserbildung und auf das Gewebewachstum. Arch. Exper. Zellforsch. 14:255, 1933.

24. Lenzi, M. A Report of a few Recent Experiments on the Biological Effects of MagneticFields. Radiol. 35:307, 1940

25. Beischer, D. E. and Furry, D. E. Personal Communication, 1964.

26. Butler, B. C. and Dean, W. W. The Inhibitory Effect of a Magnetostatic Field upon the Tissue Culture Growth of K. B. Cells. Am J. Med. Electron. 3:123, 1964.

27. Young, W. and Gofman, J. W. Magnetic Fields, Vagal Inhibition, and Acetylcholinesterase Activity. UCRL-12389, Biol. & Med., UC-48, TID-4500 (37th Ed.), Univ. of Calif., LRL, Livermore, 1965.

28. Dunlop, D. W. and Schmidt, B. L. Anomalous Development of Roots of Narcissus tazetta and Allium cepa exposed to Magnetic Fields. Third International Biomagnetic Symposium, University of Illinois, Chicago, 1966.

29. Gualtierotti, T. Effects of a Steady Magnetic Field on the Cerebellar Centers for Equilibrium and Orientation. Twelfth International Astronautical Congress, Wahington, 1961.

30. Bianchi, A., Capraro, V. and Gualtierotti, T. Decrease of the Sodium Transport Across Frog Skin in a Steady Magnetic Field. J. Physiol. 168:61, 1963.

31. Gualtierotti, T. Decrease of the Sodium Pump Activity in the Frog Skin in a Steady Magnetic Field. The Physiologist 3:150, 1964.

32. Hanneman, G. D. Changes Produced in Urinary Sodium, Potassium and Calcium Excretion in Mice Exposed to Homogeneous Electromagnetic Stress. Aerosp. Med. 38:275, 1967.

33. Barnwell, F. H. A Day-to-Day Relationship Between Oxidative Metabolism and World-Wide Geomagnetic Activity. Biol. Bull. 119:303, 1960.

34. Brown, F. A., Jr. Responses of the Planarian, Dugesia, and the Protozoan, Paramecium, to Weak Horizontal Magnetic Fields. Biol. Bull. 123:264, 1962.

35. Beischer, D. E. and Miller, E. F. Cited by Beischer, D. E. Biological Effects of Magnetic Fields in Their Relation to Space Travel. In: Schaefer, K. E. (Ed.) Bioastronautics. New York: Macmillan, 1964.

36. Becker, G. Zur Magnetfeld-Orientierung von Dipteren. Ztschr. f. vergl. Physiol. 51:135, 1965.

37. Greene, A. E. and Halpern, M. H. Response of Tissue Culture Cells to Low Magnetic Fields. Aerosp. Med. 37:251, 1966.

38. Conley, C. C., Mills, W. J. and Cook, P. A. Enzyme Activity in Macrophages from Animals Exposed to a Very Low Magnetic Field. Third International Biomagnetic Symposium, University of Illinois, Chicago, 1966.

39. Schultz, A.,Smith, J. and Dycus, A. M. Effects on Early Plant Growth from Nulled and Directional Magnetic Field Environments. Third International Biomagnetic Symposium, University of Illinois, Chicago, 1966.

40. Swain, J. and Modisette, J. L. NASA Manned Spacecraft Center, Personal Communication, 1966.

41. Cook, E. S. and Smith, M. J. Effect of Strong Magnetic Fields on Specimens in vitro: Increase of Trypsin Activity. 143rd Meeting, American Chemical Society, 1963.

42. Akoyunoglou, G. Effect of a Magnetic field on Carboxydismutase Nature 202:452, 1964.

43. Wiley, R. H., Cooke, S. L., Jr., Crawford, T. H., Fairless, B. J., Liu, H. F. and Weber, E. C. Magnetic Reactivation of Partially Inhibited Trypsin. In: Barnothy, M. J. (Ed.) Biological Effects of Magnetic Fields. New York, Plenum Press, 1964.

44. Bessey, O. A., Lowry, O. H. and Brock, M. J. (A Method for the Determination of Phosphatase Using a Ch. omogenic Substrate) J. Biol. Chem. 164:321, 1946.

45. Reitman, S. and Frankel, S. Colorimatric Method for the Determination of Serum Transaminase Activity. Am. J. Clin. Path. 28:56, 1957.

MARINER VENUS 67 MAGNETIC CONTROL*

J. G. Bastow†

J. G. Bastow, "Mariner Venus 67 Magnetic Control," spacemagnetic exploration and technology symposium (August 1967), University of Nevada, Reno.

N69-33976

ABSTRACT

Magnetic control efforts on Mariner Venus 67 were limited to reducing and stabilizing the magnetic field of existing hardware and to obtaining more meaningful information on the magnetic condition of the hardware than had been obtained in the Mariner Mars 1964 program. All type approval (TA) hardware was magnetized and demagnetized and, if no adverse effects of demagnetization were observed, all flight hardware was demagnetized to erase the effects of environmental testing and to stabilize and reduce the magnetic field. A simple facility was erected in the spacecraft assembly area at the Jet Propulsion Laboratory where assemblies and subassemblies could be magnectially mapped and magnetized or demagnetized. A similar, but smaller, facility was erected at Cape Kennedy to maintain the spacecraft magnetic integrity until launch. Magnetic mapping data were processed by computer to provide the magnetic field components of the extrapolated field in spacecraft coordinates at the spacecraft magnetometer sensor. These field components were summed and compared with the mapped field of the complete spacecraft.

Key Words: Magnetic control, spacecraft perm, magnetic mapping, magnetometer, demagnetization.

INTRODUCTION

The Mariner Venus 67 spacecraft, like its predecessor, the Mariner Mars 1964 spacecraft, carried a helium magnetometer to measure the vector components of the planetary and interplanetary magnetic fields. Because of the increased knowledge of these fields,

---

*This paper presents the results of one phase of research carried out at the Jet Propulsion Laboratory, California Institute of Technology, under Contract No. NAS 7-100, sponsored by the National Aeronautics and Space Administration.

†Senior engineer, JPL, Pasadena, California.

it was determined that more sensitivity was required. Therefore, an improvement in the magnetic environment of the spacecraft, by reducing and stabilizing its field, was necessary.

In the Mariner Mars 1964 program, an extensive effort was made to keep the use of magnetic materials to a minimum. Hardware was mapped both before and after vibration testing to determine its compliance with magnetic design requirements. It was required that the total field of an assembly not exceed 5 γ measured at 3 ft nor change by more than 0.5 γ as a result of vibration testing. Unfortunately, much of the hardware failed to meet these requirements. It was difficult to analyze the mapping results because vibration testing had introduced too much variation. Also, no attempt had been made to determine the orientation of the hardware dipole moment. Generally, hardware was mapped around three arbitrarily defined natural rectangular coordinates, which were difficult to relate to the spacecraft coordinates. Although it was found that much of the hardware had relatively high fields, it was not known (except in a few isolated instances) whether this field was abnormally high as a result of the vibration testing or if it was a result of the characteristics of the hardware.

Following launch, a study was made on the magnetic stability of magnetized and demagnetized solar panels and an extensive study was made to determine if, and to what extent, the spacecraft could be demagnetized. This latter study, in particular, was very successful in reducing the spacecraft magnetic field. Demagnetizing fields up to an 80-gauss peak at 1/20 Hz were applied to the spacecraft. In the earth's field, it was impossible to reduce the spacecraft field by more than 50%; however, by reducing the earth's field by an order of magnitude, the field was reduced to about 15% of its original value.

The Mariner Venus 67 magnetic control effort, as it evolved in late 1965, was constrained severely by both schedule and budget limitations. Improvements had to be realized utilizing essentially unmodified Mariner Mars 1964 hardware, with virtually no opportunity to further eliminate magnetic materials. Design changes were limited to those essential for a Venus rather than a Mars flight.

MARINER VENUS 67 MAGNETIC CONTROL PLAN

Based on Mariner Mars 1964 experience, it was decided that the most useful magnetic control on the Mariner Venus 67 spacecraft would be obtained by demagnetizing the flight spacecraft following its final vibration testing. Limited tests had indicated that this would be a more stable condition than the permed condition resulting from the vibration testing on magnetic shakers. It was also felt that any change in the spacecraft perm field as a consequence of the launch environment would be less if the spacecraft were in the demagnetized condition, rather than permed by the vibration testing. Hence, two major objectives evolved as a consequence of this demagnetizing program. First, to reduce the total spacecraft field from that obtained for the Mariner Mars 1964 spacecraft and, second, to ensure a more stable spacecraft magnetic field.

It was determined that the most effective control of hardware and most efficient demagnetization would be obtained if the demagnetization of flight hardware were accomplished on the assembly or subassembly level and at as late a time in the schedule as possible. By keeping the size of the test hardware small, the mapping and demagnetization, which both depend on a low and uniform ambient field, will be more effective with a smaller facility. The most opportune time for demagnetization and mapping of the flight hardware was found to be at the final inspection of the spacecraft. At this time, the spacecraft and its hardware have completed all environmental testing, the hardware is under quality assurance control, and the spacecraft is disassembled down to the subassembly level for a minute inspection before final assembly, test, and shipment to Cape Kennedy. Time did not permit mapping of each subassembly so, wherever possible, a complete bay or subsystem was demagnetized and mapped as a whole.

MAGNETIC FACILITIES

In carrying out this program, it was necessary to have a facility that was capable of magnetic mapping and demagnetizing in a low ambient field, and of sufficient size to properly accomplish these tasks on assembly-size units, approximately 1 1/2 x 2 x 2 ft. It was desired that this facility be convenient to the spacecraft hardware because the remoteness of the test facility for Mariner Mars 1964 had imposed an unnecessary obstacle to the mapping program. That facility had been developed primarily for support of the magnetometer experiment and instrument calibration with more stringent requirements than were required for merely mapping and demagnetizing hardware. Consequently, the Mariner Venus 67 magnetic facility was located in the spacecraft assembly area, fairly close to the spacecraft test stands. This location was particularly important because it was desired to demagnetize and map the spacecraft hardware after the spacecraft and its individual hardware had completed all environmental testing. This necessitated getting at the hardware rather late in the program and while the hardware was under quite rigid quality assurance control.

The facility (Fig. 1) was built around the 7-ft diam, 4000-lb demagnetizing coils, which had been developed for demagnetizing the complete Mariner Mars 1964 spacecraft and its solar panels. To reduce the earth's ambient field in the center of the demagnetizing coil structure and also to provide a mapping area, a three-axis Helmholtz system was constructed around the demagnetizing coil. A 12 1/2-ft diam coil pair was used to buck the vertical field, a 12-ft diam pair to buck the horizontal field, and a 10-ft diam pair to buck the variable east-west component. This latter coil was necessary to allow for drift in the earth's field and to eliminate the necessity of reorienting the coils as the earth's field shifted either because of natural causes or a change in local conditions.

So that the demagnetizing coil would be in the center of the Helmholtz coil system, it was necessary to raise the demagnetizing coils about 3 ft and build a work platform in the center of the system. The mapping turntable was located about 12 in. below the center line of the demagnetizing coil axis which was also oriented in the magnetic east-west direction. The magnetometer probe was mounted on the north

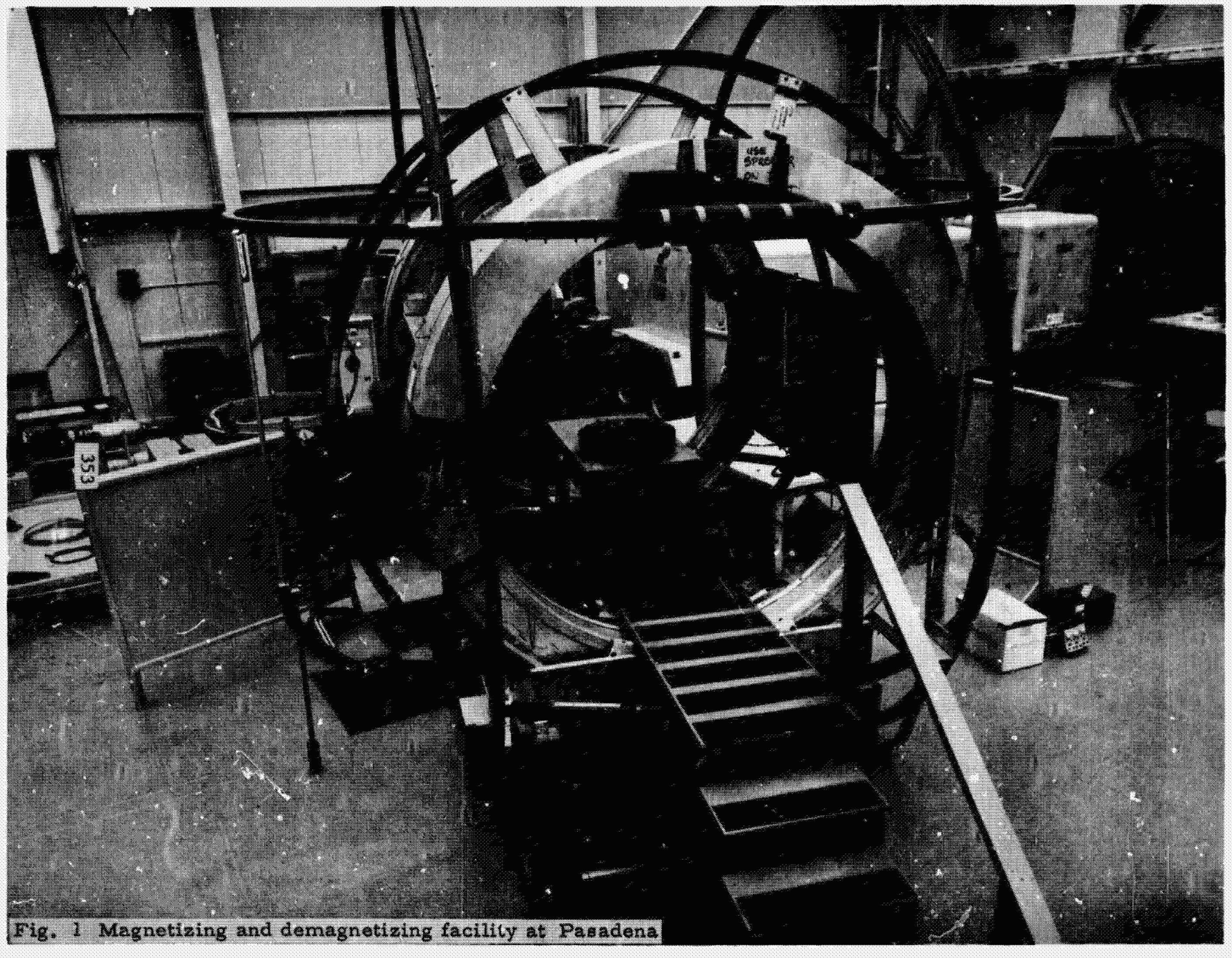


Fig. 1 Magnetizing and demagnetizing facility at Pasadena

side of the mapping turntable so that induced field effects could be determined by turning off the north-south horizontal field bucking coils. This resulted in a horizontal component of field of about 0.26 gauss.

At the center of the coil system, the field was reduced to less than 10 γ, which resulted in a magnetic field over the 2 x 2 x 2-ft volume of less than 200 γ. Field gradients were not particularly good in this area. However, because the magnitude of the field was maintained at a low level, the induced effects were negligible.

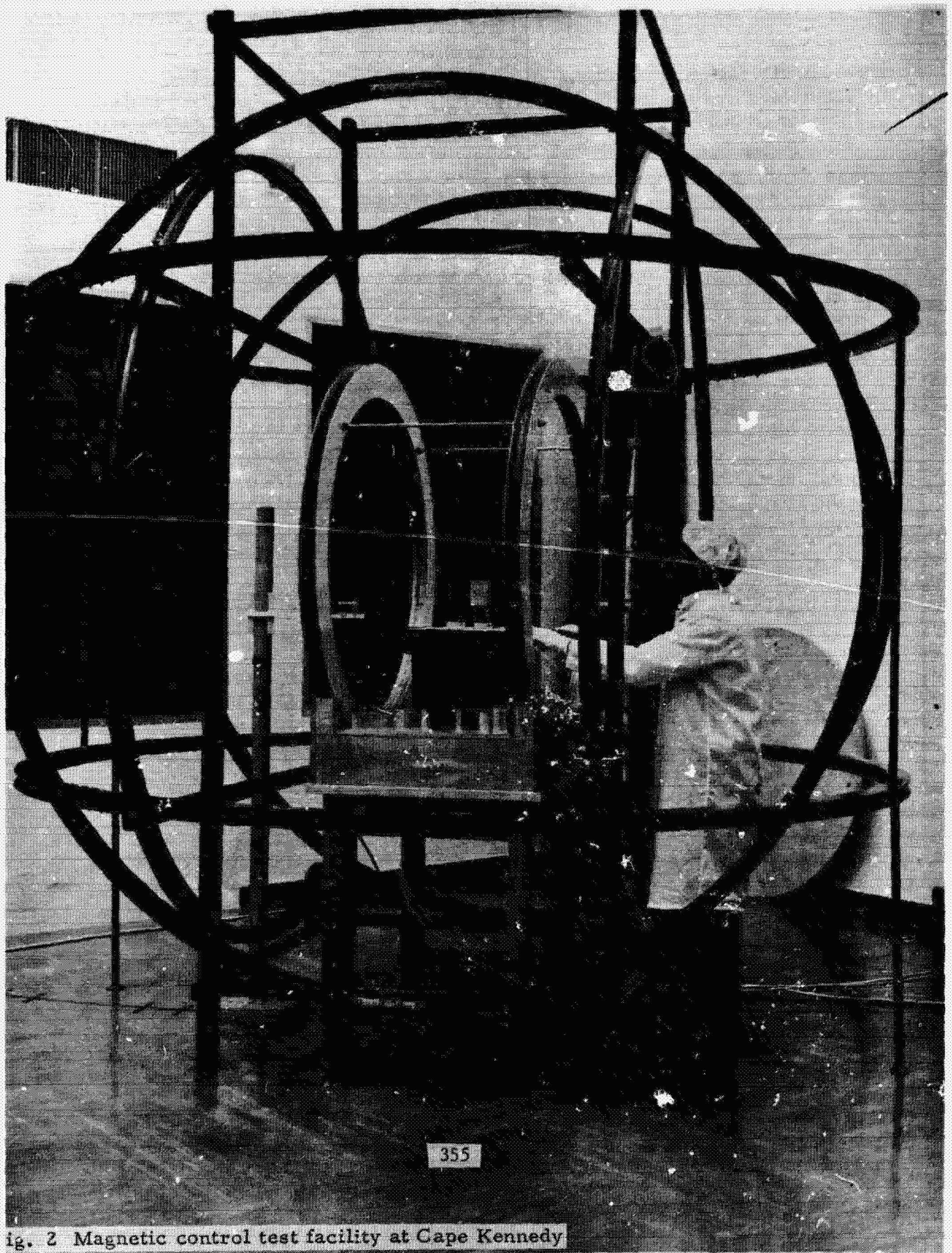
As magnetic control was to be continued at Cape Kennedy, a mapping and demagnetizing facility was also necessary at that location. To avoid the expense of shipping the large demagnetizing coils to and from Florida, a 4 1/2-ft diam Helmholtz coil pair was fabricated, capable of the 40-gauss-peak demagnetizing field used on flight hardware. At Kennedy this demagnetizing coil pair was set up in the spacecraft test area in the center of a 10-ft diam, three-axis Helmholtz coil system with a mapping turntable mounted in the center. This is shown in Fig. 2.

At times, the noise level at these sites was objectionable. In one case, the excessive noise was caused by construction work on the exterior of the next building. By waiting and making several rotations of the turntable for each position, acceptable data were obtained. Each item of hardware was mapped in each of its three coordinate axes; one of which results in redundant information that can assist in evaluation of the mapping. All mappings were obtained with the probe at a distance of approximately three times the longest dimension, up to a maximum distance of 6 ft. If other than a sine wave plot was obtained, the distance was increased (in the case of a multipolar indication) or the hardware was offset if the plot indicated the dipole was not at the center of rotation. In this way, every effort was made to obtain a dipolar mapping in order that the mapping information could be extrapolated to the magnetometer position.

From the X-Y plot of the mapping, the peak-to-peak magnetic field magnitudes were read, as well as the angular position of the maximum and the minimum. This information, the mapping distance, and the spacecraft coordinates of the center of the hardware were punched on IBM cards and fed into a 1620 computer. The 1620 computed the dipole moment and extrapolated the value of the maximum radial field to 3 ft. The computer also provided the three rectangular components of the magnetic field at the position of the spacecraft science magnetometer. The computer furnished a summation of the fields at the science magnetometer for each of the various mapping conditions.

TEST PROGRAM

To ensure that the demagnetization would have no adverse effects on the spacecraft, it was required that type approval (TA) or prototype hardware be thoroughly evaluated to determine compatibility with the demagnetization procedure to be followed on the flight hardware. The TA hardware was, therefore, subjected to a series of tests similar to what has become standard magnetic testing. The hardware was first mapped as received. This mapping had no real significance, except to determine the subsequent perming axis and the initial demagnetization axis, because the history of the hardware had not been fully determined. Next, the hardware was demagnetized in three axes and mapped in the



ig. 2 Magnetic control test facility at Cape Kennedy

same manner as the flight hardware was subsequently handled. With the 1/20-Hz demagnetizing frequency, each demagnetizing operation required about 6 min to decay from a peak field of 40 gauss. Each mapping consisted of a plot of the radial magnetic field component vs the rotation angle as the hardware was rotated about each of its three rectangular axes. Photographs were made of each mapping position to ensure that the same and a proper position was used in each mapping. Generally, the hardware was mapped in spacecraft coordinates or in such a way that a simple transformation would convert the mapping into spacecraft coordinates.

When the hardware was essentially demagnetized, it was exposed to a constant-peak amplitude perming field of 25 gauss. Actually, this field was several cycles of the 1/20-Hz field, with the final pulse being in a direction that reversed the residual field of the demagnetized condition. This helped to disclose possible hard magnet elements in the hardware. There was not enough time to perm in each axis independently, although such work probably would have been beneficial. Consequently, the hardware was only permed in one axis, the one most nearly parallel to the dipole moment determined in the "as received" mapping.

So that the TA hardware could be exposed to twice the field level specified for the flight hardware, the TA hardware was demagnetized with a peak demagnetizing field of 80 gauss over a period of about 9 min for each of its three axes. Following the three-axis demagnetization, it was again mapped.

The final test consisted of determining the effect of a 0.26-gauss inducing field as the hardware was rotated around each of its three axes. To establish a zero-field level, the hardware was withdrawn at the end of each rotation. The latter curves proved to be quite difficult to analyze because of the anisotropic nature of the induced field. The test did, however, serve as a measure of the susceptibility of the hardware to the launch environment.

In addition to the normal test procedures described previously, special tests were conducted in a few cases. Three of these special tests involved magnetic latching relays, the Canopus sensor image tube, and the tape recorder subsystem.

Special tests were conducted on latching relays because of the concern that hardware demagnetization might demagnetize the permanent magnet in the relays and render them inoperative. Tests of the latching current and the stray magnetic field indicated that magnetic fields in excess of a 500-gauss peak were necessary to alter the performance or magnetic characteristics of the relay. Essentially the same results were obtained by Goddard Space Flight Center in a similar, earlier test. The tests also alleviated the concern felt by other engineers cognizant of such devices as motors and positioners that have permanent magnet components.

The Canopus sensor, in addition to having ferromagnetic materials in the image tube, had a high-permeability shield material around the tube to protect the tube electron beam from external stray fields that might affect the sensor's accuracy. Demagnetization of the complete sensor altered the alignment of this tube by about 0.5 deg, which was considered excessive. As the sensor required disassembly to correct this alignment error, the flight Canopus sensors were granted a waiver on the demagnetization requirement.

Concern was expressed about the effect of demagnetization on the tape recorder tape. Tests on a specially prepared tape revealed that the magnetization and demagnetization of the tape recorder subassembly had no effect on the test recording on the tape.

It was only after all TA hardware had been evaluated that the flight hardware was demagnetized and mapped. Each item of hardware, as it was removed from the spacecraft for final inspection, was demagnetized with a 1/20-Hz demagnetizing field decaying from a peak field of 40 gauss in each of its three rectangular axes and then mapped by rotation around each axis. The remaining bus structure with the attitude-control gas system and the sun sensors was demagnetized as a unit. Because of its size, the structure was demagnetized in only two of the three axes and was then mapped in the earth's field on a large mapping fixture specially built for the spacecraft.

Following reassembly of the spacecraft, the nearly complete spacecraft (except for solar panels) was mapped in the earth's field to determine the three components of the spacecraft field at the position of the spacecraft magnetometer sensor.

Because the spacecraft mapping facilities were not large enough to map the spacecraft with the solar panels mounted and extended, the magnetic fields attributed to the solar panels were treated entirely separately and algebraically added to the other determinations. In the Mariner Mars 1964 program, the magnetic fields of the solar panels were a real source of concern. After vibration testing, the panels (when mounted on the spacecraft) had a combined field at the magnetometer sensor in the Z-axis of almost 100γ. It was found possible, however, to effectively demagnetize the panels to the point where they were less than 1γ each. In the Mariner Venus 67 program, there was an appreciable change in the layout of the solar panels because the flight was to be toward, rather than away from, the sun. Two changes in the panel design materially altered the magnetic effects of the panels at the magnetometer sensor. First, the solar panel active surface was to be only about two-thirds as large as the Mariner Mars 1964. The "missing" section was that part of the Mariner Mars panel which had been nearest to the spacecraft bus structure. Consequently, the offending Kovar bus bars were further from the magnetometer. Second, and more important, the Kovar buses and wires were oriented with their long axes across the width of the panel, rather than along the long axis of the panel, as was the case on the earlier program. This arrangement, shown in Fig. 3, virtually precluded the panel from acquiring a residual field from the vibration exciters. It was found that this was the case and, although demagnetization studies were made on a TA solar panel, demagnetization of the flight panels was found to be unnecessary because their residual fields were less than 0.5γ at the flight sensor.

Following the initial demagnetization and mapping of the flight hardware, strict control was maintained over the hardware and the tools used in spacecraft assembly to maintain the magnetic integrity of the spacecraft. This control was continued until the time of launch at Cape Kennedy. Any hardware that was removed from the spacecraft assembly

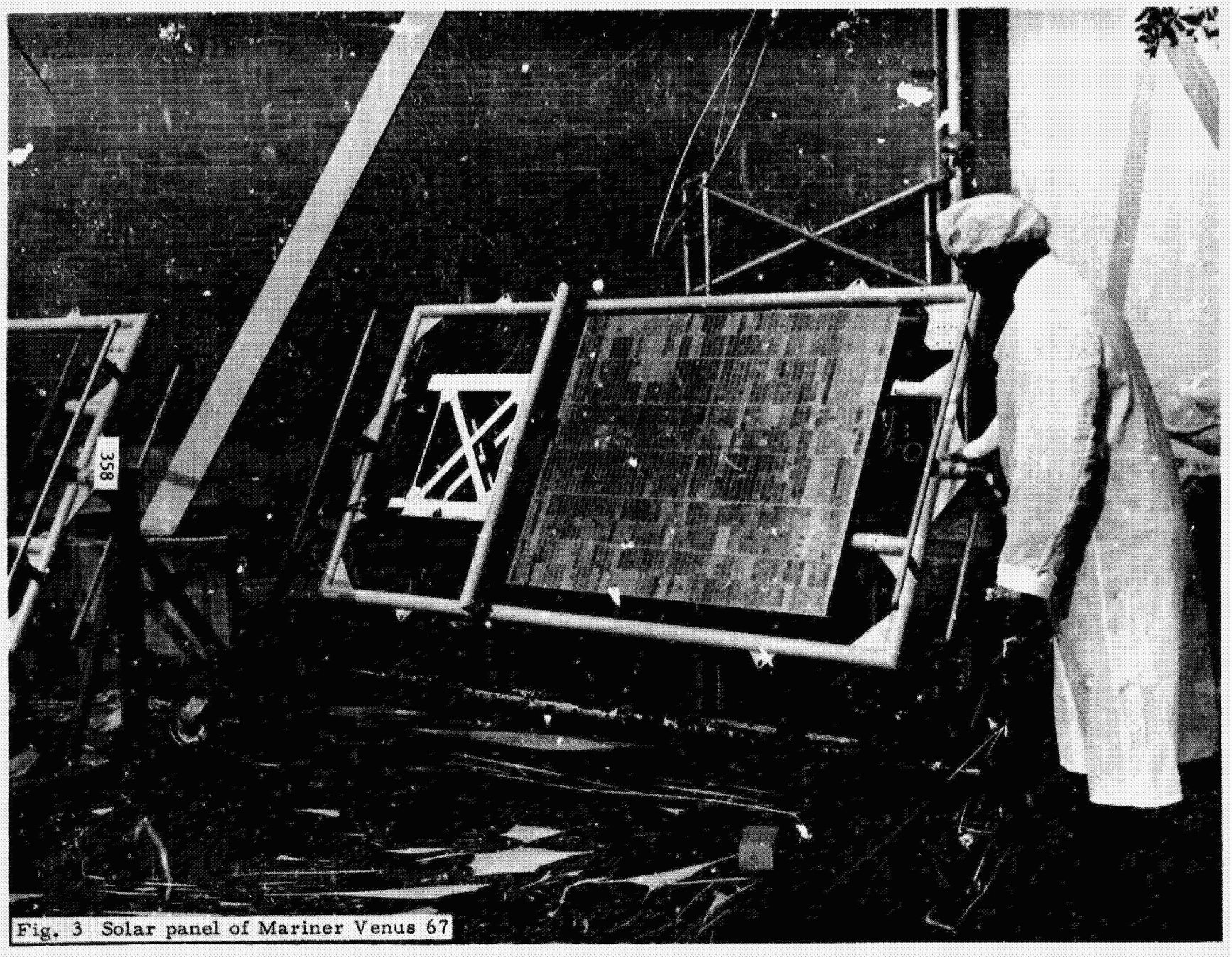


Fig. 3 Solar panel of Mariner Venus 67

area for rework was remapped on return and demagnetized again, if the field had changed by more than 10% from its previous demagnetized conditions.

At the time that the flight hardware was undergoing demagnetization and mapping, all of the spacecraft assembly tools (approximately 1,000 for each of the two flight spacecraft) were examined for a residual magnetic field. Tests on a small nickel ribbon module had indicated that tools having a field greater than 10 gauss on the surface would cause a measurable perm field in the module if they were to come in contact with the module. On this basis, any tool which displayed a magnetic field on the surface of the tool greater than 5 gauss was demagnetized until the field was reduced below this level. As the induced field of some tools was as much as from 3 to 4 gauss in the earth's field, the orientation of the tool would affect the measurement. No attempt, however, was made for precision in these measurements; if there was a question, the tool was demagnetized. The tools were tested by passing a gaussmeter probe over the surface of the tool with emphasis given to the ends of long thin tools. Approximately one-third of the tools were found to exceed the prescribed level; a few items had fields as high as 120 gauss. Not all tools were found to be permed, as expected, parallel to the long axis; sockets had fields across the diameter and crescent wrenches had fields across the jaws of the wrench. All tools could be brought below the required level by demagnetization. Subsequent rechecks of the tools did disclose a few which had reacquired a perm by one means or another.

Recheck of the tools continued at Cape Kennedy and also the tools used by the Lockheed Missiles and Space Company in matchmate of the spacecraft and Agena vehicle were checked and demagnetized there.

DISCUSSION OF PROGRAM RESULTS

This program did achieve one of its two major objectives, namely, reducing the spacecraft magnetic field at the magnetometer sensor. A comparison of the perm fields of two Mariner Mars 1964 spacecraft that were not demagnetized, and the Mariner Venus 67 flight spacecraft which were, is shown in the following table:

		X	Y	Z
Mariner Mars 1964	MC-2	2.5γ	21.0γ	17.4γ
	MC-3	5.0γ	11.5γ	30.1γ
Mariner Venus 67	MV67-1	-1.2γ	3.5γ	7.1γ
	MV67-2	-1.2γ	2.8γ	7.3γ

The second objective of obtaining a stable magnetic field was more difficult to verify. The final proof is whether the mapped field varies unexpectedly on successive mappings. Two cases of this were evident in this program. In the first case, the spacecraft was mapped without

its solar panels on February 15 and again on March 31, 1967. Although some of the hardware had been reworked during this period, this fact does not explain completely the large differences shown in the table below:

	X	Y	Z
February 15 mapping	1.5γ	3.9γ	3.1γ
March 31 mapping	-1.0γ	3.3γ	6.9γ

A review of the mapping results indicates that a few units show an excessively large variation in successive mappings of the same unit. This was particularly evident with the midcourse motor, the Canopus sensor, and the recorder subsystem.

In the second case, the field of the launched spacecraft seemed to differ unexpectedly from the field as mapped in Pasadena on April 13, 1967.

	X	Y	Z
April 13 mapping	-1.3γ	0.3γ	6.6γ
June 14-30 in-flight calibration	3.7γ	0.9γ	8.5γ

From these two cases, it is apparent that magnetic stability was not achieved. The major obstacle to magnetic stability continues to be an excessive amount of magnetic material in the spacecraft.

In addition to ensuring a low, stable residual field, we wanted to know if the magnetic fields of spacecraft assemblies could be summed to obtain an estimate of the total field of the spacecraft and if the effect of removing or installing a single assembly could be predicted. One objective was to find how the field of the individual assemblies contributed to the total field of the spacecraft. This is pertinent in any large program where assembly or subassembly restraints must conform to the over-all system requirements. It was primarily to obtain the spacecraft magnetic field components at the science magnetometer position that the magnetic mapping data were computer processed.

The results obtained by adding the field components of individual assemblies and subassemblies were in reasonably good agreement with the field determined by mapping the assembled spacecraft. This is shown in the next table for each of the two Mariner Venus 67 flight spacecraft.

		X	Y	Z
MV67-1	Sum of subassembly fields	-0.8γ	6.8γ	2.4γ
	Assembled spacecraft mapping	-1.0γ	3.3γ	6.9γ
MV67-2	Sum of subassembly fields	-1.3γ	2.5γ	5.7γ
	Assembled spacecraft mapping	-1.0γ	2.6γ	7.1γ

The large discrepancies in summed fields of the Mariner Venus 67 spacecraft appear to result almost entirely from the quadrapole field of the bay 6 radio transmitter subsystem. Although the mapping curves of this bay for the two spacecraft were similar (in that they both displayed a double-peak curve characteristic of a quadrapole and had approximately the same over-all amplitudes), the positions of the higher peaks were such as to essentially indicate a reversed field at the magnetometer sensor.

Because these computations depend on the source of magnetization being a simple dipole, deviations from this ideal are a major problem, for example, in this case, where double-humped curves were obtained. Some study is being made to determine if an equivalent dipole field can be determined from this type of curve in order that extrapolated results will be more valid. At the present time, it appears that the harmonic content of the curves is related to the dipole distribution. Additional studies are required to obtain useful relationships that could assist in evaluating the data.

In those cases where the X-Y plot indicates a simple dipole not at the center of rotation of the mapping turntable, attempts were made to correct the readings resulting from these offsets by utilizing information contained in NOLTR 64-52 ("Magnetic Moment Testing of Satellites") which gave curves of the effect of an offset dipole. It was found later that sufficiently accurate mapping data could be obtained more easily by offsetting the hardware on the mapping turntable so that the dipole was closer to the center of rotation.

In general, all of these abnormal mappings, which deviate from a simple sine curve, result in too large a peak-to-peak amplitude and, consequently, too large a value for the field components at the magnetometer sensor.

There are two major considerations that render a magnetic field summation not entirely valid. First, because of the generally random distribution and orientation of spacecraft magnetic field sources, we might expect that they would add algebraically to nearly zero, assuming similar amplitudes. Consequently, only the larger amplitude sources, or non-uniform orientations or distributions, would be apparent. Secondly, the summation depends on no interaction of neighboring fields and magnetic materials. If there is magnetic material in the hardware (as there will be unless specifically excluded), it will alter the fields caused by neighboring hardware. It would be expected that here also, the summed field would be larger than the measured field of the assembled units. This expectation was verified by comparing the sum of mappings of a few individual subassemblies with the component mappings.

CONCLUSIONS

While this program has succeeded in materially reducing the spacecraft magnetic field, it has not resolved the problem of magnetic stability. Magnetic stability remains intimately related to the amount

and type of magnetic material in the hardware while the total spacecraft field is more dependent on placement and orientation of hardware on the spacecraft. The results of this program clearly demonstrate that a spacecraft can have a low total field and yet be made up of many subassemblies with very large and potentially unstable magnetic fields.

The results of the technique of summing the subassembly fields, when compared with the total spacecraft mapped field, show significant correlation and provide insight into the effect of removing or adding a single item of hardware on the total spacecraft field. Additional work remains on the interpretation of irregular, nonsinusoidal mapping results to improve the correlation between these summed and mapped fields.

Magnetic Tests of the OGO and ERS Satellites

G. T. Inouye*

Presented at the Space Magnetic Exploration and Technology Symposium
(August 1967) University of Nevada, Reno

N69-33977

Abstract

This paper presents the results and methods used to test for the magnetic properties of the OGO and ERS satellites at the TRW Malibu Magnetic Test Facility located at Malibu. The magnetic property of the spacecraft of paramount interest are the spacecraft magnetic field at the position of the onboard magnetic sensor, both permanent and induced. Also of interest is the proportion of this field which is "hard" or permanent, and the proportion which is "soft" which may be changed by normal magnetizing environments to which the spacecraft may be subjected before being launched into orbit. Another magnetic property of interest is an overall map of the spacecraft field, and its characterization in terms of dipole and higher order multipoles, both permanent and induced, located at the center of the spacecraft.

The test site at Malibu consists of a 21 foot triaxial Fanselau-Braunbeck coil system housed in a silo, and several other buildings. A turntable is located in one of these buildings for the coil-less testing of spacecraft such as the OGO which are too large to fit into the Fanselau-Braunbeck coil system.

The testing techniques used in both the coil and coil-less methods involve the rotation of the spacecraft about two axes relative to fixed triaxial fluxgate sensors. The rotation period is required to be less than that for which an appreciable change in the ambient geomagnetic field occurs. Cancellation of these geomagnetic variations with a remote sensor eases this constraint. The fluxgate sensor outputs are recorded on both a multichannel Sanborn chart recorder and an X-Y plotter. The X-Y plot permits an immediate scaling of the magnitude of the magnetic moment in the plane of rotation, as well as giving its orientation in spacecraft coordinates. Rotation of the spacecraft about another orthogonal axis provides data for obtaining the total moment vector.

The ERS satellite to be tested is an 11 inch octahedron which easily fits into the Fanselau-Braunbeck coil system. With the coil system, of course, it is possible to measure the permanent and induced components of the spacecraft field independently.

I. Introduction

Magnetic tests have been performed on four of the Orbiting Geophysical Observatories (OGO), and the Environmental Research Satellite (ERS) designated

*Space Sciences Laboratory, Physical Research Center, TRW Systems, R1/1062, One Space Park, Redondo Beach, California 90278

as the OV5-5. The main body of the OGO, which is an oblong rectangular parallelepiped, is about 10 feet on its long dimension with the magnetic sensors located on a boom 24 feet from the center of the spacecraft. The ERS, on the other hand, is an octahedron of about 11 inches on a side, and its magnetic sensor is located about 15 inches from the center of the spacecraft. Both spacecraft were built with a certain amount of magnetic control to eliminate magnetic components wherever feasible within contract limitations. The ERS, being much smaller and less complex, permitted the use of a proportionately smaller boom than the OGO.

Both spacecraft trajectories are intended to carry the experiment out of the magnetosphere into the solar wind, so that resolutions of the order of a fraction of a gamma are required in the instrumentation. The characteristic of paramount interest in these magnetic tests was the magnitude and direction of the spacecraft field, both permanent and induced, at the location of the on-board magnetic sensors. Also of interest was the proportion of this field which was "hard" and the proportion which was "soft" and hence could be changed by normal magnetizing environments to which the spacecraft is subjected before being launched into orbit. Another property of interest was the overall map of the spacecraft field and its characterization in terms of dipole and higher order multipoles, both permanent and induced, located at the center of the spacecraft.

II. Measurement Techniques and Problems

The two main measurement problems encountered in spacecraft magnetic tests are the variations of the ambient geomagnetic field, and the sorting out of the induced effects from the permanent field. The latter problem is most easily solved by placing the spacecraft in a suitably large coil system in which the ambient field may be nulled out to the required levels over the volume of the spacecraft. Disregarding the ambient field variations for the moment, the field at the sensor location as well as an overall field map may then be obtained by first zeroing the outputs from triaxial fluxgate sensors located at the desired locations, and then placing the spacecraft on a turntable and recording the sensor outputs as the spacecraft is rotated about two mutually orthogonal axes. The dc offsets due to the introduction of the spacecraft plus the additional variations due to the two rotations would then give all the data necessary to determine the spacecraft field at the sensor location as well as the multipole expansion describing the measured field map. To determine the induction effects, the preceeding measurements would be taken at controlled field levels, and the increments in the measured fields from the zero field results could then be ascribed to the induction effects.

The problem of the ambient field variation has been solved to a large extent by means of a remote triaxial sensor whose output may be used to buck out the ambient geomagnetic field variations in the coil system. In the case of the coil-less test methods, the ambient fluctuations may either be subtracted out of the spacecraft field sensor outputs or inserted in a nulling sense into extra coil windings which are provided around each sensor. For spacecraft as large as the OGO, maneuvering of the spacecraft into or out of the test setup requires a period of about 15 minutes. For measurement resolutions of the order of 0.1 gamma, differential sensor drifts during this time

span make it difficult to obtain meaningful dc offset measurements. The data analysis techniques used and described in this paper are therefore designed to use only the sensor output variations with turntable rotation, which is in the order of 1 to 2 rpm.

The ERS satellite, being so small, is ideally suited for testing in the 21 foot triaxial Fanselau-Braunbeck coil system which is located at the TRW Magnetic Test Facility at Malibu.

III. Data Analysis - Permanent Dipole Field

The most straightforward and elegant method of analyzing the data generated is to express the spacecraft field in terms of a spherical harmonic expansion of the form

$$B = \nabla \sum_{n=1}^{\infty} \sum_{m=0}^{n} \left(G_n^m \cos n\phi + H_n^m \sin m\phi\right) P_n^m (\cos\theta) \qquad (1)$$

where the gaussian coefficients G_n^m and H_n^m include induced as well as permanent magnetization terms. As many terms are taken as required to fit the measurement data, and then the coefficients evaluated to give the best fit when the data is resynthesized from these coefficients. Such an analysis has been performed on the OGO data including permanent dipole, quadupole and octupole moments as well as induced dipole moments(1). The results are in essential agreement with the results of a less elaborate treatment which is described in the following sections.

Let us assume first that the spacecraft field is that of a permanent dipole located at the center of the spacecraft and also in the plane perpendicular to the vertical axis of rotation. The measurement setup and coordinate system is shown in Figure 1. The fields detected by the three sensors oriented as shown at a distance r vary with spacecraft rotation angle ϕ as

$$P_N = \frac{2M}{r^3} \cos\phi, \qquad P_E = -\frac{M}{r^3} \sin\phi, \quad \text{and} \quad P_V = 0. \qquad (2)$$

The component parallel to the rotation axis, P_V, shows no variation with ϕ, and the other two components vary sinusoidally with ϕ, the polar component, P_N, being twice as large as the equatorial component, P_E, and 90 degrees out of phase. In the N-E plane, the P vector traces out an ellipse with a 2:1 ratio of major to minor axes, the sense of rotation being opposite to that of the spacecraft rotation. One-fourth of the peak-to-peak P_N variation or one-half of the peak-to-peak P_E variation, then, gives the magnitude of M according to equation (2):

$$M = \frac{r^3 P_{N\,max}}{2} = r^3 P_{E\,max} \qquad (3)$$

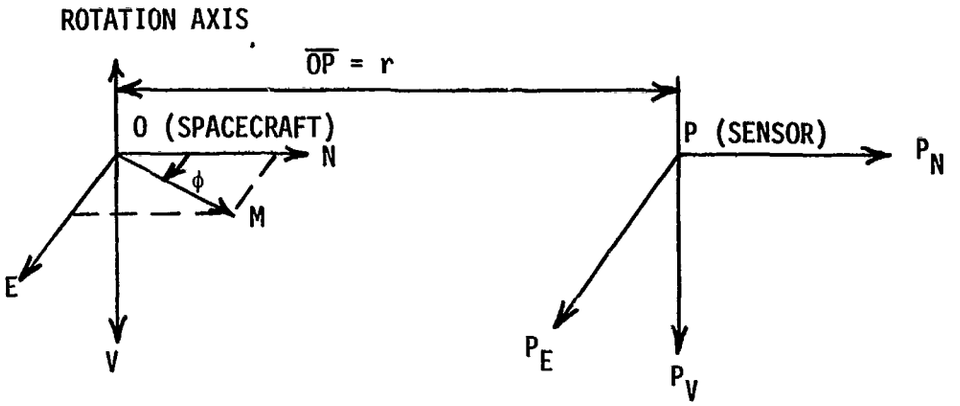


Figure 1. Measurement Set-Up and Coordinate System

In the actual case, the orientation of M within the spacecraft coordinate system is unkown and rotation must be performed about two orthogonal axes. Let X, Y, Z be the spacecraft coordinate system, and M_X, M_Y, M_Z be the components of M along these axes. Rotation of the spacecraft about its X-axis gives M_Y and M_Z, and rotation about its Z-axis gives M_X and M_Y.

If the N-E measurement coordinate system is not radial and azimuthal as shown in Figure 1, the simple 2:1 amplitude ratio and 90 degree phase relation between the N and E sensor outputs no longer obtains. However, the same ellipse is generated if the outputs are applied to an X-Y plotter, except that the major and minor axes are tilted by an angle corresponding to the rotation of the sensor axes from the radial directions. This non-radial condition existed in the OGO tests since the triaxial sensor was oriented North-East-Vertical, and the size of the building did not permit the radial direction to be North-South or East-West. The use of the X-Y plotter, then, permitted the direct scaling of the spacecraft field. In this section we have shown that if the spacecraft field is only comprised of a permanent dipole field, it may be computed from only the sinusoidally varying sensor outputs disregarding any steady-state offsets which may or may not be detected.

IV. Induced Fields

The induced moments, N, are related to the inducing field B, by a 3 by 3 matrix, $|a_{ij}|$,

$$\vec{N}\,(x\ y\ z) = |a_{ij}|\ \vec{B}\,(x\ y\ z) \qquad (4)$$

where the nine $|a_{ij}|$ terms are the induction coefficients. Expressing the induced moments in terms of the N-E-V sensor coordinate system with the spacecraft rotational angle ϕ measured as shown in Figure 2,

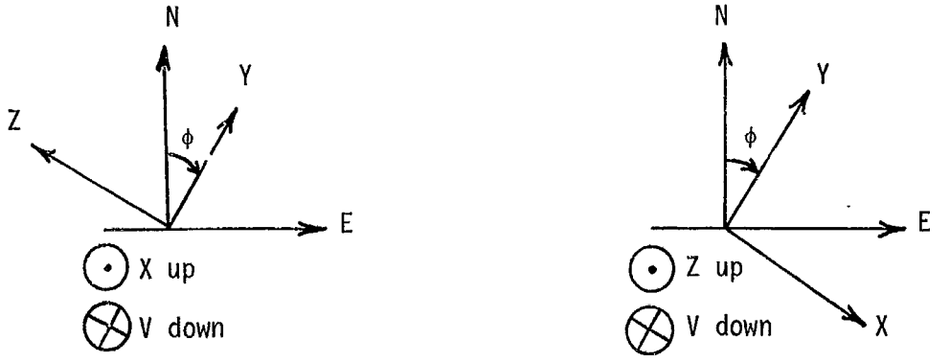


Figure 2. N-E-V Sensor and X-Y-Z Spacecraft Coordinates

$$N_{NX} = N_Y \cos\phi + N_Z \sin\phi \quad (5a)$$

$$N_{EX} = N_Y \sin\phi - N_Z \cos\phi \quad (5b)$$

$$N_{VX} = -N_X \quad (5c)$$

$$N_{NZ} = N_Y \cos\phi - N_X \sin\phi \quad (6a)$$

$$N_{EZ} = N_Y \sin\phi + N_X \cos\phi \quad (6b)$$

$$N_{VZ} = -N_Z \quad (6c)$$

The second subscript on the terms on the left signify the pertinent rotation axis.

The inducing field, B, to be used in equation (4) in spacecraft coordinates is given by

$$B_{XX} = -B_V, \quad B_{YX} = B_N \cos\phi, \quad B_{ZX} = B_N \sin\phi \quad (7)$$

$$B_{XZ} = -B_N \sin\phi, \quad B_{YZ} = B_N \cos\phi, \quad B_{ZZ} = -B_V \quad (8)$$

where B_V and B_N are the vertical (down) and northward (horizontal) components of the ambient inducing field. Again, the second of the double subscripts signify the pertinent rotation axis. The fields, I, produced at the sensor by these induced moments assuming that the sensor is located directly North of the spacecraft are given by

$$I_{NX} = \frac{2}{r^3} N_{NX}, \quad I_{EX} = \frac{-1}{r^3} N_{EX}, \quad I_{VX} = \frac{-1}{r^3} N_{VX} \quad (9)$$

$$I_{NZ} = \frac{2}{r^3} N_{NZ}, \quad I_{EZ} = -\frac{1}{r^3} N_{EZ}, \quad I_{VZ} = \frac{-1}{r^3} N_{VZ}. \quad (10)$$

Combining the expressions for B, N, and I, the induced fields are

$$I_{NX} = \frac{2}{r^3}\left[(-a_{21}\,B_V + a_{22}\,B_N\cos\phi + a_{23}\,B_N\sin\phi)\cos\phi\right. \tag{11a}$$

$$\left. + (-a_{31}\,B_V + a_{32}\,B_N\cos\phi + a_{33}\,B_N\sin\phi)\sin\phi\right]$$

$$I_{EX} = -\frac{1}{r^3}\left[(-a_{21}\,B_V + a_{22}\,B_N\cos\phi + a_{23}\,B_N\sin\phi)\sin\phi\right. \tag{11b}$$

$$\left. - (-a_{31}\,B_V + a_{32}\,B_N\cos\phi + a_{33}\,B_N\sin\phi)\cos\phi\right]$$

$$I_{VX} = \frac{+1}{r^3}(-a_{11}\,B_V + a_{12}\,B_N\cos\phi + a_{13}\,B_N\sin\phi)\,, \tag{11c}$$

with similar expressions for I_{NZ}, I_{EZ}, and I_{VZ}. The expressions for I_N and I_E have terms at the rotation frequency due to the cross-coupling of the vertical inducing field, plus second harmonic terms due to the variable induced moments. The vertical induced field has only fundamental terms, plus the steady-state terms.

All of the dipole induction cross-coefficients may be evaluated in the presence of permanent dipole moments by performing 180 degree reversals of the axes of rotation for all three orthogonal spacecraft axes, by analyzing the fundamental rotation period variations. These 180° reversals of the rotation axes shifts the phase of the induced fundamental term by 180°, but only reverses the sign of the phase angle of the permanent dipole contribution. The three diagonal terms of the induction matrix may be evaluated by analyzing the second harmonic components of the rotation frequency. Writing only these terms in equation 11,

$$I_{NX} = \frac{B_N}{r^3}\left[(a_{22} - a_{33})\cos 2\phi + (a_{23} + a_{32})\sin 2\phi\right] \tag{12a}$$

$$I_{EX} = \frac{B_N}{2r^3}\left[(a_{22} - a_{33})\sin 2\phi - (a_{23} + a_{32})\cos 2\phi\right] \tag{12b}$$

$$I_{VX} = 0\,. \tag{12c}$$

It is seen that each rotation gives only one equation involving the difference of two of the three diagonal terms. Thus, rotation about all three orthogonal axes is required to evaluate these terms.

V. Offset Permanent Dipole

The following is the analysis of a permanent dipole moment off-set from the axis of rotation, but still in the horizontal plane of the magnetometer and the origin of the spacecraft coordinate system. It is assumed again that the spacecraft is rotated in the clockwise direction about the x-axis which is vertically up. The permanent moment M, has components M_Y and M_Z and is located at z_0, y_0 or r_0, ϕ_0. R is the distance $\overline{OP}$, ϕ is the angle between the z-axis and $\overline{OP}$, r is the distance from the location of the off-set moment, Q, to the location of the magnetometer, P, and β is the angle between $\overline{OP}$ and $\overline{QP}$.

In this case of the off-set moment, the component of the moment parallel to the spin axis will cause a field change with rotation along the vertical magnetometer sensor due to the varying distance:

$$P_V = M_X r^{-3} = M_X \left[r_0^2 + R^2 - 2r_0 R \cos (\phi + \phi_0) \right]^{-3/2}. \tag{13}$$

assuming that $r_0^2 << R^2$ and discarding the dc terms:

$$P_V \doteq 3M_X \frac{r_0}{R^4} \cos (\phi + \phi_0). \tag{14}$$

The vertical component oscillation due to M_X will be at the fundamental frequency, but will be smaller than if M_X had been rotated in the horizontal plane by the ratio, $3r_0/2R:1$. If cross-induced field effects may be considered to be small, the detection of this component may be used as a criterion for the magnetic centering of the spacecraft on the turntable.

Under the assumption that $r_0^2 << R^2$, the analysis for P_E and P_N simplifies in the following manner:

$$r \doteq R \left[1 - \frac{r_0}{R} \cos (\phi + \phi_0) \right] \tag{15}$$

$$r^{-3} \doteq R^{-3} \left[1 + \frac{3r_0}{R} \cos (\phi + \phi_0) \right] \tag{16}$$

$$\cos \beta \doteq \cos 2\beta \doteq 1 \tag{17}$$

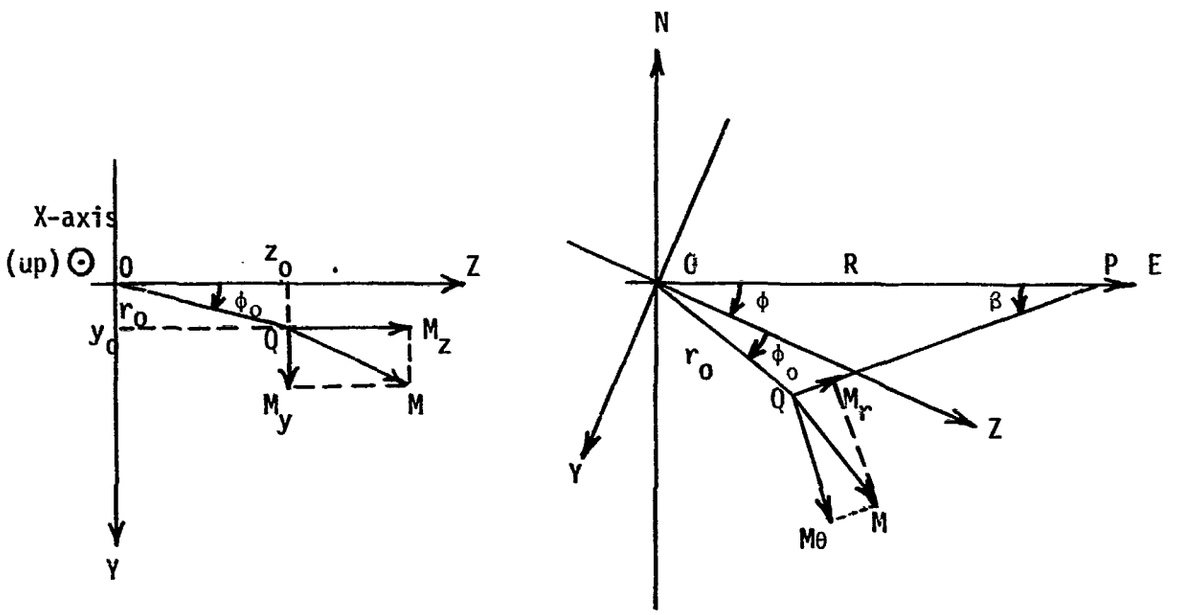


Figure 3. Coordinate System for Computing Offset Dipole Fields

$$\sin\beta \doteq \beta \doteq \frac{r_o}{R}\left[\sin(\phi+\phi_o) + \frac{r_o}{2R}\sin 2(\phi+\phi_o)\right] \tag{18}$$

$$P_E \doteq 2R^{-3}(M_Z\cos\phi - M_Y\sin\phi) + \frac{9}{2}M_Z r_o R^{-4}\cos(\phi_o+2\phi) \tag{19}$$

$$- \frac{3}{2}M_Y r_o R^{-4}\sin(\phi_o+2\phi) + \frac{3r_o}{2}R^{-4}(M_Z\cos\phi_o + M_Y\sin\phi_o)$$

$$P_N \doteq r^{-3}(M_Z\sin\phi + M_Y\cos\phi) + 3M_Z r_o R^{-4}\sin(\phi_o+2\phi) \tag{20}$$

$$+ 3M_Y r_o R^{-4}\cos\phi_o.$$

The first two terms in the expressions for P_E and P_N are recognized as the terms which would apply if the moments had no off-set from the rotation axis. The remaining terms, then are due to the off-set, and consist entirely of second harmonic terms in ϕ, and dc off-sets. Since these involve R^{-4}, they correspond to quadrupole moments. The induced moments, although they cause second harmonic variations, do not drop off as R^{-4}, and may not be described as quadrupoles.

There are two further specialized cases of interest: (i) $M = M_Z$, $M_Y = 0$, $\phi_o = 0$ and (ii) $M = M_Y$, $M_Z = 0$, $\phi_o = 0$. The first gives

$$P_E \doteq 2M R^{-3}\cos\phi + \frac{9}{2}M r_o R^{-4}\cos 2\phi + \frac{3Mr_o}{2}R^{-4} \tag{21}$$

$$P_N \doteq M R^{-3}\sin\phi + 3M r_o R^{-4}\sin 2\phi \quad . \tag{22}$$

It is seen that the second harmonic component traces out an ellipse with its major axis along $\overline{OP}$, with a 3:2 ratio of major to minor axes. The ratio of this major axis to that of the ellipse due to the centered dipole moment is $9r_o/4R$:1, so that if r_o/R were 1/10, the ratio would be 9/40, or 22-1/2%. The second specialized case gives

$$P_E \doteq -2M R^{-3}\sin\phi - \frac{3}{2}M r_o R^{-4}\sin 2\phi \tag{23}$$

$$P_N \doteq M R^{-3}\cos\phi + 3M r_o R^{-4}. \tag{24}$$

To the order of approximation made, only P_E has a second harmonic component and P_N has only a dc off-set while the P_E has no dc off-set.

Since the induced dipole field is greater with the sensor located North (or South) of the spacecraft as compared to a location East (or West), a set of sensors located in each of these directions would provide a means for sorting out the offset permanent dipole from the induced fields. The latter, of course, should give results independent of sensor direction.

Another method for sorting out the two components is to use the r^{-4} vs r^{-3} radial variation of the second harmonic terms. The induced dipole field drops off as r^{-3} while the offset permanent dipole field drops off as r^{-4}.

VI. A Method for Discrimination of Harmonics

In the preceeding sections, we have discussed methods of detecting and discriminating between permanent dipoles with offsets and induced dipole moments using the fundamental and second harmonic terms in the sensor outputs separately. It was assumed that a Fourier analysis would be performed to separate the two frequencies from the total sensor outputs. An instrumental method for accomplishing the same effect would be to tape record the outputs, playing back the record in a tape loop, and electronically filtering out the desired frequency component.

A much simpler method, which may be described as a spatial filter, which does not require a highly uniform turntable speed or tape recorder and filtering is as follows. Instead of a single triaxial sensor, two sensors are located diametrically opposite to the turntable axis. In the Förster Hoover sensors, which we use, each sensor consists of two halves, each of which could be used on opposite sides of the turntable. The two halves are supported series-aiding in the normal fashion to detect second harmonic variations, and series-bucking to detect fundamental variations. In each of these modes, the wanted signal is additive, and the undesired signal is suppressed. The polarity of the sensor output may be changed electrically rather than by a physical reversal of one of the sensors.

VII. Results

The four OGO magnetic tests showed that at the 24 foot probe distance, the spacecraft field is in the order of 0.5 gamma under demagnetized conditions. Magnetizing the spacecraft with an exposure to a 25 gauss field increases the field to about 5 gamma, but degaussing reduces this back to the initial value. An 1 cps oscillating field with an exponentially decaying envelope starting at 50 gauss is used for demagnetizing. The second harmonic components was found to be less than about 20% of the permanent dipole field, and no analysis was performed for determining induction coefficients or offset dipole contributions. Some of the X-Y plots as well as the Sanborn chart records are given in Figures 4, 5, 6, and 7.

The ERS magnetic test showed a field of about 5 gamma at the sensor location.

On the test of the first OGO the spacecraft was left in its demagnetized condition for about a month in the ambient geomagnetic field while other spacecraft tests were being performed. Another test after this period was performed and the spacecraft was found to have increased by a negligible amount of about a tenth of a gamma, which is barely within the measurement resolution.

VIII. Acknowledgements

The OGO tests, performed under NASA Contract NAS5-3900, involved a large number of TRW Space Sciences Laboratory personnel as well as the OGO mechanical handling crew. Also present as advisors as well as observers were NASA Goddard personnel such as C. L. Parsons and C. Harris. The OV5-5 tests were supported under company sponsored research.

IX. References

(1) The following are the TRW OGO magnetic test reports:

OGO-A:	2311-6099-RU000
OGO-C:	2311-6117-RU000
OGO-D:	2791-6003-RU000
OGO-E	02648-6028-R000

The authors are G. M. Crook, I. M. Green, E. W. Greenstadt, G. T. Inouye, A. Rosen, and J. L. Vogl.

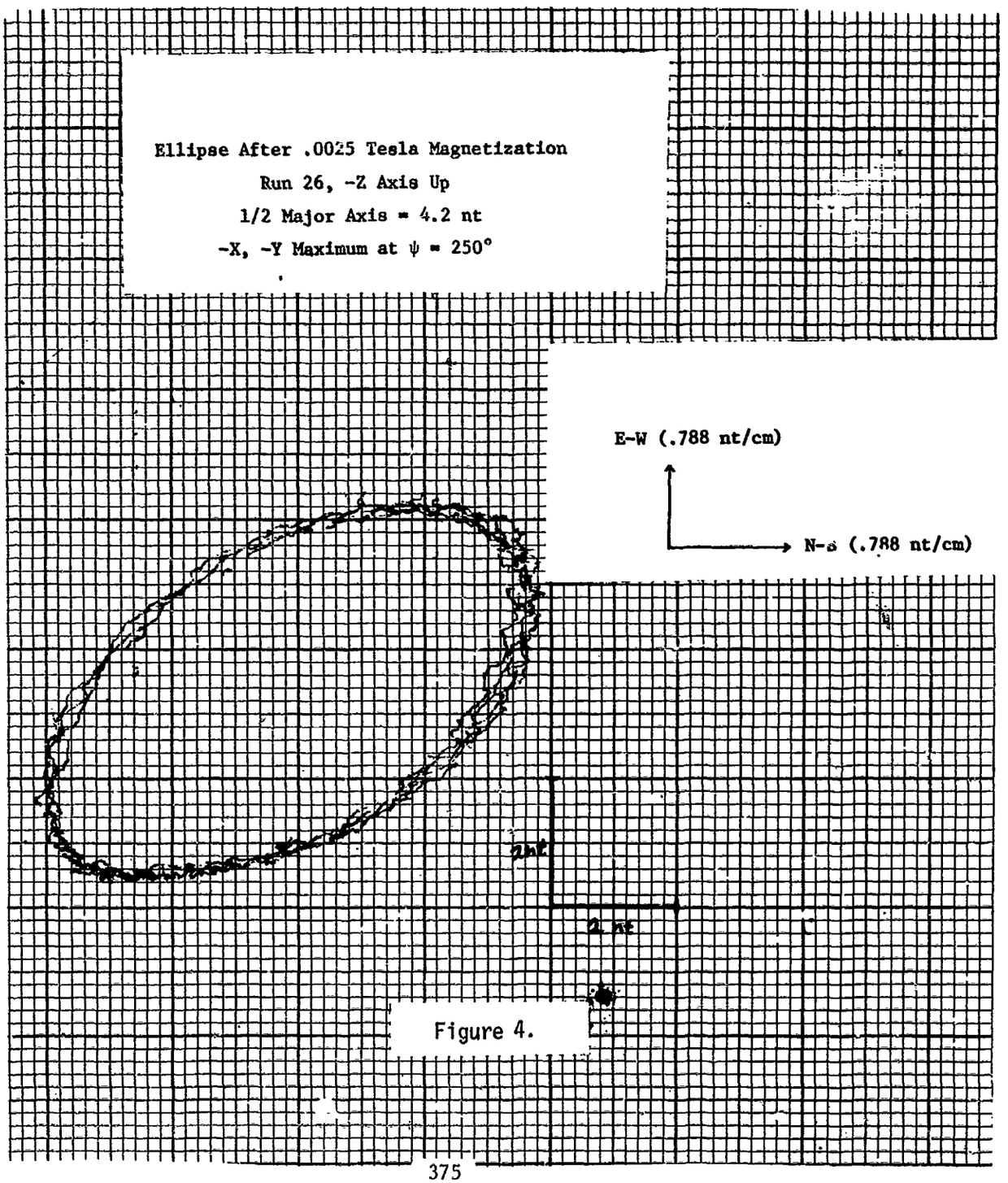

Ellipse After .0025 Tesla Magnetization
Run 26, -Z Axis Up
1/2 Major Axis = 4.2 nt
-X, -Y Maximum at ψ = 250°
E-W (.788 nt/cm)
N-S (.788 nt/cm)
2nt
2 nt

Figure 4.

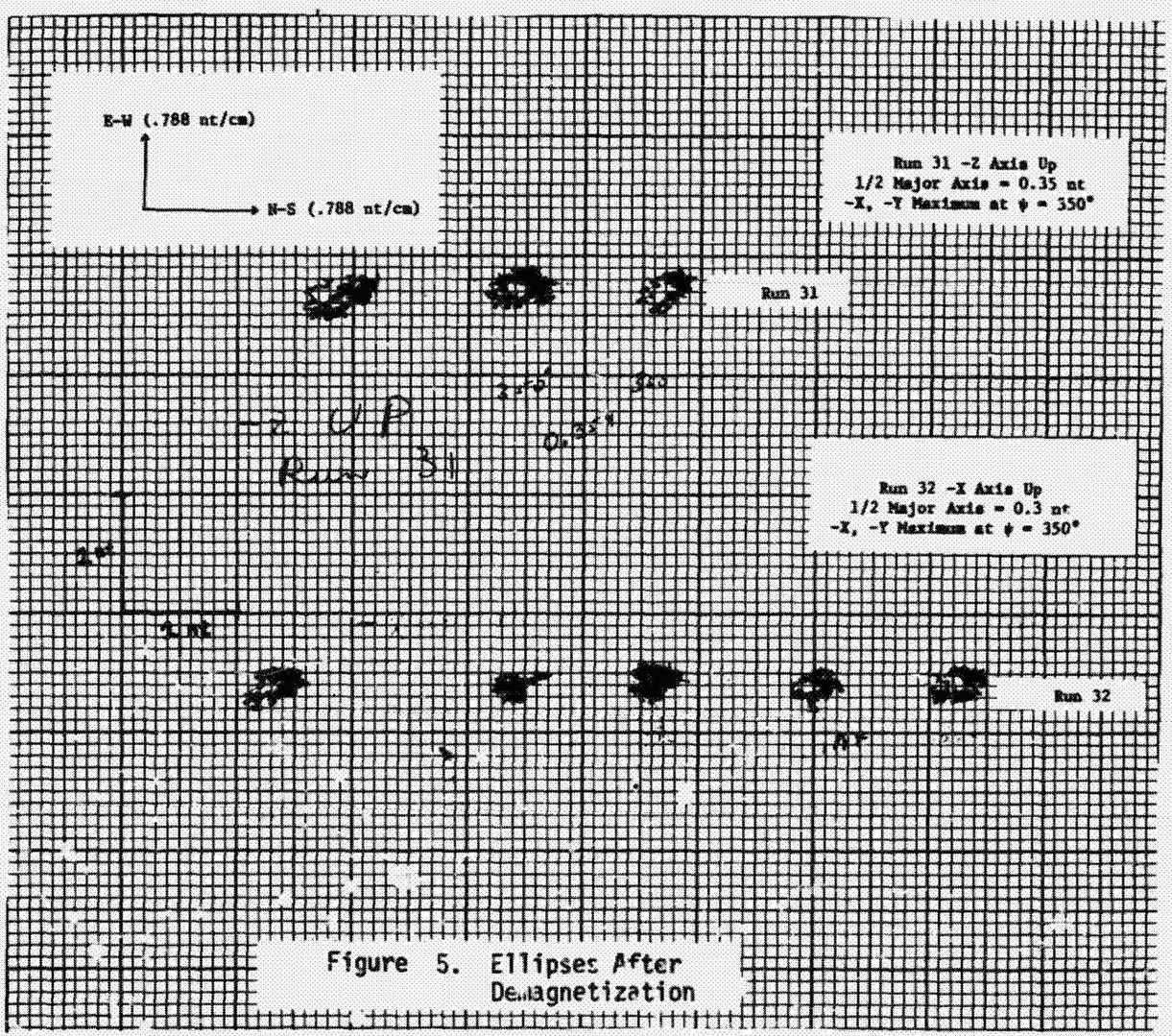


Figure 5. Ellipses After Demagnetization

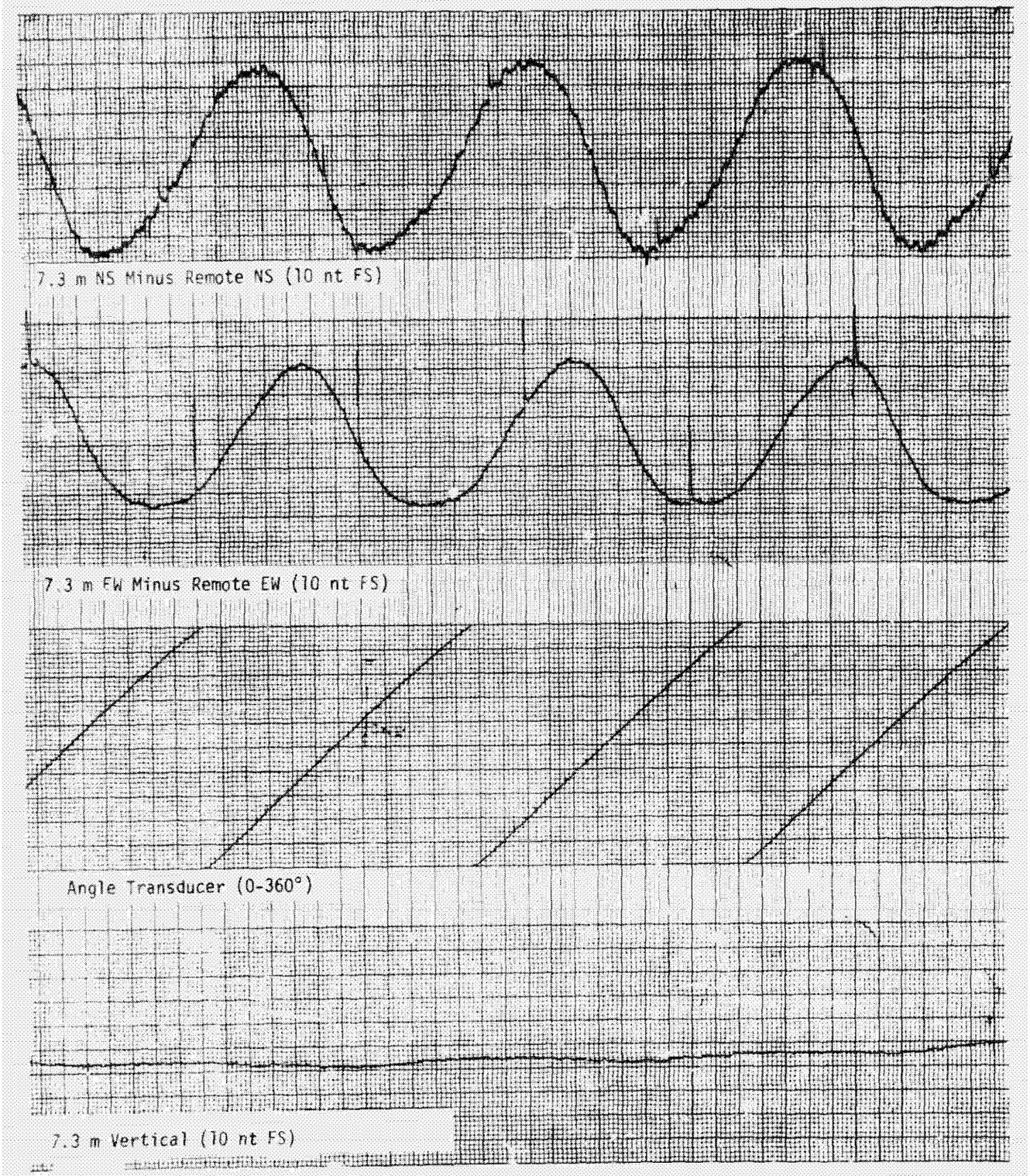


Figure 6. Run 26 (After Magnetization, 1 mm/sec, -Z up

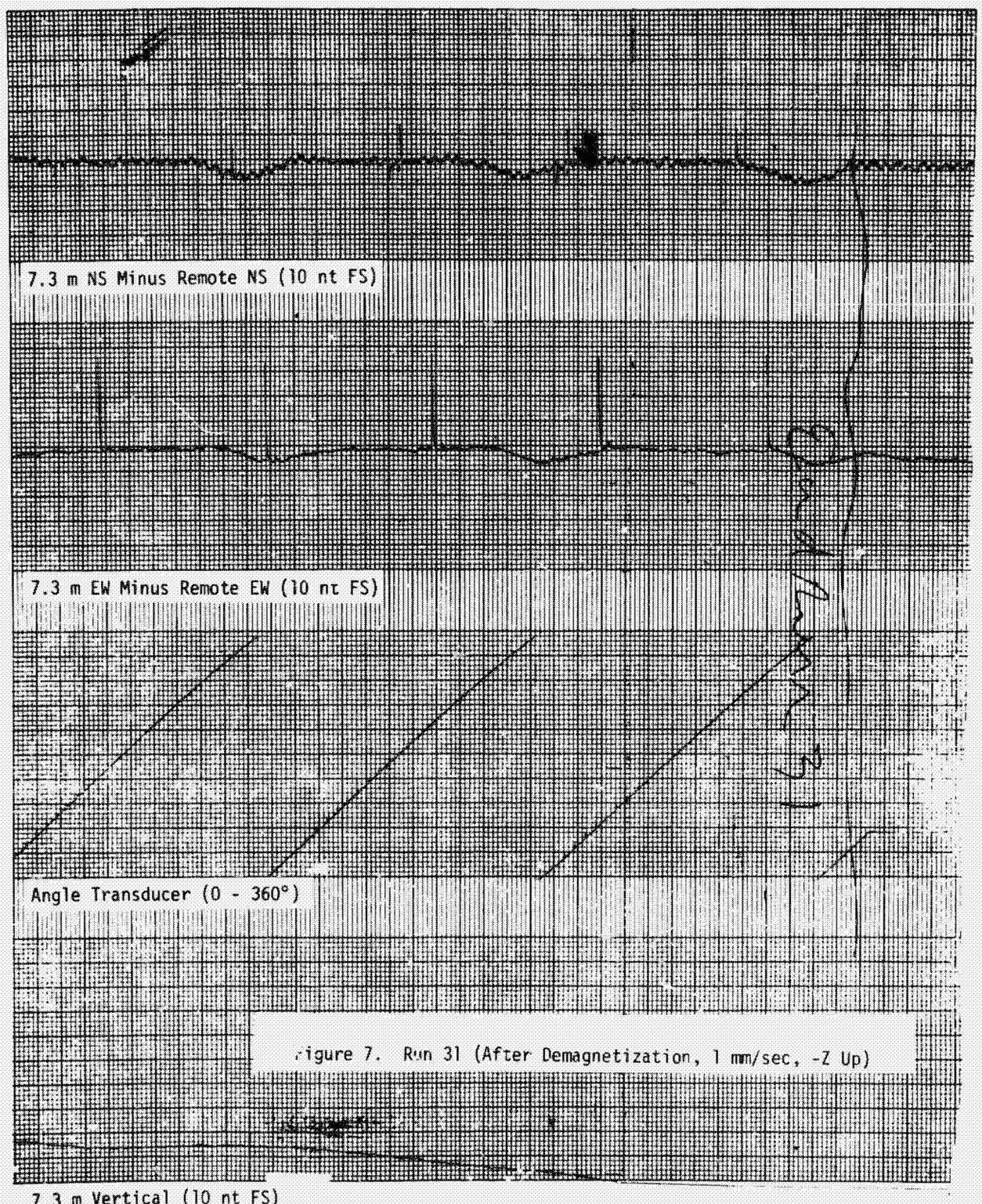


Figure 7. Run 31 (After Demagnetization, 1 mm/sec, -Z Up)

Application of Resonance Technique for Measuring Satellite Magnetic Dipole Moment

by

Barry E. Tossman

N69-33978

Reference: B. E. Tossman, "Application of Resonance Technique for Measuring Satellite Magnetic Dipole Moments," Space Magnetic Exploration and Technology Symposium, (August 1967) University of Nevada, Reno.

Magnetic torques, due to either current loops or residual permanent magnetic moment, constitute a principle source of attitude perturbation on earth satellites. In an effort to control these torques it is necessary to measure and compensate the satellite magnetic dipole moment. This paper presents the theory and application of a resonance technique which is especially designed to measure small dipole moments. In using this technique, the satellite is suspended by torsion wires in a controlled magnetic field. By changing the magnetic field sense in synchronism with the natural torsion suspension frequency the satellite is driven into resonance. The rate of change of amplitude is a direct measure of dipole moment.

This resonance technique has been successfully employed by the Applied Physics Laboratory in measuring and compensating dipole moments on 12 satellites. Testing methods have been improved to the extent that dipole moments as small as 50 pole-cm have been detected on satellites weighing up to 500 pounds. This paper discusses the application of resonance testing to several of the larger spacecraft and compares the results of dipole moment trim measurements to their in-flight attitude performance.

Key Words

Spacecraft
Magnetic Testing
Dipole Moment
Resonance Technique

---

1. The Johns Hopkins University Applied Physics Laboratory, Silver Spring, Maryland

INTRODUCTION

Magnetic torques form a major disturbance to attitude stabilization of near earth satellites. These torques are due to dipole moments created within the spacecraft by current loops, residual magnetism or permeable materials. In establishing a minimum dipole moment state it is necessary to accurately determine small magnetic moments of typically large spacecraft. Techniques which have been employed to determine magnetic characteristics include field and static torque measurement. Field measurement techniques are often confused by the presence of higher order poles while static torque tests are subject to vibration and atmospheric disturbances.

This paper describes the application of a technique (1), presented in 1965 which is particularly suited to measuring small dipole moments of large spacecraft. The spacecraft is suspended by torsion wires and an applied magnetic field is reversed synchronously with the free torsion resonance. Dipole moments within the satellite cause it to be pulsed into resonance-zero dipole moments effect no response. The magnitude of the dipole moment present is directly proportional to the rate of change of deflection amplitude.

This technique has been applied by the Applied Physics Laboratory to 12 spacecraft since March 1965. This paper summarizes the theory of this technique and describes its application to several of these spacecraft. It also compares the results of dipole moment trim measurements to in-flight attitude performance.

THEORY

It is assumed that the spacecraft contains a permanent magnetic dipole moment which resolves into three orthogonal components M_x, M_y, M_z aligned with the spacecraft axes. The spacecraft is suspended by torsion wires according to Fig. 1 such that it is constrained to rotate about a vertical axis. The suspension torsional stiffness k is adjusted to provide a natural period of oscillation τ of about 30 seconds. The motion of the satellite in this suspension is completely undamped and all aerodynamic effects are minimized by appropriate shrouding.

In order to drive the spacecraft into resonance, a magnetic field is applied in the horizontal plane and reversed periodically at a frequency matching that of the free torsion resonance of the spacecraft. Although almost any periodic function of applied field can be ultilized, the present analysis is based on a square wave generated field as shown in

Fig. 2. This field H(t) has a zero to peak amplitude h and frequency $\omega_n = 2\pi/\tau$ and is generated in such a way that its Fourier series representation consists solely of cosine functions, viz

$$H(t) = \frac{4h}{\pi} \sum_{k=1}^{m} (-1)^{k-1} \frac{\cos (2k-1)}{2k-1} \omega_n t$$

The torque equation for rotation about the torsion wire axis is of the form

$$I \ddot{\theta} + c \dot{\theta} + K\theta = - H(t) \left(M_x \sin \theta + M_y \cos \theta \right) \qquad (1)$$

It is assumed that the rotations are of small amplitude such that the dipole moment component parallel to the applied field produces little torque, while the component normal to H (t) produces a greater torque which reverses its sense as the field is reversed. Assuming no damping, small angular deflections, and $M_x H(t) \ll K$ and substituting for H(t) as given by Eq. (1), the deflection response is given by

$$\theta(t) = \frac{4hM}{\pi I \omega_n^2} \left[\frac{\omega_n t}{2} \sin \omega_n t + \frac{1}{24} (\cos 3\omega_n t - \cos \omega_n t) - \frac{1}{120} (\cos 5\omega_n t - \cos \omega_n t) + \frac{1}{366} (\cos 7\omega_n t - \cos \omega_n t) \ldots \right] + \theta_o \cos \omega_n t + \frac{\theta_1}{\omega_n} \sin \omega_n t \qquad (2)$$

Parameter θ_0 and θ_1 describe initial conditions for displacement and angular velocity respectively.

Spacecraft rotation $\theta(t)$ is tracked by means of an optical lever and screen or automatic autocollimator. The position is recorded at the instant of field reversal i.e. for $\omega_n t = (N-\frac{1}{2})\pi$ where N is a positive integer. These positions, defined as $\theta(N)$ although not deflection peaks define a linear amplitude growth

$$\theta(N) = \frac{2hM}{\omega_n^2 I} (N - \tfrac{1}{2} + \rho) \qquad (3)$$

where $\rho = \theta_1 \omega_n I/2hM$

Dipole moment magnitude is determined from Eq. (3) by

$$M = \frac{I\omega_n^2}{2h} \frac{d\,|\theta(N)|}{dN} \qquad (4)$$

and its polarity determined by the rotation sense during each half cycle.

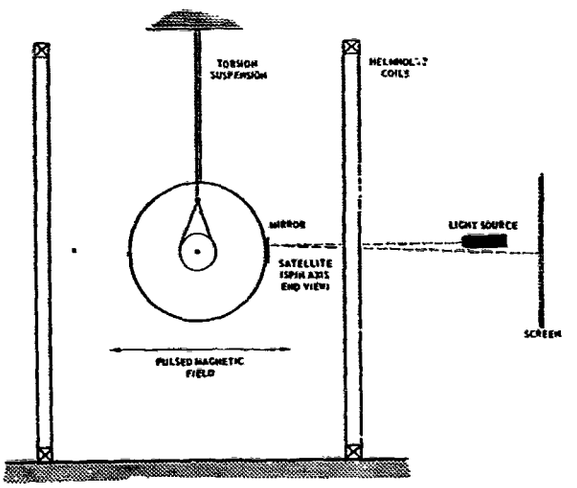


FIG. 1 MEASUREMENT OF SMALL MAGNETIC DIPOLE BY RESONANT PULSING

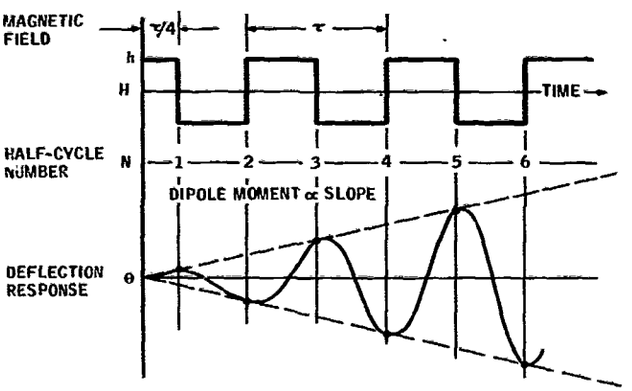


FIG. 2 MAGNETIC FIELD AND DEFLECTION RESPONSE

EXPERIMENTAL TECHNIQUES

This section presents some of the experimental procedures which have enabled pulsed resonance testing to be successfully applied to 500 pound spacecraft. In applying resonance testing to 12 satellites a technique has evolved. The following paragraphs relate the experimental conditions as pertain to spacecraft suspension, shrouding, synchronization of the field frequency, angular determination and establishing near zero initial conditions for rotational position and rate.

Spacecraft Suspension

Typically larger spacecraft are supported by a pair of long cables and strongback forming a bifilar suspension as shown in Fig. 3. The complete suspension is non-magnetic; the cable length and separation are adjusted to the spacecraft weight and inertia to provide a nominal 30 sec. period of oscillation. The spacecraft symmetry axis is typically suspended horizontally. In this way two components of dipole moment in the horizontal plane are measured, the spacecraft is rotated 90^{o} about its symmetry axis, and the third orthogonal component of dipole moment can be determined.

For payloads with moments of inertia of 3 slug-ft^2 or greater it is necessary to employ the bifilar suspension. For strength and ease of handling non-magnetic stranded cables are used. It was found that if left-lay cable was used for both lengths the bifilar spring constant became non-linear due to unwinding. The spring rate would vary depending on the sense of rotation. It was found that by using a right and left lay cable pair this nonlinear spring characteristic was resolved.

Aerodynamic Torques

Typically in the large open space of a magnetics facility drafts from windows, doors, and people moving can create significant disturbances unless painstakingly controlled. For the more sensitive tests, I have found it necessary to close all windows and doors, turn off all air-conditioning systems and shield the spacecraft with a dropcloth enclosure about 12 ft. square and 9 to 15 ft. high. Using these precautions angular disturbances can be controlled to within 10 arc sec or about 100 dyne-cm torque. Since dipole moment determination resolves from a sinusoidal response, it has not been found necessary to protect for radiator convection currents or seal windows and doors. The lower bound on dipole moment determination established by residual aerodynamic effects is currently on the order of 20 pole-cm.

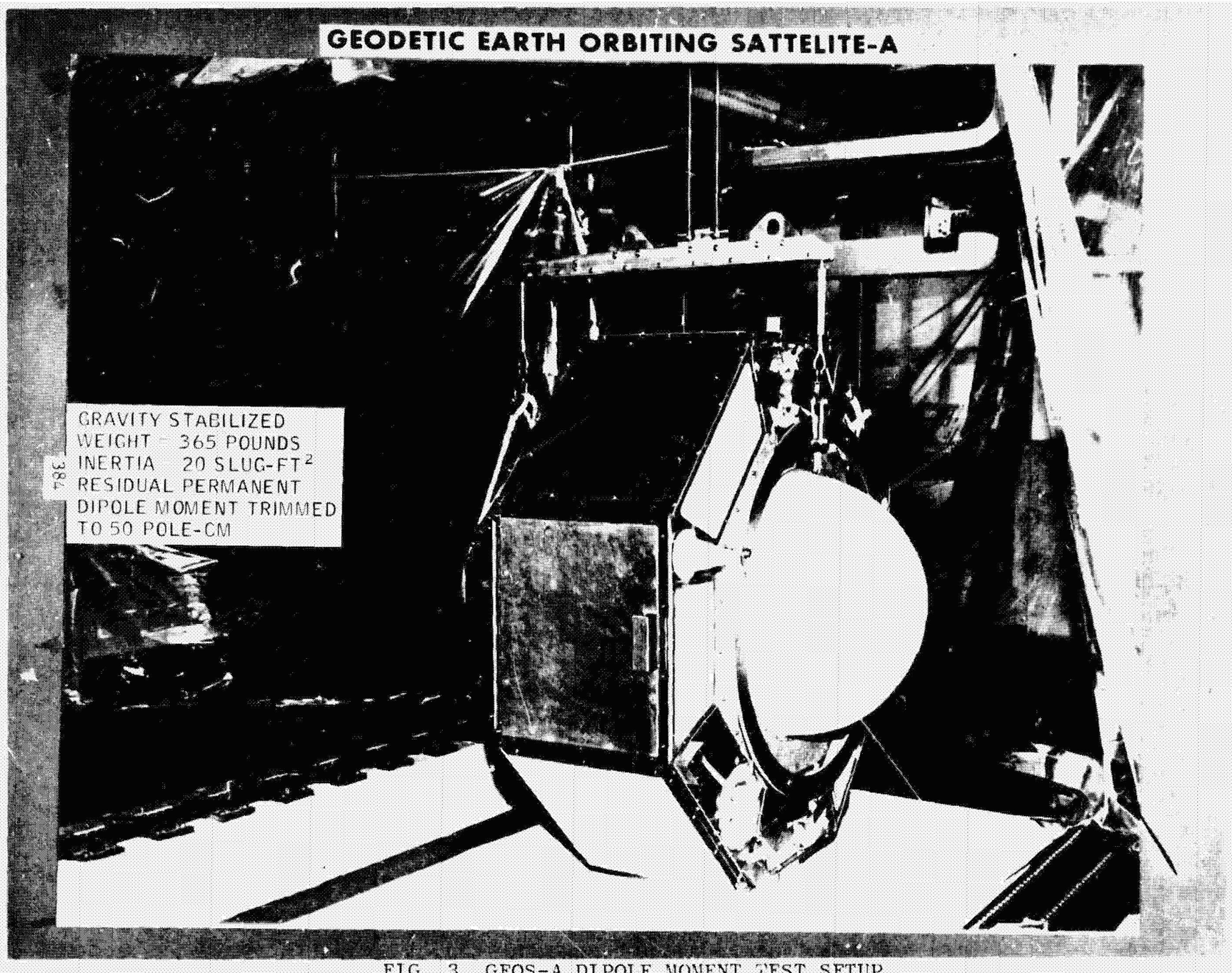


FIG. 3 GEOS-A DIPOLE MOMENT TEST SETUP

Field Synchronization

It is essential that the frequency of the applied magnetic field precisely match the free suspension resonance. By driving with a frequency off, say 10%, the response is 180° out of phase in 5 cycles. I find it necessary to match frequencies better than 1% and do it in the following manner: First the natural period of oscillation of the spacecraft is precisely determined by using a stop-watch or electronic timer and observing many periods of oscillation. The amplitude of oscillation during these timed cycles is no greater than that expected during resonance testing. In this way higher amplitude non-linearities are discounted. The degree of system damping is observed during this time as the decay is oscillation amplitude. In general the amplitude decay rate is less than 0.2% per cycle.

A clock is synchronized to the period of free oscillation. The clock, driven by a hysteresis synchronous motor is energized by a signal generator whose frequency is adjusted such that one clock revolution equals two natural periods of oscillation. The magnetic field is reversed by manual switching every quarter clock rotation. Thus, over long time periods field reversing will maintain synchronism with the satellite frequency.

An excellent verification of resonant pulsing is obtained if the deflection response and magnetic field can be continuously recorded. Frequency mismatch is noted by an increasing phase shift between amplitude peaks and field reversals.

Damper and Initial Condition Control

It was found that in order to obtain the best response for dipole moment determination, initial conditions of zero angle and rate were desirable. Since the suspension provided no damping of oscillations some mechanism was needed to establish rest conditions at the start of each run. To this end an eddy-current damper was developed.

This device, shown in Fig. 4, consists of a thin beam attached to the strongback with an aluminum vane at the end. The vane was positioned between two wheels. Each wheel had 6 permanent magnets—poles directed out. Each wheel could be independently driven clockwise by microswitch hand control. By driving the lower wheel an eddy-current reaction force on the vane would rotate the satellite clockwise (looking down); or, by driving the upper wheel, counter-clockwise. By detecting the sense of spacecraft rotation and producing opposing eddy-current torques all motion could be stopped. When the magnet wheels are motionless eddy-current damping on the satellite is negligible.

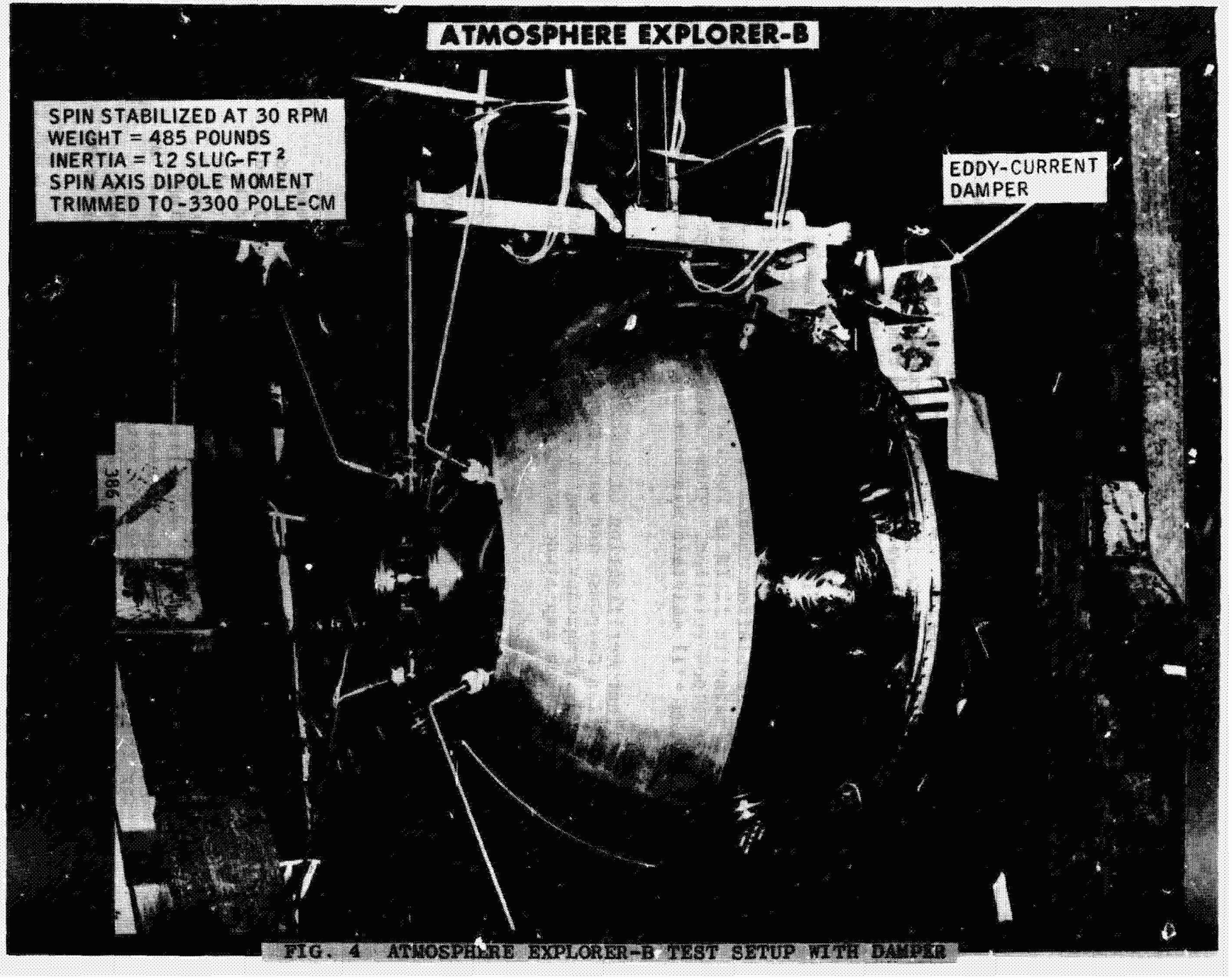


FIG. 4 ATMOSPHERE EXPLORER-B TEST SETUP WITH DAMPER

Measurement of Satellite Rotation

The deflection response is tracked by an optical lever or automatic autocollimator. If the payload moment of inertia is less than 3 slug-ft^2 an 8 meter optical lever can provide sufficient resolution of angular motion. As an example. let $I = 3$ slug-ft^2 $h = 0.400$ oe $\tau = 30$ sec and $M = 100$ pole-cm. Then from Eq. (4) $d\theta(N)/dN = 9.2$ arc sec/half cycle. The deflection of an 8 meter optical lever in this case would be 1 cm in 14 half cycles. For payloads with moments of inertia greater than 3 slug-ft^2 it becomes necessary to employ an automatic autocollimator. One excellent feature of the automatic autocollimator is that it allows for permanent recording of the deflection response. Figure 5 is a sample of such a response recorded simultaneously on 2 channel strip chart with the applied magnetic field.

Magnetics Facility

Dipole moment testing has been performed at the Naval Ordnance Laboratories magnetics testing facility — building No. 203. This facility is a 26 ft. square 4-coil system which is capable of nulling Earth's magnetic field and applying up to about 600 millioersted in any direction. The No. 203 facility provides a calibrated magnetic field uniform to .05% over a 4 feet dia spherical volume in the North-South and, vertical directions. The East-West control field volume is somewhat smaller.

When flashing fields for dipole moment testing, Earths field is cancelled by the primary field coil system and the variable field generated from a second set of coils. This second coil set is driven by a regulated power supply which is set to generate, say, 400 moe. A switch is used to reverse the current to this set of field coils. Variations in coil current during the pulsing sequence are on the order of 0.2%.

ERROR ANALYSIS

This section considers sources and magnitudes of error in the determination of dipole moment. These errors derive from assumptions made in the analysis of the torque equation, alignment and setup error as well as random errors due to disturbance torques.

Errors in Theory

Several assumptions were made in deriving the deflection response from the torque equation. Consider the magnitude of error introduced by these assumptions.

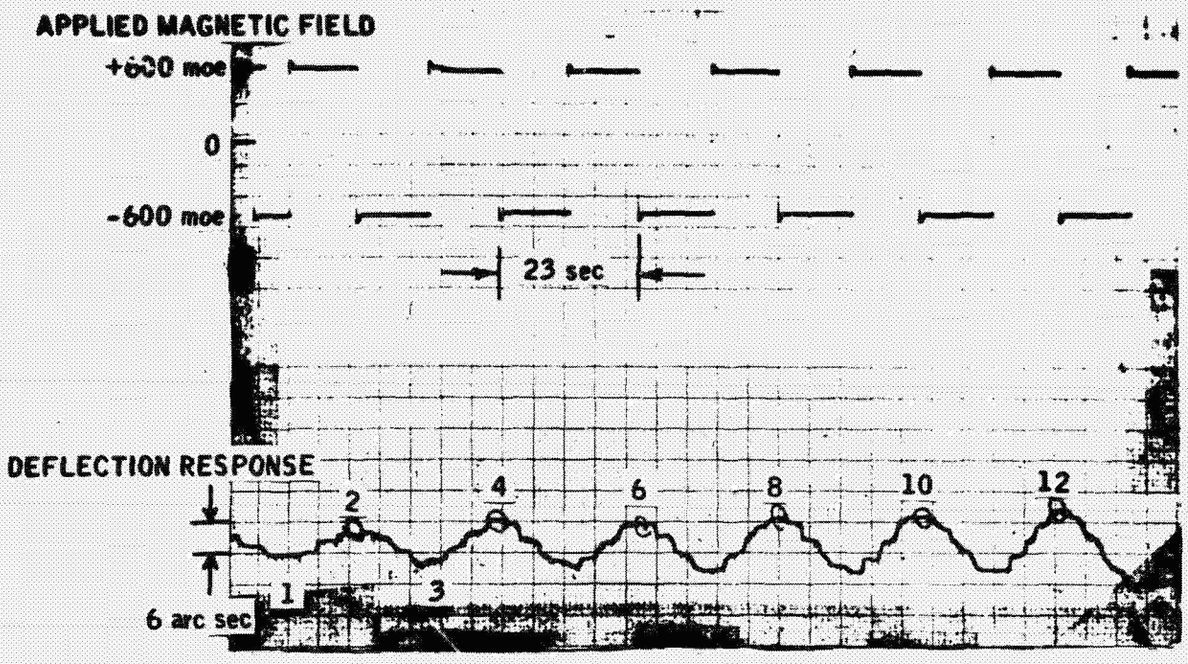


FIG. 5a **DEFLECTION RESPONSE OF DODGE TO 100 POLE-CM MAGNET**

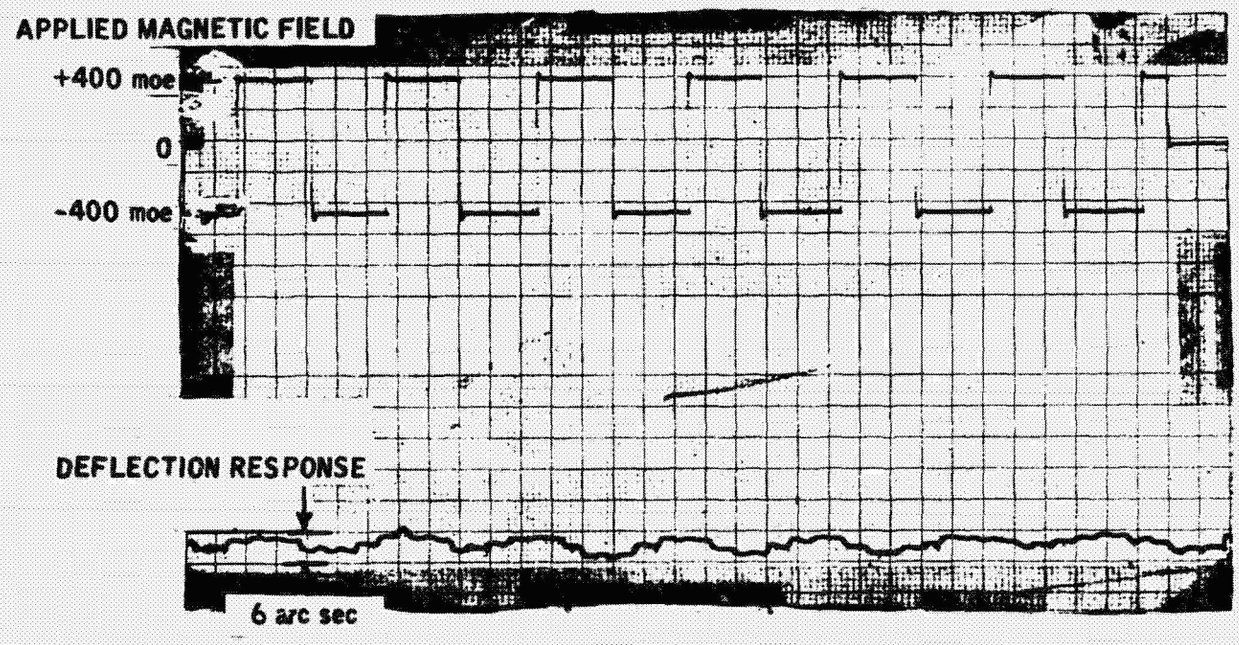


FIG. 5b **DODGE NULL DIPOLE MOMENT DEFLECTION RESPONSE**

1) It was assumed that ϑ remained small so that sin θ = ϑ and cos θ = 1.00. Peak deflections during resonance testing are on the order of 1 arc minute, thus the maximum error introduced by sin ϑ, cos θ assumptions are essentially zero.

2) It was assumed that magnetic restoring torques were negligible compared to the bifilar spring constant. For dipole moments as great as 1000 pole-cm and H = 0.4 oe, MH = 400 dyne-cm/rad as compared to typical K $\approx$ 2 x 10^6 dyne-cm/rad. This anomaly in spring rate effecting a change in resonant period is thus less than 0.2%.

Synchronization Errors

The square wave generated field must be synchronized to the free torsion suspension resonance. By accurately timing the suspension period and synchronizing a clock with a stable frequency source to this period, synchronization errors are reduced to within 0.5%. With this synchronization error it would take 100 cycles before the applied magnetic field would drive 180° out of phase to the mechanical system. Typically dipole moment determination is made within 5 cycles during which time near zero phase shift is encountered.

Consider the error in dipole moment determination due to improper synchronization. It can be shown that since θ(N) is recorded at the instant of field reversal the percent deviation from the true deflection response slope is one half the synchronization error, thus, $\approx$ 0.25%. The error in response slope due to random timing errors in field reversing is also quite small. Since the ϑ(N) positions are near deflection peaks, position rates of change are small. In addition, the response slope is an averaged determination; thus slope error due to small random timing errors is near zero.

Errors in Magnetic Field Strength

When flashing fields a power supply is preset to establish the required field strength and a reversing switch on the field coil used to change the field sense. Coil current is monitored with a DVM and standard resistor in an oil bath. Typical variations in coil current are on the order of 0.2%. When attempting to achieve a null dipole moment the error in field strength is not a factor since any resonance response indicates the presence of a dipole moment. Field strength error is a factor when using Eq. (4) to precisely determine the magnitude of a magnetic moment.

Alignment Errors

Spacecraft axes are aligned parallel to the field coil axes to within 0.5° by using spirit levels and sighting on coil references. If it is desired to trim all components of spacecraft dipole moment to zero, alignment error is not a factor. The error in precise determination of more finite dipole moments is proportional to the sine of the alignment error times the transverse axis dipole moment. For equal components of dipole moment this error could be on the order of 0.8%.

It is noted that most errors can be fairly well controlled. If a null dipole moment state is desired, the predominate error sources are that due to aerodynamic effects and sensitivity of the optical sensor. Presently, the smallest dipole moment which can be detected on a 500 pound spacecraft is about 50 pole-cm. In precisely determining the value of a more finite dipole moment the error might be on the order of 0.89% which is the RSS total of the listed errors.

SPACECRAFT APPLICATION AND ORBITAL RESULTS

Since its inception in 1965, pulsed resonance dipole moment testing has been applied to 12 spacecraft. Most spacecraft missions called for trimming residual moments to zero for which the technique is particularly suited; other missions required setting a component of dipole moment to some select value. This section describes several applications of pulsed resonance testing and compares the results of dipole moment determination to the spacecraft in flight attitude performance.

Direct Measurements Explorer-A

The DME-A spacecraft was built by APL for NASA Goddard for the purpose of sampling and measuring charged particles. It was launched in November 1965 into a near earth orbit ranging from 500 to 3000 km altitude. The spacecraft was intended to be spin stabilized with its spin axis aligned with the orbit normal. (2)

The spacecraft contains two chargeable magnets which when energized are used to precess the spin axis and maintain its alignment with the orbit normal. (The orbit regresses at the rate of 0.8°/day.) A magnetometer sensor positioned between the chargeable magnets is used to determine their magnetic state. When the chargeable magnets are nulled it is necessary that there be no precession torques, thus a prime spacecraft

requirement called for zero residual dipole moment. In order to establish and confirm this desired magnetic state throughout assembly, minor changes and vibration testing, the spacecraft was taken to NOL a total of 3 times. Figure 6 shows the DME-A spacecraft in its bifilar torsion wire suspension at NOL. The spacecraft weighed 215 pounds and had a moment of inertia of 6 slug-ft^2. The suspension natural period was 22 seconds which provided a dipole moment calibration response of

$$M = 1.36 \times 10^7 \frac{d\,\theta(N)}{dN} \text{ pole-cm}$$

and had a resolution of 20 pole-cm. The purpose of NOL testing was to trim the components of residual dipole moment normal to the spin axis to less than 50 pole-cm and to establish a calibration curve of spin axis dipole moment versus null sensor. These test objectives were met using pulsed resonance testing.

In spite of the NOL operations there remained some uncertainty as to the state of magnetic trim. The low gyrostability of DME-A made it quite sensitive to drift produced by spurious dipole moments. A test of the null dipole moment state occurred during the period January 6 through 11, 1966. The magnetometer and null sensor telemetry indicated that the spin axis dipole moment was within 10 to 20 pole-cm of zero. By tracking the spacecraft attitude during this period it was determined that any drift must have been less than one degree. This spin axis stability confirmed the null sensor calibration and indicated that there was no change in magnetic state of the spacecraft throughout shipping, vehicle installation and launch phases.

Geodetic Earth Orbiting Satellite—A

GEOS-A was built by the Applied Physics Laboratory under NASA sponsorship for the general purpose of geodetic study. It was launched on November 6, 1965 into a near earth orbit ranging from 600 to 1230 n mi at 59.4^o inclination. The satellite employed a 2 axis gravity-gradient stabilization system which was designed to have an earth pointing accuracy of 5^o or better in a circular orbit. This degree of alignment with local vertical depended on minimizing magnetic torques. Prelaunch analysis indicated that 5^o gravity stabilization could be achieved only if the spacecraft residual dipole moment along the pitch axis was less than 500 pole-cm. Somewhat greater dipole moment could be tolerated along the yaw axis (boom axis).

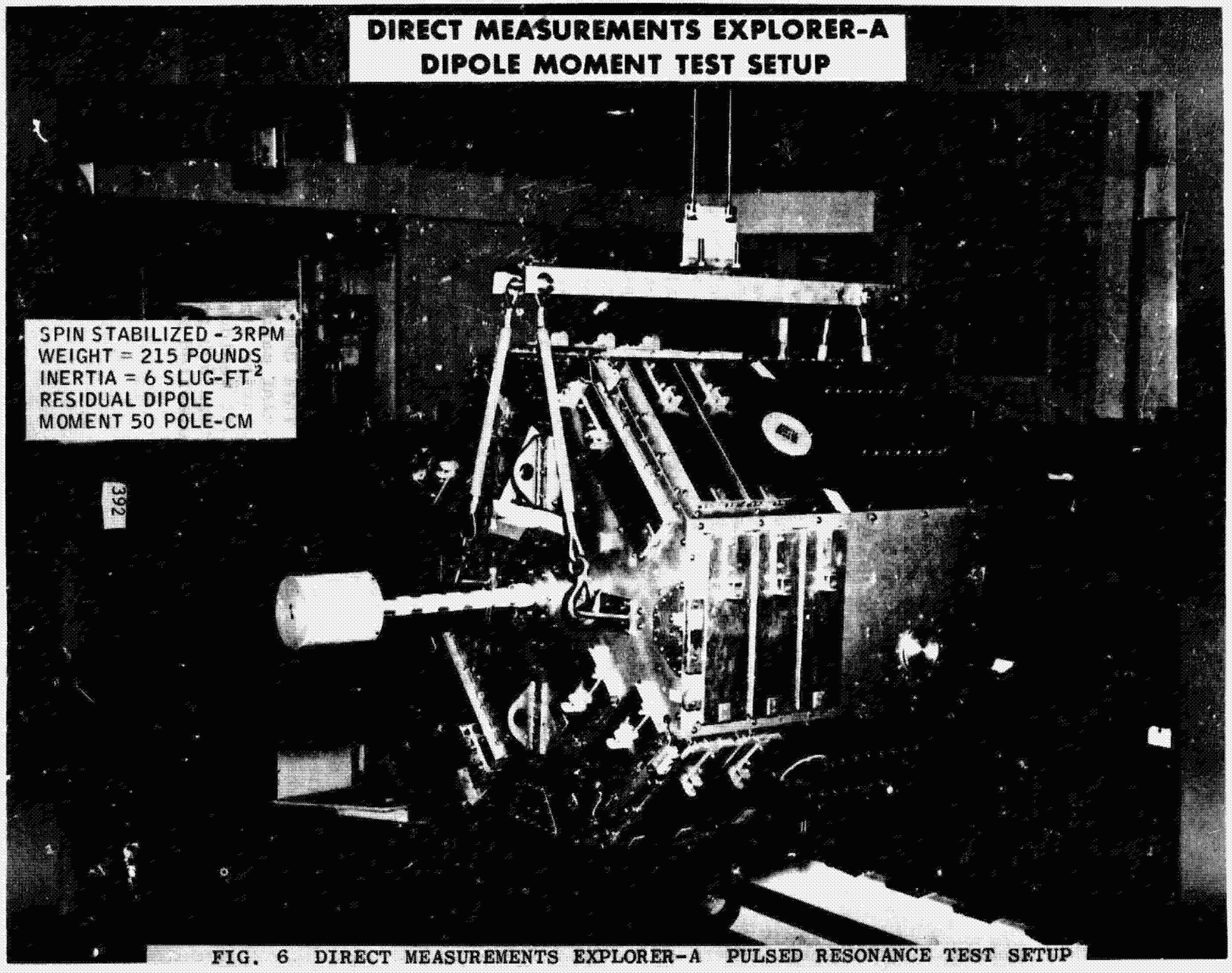


FIG. 6 DIRECT MEASUREMENTS EXPLORER-A PULSED RESONANCE TEST SETUP

The attitude stabilization configuration was a single dumbell formed by a DeHavilland A-18 extendible boom (60 ft maximum length) and a magnetically anchored eddy-current damper. This damper included as its active element a permanent magnet of 25,000 pole-cm dipole moment strength which would orient along the earth magnetic field. As the satellite librated, eddy-currents induced in a copper sphere which surrounded the magnet but was attached to the boom, would damp satellite motions. In its launch configuration the magnet was located near the spacecraft center and was free to orient in any direction. Since it was impossible to construct a perfectly non-magnetic spacecraft the major problem to be resolved by dipole moment testing was the degree and variation in magnetic perm state that this free magnet would give the spacecraft.

GEOS-A in its non-magnetic torsion suspension at NOL is shown in Fig. 3. The spacecraft weighed 365 pounds, had a maximum moment of inertia of 20 slug-ft^2 and had a bifilar period of 27 seconds. Its symmetry axis (boom axis) was suspended horizontally such that once the two components of dipole moment in the horizontal plane were determined, the third orthogonal component could be measured by rotating the spacecraft 90^o about this axis. The spacecraft was demagnetized prior to dipole moment testing. Components of residual dipole moment following deperm were M_x = +350, M_y = -471 and M_z = -183 pole-cm. These components were nulled to within 50 pole-cm of zero by adding permanent compensating magnets.

The eddy-current damper with its randomly oriented magnet was held in its launch position so as to magnetize material (especially battery cases) in its vacinity. The spacecraft components of dipole moment were determined again and this procedure repeated several times. The variation in magnetic state was M_x = ±130, M_y = ±180 and M_z = ±250 pole-cm. These variations in dipole moment strength were acceptable for the 5^o gravity stabilization intended.

Post launch analysis indicated that despite the higher orbital eccentricity steady state pitch errors in the gravity stabilized mode were less than 6^o and roll errors were within 3^o.

Atmosphere Explorer-B

The AE-B satellite was built by the Aeronomy and Meterology Division of Goddard Space Flight Center for the purpose studying the physics of the upper atmosphere. It was launched into a 64^o inclination orbit ranging from 250 km to 1200 km altitude in August 1966. The satellite is spin stabilized at

30 rpm with its spin axis normal to the orbit plane. Sampling instruments with ports on the equator of the spacecraft see both the forward and wake regions of the free-stream during each cycle and can thus compensate for forward velocity.

The attitude control system was designed and built by the Applied Physics Laboratory (3) and had the functions of controlling spin axis orientation and maintaining spin rate. Controlled spin axis precession was achieved by using a chargeable magnet system which consisted of a permanent plus a variable magnet. The magnetic state of the variable magnet was established by capacitor discharge through windings on the magnet. When the variable magnet is charged to full strength in the same sense as the permanent magnet a net dipole moment of 1.8×10^5 pole-cm results which can produce a precession rate of 1/4 deg/min. In the cancel state, i.e. where the variable magnet is fully charged in the opposite sense, a dipole moment of -3300 pole-cm was established. It was determined that this strength of spin axis dipole moment would precess the spin axis at the same rate as the precession of the orbit normal. Once proper spin axis orientation is achieved, the variable magnet would be pulsed into this cancel state thereby reducing the subsequent number of precession maneuvers. Pulsed resonance testing was used to establish this "cancel" dipole moment state.

The AE-B was taken to NOL in December 1965 and February 1966; the test setup at NOL is shown in Fig. 4. The satellite weighed 485 pounds and had a spin axis moment of inertia of 12 slug-ft^2. Deflection response was determined through the use of an automatic autocollimator. Components of dipole moment normal to the spin axis were measured at M_x = -9,090 and M_y = +2,960 pole-cm. These components were not compensated since the spin rate and gyrostability of AE-B were high. The variable magnet was then charged into its full cancel state. By adding permanent magnets the net spin axis dipole was trimmed to -2980 ±50 pole-cm as compared to the desired value of -3300 pole-cm. One of the permanent magnets was later chipped during spacecraft assembly which brought the final spin axis moment even closer to the desired value.

AE-B was launched in August 1966. After several maneuvers the spin axis was aligned with the orbit normal and the spin rate set at 30 rpm. Close watch on the AE-B attitude revealed that in fact its spin axis was drifting at nominally the same rate as the orbit normal. (4) A minimum of precession maneuvers over the following months were required to maintain the desired alignment. This attitude performance supports the conclusion that the cancel state spin axis dipole moment was quite close to the NOL established value.

Department of Defense Gravity Experiment

The DODGE satellite is designed to investigate 3 axis gravity-gradient stabilization at near synchronous altitudes. It was launched on July 1, 1967 into a 7^{o} inclination circular orbit at 18,000 n mi altitude. The satellite includes 10 motorized booms which will be extended in various configurations; libration damping is effected by using either an enhanced magnetic damping scheme or a damped gimballed boom. (5) The spacecraft, shown in Fig. 7, is 8 ft long, weighs 500 pounds and has a maximum moment of inertia of 34 slug-ft^2.

DODGE was subject to magnetics systems testing including pulsed resonance dipole moment measurements at NOL in April 1967. Aerodynamic disturbances were slightly greater on DODGE due to its stack. Additional shrouding was sufficient to reduce angular disturbances to within several arc seconds. Dipole moment sensitivity on DODGE was on the order of 50 pole-cm.

Components of residual dipole moment in the spacecraft measured at the start of testing were M_x = +150, M_y = -150 and M_z = +200 pole-cm. These components were trimmed to less than 50 pole-cm by the addition of compensating magnets. Figure 5a is the deflection response record corresponding to 100 pole-cm in the -Z direction. The deflection response sensitivity to a 100 pole-cm dipole moment is 12 arc seconds peak-to-peak in 5 cycles when using a field of $\pm$600 moe. The deflection response record of a null dipole moment is shown in Fig. 5b. The continuous angular response record was obtained from a Kollmorgan automatic autocollimator. The applied magnetic field was simultaneously recorded on the two channel Sanborn.

Pulsed resonance testing was extensively employed on DODGE in order to determine the changes in satellite perm state due to the operation of magnetic systems in the spacecraft, as well as determining the strength of current loops when operating various electrical system. Changes in the magnetic perm state were under 50 pole-cm even after exercising the 8.64×10^4 pole-cm electromagnets. Peak variations due to current loops were within 300 pole-cm in battery mode but as high as 1200 pole-cm when operating off the solar array. Compensating current loops were added onto the solar bus to alleviate this problem.

Conclusions

To date, pulsed resonance testing has proven to be an excellent technique for determining small dipole moments of large spacecraft. Measuremert sensitivity has been on the order of 20 to 50 pole-cm for spacecraft weighing up to 500

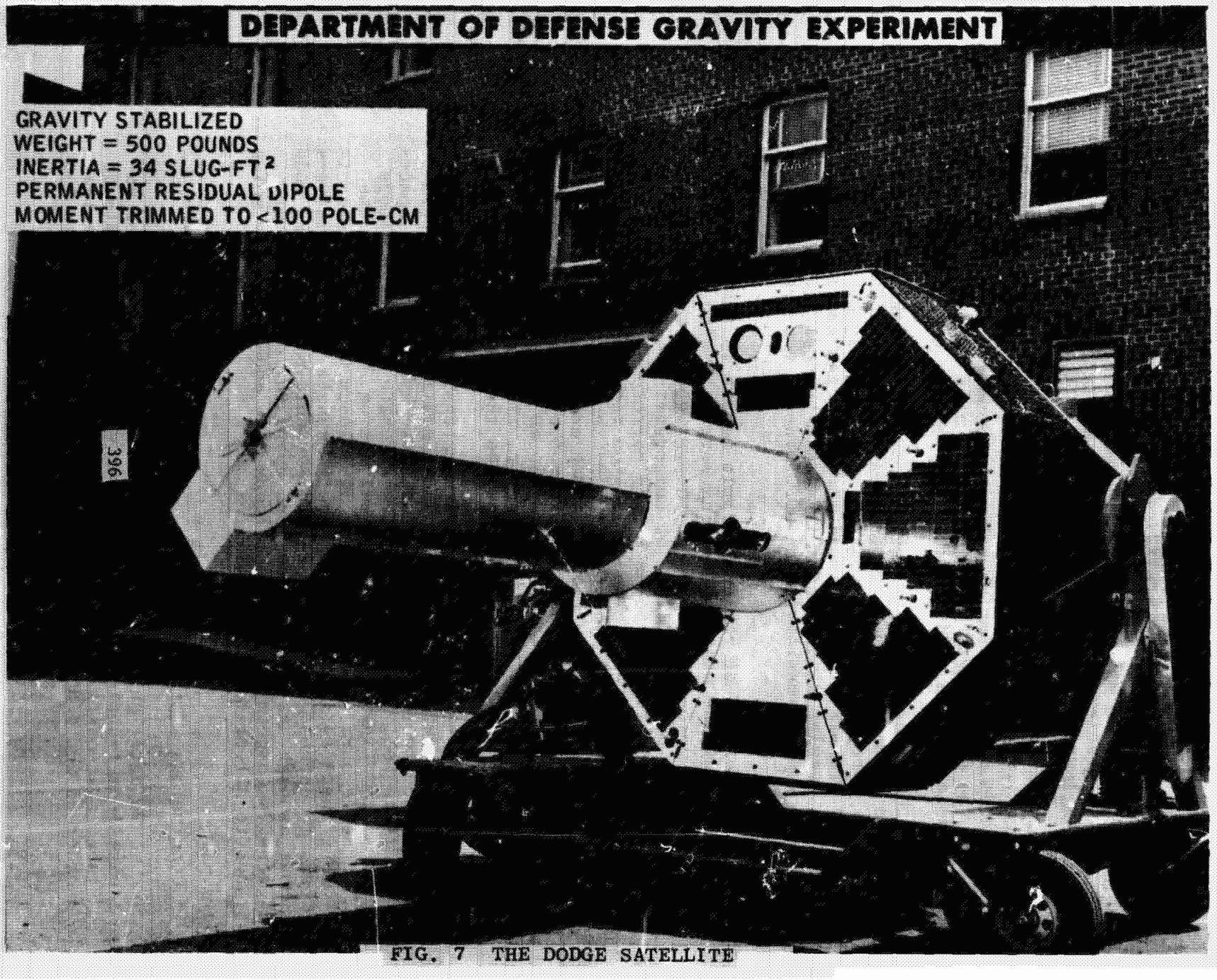


FIG. 7 THE DODGE SATELLITE

pounds. The technique is particularly suited for compensating spacecraft residual permanent dipole moments and confirming the null state. Variations in a null dipole state due to satellite current loops or changes in magnetization due to satellite operations are readily detected. Accurate dipole moment determination extends to moments as large as several thousand pole-cm as evidenced by the AE-B attitude performance. Determination of dipole moments in the 10^4 pole-cm range is probably more conveniently accomplished by field measurement techniques.

The accuracy and sensitivity of pulsed resonance testing has proven to be quite acceptable for achieving the null magnetic state required by many present near earth orbiting spacecraft. I see no serious limitations to this technique for the future.

References

1. Tossman, B. E.: "A Resonance Technique for Measurement of Satellite Magnetic Dipole Moment" Proceedings of Magnetic's Workship, JPL Technical Memo. No. 33-216, April 1965.

2. Mobley, F. F. et al: "Performance of the Spin Control System of the DME-A Satellite" Guidance and Control Conference, AIAA, August 1966.

3. Mobley, F. F.: "Attitude Control System for the Atmosphere Explorer-B Satellite" AIAA Paper No. 65-432, AIAA 2nd Annual Meeting, July 1965.

4. Werking, R.: "AE-B Definitive Attitude Report" Goddard Space Flight Center "X" Document, to be published.

5. Fischell, R. E.: "The DODGE Satellite" Proceedings AIAA/ JACC Guidance and Control Conference, Seattle, Washington, AIAA New York pp 256-267, August 1966.